

Mechanisms and Machine Science

Jose Manoel Balthazar *Editor*

# Nonlinear Vibrations Excited by Limited Power Sources




 Springer

# Mechanisms and Machine Science

Volume 116

## Series Editor

Marco Ceccarelli , Department of Industrial Engineering, University of Rome Tor Vergata, Roma, Italy

## Advisory Editors

Sunil K. Agrawal, Department of Mechanical Engineering, Columbia University, New York, USA

Burkhard Corves, RWTH Aachen University, Aachen, Germany

Victor Glazunov, Mechanical Engineering Research Institute, Moscow, Russia

Alfonso Hernández, University of the Basque Country, Bilbao, Spain

Tian Huang, Tianjin University, Tianjin, China

Juan Carlos Jauregui Correa, Universidad Autonoma de Queretaro, Queretaro, Mexico

Yukio Takeda, Tokyo Institute of Technology, Tokyo, Japan

This book series establishes a well-defined forum for monographs, edited Books, and proceedings on mechanical engineering with particular emphasis on MMS (Mechanism and Machine Science). The final goal is the publication of research that shows the development of mechanical engineering and particularly MMS in all technical aspects, even in very recent assessments. Published works share an approach by which technical details and formulation are discussed, and discuss modern formalisms with the aim to circulate research and technical achievements for use in professional, research, academic, and teaching activities.

This technical approach is an essential characteristic of the series. By discussing technical details and formulations in terms of modern formalisms, the possibility is created not only to show technical developments but also to explain achievements for technical teaching and research activity today and for the future.

The book series is intended to collect technical views on developments of the broad field of MMS in a unique frame that can be seen in its totality as an Encyclopaedia of MMS but with the additional purpose of archiving and teaching MMS achievements. Therefore, the book series will be of use not only for researchers and teachers in Mechanical Engineering but also for professionals and students for their formation and future work.

The series is promoted under the auspices of International Federation for the Promotion of Mechanism and Machine Science (IFTOMM).

Prospective authors and editors can contact Mr. Pierpaolo Riva (publishing editor, Springer) at: [pierpaolo.riva@springer.com](mailto:pierpaolo.riva@springer.com)

Indexed by SCOPUS and Google Scholar.

More information about this series at <https://link.springer.com/bookseries/8779>

Jose Manoel Balthazar  
Editor

# Nonlinear Vibrations Excited by Limited Power Sources

 Springer



*Editor*

Jose Manoel Balthazar  
UNESP-Universidade Estadual Paulista  
Bauru-SP, Brasil

UTFPR-Universidade Tecnológica Federal  
do Paraná  
Ponta Grossa, PR, Brasil

ISSN 2211-0984

ISSN 2211-0992 (electronic)

Mechanisms and Machine Science

ISBN 978-3-030-96602-7

ISBN 978-3-030-96603-4 (eBook)

<https://doi.org/10.1007/978-3-030-96603-4>

© The Editor(s) (if applicable) and The Author(s), under exclusive license to Springer Nature Switzerland AG 2022

This work is subject to copyright. All rights are solely and exclusively licensed by the Publisher, whether the whole or part of the material is concerned, specifically the rights of translation, reprinting, reuse of illustrations, recitation, broadcasting, reproduction on microfilms or in any other physical way, and transmission or information storage and retrieval, electronic adaptation, computer software, or by similar or dissimilar methodology now known or hereafter developed.

The use of general descriptive names, registered names, trademarks, service marks, etc. in this publication does not imply, even in the absence of a specific statement, that such names are exempt from the relevant protective laws and regulations and therefore free for general use.

The publisher, the authors and the editors are safe to assume that the advice and information in this book are believed to be true and accurate at the date of publication. Neither the publisher nor the authors or the editors give a warranty, expressed or implied, with respect to the material contained herein or for any errors or omissions that may have been made. The publisher remains neutral with regard to jurisdictional claims in published maps and institutional affiliations.

This Springer imprint is published by the registered company Springer Nature Switzerland AG  
The registered company address is: Gewerbestrasse 11, 6330 Cham, Switzerland

***Publisher's Note***

*The Editor also wishes to thank all the authors and the Springer Publishers remain neutral about jurisdictional claims in published chapters and institutional affiliations.*

# Preface

It is known that over the years, the construction of Models has played an important part in the discovery and dissemination of knowledge. The mathematical model of the vibrating linear systems has been studied exhaustively over the last years and significant contributions have been also made to the theory of vibrations of nonlinear dynamical systems. We also note that many oscillatory (vibrating) phenomena of real systems cannot be explained, nor solved, based on linear theory. That is why it is important to introduce nonlinear characteristics on the mathematical models of the considered vibrating systems (and to electro-mechanical systems). The main difficulty, in comparison to linear systems, is due to the absence of the superposition principle. This means that every nonlinear vibrating system must be solved individually, and a special methodology must be developed for each class of problems. Nowadays, fractional stiffness and damping are also appearing in different contexts for vibrating systems with memory and hysteresis. Such damping is defined by a fractional derivative in contrast to classical viscous damping term with the first-order derivative. As the memory of a dynamical system induced extra degree of freedom, for the phase space, the standard methods of dynamical response analysis and system identification, which relies on the knowledge of system dimensionality, cannot be used. Nevertheless, despite of great advances of the vibrating theory, vibrations still meet which cannot be explained by traditional vibrating theory. We will discuss, here, some vibrating problems belonged to this class called non-ideal vibrations (RNIS).

It is also well known that the conditions of stability (or dynamic instability) are commonly expressed in the theory of mechanical vibrations considering certain relations between the frequencies of external excitations and the natural frequencies of the vibrating system. They are called frequency relations and they are called resonance. It is noteworthy that the existence of resonant vibrations (resonance relations) and their characteristics (transient or steady state) depend on several factors related to the vibrating systems and external excitation characteristics. The steps to be used in solving a resonant vibrating problem are shown in the usual sequence:

- Establishment of the differential equations of motion.
- Obtaining differential equations of motion in time.

- Using of asymptotic representations of the solutions of the equations obtained, this procedure determines the resonance relations.
- Solution of differential equations of motion (analytical or numerical).
- Determination of the regions related to the stability and instability of the system.
- Possible use of control techniques.

Additionally, it will be mentioned that the features commonly found in vibrating engineering are

- Nonlinearities (geometric or physical characteristics).
- Energy dissipation (internal or external).
- Gyroscopic systems.
- Material imperfections.
- Stationary and non-stationary modes.
- Unlimited power sources (or ideal sources) or limited (non-ideal sources (RNIS)).
- Non-conservative dynamic (follower) or forced.

It is known that vibrations of nonlinear systems have been studied exhaustively over the last years grounded in H. Poincare, W. Ritz, V. G. Galerkin, A. Lyapunov, A. Stodola, etc. At the end of nineteenth and beginning of the twentieth century, around 1920, appeared the first works of the authors G. Duffing, Van der Pol, M. N. Krylov, N. N. Bogolyubov, S. A. Mitrosposky, J. J. Stoker, N. Minorok, C. Hayashi, H. Kauderer, etc. and other significant contributions have been also made to the theory of vibrations of nonlinear dynamical systems.

With the development of modern technology, machineries and equipment are becoming more complex every day. In this book, among all machineries, it will be restricted to a particular rotary one and the existence full interaction of between mechanical and electric parts (electro-mechanical systems) their support structures (RNIS systems).

It is known that electro-mechanical systems (taking into account a full interaction between the structure and the energy source) fall into three groups (Bishop 2000), (Premont 2006):

- The conventional electro-mechanical systems (MACRO): Small DC motors with limited power (RNIS) are usually used in laboratory test and therefore the investigation of mutual interaction of driven and driving sub-system is very important and some emergent and new nowadays areas:
- Micro-Electromechanical Systems (MEMS).
- Nano-Electromechanical Systems (NEMS).

Note that MEMS and NEMS technology is still in its infancy with global research and development actively under way.

In this point, it is important to clarify what rotary non-ideal systems (RNIS) means, in order to avoid future confusions.

Non-ideal systems (RNIS) have appeared in the literature with several meanings; as an example, some researchers use the concept of (RNIS) solutions for concentrated solutions, that is, the solutions can occur in two ways: when intermolecular

forces between solute and solvent molecules are less strong than between molecules of similar (of the same type) molecules, and when intermolecular forces between dissimilar molecules are greater than those between similar molecules.

Here, we deal with an energy transfer between the energy sources and the support structures and their possible control approaches, that is, we are interested to what happens to the motor (or electro-mechanical shaker), input, output, as the response to the rotary system support structure changes.

So, here, we discussed the physical phenomena involved, the adequate methodology to deal with (RNIS), and reported a selection of papers recently published, for emergent vibrating studies. New phenomena are addressed, concerning structures supporting unbalanced machines, capable of a limited output power, that is, Rotary Non-Ideal Systems (RNIS), and the motion of an oscillating structure under the action of such energy source was accompanied by a full interaction between these non-ideal motors and their supports.

We also analyzed possible and practical applications concerning unbalanced non-ideal DC motor-type foundation structure (RNIS) in the presence of the **Sommerfeld effect**, that is, getting stuck at resonance (energy imparted to the motor being used to excite large amplitude motions on the supporting structure), that is, jump phenomena and the increase in power supply that is required by an excitation source operating near resonance. The structural response provides a sort of energy sink. Sommerfeld suggested that the structural response provided a sort of energy sink. Thus, we pay to vibrate our structure rather than operate the machinery. One of the problems often faced by designers is how to drive a system through resonance and avoid the “energy sink” described by Sommerfeld.

This above-mentioned property of (RNIS) enabled the advance of research in engineering applications, as in the case of using, as an excitation of the system, an electro-mechanical vibrator instead of a direct current motor, in agreement as it does, classically. So, this property made it possible to increase the range of research emergent possibilities on this topic to Macro- and MEMS scales (Balthazar et al. 2018). The possibility of saturation phenomenon occurrence, *i.e.*, the transference of energy from higher frequency and lower amplitude to lower frequency and higher amplitude mode, uses 2:1 internal resonance by connecting it to a second-order controller using quadratic position coupling terms may be possible.

The study of non-ideal vibrating systems (RNIS), that is, when the excitation is influenced by the response of the system, has been considered a major challenge in theoretical and practical engineering research.

A classical book of (RNIS) was written by Prof. Kononenko (1969), entirely devoted to this subject. (Nayfeh and Mook 1979) gave a comprehensive and complete review of different approaches to the problem up to 1979 and in the books of (Evan-Iwanowski 1976), (Alifov and Frolov 1990), (Blekhman 2000), and (Cveticanin et al. 2018).

We also announced that some few papers concerning some (RNIS) problems undeserve of others. (Pontes and Balthazar 1975) dealt with friction-induced (RNIS) as a source of fatigue and (Lima et al. 2019) studied an application to robotic manipulator with a (RNIS) load. (Dantas and Balthazar 2013) by using the averaging method proved the existence of Neimark-Sacker bifurcation in a class of non-ideal (RNIS) mechanical systems. In fact, such problem drops in a more general research program on quenching for this mechanical system; (Dantas and Balthazar 2007) presented the

so-called Sommerfeld effect, as a bifurcation of periodic orbits, by using the regular perturbation theory and (Dantas and Balthazar 2003) the authors investigated the stability of the equilibrium point of the system and we obtain, in the critical case, sufficient conditions to obtain an appropriate normal form. From this, we get conditions for the appearance of Hopf bifurcation when the difference between the driving torque and the resisting torque is small. In (Felix et al. 2017), the method of Jacobi-Anger expansion in a 2DOF model of a flexible portal frame with harmonic force of varying frequency to an energy harvester is used. The frequencies of these modes are set in a two-to-one internal resonance condition. The good performance, of the harvester generator was reported, and the authors observed periodic, quasi-periodic, or chaotic oscillations, depending on the saturation phenomenon. In (Rocha et al. 2018), the authors deal with Sommerfeld effect, and saturation phenomenon using method of multiple scales was applied to find an analytical approximated solution of the equations of motion and numerical simulations of the equations of motion were carried out. In (Thomaz et al. 2017), the authors investigated the dynamical behavior of a (RNIS) Duffing oscillator, to identify new features on Duffing oscillator parameter space due to the limited power supply. An extensive numerical characterization in the bi-parameter space by using Lyapunov exponents is provided. Following this procedure, a remarkable new organized distribution of periodic windows is identified, the ones known as Arnold tongues and shrimp-shaped structures. In addition, intertwined basins of attraction for coexisting multiple attractors connected with tongues are identified. Using the approach published in (Shahlaei-Far and Balthazar 2018) an analysis of resonant behavior of the non-ideal was done based on Method of Direct Separation of Motions (MDSM). The decomposition of the equations of motion has been proposed to separate the infinitely growing coordinate, governing position of the rotor. In (Silveira et al. 2019), construction of basins of attraction was analyzed and the algorithm is tested on three systems, the classic nonlinear Duffing system, a non-ideal system exhibiting the Sommerfeld effect and an immunodynamic system. Continues The work of (Piccirillo 2021) concerned with controlling the basin erosion phenomenon of a vibrating system driven by a source with limited power supply (non-ideal excitation). In (Balthazar et al. 2018), the main properties of (RNIS) have been reviewed, such as the Sommerfeld effect, *i.e.*, jump phenomena and the increase in power supply that is required by an excitation source operating near resonance; the possibility of saturation phenomenon occurrence, *i.e.*, the transference of energy from higher frequency and lower amplitude to lower frequency and higher amplitude mode; and the existence of regular (periodic motion) and irregular (chaotic motion) behaviors, depending on the value of control parameters (voltage of a DC motor). In the paper of (Varanis et al. 2020), the authors deal with a (RNIS) system with memory by possessing a fractional damping term using three different mathematical tools, which are the 0–1 test, scale index, and wavelet technique. In (Avanco et al. 2020), the authors presented an analysis focused on the nonlinear dynamics of a solar panel opening during the trajectory of a satellite around the Earth, analyzing the dynamics between energy sources and structural response that must not be ignored in real engineering problems. In (Tusset et al. 2020), two control signals were considered in which one is the nonlinear feedforward controller to maintain the (RNIS)

system in periodic orbit and the other one is the feedback controller obtained by the SDRE, which takes the system trajectory to the desired periodic orbit. Numerical simulations demonstrated the effectiveness of the control strategy in conducting the system from any initial condition to the desired orbit and the control of chaos by time-delayed feedback control.

Finally, we mention that the subject of this book is to deal with a special class of vibrating system that combines electrical and mechanical drivelines in honor for Prof. D.T. Mook, Professor Emeritus of Biomedical Engineering and Mechanics at Virginia Tech, died June 19, 2020, that encouraged me to study this topic in 1994 and I'm still going to today.

The present book doesn't claim literature completeness since the available literature is dispersed over many distinct sources. It is restricted to the main references on the non-ideal vibrating dynamical systems (RNIS). In this new book, about non-ideal vibrations, we presented new and relevant results concerning (RNIS).

In summary, this book titled **Nonlinear Vibrations Excited by Limited Power Sources** contains 21 selected contribution chapters with participation of researchers of the 6 (six) countries : Ukraine, Poland, Cameroon, Spain, Italy, India, and Brazil and it is organized into two sections: Electromechanical systems and Nonlinear Dynamics of (RNIS) and Control of (RNIS) and Harvester Energy of (RNIS).

The Editor hopes that this publication will attract the attention of researchers and students in the field of engineering and science.

The authors of this book revisited in a systematic way many publications based on the assumptions that the external excitations are produced by non-ideal sources (RNIS). Several examples for emergent engineering applications of full interaction between mechanical and electrical (RNIS) systems that have been studied over the last year will be presented. Among these applications nonlinear phenomena such as the Sommerfeld effect, chaotic oscillations are observed, and control systems are designed. Piezoelectric material selection and the circuit design in nonlinear vibrational energy harvesting are also discussed considering the positioning of the piezoelectric layer and the effects of the nonlinearities on the behavior of the considered (RNIS) vibrating systems.



UNESP-Universidade Estadual Paulista, Bauru-SP, Brasil and  
 UTFPR-Universidade Tecnológica Federal do Paraná, Ponta Grossa, PR, Brasil  
 Email: [jose-manoel.balthazar@unesp.br](mailto:jose-manoel.balthazar@unesp.br), [jmbaltha@gmail.com](mailto:jmbaltha@gmail.com)

Bauru-SP/Ponta Grossa, Brasil

Jose Manoel Balthazar

## Support References

- Alifov, A.A., Frolov, K.V.: Interaction of Nonlinear Oscillatory Systems with Energy Sources. E. Rivin, English Edition Editor (1990)
- Balthazar, J.M., Tusset, A.M., Brasil, R.M.L.R.F. et al.: An overview on the appearance of the Sommerfeld effect and saturation phenomenon in non-ideal vibrating systems (NIS) in macro and MEMS scales. *Nonlinear Dyn* **93**, 19–40 (2018)
- Bishop, R.H. The mechatronic handbook. CR press, (2002)
- Blekhman, I.I.: Vibrational Mechanics: Nonlinear Dynamic Effects. General Approach, Applications, World Scientific, Singapore (2000)
- Cveticanin L., Miodrag Z., Jose M.B.: Dynamics of Mechanical Systems with Non-Ideal Excitation. Springer Nature (2018)
- Dantas, M.J.H., Balthazar, J.M.: On the appearance of a Hopf bifurcation in a non-ideal mechanical problem. *Mech. Res. Commun.* **30**(5), 493–503 (2003)
- Dantas, M.J.H., Balthazar, J.M.: On the appearance of Neimark -Sacker bifurcation in a non-ideal system. Z. Dimitrovová et.al. (eds.) 11th International Conference on Vibration Problems. Lisbon, Portugal, 9–12 September 2013
- Dantas, M.J.H., Balthazar, J.M.: On the existence and stability of periodic orbits in non-ideal problems: General results. *Z. angew. Math. Phys.* **58**, 940–958 (2007)
- De Souza, S.L.T., Batista, A.M., Baptista, M.S., Caldas, I.L., Balthazar, J.M.: Characterization in bi-parameter space of a non-ideal oscillator. *Physica A: Stat. Mech. Appl.* **466**, 224–231, (2017)
- Evan-Iwanowski, R.M.: Resonance Oscillators in Mechanical Systems. Elsevier (1976)
- Felix J.L.P., Bianchin R.P., Almeida A., Balthazar J.M., Rocha R.T.: Brasil R.M.L.R.F. On energy transfer between vibration modes under frequency-varying excitations for energy harvesting. *Appl. Mech. Mater.* **849**, Trans Tech Publications, Ltd., pp. 65–75. (2016)
- Lima J.L., Balthazar J.M., Rocha R. T., Janzen F.C., Bernardini D., Litak G., Bassinello D.G., Tusset A.M.: On Positioning and Vibration Control Application to Robotic Manipulators with a Nonideal Load Carrying. *Shock and Vibration*, Paper 5408519, (2019)
- Nayfeh A.H., Mook, D.T.: Nonlinear Oscillations. Wiley (1979)
- Piccirillo V., Do Prado T.G., Tusset A.M., Balthazar J.M.: Dynamic integrity analysis on a non-ideal oscillator. *Math. Eng. Sci. Aerosp.* **11**(3), 541–547 (2020)
- Pontes B., Balthazar J.M.: On Friction Induced Nonideal Vibrations: A Source of Fatigue. Inman et al. Eds. *Damage Prognosis: For Aerospace, Civil and Mechanical Systems*. Wiley (2005)
- Premont A.: *Mechatronics Dynamics of Electromechanical and Piezoelectric Systems*. Springer (2006)
- Rafael, A., Raibel, A., José, M.B., Ângelo, M.T., Maurício Aparecido Ribeiro, Frederic Conrad Janzen, Átila Madureira Bueno. A Brief Analysis of Artificial Satellites Solar Panels Deployment Considering a Nonlinear Dynamic Model. In: Altenbach H., Amabili M., Mikhlin Y.V. (eds) *Nonlinear Mechanics of Complex Structures*. Advanced Structured Materials, vol 157. Springer, Cham (2021)
- Rocha R.T., Balthazar J.M., Tusset A.M., Quinn D.D.: An analytical approximated solution and numerical simulations of a non-ideal system with saturation phenomenon. *Nonlinear Dyn* **94**, 429–442 (2018)



- Shahlaei-Far S., Balthazar J.M. (2018) Method of Direct Separation of Motions Applied to a Non-ideal Electromechanical Pendulum System. In: Awrejcewicz J. (eds) *Dynamical Systems in Applications. DSTA 2017. Springer Proceedings in Mathematics & Statistics*, vol. 249. Springer, Cham, (2017).
- Silveira, M., Gonçalves, JP, Balthazar JM.: Multi-core and many-core SPMD parallel algorithms for construction of basins of attraction. *J Theor Appl Mech.* **57**(4), 1067–1079 (2019)
- Tusset A.M., Balthazar J.M., Rocha R.T., Ribeiro M.A., Lenz W.B., Janzen F.C.: Time-Delayed Feedback Control Applied in a Nonideal System with Chaotic Behavior. In: Lacarbonara W., Balachandran B., Ma J., Tenreiro Machado J., Stepan G. (eds) *Nonlinear Dynamics and Control*. Springer, Cham (2020)
- Varanis M., Marcelo A. M. Tusset, Balthazar J M, Litak GDe Oliveira C., Rocha R.T., Nabarrete A., Piccirillo, V.: Dynamics and control of periodic and non-periodic behavior of Duffing vibrating system with fractional damping and excited by a non-ideal motor. *J. Franklin Inst.* **357**(4), 2067–2082 (2020)

# Acknowledgments

Acknowledgements are due to all the authors and co-authors, to the reviewers for all their time and collaboration.

The Editor declares that he has no conflicts of interest regarding the publication of this special issue.

The Editor also wishes to thank Pierpaolo Riva- Editor Engineering and Applied Sciences Springer for his invaluable help in editing this book.

The authors wish to express their appreciation for the support provided by grant from the National Council for Scientific and Technological Development (CNPq).

# Contents

<b>Electromechanical Systems and Nonlinear Dynamics of RNIS</b>	
<b>A Tutorial on the Simplification of Electromechanical Dynamic Models</b> .....	3
Rafael Henrique Avanço, Danilo Antonio Zanella, Americo Cunha Jr., Angelo Marcelo Tusset, and Jose Manoel Balthazar	
<b>Cardiorespiratory System as the System with Limited Power</b> .....	15
Evgeniy D. Pechuk, Tatyana S. Krasnopolskaya, and Oleh A. Savytskyi	
<b>Slow Oscillations in Systems with Inertial Vibration Exciters</b> .....	29
Nikolay P. Yaroshevich, Oleksiy S. Lanets, and Olha M. Yaroshevych	
<b>Bifurcations “Cycle–Chaos–Hyperchaos” in Some Nonideal Electroelastic Systems</b> .....	43
S. V. Donetskyi and A. Yu. Shvets	
<b>Nonlinear Dynamics of Self and Parametrically Excited Systems with Non-ideal Energy Source</b> .....	53
Jerzy Warminski	
<b>A Study of the Sommerfeld Effect in a Rotor Machine Foundation Model with 4 DOF</b> .....	73
Sara Prates Lima and Reyolando Manoel Lopes Rebello da Fonseca Brasil	
<b>Three Kinds of Sommerfeld Effect in Rotor Dynamics</b> .....	85
A. K. Samantaray	
<b>Nonlinear Modal Analysis of Vibrating Systems with Limited Power Supply</b> .....	127
V. Piccirillo, A. M. Tusset, Jose Manoel Balthazar, and A. G. Martinez	
<b>Resonance Dynamics of the Non-ideal System Having the Pendulum as Absorber of Elastic Vibrations</b> .....	139
Y. O. Lebedenko, Y. V. Mikhlin, and M. A. Pinsky	

**On a Vehicular Suspension for a Non-ideal and Nonlinear Orchard Tower Sprayer Through an Inverted Pendulum Using Reologic Magneto (MR) . . . . . 151**  
R. N. Silva, J. L. P. Felix, Jose Manoel Balthazar, A. M. Tusset, M. A. Ribeiro, W. B. Lenz, and A. Cunha

**On the Use of Synchrosqueezing Transform for Chaos and Nonlinear Dynamics Analysis in Fractional-Order Systems . . . . . 175**  
M. Varanis, C. Oliveira, M. A. Ribeiro, W. B. Lenz, A. M. Tusset, and Jose Manoel Balthazar

**On the Stability and Long-Term Behaviour of Structural Systems Excited by Nonideal Power Sources . . . . . 191**  
Javier González-Carbajal, Daniel García-Vallejo, and Jaime Domínguez

**Nonlinear Dynamics of RNIS, Control of RNIS and Harvester Energy of RNIS**

**Nonlinear Control Applied in Jump Attenuation of a Non-ideal System . . . . . 241**  
A. M. Tusset, A. Kossoski, A. M. Bueno, Jose Manoel Balthazar, J. L. P. Felix, A. Cunha Jr, and R. H. Avanço

**Chaos Control in a Nonideal Vibrating Systems . . . . . 253**  
A. M. Tusset, V. Piccirillo, S. L. T. de Souza, A. M. Batista, Jose Manoel Balthazar, R. M. L. R. F. Brasil, C. Oliveira, and M. Varanis

**Nonlinear Control of Rotating Flexible Structures Considering Aerodynamic Effects and Non-ideal Interactions . . . . . 263**  
André Fenili

**Control of the Dynamics of Mechanical Structures Supporting DC Motors with Limited Power Supply . . . . . 311**  
A. A. Nanha Djanan, B. R. Nana Nbandjo, and P. Woafu

**Dynamic Analysis and PID Control of a Double Pendulum Arm Excited by a Nonideal Source . . . . . 343**  
A. M. Tusset, P. L. Paula Filho, V. Piccirillo, G. G. Lenzi, Jose Manoel Balthazar, C. Oliveira, and M. Varanis

**Fractional Dynamics of Harvester with Nonideal Source Excitation . . . . 357**  
M. A. Ribeiro, W. B. Lenz, A. M. Tusset, Jose Manoel Balthazar, C. Oliveira, and M. Varanis

**Piezoelectric Energy Harvesting from a Non-ideal Portal Frame System Including Shape Memory Alloy Effect . . . . . 369**  
A. M. Tusset, V. Piccirillo, I. Iliuk, G. G. Lenzi, M. E. K. Fuziki, Jose Manoel Balthazar, G. Litak, and D. Bernardini

**LQR Optimal Control Applied in an Energy Harvesting System  
with Non-ideal Excitation Operating with Uncertain Parameters . . . . . 381**  
Estevão Fuzaro de Almeida and Fábio Roberto Chavarette

**A Hybrid PID-LQR Control Applied in Positioning Control  
of Robotic Manipulators Subject to Excitation from Non-ideal  
Sources . . . . . 393**  
A. M. Tusset, J. J. De Lima, F. C. Janzen, P. L. Paula Filho,  
J. A. G. Luz Junior, Jose Manoel Balthazar, and A. Kossoski

# **Electromechanical Systems and Nonlinear Dynamics of RNIS**

# A Tutorial on the Simplification of Electromechanical Dynamic Models



Rafael Henrique Avanço , Danilo Antonio Zanella , Americo Cunha Jr. , Angelo Marcelo Tusset , and Jose Manoel Balthazar 

**Abstract** DC motors are electromechanical systems designed to convert electric power to mechanical power. Their dynamics depend on the features of the motor and the load which they move. The dynamics of the motor is influenced by the external loads acting during the rotation. The electromagnetic forces interact according to the mechanical and electric characteristics of the motor. A common procedure is to neglect the effect of inductance in the steady-state speed and constant current. However, a recent analysis in literature claimed the inductance may be highly relevant in some cases in a steady-state regime. However, including the inductance in computer simulations causes highly time-consuming. Therefore, the intention in the present text is to investigate when it is mandatory to consider the motor inductance in the numerical simulation. The conclusion is that the inductance is relevant when the external loads are relatively high and vary in time.

## 1 Introduction

This chapter focuses on a discussion on a relatively classic theme in dynamical systems, the modeling of nonlinear dynamics of electromechanical systems involving DC motors [1–5]. In addition to contributing to the formation of new researchers on the subject, the text also aims to clarify some points that still confuse the literature. In

---

R. H. Avanço (✉) · D. A. Zanella  
Federal University of Maranhão, Rodovia MA-140, KM 04, Balsas, MA, Brazil

A. Cunha Jr.  
Rio de Janeiro State University, Rua São Francisco Xavier, 524, Rio de Janeiro, RJ, Brazil  
e-mail: [americo.cunha@uerj.br](mailto:americo.cunha@uerj.br)

A. M. Tusset  
Federal University of Technology - Paraná, R. Doutor Washington Subtil Chueire, 330, Ponta Grossa, PR, Brazil  
e-mail: [tusset@utfpr.edu.br](mailto:tusset@utfpr.edu.br)

J. M. Balthazar  
São Paulo State University, Av. Eng. Luís Edmundo Carrijo Coube, 2085, Bauru, SP, Brazil

this sense, the text presents a discussion of the most important aspects of modeling a system where a cart is coupled to a DC motor via a scotch yoke mechanism.

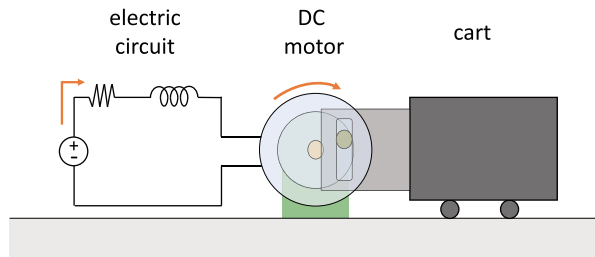
A DC motor is an electric machine that converts direct current electrical energy into mechanical energy. These motors have a permanent magnet stator with the poles N and S, where the electromagnetic forces arise from the current subject to the magnetic field of the stator [2]. The main goal of this analysis is to understand the influence of the inductance in the dynamics of the DC motors. The inductance may be defined as a tendency of an electrical conductor to oppose a change in the electric current flowing through it. In DC motors, the current flows in coils, what causes a higher effect in the magnetic field. Therefore, the consequence is that in some cases the inductance interferes in the dynamics, but in others, it could be neglected. A DC motor is governed by a set of differential equations. An electric equation considering current and voltage. The other is a mechanic differential equation based on the equilibrium of torque. In literature, a useful approach does not consider the inductance of the motor after the transient condition [5, 6]. However, recent analysis claimed that this approach is not reasonable in all cases. An analysis with a motor with a mass and scotch yoke was performed in [7], neglecting the inductance in this case caused a discrepancy when compared with a complete model which considers the inductance. In the present text, some simulations are worked out where is possible to verify that under some conditions there is a divergence in results when the inductance is considered or not. On the other hand, in some situations, the inductance does not interfere significantly in the dynamics, and the act of disregarding it does not have great losses, with the advantage of simplifying the mathematical model.

## 2 Electromechanical System

The mechanism comprehends a cart moved to left and right through a scotch yoke mechanism. This mechanism is powered by a DC motor and it is illustrated in (Fig. 1). This type of motor has its electric equation written in as

$$L \ddot{Q} + R \dot{Q} + G \Theta' = \mathcal{V}, \quad (1)$$

**Fig. 1** Illustration of the electromechanical system, which consists of a cart coupled to a DC motor by a scotch yoke mechanism





while the Newton Laws of rotation applied over the rotor in the motor results in the mechanical equation

$$J \Theta'' + B \Theta' - G Q' = \mathcal{T}. \quad (2)$$

In the last two equations we have  $Q' = Q'(T)$  and  $\Theta = \Theta(T)$  respectively denote the electrical current and angular displacement of rotor in time  $T$ ; the upper prime is an abbreviations for physical time derivative, i.e.,  $\square' = d\square/dT$ ;  $L$  represents an electrical inductance of the motor armature;  $R$  stands for the internal electrical resistance of the motor;  $J$  the rotational inertia of the rotor;  $B$  describes a damping coefficient related to a viscous friction; while  $G$  is an electromechanical coupling coefficient, it is equal to the torque constant and speed constant. The voltage source  $\mathcal{V} = \mathcal{V}(T)$  and the external torque  $\mathcal{T} = \mathcal{T}(T)$  acting over the motor correspond to (possibly) time-dependent external excitations. The torque may also be a function of the electromechanical system coordinates and their derivatives, i.e.,  $\mathcal{T} = \mathcal{T}(\Theta, \Theta', \Theta'', T)$ . In the present problem the external torque  $\mathcal{T}$  is a consequence of the cart reaction and is written as

$$\mathcal{T} = F D \sin \Theta. \quad (3)$$

The position of the cart is represented in Eq.(4), where the cart depends on the angular position of the rotor

$$X = D \cos \Theta. \quad (4)$$

The force of the motor acting over the cart is

$$M X'' = F, \quad (5)$$

and the resultant torque over the motor is given by

$$\mathcal{T} = -M D^2 \sin \Theta \left( \sin \Theta \Theta'' + \cos \Theta \Theta'^2 \right). \quad (6)$$

The initial conditions for the dynamic system are represented by

$$Q'(0) = Q'_0, \quad \Theta'(0) = \Theta'_0, \quad \text{and} \quad \Theta(0) = \Theta_0, \quad (7)$$

The dynamic system described by Eqs.(1) and (2) is considered the full-order dynamic model. In the next section we will introduce and comment the reduced model.

### 3 Reduced-Order Dynamic System

The *electrical characteristic time* of the problem is defined by

$$T_Q = \frac{L}{R}, \quad (8)$$

which in a Resistor-Inductor circuit means 63.2% of the time necessary to reach a steady-state current. Additionally, the *mechanical time constant*

$$T_\Theta = \frac{J R}{G^2}, \quad (9)$$

represents 63.2% of the time used to reach the maximum speed without external loads on the DC motor.

In literature, it is common authors [5, 6, 8–14] affirm the inductance could be neglected when the electrical characteristic time  $T_Q$  is much smaller than the  $T_\Theta$  mechanical characteristic time. Although this approach is very useful, [7, 15] demonstrated an example where the models highly diverge in results. The reduced-order dynamic model considers the inductance multiplied by the derivative of the current is irrelevant in steady-state conditions. Therefore, a set of equations may be resumed in a single equation.

When inductance is neglected the Eq. (1) turns into

$$Q' = \frac{\mathcal{V}}{R} - \frac{G}{R}, \quad \Theta' \quad (10)$$

which, after isolating the term  $Q'$  and substituting in the mechanical equation Eq. (2) we obtain the reduced-order equation including both electrical and mechanical aspects

$$J \Theta'' + B \Theta' - \frac{G \mathcal{V}}{R} \mathcal{V} + \frac{G^2 \Theta'}{R} = \mathcal{T}. \quad (11)$$

The initial conditions now do not consider the current. The electrical part depends on the voltage set. Therefore the initial conditions are simply

$$\Theta'(0) = \Theta'_0, \quad \text{and} \quad \Theta(0) = \Theta_0. \quad (12)$$

## 4 Dimensionless Formulation

In this sections the dimensionless parameters are introduced. A method commonly applied is the Buckingham  $\Pi$  theorem. The theorem states one can combine parameters from a physical problem and find dimensionless parameters. Some of the most known are the Reynolds number and Mach number in fluid dynamics. In the present problem the dimensionless parameters considered are

$$\begin{aligned} t &= \frac{T}{JR/G^2}, \quad \theta = \Theta, \quad \dot{\theta} = \frac{\Theta'}{G^2/JR}, \\ \dot{q} &= \frac{Q'}{G^3/JR^2}, \quad \ell = \frac{L}{JR^2/G^2}, \\ v &= \frac{\mathcal{V}}{G^3/JR}, \quad b = \frac{B}{G^2/R}, \quad d = \frac{D}{\sqrt{J/M}}. \end{aligned} \quad (13)$$

Here the lower case letters represent the dimensionless parameters and the upper case letters are physical parameters previously mentioned. The electric equation of the DC motor represented in Eq. (1) turns into the dimensionless electric equation

$$\ell \ddot{q} + \dot{q} + \dot{\theta} = v, \quad (14)$$

while the mechanical equation in Eq. (2) become the dimensionless equation

$$\ddot{\theta} + b\dot{\theta} - \dot{q} = \tau, \quad (15)$$

which the right-hand-side is given by the dimensionless external torque

$$\tau = -d^2 \sin \theta (\sin \theta \ddot{\theta} + \cos \theta \dot{\theta}^2). \quad (16)$$

The dimensionless initial conditions are

$$\dot{q}(0) = \dot{q}_0, \quad \dot{\theta}(0) = \dot{\theta}_0, \quad \text{and} \quad \theta(0) = \theta_0. \quad (17)$$

In the reduced model we consider the dimensionless electric equations as

$$\dot{q} + \dot{\theta} = v, \quad (18)$$

so that when the dimensionless current  $\dot{q}$  is replaced in Eq. (15), results in the reduced dimensionless mechanical equation

$$\ddot{\theta} + (b + 1)\dot{\theta} - v = \tau. \quad (19)$$

In consequence, the initial conditions for the reduced model does not contain the electric current

$$\dot{\theta}(0) = \dot{\theta}_0, \text{ and } \theta(0) = \theta_0. \quad (20)$$

## 5 Results and Discussion

In figures from Fig. 2, 3, 4, 5, 6, 7, 8 and 9 we have in each one the graphics of electric current  $\dot{q}$  versus angular velocity  $\dot{\theta}$ , the time history of the motor angular speed  $\dot{\theta}$  and the time history of the motor angular position  $\theta$ . The intention is to vary some parameters and find some conclusion about the influence of the different parameters. There are many parameters in the present problem and all of them may have its own relevance. However, for practical purposes we considered that three of them are more important. A dimensionless parameter for inductance represented through the parameter  $\ell$  which is varied from Figs. 2, 3 and 4, while the others parameters are maintained constant. In Fig. 2, the value of  $\ell$  is 0.02, a relatively small inductance

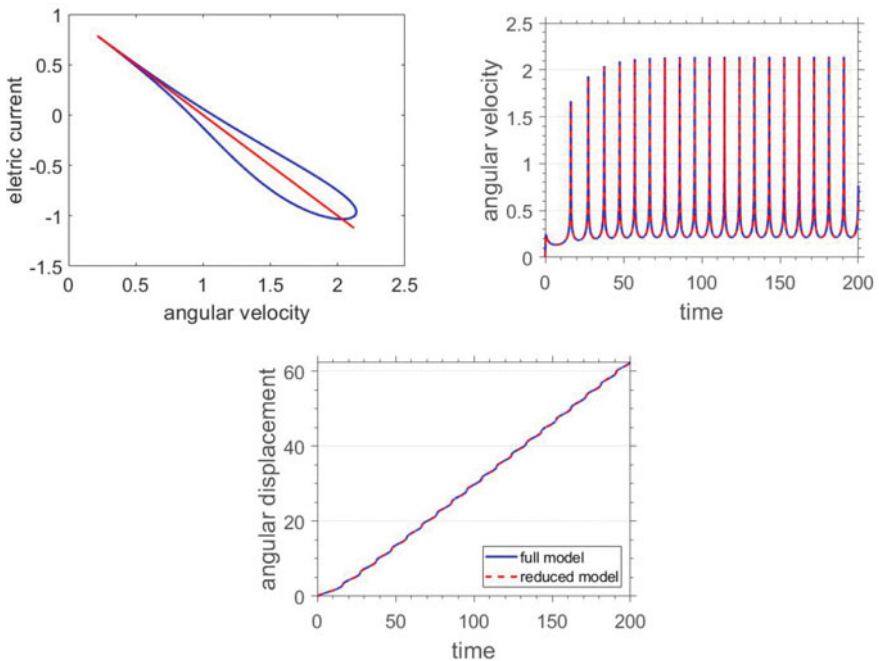


**Fig. 2** Phase-space of electric current  $\dot{q}$  versus angular velocity  $\dot{\theta}$ , angular velocity  $\dot{\theta}$  versus  $t$  and angular displacement  $\theta$  versus  $t$ . Dimensionless parameters:  $\ell = 0.02$ ,  $\nu = 1$ ,  $b = 1$ ,  $d = 10$ . Initial conditions:  $(\theta_0, \dot{\theta}_0, \dot{q}_0) = (0, 0, 3\nu)$

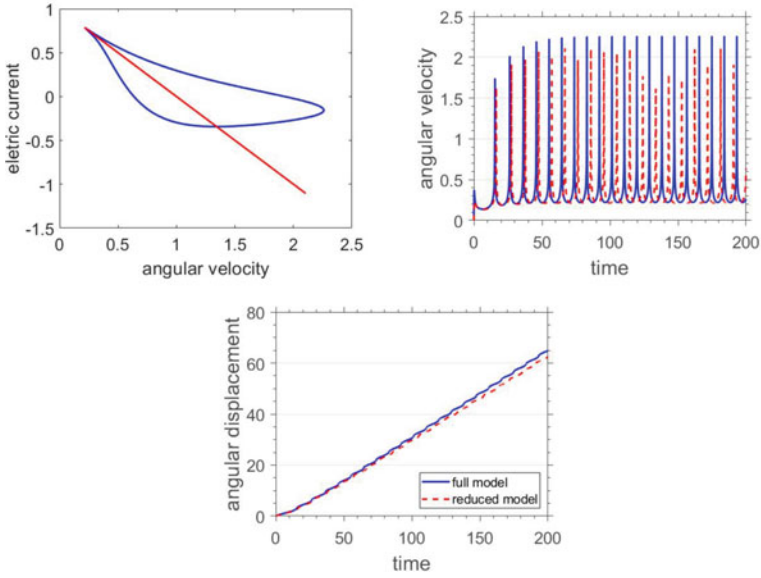


**Fig. 3** Phase-space of electric current  $\dot{q}$  versus angular velocity  $\dot{\theta}$ , angular velocity  $\dot{\theta}$  versus  $t$  and angular displacement  $\theta$  versus  $t$ . Dimensionless parameters:  $\ell = 0.2, \nu = 1, b = 1, d = 10$ . Initial conditions:  $(\theta_0, \dot{\theta}_0, \dot{q}_0) = (0, 0, 3\nu)$

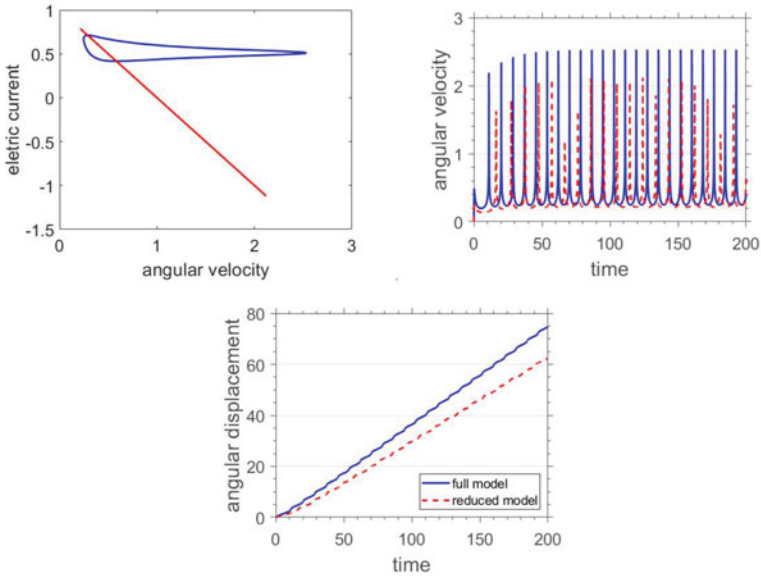


**Fig. 4** Phase-space of electric current  $\dot{q}$  versus angular velocity  $\dot{\theta}$ , angular velocity  $\dot{\theta}$  versus  $t$  and angular displacement  $\theta$  versus  $t$ . Dimensionless parameters:  $\ell = 2, \nu = 1, b = 1, d = 10$ . Initial conditions:  $(\theta_0, \dot{\theta}_0, \dot{q}_0) = (0, 0, 3\nu)$

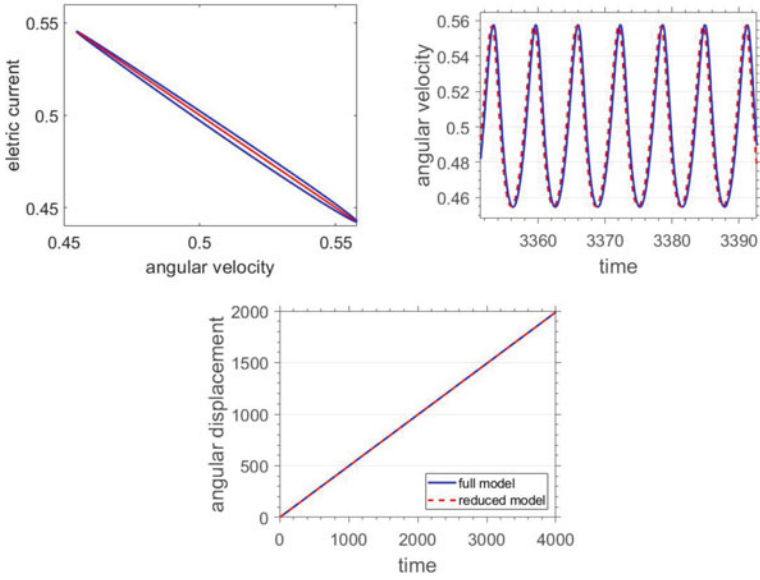


**Fig. 5** Phase-space of electric current  $\dot{q}$  versus angular velocity  $\dot{\theta}$ , angular velocity  $\dot{\theta}$  versus  $t$  and angular displacement  $\theta$  versus  $t$ . Dimensionless parameters:  $d = 1, \ell = 0.05, \nu = 1, b = 1$ . Initial conditions:  $(\theta_0, \dot{\theta}_0, \dot{q}_0) = (0, 0, 3 \nu)$

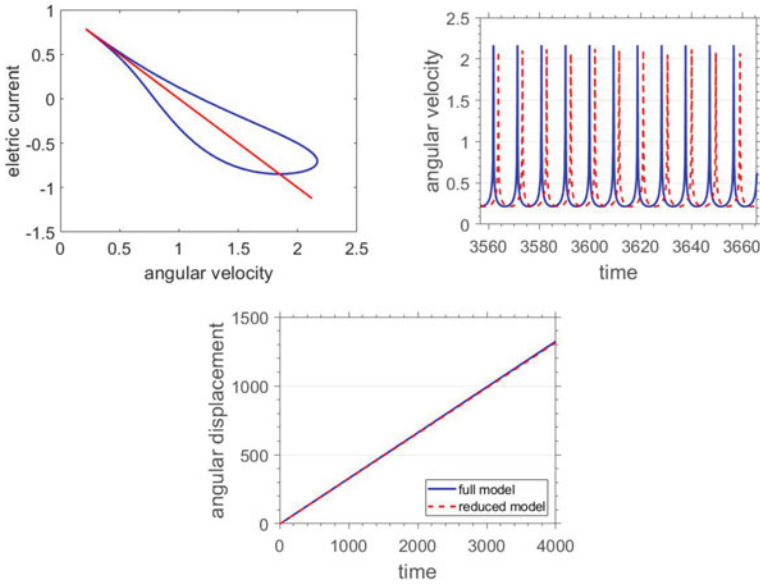


**Fig. 6** Phase-space of electric current  $\dot{q}$  versus angular velocity  $\dot{\theta}$ , angular velocity  $\dot{\theta}$  versus  $t$  and angular displacement  $\theta$  versus  $t$ . Dimensionless parameters:  $d = 10, \ell = 0.05, \nu = 1, b = 1$ . Initial conditions:  $(\theta_0, \dot{\theta}_0, \dot{q}_0) = (0, 0, 3 \nu)$

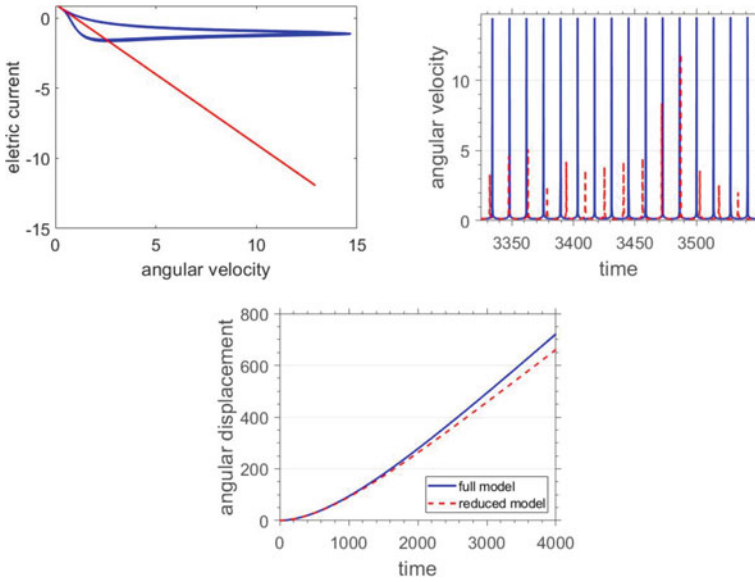


**Fig. 7** Phase-space of electric current  $\dot{q}$  versus angular velocity  $\dot{\theta}$ , angular velocity  $\dot{\theta}$  versus  $t$  and angular displacement  $\theta$  versus  $t$ . Dimensionless parameters:  $d = 100, \ell = 0.05, \nu = 1, b = 1$ . Initial conditions:  $(\theta_0, \dot{\theta}_0, \dot{q}_0) = (0, 0, 3 \nu)$

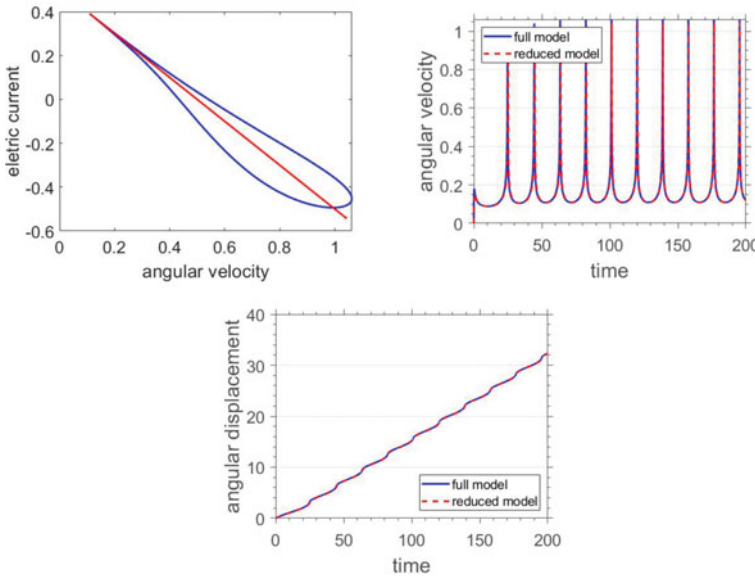


**Fig. 8** Phase-space of electric current  $\dot{q}$  versus angular velocity  $\dot{\theta}$ , angular velocity  $\dot{\theta}$  versus  $t$  and angular displacement  $\theta$  versus  $t$ . Dimensionless parameters:  $\nu = 0.5, d = 10, \ell = 0.05, b = 1$ . Initial conditions:  $(\theta_0, \dot{\theta}_0, \dot{q}_0) = (0, 0, 3 \nu)$

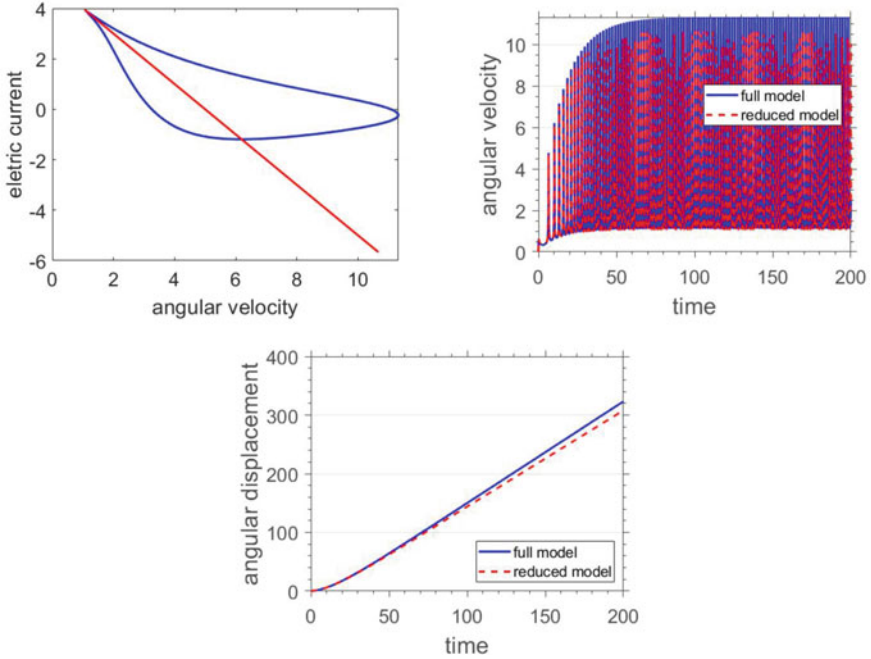


**Fig. 9** Phase-space of electric current  $\dot{q}$  versus angular velocity  $\dot{\theta}$ , angular velocity  $\dot{\theta}$  versus  $t$  and angular displacement  $\theta$  versus  $t$ . Dimensionless parameters:  $v = 5, d = 10, \ell = 0.05, b = 1$ . Initial conditions:  $(\theta_0, \dot{\theta}_0, \dot{q}_0) = (0, 0, 3v)$

where the results demonstrated low divergence when the full and reduced model are compared. An intermediate condition of divergence may be found in Fig. 3 when the value of  $\ell$  is 0.2. Finally, in Fig. 4 which the highest value of inductance with  $\ell$  equal to 2, the diverge appears clearly. This comparisons among these three figures evidence the relevance of the inductance on the present eletromechanical system. Larger values for the inductance have more impact in the divergence between the two models.

Another parameter that is took into account is the  $d$ . According the Eq. 13, the term  $d$  depends on the mass displaced, the moment of inertia of the rotor and the crank radius. From Figures 5, 7 and 7 the parameter  $d$  is varied while the inductance is fixed with  $\ell$  equal to 0.05. The results show good accordance between reduced and full model in Fig. 5. Differences begin to rise in Fig. 6, specially in the graphics for the angular velocity time histories. Lastly, in Fig. 7 the difference are obvious in the three graphics.



The third parameter analyzed is the  $\nu$ . Higher values for the voltage will exhibit divergence for the two models. In the Fig. 8 where  $\nu$  equal to 0.5 the two models have good accordance in the results of motion, while in Fig. 9 with  $\nu$  equal to 5 the reduced and the full models demonstrate a relevant divergence.

## 6 Conclusion

The conclusion begins pointing the importance to express the system in dimensionless terms. The common reason for this advice is the purpose to obtain a more generic result, suitable for diverse range of conditions. However, in this eletromechanical system when you turn the differential equations into dimensionless differential equations you avoid very small coefficients that oblige the usage of tiny step for integration. In other words, very small values in the coefficients cause difficulties for the computer calculus. The effect of high inductance is easier to understand. It follows the derivative of the current, the consequence is that higher the inductance, higher is the effect to the dynamics of the eletromechanical system. Not so obvious is the influence of the parameter  $d$ . This parameter is not composed by electric parts. The parameter  $d$  is essentially mechanical and it is responsible for the external loads acting on the motor. A higher value of  $d$  means high external forces alternating during time. It is similar to a motor in the transient regime, while it is accelerating. The voltage represented by the parameter  $\nu$  also provokes divergences between the two models. The explanation is that high voltage causes a higher current and also contributes for a greater forces involved in the mechanism. A mathematical note is that in Eqs. 1 and 14 when the speed of motor is reduced near to stall, the electric part of the equation will have higher influence. It means a higher influence for inductance and electric resistance. Therefore, the main advice for electromechanical systems with DC motor is to test different models including and disregarding the inductance. Operating in high speeds and with constant load are the best conditions to neglect the influence of the inductance in DC motors. For more details on the problem discussed in this chapter the reader is invited to see reference [16].

## Code Availability

The simulations of this chapter used a Matlab code dubbed **ElectroM - ElectroMechanical Dynamic Code**. To facilitate the reproduction of the results, this code is available for free on GitHub [17]. Other animations of electromechanical dynamics are available on a YouTube playlist [18].

**Acknowledgements** This research received financial support from the Brazilian agencies Coordenação de Aperfeiçoamento de Pessoal de Nível Superior - Brasil (CAPES) - Finance Code 001, the Brazilian National Council for Scientific and Technological Development (CNPq), grants

306525/2015-1 and 307371/2017-4, and the Carlos Chagas Filho Research Foundation of Rio de Janeiro State (FAPERJ) under the following grants: 211.304/2015, 210.021/2018, 210.167/2019, 211.037/2019 and 201.294/2021.

## References

1. Cveticanin, L., Zukovic, M., Balthazar, J.M.: Dynamics of Mechanical Systems with Non-Ideal Excitation. Springer (2018)
2. Chapman, S.J.: Electric Machinery Fundamentals, 5th edn. McGraw-Hill (2012)
3. Toliyat, H.A., Kliman, G.B.: Handbook of Electric Motors, 2nd edn. Taylor & Francis (2004)
4. Nayfeh, A.H., Mook, D.T.: Nonlinear Oscillations, 1st edn. Wiley-VCH (1979)
5. Kononenko, V.O.: Vibrating Systems with a Limited Power Supply Iliffe (1969)
6. Avanço, R.H., Tusset, A.M., Balthazar, J.M., Nabarrete, A., Navarro, H.A.: J. Brazilian Soc. Mech. Sci. Eng. **40**, 23 (2018). <https://doi.org/10.1007/s40430-017-0955-x>
7. Lima, R., Sampaio, R.: In: Proceeding Series of the Brazilian Society of Computational and Applied Mathematics, vol. 6, pp. 010,310–1 (2018). <https://doi.org/10.5540/03.2018.006.02.0310>
8. Balthazar, J., Mook, D.T., Weber, H.I., Brasil, R.M.L.R.F., Fenili, A., Belato, D., Felix, J.L.P.: Meccanica **38**, 613 (2003). <https://doi.org/10.1023/A:1025877308510>
9. Balthazar, J.M., Tusset, A.M., Brasil, R.M.L.R.F., Felix, J.L.P., Rocha, R.T., Janzen, F.C., Nabarrete, A., Oliveira, C.: Nonlinear Dyn. **93**, 19 (2018). <https://doi.org/10.1007/s11071-018-4126-0>
10. Belato, D., Weber, H.I., Balthazar, J.M., Mook, D.T.: Int. J. Solids Struct. **38**, 1699 (2001). [https://doi.org/10.1016/S0020-7683\(00\)00130-X](https://doi.org/10.1016/S0020-7683(00)00130-X)
11. Gonçalves, P.J.P., Silveira, M., Petrocino, E.A., Balthazar, J.M.: Meccanica **51**, 2203 (2016). <https://doi.org/10.1007/s11012-015-0349-z>
12. Gonçalves, P.J.P., Silveira, M., Pontes Junior, B.R., Balthazar, J.M.: J. Sound Vibr. **333**, 5115 (2014). <https://doi.org/10.1016/j.jsv.2014.05.039>
13. Rocha, R.T., Balthazar, J.M., Tusset, A.M., Piccirillo, V.: J. Vibr. Control **24**, 3684 (2018). <https://doi.org/10.1177/1077546317709387>
14. Rocha, R.T., Balthazar, J.M., Tusset, A.M., Quinn, D.D.: Nonlinear Dyn. **94**, 429 (2018). <https://doi.org/10.1007/s11071-018-4369-9>
15. Lima, R., Sampaio, R., Hagedorn, P., Deü, J.F.: J. Brazilian Soc. Mech. Sci. Eng. **41**, 552 (2019). <https://doi.org/10.1007/s40430-019-2032-0>
16. Cunha, A., Jr., Pereira, M., Avanço, R., Tusset, A.M., Balthazar, J.M.: On the reduction of nonlinear electromechanical systems, under review (2022)
17. Cunha, A., Jr., Pereira, M., Avanço, R., Tusset, A.M., Balthazar, J.M. ElectroM - ElectroMechanical Dynamic Code (2021). <https://americocunhajr.github.io/ElectroM>
18. Cunha, A., Jr.: Electromechanical dynamics. <https://bit.ly/3CQGei8> (2021). Accessed 10 Aug 2021

# Cardiorespiratory System as the System with Limited Power



Evgeniy D. Pechuk , Tatyana S. Krasnopolskaya ,  
and Oleh A. Savytskyi 

**Abstract** A modified cardiorespiratory model based on the famous De Boer beat-to-beat model and Zaslavsky map (which describes dynamics of the respiratory system as a generator of central type) was studied in details. The purpose of this work is twofold: it is to show and study the occurrence of chaotization in a generalized model of the interaction of the cardiovascular and respiratory subsystems, when modeling the entire cardiorespiratory system as a system with limited power. The second goal is to examine the dynamics of the entire system when changing heart rhythms. Chaotic modes were revealed, which were produced by the interaction between the subsystems. It was proved that the irregularity of the behavior of phase trajectories (which is characteristic of the dynamics of the cardiovascular system of a healthy person) depends on the intensity of the feedback effect produced by the heart rate on breathing. Thus, in order to construct right model of cardiorespiratory system of a healthy person necessary to consider such system as nonideal system with limited excitation. The second part of the article addresses the strategy to study the influence of increasing the pulse from 60 to 90 beats per minute on the dynamics of cardiorespiratory system.

**Keywords** Heart rate · Cardiovascular system · Respiratory system · Feedback · Chaos

## 1 Introduction

Today the problems of modeling processes in biophysics receive greatest demand because of Covid-19 epidemic. It is known that the functioning of the heart is closely related to the dynamics of the lungs, and modeling their interaction is an important and relevant task. The heart of a healthy person works irregularly, as was shown by

---

E. D. Pechuk · T. S. Krasnopolskaya (✉) · O. A. Savytskyi  
Institute of Hydromechanics NASU, 8/4 M. Kapnist Str., Kyiv 03057, Ukraine  
e-mail: [t.krasnopolskaya@tue.nl](mailto:t.krasnopolskaya@tue.nl)

O. A. Savytskyi  
e-mail: [osavitsky@ukr.net](mailto:osavitsky@ukr.net)

Goldberger [4] only 13 h before cardiac arrest and death of a person, his heart rate is periodic, that is, regular. Thus, after discovering the phenomenon of deterministic chaos, the modern theory of dynamic systems should be used for modeling and diagnostics of heart rates. The goal of our present paper was to study the interaction between the cardiovascular and respiratory systems taking into account the direct and inverse relations of the respiratory and cardiovascular subsystems. The interaction between the cardiovascular and respiratory subsystems was described by the De Boer model [2], the solution of which is regular. This model has been widely used in many studies of heart dynamics for the past 30 years. Based on the De Boer model, the interaction between the cardiovascular and respiratory subsystems will be considered with regard to the equations of direct (from respiratory to cardio) and inverse (from cardio to respiratory) relations of the subsystems. Thus, the cardiorespiratory system will be modeled and studied as the system with limited power. For that the respiratory system will be modeled as a Zaslavsky generator, which is described by the known equations of the dissipative standard map [18, 24]. Chaotic steady-state regimes will be revealed, and we stress out that they are produced by the interaction between the subsystems. It will be proved that the irregularity of the behavior of phase trajectories in a generalized model depends on the intensity of the effect produced by the heart rate on breathing, which is characteristic of the dynamics of the cardiovascular system of a healthy person. The novelty of this paper is also that we use the De Boer model of a cardiovascular system with heart beats around 60 beats/min and compare results for the model with 90 beats/min.

## 2 The Mathematical Model of Direct and Feedback Interactions

A well-known and physiologically correct model of the cardiac system is the De-Boer model of the cardiovascular system [2], which, in particular, does not take into account the reverse effect of heart activity on respiration parameters. For the first time for this model, the indicated inverse effect was taken into account in the Grinchenko-Rudnitsky model [5], where, in accordance with the principles of optimal control, the regulation and interactions of pressure in the cardiac system and the amplitudes of respiratory oscillations were investigated, but chaotic regimes (which are typical for healthy man) were not found.

Subsequently, the De Boer model was significantly developed in the work of Seidel and Herzel [19], where the so-called SH-model is constructed, which differs from the De Boer model by taking into account some elements of the sinus node activity and the dynamics of the ventricles. At the same time, the existence of chaotic dynamics in this model was revealed. The SH model was further developed by Kotani et al. [7], which took into account the reverse effect of the cardiac system on respiratory activity.

The human cardiovascular system directly and indirectly interacts with different systems of entire organism. Realized self-oscillations in a cardiovascular system are under an activity of practically all organs (see [2–4, 6, 7, 15–17, 22, 23]). There are numerous interactions of heart rhythms between itself and with an internal and external environment. Cardiac and respiratory rhythms form up during embryo stage, and even the brief break of these rhythms after a birth result in death.

Existence of breathing and heart rhythm synchronization effect, found experimentally in the cardiovascular system both for healthy people and with pathologies, is well-proven in work Toledo [22] in 2002. It is well-known, the dynamic process of mutual synchronization can be realized only in a case of presence of a subsystem mechanical interaction. Therefore, the indicated effect display testifies the presence of both direct and feedback interactions between the cardiovascular and respiratory systems.

A heart system and organism of man in general have one of major descriptions of activity, such as a blood pressure dynamic. His time-history, along with electrocardiogram (ECG), is an important information generator for research and diagnostics of laws and pathologies of the cardiovascular system, see Fig. 1. The task of mathematical model construction, describing the dynamics of arterial blood pressure, is far from complete. Complications of such design are related to the necessity of taking into account of influence on the cardiac rhythms not only the cardiovascular system but also other organs and systems of organism, in particular a respiratory system. According to studies in healthy people, the heart rate is on average about 60 beats/min and can fluctuate within 20 beats/min for every few beats. During the day, the heart rate can vary from 40 to 180 beats/min.

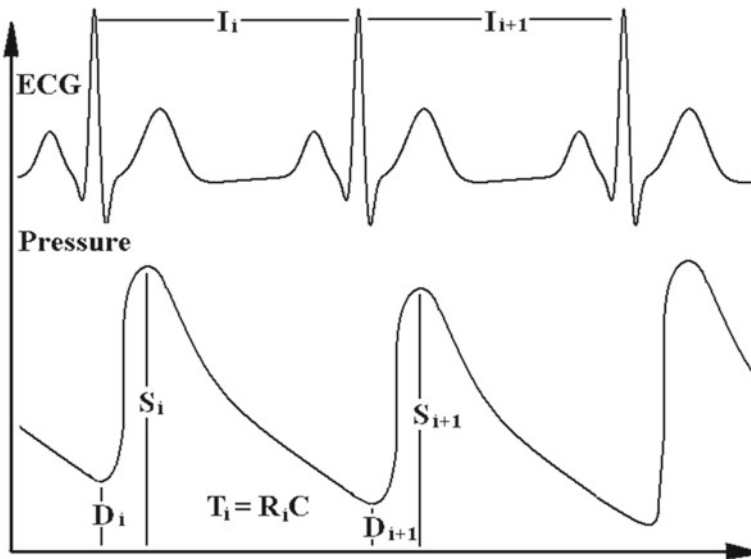
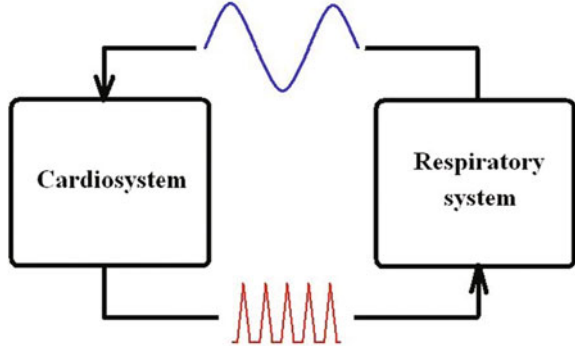


Fig. 1 Characteristics of the heartbeat in De Boer model

**Fig. 2** Interaction of the cardiovascular and respiratory system



However, this model does not consider the reverse mechanical influence effect of the heartbeat changes on a breathing phase (frequency). In the present study, we add to the De Boer model a self-oscillating system (which describes dynamics of the respiratory system as a generator of central type [6], shown in Fig. 2) which is under impulsive influence of heartbeat.

The De Boer model describes the followings main characteristics of the heartbeat system: systolic pressure  $S$ , diastolic pressure  $D$ , R-R interval  $I$  and arterial time constant  $T$  (in a state of rest for a healthy man  $S = 120$  mmHg,  $D = 80$  mmHg,  $I = 800$  ms,  $T = 1500$  ms for the middle heart beats as 75 beats/min). This mathematical model is a system of five discrete nonlinear maps. This model contains only a direct mechanical influence of the respirator system on the cardiovascular system and can be written in the form:

$$\begin{aligned}
 D'_i &= c_1 S'_{i-1} \exp\left(-\frac{I'_{i-1}}{T'_{i-1}}\right); \\
 S'_i &= D'_i + \gamma \frac{T_0}{S_0} I'_{i-1} + \frac{A}{S_0} \sin(2\pi f T_0 t_i) + \frac{c_2}{S_0}; \\
 I'_i &= G_v \frac{S_0}{T_0} \hat{S}'_{i-\tau_v} + G_\beta \frac{S_0}{T_0} F(\hat{S}', \tau_\beta) + \frac{c_3}{T_0}; \\
 T'_i &= 1 + G_\alpha \frac{S_0}{T_0} - G_\alpha \frac{S_0}{T_0} F(\hat{S}', \tau_\alpha); \\
 \hat{S}'_i &= 1 + \frac{18}{S_0} \arctan \frac{S_0 (S'_i - 1)}{18},
 \end{aligned} \tag{1}$$

where  $i \geq 1$ ,  $D' = D/S_0$ ,  $S' = S/S_0$ ,  $I' = I/T_0$ ,  $T' = T/T_0$ ,  $F(\hat{S}, \tau) = (\hat{S}_{i-\tau-2} + 2\hat{S}_{i-\tau-1} + 3\hat{S}_{i-\tau} + 2\hat{S}_{i-\tau+1} + \hat{S}_{i-\tau+2})/9$ ,  $t_i = \sum_{k=0}^{i-1} I'_k$  is a real time,  $A = 3$  mmHg is a breathing amplitude,  $f = 0.25$  Hz is a breathing frequency,  $c_1 = D_0/S_0 \exp(I_0/T_0)$ ,  $c_2 = S_0 - D_0 - \gamma I_0$ ,  $c_3 = I_0 - S_0(G_v + G_\beta)$ ,  $\gamma = 0.016$  mmHg,  $G_\alpha = 18$  ms/mmHg,  $G_\beta = 9$  ms/mmHg,  $G_v = 9$  ms/mmHg,

$\tau_\alpha = \tau_\beta = 4$ ,  $\tau_v$  is equal to 0 if frequency of heartbeat is less than 75 beat/min, and  $\tau_v$  is equal to 1, if frequency is more than 75 beat/min.

Generation of body rhythms, according to the theory of Glass [6] is carried out by the generators of the central type. Breathing is related to the movement of the chest and its dynamics can be modeled as the dynamics of the central generator. We suppose that a healthy man at rest breathes periodically with a permanent frequency and an amplitude of motions of thorax. In that case a breathing process can be described as the self-oscillating system, which has a steady limit circle. Thus, for the mathematical modeling of a such system equations of the Zaslavsky map could be used. Famous Zaslavsky map is the system of equations [18, 24] which describes the dynamics of an amplitude  $r_n$  and a phase  $\varphi_n$  of the system (in which periodic self-oscillations with a frequency  $\omega$  are realized) which is under  $T$ -periodic impulsive action of constant intensity  $\eta$ .

The system of Zaslavsky map has the following form:

$$r_{n+1} = (r_n + \eta \sin \varphi_n) \exp(-\kappa T), \quad (2)$$

$$\varphi_{n+1} = \varphi_n + \omega T + \nu(r_n + \eta \sin \varphi_n) \frac{1 - \exp(-\kappa T)}{\kappa}, \quad (3)$$

where  $\kappa$ ,  $\nu$  are constant parameters of interaction.

In our approach these Eqs. (2) and (3) are used to describe changes of an amplitude and phase of a respiratory system effect for every R-R interval with an intensity proportional to systolic pressure as discrete nonlinear maps

$$\tilde{\eta} = -\eta (S_n - S_0) \quad (4)$$

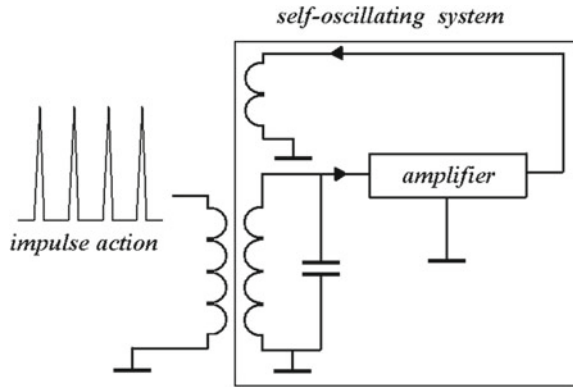
$$r_{n+1} = [r_n - \eta (S_n - S_0) \sin \varphi_n] \exp(-\kappa I_n), \quad (5)$$

$$\varphi_{n+1} = \varphi_n + 2\pi f I_n + \nu[r_n - \eta (S_n - S_0) \sin \varphi_n] \frac{1 - \exp(-\kappa I_n)}{\kappa}, \quad (6)$$

where  $I$  is R-R interval,  $\eta > 0$ .

Thus, we study the dynamics of the modified model of cardiorespiratory system, which consists of the De Boer model with direct respiratory influence  $(A + r_i) \sin \varphi_i$ , and with reverse influence modeled by the Zaslavsky discrete map system (4)–(6) (see Fig. 3). In other words, we consider cardio subsystem as oscillating system with a limited excitation from the respiratory subsystem [1, 3, 8–14, 20, 21]. This is the basic novelty of our approach.

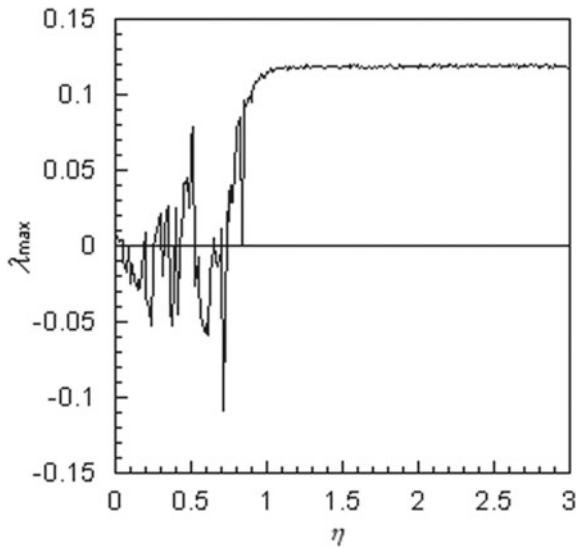
**Fig. 3** Schema of Zaslavsky generator as self-oscillating system with amplifier under impulse action



### 3 Numerical Simulations Results for the Heart Beats 75 beats/min

The following values of variables and constants are used in our numerical simulations of system of Eqs. (1), (4)–(6) for the cardiorespiratory system with heart beats equal to 75 beats/min:  $I' [0] = 0.53$ ,  $S' [-j] = 1.08$ ,  $j = 0, 1, \dots, 6$ ,  $r' [0] = 0$ ,  $\varphi' [0] = 0$ ,  $\kappa = 0.001$  1/ms,  $\nu = 0.001$  1/(ms mmHg). In order to study steady-state regimes the largest non-zero Lyapunov exponent [1, 8, 15] was calculated. The dependence of the largest non-zero Lyapunov exponent of the system on values of the bifurcation parameter  $\eta$  is shown in Fig. 4. The dynamics of the system changes with increasing of this parameter. There is the region where this Lyapunov exponent

**Fig. 4** The largest non-zero Lyapunov exponent  $\lambda_{\max}$  of the complex system





is equals to zero ( $\eta = 0.2$ ), what means that a limit circle is realized as steady-state regimes [1, 8, 15]. We emphasize that  $\eta$  describes intensity of heart influence on a respiratory system. The next Fig. 5 illustrates a behavior of systolic pressure, power spectra and projection of the phase portrait for this value of intensity. The spectrum in Fig. 5b has discrete peaks one of which corresponds to a peak on the Meyer frequency in the spectrum. So that, graphs indicate that there are regular regimes in the system. With increasing value of  $\eta$  the transition to chaos occurs. Thus, at  $\eta = 0.8$  chaos is realized in the system, when the spectrum in Fig. 6b is continuous and the projection of the phase portrait occupies some area in the phase space.

Finally, at  $\eta = 1.0$  the largest non-zero Lyapunov exponent is steady positive and the chaotic regime is fully developed, the power spectrum is continuous (Fig. 7b). So, we have found such steady-state basic regimes: at  $\eta = 0.2$  periodic regime (Fig. 5), at  $\eta = 0.8$  and for  $\eta \geq 1.0$  chaotic regimes (Figs. 6 and 7).

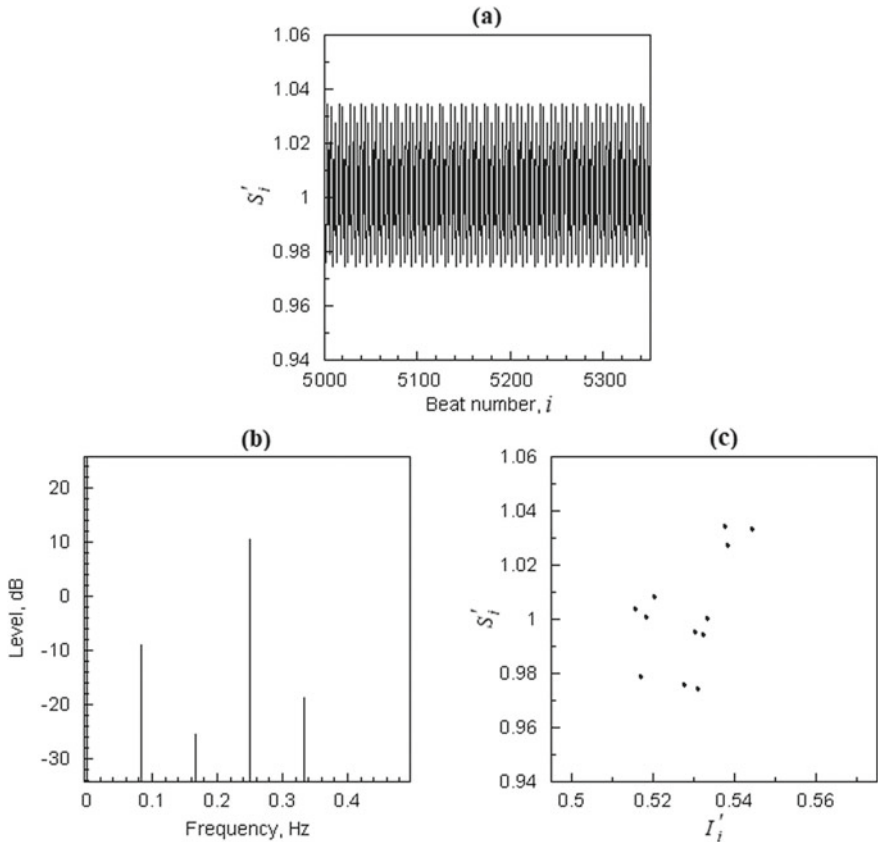


**Fig. 5** Graphs of simulated systolic pressure data **a**, power spectra **b** and projection of the phase portrait **c** for  $\eta = 0.2$

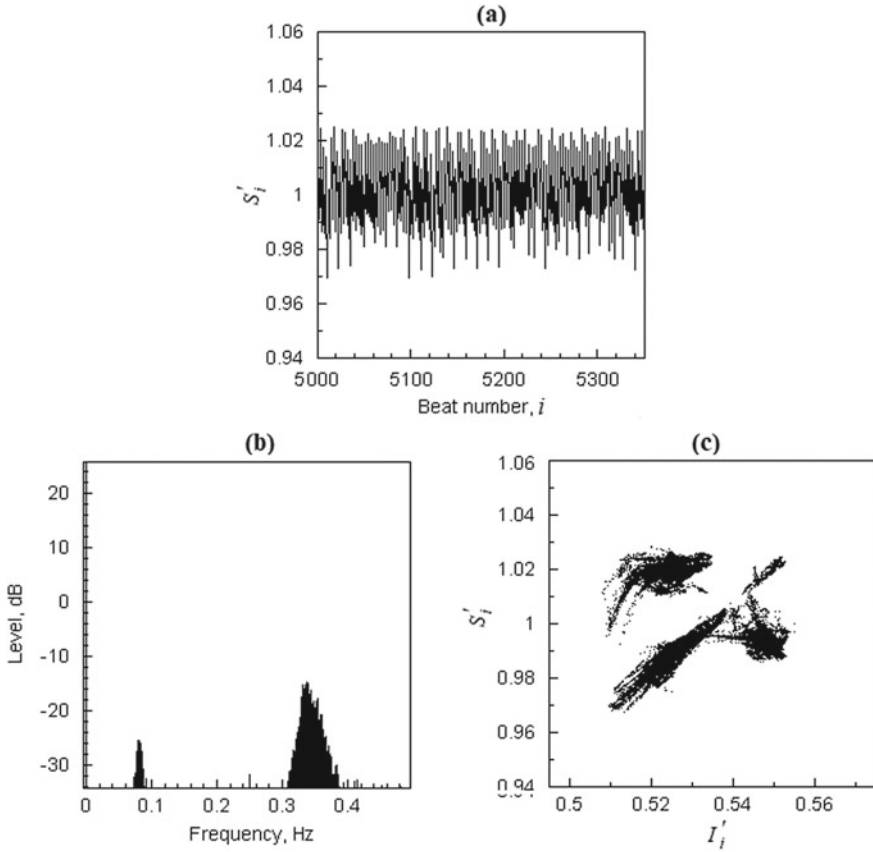


**Fig. 6** Graphs of simulated systolic pressure data **a**, power spectra **b** and projection of the phase portrait **c** for  $\eta = 0.8$

#### 4 The Cardiorespiratory System Regimes for Different Heart Rates

Now consider the behavior of the system (1), (4)–(6) when the heart rate increases from 60 to 90 beats/min. For numerical simulation, we take the following initial values:

$$I'[0] = 0.67, \quad \text{for a pulse 60 beats/min,}$$

$$I'[0] = 0.45, \quad \text{for a pulse 90 beats/min,}$$

$$S'[-j] = 1.08, \quad j = 0, \dots, 6.$$

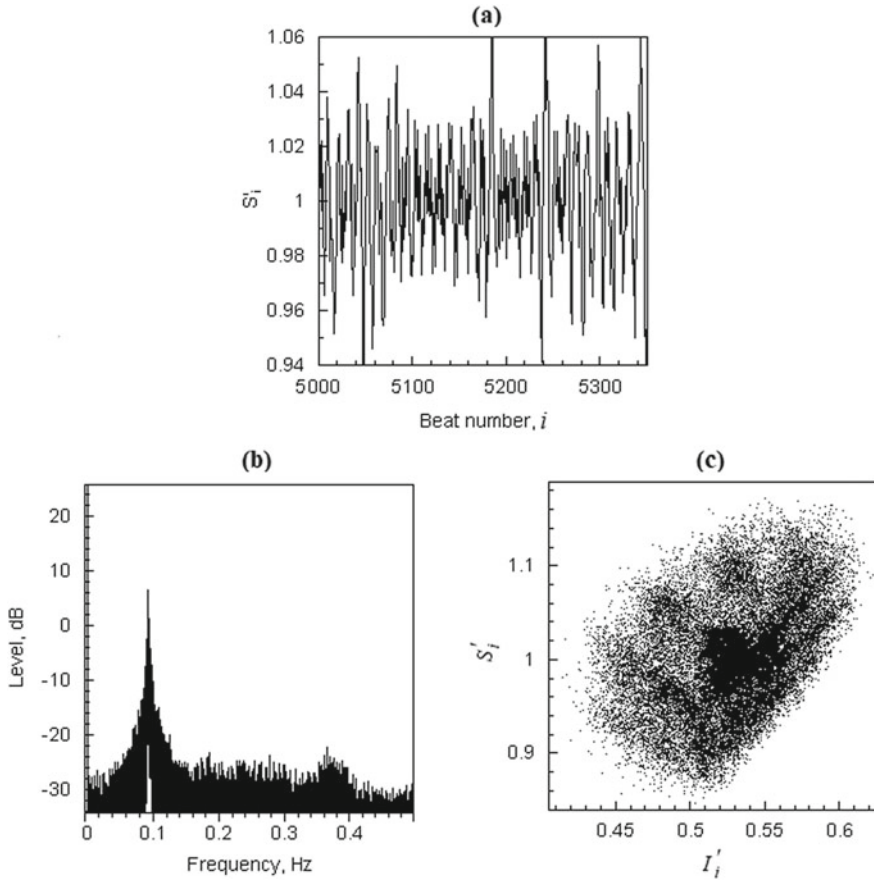


**Fig. 7** Graphs of simulated systolic pressure data **a**, power spectra **b** and projection of the phase portrait **c** for  $\eta = 1$

In Fig. 8 shows the projection of the phase space on the plane of the cardio interval and systolic pressure for the case of pulse equals 60 and values  $\eta = 0.03, \eta = 0.07, \eta = 0.1, \eta = 0.17$  (from left to right and from top to bottom). As can be seen from the graphs, a chaos is observed only when  $\eta = 0.17$  and projection occupies continuous area in space and quasiperiodic regimes are realized at smaller value of  $\eta \leq 0.1$ . Similar curves for the case of a pulse of 90 beats per minute are shown in Fig. 9. In this case, the solutions of the system are characterized by chaotic steady-state regimes even for the smallest value of  $\eta = 0.03$ . In Fig. 10 the corresponding wave realizations of the value of the cardio interval according to these solutions for 60 s are shown. Power spectrum for parameter values  $\eta = 0.03$  and  $\eta = 0.17$  is built on Fig. 11. Both spectra have a continuous structure (which proves the realization of precisely chaotic regimes) with well-defined bursts in the Mayer wave region (0.1 Hz) at a smaller value of the parameter  $\eta = 0.03$ . At  $\eta = 0.17$  the spectrum

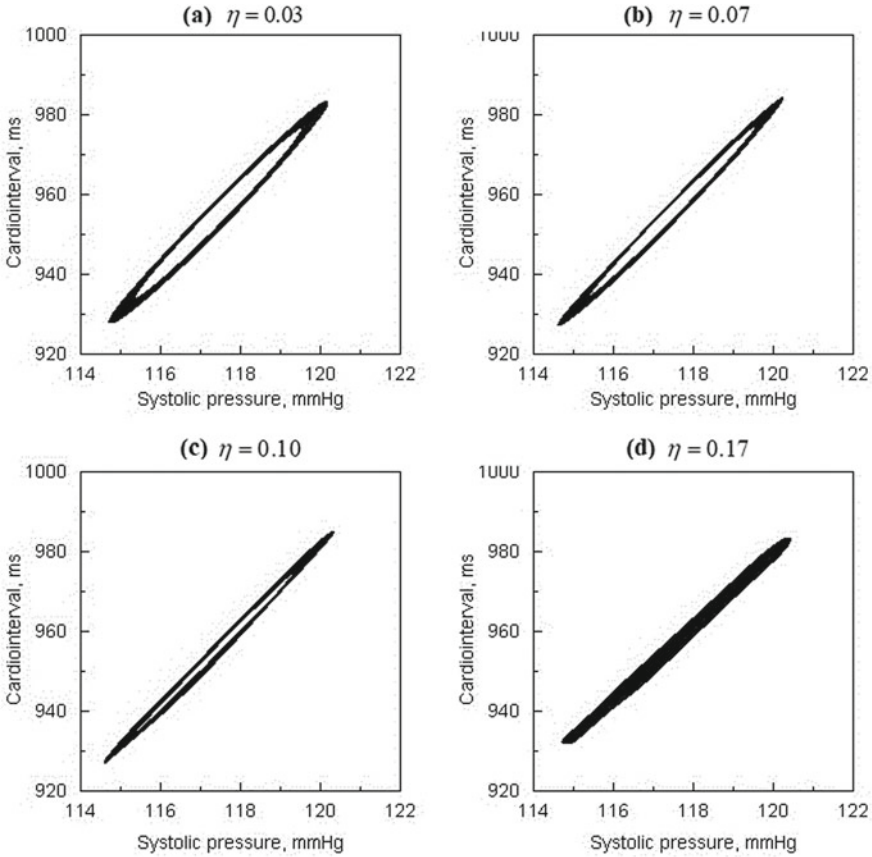


**Fig. 8** Projection of phase space on the plane of the cardiointerval and systolic pressure for the case of pulse 60 beats/min and values **a**  $\eta = 0.03$ , **b**  $\eta = 0.07$ , **c**  $\eta = 0.10$ , **d**  $\eta = 0.17$

is also continuous with two characteristic peaks at the frequency 0.17 Hz and in the area 0.335 Hz, which corresponds to a slightly increased frequency of respiratory waves. Frequency is considered to be as the standard rate of respiration equals to 0.25 Hz [5], which corresponds to a wave period of 4 s. That is, the model shows an increase in respiration rate with increasing heart rate, which also coincides with the experimental data.

## 5 Conclusions

On the basis of the De Boer model an interaction of the cardio and the respiratory subsystems is studied and modeled as the system with limited power. This model takes into account both direct and reverse influence of subsystems—cardiovascular

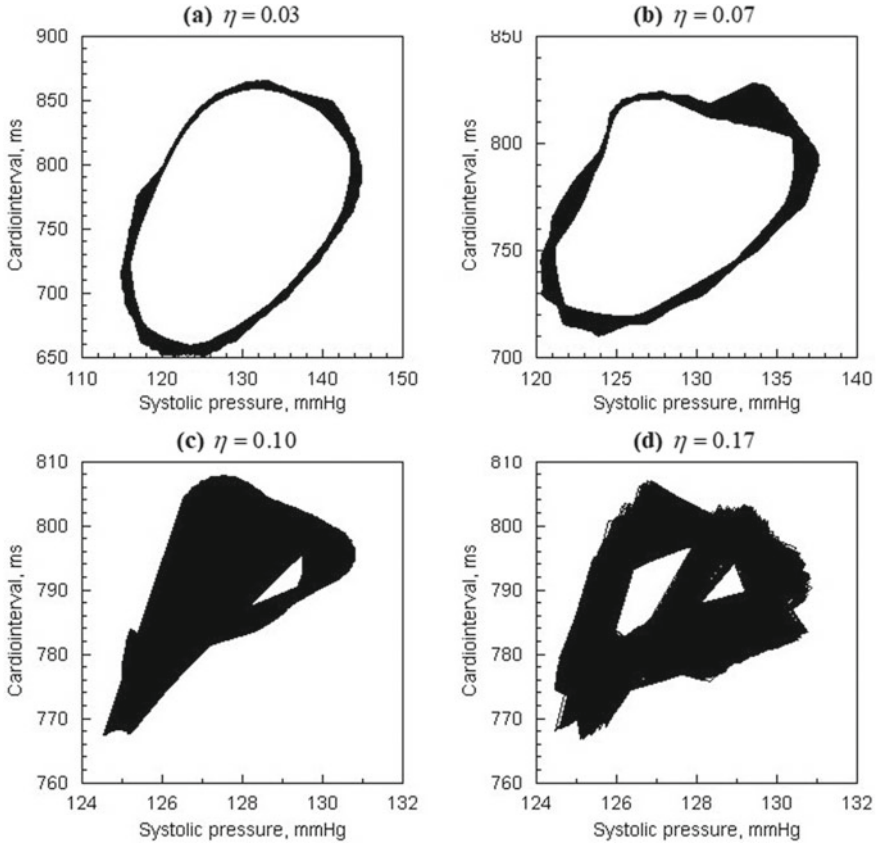


**Fig. 9** Projection of phase space on the plane of the cardiointerval and systolic pressure for the case of pulse 90 beats/min and values **a**  $\eta = 0.03$ , **b**  $\eta = 0.07$ , **c**  $\eta = 0.10$ , **d**  $\eta = 0.17$

and respiratory. The methods of modern theory of the dynamical systems are used to study laws of the steady-state regimes of the modified model for the pulse equals to 75 beats/min. It is established that the irregularity of the behavior of the phase trajectories depends on the intensity of the action of the heart rhythm on breathing, which is characteristic of the dynamics of the cardiorespiratory system of a healthy person.

The pulse of an adult without significant pathologies in the cardiovascular system may be about 60 beats per minute. With increasing body temperature due to viral infections, its value increases significantly. In the model of De Boer et al., which is generalized by taking into account the inverse effect of heart activity on the characteristics of chest movements, the effect of increasing the pulse to 90 beats/min was studied. It is revealed that the process of chaoticity of the dynamic regime occurs at smaller values of the bifurcation parameter. The chaotic regimes and some of its characteristics are shown. This may mean that an increase in heart rate leads to

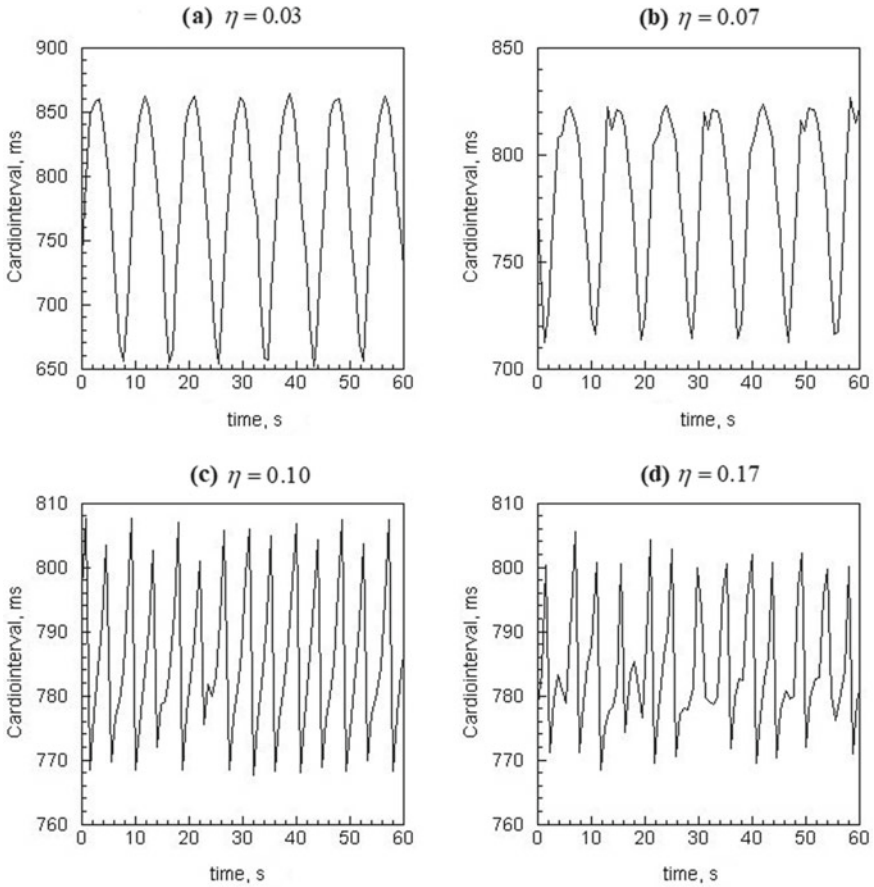


**Fig. 10** Time realizations of the value of the cardiointerval for the case of pulse 90 beats/min and values **a**  $\eta = 0.03$ , **b**  $\eta = 0.07$ , **c**  $\eta = 0.10$ , **d**  $\eta = 0.17$

an increase in the overall sensitivity of the body, due to the sensitive dependence of chaotic processes on the initial conditions and small changes in parameters. The effect of increasing the frequency of respiratory oscillations on the frequency spectrum of the chaotic steady-state regimes of the cardio interval was also revealed.

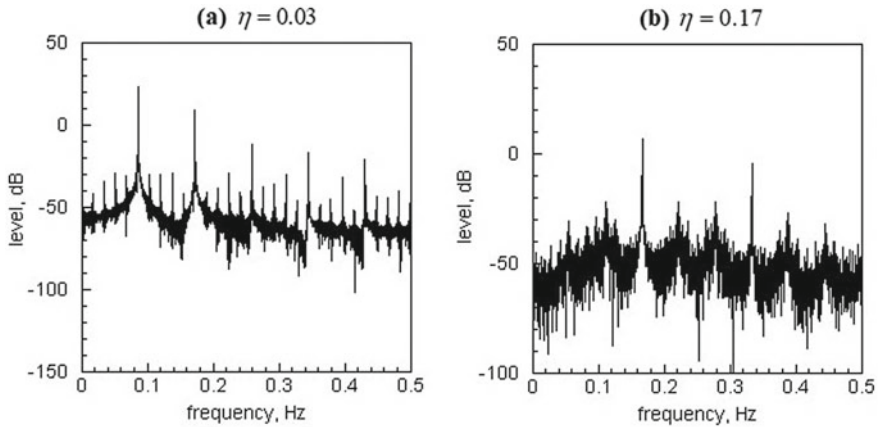


**Fig. 11** Power spectrum  $i$  of systolic pressure for the case of pulse 90 and values **a**  $\eta = 0.03$ , **b**  $\eta = 0.17$

## References

1. Balthazar, J.M., Palacios Felix, J.L. et al.: Nonlinear interactions in a piezoceramic bar transducer powered by a vacuum tube generated by a nonideal source. *J. Comput. Nonlinear Dyn.*, **4**(1), 1–7, 011013 (2009)
2. De Boer, R.W., Karemaker, J.M., Strakee, J.: Hemodynamic fluctuations and baroreflex sensitivity in humans: a beat-to-beat model. *Am. J. Physiol.* **253**, 680–689 (1987)
3. Frolov, K.V., Krasnopol'skaya, T.S.: Sommerfeld effect in systems without internal damping. *Sov. Appl. Mech.* **23**, 1122–1126 (1987)
4. Goldberger, A.L.: *Clinical Electro-cardiography: A Simplified Approach*, 7th edn. Mosby Elsevier, Philadelphia (2006)
5. Grinchenko, V.T., Rudnitskiy, A.G.: A model of intersection of the cardiovascular and respiratory systems. *Acoust. Bull.* **9**(3), 16–26 (2006)
6. Glass, L., Mackey, M.C.: *From Clocks to Chaos. The Rhythms of Life*. Princeton University Press, Princeton, Princeton (1988)
7. Kotani, K., et al.: Model for cardiorespiratory synchronization in humans. *Phys. Rev. E.* **65**, 051923–051932 (2002)
8. Krasnopol'skaya, T.S., Shvets, A.Y.: Chaotic oscillations of a spherical pendulum as an example of interaction with energy source. *Int. Appl. Mech.* **28**, 669–674 (1992)
9. Krasnopol'skaya, T.S., Shvets, A.Y.: Properties of chaotic oscillations of the liquid in cylindrical tanks. *Prikladnaya Mekhanika* **28**(6), 52–61 (1992)
10. Krasnopol'skaya, T.S., Shvets, A.Y.: Chaotic surface waves in limited power-supply cylindrical tank vibrations. *J. Fluids Struct.* **8**(1), 1–18 (1994)
11. Krasnopol'skaya, T.S.: Acoustic chaos caused by the Sommerfeld effect. *J. Fluids Struct.* **8**(7), 803–815 (1994)
12. Krasnopol'skaya, T.S.: Chaos in acoustic subspace raised by the Sommerfeld-Kononenko effect. *Meccanica* **41**(3), 299–310 (2006)
13. Krasnopol'skaya, T.S., Shvets, A.Y.: Deterministic chaos in a system generator-piezoceramic transducer. *Nonlinear Dyn. Syst. Theor.* **6**(4), 367–387 (2006)
14. Krasnopol'skaya, T.S., Shvets, A.Y.: Dynamical chaos for a limited power supply for fluid oscillations in cylindrical tanks. *J. Sound Vibr.* **322**(3), 532–553 (2009)
15. Krasnopol'skaya, T.S., Pechuk, E.D.: Cardiorespiratory system with strong interaction. *Chaotic Model. Simul. (CMSIM)* **NI**, 141–146 (2017)

16. Pechuk, E.D. et al.: Influence of the heart rate on dynamics of cardiorespiratory system. In: Skiadas, C.H., Dimotikalis, Y. (eds.) 12th Chaotic Modeling and Simulation International Conference. Springer Nature Switzerland AG 2020, pp. 211–216 (2020)
17. Pechuk, E.D., Krasnopolskaya, T.S., Rudnytska, M.O.: Cardiorespiratory system as nonideal system with limited excitation, *Chaotic Model. Simul. (CMSIM)*, N1, January, pp. 19–27 (2021)
18. Sagdeev, R.Z., Usikov, D.A., Zaslavsky, G.M.: *Nonlinear Physics: From the Pendulum to Turbulence and Chaos*. Harwood Academic Publishers, New-York (1988)
19. Seidel, H., Herzel, H.: Bifurcations in a nonlinear model of the baroreceptor-cardiac reflex. *Acoust. J.* **115D**, 145–160 (1998)
20. Shvets, A.Y.: Deterministic chaos of a spherical pendulum under limited excitation. *Ukr. Math. J.* **59**, 602–614 (2007)
21. Shvets, A.Y., Krasnopolskaya, T.S.: Hyper-Chaos in Piezoceramic Systems with Limited Power-Supply IUTAM Symposium on Hamiltonian Dynamics, Vortex Structures, Turbulence, pp. 313–322 (2008)
22. Toledo, E., et al.: Does synchronization reflect a true interaction in the cardiorespiratory system. *Med. Eng. Phys.* **24**, 45–52 (2002)
23. Yang, T., Jacobstein, M.D., Levy, M.N.: Synchronization of automatic cells in S-A node during vagal stimulation in dogs. *Am. J. Phys.* **246**, 585–591 (1984)
24. Zaslavsky, G.M.: The simplest case of a strange attractor. *Phys. Lett. A* **69**, 145–147 (1978)



# Slow Oscillations in Systems with Inertial Vibration Exciters



Nikolay P. Yaroshevich, Oleksiy S. Lanets, and Olha M. Yaroshevych

**Abstract** Oscillations of the inertial drive of a vibration machine with a limited-power motor during passage through the resonance zone are considered. It was found that in case of “stucking” of vibration exciter’s speed in the resonance zone, its relatively slow damped oscillations with relatively large amplitudes are excited. It is shown that during “stucking” of exciter’s speed, oscillations of the vibration machine’s drive can also be quite large. The critical frequencies of the drive of vibration machines with unbalanced vibration exciters have been specified.

**Keywords** Vibration machine · Unbalanced drive · Slow oscillations · Sommerfeld effect

## 1 Introduction

Vibration machines driven by inertial vibration exciters are used in various industries. Typically, such vibration machines operate in an above resonant mode. When starting vibration machines (run-out) there is a problem of passing through the zone of their resonance. During this period of movement, slowing down of the electric motor’s run is possible, up to the “stucking” of its frequency, i.e. occurrence of the Sommerfeld effect [1]. In this case, a stable resonant mode of vibration machine’s oscillations takes place; thus all the energy of the motor is consumed to maintain resonance oscillations. The result of it can also be the excitation of significant oscillations of the drive of vibration machine.

Investigation of dynamic processes in drives of vibration machines with a limited-power motor that are driven by inertial vibration exciters—is an urgent task of vibration engineering.

---

N. P. Yaroshevich (✉) · O. M. Yaroshevych  
Lutsk National Technical University, Lutsk 43018, Ukraine

O. S. Lanets  
Institute of Engineering Mechanics and Transport, Lviv Polytechnic National University, Lviv 79013, Ukraine

## 2 An Analysis of Studies on the Dynamics of Vibration Machines with Unbalanced Drive

A detailed consideration of the theory of oscillatory systems with limited excitation (non-ideal energy source) is given in the works [2–5].

Review of later works, as well as recent achievements in the field of non-ideal vibrating systems, are reflected in the works [6, 7].

So, in the paper [6], the main characteristics of non-ideal vibrating systems (first of all, the Sommerfeld effect) and the methodology for solving relevant problems are analyzed.

In [7], attention is drawn to the fact that a relatively simple theoretical description of the Sommerfeld effect is obtained using the method of direct separation of motions.

The effectiveness of application of the method of direct separation of motions for this class of problems is also demonstrated in articles [8–11].

So, in [8], when studying the dynamics of a machine unit with additional degrees of freedom, it is recommended to use the equation of slow motions rather than the initial equations of motion. The equation of slow motions takes the form of the classical equation of a machine unit, but at the same time, it contains an additional load moment that takes into account resonance phenomena.

In [9], a modification of the method of direct separation of motions is used to study a non-ideally excited electromechanical pendulum system consisting of three masses and a DC motor.

The paper [11] demonstrates the effectiveness of the use of continuous wavelet transform and wavelet packet transform for the characterization of the Sommerfeld effect in mechanical systems.

Interest in this issue has not waned to the present time. Of the latest publications, we also note the works [12, 13].

A number of papers are devoted to the issues of starting of vibration machines with inertial exciters, in particular [14–17].

The starting of vibration machines with several inertial vibration exciters is studied in [14]. Based on the results of numerical experiments, it is concluded that sequential starting of motors can significantly reduce the maximum amplitudes of resonant oscillations during starting.

The dynamics of starting of vibration machines taking into account the elasticity of connection of the vibration exciter with a limited power motor is analyzed in [15, 16]. An expression that describes relative torsional oscillations of the vibration exciter in stationary modes of motion and the formula for the vibration moment are obtained in these papers.

In [17] it is shown that a two-mass oscillation system with an eccentric-pendulum drive in the mode of resonant oscillations is characterized by instantaneous start and stop of the drive without long transient modes.

In [7], attention is drawn to the fact that the mode of behavior of vibration machines with inertial exciters during the passage of resonance is characterized by a number of rules that have applied significance. So, during the starting in the resonance zone,

oscillations of the vibration exciter occur with a frequency significantly lower than the frequency of its rotation [18–20]. In some papers, such oscillations are called semi-slow. The works [10, 22] are devoted to the applied use of slow oscillations to facilitate the starting of inertially excited vibration machines.

This chapter is devoted to the further development of the results of works [16, 18, 21].

### 3 Investigation of Vibration machine’s Drive Oscillations During Passing Through the Resonance Zone

#### 3.1 Formulation of the Problem and Equations of Motion of Vibration Machine

Analytical model of vibration machine (Fig. 1) corresponds to the simplest case, when the vibrational part of the system is linear and has one degree of freedom. In such a model, all the studied effects are fully demonstrated. This model is one of the basic models of the theory of oscillatory systems with limited excitation (excluding the elastic-damping connection of the rotors of electric motor and vibration exciter).

It should be noted that the elastic-damping connection can be represented by a belt drive, elastic coupling, flexible shaft or some other deformable element; an element considered to be inertialess. In this case, let it be a coupling.

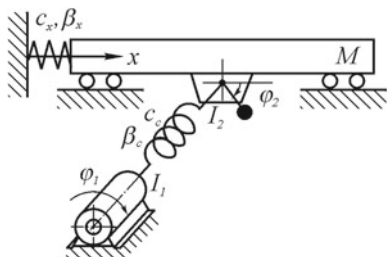
The motion equations of such a system are as follows:

$$I_1 \ddot{\varphi}_1 + \beta_c (\dot{\varphi}_1 - \dot{\varphi}_2) + c_c (\varphi_1 - \varphi_2) = L(\dot{\varphi}_1),$$

$$I_2 \ddot{\varphi}_2 - \beta_c (\dot{\varphi}_1 - \dot{\varphi}_2) - c_c (\varphi_1 - \varphi_2) = -R(\dot{\varphi}_2) + m\varepsilon(\ddot{x} \sin \varphi_2 + g \cos \varphi_2), \quad (1)$$

$$M\ddot{x} + \beta_x \dot{x} + c_x x = m\varepsilon(\ddot{\varphi}_2 \sin \varphi_2 + \dot{\varphi}_2^2 \cos \varphi_2), \quad (2)$$

Fig. 1 Dynamic model of vibration machine



where  $\varphi_1, \varphi_2$ —are angles of rotation of rotors of electric motor and vibration exciter;  $I_1, I_2$ —are moments of inertia of rotors;  $x$ —is horizontal deflection of bearing body;  $M$ —is the total mass of the elastically fixed bearing body of vibration machine;  $m, \varepsilon$ —are the mass of the vibration exciter and its eccentricity;  $c_x$ —is the axial rigidity of the elastic elements of the suspension bracket of the bearing body;  $c_c$ —is the stiffness of the coupling;  $\beta_x, \beta_c$ —is the coefficient of viscous friction of suspension bracket and coupling springs;  $L(\dot{\varphi}), R(\dot{\varphi})$ —is the torque of the electric motor (static characteristic) and the moment of resistance forces of rotation of the vibration exciter;  $g$ —is gravity acceleration.

### ***3.2 The Slow Motion Equations of Rotors of Electric Motor and Vibration Exciter in the Zone of the Sommerfeld Effect***

To study the motion of the rotors during slow passage through the resonance zone, we will use the method of direct separation of motions [4]. In accordance with the basic condition of the method, we assume that considered motions can be represented in the form:

$$\dot{\varphi}_i = \omega(t) + \dot{\psi}_i(t, \omega t), \quad x = x(t, \omega t), \quad i = 1, 2, \quad (3)$$

where  $t$ —“slow”,  $\tau = \omega(t)t$ —“fast” time;  $\omega(t)$ —are slow,  $\dot{\psi}_i$  and  $x$ —are fast time functions, whilst the latter  $2\pi$ - being periodic for  $\tau$  and their average values during this period are equal to zero.

Coordinates  $\varphi_i$ , taking into account (3), will be determined as follows:

$\varphi_i = \omega(t)t + \alpha_i(t) + \psi_i(t, \omega t)$ , where  $\alpha_i(t)$ —is some function  $t$ , that will be considered slow.

Such a representation of the solutions of system (1) and (2) during analyzing the slow passage of the rotors through the resonance zone, when there is an occurrence of the Sommerfeld effect, and, accordingly, the frequency  $\omega(t)$  changes rather slowly, seems to be reasonable.

It should be noted that the period of passage through the resonance zone is of particular interest as the maximum loaded operating mode of the vibration machine.

In accordance with the method used, let's write down the equations of slow motions of the motor and exciter rotors in the form:

$$I_1 \dot{\omega} + c_c(\alpha_1 - \alpha_2) = L(\omega),$$

$$I_2 \dot{\omega} - c_c(\alpha_1 - \alpha_2) = -R(\omega) - V(\omega), \quad (4)$$

where  $V(\omega) = -\langle \Phi(\ddot{x}, \varphi_2) \rangle$ —is so-called vibration moment [4];  $\Phi(\ddot{x}, \varphi_2) = m\varepsilon(\ddot{x} \sin \varphi_2 + g \cos \varphi_2)$ .

Here and down the text, angle brackets  $\langle \dots \rangle$  indicate the averaging over a period  $2\pi$  by  $\tau$ . When receiving the system (4), moments  $L(\dot{\varphi}_1)$  and  $R(\dot{\varphi}_2)$  were linearized near the value  $\dot{\varphi}_i = \omega$  according to the formulas:  $L(\dot{\varphi}_1) = L(\omega) - k_1 \dot{\varphi}_1$ ,  $R(\dot{\varphi}_2) = R(\omega) + k_2 \dot{\varphi}_2$  (where  $\omega$ —is the “sticking” frequency of exciter’s speed in the resonance zone of the vibration machine);  $k_1$ ,  $k_2$ —electrical and mechanical damping coefficients [4].

Thus, the high-frequency vibration of bearing body leads to the appearance of a vibration moment in the equation of slow motions of the vibration exciter (additional moment of forces of resistance to rotation, due to energy losses during oscillations). When analyzing the equations of slow motions, nature of the change in vibration moment is very important. The expression for vibration moment in [4] was obtained in the form  $V(\omega) = -V_{max} \sin \gamma_x$ , where its detailed analysis was made. We represent this expression in a more informative form

$$V(\omega) = -\frac{1}{2} k_d^2 A_{st}^2 \beta_x p_x, \quad (5)$$

where  $V_{max} = \frac{m\varepsilon\omega^2}{2} A_x$ ;  $\sin \gamma_x = \frac{2b_x\omega}{\sqrt{(\omega^2 - p_x^2)^2 + 4b_x^2\omega^2}}$ ;  $p_x^2 = \frac{c_x}{M}$ ,  $p_x \approx \omega$ ;  $b_x = \frac{\beta_x}{2M}$ ;  $A_x = \frac{m\varepsilon\omega^2}{M\sqrt{(\omega^2 - p_x^2)^2 + 4b_x^2\omega^2}}$ ;  $A_{st} = \frac{m\varepsilon}{M}$ —is the amplitude of oscillations of vibration machine in an above resonant operating mode;  $k_d = \frac{\lambda_x^2}{\sqrt{(1 - \lambda_x^2)^2 + 4h_x^2\lambda_x^2}}$ —is the dynamic coefficient;  $\lambda_x = \frac{\omega}{p_x}$ ;  $h_x = \frac{b_x}{p_x}$ —is the relative damping coefficient.

Note that the expression (5) indicates both significant and rapid (proportional to square of the dynamic coefficient) load increase on the electric motor when the Sommerfeld effect occurs.

According to the Eq. (4), in this mode of motion, the static deformation of the drive (average deformation value) will be maximum,  $\alpha_{12} \approx L_{max}/c_c$ , where  $L_{max}$ —is the maximum vibration moment of electric motor;  $\alpha_{12} = \alpha_1 - \alpha_2$ , at the same time, it is more than twice its static deformation in an above resonant operating mode ( $\alpha_{12} \approx L_{nom}/c_c$ , where  $L_{nom}$ —is the nominal vibration moment of the electric motor).

Summing up the Eqs. (4), we get the equations of slow motions of the vibration exciter rotor when passing through the resonance zone in the following form

$$I\dot{\omega} = L(\omega) - R(\omega) + V(\omega), \quad (6)$$

where  $I = I_1 + I_2$ .

Then, the equation for the frequency of rotation of the vibration exciter in stationary modes of motion can be written in the form  $L(\omega) = R(\omega) - V(\omega)$ . The last two equations do not differ from those given in [4] for the basic dynamic

model. Consequently, the conclusions made in [4] regarding the possible stationary modes of motion of the vibration exciter and their stability are also valid for the model under consideration. Naturally, the presence of an elastic-damping element in the drive of the vibration machine does not affect the slow motions of the exciter's rotor; it cannot be said about the equation of fast motions. In addition, an abrupt (proportional to  $k_d^2$ ) increase in the vibration moment in the resonance zone of the vibration machine can lead to the occurrence of nonstationary oscillations of the vibration exciter's rotor.

### 3.3 Equations of Rapid Motions of the Rotors of Electric Motor and Vibration Exciter and Their Analysis

To analyze oscillatory processes in a vibration machine's drive in the zone of the Sommerfeld effect, it is important to consider the equations of fast motion of rotors:

$$I_1 \ddot{\psi}_1 + \beta_c(\dot{\psi}_1 - \dot{\psi}_2) + c_c(\psi_1 - \psi_2) + k_1 \dot{\psi}_1 = 0,$$

$$I_2 \ddot{\psi}_2 - \beta_c(\dot{\psi}_1 - \dot{\psi}_2) - c_c(\psi_1 - \psi_2) + k_2 \dot{\psi}_2 = \Phi(\ddot{x}, \varphi_2) - \langle \Phi(\ddot{x}, \varphi_2) \rangle. \quad (7)$$

Assuming that  $\varphi_i = \omega t + \psi_i$ , we represent the equations of fast motions of the vibration exciter's rotor in the form

$$I_2 \ddot{\psi}_2 + k_2 \dot{\psi}_2 = m\varepsilon(\ddot{x} \sin \omega t + \ddot{x} \psi_2 \cos \omega t - \langle \ddot{x} \sin \omega t \rangle). \quad (8)$$

When deriving Eq. (8), the assumption [17] was taken into account; in accordance with it, in the initial approximation, the oscillations of the speed of the motor's rotor do not have a noticeable effect on the oscillations of the vibration exciter's speed,  $I_1 \ll I_2$  (that is also confirmed by the results of computer simulation); the linearization of the right side (7) is performed according  $\psi_2$ ; the effect of the gravity moment of the debalance is not taken into account.

Taking into account the solution of Eq. (2), corresponding to the steady-state forced oscillations of the bearing body when the vibration exciter rotates with frequency  $\omega$ , we represent (8) in the form:

$$I_2 \ddot{\psi}_2 + k_2 \dot{\psi}_2 + c_\psi \psi_2 = -V_{\max} [\sin(2\omega t - \gamma_x) - \psi_2 \cos(2\omega t - \gamma_x)], \quad (9)$$

where  $c_\psi = V_{\max} \cos \gamma_x$ .

On the right side of (9), the first and second summands represent the destabilizing moments; at the same time, the value of the second summand is significantly less than the first one and, therefore, it can be neglected. Let us write Eq. (9) in the form

$$\ddot{\psi}_2 + 2b_\psi \dot{\psi}_2 + p_\psi^2 \psi_2 = \Phi_x \sin 2\omega t, \quad (10)$$

where  $b_\psi = \frac{k_2}{2I_2}$ ;  $\Phi_x = -\frac{V_{\max}}{I_2}$ .

Thus, in the zone of the Sommerfeld effect, Eqs. (9) and (10) of fast motions of the vibration exciter take the form of the equation of small forced oscillations of a point relative to the stable equilibrium position. In (9) term  $c_\psi \psi_2$  is a kind of elastic force, and the factor  $c_\psi$  can be called a dynamic or vibrational stiffness coefficient. As you can see, the value  $c_\psi$  is proportional to  $V_{\max}$ . Consequently, in the resonance zone of the vibration machine, the coefficient  $c_\psi$  is significant and it seems important to analyze the possible oscillations in the speed of the vibration exciter.

In Eq. (10), the term  $p_\psi$  is the frequency of natural rotational oscillations of the vibration exciter's rotor in the zone of the Sommerfeld effect,  $p_\psi = A_x p_x \sqrt{\frac{M}{2I_2} |1 - \lambda_x^2|}$ . In [18], this frequency is called the frequency of free oscillations of the "inner pendulum"; at the same time, it was found that for vibration machines with an inertial drive, the following inequality is usually valid  $\omega/p_\psi > 3$ . Note that when the rotor passes through the resonance zone and the rotation frequency reaches  $p_x$ , the frequency of slow oscillations of the vibration exciter turns into zero.

Obviously, the oscillation amplitudes described by linear Eqs. (9) and (10) are primarily determined by the correlation between the frequencies  $p_\psi$  and  $2\omega$ ; in the case under consideration, when the frequency of excitation of oscillations significantly exceeds the natural frequency of the system ( $2\omega \gg p_\psi$ ), along with establishment of a stationary mode, a pronounced transient process with increased initial amplitudes will take place. Complex oscillations excited during this period of movement represent the superposition of low-frequency (with frequency  $p_\psi$ ) damped oscillations of the system with relatively large amplitudes on forced fast (with frequency  $2\omega$ ) oscillations with significantly lower amplitudes.

Note that in the frequency range  $\omega \approx p_x$ , the values of the coefficients of viscous resistance  $k_2$  and damping  $b_\psi$  in Eqs. (9) and (10) are relatively small; they are smaller than for the case of the basic model [4]:  $k = k_1 + k_2$  и  $b_\psi = \frac{k_1 + k_2}{2(I_1 + I_2)}$  ( $k_2 < k_1$ ,  $I_1 \ll I_2$ ). Consequently, the damping of accompanying free oscillations described by Eqs. (9) and (10) will occur relatively slowly.

Thus, when analyzing the process of establishing of a stationary mode of rotation of the vibration exciter's rotor in the zone of the Sommerfeld effect, it is not enough to take into account only its forced oscillations; free oscillations will have a decisive influence on the emerging movement of the vibration exciter.

Let us find the general solution of Eq. (10). When determining the initial conditions, we take into account that:

- the Sommerfeld effect occurs with a rapid increase in the vibrational moment to the value  $V_{\max}$ ; the impact of it can be estimated by impulse (the frequency of the vibration moment  $2\omega$  is significantly higher than the natural frequency  $p_\psi$ ,  $2\omega \gg p_\psi$ );
- the braking effect of the vibration moment takes place during half of the period;

- before the occurrence of the Sommerfeld effect, the oscillatory motions of the exciter's rotor are relatively small.

For greater clarity of the sought solution, we neglect in (10) the moment of resistance  $b_\psi \dot{\psi}_2$ . This simplification is evidenced by the fact that at  $p_\psi \ll 2\omega$  the influence of the resistance forces on the forced oscillations is insignificant, and on free oscillations—is reduced only to the gradual damping of the latter (it can be taken into account when analyzing a solution).

Solution of Eq. (10) taking into account the initial conditions  $\psi_{20} = 0$ ,  $\dot{\psi}_{20} = -V_{\max}/I\omega$ , as well as conditions  $p_\psi^2 \ll \omega^2$ , can be written in the form

$$\psi_2 \approx -\frac{3V_{\max}}{2\omega p_\psi I_2} \sin p_\psi t + \frac{V_{\max}}{4\omega^2 I_2} \sin 2\omega t. \quad (11)$$

The rotor oscillation is best judged by its speed oscillations. The expression describing oscillations of the rotor frequency when the stationary mode is established can be represented in the form

$$\dot{\psi}_2 \approx \frac{V_{\max}}{2\omega I_2} (3 \cos p_\psi t + \cos 2\omega t). \quad (12)$$

Naturally, under the assumptions made above, expression (12) coincides with that obtained in [21] for the case of the absence of an elastic-damping connection of the rotors of the electric motor and vibration exciter. Taking into account the assumption that friction forces are neglected (i.e., that in (10) the amplitudes of the first harmonic actually gradually decrease), we can conclude:

- when a stationary mode of rotation of the exciter rotor is established, a transient process takes place, that is representing biharmonic damped oscillations of the rotor speed with the fundamental frequency  $p_\psi$ ; since  $p_\psi \ll 2\omega$ , the nonstationary process represents relatively slow oscillations;
- the emergence of slow oscillations in the speed of the vibration exciter is a consequence of an abrupt increase in the vibration moment in the resonance zone of the vibration machine;
- the maximum (initial) amplitudes of these oscillations are large enough—at least three times the amplitudes of the subsequently established stationary mode;
- damping of nonstationary oscillations in the zone of the Sommerfeld effect occurs relatively slowly;
- at the same time, the amplitudes of the steady-state stationary mode are also relatively large, and that is a consequence of the resonant value of the vibration moment,  $V(\omega) \approx V_{\max}$ .

Since the condition of vibration isolation of the drive in the zone of natural frequencies of the vibration machine is not satisfied, oscillations in the exciter's speed can cause significant oscillations of the drive.



### 3.4 Equations of Fast Motions of a Vibration machine's Drive

Consider the torsional oscillations of a vibration machine's drive. We transform the equations of fast motions of the electric motor's rotor into the equation of oscillations of the drive; in this case, we will take into account the estimates of the summands of the equations of fast motions made in [4]. Then we get the equation

$$\ddot{\psi}_{12} + 2b_{12}\dot{\psi}_{12} + p_c^2\psi_{12} = \Psi_{\psi} \sin p_{\psi}t + \Psi_{\omega} \sin 2\omega t, \quad (13)$$

where  $b_{12} = \frac{\beta_c + k_1}{2I_1}$ ;  $\Psi_{\psi} = -\frac{3V_{\max}p_{\psi}}{2I_2\omega}$ ;  $\Psi_{\omega} = \frac{V_{\max}}{I_2}$ .

It is easy to make sure that the damping coefficient  $b_{12}$  in the equation of the drive oscillations (13) significantly exceeds the coefficient  $b_{\psi}$  in the equation of motion of the vibration exciter (10). In addition, from the strength condition (unacceptability of large deformations) of the drive, it follows that its natural frequency cannot be significantly lower than the oscillation excitation frequencies  $p_{\psi}$ ,  $2\omega$ . Consequently, when the stationary mode is established, the transient process will not be as significant as for the vibration exciter. Then we represent the solution of Eq. (13) in the form

$$\psi_{12} = \Phi_{\psi}k_{\psi} \sin p_{\psi}t + \Phi_{\omega}k_{\omega} \sin 2\omega t, \quad (14)$$

where  $\Phi_{\psi} = -\frac{3\lambda_p}{2} \frac{V_{\max}}{I_2 p_c^2}$ ,  $\Phi_{\omega} = \frac{V_{\max}}{I_2 p_c^2}$ ;—are the static deformations of the drive;

$k_{\omega} = \frac{1}{\sqrt{(1-\lambda_{\omega}^2)^2 + 4h^2\lambda_{\omega}^2}}$ ,  $k_{\psi} = \frac{1}{\sqrt{(1-\lambda_{\psi}^2)^2 + 4h^2\lambda_{\psi}^2}}$ —are the dynamic coefficients;  $h_c = \frac{b_{12}}{p_c}$ ;  $\lambda_{\psi} = \frac{p_{\psi}}{p_c}$ ;  $\lambda_{\omega} = \frac{2\omega}{p_c}$ .

Solution (14) makes it possible to estimate the amplitudes of rotary oscillations of the drive when starting the vibration machine in case of the Sommerfeld effect. Comparing in (14) the static deformations of the drive (constant components) from the action of exciting moments with slow and fast frequencies, it is easy to find that the value of the second is approximately twice the first; moreover, the amplitudes of the slow harmonic actually decrease. Consequently, the main oscillations of the drive in the zone of the Sommerfeld effect are its fast oscillations with a frequency  $2\omega$ .

As you can see, in (14) the value of the amplitudes of both harmonics is proportional to  $V_{\max}$ . Consequently, in the resonance zone of the vibration machine, the oscillations of the drive can abruptly increase. At the same time, in case of a hard drive ( $p_c \gg \omega_w$ , i.e. when  $p_c \gg p_{\psi}$ ,  $p_c > 2\omega$ ,  $\omega_w$ —is the vibration exciter's rotation frequency in operating mode), dynamic coefficients will be smaller than in case of a soft drive ( $\frac{\omega_w}{p_c} > \sqrt{2}$ ) and, accordingly, the oscillation amplitudes of such a drive in the resonance zone of the vibration machine will also be significantly smaller than the oscillation amplitudes of the soft drive. In addition, the possibility of coincidence of the frequencies of excitation of oscillations in the resonance zone

( $p_{\psi, \omega} \approx p_x, 2\omega$ ) with the natural frequency of the drive  $p_c$  is excluded. Thus, oscillations of the soft drive of the vibration machine when it slowly passes through the resonance zone will be large.

### 3.5 Computer Simulation of Oscillations in Drives of Vibration Machines in the Resonance Zone

The joint numerical solution of the original system of Eqs. (1) and (2) and the system of differential equations of the dynamic model of an asynchronous electric motor [23] was carried out with the following basic values of the mechanical system parameters:  $M = 300 \text{ kg}$ ;  $m = 39, 24 \text{ kg}$ ;  $\varepsilon = 0, 035 \text{ m}$ ;  $I_1 = 0, 0068 \text{ kg} \cdot \text{m}^2$ ;  $I_2 = 0, 068 \text{ kg} \cdot \text{m}^2$ ;  $c_x = 6, 9 \cdot 10^5 \text{ N/m}$ ;  $\beta_x = 1500 \text{ kg/s}$ ; in addition, there were also used the parameters of the three-phase asynchronous electric motor 4A serie with power  $P_{mot} = 2, 2 \text{ kW}$  and synchronous rotation frequency  $n_s = 1500 \text{ rpm}$ .

According to Fig. 2 (curves 1), when the speed of rotation of the vibration exciter “sticks” in the natural frequency zone  $p_x$  ( $p_x = 48 \text{ s}^{-1}$ ), its oscillations are excited with large initial amplitudes, which are the result of superposition of high-frequency forced (with the doubled “sticking” frequency,  $2\omega \approx 92 \text{ s}^{-1}$ ;  $\omega \approx p_x$ ) and low-frequency damped (with natural frequency) oscillations.

Thus, when the Sommerfeld effect occurs, a clearly pronounced relatively long transient process takes place; the process represents biharmonic damped oscillations of the speed of a vibration exciter with a slow basic frequency  $p_{\psi}$  ( $p_{\psi} \ll \omega$ ). In this case, the total oscillations have a distinctive shape: the amplitude of the low-frequency

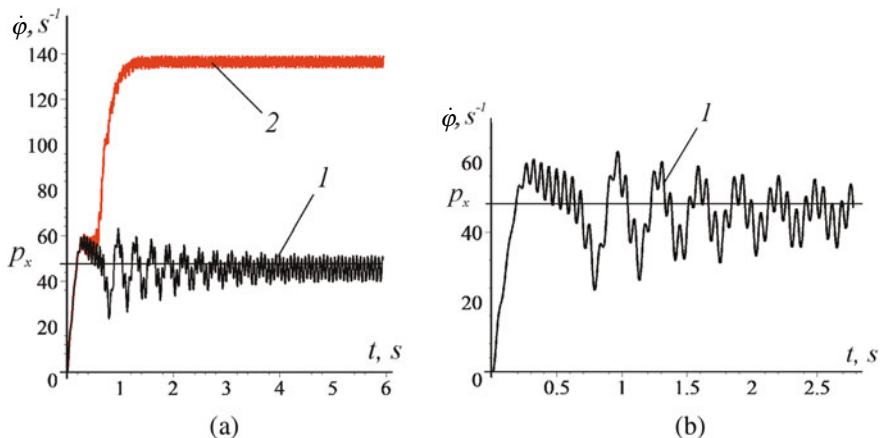


**Fig. 2** Time dependences of the vibration exciter speed for periods of movement of different duration (a, b), in the case of: 1—“sticking” of the vibration exciter speed ( $m\varepsilon = 1, 199 \text{ kg m}$ ); 2—passing of vibration exciter through the resonance zone ( $m\varepsilon = 1, 197 \text{ kg m}$ )

harmonic noticeably exceeds the amplitude of the high-frequency harmonic. The initial amplitudes of the oscillations under consideration are relatively large (the maximum reaches  $19,5\text{ s}^{-1}$ , while subsequently, in a steady state, the amplitudes decrease to  $11\text{ s}^{-1}$ ); damping of oscillations is relatively slow (more than  $5\text{ s}$ ).

The graphs in Fig. 2 convincingly demonstrate that slow oscillations of the vibration exciter speed are a transient process to its steady motion in the zone of the Sommerfeld effect.

It seems important to analyze the oscillations of the vibration machine’s drive during considered period of movement, and in the process to compare the cases of using the “hard” and “soft” drives. Note that no significant differences are observed on the graphs of the vibration exciter speed changing for drives of different stiffness.

According to the results obtained (Fig. 3): when the Sommerfeld effect occurs, no increased initial amplitudes of the drive oscillations are observed in all the cases under consideration; i.e. a clearly pronounced transition process does not occur. At the same time, it is clearly seen that along with fast oscillations of the drive with doubled rotation frequency of the vibration exciter, slow oscillations with a frequency  $p_\psi$  occur; the amplitudes of the slow harmonic are noticeably smaller than those of the fast one, and at the same time, they are damped.

It was found that when using a “soft drive”, its oscillations in the Sommerfeld zone will be very large. So, as follows from Fig. 3, a, the maximum amplitudes of the drive oscillations during this period of motion noticeably exceed the maximum amplitudes of the drive at the moment of the engine start, and much more than the amplitudes in the above resonant steady-state mode. Note that the parameters of the system, both when the rotor is “stuck” and when it passes through the resonance zone, are almost the same, excepting a slight difference in the static moments of the vibration exciters ( $m\varepsilon = 1,199\text{ kg m}$  and  $m\varepsilon = 1,197\text{ kg m}$ , consequently).

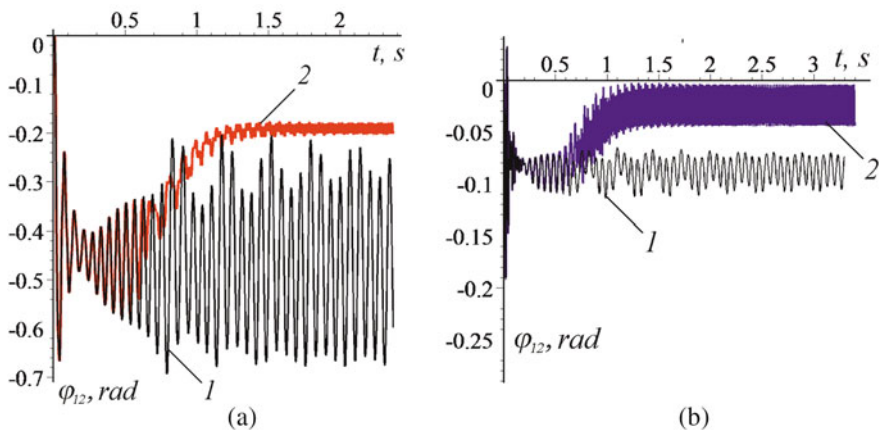


**Fig. 3** Change in angular deformation of the drive: **a**  $p_c = 88, 1^{-1}$ ,  $p_c \approx 2\omega$ ; **b**  $p_c \approx 203, 5^{-1}$ ;  $p_c \approx p_\psi$ , in the case of: 1—“stucking” of the rotors in the zone of the Sommerfeld effect; 2—passing through the resonance zone with exit to the operating mode

Note that in the example in Fig. 3a, due to the proximity of the frequency of the disturbing moment  $2\omega \approx 92 \text{ s}^{-1}$  and the natural frequency of the drive  $p_c = 88, 1 \text{ }^{-1}$ , the excited oscillations have the character of beats; this process is not steady; accompanying free oscillations quickly disappear; at the same time, the amplitudes of the continuing oscillations remain practically the same.

## 4 Results and Discussion

In accordance with the results obtained, when starting a vibration machine with a limited-power motor in the zone of the Sommerfeld effect, significant low-frequency (comparatively to the rotational speed) oscillations of the vibration exciter speed can be excited; the damping of these oscillations is quite long. Their amplitudes are the greater, the greater the value of the vibrational moment in the resonance zone.

It is shown that the oscillation amplitudes of the vibration machine's drive in the resonance zone substantially depend on the relation of its natural frequency  $p_c$  to the frequencies  $p_\psi$ ,  $\omega$  and  $2\omega$  ( $\omega$ —is the frequency of “stucking”). This means that the oscillations of the “soft drive” of the class of soft vibroisolating machines ( $\frac{\omega_w}{p_x} > 3$ ), in case of the Sommerfeld effect, can be quite large. Consequently, the occurrence of a stationary mode of motion in the zone of the Sommerfeld effect is dangerous for the drive of the vibration machine, as the maximum loaded mode of its operation.

It seems important that slow oscillations in the speed of a vibration exciter are the physical basis for the effectiveness of methods for controlling the start-up of devices with inertial vibration exciters. In addition, slow oscillations are at the heart of the “double start” method of vibration machines with inertial drive. These methods are based on the fact that in the resonance zone of the vibration machine, the periodic exchange of kinetic energy between the rotating vibration exciter and the oscillating bearing body is especially significant.

The results obtained will contribute to the choice of the parameters of the algorithms for the control systems of the start-up of vibration machines to facilitate their passage through the resonance zone.

## 5 Conclusions

When the frequency of the electric motor gets stuck in the resonance zone of the vibration machine, biharmonic damped oscillations of the speed of the vibration exciter are excited with the basic relatively slow frequency and rather large amplitudes. These oscillations represent a transient process to a steady-state mode of vibration exciter rotation in the zone of the Sommerfeld effect.

When the Sommerfeld effect occurs, the oscillations of the “soft drive” of vibration machines with inertial excitation will be large.

The critical frequencies of the drive, along with its natural frequency  $p_c$  (multiple frequencies), can also be considered the frequency of “stucking” of the electric motor in the resonance zone of the vibration machine  $\omega \approx p_x$ , the double frequency of “stucking”  $2\omega$ , as well as the frequency of slow oscillations of the speed of the vibration exciter  $p_\psi$  in the zone of the Sommerfeld effect.

## References

1. Sommerfeld, A.: Beiträge zum dynamischen ausbau der festigkeitslehre. Phys. Z.3, 266–286 (1902)
2. Kononenko, V.O.: Vibrating System of Limited Power Supply. Illife Books, London (1969)
3. Alifov, A.A., Frolov, K.V.: Interaction of Non-linear Oscillatory Systems with Energy Sources. CRC Press, New York (1990)
4. Blekhman, I.I.: Vibrational mechanics. Nonlinear dynamic effects, General approach, Applications. World Scientific, Singapore et al. (2000)
5. Balthazar, J.M., Mook, D.T., Weber, H.I., et al.: An overview on non-ideal vibrations. *Meccanica* **38**(6), 613–621 (2003)
6. Balthazar, J.M., Tusset, A.M., Brasil, R.M.L.R.F., et al.: An overview on the appearance of the Sommerfeld effect and saturation phenomenon in non-ideal vibrating systems (NIS) in macro and MEMS scales. *Nonlinear Dyn* **93**, 19–40 (2018)
7. Blekhman I.I.: Vibrational mechanics and vibrational rheology (theory and applications). M.: Fizmatlit (2018)
8. Blekhman, I.I., Kremer, E.B.: The dynamics of a complex machine assembly: vibration-induced drag on the rotation. *J. Mach. Manuf. Reliab.* № 4, 330–335 (2017)
9. Shahlaei-Far, S., Balthazar, J.M.: Method of direct separation of motions applied to a non-ideal electromechanical pendulum system. In: Awrejcewicz, J. (ed.) *Dynamical Systems in Applications. DSTA 2017. Springer Proceedings in Mathematics & Statistics*, vol. 249 (2018)
10. Beletskiy, V., Indeytsev, D., Fradkov, A.: Nonlinear problems of theory of oscillation and theory of control *Vibrational Mechanics. IMEP of RAS*, p. 528 (2009). (under redact.–SPb.: Nauka).
11. Varanis, M., Balthazar, J.M., Silva, A., Mereles, A.G., Pederiva, R.: Remarks on the Sommerfeld effect characterization in the wavelet domain. *J. Vib. Control* **25**(1), 98–108 (2019)
12. Filimonikhin, G., Yatsun, V., Kyrchenko, A., Hrechka, A., Shcherbyna, K.: Synthesizing a resonance anti-phase two-mass vibratory machine whose operation is based on the Sommerfeld effect. *East. Eur. J. Enterp. Technol.* **6/7**(108), 42–50 (2020)
13. Kossoski, A., Tusset, A.M., Janzen, F.C., Ribeiro, M.A., Balthazar, J.M.: Attenuation of the vibration in a non-ideal excited flexible electromechanical system using a shape memory alloy actuator In: *Vibration Engineering and Technology of Machinery: Proceedings of VETOMAC XV 2019*, pp. 431–444 (2021)
14. Shikhov, A.M., Rumyantsev, S.A., Azarov, E.B.: Enhanced energy efficiency in actuation and operation. *Min. Inf. Anal. Bull.* **4**, 137–145 (2020)
15. Yaroshevich, N., Zabrodets, I., Shymchuk, S., Yaroshevich, T.: Influence of elasticity of unbalance drive in vibration machines on its oscillations. *East. Eur. J. Enterp. Technol.* **5**(7)(95), 62–69 (2018)
16. Yaroshevich N., Yaroshevych O., Lyshuk, V.: Drive dynamics of vibratory machines with inertia excitation. In: Balthazar, J.M. (ed.) *Vibration Engineering and Technology of Machinery. Mechanisms and Machine Science*, vol. 95. Springer (2021)
17. Lanets, O.S., Dmytriv, V.T., Borovets, V.M., Derevenko, I.A., Horodetsky, I.M.: Analytical model of the two-mass above resonance system of the eccentric-pendulum type vibration table. *Int. J. Appl. Mech. Eng.* **25**(4), 116–129 (2020)

18. Blekhman, I.I., Indeitsev, D.A., Fradkov, A.L.: Slow motions in systems with inertial excitation of vibrations. *J. Mach. Manuf. Reliab.* **37**(1), 21–27 (2008)
19. Neishtadt, A.I.: Passage through a resonance in a two-frequency problem. *Dokl. Akad. Nauk SSSR* **221**, 301–304 (1975)
20. Pechenev, A.V.: On the motion of a vibrational system with limited excitation near a resonance. *Dokl. Akad. Nauk SSSR* **290**, 12–15 (1986)
21. Yaroshevich, N., Puts, V., Yaroshevich, T., Herasymchuk, O.: Slow oscillations in systems with inertial vibration exciters. *Vibroengineering Procedia* **32**, 20–25 (2020)
22. Tomchin, D.A., Fradkov, A.I. (2005) Control of rotor passing through the resonance zone on the basis of the method of velocity gradient. *Problems of machine building and reliability of machines*, Issue 5, pp. 66–71
23. Tchaban, V., Lyshuk, V.: Mathematical model vnit power asynchronous machines. Lutsk, LNTU, p. 116 (2013)

# Bifurcations “Cycle–Chaos–Hyperchaos” in Some Nonideal Electroelastic Systems



S. V. Donetskyi  and A. Yu. Shvets 

**Abstract** A non-ideal dynamic system “piezoceramic transducer—LC generator” is considered. Various scenarios of transition to deterministic chaos in such a system are described. For the first time, the implementation of the “chaos-chaos” and “chaos-hyperchaos” transitions according to the scenarios of generalized intermittency has been discovered.

## 1 Introduction

Any oscillatory system consists of two main elements, namely, a source of excitation of oscillations and the actual oscillatory load. If the power of the oscillation excitation source is comparable to the power consumed by the oscillatory load, then such systems are called nonideal systems or systems with limited excitation. In nonideal nonlinear dynamical systems, the interaction between the source of oscillation excitation and the oscillatory subsystem can lead to completely unexpected steady-state regimes, in particular to the emergence of the deterministic chaos. Especially interesting cases are when the occurrence of chaos is associated exclusively with the interaction between the excitation source and the oscillatory load, and not with the internal properties of the subsystems.

For the first time, studies of limited excitation were started in the works of Arnold Sommerfeld [27, 28]. In the future, such studies were continued by Timoshenko [29], Kononenko 1969, Nayfeh and Mook [19]. Among the works of recent decades, significant contribution was made by Krasnopolskaya [12, 13], Warminski and Balthazar [30], Balthazar et al. [2], Palacios Felix and Balthazar [20] and many others.

The main purpose of this paper is to study new bifurcations of the transition to deterministic chaos in some nonlinear dynamic system “piezoceramic transducer— analog generator of limited power.

---

S. V. Donetskyi · A. Yu. Shvets (✉)  
National Technical University of Ukraine “Igor Sikorsky Kyiv Polytechnic Institute”, Kyiv,  
Ukraine

## 2 Mathematical Model of System “piezoceramic Transducer-LC-Generator”

Let us consider a piezoceramic rod transducer, which is loaded on the acoustic medium and to which electrodes the electrical voltage is affixed, raised by the LC-generator (Fig. 1). The selection of the generator of such type is caused by the renaissance of its application observable now in the up-to-date technique. This is related to facts that the electrovacuum-tube (analogue) devices ensure higher metrological characteristic to comparison with the numeral devices.

In papers [14, 16] in strict accordance with the theory of the relationship between mechanical and electrical fields in piezoceramic media [1, 4, 9], as well as based on the general principles of the theory of systems with limited excitation (Kononenko 1969), a mathematical model of the “transducer-generator” system was derived. It is proved that such a mathematical model can be written in the form of the following system of ordinary differential equations:

$$\begin{aligned} \ddot{\varphi} + \omega_0^2 \varphi &= a_1 \dot{\varphi} + a_2 \dot{\varphi}^2 - a_3 \dot{\varphi}^3 - a_4 V, \\ \ddot{V} + \omega_1^2 V &= a_5 \varphi + a_6 \dot{\varphi} - a_7 \dot{V}. \end{aligned} \tag{1}$$

Here  $V(t)$ —voltage in the electrodes of the transducer;  $t$ —time;  $\varphi(t) = \int_0^t (e_g - E_g) dx$ ;  $e_g$ —tube grid voltage;  $E_g$ —the constant component of voltage  $e_g$ . A detailed description of all parameters of the mathematical model (1), each of which depends on many electrical and elastic properties of the “transducer-generator” system is given in the paper [16].

Note that the mathematical model (1) was derived for one specific type of dynamical systems. However, as it was subsequently established in this dynamic system, a unique variety of steady-state dynamic regimes is realized. So, in this system, all the main types of regular attractors were discovered, such as equilibrium positions, limit cycles and invariant tori [3, 16, 25]. Chaotic attractors, including hyperchaotic ones, were also found in the system [1, 3, 13, 22]. Transitions to chaos (hyperchaos)

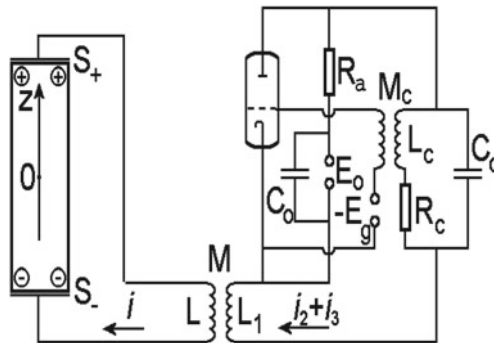


Fig. 1 Scheme of viewed system



through a cascade of period doubling bifurcations [7, 8] and through intermittency [18, 21] were identified. And at last, in papers [25, 26] self-excited, hidden and rare attractors were discovered in this system.

The dynamical system [1] has a wider variety of steady-state regimes and scenarios for the transition from one type of regime to another than, for example, the classical systems of Lorenz and Roessler. Such system is the “library” of regular and chaotic dynamics and can be used as a basic one in the study of general theory of dynamical systems.

### 3 Research Methodology and Numerical Results

The system of Eq. (1) is a nonlinear system of differential equations with a four-dimensional phase space. Therefore, in the general case, a solution to such a system can only be found using numerical or numerical-analytical methods. For the convenience of using such methods, we bring the system of Eq. (1) to a normal form. We introduce new “dimensionless” phase variables and “dimensionless” time by the formulas:

$$\xi = \frac{\varphi\omega_0}{E_g}, \quad \frac{d\xi}{d\tau} = \zeta, \quad \beta = \frac{V}{E_g}, \quad \frac{d\beta}{d\tau} = \gamma, \quad \tau = \omega_0 t. \quad (2)$$

Then the system of Eq. (1) can be written in the form:

$$\begin{aligned} \frac{d\xi}{d\tau} &= \zeta, & \frac{ds}{d\tau} &= -\xi + \alpha_1 s + \alpha_2 s^2 - \alpha_3 s^3 + \alpha_4 \beta, \\ \frac{d\beta}{d\tau} &= \gamma, & \frac{d\gamma}{d\tau} &= \alpha_5 \xi + \alpha_6 \zeta - \alpha_0 \beta - \alpha_7 \gamma. \end{aligned} \quad (3)$$

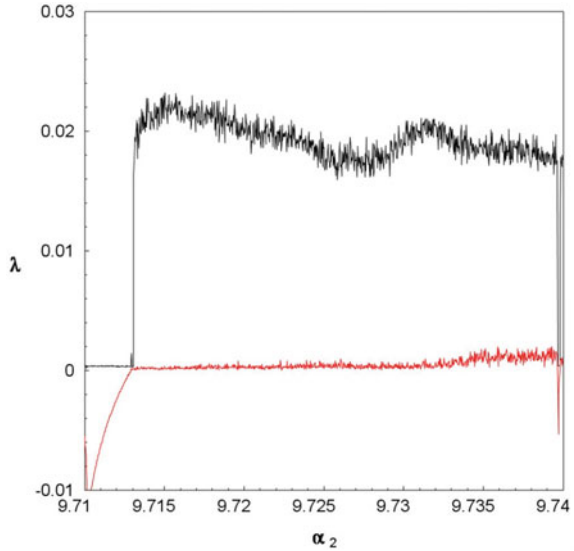
where the coefficients are equal to

$$\begin{aligned} \alpha_0 &= \omega_1^2/\omega_0^2, & \alpha_1 &= a_0/\omega_0, & \alpha_2 &= a_2 E_g/\omega_0, & \alpha_3 &= a_3 E_g^2/\omega_0, \\ \alpha_4 &= -a_4/\omega_0, & \alpha_5 &= a_5/\omega_0^3, & \alpha_6 &= a_6/\omega_0^2, & \alpha_7 &= a_7/\omega_0. \end{aligned}$$

For construction and study of attractors of system (3) (both regular and chaotic), a whole complex of numerical methods was applied. Such as, the fifth order method of Runge–Kutta with the application of correcting procedure of Dormand–Prince [10], the algorithm of Benettin [6, 5], the method of Henon [11] and some other methods. A detailed methodology for applying the above methods is described in the papers [17, 23].

At studying attractors of dynamical systems, a description of scenarios (a sequence of bifurcations) of transitions from an attractor of one type to an attractor of another type have great interest. In particular, investigation of scenarios of transitions from regular to chaotic attractors, as well as transitions from a chaotic attractor of one type to a chaotic attractor of another type. As noted earlier, transitions to chaos were

**Fig. 2** Dependence of two Lyapunov characteristic exponents on the parameter  $\alpha_2$



found in the “transducer-generator” system according to the Feigenbaum scenario (a cascade of period doubling bifurcations) and according to the Manneville-Pomeau scenario (through intermittency).

Let us show that in system (3) a transition is realized from a chaotic attractor of one type to a chaotic attractor of another type according to a more complex scenario of generalized intermittency. The scenario of generalized intermittency for nonideal hydrodynamic systems was described in papers [15, 16, 24].

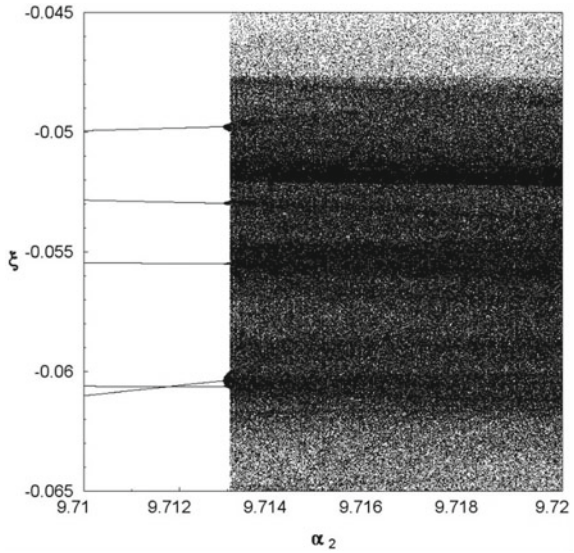
Suppose that the parameters of system (3) are respectively equal to  $\alpha_0 = -0.104$ ;  $\alpha_1 = 0.0535$ ;  $\alpha_3 = 9.95$ ;  $\alpha_4 = 0.103$ ;  $\alpha_5 = 0.0604$ ;  $\alpha_6 = 0.12$ ;  $\alpha_7 = 0.01$ . We choose  $\alpha_2$  as the bifurcation parameter.

In Fig. 2, the dependences of two Lyapunov characteristic exponents on the parameter  $\alpha_2$  are plotted. The maximal exponent  $\lambda_1$  is shown in black and the second  $\lambda_2$  is shown in red.

As can be seen from Fig. 2 for  $\alpha_2 < 9.7128$  maximal Lyapunov exponent will be zero, while the second exponent will be negative. This means that the attractor of system (3) for such values will be the limit cycle. At  $\alpha_2 > 9.7128$  maximal Lyapunov exponent becomes positive, which indicates the appearance of a chaotic attractor in system (3). Chaos in the system will exist for almost all the values of  $\alpha_2$  considered in Fig. 2, with the exception of a very narrow periodicity window at the right boundary of the interval  $9.7128 < \alpha_2 < 9.74$ . As for the second Lyapunov exponent, it (up to the error of the Benettin et al. method) will be zero at  $9.7128 < \alpha_2 < 9.7348$ . At  $\alpha_2 > 9.7348$  the second, the Lyapunov exponent becomes positive. The presence of two positive Lyapunov indicators indicates the emergence of a hyperchaotic attractor.

In Fig. 3 the phase-parametric characteristic (bifurcation tree) of the system (3) is shown. Limit cycles correspond to individual branches of this tree, and chaotic

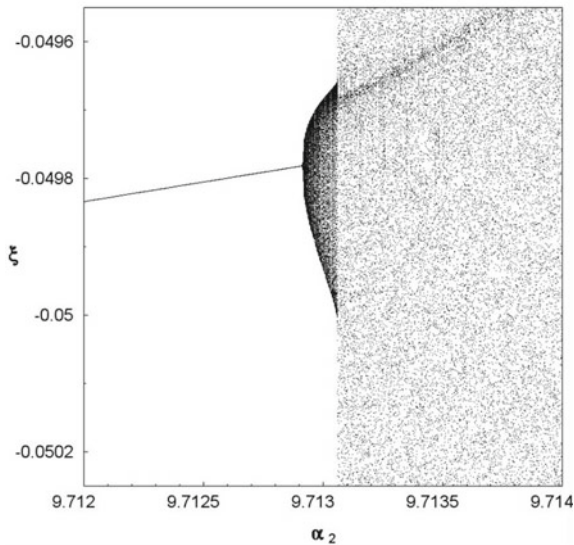
**Fig. 3** Phase-parametric characteristic



attractors correspond to densely black areas. In Fig. 3, two types of densely black areas are clearly visible. These densely black areas correspond to different types of chaotic attractors, which differ noticeably in the size of the attractor localization region in the phase space.

Figure 4 shows an enlarged fragment of the phase-parametric characteristics of the system (3). This figure makes it possible to very clearly illustrate the transitions

**Fig. 4** Enlarged fragment of phase-parametric characteristic



from one type of attractor to another. Thus, with an increase in the value of the parameter  $\alpha_2$  the limit cycle is replaced by a chaotic attractor with a small region of localization in the phase space. In turn, this chaotic attractor is replaced by a chaotic attractor of another type with a much larger area of localization in the phase space. In addition, Fig. 3 and Fig. 4 allow us to make an assumption about the scenario of the transition from a chaotic attractor of one type to a chaotic attractor of another type through generalized intermittency [16, 24]. However, most clear the scenario of such a transition can be revealed when studying the projections of the phase portraits of attractors and the distributions of invariant measures over the phase portraits.

Let us consider the dynamic behavior of system (3) with increasing parameter  $\alpha_2$ . In Fig. 5a), a projection of the phase portrait of the limit cycle at  $\alpha_2 = 9.7125$  is shown. As the parameter  $\alpha_2$  increases up to  $\alpha_2 \approx 9.7128$ , the limit cycle disappears and a chaotic attractor arises in the system. The projection of the phase portrait of a chaotic attractor constructed at  $\alpha_2 \approx 9.71305$  is shown in Fig. 5b). The transition from a limit cycle to a chaotic attractor occurs through intermittency trough one rigid bifurcation [18]. Despite the fact that the chaotic attractor is very similar in shape

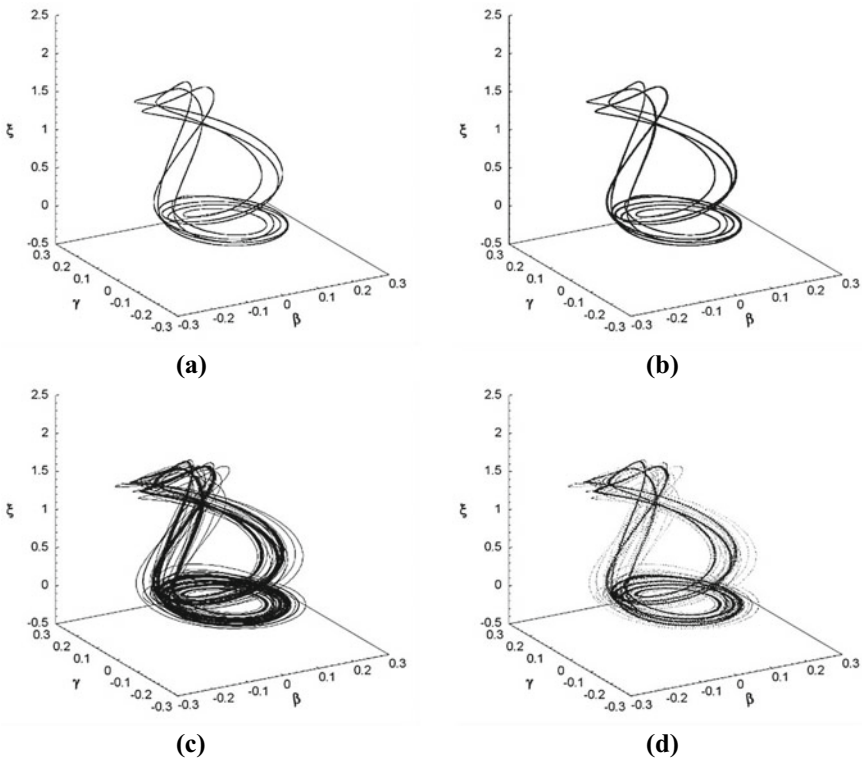


**Fig. 5** Limit cycle at  $\alpha_2 = 9.7125$  (a); Chaotic attractor at  $\alpha_2 = 9.7125$  (b); Chaotic attractor at  $\alpha_2 = 9.7131$  (c); Distribution of invariant measure at  $\alpha_2 = 9.713$  (d)

to the disappeared limit cycle, there are fundamental differences between them. The limit cycle consists of one orbitally stable trajectory along which the movement is strictly periodic. A chaotic attractor consists of an infinite set of arbitrarily close to each other open trajectories along which the motion is unpredictable.

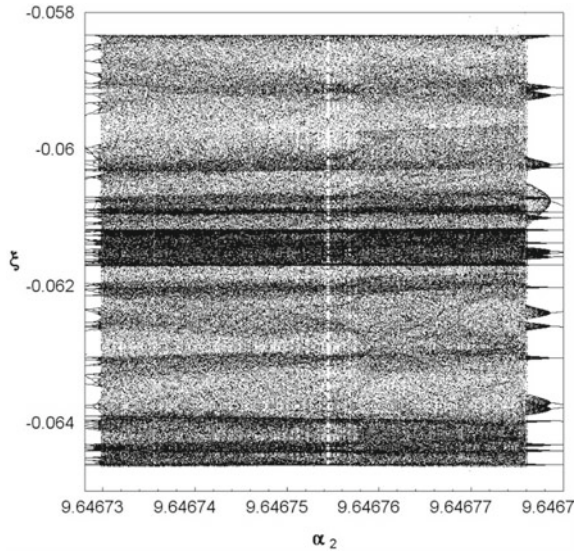
Note that such a chaotic attractor exists on a very small interval of variation of the parameter  $\alpha_2$ , and small increase in parameter  $\alpha_2$ , namely  $\alpha_2 \approx 9.7131$  leads to next rigid bifurcation after which chaotic attractor of another type arises. The existing chaotic attractor disappears and a chaotic attractor of a different type appears in the system. The projection of the phase portrait of the new chaotic attractor is shown in Fig. 5c). The distribution of the Krylov-Bogolyubov measure over the projection of the phase portrait of the new chaotic attractor is shown in Fig. 5d).

The scenario of such a transition from a chaotic attractor of one type to a chaotic attractor of another type is called generalized intermittency [16, 24]. In this scenario, after passing the bifurcation point, the chaotic attractor disappears and a chaotic attractor of a new type appears. Motion along the trajectory new chaotic attractor consists of two alternating phases, namely rough-laminar phase and turbulent phase. In the rough-laminar phase, the trajectory makes chaotic movements in a neighborhood of the trajectories of the disappeared chaotic attractor. Then, at an unpredictable moment of time, the trajectory leaves the localization region of the disappeared attractor and moves to more distant regions of the phase space. Rough-laminar phase corresponds to the much blacker areas in Fig. 5c, d. In turn, turbulent phase corresponds to much less darkened areas in Fig. 5c, d. After some time, the movement of the trajectory returns to the rough-laminar phase again. Then, trajectories switch to turbulent phase again. Such transitions are repeated an infinite number of times. From Fig. 5b, d it is especially clearly seen that the contours of the disappeared chaotic attractor are essentially rough laminar phase of a new chaotic attractor. Note that the duration of both rough-laminar and turbulent phases is unpredictable as are the moments of times of transition from one phase to another.

With a further increase in the value of the parameter  $\alpha_2$ , the second Lyapunov characteristic exponent also becomes positive. A chaotic attractor turns into a hyperchaotic one. Hyperchaotic attractors have two directions in the phase space along which the trajectories of the hyperchaotic attractor run away.

Finally, let us consider on one more interesting feature of the “transducer-generator” system. Figure 6 shows the phase-parametric characteristic for another interval of variation of the parameter  $\alpha_2$ . Here, as before, the separated “branches” of the bifurcation tree correspond to the limit cycles, and the densely black areas correspond to chaotic attractors. Clearly, it can be identified the transitions from densely black areas to densely black areas with noticeably greater size. At such transitions, the chaotic attractor of one type is replaced by a chaotic attractor of another type. As before, such transition is carried out according to the scenario of generalized intermittency. However, there is difference in sequence of bifurcations with such transitions. Therefore, on transitions corresponding to the Fig. 3, following bifurcation sequence occurs: limit cycle–intermittency–chaotic attractor of one type–generalized intermittency–chaotic attractor of another type. In turn, Fig. 6 corresponds to the following sequence of bifurcations: limit cycle–cascade of bifurcations of

**Fig. 6** Phase-parametric characteristic



period doubling–intermittency–chaotic attractor of one type–generalized intermittency–chaotic attractor of another type. Thus, first transition to chaos corresponding to Fig. 3 is carried out through one rigid bifurcation, and the first transition to chaos corresponding Fig. 6 is carried out through an infinite number of soft bifurcations.

In conclusion, we emphasize that implementation of the scenario of generalized intermittency for the “transducer-generator” system was found for the first time.

## References

1. Auld, B.A.: *Acoustic Fields and Waves in Solids*. Wiley, New York (1973)
2. Balthazar, J.M., Mook, D.T., et al.: An overview on non-ideal vibrations. *Meccanica* **38**(3), 613–621 (2003)
3. Balthazar, J.M., Palacios Felix, J.L., et al.: Nonlinear interactions in a piezoceramic bar transducer powered by vacuum tube generated by a nonideal source. *J. Comput. Nonlinear Dyn.* **4**(011013), 1–7 (2009)
4. Bazenov, V.M., Ulitko, A.F.: Examination dynamic behaviour of a piezoceramic stratum at instantaneous electrical loading. *Appl. Mech.* **11**(1), 22–27 (1975). (in russian)
5. Benettin, G., Galgani, L., et al.: Lyapunov Characteristic exponents for smooth dynamical systems and for Hamiltonian systems: a method for computing all of them. *Meccanica* **15**(1), 21–30 (1980)
6. Benettin, G., Galgani, L., Strelcyn, J.M.: Kolmogorov entropy and numerical experiments. *Phys. Rev. A* **14**, 2338–2342 (1976)
7. Feigenbaum, M.J.: Quantative universality for a class of nonlinear transformations. *J. Stat. Phys.* **19**(1), 25–52 (1978)
8. Feigenbaum, M.J.: The universal metric properties of nonlinear transformations. *J. Stat. Phys.* **21**(6), 669–706 (1979)

9. Grinchenko, V.T., Ulitko, A.F., Shulga, N.A.: *Electroelasticity*. Naukova Dumka, Kyiv (1989). (in russian)
10. Hairer, E., Norsett, S.P. et al.: *Solving ordinary differential equations. Nonstiff problems*. Springer, Berlin (1987)
11. Henon, M.: On the numerical computation of Poincaré maps. *Physica. D.* **5**, 412–415 (1982)
12. Krasnopolskaya, T.S.: Acoustic chaos caused by the Sommerfeld effect. *J. Fluids Struct.* **8**(7), 803–815 (1994)
13. Krasnopolskaya, T.S.: Chaos in acoustic subspace raised by the Sommerfeld-Kononenko effect. *Meccanica* **41**(3), 299–310 (2006)
14. Krasnopolskaya, T.S., Shvets, A.Yu.: Chaos in vibrating systems with limited power-supply. *Chaos* **3**(3), 387–395 (1993)
15. Krasnopolskaya, T.S., Shvets, A.Yu.: Chaotic surface waves in limited power-supply cylindrical tank vibrations. *J. Fluids Struct.* **8**(1), 1–18 (1994)
16. Krasnopolskaya, T.S., Shvets, A.Yu.: Deterministic chaos in a system generator-piezoceramic transducer. *Nonlin. Dyn. Syst. Theory* **6**(4), 367–387 (2006)
17. Krasnopolskaya, T.S., Shvets, A.Yu.: Dynamical chaos for a limited power supply oscillations in cylindrical tanks. *J. Sound Vibr.* **322**(3), 532–55 (2009)
18. Manneville, P., Pomeau, Y.: Different ways to turbulence in dissipative dynamical systems. *Physica D. Nonlinear Phenom* **1**(2), 219–226 (1980)
19. Nayfeh, A.H., Mook, D.T.: *Nonlinear Oscillations*. Wiley, New York (1979)
20. Palacios Felix, J.L., Balthazar, J.M.: Comments on a nonlinear and nonideal electromechanical damping vibration absorber, Sommerfeld effect and energy transfer. *Nonlinear Dyn.* **55**, 1–11 (2009)
21. Pomeau, Y., Manneville, P.: Intermittent transition to turbulence in dissipative dynamical systems. *Comm. Math. Phys.* **74**(2), 189–197 (1980)
22. Shvets, A.Yu., Krasnopolskaya, T.S.: Hyperchaos in piezoceramic systems with limited power-supply. *IUTAM Symposium on Hamiltonian Dynamics, Vortex Structures, Turbulence*, 313–322 (2008)
23. Shvets, A.Yu.: Deterministic chaos of a spherical pendulum under limited excitation. *Ukr. Math. J.* **59**, 602–614 (2007)
24. Shvets, A.Yu., Sirenko, V.A.: Scenarios of Transitions to Hyperchaos in Nonideal Oscillating Systems. *J. Math. Sci.* **243**(2), 338–346 (2019)
25. Shvets, A., Donetskiy, S.: Transition to deterministic chaos in some electroelastic systems In: Skiadas, C., Lubashevsky, I. (eds.) *11th Chaotic Modeling and Simulation International Conference. CHAOS 2018*. Springer Proceedings in Complexity. Springer, Cham, pp 257–264 (2019)
26. Shvets, A., Donetskiy, S.: Identification of Hidden and Rare Attractors in Some Electroelastic Systems with Limited Excitation In: Skiadas, C., Dimoticalis, Ya. (eds.) *13th Chaotic Modeling and Simulation International Conference. CHAOS 2020*. Springer Proceedings in Complexity. Springer, Cham, pp 865–878 (2021)
27. Sommerfeld, A.: Beiträge zum dynamischen Ausbau der Festigkeitslehre. *Physikalische Zeitschrift* **3**, 266–271 (1902)
28. Sommerfeld, A.: Beiträge zum dynamischen Ausbau der Festigkeitslehre. *Z. Ver. Dtsch. Ing.* **46**, 391–394 (1902)
29. Timoshenko, S.: *Vibration Problems in Engineering*. Van Nostrand Co., New York (1928)
30. Warminski, J., Balthazar, J.M., et al.: Vibrations of a non-ideal parametrically and self-excited model. *J. Sound Vibr.* **245**(2), 363–374 (2001)

# Nonlinear Dynamics of Self and Parametrically Excited Systems with Non-ideal Energy Source



Jerzy Warminski

**Abstract** Vibrations of a non-ideal system with nonlinear damping and periodically varying stiffness are presented in the chapter. The system is excited by rotating unbalanced mass attached to the DC motor with limited power. Rotation of the motor is tuned to the period of varying stiffness in 1:2 ratio which corresponds to the principal parametric resonance. Nonlinear damping is represented by Rayleigh model which may generate self-excitation. The analytical solutions obtained by Krylov–Bogoliubov–Mitropolsky method for the two degree of freedom model show an existence of the internal loop on the resonance curve and transition zones from periodic to quasi-periodic oscillations. Chaotic or hyper-chaotic vibrations are detected by numerical simulations and an influence of the non-ideal energy source on the motion type is presented.

## 1 Introduction

Structural elements of mechanical, aerospace or civil engineering objects are subjected to various excitation sources. Self-excited vibrations belong to a special class of vibrations occurring in the nature or in the structures produced by men. Their characteristic feature is that they are generated by constant input, independent of time [10, 13]. An energy transfer is controlled by the system itself and oscillation arise due to its internal properties. Classical examples are flutter of airplane wings, chatter in machining or shimmy of vehicle wheels. The self-excitation can be soft, with a stable limit cycle, or hard (catastrophic) when a limit cycle is unstable and a solution may tend to zero or to infinity. The second, totally different class, are vibrating systems with periodically varied coefficients [4, 9, 10]. In machine dynamics the coefficients are related to periodically changing stiffness or mass moment of inertia. The main feature of parametric oscillations is that for selected parameters instability zones occur and the amplitude of oscillations gets large values. These zones, called

---

J. Warminski (✉)

Mechanical Engineering Faculty, Department of Applied Mechanics,  
Lublin University of Technology, Lublin, Poland  
e-mail: [j.warminski@pollub.pl](mailto:j.warminski@pollub.pl)



parametric resonances, are dependent on amplitude and frequency of varied coefficients and damping of the system. Apart from self and parametric vibrations also the system can be excited by direct applied periodic force. Then the periodic component occurs on the right side of the equations and the model becomes inhomogeneous. In some cases all mentioned above vibrations may exist at the same time and then due to interactions interesting, and sometimes unexpected, phenomena may arise [1, 14, 15, 17]. If the model consists of self-excited terms and parametric with external excitations are tuned 1:2 they interact strongly in the vicinity of the principal parametric resonance [15]. Inside the resonance zone even five periodic solutions are possible but only two of them are stable. Moving away from the resonance the interaction with self-excitation becomes strong and then quasi-periodic oscillation takes place, followed by the second kind Hopf bifurcation.

Often in mathematical models excitations are defined by simple harmonic force and dynamics of the energy source (DC motor for example) and its interactions with the main system are neglected. This kind of model is called ideal [2]. In contrast, systems with limited power have to consider interactions with the main structure [5–7]. The effect of non-ideal energy source was first detected by Sommerfeld [11]. During the experimental tests Sommerfeld observed instabilities in a linear structure with one degree of freedom. The explanation was found when the characteristic of the motor was taken into account. The formulated complete model considered coupling with the energy source confirmed results obtained by experiment.

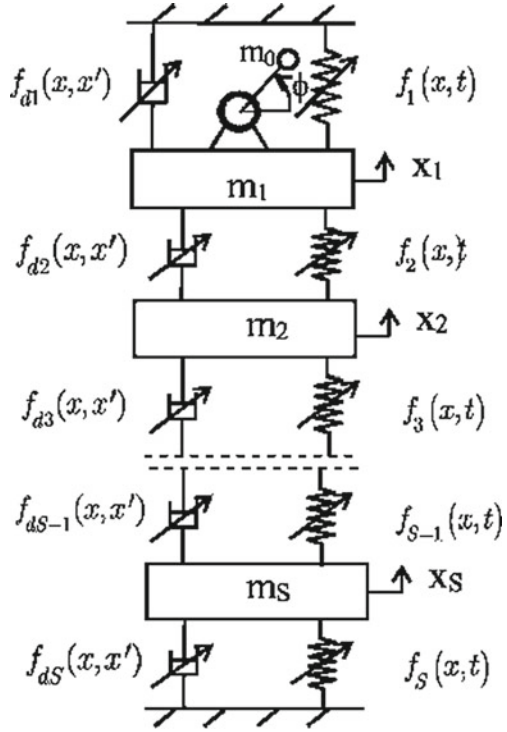
The non-ideal energy source introduces an additional degree of freedom and differential equations of motion are expressed by a coordinate describing motion of the energy source. In consequence the model is represented by autonomous equations without time given in a direct form [2]. The introduction of new coordinate  $\phi$  transforms harmonic excitation  $\sin\omega t$  into  $\sin\phi$ , which is a nonlinear function of the coordinate. A non-ideal model of a parametric and self-excited system with one degree of freedom was analyzed in paper [16] where the importance of the proper modelling of the energy source was presented, either for regular or chaotic oscillations. In the present chapter the model is extended for a chain of coupled oscillators. Detailed analysis is demonstrated for two coupled Rayleigh-Mathieu-Duffing oscillators with a non-ideal energy source.

## 2 Model of the Structure

A model of the studied structure is a chain of coupled oscillators excited by rotating unbalanced mass attached to the DC motor with limited power. Due to this fact the motor plays a role of a non-ideal energy source. The rotating mass excites the system with  $S$ -degrees of freedom but the oscillators influence the rotor motion as well. Thus, the coupled oscillators together with the rotor are represented by  $S + 1$  generalized coordinates.

As presented in Fig. 1 motion of oscillators is described by  $x_i$  coordinates,  $i = 1, 2, \dots, S$ , while  $\phi$  and is angle of rotation of the DC motor. The oscillators are connected

**Fig. 1** Non-ideal system with parametric and self-excitation with many degrees of freedom



by springs, considered in further investigation as nonlinear of Mathieu–Duffing type which are nonlinear and may produce parametric vibrations. Dampers in Fig. 1 are represented by nonlinear Rayleigh functions which may generate self-excitation.

Kinetic energy of the system takes the form

$$T = \frac{1}{2}(J_0 + m_0r^2)\dot{\phi}^2 + \frac{1}{2}m_0\dot{x}_1^2 + \dot{x}_1\dot{\phi}rm_0\cos\phi + \sum_{i=1}^s \frac{1}{2}m_i\dot{x}_i^2 \quad (1)$$

where  $r, m_0, J_0$  are radius, unbalanced mass and mass moment of inertia of the rotor and  $m_i$  is mass of the selected oscillator.

Let us assume temporarily that the system is linear and conservative, then its potential energy is defined as

$$V = \frac{1}{2}k_1x_1^2 + m_0g(x_1 + r\sin\phi) + \sum_{i=1}^{s-1} \frac{1}{2}k_{i,i+1}(x_i - x_{i+1})^2 + \frac{1}{2}k_Sx_S^2 \quad (2)$$

where,  $g$  is gravity acceleration,  $x_i$  displacement of  $m_i$  mass,  $k_I$ ,  $k_S$ ,  $k_{i,i+I}$  linear stiffness of the first spring, the last spring, and springs connecting  $i$  and  $i + I$  oscillators. Applying kinetic and potential energies to Lagrange equations of the second kind, and considering notation presented in Fig. 1, we obtain a set of  $S + I$  ordinary differential equations of motion of coupled oscillators with the DC motor. The terms related to static displacements and gravity force components are equal therefore they are pared. The term  $m_0 g r \cos\phi$  is also assumed as small and can be neglected [7].

To include nonlinear damping and stiffens the additional nonlinear functions  $\tilde{f}$  are added to the model. These functions depend on generalized coordinates and velocities. We assume that nonlinearities are of  $\varepsilon$  order, where  $\varepsilon$  is a formal small parameter. Thus, equations of motion of the complete nonlinear system take the final form

$$\begin{aligned} \ddot{\phi} &= \varepsilon \left[ \tilde{G}(\dot{\phi}) - \tilde{q}_2 \ddot{X}_1 \cos\phi \right] \\ \ddot{X}_1 + M_1(a_{11}X_1 + a_{12}X_2 + \dots + a_{1S}X_S) &= \varepsilon M_1 \tilde{f}_1 + \tilde{q}_1 \dot{\phi}^2 \sin\phi - \tilde{q}_1 \ddot{\phi} \cos\phi \\ \ddot{X}_2 + M_2(a_{21}X_1 + a_{22}X_2 + \dots + a_{2S}X_S) &= \varepsilon M_2 \tilde{f}_2 \\ &\vdots \\ \ddot{X}_S + M_S(a_{S1}X_1 + a_{S2}X_2 + \dots + a_{SS}X_S) &= \varepsilon M_S \tilde{f}_S \end{aligned} \quad (3)$$

Functions with tilde are expressed by small parameter,  $\tilde{G}(\dot{\phi}) = \varepsilon G(\dot{\phi})$  and  $\tilde{f}_i = \varepsilon f_i$ . Furthermore, Eq. (3) are expressed in dimensionless form by introducing dimensionless time  $\tau = \omega_1 t$  and coordinates  $X_j = \frac{x_j}{x_0}$ , where  $\omega_1 = \sqrt{\frac{k_1}{m_1}}$ ,  $x_0 = \frac{m_1 g}{k_1}$ . Parameters  $a_{ij}$  represent linear parts of stiffness coefficients,  $M_i = \frac{m_i}{m_1}$ ,  $q_1 = \frac{m_0 r}{M + m_0}$ ,  $q_2 = \frac{m_0 r}{J_0 + m_0 r^2}$ ,  $\tilde{q}_1 = \varepsilon q_1$  and functions  $\tilde{f}_i = \tilde{f}_i(X_1, X_2, \dots, X_S, \dot{X}_1, \dot{X}_2, \dots, \dot{X}_S, \tau)$  are nonlinear functions of dimensionless time and coordinates.

The first equation of set (3) is a driving equation of the DC motor defined as

$$G(\dot{\phi}) = L(\dot{\phi}) - H(\dot{\phi}) \quad (4)$$

where  $H(\dot{\phi})$  is a resistant torque and  $L(\dot{\phi})$  is torque generated by the motor. According to [2, 7],  $G(\dot{\phi})$  can be accepted by the linear function

$$G(\dot{\phi}) = u_1 - u_2 \dot{\phi} \quad (5)$$

approximating the resultant torque generated by the rotor. Coefficient  $u_1$  represent voltage supplied to the DC motor while  $u_2$  depends on the motor characteristic. Excitation of the system occurs in the second equation of Eq. (3). It is worth mentioning that the model is *time independent* which is characteristic feature of *non-ideal systems*.

### 3 Two Degrees of Freedom Model with Non-ideal Energy Source

Detailed analysis of the considered system is performed for two degrees of freedom model presented in Fig. 2.

Equation of motion of the presented model take the form

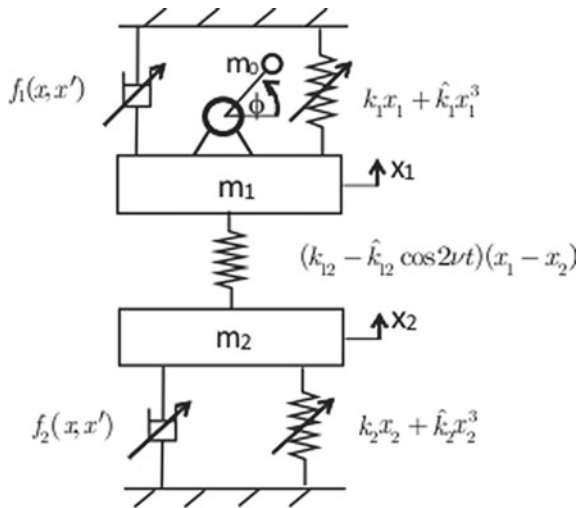
$$\begin{aligned}
 (J_0 + m_0 r^2) \phi'' &= G(\phi') - m_0 r x''_1 \cos \phi \\
 m_1 x''_1 + f_1(x, x') + k_1 x_1 + \hat{k}_1 x_1^3 + (k_{12} - \hat{k}_{12} \cos 2\nu t)(x_1 - x_2) & \\
 &= m_0 r \phi'^2 (\sin \phi - \phi'' \cos \phi) \\
 m_2 x''_2 + f_2(x, x') + k_2 x_2 + \hat{k}_2 x_2^3 - (k_{12} - \hat{k}_{12} \cos 2\nu t)(x_1 - x_2) &= 0
 \end{aligned}
 \tag{6}$$

where prime denotes derivative with respect to time.

The system is composed of two self-excited oscillators with nonlinear damping of Rayleigh type defined as:  $f_1 = -\alpha_1 X'_1 + \beta_1 X_1^3$ ,  $f_2 = -\alpha_2 X'_2 + \beta_2 X_2^3$  and nonlinear Duffing springs:  $k_1 x_1 + \hat{k}_1 x_1^3$ ,  $k_2 x_2 + \hat{k}_2 x_2^3$ . The oscillators are coupled by a linear spring with periodically varied stiffness  $\hat{k}_{12} \cos 2\nu t$ . The system is excited by non-ideal energy source—DC motor with the rotating unbalanced mass.

Introducing dimensionless time  $\tau = \omega_1 t$ , where  $\omega_1^2 = \frac{k_1}{m_1}$ ,  $m_1 = m_{10} + m_0$ , and small formal parameter  $\varepsilon$ , Eq. (6) is transformed to the form

**Fig. 2** Non-ideal system with parametric and self-excitation with two degrees of freedom



$$\begin{aligned}
\ddot{\phi} &= \varepsilon \left[ \tilde{G}(\phi) - \tilde{q}_2 \ddot{X}_1 \cos\phi \right] \\
\ddot{X}_1 + \delta_1 X_1 + \delta_{12}(X_1 - X_2) &= \varepsilon \left[ \tilde{f}_1(X_1, X_2, \dot{X}_1, \dot{X}_2, \tau) + \tilde{q}_1(\dot{\phi}^2 \sin\phi - \ddot{\phi} \cos\phi) \right] \\
\ddot{X}_2 + M\delta_2 X_2 - M\delta_{12}(X_1 - X_2) &= \varepsilon \left[ M \tilde{f}_2(X_1, X_2, \dot{X}_1, \dot{X}_2, \tau) \right]
\end{aligned} \tag{7}$$

where dot denotes derivative with respect to dimensionless time  $\tau$ .

Equations (7) are transformed from generalized coordinates  $X_i$  to quasi-normal coordinates  $Y_i$  by a linear transformation

$$\begin{aligned}
Y_1 &= X_1 + \lambda_{21} X_2 + \dots + \lambda_{s1} X_s \\
Y_2 &= X_1 + \lambda_{22} X_2 + \dots + \lambda_{s2} X_s \\
&\vdots \\
Y_s &= X_1 + \lambda_{2s} X_2 + \dots + \lambda_{ss} X_s
\end{aligned} \tag{8}$$

where  $\lambda_{ij}$  are coefficients of linear modes normalized to the first coordinate, therefore,  $\lambda_{i1} = I$ .

After transformation to normal coordinates we get

$$\ddot{\phi} = \varepsilon \left[ \tilde{\Gamma}(\omega) + \tilde{q}_2(\psi_1 \ddot{Y}_2 - \psi_2 \ddot{Y}_1) \cos\phi \right] \tag{9}$$

$$\begin{aligned}
\ddot{Y}_1 + p_1^2 Y_1 &= \varepsilon \left[ -\tilde{F}_{d1} - \tilde{\gamma}_1(Y_2 \psi_1 - Y_1 \psi_2)^3 + (Y_2 \eta_1 - Y_1 \eta_2) \tilde{\mu} \cos 2\phi \right] \\
&\quad + M\lambda_{12} \left[ -\tilde{F}_{d2} - \tilde{\gamma}_2 \chi^3 (Y_1 - Y_2)^3 - (Y_2 \eta_1 - Y_1 \eta_2) \tilde{\mu} \cos 2\phi \right]
\end{aligned} \tag{10}$$

$$\begin{aligned}
\ddot{Y}_2 + p_2^2 Y_2 &= \varepsilon \left[ -\tilde{F}_{d1} - \tilde{\gamma}_1(Y_2 \psi_1 - Y_1 \psi_2)^3 + (Y_2 \eta_1 - Y_1 \eta_2) \tilde{\mu} \cos 2\phi \right] \\
&\quad + M\lambda_{22} \left[ -\tilde{F}_{d2} - \tilde{\gamma}_2 \chi^3 (Y_1 - Y_2)^3 - (Y_2 \eta_1 - Y_1 \eta_2) \tilde{\mu} \cos 2\phi \right]
\end{aligned} \tag{11}$$

where

$$\begin{aligned}
\tilde{F}_{d1} &= \left[ -\tilde{\alpha}_1 + \tilde{\beta}_1 (\psi_1 \dot{Y}_2 - \psi_2 \dot{Y}_1)^2 \right] (\psi_1 \dot{Y}_2 - \psi_2 \dot{Y}_1), \\
\tilde{F}_{d2} &= \left[ -\tilde{\alpha}_2 + \tilde{\beta}_2 \chi^2 (\dot{Y}_1 - \dot{Y}_2)^2 \right] \chi (\dot{Y}_1 - \dot{Y}_2),
\end{aligned}$$

are Rayleigh damping functions expressed in normal coordinates,  $p_1$  and  $p_2$  are natural frequencies of the system. Parametric excitation is represented by term  $\tilde{\mu} \cos 2\phi$  with amplitude  $\tilde{\mu}$  and frequency  $2\dot{\phi}$

If  $\varepsilon$  is equal to zero then the system is fully uncoupled. However, if  $\varepsilon$  is a small positive number then all coordinates are fully coupled and depending on the angular velocity of the DC motor and frequency of the periodically varying stiffness various resonance states can occur. We focus on the resonance zone when the rotor

speed is synchronized with the parametric excitation in the ration 1:2. This situation corresponds to the principal parametric resonance. Additionally the system includes self-excitations which interact with parametric and externally excited vibrations.

### 3.1 Analytical Solutions

Let us consider vibrations around the principal parametric resonance. The rotor rotates with angular velocity  $\dot{\phi} = \omega_1$  in the vicinity of the first natural frequency  $p_1$ , thus we can write

$$p_1 - \omega_1 = \varepsilon \Delta_1 \tag{12}$$

where  $\Delta_1$  is a frequency detuning parameter. Parametric excitation frequency is tuned with the rotor speed.

We also assume that system is weakly nonlinear and therefore the first quasi-normal coordinate  $Y_1$  plays the main role in the response and the second  $Y_2$  is close to zero in the first order approximation. Thus, Eqs. (9)–(11) are reduced to the form

$$\frac{d^2\phi}{dt} = \varepsilon[\Gamma(\omega_1) + \tilde{q}_2\psi_2\ddot{Y}_1\cos\phi] \tag{13}$$

$$\begin{aligned} \ddot{Y}_1 + p_1^2 Y_1 = \varepsilon \left\{ -\tilde{\alpha}_1\psi_2\dot{Y}_1 + \tilde{\beta}_1\psi_2^3\dot{Y}_1^3 + \tilde{\gamma}_1\psi_2^3Y_1^3 - Y_1\eta_2\tilde{\mu}\cos2\phi \right. \\ \left. + \tilde{q}_1(\omega^2\sin\phi - \ddot{\phi}\cos\phi) + M\lambda_{12} \left[ \tilde{\alpha}_2\chi\dot{Y}_1 - \tilde{\beta}_2\chi^3\dot{Y}_1^3 - \tilde{\gamma}_2\chi^3Y_1^3 + Y_1\eta_2\tilde{\mu}\cos\phi \right] \right\} \end{aligned} \tag{14}$$

For the weakly nonlinear system we assume that vibrations amplitude and the angular velocity  $\omega_1$  are slowly varying in time. To determine analytical solutions it is convenient to introduce new coordinates

$$Y_1 = A\cos(\phi + \psi) \tag{15}$$

$$\dot{Y}_1 = -Ap_1\cos(\phi + \psi) \tag{16}$$

Computing the first time derivative of  $Y_1$  and comparing with Eq. (16) we get

$$\frac{dA}{dt}\cos(\phi + \psi) - \frac{d\psi}{dt}A\sin(\phi + \psi) = (\omega_1 - p_1)A\sin(\phi + \psi) \tag{17}$$

The second time derivative takes the form

$$\ddot{Y}_1 = -\frac{dA}{dt}p_1\sin(\phi + \psi) - \left(\omega_1 + \frac{d\psi}{dt}\right)Ap_1\cos(\phi + \psi) \quad (18)$$

Substituting (15)–(18) into Eqs. (13)–(14) we get a set of the first order differential equations

$$\frac{d\omega_1}{dt} = \varepsilon \left\{ \tilde{\Gamma}(\omega_1) - \tilde{q}_2\psi_2A_1p_1\omega\cos\phi\cos(\phi + \psi) \right\} \quad (19)$$

$$\frac{dA}{dt} = \varepsilon \{ f_{1A}(A, \phi, \psi) + M\lambda_{12}f_{2A}(A, \phi, \psi) \} \sin(\phi + \psi) + \varepsilon^2 \dots \quad (20)$$

$$\frac{d\psi}{dt} = \varepsilon \left\{ \Delta_1 + \frac{1}{A} [f_{1A}(A, \phi, \psi) + M\lambda_{12}f_{2A}(A, \phi, \psi)] \right\} \cos(\phi + \psi) + \varepsilon^2 \dots \quad (21)$$

where

$$\begin{aligned} f_{1A}(A, \phi, \psi) &= -\frac{\tilde{q}_1\omega_1^2}{p_1}\sin\phi - A\tilde{\alpha}_1\psi_2\sin(\phi + \psi) + \frac{3}{4}A^3p_1^2\tilde{\beta}_1\psi_2^3\sin(\phi + \psi) \\ &\quad - \frac{1}{4}A^3p_1^2\tilde{\beta}_1\psi_2^3\sin 3(\phi + \psi) + \frac{A\tilde{\mu}}{2p_1}\eta_2\cos(\phi - \psi) + \frac{A\tilde{\mu}}{2p_1}\eta_2\cos(3\phi + \psi) \\ &\quad - \frac{3}{4}\frac{A^3\tilde{\gamma}_1}{p_1}\psi_2^3\cos(\phi + \psi) - \frac{1}{4}\frac{A^3\tilde{\gamma}_1}{p_1}\psi_2^3\cos 3(\phi + \psi) \\ f_{2A}(A, \phi, \psi) &= A\tilde{\alpha}_2\chi\sin(\phi + \psi) - \frac{3}{4}A^3p_1^2\tilde{\beta}_2\chi^3\sin(\phi + \psi) \\ &\quad + \frac{1}{4}A^3p_1^2\tilde{\beta}_2\chi^3\sin 3(\phi + \psi) - \frac{A\tilde{\mu}}{2p_1}\eta_2\cos(\phi - \psi) - \frac{A\tilde{\mu}}{2p_1}\eta_2\cos(3\phi + \psi) \\ &\quad + \frac{3}{4}\frac{A^3\tilde{\gamma}_2}{p_1}\chi^3\cos(\phi + \psi) + \frac{1}{4}\frac{A^3\tilde{\gamma}_2}{p_1}\chi^3\cos 3(\phi + \psi) \end{aligned}$$

Functions  $A(t)$ ,  $\phi(t)$ ,  $\psi(t)$  are slowly changing in time. To find the approximate solutions we apply Krylov–Bogoliubov–Mitropolsky method [3]. In the first approximation we write

$$\omega_1 = \Omega_1 + \varepsilon U_1(\phi_1, \Omega_1, a_1, \xi_1) \quad (22)$$

$$A = a_1 + \varepsilon U_2(\phi, \Omega_1, a_1, \xi_1) \quad (23)$$

$$\psi = \xi_1 + \varepsilon U_3(\phi_1, \Omega_1, a_1, \xi_1) \quad (24)$$

where  $U_1(\phi, \Omega, a, \xi)$ ,  $U_2(\phi, \Omega, a, \xi)$ ,  $U_3(\phi, \Omega, a, \xi)$  are also slowly varying functions. To get solutions for  $\Omega_I$ ,  $a_I$ ,  $\xi_I$ , we average the right sides of Eqs. (19)–(21) through the vibration period

$$\frac{d\Omega_1}{dt} = \frac{\varepsilon}{2\pi} \int_0^{2\pi} f_{\Omega_1} d\varphi, \quad \frac{da_1}{dt} = \frac{\varepsilon}{2\pi} \int_0^{2\pi} f_{a_1} d\varphi, \quad \frac{d\xi_1}{dt} = \frac{\varepsilon}{2\pi} \int_0^{2\pi} f_{\xi_1} d\varphi \quad (25)$$

and we obtain

$$\frac{d\Omega_1}{dt} = \varepsilon \left\{ \Gamma(\Omega_1) - \frac{1}{2} a_1 p_1 \tilde{q}_2 \Omega_1 \psi_2 \cos \xi_1 \right\} \quad (26)$$

$$\begin{aligned} \frac{da_1}{dt} = \varepsilon \left\{ -\frac{1}{2} \tilde{\alpha}_1 \psi_1 a_1 + \frac{3}{8} a_1^3 p_1^2 \tilde{\beta}_1 \psi_2^3 + \frac{1}{4} a_1 \frac{\tilde{\mu}}{p_1} \eta_2 \sin 2\xi_1 \right. \\ \left. + M\lambda_{12} \left[ \frac{1}{2} \tilde{\alpha}_2 \chi a_1 - \frac{3}{8} a_1^3 p_1^2 \tilde{\beta}_2 \chi^3 - \frac{1}{4} a_1 \frac{\tilde{\mu}}{p_1} \eta_2 \sin 2\xi_1 \right] - \frac{1}{2} \tilde{q}_1 \frac{\Omega_1^2}{p_1} \cos \xi_1 \right\} \end{aligned} \quad (27)$$

$$\begin{aligned} \frac{d\xi_1}{dt} = \varepsilon \left\{ \Delta_1 - \frac{3}{8} a_1^2 \frac{\tilde{\gamma}_1}{p_1} \psi_2^3 + \frac{1}{4} \frac{\tilde{\mu}}{p_1} \eta_2 \cos 2\xi_1 \right. \\ \left. + M\lambda_{12} \left[ \frac{3}{8} a_1^2 \frac{\tilde{\gamma}_2}{p_1} \chi^3 - \frac{1}{4} \frac{\tilde{\mu}}{p_1} \eta_2 \cos 2\xi_1 \right] + \frac{1}{2} \tilde{q}_1 \frac{\Omega_1^2}{a_1 p_1} \sin \xi_1 \right\} \end{aligned} \quad (28)$$

In a steady state  $\frac{d\Omega_1}{dt} = 0$ ,  $\frac{da_1}{dt} = 0$ ,  $\frac{d\xi_1}{dt} = 0$ , thus Eqs. (26)–(28) become nonlinear algebraic equations enabling determining amplitude and phase of vibrations and angular velocity of the motor in the vicinity of the first principal parametric resonance.

### 3.2 Stability Analysis

Stability analysis of the obtained solutions is based on Eqs. (26)–(28) which can be written in the consistent form

$$\begin{aligned} \frac{d\Omega_1}{dt} &= \Gamma_1(a_1, \Omega_1, \xi_1) \\ \frac{da_1}{dt} &= \Gamma_2(a_1, \Omega_1, \xi_1) \\ \frac{d\xi_1}{dt} &= \Gamma_3(a_1, \Omega_1, \xi_1) \end{aligned} \quad (29)$$

Perturbing above equations and subtracting unperturbed from perturbed we get a set of equations in perturbations

$$\begin{aligned} \frac{d\delta_{\Omega_1}}{dt} &= \left( \frac{\partial \Gamma_1}{\partial \Omega_1} \right)_0 \delta_{\Omega_1} + \left( \frac{\partial \Gamma_1}{\partial a_1} \right)_0 \delta_{a_1} + \left( \frac{\partial \Gamma_1}{\partial \xi_1} \right)_0 \delta_{\xi_1} \\ \frac{d\delta_{a_1}}{dt} &= \left( \frac{\partial \Gamma_2}{\partial \Omega_1} \right)_0 \delta_{\Omega_1} + \left( \frac{\partial \Gamma_2}{\partial a_1} \right)_0 \delta_{a_1} + \left( \frac{\partial \Gamma_2}{\partial \xi_1} \right)_0 \delta_{\xi_1} \\ \frac{d\delta_{\xi_1}}{dt} &= \left( \frac{\partial \Gamma_3}{\partial \Omega_1} \right)_0 \delta_{\Omega_1} + \left( \frac{\partial \Gamma_3}{\partial a_1} \right)_0 \delta_{a_1} + \left( \frac{\partial \Gamma_3}{\partial \xi_1} \right)_0 \delta_{\xi_1} \end{aligned} \quad (30)$$



where  $\delta$  means variation of the selected function and the subscript "0" denotes derivatives in the steady state. Stability depends on the values of the roots of the characteristic determinant of (30). The solution is stable if all real parts of the roots are negative, otherwise the system is unstable.

The derivatives take definitions

$$\begin{aligned} \left(\frac{\partial \Gamma_1}{\partial \Omega_1}\right) &= -\varepsilon \tilde{U}_2 - \frac{1}{2} \varepsilon a p_1 \tilde{q}_2 \psi_2 \cos \xi_1, \quad \left(\frac{\partial \Gamma_1}{\partial a}\right) = -\frac{1}{2} \varepsilon p_1 \tilde{q}_2 \psi_2 \Omega_1 \cos \xi_1, \\ \left(\frac{\partial \Gamma_1}{\partial \xi_1}\right) &= \frac{1}{2} \varepsilon a p_1 \tilde{q}_2 \psi_2 \Omega_1 \sin \xi_1, \quad \left(\frac{\partial \Gamma_2}{\partial \Omega_1}\right)_0 = -\varepsilon \frac{\tilde{q}_1 \Omega_1}{p_1} \cos \xi_1, \\ \left(\frac{\partial \Gamma_2}{\partial a}\right)_0 &= \frac{1}{2} \varepsilon \left[ -\tilde{\alpha}_1 \psi_2 + \frac{9}{4} a^2 p_1^2 \tilde{\beta}_1 \psi_2^3 + \frac{\eta_2}{2 p_1} \tilde{\mu} \sin 2 \xi_1 + M \lambda_{21} \left( \tilde{\alpha}_2 \chi - \frac{9}{4} a^2 p_1^2 \tilde{\beta}_2 \chi^3 - \frac{\eta_2}{2 p_1} \tilde{\mu} \sin 2 \xi_1 \right) \right] \\ \left(\frac{\partial \Gamma_2}{\partial \xi_1}\right) &= \frac{1}{2 p_1} \varepsilon (a \tilde{\mu} \eta_2 \cos 2 \xi_1 - M \lambda_{21} a \tilde{\mu} \eta_2 \cos 2 \xi_1 + \tilde{q}_1 \Omega_1^2 \sin \xi_1), \\ \left(\frac{\partial \Gamma_3}{\partial a}\right) &= \frac{1}{2 p_1} \varepsilon \left( -\frac{3}{2} a \tilde{\gamma}_1 \psi_2^3 + \frac{3}{2} M \lambda_{21} a \tilde{\gamma}_2 \chi^3 - \frac{1}{a^2} \tilde{q}_1 \Omega_1^2 \sin \xi_1 \right), \\ \left(\frac{\partial \Gamma_3}{\partial \xi_1}\right)_0 &= \frac{1}{2 p_1} \varepsilon \left( \frac{\tilde{q}_1}{a} \Omega_1^2 \cos \xi_1 - \tilde{\mu} \eta_2 \sin 2 \xi_1 - M \lambda_{21} \eta_2 \tilde{\mu} \sin 2 \xi_1 \right). \end{aligned}$$

## 4 Numerical Analysis of Regular Oscillations

Nonlinear oscillations of the two degrees freedom model with non-ideal energy source and parametric and self-excitations are analyzed for the following data

$$\alpha_1 = 0.1, \beta_1 = 0.05, \gamma_1 = 0.1, \alpha_2 = 0.1, \beta_2 = 0.05, \gamma_2 = 0.1,$$

$$\mu = 0.2, M = 0.5, \delta_1 = 1, \delta_{12} = 0.3, \delta_2 = 1 \quad (31)$$

Natural frequencies of the system, modal coefficients and coefficients related to coordinate transformation take values

$$p_1 = 0.766, p_2 = 1.168, \lambda_{12} = 4.754, \lambda_{22} = -0.421$$

$$\chi = 0.192, \psi_1 = 0.919, \psi_2 = 0.0813, \eta_1 = 1.112, \eta_2 = 0.112 \quad (32)$$

Let us assume that the characteristic of the DC motor is defined by function  $\Gamma(\dot{\phi})$  (Eq. (5)). Parameter  $u_1$  (related to the supplied voltage) is varied in domain  $u_1 \in (0, 1.8)$ , parameter  $u_2$  is fixed,  $u_2 = 1.5$ .

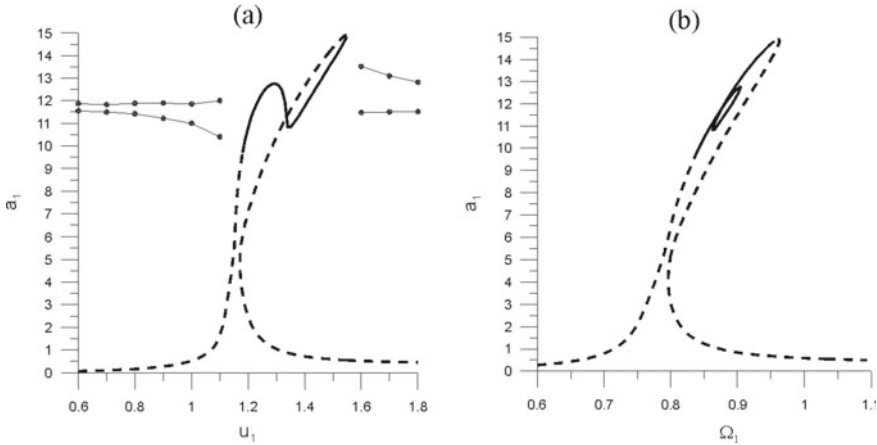


**Fig. 3** Vibration amplitudes in the vicinity of the principal parametric resonance around frequency  $p_1$ , **a** amplitude against  $u_1$  parameter and **b** amplitude against excitation frequency  $\Omega_1$

Resonance curves for the principal parametric resonance are presented in Fig. 3. The curves in black are determined for the steady state on the basis of analytical solutions (26)–(28) while the stability checked by computing characteristic roots of Eq. (30). Unstable solutions are marked by dashed lines. The analytical solutions are stable close to the first natural frequency  $p_1$ . Moving away from this frequency solutions become unstable and the quasi periodic oscillations occur (Fig. 3a).

The quasi-periodic solutions are obtained by a direct integration of equations of motion (7) and then solutions are transformed from generalized (physical) coordinates to quasi-normal coordinates using transformation (8). Because the motion has a beating nature with modulated amplitude it is denoted by dots indicating maximal and minimal values of the amplitude. As we can observe quasi-periodic motion starts when the stability of periodic solution is lost. The modulation of the amplitude decreases moving away from the resonance zone. The periodic solution bifurcates to quasi-periodic via the second kind Hopf bifurcation, not indicated in the figure. Varying parameter  $u_1$  we can observe also change in the angular speed of the DC motor. Therefore, the shape of the resonance curve against angular velocity  $\Omega_1$  is different than against parameter  $u_1$  as presented in Fig. 3b. The additional fully stable loop occurs on the left branch of the resonance curve. This solution is in agreement with results published in the paper [16] for one degree of freedom model. For the ideal system [15], excited by a motor with infinite power, the loop arises on the declining branch and it is only partially stable. In contrast the loop existing in the non-ideal model arises on the inclining branch and is fully stable.

The detailed changes in the amplitude and angular velocity can be observed on the basis of the averaged Eqs. (26)–(28) which have been modelled in the Matlab–Simulink package and then solved numerically. Figure 4 and Fig. 5 present solutions  $a_1(t)$  and  $\Omega_1(t)$  while supplied voltage is slowly increasing and decreasing, respectively.

**Fig. 4** Amplitude and angular velocity of the motor against slowly increasing in time parameter  $u_1 \in (0.4 - 2.4)$

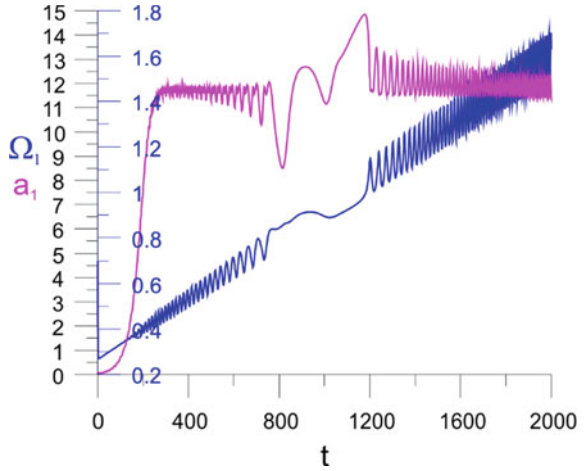
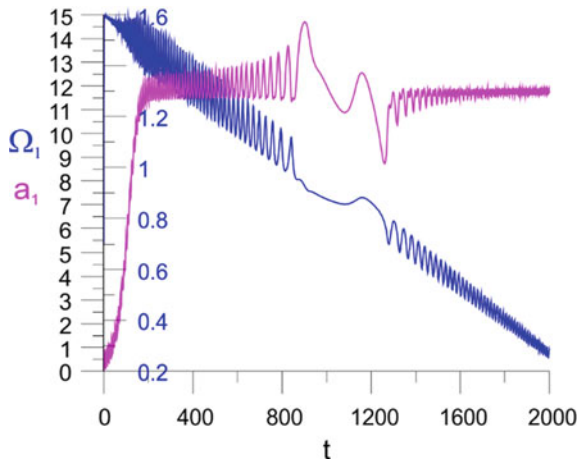


**Fig. 5** Amplitude and angular velocity of the motor against slowly decreasing in time parameter  $u_1 \in (2.4 - 0.4)$



Two different scales are used in the figures, red color represents amplitude while blue angular velocity (frequency of excitation) of the computed solutions. Modulation of amplitude are clearly visible out of the resonance zone. This result is an effect of interactions between parametric and external vibrations and additional interaction with the non-ideal energy source. Therefore, quasi-periodic oscillations are observed on the angular velocity curves (blue line).

Modulation of the oscillations increases close to the resonance zone and inside the resonance zone transits to periodic with constant amplitude, both either for the main system or angular velocity of the motor. Inside the resonance zone two local maxima occur. The drop of angular velocity in the middle of the resonance zone (blue line in Fig. 4) is related with the *limited power supply* which is too small to maintain the response to be continuously increasing.

Time histories of amplitude  $a_I$  and angular velocity  $\Omega_I$  outside and inside the resonance region for selected parameters  $u_I$  are presented in Fig. 6. Amplitude modulations very close to the frequency locking for  $u_I = 1.1$  and  $u_I = 1.53$  are presented in Fig. 6a, c.

Inside the resonance for  $u_I = 1.2$  where the frequency locking takes place amplitude is constant (Fig. 6b). For  $u_I = 1.7$  (Fig. 6d), far away from the resonance, amplitude modulations are much smaller and oscillation frequency is increased.

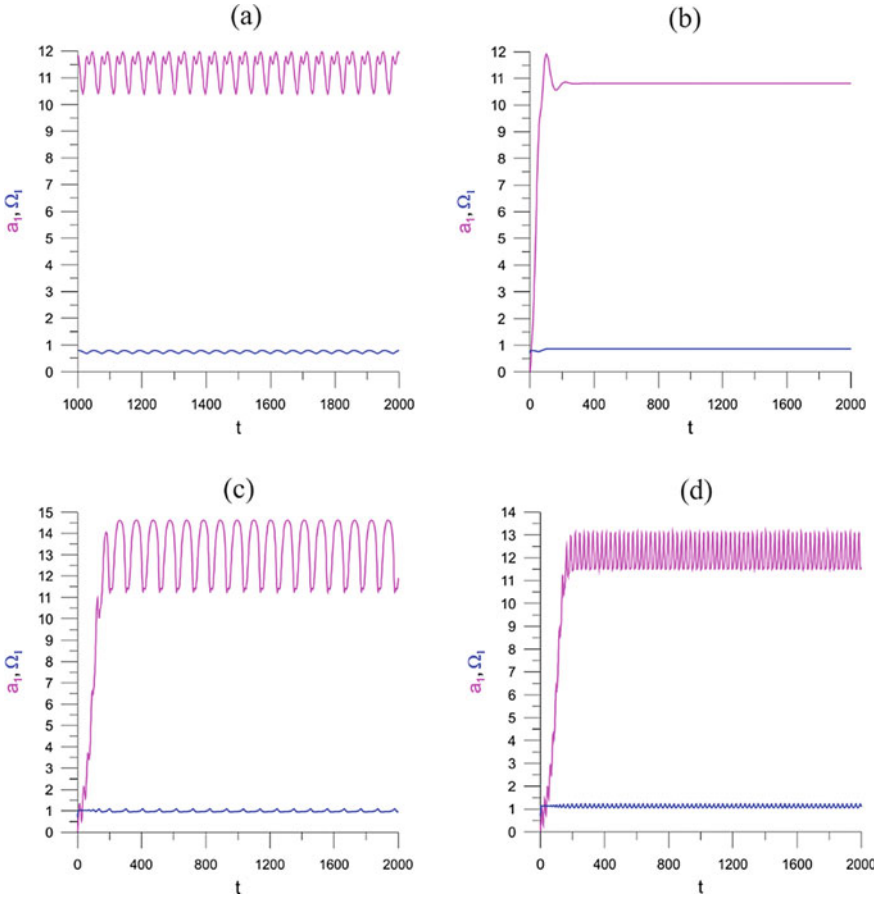


**Fig. 6** Time histories of vibration amplitudes and angular velocity against parameter  $u_I$  parameter; **a**  $u_I = 1.1$ , **b**  $u_I = 1.2$ , **c**  $u_I = 1.53$ , **d**  $u_I = 1.70$

## 5 Chaotic Oscillations of Nonlinear Two Degrees of Freedom System with Non-ideal Energy Source

Apart from regular oscillations which can be periodic or quasi-periodic also more complex chaotic oscillations may occur [12]. One of the main criterion for the motion classification is based on Lyapunov exponent. Parameters (31) are accepted to check regular periodic or quasi-periodic dynamics. For this purpose bifurcation diagrams based on Lyapunov exponents are computed for varied parameter  $u_I$  in domain  $u_I \in (0 - 6)$ . The computations have been performed till steady state has been achieved, transient solutions have been rejected.

Lyapunov exponents diagram is presented in Fig. 7. As we can see values of the exponents do not exceed zero values which confirms regular oscillations in the analyzed domain of bifurcation parameter  $u_I$ . Examples of Poincaré maps for  $X_1, \dot{X}_1$  coordinates are presented in Fig. 8.

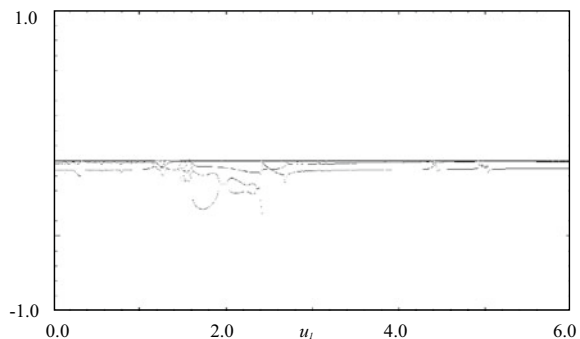
As it has been mentioned the considered system is autonomous and time is not present in the direct form therefore the base of solution sampling and then plotting period  $T = \pi$  has been applied.

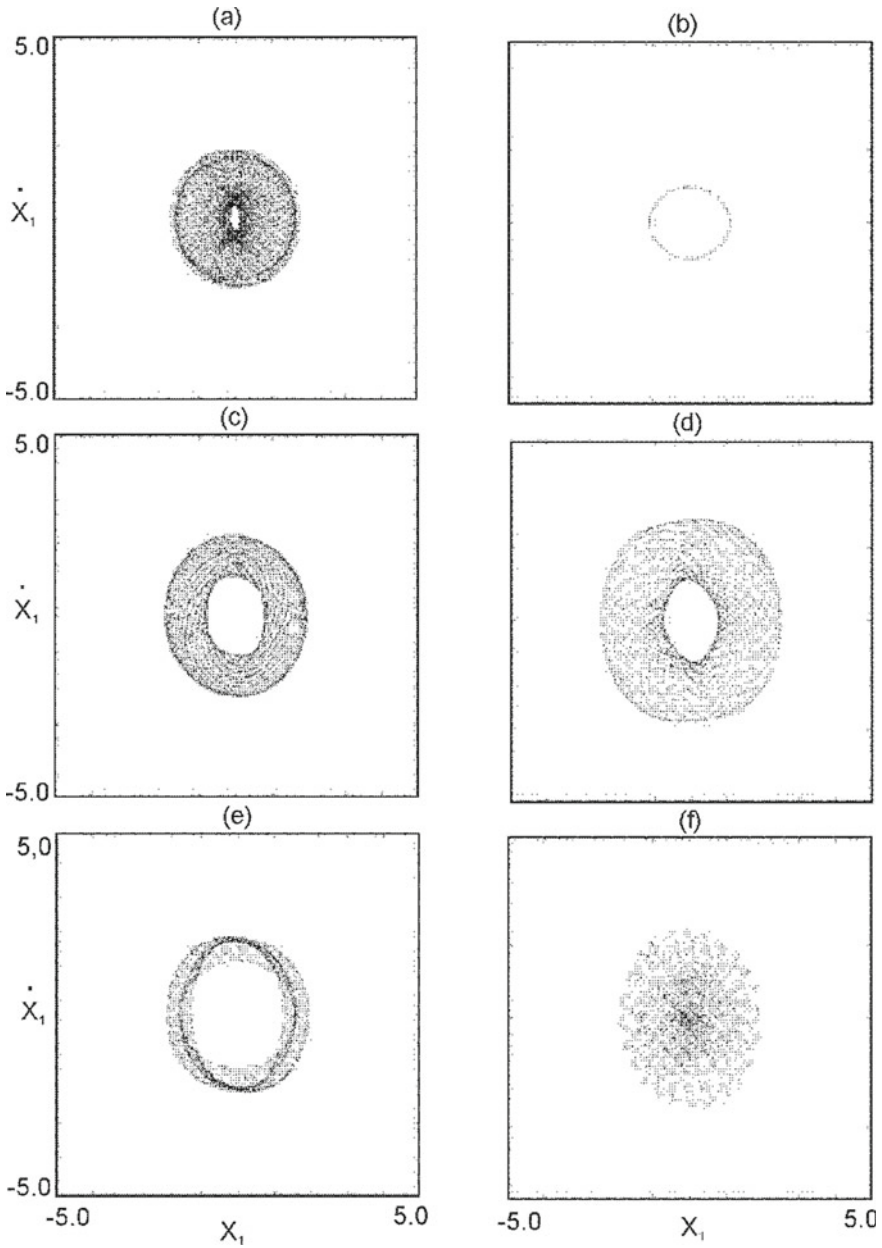
The map in Fig. 8b corresponds to a periodic solution and the attractor gets a shape of a single closed curve. In the rest maps the oscillations are quasi-periodic occurring due to nonlinear dynamics of the whole coupled system. The most complex structure of the attractor is presented in Fig. 8a, f, just before and after the resonance zone. Then, a very strong impact of self-excitation on the system dynamics takes place. In Fig. 8c–e the quasi-periodic motion is related to couplings of the whole structure and smaller influence of self-excitation.

A detailed motion classification based on Lyapunov exponents is proposed in Table 1.

For periodic motion just one, out of six, Lyapunov exponent is equal to zero, rest get negative values. Quasi-periodic motion is characterized by two or three exponents equal to zero and they are called respectively as quasi-periodic oscillations of the first or the second kind (see Fig. 8f).

**Fig. 7** Lyapunov exponents against  $u_I$  parameter for the non-ideal system with two degrees of freedom, parameters (31);  $\mu = 0.2$

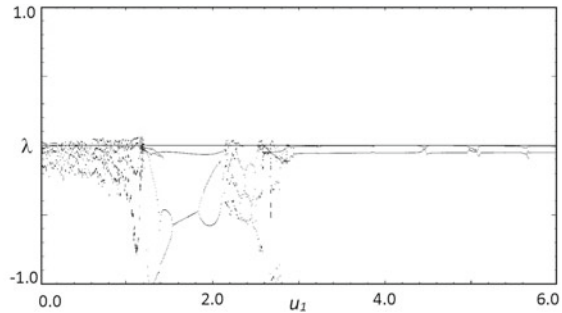




**Fig. 8** Phase portraits for selected parameters  $u_1$ ,  $\mu = 0.2$ , **a**  $u_1 = 0.80$ , **b**  $u_1 = 1.30$ , **c**  $u_1 = 1.70$ , **d**  $u_1 = 2.2$ , **e**  $u_1 = 2.6$ , **f**  $u_1 = 3.2$

**Table 1** Type of attractors and Lyapunov exponents for selected parameter  $u_1$ ;  $\mu = 0.2$ 

$u_1$	Attractor	$\lambda_1$	$\lambda_2$	$\lambda_3$	$\lambda_4$	$\lambda_5$	$\lambda_6$
0.80	Quasi-periodic	0.0	0.0	-0.0167	-0.0167	-0.0691	-1.5213
1.30	Periodic	0.0	-0.0285	-0.0296	-0.0296	-0.0738	-1.4178
1.70	Quasi-periodic	0.0	0.0	-0.0381	-0.0924	-0.3185	-1.288
2.20	Quasi-periodic	0.0	0.0	-0.0664	-0.1533	-0.2060	-1.4447
2.60	Quasi-periodic	0.0	0.0	-0.0519	-0.0823	-0.0823	-1.5788
3.20	Quasi-periodic type II	0.0	0.0	0.0	-0.0200	-0.0643	-1.5637

**Fig. 9** Lyapunov exponents against  $u_1$  parameter for non-ideal system with two degrees of freedom, parameters (31);  $\mu = 1.0$ 

Dynamics of the non-ideal system is analyzed also for larger parametric excitation by increasing  $\mu$  parameter up to  $\mu = 1.0$  and keeping the same values of the rest coefficients. Now, the maximal Lyapunov exponent gets positive values as presented in diagram in Fig. 9. These zones indicate chaotic oscillations of the system. The first chaotic region occurs out of the resonance for  $u_1 \in (0, 1.2)$  with a minor windows of regular motion. On Poincaré map for  $u_1 = 0.6$  we obtain periodic oscillations while for  $u_1 = 0.7$  and  $u_1 = 1.1$  oscillations become chaotic (Fig. 10a–c).

Other two chaotic regions occur next to  $u_1 \approx 2.2$  and  $u_1 \approx 2.5$  with quasi-periodic oscillations between them (Fig. 10f). For large values of  $u_1$  parameter the only regular motion takes place (Fig. 10h).

The Lyapunov exponents corresponding to bifurcation diagram in Fig. 9 and Poincaré maps are collected in Table 2. For  $u_1 = 0.70$ ,  $u_1 = 2.22$ ,  $u_1 = 2.55$ , values of the maximal Lyapunov exponent are positive, which means that for these parameters oscillations are chaotic. This fact is also confirmed by strange chaotic attractors presented on Poincaré maps. For  $u_1 = 1.1$ , and attractor presented in Fig. 10c, two exponents are positive. This motion is called hyper-chaotic. In the rest cases one or two exponents are equal to zero what indicates periodic or quasi-periodic motion.

The additional numerical simulations (not presented here) show that the model with non-ideal energy source has much higher tendency in transition to complex dynamics, including chaos or hyper-chaos, than its ideal counterpart. This is the effect of the additional degree of freedom related to nonlinear DC motor dynamics.

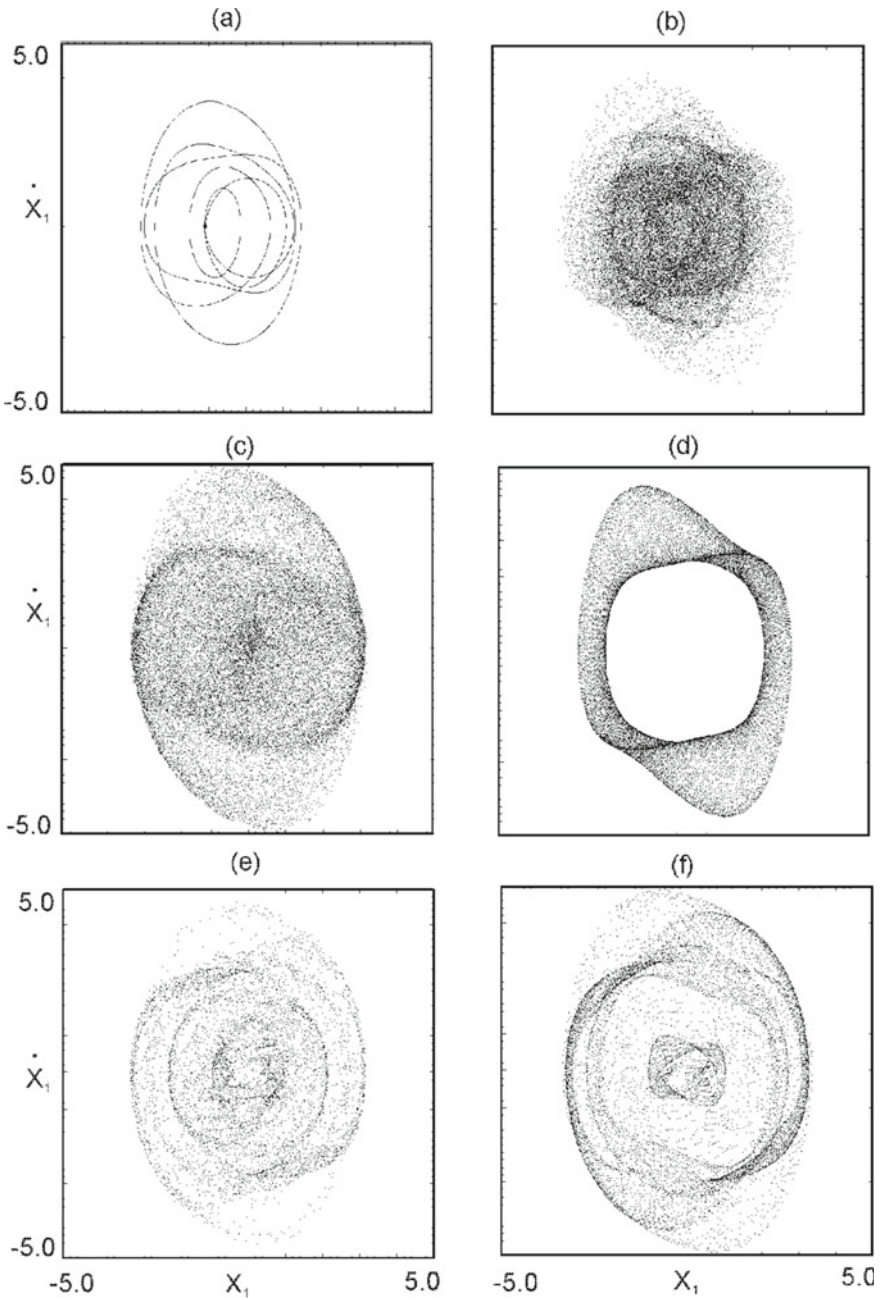


**Fig. 10** Phase portraits for selected parameters  $u_1, \mu = 1.0$ , **a**  $u_1 = 0.60$ , **b**  $u_1 = 0.70$ , **c**  $u_1 = 1.10$ , **d**  $u_1 = 1.80$ , **e**  $u_1 = 2.22$ , **f**  $u_1 = 2.40$ , **g**  $u_1 = 2.55$ , **h**  $u_1 = 2.80$



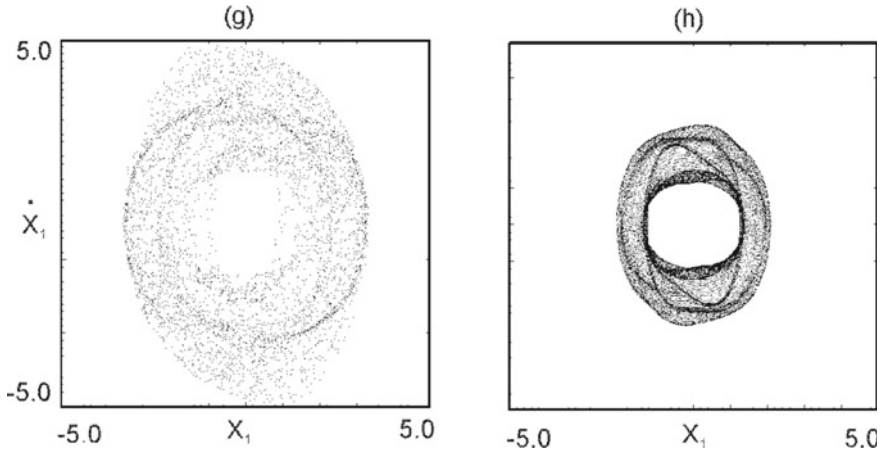


Fig. 10 (continued)

Table 2 Type of attractors and Lyapunov exponents for selected parameter  $u_1$ ;  $\mu = 1.0$

$u_1$	attractor	$\lambda_1$	$\lambda_2$	$\lambda_3$	$\lambda_4$	$\lambda_5$	$\lambda_6$
0.60	periodic	0.0	-0.0013	-0.0268	-0.1308	-0.2129	-1.4659
0.70	chaotic	0.0404	0.0	-0.0254	-0.0925	-0.2236	-1.4681
1.10	chaotic	0.0490	0.0027	-0.0002	-0.1951	-0.6851	-1.4755
1.80	quasi-periodic	0.0	0.0	-0.0641	-0.4832	-0.4834	-1.4884
2.22	chaotic	0.0280	0.0	-0.0822	-0.2048	-0.4496	-1.4382
2.40	quasi-periodic	0.0	0.0	-0.1507	-0.3651	-0.5436	-1.5040
2.55	chaotic	0.0289	0.0	-0.0060	-0.3707	-0.7586	-1.4469
2.80	quasi-periodic	0.0	0.0	-0.0406	-0.0869	-0.1244	-1.5715

## 6 Conclusions

The interactions between external, parametric and self-excited vibrations are studied in the paper. The model assumed as non-ideal, includes the additional degree of freedom of the energy source (DC motor). The parametric and external excitations are tuned in 1:2 ratio which leads to very strong interactions in the principal parametric zone. The analytical solutions based on the Krylov–Bogoliubov–Mitropolsky method show that in the vicinity of this zone the phenomenon of frequency locking takes place. The system vibrates periodically. The influence of the non-ideal energy source is observed by local decrease of the amplitude and angular velocity inside the resonance zone against the supplied voltage. On the resonance characteristic—amplitude against excitation frequency—this effect creates a loop on the increasing branch of the resonance curve and the loop is fully stable. The phenomenon is in contrast to the ideal system where the loop arises on the declining branch and its upper part

is stable [15]. Outside the principal parametric resonance, after the Hopf bifurcation of the second kind, the system transits to quasi-periodic oscillations. Based on the extended numerical simulation, apart from periodic or quasi-periodic, also chaotic or hyper-chaotic vibrations may arise while parametric excitation is increased. This fact is confirmed by computed Lyapunov exponents and strange chaotic attractors plotted on Poincaré maps. The dynamics of the non-ideal model differs from the ideal system in a case of regular vibrations as well as chaotic motion. The non-ideal model is more sensitive in the transition to chaotic oscillations when compared with its counterpart.

**Acknowledgements** The research has been financed within the framework of the project "Lublin University of Technology—Regional Excellence Initiative", funded by the Polish Ministry of Science and Higher Education (contract no. 030/RID/2018/19).

## References

1. Alifov, A., Frolov, K.W.: Interaction of Nonlinear Oscillatory Systems with Energy Sources (in Russian) Moscow, Nauka (1985)
2. Balthazar, J.M., Cheshankov, B.I., Ruschev, D.T., Barbanti, L., Weber, H.I.: Remarks on the passage through resonance of a vibrating system with two degrees of freedom. *J. Sound Vib.* **239**, 1075–1085 (2001)
3. Bogoliubov, N.N., Mitropolsky, J.A.: Asymptotic methods in the theory of nonlinear oscillations, (in Russian) Moscow GIF-ML (1958), translated from Russian: Gordon & Breach, Delhi (1961)
4. Cartmell, M.P.: Introduction to Linear, Parametric and Nonlinear Vibrations, Chapman and Hall, London (1990)
5. Dimentberg, R.M., McGovern, L., Norton, R.L., Chapdelaine, J., Harrison, R.: Dynamics of an unbalanced shaft interacting with a limited power supply. *J. Nonlinear Dyn.* **13**, 171–187 (1997)
6. Dimentberg, M., Chapdelaine, J., Harrison, R., Norton, R.L.: Passage through critical speed with limited power by switching system stiffness. *Nonlinear Stochastic Dyn. AMD, Vol. 192, DE* **78**, 57–67 (1994)
7. Kononenko, V.O.: Vibrating Systems with Limited Power Supply. Illife, London (1969)
8. Krasnopolskaja, T.S., Shvets, A.Ju.: Chaos in systems with a limited power supply. *Chaos* **3**, 387, <https://doi.org/10.1063/1.165946> (1993)
9. Nayfeh, A.H.: The response of two-degree-of-freedom systems with quadratic non-linearities to a parametric excitation. *J. Sound Vib.* **88**(4), 547–557 (1983)
10. Nayfeh, A.H., Balachandran, B.: Applied nonlinear dynamics. Wiley, New York (1995)
11. Sommerfeld, A.: Beiträge zum dynamischen ausbau der festigkeitslehe. *Physikal Zeitschr* **3**, 266–286 (1902)
12. Szemplińska-Stupnicka, W.: The analytical predictive criteria for chaos and escape in nonlinear oscillators: a survey. *Nonlinear Dyn.* **7**, 129–147 (1995)
13. Thomsen, J.: Vibrations and Stability, Order and Chaos, McGraw Hill, London (1997)
14. Tondl, A.: On the interaction between self-excited and parametric vibrations, Monographs and Memoranda, No. 25, National Research Institute for Machine Design, Prague (1978)

15. Warminski, J.: Nonlinear dynamics of self-, parametric, and externally excited oscillator with time delay: van der Pol versus Rayleigh models. *Nonlinear Dyn.* **99**, 35–56 (2020)
16. Warminski, J., Balthazar, J.M.: Brasil, RMLRF, Vibrations of a non-ideal parametrically and self-excited model. *J. Sound Vib.* **245**(2), 363–374 (2001)
17. Yano, S.: Considerations on self-and parametrically excited vibrational systems. *Ingenieur-Archiv* **59**, 285–295 (1989)

# A Study of the Sommerfeld Effect in a Rotor Machine Foundation Model with 4 DOF



Sara Prates Lima   
and Reylando Manoel Lopes Rebello da Fonseca Brasil 

**Abstract** This paper addresses the nonlinear dynamical analysis of a block foundation structure for an unbalanced rotating machine, with limited power supply, leading to interaction between the motor and the structure. This aspect is often not considered during usual design practice, although all real motors are, in this sense, non-ideal power sources. Our mathematical model considers this system as non-ideal, subjected to the Sommerfeld effect, which may manifest close to foundation/machine's resonances, with possible jumps from lower to higher frequency rotation regimes, no intermediate stable steady states in between. The model proposed is defined by three degrees of freedom, vertical and horizontal translations of the block and rotation about its axis, and an additional one associated with the rotation of the rotor shaft (intrinsic to the so-called non-ideal systems). The mathematical model that describes the system's motion is derived via Lagrange's equations. The solution of this system of differential equations can in principle be carried out analytically, but this can be difficult or even impossible in some cases, particularly when these equations are nonlinear, such as the proposed model. The numerical solution adopted here was implemented in Matlab® software. This paper aims to analyze this little studied problem of practical importance.

**Keywords** Machine-foundation interaction · Sommerfeld effect · Non-ideal systems

## 1 Introduction

For many systems, disregarding the influence of the structure motion on their excitation source is an acceptable simplification, but for many others it is not. Sommerfeld (1904) was the first to study the phenomenon of this interaction, later called the

---

S. P. Lima · R. M. L. R. da F. Brasil (✉)  
CECS, Federal University of ABC, Av. dos Estados, nº 5001, 09210-580 Santo André, Brasil  
e-mail: [reylando.brasil@ufabc.edu.br](mailto:reylando.brasil@ufabc.edu.br)

S. P. Lima  
e-mail: [sara.lima@ufabc.edu.br](mailto:sara.lima@ufabc.edu.br)

Sommerfeld Effect, making an experiment of an elastic base supporting an unbalanced machine. A few years later this experiment was replicated by Kononenko and Korablev [1], who had their work re-analyzed by Nayfeh and Mook [2].

Non-ideal systems are those in which the structural motion influences its source of excitation. These systems can be linear, or nonlinear, regardless of its excitation. In general, the more the power supply is limited, the more the system moves further away from the ideal system, and the greater the machine-structure interaction is. Mathematically it is imperative to include to the model an equation that describes the dynamics of the motor. Therefore, an additional degree of freedom is required to model non-ideal systems [1–5].

In this work, we develop a non-ideal system model of a supported machine with an unbalanced rotor. This non-ideal system is composed of a rigid foundation block directly supported by springs and dashpots.

This work aims to present ongoing research of the machine-foundation interactions. The mathematical development of the proposed non-ideal system is carried out via Lagrange's equations. In Sect. 2, the physical model representing the foundation structure and its driver source, the machine, will be presented. Next, Sect. 3 presents the mathematical model composed of equations that describe the displacements and velocities of the physical model, obtained using Lagrange's equations. Numerical simulations and graphical displays are presented in Sect. 5, using assumed stiffness, mass and damping parameters. Sections 5 and 6 will present the final discussion and conclusions.

## 2 Physical Model

The proposed physical model considers the machine and structure interaction and consists of four degrees of freedom: the two translations (vertical and horizontal), one rotation (about the axis of the foundation) and the last one associated with the motor shaft. This additional degree of freedom is typical of the so-called non-ideal systems, as can be seen in Fig. 1.

$C_i$  ( $i = 1, 2, 3$ ) and  $K_i$  ( $i = 1, 2, 3$ ) are, respectively, conveniently adopted damping and stiffness coefficients of the machine foundation.

## 3 Mathematical Model

In this mathematical model, time functions  $q_1$ ,  $q_2$  and  $q_3$  are, respectively, the generalized coordinates related the horizontal, vertical, and rotational motions of the block foundation, while time function  $q_4$  is the angular displacement of the motor shaft. The eccentricity  $e$  is obtained through the quality of the balance of the rotating machine, while  $h$  is the height between the motor shaft and the foundation axes (Fig. 1).

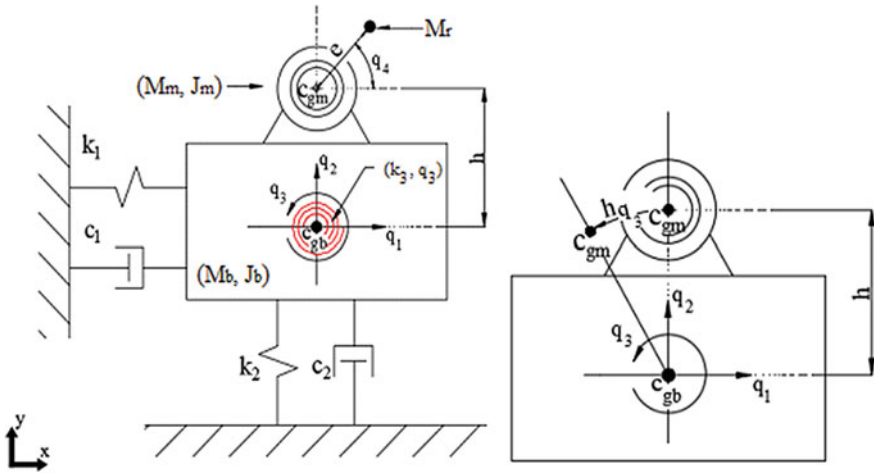


Fig. 1 Model of a foundation structure with unbalanced excitation source

**Unbalanced mass ( $M_r$ )**

The coordinates and velocities of the unbalanced mass from Fig. 1 are:

$$x_r = q_1 - hq_3 + e\cos q_4 \quad y_r = q_2 + e\sin q_4 + h \tag{1}$$

$$\dot{x}_r = \dot{q}_1 - h\dot{q}_3 - e\dot{q}_4\sin q_4 \quad \dot{y}_r = \dot{q}_2 + e\dot{q}_4\cos q_4 \tag{2}$$

**Mass of the foundation block ( $M_b$ )**

The coordinates and velocities of the machine foundation block mass presented in the Fig. 1 are:

$$x_b = q_1 \quad y_b = q_2 \tag{3}$$

$$\dot{x}_b = \dot{q}_1 \quad \dot{y}_b = \dot{q}_2 \tag{4}$$

**Motor mass ( $M_m$ )**

The coordinates and velocities of the mass of the motor are:

$$x_m = q_1 - hq_3 \quad y_m = q_2 + h \tag{5}$$

$$\dot{x}_m = \dot{q}_1 - h\dot{q}_3 \quad \dot{y}_m = \dot{q}_2 \tag{6}$$

### Kinetic Energy ( $T$ )

The kinetic energy of this model is obtained as follows:

$$T = 1/2 \left[ \begin{array}{l} M_b(\dot{q}_1^2 + \dot{q}_2^2) + M_m[(\dot{q}_1 - h\dot{q}_3)^2 + \dot{q}_2^2] \\ + J_b\dot{q}_3^2 + M_r(\dot{q}_1 - h\dot{q}_3 - \dot{q}_4 e \sin q_4)^2 \\ + M_r(\dot{q}_2 + \dot{q}_4 e \cos q_4) + J_m\dot{q}_4^2 \end{array} \right] \quad (7)$$

in which  $J_m$  is the moment of inertia of the machine rotor and  $J_b$  the moment of inertia of foundation block.

### Strain energy ( $U$ )

In this case the strain energy can be obtained by:

$$U = 1/2(K_1q_1^2 + K_2q_2^2 + K_3q_3^2) \quad (8)$$

in which  $K_i (i = 1, 2, 3)$  are the stiffness coefficients.

### Work of conservative forces ( $W$ )

The work of the weight forces is given by:

$$W = -g[(M_b + M_m + M_r)q_2 + M_r(q_2 + e \sin q_4)] \quad (9)$$

in which  $g$  it is the acceleration due to gravity.

### Total Potential Energy ( $V$ )

The total potential energy will be determined by:

$$V = U - W \quad (10)$$

### Lagrange's equation

In this model, Lagrange's equation can be presented as:

$$\frac{d}{dt} \left( \frac{\partial \mathcal{L}}{\partial \dot{q}_i} \right) - \frac{\partial \mathcal{L}}{\partial q_i} = N_i (i = 1, 2, 3, 4) \quad (11)$$

in which  $\mathcal{L} = T - V$  is the Lagrangean function and  $N_i$  are the non-conservative generalized forces.

## Equations of Motion

### First degree of freedom

For the first degree of freedom the equation of motion is:

$$(M_b + M_m + M_r)\ddot{q}_1 + C_1\dot{q}_1 + K_1q_1 = (M_m + M_r)h\ddot{q}_3 + M_re(\ddot{q}_4 \sin q_4) + M_re(\dot{q}_4^2 \cos q_4) \quad (12)$$

### Second degree of freedom

For the second degree of freedom the equation of motion is:

$$(M_b + M_r + M_m)\ddot{q}_2 + C_2\dot{q}_2 + K_2q_2 = -g(M_b + M_r + M_m) - M_re(\ddot{q}_4 \cos q_4 - \dot{q}_4^2 \sin q_4) \quad (13)$$

### Third degree of freedom

For the third degree of freedom the equation of motion is:

$$(M_m h^2 + M_r h^2 + J_b)\ddot{q}_3 + C_3\dot{q}_3 + K_3q_3 = (M_b + M_m)h\ddot{q}_1 - M_re(\ddot{q}_4 \sin q_4 - \dot{q}_4^2 \cos q_4) \quad (14)$$

### Fourth degree of freedom

For the fourth degree of freedom the equation of motion is:

$$M_re(\ddot{q}_1 \sin q_4 + \ddot{q}_2 \cos q_4 + h\ddot{q}_3 \sin q_4) + (M_re^2 + J_m)\ddot{q}_4 = L(\dot{q}_4) - H(\dot{q}_4) + M_re g \cos q_4 \quad (15)$$

in which  $L(\dot{q}_4)$  is the total torque of the rotor and  $H(\dot{q}_4)$  is its the motor damping torque due to internal friction.

### Matrix formulation

Let us re-write the equations of motion (12 to 15) in matrix form:

$$[M]\{\ddot{q}\} + [C]\{\dot{q}\} + [K]\{q\} = \{p\} \quad (16)$$

where



$$[M] = \begin{bmatrix} M_b + M_r + M_m & 0 & -(M_m + M_r)h & -M_r e \sin q_4 \\ 0 & M_b + M_r + M_m & 0 & M_r e \cos q_4 \\ -(M_m + M_r)h & 0 & (M_m + M_r)h^2 + J_b & M_r h e \sin q_4 \\ -M_r e \sin q_4 & M_r e \cos q_4 & M_r h e \sin q_4 & M_r e^2 + J_m \end{bmatrix} \quad (17)$$

$$\{\ddot{q}\} = \begin{Bmatrix} \ddot{q}_1 \\ \ddot{q}_2 \\ \ddot{q}_3 \\ \ddot{q}_4 \end{Bmatrix} \quad (18)$$

$$[C] = \begin{bmatrix} C_1 & 0 & 0 & 0 \\ 0 & C_2 & 0 & 0 \\ 0 & 0 & C_3 & 0 \\ 0 & 0 & 0 & 0 \end{bmatrix} \quad (19)$$

$$\{\dot{q}\} = \begin{Bmatrix} \dot{q}_1 \\ \dot{q}_2 \\ \dot{q}_3 \\ \dot{q}_4 \end{Bmatrix} \quad (20)$$

$$[K] = \begin{bmatrix} K_1 & 0 & 0 & 0 \\ 0 & K_2 & 0 & 0 \\ 0 & 0 & K_3 & 0 \\ 0 & 0 & 0 & 0 \end{bmatrix} \quad (21)$$

$$\{q\} = \begin{Bmatrix} q_1 \\ q_2 \\ q_3 \\ q_4 \end{Bmatrix} \quad (22)$$

$$\{p\} = \begin{Bmatrix} -M_r e \dot{q}_4^2 \cos q_4 \\ -M_r e \dot{q}_4^2 \sin q_4 - (M_b + M_m + M_r)g \\ -M_r h e \dot{q}_4^2 \cos q_4 \\ L(\dot{q}_4) - H(\dot{q}_4) + M_r e g \cos q_4 \end{Bmatrix} \quad (23)$$

Equations of this type are difficult to solve in closed form, so is convenient to transform the second order differential equation system into a first order differential equations system and then choose a numerical method to solve the problem, as the Runge-Kutta method implemented in Matlab®.

## 4 Torque Relationships

A steady state constant motor frequency condition is given by the torque relationship

$$S(\dot{q}_4) = H(\dot{q}_4) + R(\dot{q}_4) \quad (24)$$

In Eq. (21), remembering that torque and energy have the same unities,  $S(\dot{q}_4)$  is the total energy dissipated by the motor/structure system and  $R(\dot{q}_4)$  the energy dissipated by damping of the support structure, given by

$$R(\dot{q}_4) = \sum_{i=1}^3 \frac{C_i}{2q_4} \omega_i^2 a_i^2 \quad (25)$$

where  $\omega_i$  are the undamped frequencies of vibration of the support structure (rad/s). The amplitudes of vibration of these three modes are

$$a_i = \frac{M_r e}{Modemass} D_i \beta_i^2 \quad (26)$$

where the nondimensional Coefficients of Dynamic Amplification are

$$D_i = \frac{1}{\sqrt{(1 - \beta_i^2)^2 + (2\xi_i \beta_i)^2}} \quad (27)$$

defining the nondimensional relationships

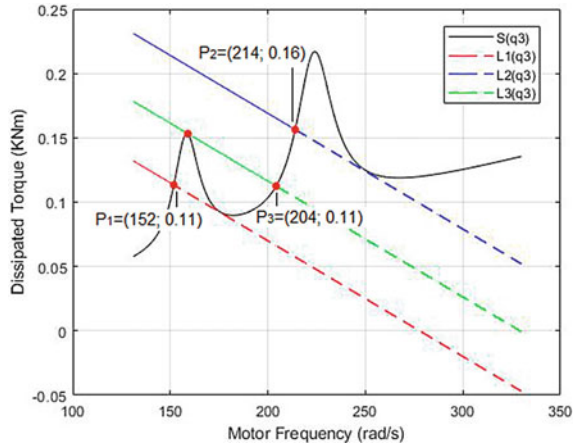
$$\beta_i = \frac{q_4}{\omega_i} \xi_i = \frac{C_i}{2(Modemass)\omega_i} \quad (28)$$

## 5 Numerical Simulations

Next, numerical parameters are adopted:  $M_b + M_r + M_m = 2$  t,  $K_1 = 50,000$  KN/m,  $K_2 = 100,000$  KN/m,  $K_3 = 75,000$  KNm/rad,  $M_r = 0.1$  t,  $e = 0.01$  m,  $\xi_1 = \xi_2 = \xi_3 = 0.05$ ,  $J_m = 1.7 \times 10^{-4}$  tm<sup>2</sup>,  $H(\dot{q}_4) = 4 \times 10^{-4} \dot{q}_4$  KNm. Figure 2 displays the  $S(\dot{q}_4)$  energy dissipation curve of this system (in black), from Eq. (21), and three possible  $L_k(\dot{q}_4)$  available torque characteristic curves of the motor (in red, green and blue), for three different possible energy levels, considered as linear, in KNm,

$$L_1(\dot{q}_4) = 0.25 - 0.0009\dot{q}_4 \quad L_2(\dot{q}_4) = 0.35 - 0.0009\dot{q}_4$$

**Fig. 2**  $S(\dot{q}_4)$  curve, in black,  $L_1(\dot{q}_4)$  line, in red,  $L_2(\dot{q}_4)$  blue and  $L_3(\dot{q}_4)$  blue line, in green



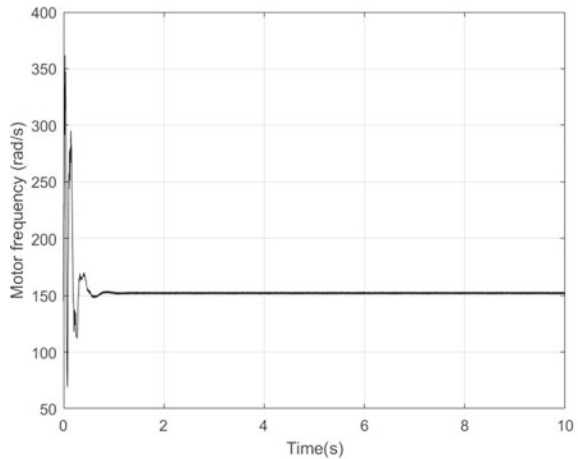
$$L_3(\dot{q}_4) = 0.30 - 0.0009\dot{q}_4$$

Figure 2 displays only the first two resonance peaks of this system. The third one, related to the roll mode of the foundation block is not of interest for the adopted parameters.

The computed stable steady state constant motor frequencies (rad/s) and corresponding torques, for positive increase of the motor power (KNm) are:  $P1 \cong (152; 0.11)$ ,  $P2 \cong (214; 0.16)$  and  $P3 \cong (204; 0.11)$ .

Next, it is performed a time step-by-step numerical integration of the equations of motion, using Runge–Kutta’s 4th and 5th order algorithm, implemented in Matlab® software. The first steady state regime, P1, is displayed in Fig. 3, the second, P2, is displayed in Fig. 4 and P3, displayed in Fig. 5.

**Fig. 3** Steady state constant motor frequency regime, P1



**Fig. 4** Steady state constant motor frequency regime, P2

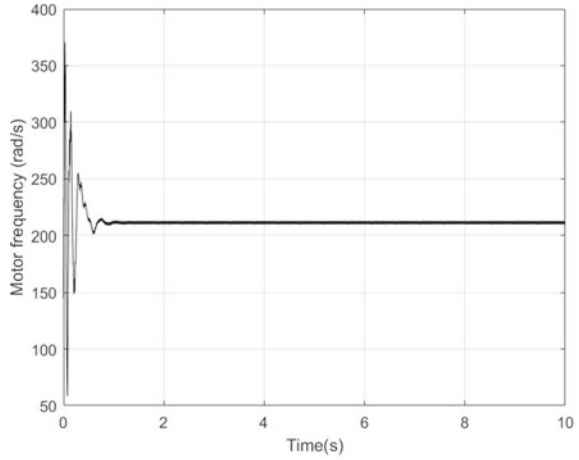
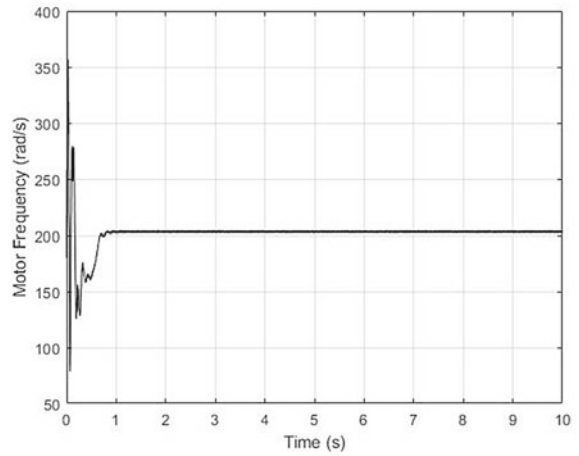


**Fig. 5** Steady state constant motor frequency regime, P3



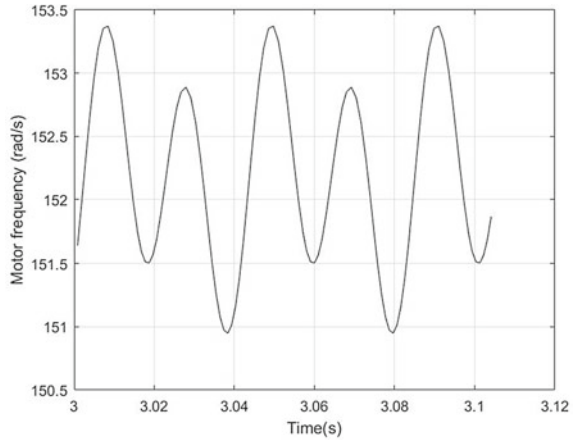
In Figs. 3, 4 and 5, a fairly good agreement with Fig. 2 results is obtained. As expected, the effect of gravity on  $m_r$  leads to a complex steady state behavior, as is possible to see in Fig. 6, a zoom of part of Fig. 3.

## 6 Discussion

Let us discuss simulations results presented in Figs. 2, 3, 4 and 5.

In steady state P1, the amount of energy provided by the motor through torque curve  $L_1(\dot{q}_4)$ , in red, is not enough to surpass the first resonance peak of the energy dissipation curve, resulting in stagnation of the angular speed regime of the machine.

**Fig. 6** Zoom of steady state constant motor frequency P1



If some more energy is provided, through torque curve  $L_3(\dot{q}_4)$ , in green, the system reaches a point at this first resonance peak and **jumps** to far away point P3 where a steady state regime is again possible, no **stable** steady states in between. This is the so called **Sommerfeld Effect**.

Finally, if more energy is applied, through torque curve  $L_2(\dot{q}_4)$ , in blue, it is possible to reach higher steady state angular velocity regimes as point P2.

## 7 Conclusions

Studies of models considering non-ideal systems are important for a better practice of engineering, but are not usually done, being replaced by approximations. The system of differential equations of the model studied here is coupled, nonlinear and of second order, quite difficult to solve analytically. So, it is necessary to use a numerical method.

Among the possible solver methods to this model, the solution for this model was carried out in the Matlab® program using the ode45 function, that uses a combination of fourth and fifth order Runge Kutta methods. The implementation of this algorithm requires the transformation of the of second-order differential equations into a first order system [6, 7].

A study of non-ideal behavior of a four degrees of freedom support structure for a limited power unbalanced motor was presented. The expected Sommerfeld Effect of rotation frequency stagnation near resonances was observed, as well as a jump phenomenon due to instability. Modeling of this type of foundation as non-ideal systems can be of importance in practice.

**Acknowledgements** The authors acknowledge support by CAPES, CNPq and FAPESP, all Brazilian research funding agencies.

**Authorship statement**

The authors hereby confirm that they are the sole liable persons responsible for the authorship of this work, and that all material that has been herein included as part of the present paper is either the property (and authorship) of the authors or has the permission of the owners to be included here.

**References**

1. Kononenko, V.O., Koralev, S.S.: An experimental investigation of the resonance phenomena with a centrifugally excited alternating force. Tr, rt. Mr. Mosk. Tekhn, tekhn. Mr. Inst. Mr. Lekh. Prom, no. 14,224 (1959)
2. Nayfeh, A.H., Mook, D.T.: *Nonlinear Oscillations*, p. 705. Wiley, Virginia (1995)
3. Balthazar, J.M., Tusset, A.M., Brasil, R.M.L.R.F., Nabarrete, A.: An overview on the appearance of the Sommerfeld effect and saturation phenomenon in non-ideal vibrating systems (NIS) in macro and MEMS scales. *Nonlinear Dyn.* **91**, 1–12 (2018)
4. Balthazar, J.M., Mook, D.T., Weber, H.I., Brasil, R.M.L.R.F., Fenili, A.: An overview on non-ideal vibrations. *Meccanica* **38**, 613–621 (2003)
5. Warminski, J., Balthazar, J.M., Brasil, R.M.L.R.F.: Vibrations of non-ideal parametrically and self-excited model. *J. Sound Vib.* **245**, 363–374 (2001)
6. Brasil, R.M.L.R.F., Silva, M.A.: *Introdução à Dinâmica das Estruturas Para a Engenharia Civil*. 2nd ed. São Paulo: Blucher, 2015.268 p. (in Portuguese)
7. Bachmann, H., et al.: *Vibration problems in structures: practical guidelines*, p. 234. Birkhauser, Basel (1995)

# Three Kinds of Sommerfeld Effect in Rotor Dynamics



A. K. Samantaray

**Abstract** When transverse or torsional vibration amplitudes in a rotor dynamic system is high, energy is often drawn from the drive to sustain those motions. Therefore, the part of the drive energy available for spinning the rotor reduces in that condition. This can lead to perpetual or transient capture of the rotor speed in the regime where large amplitude vibrations occur. A critical amount of additional drive power is often needed to escape the capture of the rotor speed and such an escape is often associated with a sudden jump to a higher rotor speed and reduction in the vibration amplitudes, which is formally recognised as the Sommerfeld effect. Till now, Sommerfeld effect and resonance capture has been studied for rotor dynamic systems with unbalanced rotor disc under synchronous whirl condition. In this chapter, it will be shown that two more kinds of Sommerfeld effects can exist even if the rotor shaft and disc are perfectly balanced. One of those is related to high amplitude transverse asynchronous whirl of the non-circular rotor shaft due to parametric instability. The other is related to resonance capture in torsional vibrations of the transmission shaft in a universal joint driveline. In this chapter, three simple academic examples have been considered for each of these kinds of Sommerfeld effect.

## 1 Introduction

Rotating equipment often operate at a speed which is above one or more of its critical speeds. This is desired for good vibration isolation behaviour. However, in a rotor system, a small unbalance may exist due to manufacturing defects, installation error, faults in the rotor blades or bearings, asymmetric loading, or due to natural wear and tear process. Sometimes, the unbalance may be intentionally added to create vibrations, such as in vibrating screens, mixers, and drying cycle of washing machines. A rotor system has large vibration amplitude at its critical speeds and sustained operation at any of these critical speeds can cause failure of the entire

---

A. K. Samantaray (✉)

Department of Mechanical Engineering, Indian Institute of Technology Kharagpur, Kharagpur  
721302, West Bengal, India

e-mail: [samantaray@mech.iitkgp.ac.in](mailto:samantaray@mech.iitkgp.ac.in)

system [1]. In the region of resonance, most of the power supply to the rotating system from the drive of the rotor, such as an engine or motor, goes to increase the structural vibration rather than increasing the rotor spin speed [2, 3]. Hence, the rotor speed may get caught at the resonance with excessive vibration or whirl amplitude.

There is always an energy interaction between the source (drive) and the rotor system, and any real drive (motor, engine, etc.) has power saturation behaviour. These drives follow specific torque-speed characteristic and can deliver a limited amount of torque/power at a given speed. Therefore, the output torque/power of such a drive is influenced by the load and such a drive is often termed as a non-ideal drive/source to distinguish it from an ideal drive that can provide unlimited amount of power output at any speed. In a non-ideally driven rotor, as the rotor speed approaches a critical speed with gradually increasing input power, the rate of increase in rotor speed slows down (almost remains constant) and the vibration amplitudes start to increase at a faster rate. For passage through the resonance or to accelerate through the critical speed, the rotor requires a minimum (just sufficient) amount of power supply from the drive, termed as the critical power. If the available power is a little less than this critical power limit then the rotor speed remains nearly at the critical speed with large vibration amplitude, and a slightly higher power causes the rotor speed to attain a much higher value with a corresponding reduction in the vibration amplitude. Similar phenomenon is also present during gradual rotor speed reduction from a speed above the critical speed. This non-linear jump phenomenon is called the Sommerfeld effect. In fact, there exists a missing speed range in the neighbourhood of a critical speed which is neither reached during the rotor coast up (speed increase) nor during coast down (speed reduction). Three different kinds of Sommerfeld effect due to large vibration amplitudes or load, and consequent drive power saturation in non-ideally driven rotor dynamic systems will be discussed in this chapter.

Arnold Sommerfeld is credited with being the first to study non-ideal sources [4]. The power saturation phenomenon was first experimentally observed by Sommerfeld in 1902 and it has been named in his honor as the Sommerfeld effect [5]. Sommerfeld's observation was that the structural response of the system to which a non-ideal source, such as an electric motor, is connected may act like energy sink under certain conditions so that a part of the energy supplied by the source is spent to vibrate the structure rather than to increase the drive speed. Sommerfeld put it as "*the plant owner spends expensive coal not to rotate his shaft, but rather to shake the foundation*". Further to that, Kononenko [6] described an experiment where a cantilever beam supports a non-ideal energy source (i.e., an unbalanced motor) at its free end and exhibits large amplitude motions in the region of resonance for a sufficiently large range of motor power increase and it is then followed by a sudden amplitude reduction on increasing the input power beyond the critical power input. Sommerfeld effect has been a subject of discussion in several books [2, 3, 7–9].



## 2 Types of Sommerfeld Effect

Generally, the Sommerfeld effect is described by the dynamics of an unbalanced electric motor, particularly a DC motor, placed on an elastic support [10–12]. With increase in the input voltage to the motor (coast up operation), the motor speed increases almost proportionally at the beginning. Due to the unbalance in the rotor, resonance effect sets in as the motor speed approaches the elastic foundation's natural frequency. Therein, the high vibration amplitude of foundation produces a large dynamic load on the motor and hence, the input power supply from motor goes to the foundation to overcome this. If the motor supply voltage is increased and still the motor output power is insufficient to overcome the power diverted to the foundation then the motor speed remains perpetually caught near the resonance speed. In fact, a large amount of motor power is delivered to increase the support's flexural vibration rather than to increase the motor speed [13]. There is a critical amount of motor power beyond which a non-linear jump phenomenon occurs. This results in a sudden jump of motor/rotor speed to a higher speed with a simultaneous sudden reduction in the foundation vibration amplitude. This jump phenomenon is termed as the *Sommerfeld effect of first kind*. Similar jump phenomenon occurs during coast down operation, however, the transition points for this kind of sudden jump are different for coast up and coast down operations. This non-linear jump phenomenon is characterized by the inability to obtain certain common motor steady-state speeds near the resonance frequency [14, 15].

Sommerfeld effect of first kind has been widely studied for mechanical engineering applications in [16–19]. Moreover, several techniques to encourage passage through resonance with a limited power supply and to prevent the growth of large amplitude vibration, thereby extending the machine life, has been proposed in [6, 20]. Tuned Sommerfeld effect suppression is proposed in [21], where the effect of a vibration absorber near the zone of the Sommerfeld effect is described. Sommerfeld effect in wind turbine [22], vehicle dynamics [23] and slider-crank mechanism are also reported in [24]. Balthazar and his co-workers [25–31] have published several studies on different kinds of non-ideal source and system interactions leading to Sommerfeld effect of first kind. Sommerfeld effect of first kind can also appear without rotor unbalance. One example is resonance in the torsional vibration modes due to fluctuating input speed or load [32].

Many rotor dynamic systems exhibit parametric instability. In some specific rotor dynamic applications, the cross-section of the shaft is purposefully designed to be non-circular (asymmetric). Considerable amount of research has been reported on the dynamics of asymmetric rotor shaft mounted on rigid or flexible supports [33–38]. One unstable speed region appears between the two major critical speeds for a flexible asymmetric rotor shaft with a centrally placed rotor disc and rigid/ideal support bearings at the shaft ends [36, 39]. The asymmetry in shaft bending stiffness combined with flexible and asymmetric supports produce many additional unstable regions near at the combined parametric resonance regions, as reported by several

researchers [37, 40–42]. The lumped parameter model of asymmetric shaft-rotor system is studied in both rotating and inertial frames in [43, 44]. These studies assume that the rotor can be driven to and through the unstable regions to reach any operating desired speed, i.e. those do not consider the drive dynamics. The situation under real drive conditions is significantly different due to drive power saturation. The power scarcity to escape through the parametric instability regimes leads to a different kind of Sommerfeld effect, which is termed here as the *Sommerfeld effect of second kind* [45]. Parametric instabilities occur in other types of rotor assemblies, such as geared shaft systems and shafts with universal joints and flexible foundation, and thus, there can be Sommerfeld effect of second kind present in many as yet unsolved problems.

When the rotor shaft has material damping, it exhibits a permanent instability at certain threshold speed. Such permanent instability thresholds also exist in shafts with internal friction such as splined joints, and shafts supported on journal bearings [46–50]. Fluid film forces from bearings and Alford forces on bladed disc systems produce non-conservative circulatory forces and lead to rotor system instability. The permanent instability threshold is a speed above which there is no further stable operating speed. A real rotor cannot operate at any speed higher than this permanent instability speed and shows saturation behaviour termed as the *Sommerfeld effect of third kind* [51].

The nature of the above-mentioned three types of Sommerfeld effects is detailed with example applications in the following sections.

### 3 The Sommerfeld Effect of First Kind Due to Lateral Vibrations

Most studies on Sommerfeld effect reported in literature have focused on the unbalance-induced excitation of natural frequencies with forward precession modes only, while considering the synchronous critical speeds. However, a backward precession mode can also be excited by using just the rotor unbalance as the chief driving force. This has been documented before in some crucial works in this area [52–57]. The occurrence of such a backward whirl response is strongly dependent on stiffness asymmetry at the support ends. Therefore, Sommerfeld effect can also exist at various speed ranges in addition to that at the forward critical speed.

The influence of anisotropy in support flexibility of a rigid rotor shaft on the rotor whirl dynamics is studied here for the case when the rotor shaft carries single unbalanced rotor disc and is driven by a permanent magnet DC (PMDC) motor, as shown in Fig. 1. The rigid disc is firmly placed away from the middle portion of the rigid rotor shaft and this introduces a strong gyroscopic coupling to the rotor dynamic formulation. The rotor dynamic system is studied here for the chosen parameter values listed in Table 1.

The rotor shaft's length is  $l$  and as the rotor disc is placed asymmetrically at one-third of shaft length from the left end support. The rigid hollow shaft has a uniform

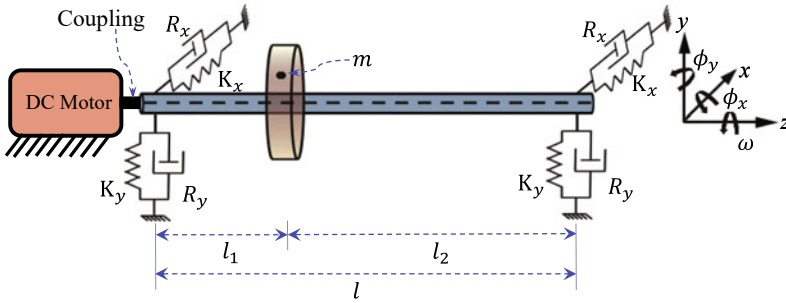


**Fig. 1** Non-ideal rotor dynamic system with anisotropic bearings

**Table 1** The system parameters, their description and values

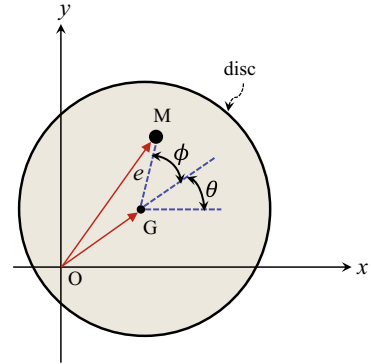
Parameter	Description	Value
$L$	Shaft length	0.9 m
$l_1$	Distance between left end bearing and disk	0.3 m
$l_2$	Distance between disk and right end bearing	0.6 m
$I_p$	Polar moment of inertia of rotor disc	0.48 kgm <sup>2</sup>
$I_d$	Diametral moment of inertia of rotor disc	0.24 kgm <sup>2</sup>
$m$	Mass of the rotor disc	15 kg
$e$	eccentricity of the rotor disc	0.001 m
$R_e$	Translational aerial damping coefficient on rotor disc	20 Ns/m
$R_{e\phi}$	Rotational aerial damping coefficient on rotor disc	1 Nms/rad
$R_x$	Bearing damping coefficient in x-direction	5 Ns/m
$R_y$	Bearing damping coefficient in y-direction	10 Ns/m
$K_x$	Bearing stiffness in x-direction	20,000 N/m
$K_y$	Bearing stiffness in y-direction	40,000 N/m
$R_b$	Spin rotational damping coefficient	0.0005 Nms/rad

circular cross-section. The disc mass is  $m$  and the position of the mass centre of the rotor disc is assumed to be at a distance  $e$  from the shaft geometric centre. The position of the mass centre  $M$  is given as  $(x_m, y_m)$  and that of the geometric centre  $G$  as  $(x, y)$  according to the co-ordinate axes shown in Fig. 2. Thus, the coordinates of mass centre  $(x_m, y_m)$  are expressed as

$$x_m = x + e\cos(\theta + \varphi) \text{ and } y_m = y + e\sin(\theta + \varphi) \tag{1}$$

where  $\theta$  is the angle of rotation of the rotor disc about the spin axis (i.e. z-axis) and  $\varphi$  is a constant phase corresponding to the initial position of the mass centre of the disc. The angles  $\phi_x$  and  $\phi_y$  describe the small angular motions of the rotor about the positive  $x$  and  $y$  directions, respectively. In steady state, the unbalance response

**Fig. 2** Positions of the geometric and mass centre of the rotor disc



is a synchronous whirl at same frequency as the constant angular speed  $\omega$  about the spin or z-axis. The instantaneous angle between the x-axis and the line passing from origin to the geometric centre is then expressed as  $\theta = \omega t$ .

With reference to Fig. 1,  $l_1$  and  $l_2$  are the distance of disc from the left and the right support ends, respectively.  $K_x$  and  $R_x$  are the bearing stiffness and damping in the x-direction for both ends of the shaft; whereas,  $K_y$  and  $R_y$  represent the same in the y-direction. For the disc,  $R_e$  and  $R_e\phi$  represent the external translational and rotational damping values acting at the geometric centre of the disc, respectively.  $I_p$  is the rotary inertia of disc about the spin axis and  $I_d$  is the disc diametral moment of inertia. For this analysis, the disc is assumed to be thin and laterally symmetric, which implies  $I_p = 2I_d$ .

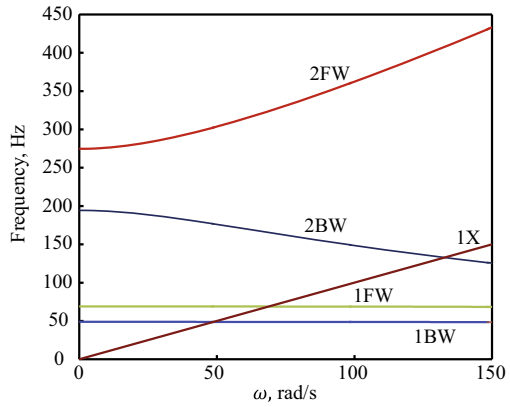
### 3.1 Modal Analysis

A constant angular speed  $\omega$  about the spin z-axis, which is the synchronous frequency, is assumed to analyse the ideal drive system. The equations of motion for the rotor disc system (excluding the non-ideal motor) are obtained as

$$\begin{aligned}
 m\ddot{x} + 2K_x x + (l/3)K_x \phi_y + (2R_x + R_e)\dot{x} + (l/3)R_x \dot{\phi}_y &= me\omega^2 \cos(\omega t) \\
 m\ddot{y} + 2K_y y - (l/3)K_y \phi_x + (2R_y + R_e)\dot{y} - (l/3)R_y \dot{\phi}_x &= me\omega^2 \sin(\omega t) \\
 I_d \ddot{\phi}_y + (l/3)K_x x + (5l^2/9)K_x \phi_y + (l/3)R_x \dot{x} + ((5l^2/9)R_x + R_{e\phi})\dot{\phi}_y - \omega I_p \dot{\phi}_x &= 0 \\
 I_d \ddot{\phi}_x - (l/3)K_y y + (5l^2/9)K_y \phi_x - (l/3)R_y \dot{y} + ((5l^2/9)R_y + R_{e\phi})\dot{\phi}_x + \omega I_p \dot{\phi}_y &= 0 \quad (2)
 \end{aligned}$$

These equations are then written in state-space form by excluding the excitation forces and the critical speeds of the system are obtained from the Campbell diagram, as shown in Fig. 3, through modal or eigenvalue analysis. The first backward and

**Fig. 3** Campbell diagram showing critical speed versus shaft spin speed ( $\omega$ )



the first forward critical speeds of the shaft are  $\omega_{cr1} = 48.97$  rad/s and  $\omega_{cr1} = 68.9$  rad/s, respectively.

The frequency response plots for the system (operating at constant speed) are obtained by assuming harmonic solutions in the form  $x = A\cos(\omega t + \alpha)$ ,  $y = B\sin(\omega t + \beta)$ ,  $\phi_x = -C\sin(\omega t + \gamma)$ , and  $\phi_y = D\cos(\omega t + \delta)$ , where  $A$ ,  $B$ ,  $C$  and  $D$  are whirl amplitudes and  $\alpha$ ,  $\beta$ ,  $\gamma$  and  $\delta$  are the phases. Substitution of these harmonic solutions into Eq. (2) and separation of sine and cosine terms give eight equations which are then solved to determine the eight unknown variables, i.e. the four amplitudes and four phase angles, at any given speed  $\omega$ . Further details on these frequency responses are available in [58]. The normalized whirl amplitudes are defined as  $x^* = 0.33(\omega_{cr1})^2 A(\omega)/g$ ,  $y^* = 0.4(\omega_{cr1})^2 B(\omega)/g$ ,  $\phi_x^* = 100C(\omega)$  and  $\phi_y^* = 120D(\omega)$ , where  $g$  is the acceleration due to gravity. The spin speed is also normalized as  $\omega^* = \omega/\omega_{cr1}$ . The steady-state amplitudes of the rotor at various constant operating speeds, as would happen in an ideal system, are obtained in the form of frequency response plots presented in Fig. 4.

### 3.2 Interfacing the Non-ideal Drive

The permanent type DC motor, whose parameter values are given in Table 2, is considered here as the non-ideal drive. The DC motor produces torque to rotate the rotor shaft instead of a constant speed motor considered for ideal drive. The power developed by a DC motor is given as

$$P_m = \tau_m \dot{\theta} = \frac{k_m(V_i - k_m \dot{\theta})}{k_m} \dot{\theta} \tag{3}$$

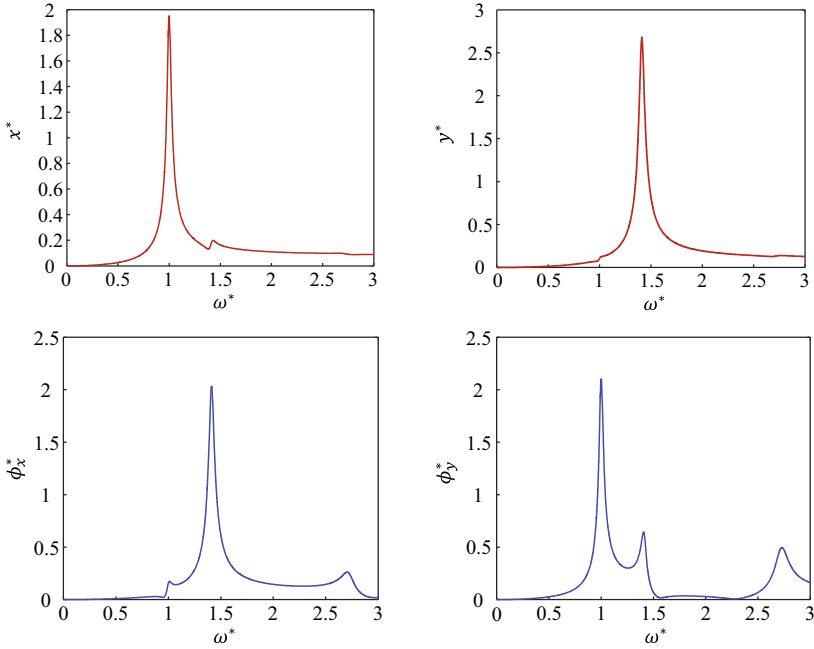


**Fig. 4** Normalized steady state whirl amplitudes versus spin speed ( $\omega^*$ )

**Table 2** DC motor parameters

Notation	Description	Value
$V_i$	DC motor voltage supply	<Variable>
$R_m$	DC motor electrical armature resistance	5 $\Omega$
$k_m$	DC motor characteristic constant	0.5 Nm/A

with  $\tau_m = k_m i_m$ ,  $i_m = \frac{V_i - V_e}{R_m} = \frac{(V_i - k_m \dot{\theta})}{R_m}$ , where  $V_i$  is the voltage supplied across the motor terminal,  $V_e$  is the back emf developed in motor coils,  $k_m$  is the motor characteristic (torque or speed) constant,  $i_m$  is the armature current,  $R_m$  is the armature resistance of the coils,  $\tau_m$  is the mechanical torque developed by the motor and  $\dot{\theta}$  is the rotor angular velocity.

Under steady state conditions,  $\dot{\theta} = \omega$ ; with no angular accelerations. Since the synchronous whirl response is periodic, an energy balance is carried out by integrating the motor power and dissipated power over a cycle, i.e. a complete whirl orbit. The steady state response presented in Fig. 4 is then used in an averaged steady state energy balance between the energy produced by non-ideal DC motor and the energy dissipated through the rotor whirl. The energy dissipation occurs through the external damping  $R_e$  and  $R_{e\phi}$ , and also through the damping in the bearings, i.e.  $R_x$  and  $R_y$ . In addition, some dissipation also occurs at the bearings in the motor and spin resistance in the support bearings, which is represented by a viscous resistance  $R_b$ . Overall, the

net work done by all the dissipative forces over a fixed cycle can be expressed as

$$W_d = \int_0^{2\pi/\omega} (P_{d,\text{left}} + P_{d,\text{right}} + P_{d,\text{disc}} + R_b\omega^2)dt \quad (4)$$

where

$$\begin{aligned} P_{d,\text{left}} &= \dot{q}_L^T \begin{bmatrix} R_x & 0 & 0 & 0 \\ 0 & 0 & 0 & 0 \\ 0 & 0 & R_y & 0 \\ 0 & 0 & 0 & 0 \end{bmatrix} \dot{q}_L, \quad P_{d,\text{right}} = \dot{q}_R^T \begin{bmatrix} R_x & 0 & 0 & 0 \\ 0 & 0 & 0 & 0 \\ 0 & 0 & R_y & 0 \\ 0 & 0 & 0 & 0 \end{bmatrix} \dot{q}_R, \\ P_{d,\text{disc}} &= \dot{q}_d^T \begin{bmatrix} R_e & 0 & 0 & 0 \\ 0 & R_{e\phi} & 0 & 0 \\ 0 & 0 & R_e & 0 \\ 0 & 0 & 0 & R_{e\phi} \end{bmatrix} \dot{q}_d, \\ \dot{q}_L^T &= [(\dot{x} - l_1\dot{\phi}_y) \ 0 \ (\dot{y} + l_1\dot{\phi}_x) \ 0], \\ \dot{q}_R^T &= [(\dot{x} + l_2\dot{\phi}_y) \ 0 \ (\dot{y} - l_2\dot{\phi}_x) \ 0] \quad \text{and} \quad \dot{q}_d^T = [\dot{x} \ \dot{\phi}_y \ \dot{y} \ -\dot{\phi}_x] \end{aligned} \quad (5)$$

The energy supplied by the motor in each cycle is given by

$$W_m = \int_0^{2\pi/\omega} P_m dt = \int_0^{2\pi/\omega} \frac{k_m(V_i - k_m\omega)}{R_a} \omega dt.$$

The steady state energy balance

$$W_m = W_d. \quad (6)$$

Equation (6) is expanded by using the assumed harmonic solutions and treating the whirl amplitudes ( $A, B, C, D$ ) and phases ( $\alpha, \beta, \gamma, \delta$ ) as constants at any given steady-state speed  $\omega$  during the integrations mentioned in Eq. (4). Further simplification and reorganization of Eq. (6) gives

$$\begin{aligned} \frac{2k_m(V_i - k_m\omega)}{R_m} &= [(2R_x + R_e)A^2 + (2R_y + R_e)B^2 + (5L^2/9R_x + R_{e\phi})C^2 + (5L^2/9R_y + R_{e\phi})D^2 \\ &\quad + (2L/3R_x AD\cos(\alpha - \delta)) + (2L/3R_y BC\cos(\beta - \gamma)) + 2R_b]\omega. \end{aligned} \quad (7)$$

For a fixed speed  $\omega$ , and given parameter values and computed parameters of the frequency response, Eq. (7) is used to compute the motor supply voltage  $V_i$ . Interestingly, it is found that there are ranges of speed where three  $\omega$  values give the same  $V_i$ , i.e. the map from  $V_i$  to  $\omega$  is not unique. Out of those three solutions,

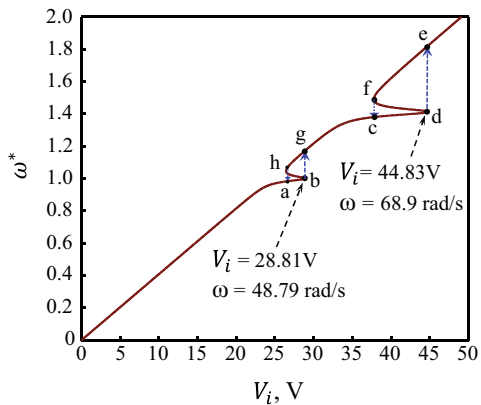
two are stable (attainable) and one is not. The solutions that satisfy the condition  $d(W_m - W_d)/d\omega < 0$  are attainable [18].

Accordingly, the non-ideal rotor system’s response is predicted and multiple jump phenomena due to Sommerfeld effect in the non-ideal system are revealed at the forward and backward critical speeds as shown in Fig. 5. Therein two jumps in the rotor speed, which correspond to the two resonance zones are shown– the first occurs from first backward whirl critical speed  $\omega_{cr1}$  to  $\omega = 57.07\text{rad/s}$  (i.e. near  $\omega^* = 1$ ) and the second takes place from the first forward whirl critical speed  $\omega_{cr2}$  to  $\omega = 89.1\text{ rad/s}$  (i.e. near  $\omega^* = 1.41$ ).

During the rotor coast up operation, the rotor speed continues to increase almost linearly until it reaches point ‘a’. Thereafter, further increase in supply voltage does not result in appreciable change in rotor speed. For the region ‘a’ to ‘b’, although the supply voltage is being increased, the rotor speed does not increase and is stuck at the first backward critical speed for the voltage range 26.43 V to 28.81 V. When the voltage is increased above 28.81 V, the rotor speed suddenly jumps from point ‘b’ to a much higher value at point ‘g’. Afterwards, by increasing voltage, the shaft speed again increases linearly till point ‘c’ (at 37.7 V). This is the zone for the first forward critical speed. Here, the rotor speed is stuck again, from ‘c’ to ‘d’ i.e. for the voltage range 37.77 V to 44.83 V. Subsequently, the second jump takes place from ‘d’ to ‘e’. Thereafter, from point ‘e’ onwards, the speed increases linearly with increase in voltage. The Sommerfeld effect is thus observed for both the first backward and first forward whirl modes of the system; thus, it is termed as ‘Multi-Sommerfeld effect’. Between the two, the jump size is comparatively higher for the first forward critical speed.

On the other hand, during coast down operation from a very high speed, the spin speed reduces linearly as the supply voltage is decreased along the line connecting points ‘e’ to ‘f’. As the voltage is reduced just below 37.77 V (point ‘f’), the speed jumps from point ‘f’ to ‘c’, i.e. there is a sudden reduction in the speed. On further voltage reduction, the voltage-speed curve traces the path along the line joining points ‘c’ to ‘h’ and a second jump occurs from point ‘h’ to ‘a’.

**Fig. 5** Normalized spin speed ( $\omega^*$ ) versus voltage supply  $V_i$



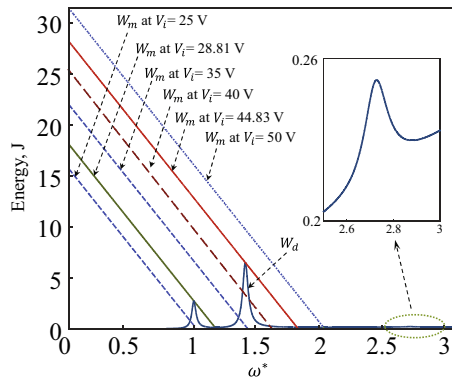


Note that there are three possible rotor speeds for the voltage ranges ‘a’ to ‘b’ and ‘c’ to ‘d’. However, the speed ranges 48.79 to 51.1 rad/s and 68.9 to 72.7 rad/s, are not physically achievable either during rotor coast-up or coast-down. This is because the branches in between ‘d’ to ‘f’ and ‘b’ to ‘h’ are unstable in nature [60, 69]. As a result, only two possible speeds exist near the resonance region; one of these can be reached during rotor coast-up and the other during rotor coast-down.

Further note that the whirl amplitudes are also functions of speed. As a direct consequence, there is an amplitude jump associated with the speed jump at the respective resonance zones. Near the resonance, the energy from the non-ideal motor is not used to increase the spin speed; instead, this energy is transferred to the vibration or whirl amplitudes. Consequently, as speed saturation occurs on approaching a critical speed during the rotor coast up, the whirl amplitudes increase. Such continuous large amplitudes of vibration may severely affect the performance of the rotor and its support structures. This happens for a voltage range in the immediate pre-jump scenario. Afterwards, as the speed jumps to a higher value, the whirl amplitudes promptly reduce. Likewise, during rotor coast down, the discrete jump in speed from a higher value to a lower value is associated with a discrete jump in amplitude from a lower value to a higher value. This dependency comes from the energy balance.

The tendency to get stuck near resonance, also called resonance capture, which occurs due to power saturation, is a typical feature of non-ideal systems. The motor energy  $W_m$  for different supply voltages and the dissipated energy  $W_d$  are plotted against the normalized rotor speed  $\omega^*$  in Fig. 6. The  $W_m$  curve for 28.81 V supply voltage grazes the dissipated energy curve at  $\omega^* = 1$  and intersects it at  $\omega^* = 1.19$ . Likewise, the  $W_m$  curve for 44.83 V supply voltage grazes the dissipated energy curve  $W_d$  at  $\omega^* = 1.41$  and intersects it at  $\omega^* = 1.85$ . The grazing or intersecting points indicate exact energy balance equation  $W_m = W_d$  given in Eq. (6) and hence those are the possible steady-state operating points. There can be one or two or three operating points. One operating point indicates that the operation is away from the resonance regime, two means operation at the exact point from which jumps occur. When there are three intersection points, the one giving the middle speed is an unstable solution. As an example of one operating point, the  $W_m$  curve for 25 V

**Fig. 6** Energy versus Normalized spin speed ( $\omega^*$ )



intersects the  $W_d$  curve once and it is at a point below first backward critical speed, and the  $W_m$  curve for 35 V intersects the  $W_d$  curve once and it is at a point below first forward critical speed. If the input voltage is increased slowly from 25 V or 35 V, then there is a resonance capture at the respective critical speeds. On the other hand, the  $W_m$  curve for 40 V intersects the dissipated energy  $W_d$  curve at three points, out of which two are stable [59] and there is resonance capture during rotor coast up at the lowest of the three speed values corresponding to the intersection points.

The inset in Fig. 6 shows a zoomed view of the resonance condition at 2BW critical speed. It is seen that the energy dissipation at 2BW critical speed and its neighbourhood is too small, and hence, no Sommerfeld effect is observed at 2BW critical speed. However, with a weakly damped bearing support system and large translational and small rotational damping on the rotor disc, it is possible to encounter Sommerfeld effect the 2BW speed. High damping often suppresses Sommerfeld effect [18]. The net external damping in 1FW and 1BW modes comes from the bearing supports and the translational external damping ( $R_e$ ) whereas the net external damping on 2BW and 2FW modes some from the bearing supports and the rotational external damping.

The steady state analysis of the non-ideal system is valid only if the rotor acceleration is negligible, i.e. when voltage increment is done gradually or the rotor disc has large polar moment of inertia. For step input voltages, the steady-state analysis may not give accurate results. To address that, a separate transient analysis for the rotor-motor system, with non-ideal source loading, is carried out.

### 3.3 Transient Analysis

The frequency response and power balance are obtained analytically, but with the assumption that the rotor system operates at a steady-state. These analytical results are then validated through direct numerical simulations of the non-ideal system. To include interaction with the non-ideal drive, the equations of motion are modified with introduction of angular acceleration terms as well as one additional equation describing the spin dynamics of the motor/rotor. From Eq. (1), it can be shown that  $m\ddot{x}_m = m\ddot{x} - m\dot{\theta}^2 \cos(\theta + \varphi) - m\ddot{\theta} \sin(\theta + \varphi)$  and  $m\ddot{y}_m = m\ddot{y} - m\dot{\theta}^2 \sin(\theta + \varphi) + m\ddot{\theta} \cos(\theta + \varphi)$ . These inertia forces produce reactive moment about the axis of the motor rotation. The new set of equations are then given as

$$m\ddot{x} + 2K_x x + (l/3)K_x \phi_y + (2R_x + R_e)\dot{x} + (l/3)R_x \dot{\phi}_y = m\dot{\theta}^2 \cos(\theta + \varphi) + m\ddot{\theta} \sin(\theta + \varphi)$$

$$m\ddot{y} + 2K_y y - (l/3)K_y \phi_x + (2R_y + R_e)\dot{y} - (l/3)R_y \dot{\phi}_x = m\dot{\theta}^2 \sin(\theta + \varphi) - m\ddot{\theta} \cos(\theta + \varphi)$$

$$I_d \ddot{\phi}_y + (l/3)K_x x + \left(5l^2/9\right)K_x \phi_y + (l/3)R_x \dot{x} + \left(\left(5l^2/9\right)R_x + R_{e\phi}\right)\dot{\phi}_y - \omega I_p \dot{\phi}_x = 0$$

$$I_d \ddot{\phi}_x - (l/3)K_y y + \left(5l^2/9\right)K_y \phi_x - (l/3)R_y \dot{y} + \left(\left(5l^2/9\right)R_y + R_{e\phi}\right)\dot{\phi}_x + \omega I_p \dot{\phi}_y = 0$$

$$(I_p + me^2)\ddot{\theta} - me\ddot{x}\sin(\theta + \varphi) + me\ddot{y}\cos(\theta + \varphi) + R_b\dot{\theta} = \frac{k_m(V_i - k_m\omega)}{R_a} \quad (8)$$

The above equation of motion is numerically integrated to obtain the transient response of the system. The initial phase  $\varphi$  does not influence the key aspects of the results and can be taken zero during the analysis. In Fig. 7a, the transient response amplitude for a step input voltage of  $V_i = 28.8$  V is shown, for which the shaft speed is stuck at  $\omega^* = 1$ , i.e. at the first backward critical speed. Note that the line styles and colors used to plot the variables are mentioned in the y-axis label of these graphs. At this point, with a slight increase of input voltage to  $V_i = 28.81$  V, the first jump is detected as shown in Fig. 7b. It can be seen that the normalized amplitudes  $x^*$  and  $\phi_y^*$  are comparatively larger than  $y^*$  and  $\phi_x^*$ . Similarly, the second jump is also detected when supply voltage is increased from  $V_i = 44.73$  V (Fig. 8a) to  $V_i = 44.74$  V (Fig. 8b). This is the resonance zone corresponding to the first forward

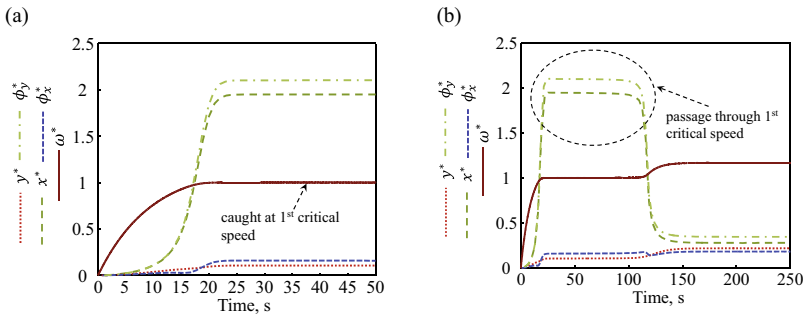


**Fig. 7** Transient response during coasting up for **a** constant  $V_i = 28.8$  V and **b** constant  $V_i = 28.81$  V, showing resonance capture and escape through the 1st critical speed

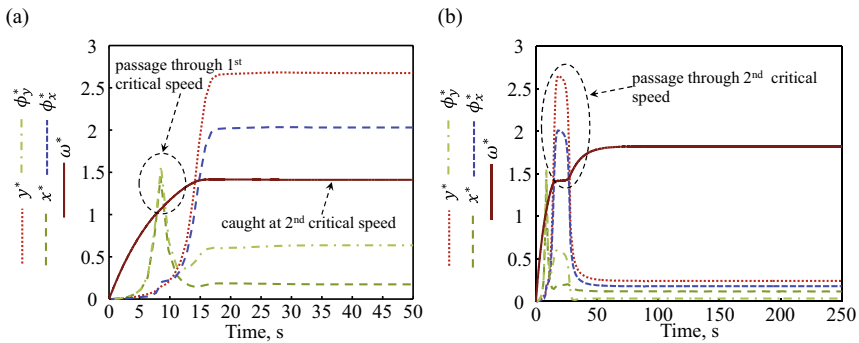


**Fig. 8** Transient response during coasting up for **a** constant  $V_i = 4.73$  V and **b** constant  $V_i = 44.74$  V, showing resonance capture and escape through the 2nd critical speed

critical speed. Here, i.e. in the second resonance zone, the normalized amplitudes  $y^*$  and  $\phi_x^*$  are larger than  $x^*$  and  $\phi_y^*$ .

The numerical simulation results differ a little from the analytically predicted results. Numerical simulations show that the voltage required to escape resonance capture can be slightly less than the theoretically predicted values through steady state analysis. In fact, the discrepancy can be more when the rotary inertia of the rotor disc and the shaft is too small. For large rotary inertia of rotor disc, it acts like a flywheel that reduces the angular accelerations (speed variation due to load transients) and hence, the simulation results tend to be more agreeable with the steady state analysis results.

The severity of the Sommerfeld effect of first kind depends on the system parameters. Especially, if the support and external damping are small then there can be resonance capture for a significantly large range of input power variation. In fact, in the absence of damping in the system, a rotor cannot be operated above the critical speed because it would theoretically require infinite amount of energy to do so. With very high values of damping in the system, Sommerfeld effect can disappear at one or more of the critical speeds. The influence of system damping on the Sommerfeld effect is detailed in [18].

Another interesting phenomenon occurs in the considered system when the two critical speeds are closely spaced and the system is weakly damped. In that case, escape from the 1BW critical speed directly leads to resonance capture at the 1FW critical speed. More such interesting results can be seen in [58].

## 4 Sommerfeld Effect of First Kind Due to Torsional Vibrations

Universal joints (U-joints) or Cardan joints are used for power transmission while accommodating parallel or angular misalignment between the input and output shafts. Torsional dynamics of rotor-shafts with a single U-joint driveline and small misalignment angle was analysed in [61–63]. The single U-joint transmission shaft system with lateral vibrations leads to parametric resonance, quasi-periodic and chaotic motions in certain speed ranges [64–66]. Double U-joints driveline also shows parametric instabilities [67]. Only very recently, the resonance capture phenomenon in a Double U-joints driveline is reported by [68] under combined torsional and lateral vibrations. However, the analysis of Sommerfeld effect purely due to resonance in torsional vibrations in the presence of large U-joint angle and large twist of the elastic shaft has not been studied so far.

Now, we discuss another system of double Cardan joint driveline which shows the Sommerfeld effect of first kind. The schematic representation of the system under consideration is shown in Fig. 9. A non-ideal motor (DC motor) drives a short and rigid input shaft which transmits power to the drive shaft through a U-joint. The hollow drive shaft is long and makes an angle  $\beta$  with the input shaft. The drive shaft

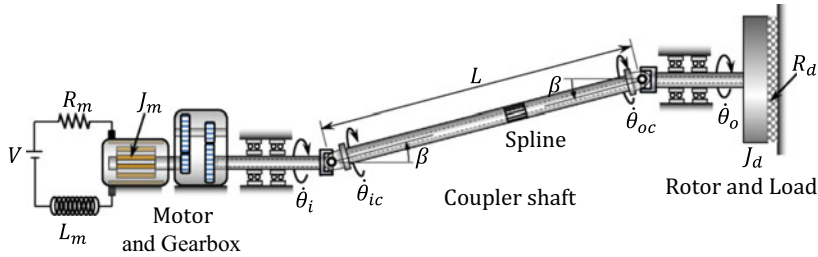


**Fig. 9** Schematic representation of double U-joint transmission system with parallel offset

is assumed to be flexible and it is connected to a short and rigid output shaft at its other end. The input and output shafts have parallel misalignment due to which the double U-joint configuration is called Z-configuration. A heavy rotor disc is mounted on the output shaft. It is assumed that the coupler shaft is massless and its flexural vibrations are prevented by suitably placed idealized rigid bearings. Furthermore, the idealized rigid bearings supporting the shafts (including the coupler shaft) and the spline joint (which is needed for in-phase assembly) are supposed to prevent warping/buckling of the shaft due to combined torsion and bending. Therefore, only torsional vibrations of the system will be considered here. Furthermore, the rotary inertia of the U-joints, clearance/backlash and friction effects are neglected. The two U-joints are assumed to be initially in phase, i.e. the yokes are initially aligned in a plane. Here, the input shaft is driven by either an open-loop controlled torque or a torque applied by a DC motor.

### 4.1 Equations of Motion

The torque applied by the DC motor is denoted by  $T_i$  and the angular velocity of the input shaft of the transmission line is  $\omega_i = \dot{\theta}_i$ . The angular velocity of the output shaft is  $\omega_o = \dot{\theta}_o$ . The angular speed of the motor and load sides (input and output shaft sides) of the coupler shaft are denoted by  $\dot{\theta}_{ic}$  and  $\dot{\theta}_{oc}$ , respectively. It is assumed that while the shaft angle of twist  $\theta_t = \theta_{ic} - \theta_{oc}$  can be large, the maximum dynamic shear stress remains well within the yield stress, and preferably within the endurance limit (for fatigue). The angular velocities at the two ends of the coupler shaft are given by using the transmission ratio at the U-joints as

$$\dot{\theta}_{ic} = \frac{\cos\beta}{1 - \sin^2\beta\cos^2\theta_i}\dot{\theta}_i \text{ and } \dot{\theta}_{oc} = \frac{\cos\beta}{1 - \sin^2\beta\cos^2\theta_o}\dot{\theta}_o \quad (9)$$

Further, by assuming no power loss (friction) at the universal joint, the reaction torque on the input shaft  $T_i$  and active torque  $T_o$  on the output shaft are given, respectively, as

$$T_i = \frac{\cos\beta}{1 - \sin^2\beta\cos^2\theta_i} T_c \text{ and } T_o = \frac{\cos\beta}{1 - \sin^2\beta\cos^2\theta_o} T_c \quad (10)$$

where  $T_c = k_t\theta_t + c_t\dot{\theta}_t$  is the torque transmitted through the coupler shaft, and  $k_t$  and  $c_t = \lambda k_t$ , with  $\lambda$  as a material constant, are the torsional stiffness and damping of the coupler shaft, respectively. The equations of motion of this two-degrees-of-freedom mechanical sub-system are given as

$$J_m\ddot{\theta}_i + \frac{\cos\beta}{1 - \sin^2\beta\cos^2\theta_i} \times (k_t\theta_t + c_t\dot{\theta}_t) = T \quad (11)$$

$$J_d\ddot{\theta}_o - \frac{\cos\beta}{1 - \sin^2\beta\cos^2\theta_o} \times (k_t\theta_t + c_t\dot{\theta}_t) + R_d\dot{\theta}_o = 0 \quad (12)$$

$$\dot{\theta}_t = \frac{\cos\beta}{1 - \sin^2\beta\cos^2\theta_i} \dot{\theta}_i - \frac{\cos\beta}{1 - \sin^2\beta\cos^2\theta_o} \dot{\theta}_o \quad (13)$$

where,  $T$  (or  $T_i$ ) is the motor torque that applied on the input shaft.

## 4.2 Numerical Simulation Results

A representative set of parameter values given in Table 3 is chosen for this system. The natural frequency of torsional vibration is  $\omega_{n0} = \sqrt{k_t(1/J_m + 1/J_d)}$ , which, for the given data, turns out to be 176.21 rad/s, when  $\beta = 0$  or the input, output and

**Table 3** Parameter values of the double Cardan joint transmission shaft system

Parameter	Description	Value
$J_m$	Moment of inertia of rotor of motor	0.2 kg.m <sup>2</sup>
$J_d$	Moment of inertia of output side large rotor disc	2.8 kg.m <sup>2</sup>
$G$	Modulus of rigidity of shaft material	80 GPa
$\tau_{max}$	Allowable shear stress of ASTM A514 alloy steel	414 MPa
$d_{oc}$	Outer diameter of coupler shaft	5 cm
$L$	Length of coupler shaft	5 m
$I_p$	Polar moment of area of coupler shaft	$3.62265 \times 10^{-7} \text{ m}^4$
$k_t$	Torsional stiffness of coupler shaft	5796 Nm/rad
$\lambda$	Material / internal damping (beta-damping) factor	$0.002 \text{ s}^{-1}$
$c_t$	Torsional damping of coupler shaft	11.592 Nms/rad
$R_d$	Load damping on large rotor disc	3 Nms/rad
$\beta$	U-joint angle	1 rad
$T$	External torque applied by motor on input shaft	<Variable>

coupler shafts are perfectly aligned in a line. For the considered parameter values in Table 3, numerical simulations are done for the different constant input torque values ( $T = 200 \text{ Nm}$ ,  $300 \text{ Nm}$  and  $474 \text{ Nm}$ ) and the respective results for the input side rotor speed, the output side rotor speed and angle of twist of the coupler shaft are shown in Fig. 10.

Due to flywheel effect, the angular velocity of the bigger rotor is steadier with respect to that of the rotor of the motor. At this nearly steady speed of the output rotor, a ball park estimate of the average speed can be obtained as  $\bar{\Omega}_o = T/R_d$  and the actual average output shaft speed  $\Omega_o$ . Since, the input shaft is directly connected to the geared motor the speed of the output shaft of the motor, the motor output speed  $\dot{\theta}_m = \omega_i = \dot{\theta}_i$ . Likewise, since the rotor disc is rigidly fixed to the output drive shaft, the rotor disc speed  $\dot{\theta}_d = \omega_o = \dot{\theta}_o$ .

The results show that the output shaft speed almost reaches the estimated speed for low values of torque. For example, consider the simulation results presented in Fig. 10 for a constant input torque  $T = 200 \text{ Nm}$ . With chosen value  $R_d = 3 \text{ Nms/rad}$  (see Table 3), the estimated output shaft speed  $\bar{\Omega}_o$  is  $66.67 \text{ rad/s}$  whereas the simulation results show that the average actual speed of output shaft  $\Omega_o$  is less, about  $62.1 \text{ rad/s}$  (see Fig. 10). The estimation error is about  $4.5 \text{ rad/s}$  or about  $7\%$ . This is because a part of the energy is lost through damping in torsional vibration (see Fig. 10). Also, the output shaft speed has less fluctuation due to heavy rotor inertia whereas there is significant fluctuation in the input shaft speed.

When the torque is increased to  $T = 300 \text{ Nm}$ , the estimated output shaft speed  $\bar{\Omega}_o$  is  $100 \text{ rad/s}$ . However. The corresponding results given in Fig. 10 show that the average output shaft speed  $\Omega_o$  is about  $78.5 \text{ rad/s}$ ; i.e. the estimation error is about  $21.5 \text{ rad/s}$  or  $27\%$ . This increase in error is due to the increased torsional vibration

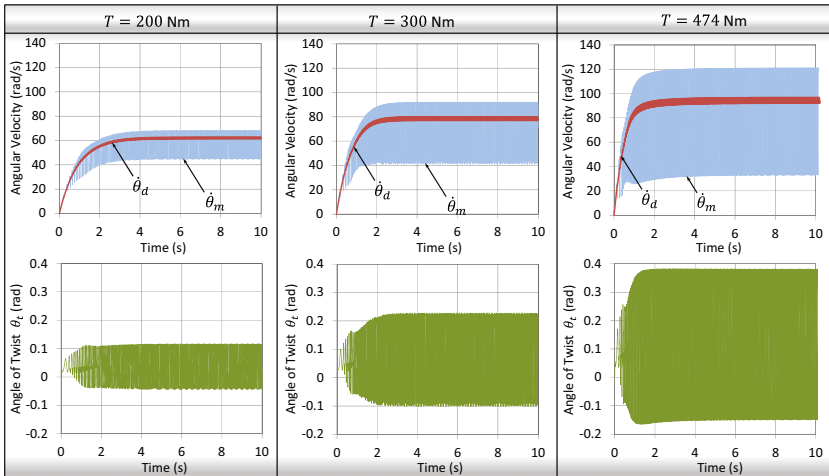


**Fig. 10** The angular velocities of input side rotor  $\dot{\theta}_m$  and output side rotor  $\dot{\theta}_d$ , and angle of twist of the coupler shaft  $\theta_t$  for constant input torque. Column 1:  $T = 200 \text{ N.m}$ , Column 2:  $T = 300 \text{ N.m}$  and Column 3:  $T = 474 \text{ N.m}$

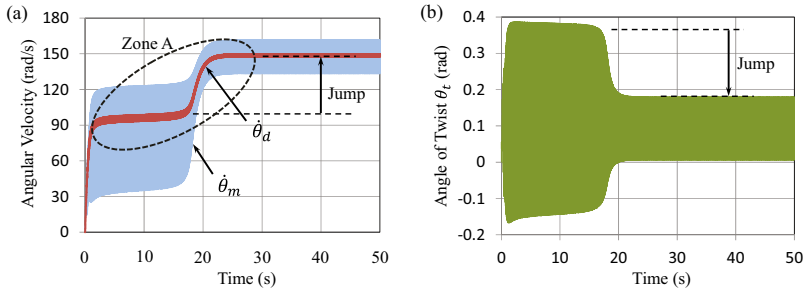


**Fig. 11** **a** The angular velocities of input side rotor  $\dot{\theta}_m$  and output side rotor  $\dot{\theta}_d$ , **b** angle of twist of the coupler shaft  $\theta_t$ , for constant input torque  $T = 480$  N.m

amplitude. In this case, the output shaft speed is closer to half of the torsional natural frequency of the zero-offset configuration ( $\beta = 0$ ) of the system. Apparently, the high torsional vibration amplitudes are due to approaching the resonance speed (twice the shaft speed is closer to the zero-offset configuration natural frequency). In fact, this shows that a kind of saturation phenomena is starting to take hold and more and more energy from the source is being wasted in torsional vibrations rather than being used to accelerate the output shaft.

For  $T = 474$  Nm, the estimated output shaft speed  $\bar{\Omega}_o$  is 158 rad/s. However, the actual average output shaft speed  $\Omega_o$  is 94.7 rad/s as shown in simulation results in Fig. 10. The torsional vibration amplitudes have reached peak twist of 0.38 rad and that vibration amplitude persists thereafter. Therefore, with the increase in torque  $T$  from 300 to 474 Nm, the output shaft speed has changed by a small margin because the additional energy is diverted to sustain the torsional vibrations. This is a classic symptom associated with the Sommerfeld effect of first kind and is termed as the capture at the resonance or resonance capture.

If input torque is increased to  $T = 480$  Nm, the estimated output shaft speed is 160 rad/s and the simulated average output shaft speed (see Fig. 11a) is 148.5 rad/s. Hence by increasing the input torque up to the critical value, system has escaped the resonance capture at about 20 s which is associated with an upward speed jump, together with a simultaneous reduction in torsional vibration amplitude and speed fluctuations of the input shaft. As soon as there is escape from resonance, less drive power is lost in torsional vibrations and the extra power is able to accelerate the output shaft rotor disc. An important observation is that during the rotor coast up, the range of steady average output shaft speeds between 94.7 to 148.5 rad/s are unreachable (excluding the transient period). The resonance capture and escape at this sub-critical speed would be henceforth referred to as Zone-A dynamics.

When the torque is increased further, the output shaft speed continues to increase in a nonlinear manner showing a second speed saturation or resonance capture. The response of the system for  $T = 540$  N.m given in Fig. 12 shows that after escaping Zone-A capture, the output shaft speed initially increases to 170 rad/s and then



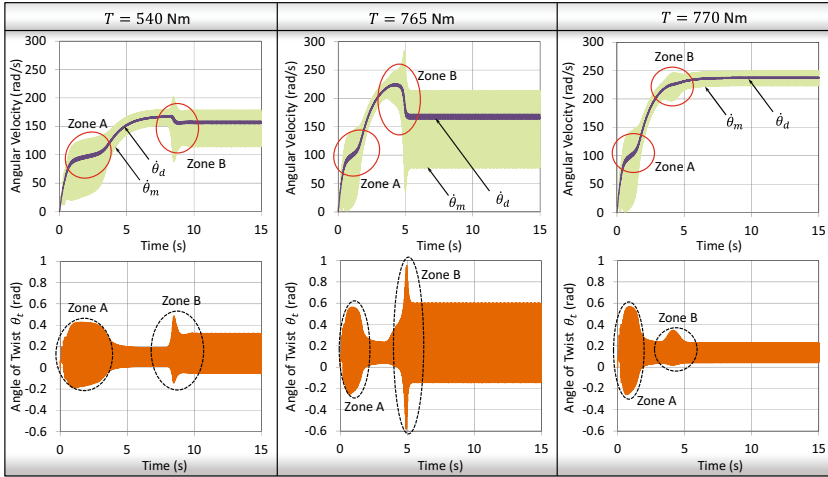


**Fig. 12** The angular velocities of input side rotor  $\dot{\theta}_m$  and output side rotor  $\dot{\theta}_d$ , and angle of twist of the coupler shaft  $\theta_t$  for constant input torque. Column 1:  $T = 540$  N.m, Column 2:  $T = 765$  N.m and Column 3:  $T = 770$  N.m

reduces to approximately steady mean speed of 156 rad/s (marked as Zone-B in the Fig. 12).

The estimated average output shaft speed at  $T = 540$  Nm is 180 rad/s. When the input torque is increased further, there is very little increase in the approximate steady average output shaft speed. For example, with  $T = 765$  Nm, the estimated output shaft speed is 255 rad/s whereas the actual average output shaft speed initially reaches 225 rad/s and then reduces to a steady average output shaft speed of 166 rad/s (see Fig. 12). Thus, for input torque changing from 480 Nm (see Fig. 11) to 765 Nm (see Fig. 12) or about 60%, the average output shaft speed has changed from 148.5 to 166 rad/s or about 12%. This indicates presence of another resonance capture in the neighbourhood of the critical speed of the straight-line assembly configuration of the system, which is 176.21 rad/s.

Figure 12 also shows the transient response of the system for constant input torque  $T = 770$  Nm, where the resonance capture is escaped and the average output shaft speed reaches 237 rad/s. So, an abrupt speed increase or jump of more than 70 rad/s is obtained with a small increase in torque from 765 to 770 Nm. Moreover, the torque change from 480 to 770 Nm (about 60.4%) produces 148.5 to 237 rad/s speed change (about 60%). Such almost commensurate change occurs when the resonance capture is avoided.

Further, note that the upward speed jump is associated with a corresponding reduction in torsional vibration amplitude. In fact, the peak vibration amplitude (almost 1 rad) at  $T = 765$  Nm exceeds the allowable limit and the steady vibration amplitude is large enough to cause quick fatigue failure. However, if the applied torque is more than the threshold value ( $T \geq 770$  Nm) to escape the resonance capture

then the peak as well as steady torsional vibration amplitudes reduce significantly and the system can be operated safely. This establishes the need for dynamic analysis of the system because an undersized actuator can lead to resonance capture and system failure.

In addition to the resonance capture and escapes seen during rotor coast up, discrete speed jumps are also observed for this system during rotor coast down. More such results can be consulted in [32]. In this section, a pre-computed open-loop controlled torque  $T = \overline{\Omega}_o R_d$  is applied for any desired mean speed  $\overline{\Omega}_o$ . Similar phenomena are also observed in the case the drive is a non-ideal source, such as a DC motor. To include the DC motor dynamics in the model, the following set of modified system equations are considered.

$$J_m \ddot{\theta}_i + \frac{\cos\beta}{1 - \sin^2\beta \cos^2\theta_i} \times (k_t \theta_t + c_t \dot{\theta}_t) = k_m i_a \quad (14)$$

$$J_d \ddot{\theta}_o - \frac{\cos\beta}{1 - \sin^2\beta \cos^2\theta_o} \times (k_t \theta_t + c_t \dot{\theta}_t) + R_d \dot{\theta}_o = 0 \quad (15)$$

$$\dot{\theta}_t = \frac{\cos\beta}{1 - \sin^2\beta \cos^2\theta_i} \dot{\theta}_i - \frac{\cos\beta}{1 - \sin^2\beta \cos^2\theta_o} \dot{\theta}_o \quad (16)$$

$$L_m \frac{di_a}{dt} + k_m \dot{\theta}_i + R_m i_a = V \quad (17)$$

where the motor torque that applied on the input shaft is given as  $T = k_m i_a$ ,  $i_a$  is the armature current,  $k_m$  is the effective motor characteristic constant, and  $L_m$  and  $R_m$  are, respectively, the motor armature coil inductance and resistance. The two-way coupling between Eqs. (14) and (17) establishes an energy transfer pipeline. Note that while many authors do not consider the inductance term  $L_m$  in the model, here it is important to retain it because of large speed fluctuations of the input shaft which is connected to the rotor of the motor [26, 69–72]. The motor is assumed to be geared and hence a large motor characteristic constant  $k_m = 5 \text{ Nm/A}$  is chosen here. The other chosen motor parameters are  $L_m = 0.01 \text{ H}$  and  $R_m = 10\Omega$ . The motor supply voltage  $V$  is the controllable input.

A consolidated result showing gradual coast up and coast down dynamics is given in Fig. 13. Here, the motor input voltage is increased @50 V/s till 80 s, held at 4 kV for the next 40 s and then reduced @50 V/s for the next 80 s.

The trend for average output shaft speed, in time sequence, shows escape through Zone-A resonance capture at sub-critical speed, a small downward speed jump at the onset of resonance capture at the critical speed (Zone-B<sub>1</sub>), gradual speed increase at a slow rate followed by a sudden upward speed jump to escape resonance capture at the critical speed (Zone-B<sub>2</sub>), constant speed for the duration of constant input torque, gradually decreasing speed and then a sudden downward speed jump through the critical speed (Zone-C) and a small downward jump through the sub-critical speed resonance (Zone-D). Note that sudden speed jumps in Zones A and C are not clearly

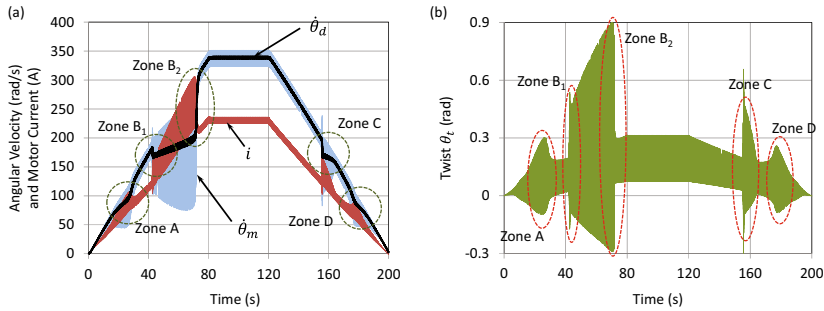


**Fig. 13** **a** The angular velocities of input side rotor  $\dot{\theta}_m$  and output side rotor  $\dot{\theta}_d$ , and motor current  $i$ , and **b** angle of twist of the coupler shaft  $\theta_t$ , when the DC motor voltage is ramped up @50 V/s from  $t = 0$  s to 80 s, held constant at 4 kV up to  $t = 120$  s and then ramped down @50 V/s up to  $t = 200$  s

visible in this result due to faster rate of input voltage ramp. The resonance capture and escape symptoms are also present in the motor current signature. Interested readers may refer to [32] for more such information.

Hence, two instances of Sommerfeld effect were observed in the system for large joint angle at the U-joints. If a so-called critical speed is defined as the fundamental torsional vibration natural frequency of the system with zero joint angle then these Sommerfeld effects occur in the neighborhood of half of the so-called critical speed, termed sub-critical speed resonance capture and escape, and further in the vicinity of the critical speed itself, called critical speed resonance capture and escape. The zone of the resonance can be determined through a simplification by assuming the mean output shaft speed to be  $\bar{\Omega}_o$ , and initially neglecting the small fluctuations over it. Then the angular speed fluctuations in the output shaft side of the coupler shaft are obtained from Eq. (9), which is periodic with time period  $\tau = 2\pi/\bar{\Omega}_o$  and can be expanded as a Fourier series

$$\dot{\theta}_{oc} = \left( \frac{a_0}{2} + \sum_{i=1}^n a_{2i} \cos 2i \bar{\Omega}_o t \right) \bar{\Omega}_o, \quad (18)$$

where

$$a_i = \frac{2}{\tau} \int_0^{\tau} \frac{\cos \beta \cos i \bar{\Omega}_o t}{1 - \sin^2 \beta \cos^2 \bar{\Omega}_o t} dt = \frac{1}{\pi} \int_0^{2\pi} \frac{\cos \beta \cos i \theta}{1 - \sin^2 \beta \cos^2 \theta} d\theta, \quad i = 0, 1, 2, \dots$$

All the  $\sin(\cdot)$  terms of regular Fourier series are absent because the function is even and odd coefficients ( $i = 1, 3, \dots$ ) of  $\cos(\cdot)$  terms also vanish on integration; thus only even coefficients are shown as  $a_{2i}$  ( $i = 0..n$ ) in Eq. (18). These coefficients depend only on the value of  $\beta$ . For the chosen value  $\beta = 1$  rad, a good convergence is obtained by considering the first five coefficients  $a_0 = 2, a_2 = 0.5969, a_4 = 0.1781,$

$a_6 = 0.0532$  and  $a_8 = 0.0159$ . From Eq. (18), it is evident that the mean  $\dot{\theta}_{oc}$  is  $\frac{a_6}{2}\bar{\Omega}_o = \bar{\Omega}_o$  and the fluctuating parts have frequencies  $2\bar{\Omega}_o, 4\bar{\Omega}_o, 6\bar{\Omega}_o, \dots$ . Thus, resonance occurs when the average output shaft speed approaches natural frequency or any of its even fractions. However, Sommerfeld effect is not observed at all those speeds because of the presence of damping in the system. If the system has smaller torsional damping and/or stiffness, then it is possible to obtain resonance capture and escape at further subcritical speed ranges. On the other hand, Sommerfeld effect may disappear at lower values of angular misalignment and higher values of shaft stiffness and damping. Thus, the severity of Sommerfeld effect in the considered system depends on a whole lot of system parameters, mostly the torsional stiffness and damping, motor constant and the shaft misalignment angle.

## 5 The Sommerfeld Effect of Second Kind

There are some specific applications in rotor dynamic systems, in which the rotor shaft is designed with non-circular or asymmetric cross section. For example, rotor shafts of multi-pole electric motors, twisted brush motors, shafts with keyways or flats to allow coupling, spade drill bits, rotary broaches, etc. Due to this rotating asymmetry, the vibrational characteristics of the rotor system have unstable dynamics in certain conditions. The asymmetry appears in the form of different bending stiffness or different moment of inertia of rotor shaft or rotor disc along the principal axes in the shaft cross-section. A rotor system with asymmetry in its bending flexibility has unstable speed range near the vicinity of the natural frequencies. The dynamics of such a system is governed by differential equations with time-varying parametric coefficients which lead to parametric instability in certain rotor speed range. Therefore, the unstable speed range is bounded by a lower stable speed range and an upper stable speed range.

However, to reach the upper stable speed range, the rotor system has to transit through the unstable speeds. This consideration is not made when mathematical analysis of the system is done with an ideal drive assumption. In reality, the whirl amplitudes grow exponentially at any speed lying in the unstable speed range and such whirl loads the drive, thereby limiting the amount of energy available to accelerate the shaft spin. The transition from the lower stable range to higher stable range would require the rotor spin to accelerate quickly through the unstable speed range before the whirl amplitudes grow substantially and create energy scarcity for rotor spin acceleration. As a consequence, when rotor spin escapes the unstable speed range, it would reach a substantially higher speed with decaying whirl amplitudes. Similar behavior occurs during rotor coast down through unstable speed range. This kind of non-linear jump phenomena is termed as *the Sommerfeld effect of second kind*. Unlike regular Sommerfeld effect (of first kind) where the power scarcity at the resonance is the cause of speed capture, Sommerfeld effect of the second kind relates to power scarcity at the parametric instability regions.

### 5.1 Flexible Asymmetric Rotor Shaft with Rigid Supports

We consider an asymmetric flexible rotor shaft which is mounted on two ideal or rigid bearings at its two ends and carries a heavy centrally placed rotor disc. A permanent magnet type DC motor is used to drive the rotor. A schematic representation of this rotor dynamic system is shown in Fig. 14, in which the shaft’s cross-section is rectangular. The two ends of the rotor shaft, where the shaft is supported on the rigid bearings, are cylindrical for negligibly small lengths. The rotor shaft mass is referred to the rotor disc position, as it is common in a Jeffcott rotor model, and the torsional vibrations are neglected.

A rotating coordinate frame is aligned parallel to the principal axes in the shaft cross-section so that the shaft bending stiffness remains constant in that reference frame. In the fixed or inertial coordinate frame, the shaft bending stiffness change with time as the shaft rotates. Here,  $x, y, z$  is the fixed coordinate system and  $\eta, \zeta, z$  is the rotating coordinate system, as shown in Fig. 14, with the rotation  $\theta$  about the common or parallel  $z$ -axis defining the angle between the two coordinate systems at any particular time and  $\Omega = \dot{\theta}$  is the angular rotational speed of shaft about  $z$ -axis (shaft spin axis). The coordinates  $(x, y)$  and  $(\eta, \zeta)$  refer to position of deflected shaft centre  $C$  in the respective frames. The shaft stiffness in  $\eta, \zeta$ —directions are  $k_\eta$  and  $k_\zeta$ , respectively.

An overall viscous damping  $c$  is assumed to act at the geometric centre  $C$  of the rotor disc. Since the rotor disc is symmetrically mounted on the rotor shaft and the rotor whirls in cylindrical mode, only two degrees of freedom of the system are considered. For studying the Sommerfeld effect of second kind, there is no need for rotor disc eccentricity. However, if the system is ideally at equilibrium (zero whirl amplitude) then it cannot show exponential whirl amplitude growth at instability. Therefore, one needs to disturb the system from equilibrium to initiate the whirl. This disturbance is naturally present in a real working environment. However, for simulation or analysis, this disturbance can be given as an initial condition such as impact or as small residual unbalance [73]. An ideal coupling which is flexible in

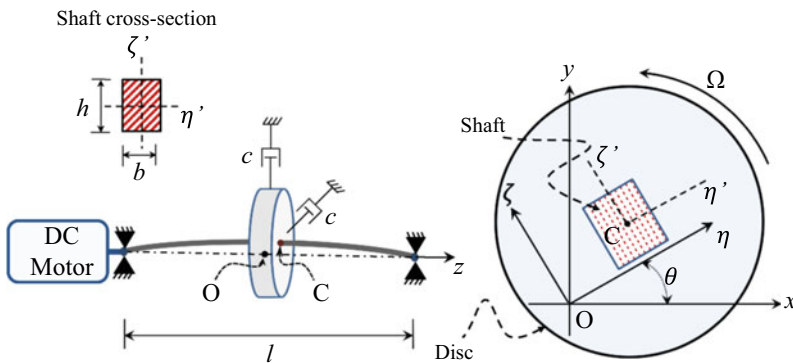


Fig. 14 Rectangular flexible rotor shaft with central rotor disc driven by a DC motor

bending and rigid in torsion is assumed between the DC motor and the rotor shaft. Since the torsion of the rotor shaft is neglected, the motor torque is directly applied to the rotor disc.

## 5.2 Equations of Motion of the System

Only lateral displacements of the disc in the first bending (whirl) mode of the rotor shaft are considered with no rotation of the disc about diametral ( $\eta - \zeta$ ) axes. To derive the stability domain of the rotor system at various rotor spin speeds, initially, the rotor speed is assumed to be constant; i.e.,  $\theta = \Omega t$ ,  $\dot{\theta} = \Omega$  and  $\ddot{\theta} = 0$ . The equations of motion of the rotor in the lateral directions can be written as

$$\mathbf{M}\ddot{\mathbf{z}} + \mathbf{D}\dot{\mathbf{z}} + \tilde{\mathbf{k}}_s \mathbf{z} = \mathbf{f} \quad (19)$$

where mass matrix  $\mathbf{M} = m\mathbf{I}$ , damping matrix  $\mathbf{D} = c\mathbf{I}$ ,  $\mathbf{I}$  is a  $2 \times 2$  identity matrix,  $\tilde{\mathbf{k}}_s$  is a time-varying shaft bending stiffness matrix, rotor's lateral displacement vector in the fixed frame  $\mathbf{z} = [x \ y]^T$ ,  $\mathbf{f}$  is a forcing vector which is zero in the present case,  $m$  is rotor disc mass (including referred shaft mass) and  $c$  is the viscous damping coefficient at the rotor disc position. At constant spin speed, the rotation matrix from rotating to fixed frame is  $\mathbf{R} = \begin{bmatrix} \cos\Omega t & -\sin\Omega t \\ \sin\Omega t & \cos\Omega t \end{bmatrix}$ . If  $\mathbf{t} = [\eta \ \zeta]^T$  is the rotor's lateral displacement vector then the restoring force vector in rotating frame is  $\mathbf{k}_s \mathbf{t} = \mathbf{k}_s \mathbf{R}^T \mathbf{z}$  where  $\mathbf{k}_s = \begin{bmatrix} k_\eta & 0 \\ 0 & k_\zeta \end{bmatrix}$ . Transformation of the restoring forces from rotating coordinate system to fixed coordinate system gives the restoring force vector in fixed frame as  $\mathbf{Rk}_s \mathbf{R}^T \mathbf{z} = \tilde{\mathbf{k}}_s \mathbf{z}$  where time varying matrix  $\tilde{\mathbf{k}}_s = \mathbf{Rk}_s \mathbf{R}^T = \begin{bmatrix} k_s + \Delta k_s \cos 2\Omega t & \Delta k_s \sin 2\Omega t \\ \Delta k_s \sin 2\Omega t & k_s - \Delta k_s \cos 2\Omega t \end{bmatrix}$  with  $k_s = \frac{k_\eta + k_\zeta}{2}$  as the mean shaft bending stiffness and  $\Delta k_s = \frac{k_\eta - k_\zeta}{2}$  as the deviatoric shaft bending stiffness. Thus the equation of motion in fixed coordinate system is obtained as

$$\mathbf{M}\ddot{\mathbf{z}} + \mathbf{D}\dot{\mathbf{z}} + \mathbf{K}_0 \mathbf{z} + \Delta \mathbf{K}_1 \mathbf{z} \cos(\tilde{\Omega} t) + \Delta \mathbf{K}_2 \mathbf{z} \sin(\tilde{\Omega} t) = 0 \quad (20)$$

where  $\mathbf{K}_0 = \begin{bmatrix} k_s & 0 \\ 0 & k_s \end{bmatrix}$ ,  $\Delta \mathbf{K}_1 = \begin{bmatrix} \Delta k_s & 0 \\ 0 & -\Delta k_s \end{bmatrix}$ ,  $\Delta \mathbf{K}_2 = \begin{bmatrix} 0 & \Delta k_s \\ \Delta k_s & 0 \end{bmatrix}$  and  $\tilde{\Omega} = 2\Omega$ .

It can be seen that Eq. (20) is a second order differential equation containing time dependent coefficients. Usually, the boundaries of unstable regions of systems described by differential equations with parametric coefficients are determined by using Floquet theory. Hence, the state space form of Eq. (20) is first obtained as

**Table 4** The asymmetric rotor shaft and rotor disc system parameters

Parameter	Description	Value
$l$	Length of rotor shaft	0.9 m
$b$	Width of rotor shaft	1.49 cm
$h$	Depth of rotor shaft	2.11 cm
$\rho$	Density of rotor shaft material	7850 kg/m <sup>3</sup>
$E$	Young's modulus of rotor shaft material	210 GPa
$J$	Rotary inertia of rotor disc	0.02 kgm <sup>2</sup>
$m$	Mass of rotor disc	10 kg
$c$	External viscous damping coefficient	60 Ns/m
$k_\eta$	Shaft stiffness in $\eta$ direction: $k_\eta = 4Eh(b/l)^3$	80,000 N/m
$k_\zeta$	Shaft stiffness in $\zeta$ direction: $k_\zeta = 4Eb(h/l)^3$	160,000 N/m

$$\begin{bmatrix} \ddot{x} & \ddot{y} & \dot{x} & \dot{y} \end{bmatrix}^T = \mathbf{S}_{4 \times 4} \begin{bmatrix} \dot{x} & \dot{y} & x & y \end{bmatrix}^T \text{ or } \dot{\mathbf{A}}^T = \mathbf{S}(t)\mathbf{A}^T \quad (21)$$

$$\text{where } \mathbf{S}(t) = \begin{bmatrix} -c/m & 0 & -(k_s + \Delta k_s \cos 2\Omega t)/m & -(\Delta k_s \sin 2\Omega t)/m \\ 0 & -c/m & -(\Delta k_s \sin 2\Omega t)/m & -(k_s - \Delta k_s \cos 2\Omega t)/m \\ 1 & 0 & 0 & 0 \\ 0 & 1 & 0 & 0 \end{bmatrix}.$$

As  $\mathbf{S}(t)$  is  $T$ -periodic with  $T = 2\pi/\Omega$ , the monodromy matrix is obtained by numerical integration of Eq. (21) from 0 to  $T$  with initial conditions set to  $[I]_{4 \times 4}$  ( $4 \times 4$  identity matrix) and then the eigenvalues  $\sigma_i$  ( $i = 1..4$ ) of the monodromy matrix are used to conclude the stability of the system. The real parts of the eigenvalues  $\sigma$ , i.e.  $\sigma_{\text{Re}}$ , indicate the system's stability. Positive real part indicates instability whereas negative real part indicates stability. The parameter values chosen for this study are listed in Table 4.

### 5.3 Numerical Results

In the absence of external damping ( $c = 0$ ), available theoretical results indicate instability speed range appears between the non-rotating beam natural frequencies in principal directions, i.e. between  $\Omega_\eta = \sqrt{(k_s - \Delta k_s)/m} = 89.44$  rad/s and  $\Omega_\zeta = \sqrt{(k_s + \Delta k_s)/m} = 126.49$  rad/s. The eigenvalues are evaluated numerically in the frequency range of interest. The real parts of the eigenvalues are plotted with respect to rotor spin speed in Fig. 15. In Fig. 15, real parts of all the four eigenvalues are equal and negative everywhere except between a narrow region identified as  $U_1$ . The absolute values of eigenvalues are plotted Fig. 16, in which the region for  $\|\sigma\| > 1$  indicates instability.

Hence for the chosen parameter values given in Table 4, the unstable speed range is 89.63 to 126.2 rad/s. It is evident that the system has one unstable region  $U_1$  which

**Fig. 15** Real parts of eigenvalues versus rotor spin speed from  $x - y$  frame model

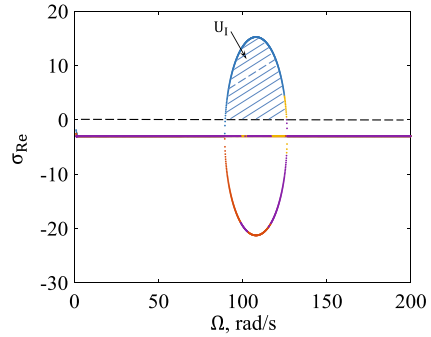
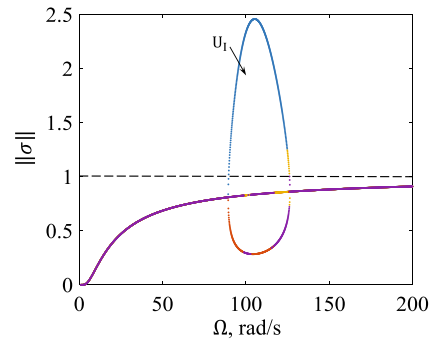


**Fig. 16** Absolute values of eigenvalues versus rotor spin speed from  $x - y$  frame model



appears near the critical speeds of system, as previously reported in [39, 74]. Only principal parametric resonance appears, in which the instability boundaries are near the major natural frequencies, i.e.  $\Omega_\eta$  and  $\Omega_\zeta$ . The combined resonance and other parametric resonances do not appear for this system with rigid supports.

Let us introduce a shaft non-circularity parameter  $\kappa = \Delta k_s/k_s$  and a non-dimensional rotor speed  $\Omega^* = \Omega/\Omega_{avg}$  with  $\Omega_{avg}^2 = (\Omega_\eta^2 + \Omega_\zeta^2)/2$ . The stability domain for constant zero damping  $c = 0$  Ns/m, evaluated from Eq. (21), is shown in Fig. 17, wherein the hatched area shows the unstable region which has two bound-

**Fig. 17** Shaft non-circularity  $\kappa$  versus non-dimensional rotor speed  $\Omega^*$  and  $c = 0$  Ns/m

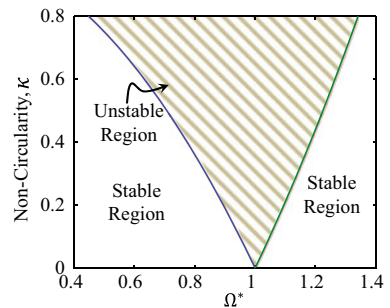




**Fig. 18** Absolute magnitude of eigenvalues versus rotor speed,  $\kappa = 1/3$  and  $c = 365$  Ns/m

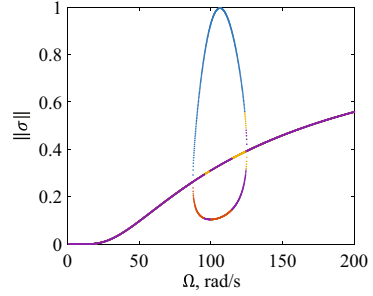
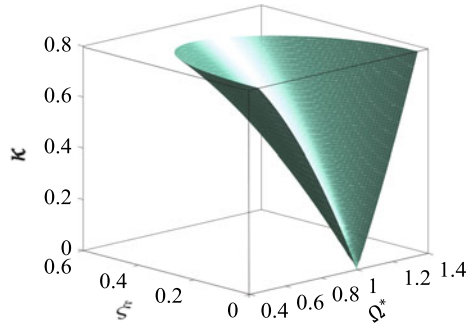


**Fig. 19** Stability domain of rotor for different values of  $\kappa$ ,  $\xi$  and  $\Omega^*$



aries. From Fig. 17, it is observed that unstable speed range increases as the shaft stiffness asymmetry or non-circularity ( $\kappa$ ) increases. It is known that increasing system damping reduces the parametric instability region [75]. As  $c$  increases, the unstable zone starts shrinking in size. In the present model with  $\kappa = 1/3$ , for damping value  $c = 365$  Ns/m, the unstable zone vanishes completely (absolute magnitude of the eigenvalues  $\leq 1$ ) as shown in Fig. 18.

Let us introduce a damping coefficient ratio  $\xi = c/(2m\Omega_{avg})$ . The stability domain variation with shaft non-circularity  $\kappa$ , damping coefficient ratio  $\xi$  and non-dimensional rotor spin speed  $\Omega^*$  is shown in Fig. 19. Note that Fig. 17 is a cross-section of Fig. 19 at  $\xi = 0$ .

### 5.4 Transient Analysis of the Non-ideal System

The permanent type DC motor is considered here as the non-ideal drive with suitable motor parameters needs to be considered, as given in Table 3. The DC motor produces torque to rotate the rotor shaft instead of a constant speed motor considered for ideal drive.

It can be shown that the reactive load torque applied on the motor is  $\Gamma_l = 2\Delta k_s \eta \zeta = (k_\eta - k_\zeta)(x \cos \theta + y \sin \theta)(-x \sin \theta + y \cos \theta)$  [45]. Thus, the equations

**Table 5** DC motor specifications

Parameters	Description	Value
$V_i$	Supply voltage	<Input>
$R_m$	Armature resistance	5 $\Omega$
$L_m$	Armature inductance	0.01 H
$k_m$	Motor's constant	0.5 Nm/A

of motion for transient analysis are given as

$$m\ddot{x} + c\dot{x} + (k_s + \Delta k_s \cos 2\theta)x + (\Delta k_s \sin 2\theta)y = 0 \quad (22)$$

$$m\ddot{y} + c\dot{y} + (\Delta k_s \sin 2\theta)x + (k_s - \Delta k_s \cos 2\theta)y = 0 \quad (23)$$

$$J\ddot{\theta} + 2\Delta k_s(x\cos\theta + y\sin\theta)(-x\sin\theta + y\cos\theta) = k_m i_a \quad (24)$$

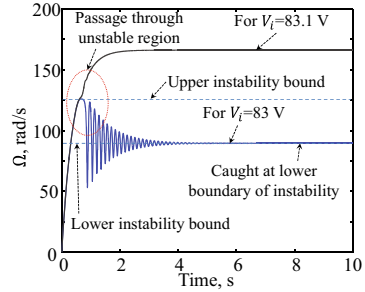
$$L_m \frac{di_a}{dt} + k_m \dot{\theta}_i + R_m i_a = V_i \quad (25)$$

where  $J$  is the rotary inertia of the rotor disc (including the rotor of the motor and the rotor shaft) about the spin axis,  $k_m$  is the motor constant,  $i_a$  is the armature current,  $L_m$  and  $R_m$  are, respectively, the motor armature coil inductance and resistance, and  $V_i$  is the voltage applied across the motor terminals. The parameters of the DC motor chosen for the transient analysis are given in Table 5.

The theoretical analysis provides the stable and unstable speed ranges, but does not reveal the process to reach stable speed regions beyond the unstable regions when the energetic coupling between the motor and the rotor is considered. Thus, the transition through the unstable speed ranges is analyzed here through numerical simulations. The power supply by motor is used to overcome the load produced by rotor system. If the amount of available power is insufficient then the rotor may get stuck in boundary of the unstable zone. So it is essential to determine the critical amount of power to smoothly escape the instability for the motor sizing and overall system design perspectives.

The transient analysis of the rotor system with a non-ideal DC motor is carried out through numerical simulation; therein an initial momentum of 1 kg.m/s is given to the rotor disc in  $x$ -direction. Note that the dynamics of the system is governed by the initial conditions because the excitation here is of multiplicative nature. If there is no whirl in the rotor ( $\eta = 0$  or  $\zeta = 0$ ) then there is no load on the motor. Even a small residual unbalance is sufficient to initiate the load on the motor. The rotor speed response and amplitude response are plotted with time for coast up operation, as shown in Figs. 20 and 21. When constant input voltage is applied, the speed saturation starts to occur from about  $V_i = 44.83$  V. Such saturation behavior

**Fig. 20** Rotor speed response for motor supply voltages  $V_i = 83 \text{ V}$  and  $83.1 \text{ V}$  showing passage through parametric instability



continues up to  $V_i = 83 \text{ V}$  (see Fig. 21). When the speed is saturated, i.e. captured at the lower instability bound (89.66 rad/s), the whirl amplitude increases with applied voltage (see Fig. 21) and more and more energy is dissipated through the external viscous damping. During transient phase, the maximum speed does not exceed the upper instability bound.

At the steady-state, the motor power is balanced by the dissipated power. The steady-state whirl amplitude depends on the excess motor power, i.e., it is zero at  $V_i = 44.83 \text{ V}$  and increases as  $V_i$  increases, until it reaches  $83 \text{ V}$ , where the whirl amplitudes are very large and the system is still captured at the lower instability threshold.

When the supply voltage reaches or exceeds a critical value,  $V_i = 83.1 \text{ V}$ , then the rotor system escapes from capture at the lower instability threshold and reaches a higher speed. Thus, between  $V_i = 83 \text{ V}$  and  $V_i = 83.1 \text{ V}$ , there is a sudden speed jump. Also, the whirl amplitude converges to 0 at  $V_i = 83.1 \text{ V}$ , i.e. there is also an associated amplitude jump (see Fig. 21). Note that at  $V_i = 83 \text{ V}$ , the rotor speed just about reaches the upper instability threshold speed  $\Omega = 126.2 \text{ rad/s}$  (indicated by dashed line in Fig. 20).

When the voltage is reduced from a value  $V_i > 83.1 \text{ V}$  or above, there is also a similar jump phenomenon where the rotor speed suddenly jumps from the upper instability threshold to the lower instability threshold (see Figs. 22 and 23), but there is no speed capture at the upper stability threshold. The results in Figs. 22 and 23 are obtained under the initial conditions that correspond to initial rotor spin speed 200

**Fig. 21** Rotor amplitude response for motor supply voltages  $V_i = 83 \text{ V}$  and  $83.1 \text{ V}$  showing passage through parametric instability

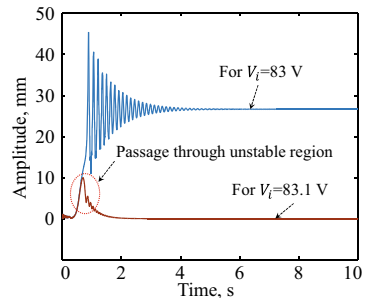


**Fig. 22** Rotor speed response for motor supply voltages  $V_i = 63 \text{ V}$  and  $63.1 \text{ V}$  showing passage through parametric instability

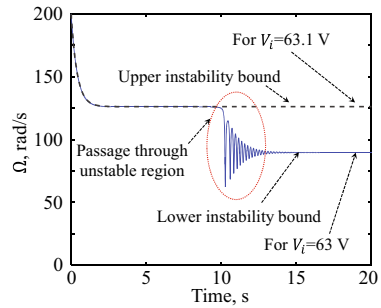
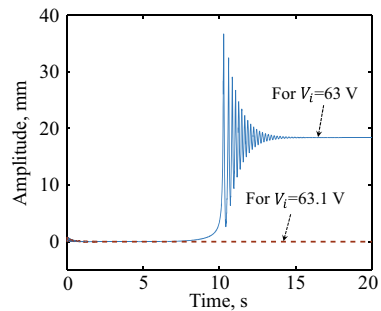


**Fig. 23** Rotor amplitude response for motor supply voltages  $V_i = 63 \text{ V}$  and  $63.1 \text{ V}$  showing passage through parametric instability



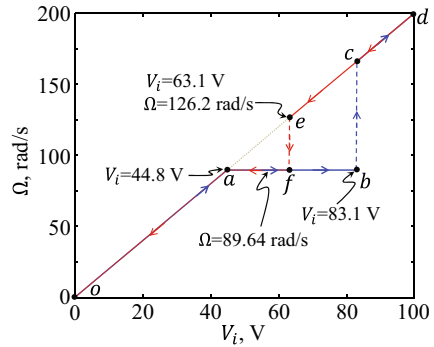
rad/s (above the upper stability threshold) and  $0.1 \text{ m/s}$  initial velocity of the rotor disc in  $x$ -direction. The initial input voltage is  $100 \text{ V}$  and it is reduced suddenly (a step drop) to a lower value.

Note that in this case, the induced emf is initially larger than the supplied voltage to the motor and hence, the motor applies brake or negative torque on the rotor. Up to  $V_i > 63.1 \text{ V}$ , the whirl amplitude converges to zero and the steady rotor speed reaches  $V_i/k_m > 126.2 \text{ rad/s}$ . When  $V_i$  is reduced just below  $63.1 \text{ V}$ , the rotor becomes unstable and whirl amplitudes start growing. This causes dissipation of energy through the viscous damping on the rotor and hence the rotor speed reduces until it reaches the lower instability threshold speed, i.e.  $89.66 \text{ rad/s}$  and it remains captured there until the motor supply voltage is reduced below  $49.83 \text{ V}$ . The bending stresses in the rotor shaft remain below yield stress when there is smooth passage through instability; whereas, capture at the lower instability threshold may lead to failure of the rotor shaft.

### 5.5 Jump Phenomena Characteristics

From the results, there is a clear similarity with the Sommerfeld effect of the first kind, although the Sommerfeld effect of the second kind happens here due to instability of whirl mode. This characteristic of the non-linear jump phenomena is shown in Fig. 24.

**Fig. 24** Characterization of the Sommerfeld effect of second kind in asymmetric rotor



During the rotor coast up (speed increase), the steady-state rotor speed follows the path  $o \rightarrow a \rightarrow b \rightarrow c \rightarrow d$  containing a capture at lower stability threshold in the path  $a \rightarrow b$  and a jump  $b \rightarrow c$ , as shown in Fig. 24. During rotor coast down (speed decrease), the steady-state rotor speed follows the path  $d \rightarrow e \rightarrow f \rightarrow a \rightarrow o$  containing a capture at lower stability threshold in the path  $f \rightarrow a$  and a jump  $e \rightarrow f$ , as shown in Fig. 24. Note that there is no speed capture at the upper instability threshold speed. Further note that steady-state speeds in the range lying between points  $a$  to  $e$ , i.e. the unstable speed range, can neither be reached during rotor coast-up nor during rotor coast-down.

Additionally, the plot between the non-circularity  $\kappa$  and the rotor speed  $\Omega$  is presented together with plot between input voltage supply  $V_i$  and the rotor speed  $\Omega$ , for coast up and coast down operation in Figs. 25 and 26, respectively. In Fig. 25, the blue colored lines indicate stability boundaries for different values of  $\kappa$ . Here, the Sommerfeld effect is shown for a fixed value  $\kappa=0.4$  and  $c = 0$  Ns/m, for which the shaded area is unstable speed range (69.28 rad/s to 105.8 rad/s). During coast up operation, the input voltage and speed variation (red line) takes the linear path  $a$  to  $b$  till the voltage reaches 34.6 V and speed reaches 69.28 rad/s. After point  $b$ ,

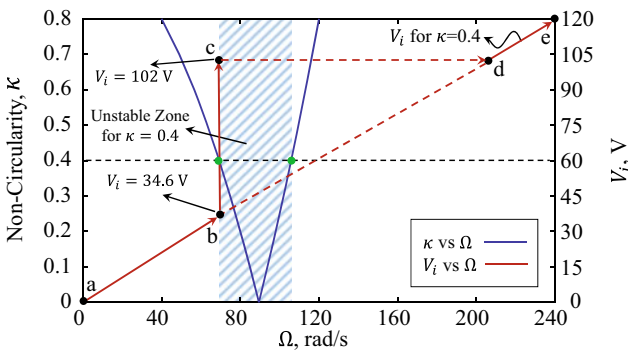


**Fig. 25** Non-circularity versus rotor speed (stability map), and motor supply voltage versus rotor speed with  $\kappa = 0.4$  for coast up dynamics

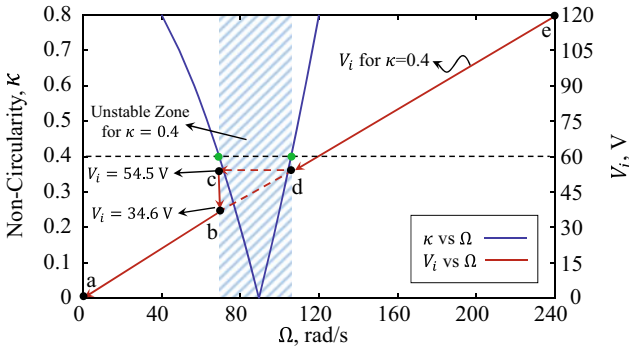


**Fig. 26** Non-circularity versus rotor speed (stability map), and motor supply voltage versus rotor speed with  $\kappa=0.4$  for coast down dynamics

i.e. at the stability boundary, the rotor speed gets stuck at 69.28 rad/s even as the input voltage is increased. During this period, the vibration amplitude increases as the energy supplied by motor contributes to increase in the whirl amplitude. At point c, for the input voltage of 102 V, enough energy is available to escape from this unstable region and a sudden speed jump occurs from c to d, i.e. the rotor speed increases to 204 rad/s from 69.28 rad/s (shown by dashed line). After that, the rotor speed increases linearly with the input voltage along the path d to e.

Similarly, for the coast down operation, the variation of the rotor speed with voltage follows the path  $e \rightarrow d \rightarrow c \rightarrow b \rightarrow a$  as shown in Fig. 26. Once the rotor speed reaches the speed corresponding to the upper stability boundary (point d, 105.8 rad/s at 54.5 V), further reduction in voltage reduces the rotor speed to that corresponding to the lower stability boundary (point c, 69.28 rad/s at 54.5 V). Further reduction in voltage up to 34.6 V does not change the rotor speed and thereafter, a linear reduction in speed with voltage occurs in the path b to a.

Mathematically, the location of points c and d depend on the initial conditions during rotor coast up. With large rotor inertia and sufficiently high constant supply voltage, realistic initial disturbances die out by the time the rotor speed starts from zero and reaches the stability boundary. Thus, the whirl amplitude is usually small at point b if sufficient time has elapsed to reach there and then point c appears closer to point b. However, for large initial conditions or rotor unbalance, the whirl amplitude on reaching point b can be large and then it grows very fast at the stability boundary. In that case, point c shifts upwards. Likewise, if the supply voltage is gradually increased then the rotor speed gets permanently captured at the stability boundary, i.e. the voltage at point c in Fig. 25 tends to infinity. On the other hand, location of points b, c and d during rotor coast down are mostly unaffected by the initial conditions.

## 6 The Sommerfeld Effect of Third Kind

Rotor systems become permanently unstable beyond a certain threshold speed due to the effect of non-conservative circulatory forces, which can arise out of shaft material/internal damping, anti-symmetric bearing stiffness, Alford forces, etc. These physical phenomena create an energy pipeline for continuous pumping of motor power to the rotor whirl. In fact, the material damping increases the effective damping for rotor speeds below the shaft natural frequency and the destabilizing effect (effective damping reduction) starts for rotor speeds after the shaft natural frequency [76]. The material damping effect is present during asynchronous rotor whirl and it vanishes during synchronous rotor whirl. The material damping is modeled in a rotating frame just like the asymmetric shaft stiffness and for higher frequencies, it is found to be proportional to the shaft's stiffness, with the proportionality constant  $\lambda$ . Here, the material damping parameter  $\lambda = 0.002 \text{ s}^{-1}$ , which is a standard material constant, is chosen for the steel rotor shaft.

### 6.1 Flexible Asymmetric Rotor Shaft Mounted on Rigid Support

Here, we consider the same asymmetric rotor shaft system as in the previous section (Sect. 5). The material damping of the shaft  $\mathbf{C}_{\text{si}}$  is given as  $\begin{bmatrix} c_{\eta i} & 0 \\ 0 & c_{\zeta i} \end{bmatrix}$  in rotating coordinate system where,  $c_{\eta i} = \lambda k_{\eta}$  and  $c_{\zeta i} = \lambda k_{\zeta}$ . Thus, the force due to shaft's material damping in fixed coordinate system is determined as  $\tilde{\mathbf{C}}_{\text{si}}^1 \dot{\mathbf{z}} + \tilde{\mathbf{C}}_{\text{si}}^2 \mathbf{z}$  where,

$$\tilde{\mathbf{C}}_{\text{si}}^1 = \begin{bmatrix} c_{si} + \Delta c_{si} \cos 2\Omega t & \Delta c_{si} \sin 2\Omega t \\ \Delta c_{si} \sin 2\Omega t & c_{si} - \Delta c_{si} \cos 2\Omega t \end{bmatrix},$$

$$\tilde{\mathbf{C}}_{\text{si}}^2 = \begin{bmatrix} -\Delta c_{si} \sin 2\Omega t & c_{si} + \Delta c_{si} \cos 2\Omega t \\ -c_{si} + \Delta c_{si} \cos 2\Omega t & \Delta c_{si} \sin 2\Omega t \end{bmatrix},$$

$c_{si} = \frac{c_{\eta i} + c_{\zeta i}}{2}$  is mean shaft material damping and  $\Delta c_{si} = \frac{c_{\eta i} - c_{\zeta i}}{2}$  is deviatoric shaft material damping. Finally, in form of matrices and vectors representation, the system's equation in fixed coordinate system is obtained as.

$$\begin{aligned} & \mathbf{M}\mathbf{z} + (\mathbf{D} + \mathbf{C}_o)\mathbf{z} + (\mathbf{K}_o + \Omega\mathbf{C}_o^1)\mathbf{z} + \Delta\mathbf{C}_1\mathbf{z} \cos(\Omega t) + \Delta\mathbf{C}_2\mathbf{z} \sin(\Omega t) \\ & + \Delta\mathbf{K}_1\mathbf{z} \cos(\Omega t) + \Delta\mathbf{K}_2\mathbf{z} \sin(\Omega t) + \Omega\Delta\mathbf{C}_2\mathbf{z} \cos(\Omega t) \\ & - \Omega\Delta\mathbf{C}_1\mathbf{z} \sin(\Omega t) = \mathbf{0} \end{aligned} \quad (26)$$

where,  $\mathbf{D} = \begin{bmatrix} c & 0 \\ 0 & c \end{bmatrix}$ ,  $\mathbf{K}_0 = \begin{bmatrix} k_s & 0 \\ 0 & k_s \end{bmatrix}$ ,  $\mathbf{C}_0 = \begin{bmatrix} c_{si} & 0 \\ 0 & c_{si} \end{bmatrix}$ ,  $\mathbf{C}_0^1 = \begin{bmatrix} 0 & c_{si} \\ -c_{si} & 0 \end{bmatrix}$ ,  $\Delta\mathbf{C}_1 = \begin{bmatrix} \Delta c_{si} & 0 \\ 0 & -\Delta c_{si} \end{bmatrix}$ ,  $\Delta\mathbf{C}_2 = \begin{bmatrix} 0 & \Delta c_{si} \\ \Delta c_{si} & 0 \end{bmatrix}$  and  $\tilde{\Omega} = 2\Omega$ .

## 6.2 Stability Analysis

The boundaries of unstable regions of system are determined by using Floquet theory. Hence, Eq. (26) written in state space form as  $\dot{\mathbf{A}}^T = \mathbf{P}(t)\mathbf{A}^T$ .

$$\text{where } \mathbf{P}(t) = \begin{bmatrix} \frac{p_{11}}{m} & \frac{p_{12}}{m} & \frac{p_{13}}{m} & \frac{p_{14}}{m} \\ \frac{p_{21}}{m} & \frac{p_{22}}{m} & \frac{p_{23}}{m} & \frac{p_{24}}{m} \\ 1 & 0 & 0 & 0 \\ 0 & 1 & 0 & 0 \end{bmatrix} \quad (27)$$

and,  $p_{11} = c + c_{si} + \Delta c_{si} \cos 2\Omega t$ ,  $p_{12} = \Delta c_{si} \sin 2\Omega t$ ,  $p_{13} = k_s + \Delta k_s \cos 2\Omega t - \Omega \Delta c_{si} \sin 2\Omega t$ ,  $p_{14} = \Omega c_{si} + \Omega \Delta c_{si} \cos 2\Omega t + \Delta k_s \sin 2\Omega t$ ,  $p_{21} = \Delta c_{si} \sin 2\Omega t$ ,  $p_{22} = c + c_{si} - \Delta c_{si} \cos 2\Omega t$ ,  $p_{23} = -\Omega c_{si} + \Omega \Delta c_{si} \cos 2\Omega t + \Delta k_s \sin 2\Omega t$ , and  $p_{24} = k_s - \Delta k_s \cos 2\Omega t + \Delta c_{si} \sin 2\Omega t$ .

As the monodromy matrix is obtained by numerical integration of  $\mathbf{P}(t)$  and then the eigenvalues  $\sigma_i$  ( $i = 1..4$ ) of the monodromy matrix are used to conclude the stability of the system by inputting the values of parameters that are given in Table 4. The real parts of the eigenvalues  $\sigma_{Re}$  are plotted with respect to rotor spin speed without considering the internal damping in Fig. 27. It can be seen that only one unstable region ( $U_1$ ) due to parametric instability appears in entire speed range of the rotor. The real parts of the eigenvalues  $\sigma_{Re}$  are plotted for the same parameters with internal damping ( $\lambda = 0.002 \text{ s}^{-1}$ ) in Fig. 28. Now, there is a similar unstable operation region due to parametric instability (speeds  $u_1$  to  $u_2$  i.e., 89.7 to 126.2 rad/s, corresponding to region  $U_1$ ) and another permanent instability region (from 133.2 rad/s i.e.,  $u_3$  onwards). Thus, the instability threshold speed  $\Omega_{th} = 133.2 \text{ rad/s}$  and there is no

**Fig. 27** Real parts of eigenvalues versus rotor speed for the rotor and  $\lambda = 0\text{s}^{-1}$

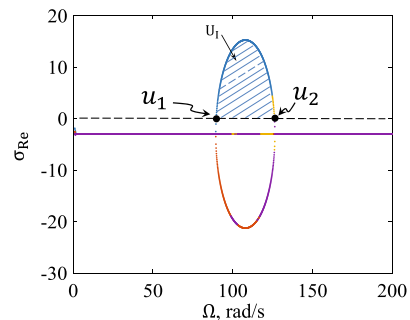
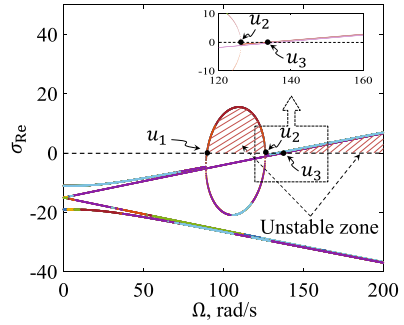




**Fig. 28** Real parts of eigenvalues versus rotor speed for the rotor and  $\lambda = 0.002 \text{ s}^{-1}$



stable operating speed beyond this permanent instability threshold. The range of parametric instability and the onset of permanent flutter instability strongly depend upon the damping in the system. For example, if the external damping is increased to  $c = 100 \text{ Ns/m}$  then the system has parametric instability region from  $u_1 = 90 \text{ rad/s}$  to  $u_2 = 125.7 \text{ rad/s}$ , i.e. there is a very small change in the unstable speed range, whereas the permanent instability threshold value increases significantly to  $u_3 = 151.9 \text{ rad/s}$ .

### 6.3 Transient Analysis of Non-ideal System

Some sample simulation results are discussed here corresponding to the stability behavior shown in Fig. 28 where the parametric instability region appears for speed range 89.7–126.2 rad/s, and the stability threshold speed is 133.2 rad/s. The excitation to initiate rotor whirl is provided by the initial momentum of 1 kg-m/s in x-direction of disc centre. The rotor speed reaches the desired steady-state value  $\Omega = V_i/k_m$  for  $V_i \leq 44.9 \text{ V}$ . The results show that the rotor spin speed is stuck at 89.65 rad/s (near lower unstable boundary  $U_1$ ) for  $V_i = 45 \text{ V}$ . After that, it never escapes through the unstable regions for any further increase in the supply voltage. This is because when there is sufficient power given to accelerate the rotor speed outside the capture at the parametric instability boundary, the rotor speed would actually reach a value beyond the permanent stability threshold (133.2 rad/s, here). Thus, the vibration amplitudes start to increase and reduce the shaft speed back to the lower limit of the parametric instability boundary. Such a behavior is observed when the permanent instability speed is very close to the parametric instability region.

For the case of higher value of external-damping, i.e.  $c = 100 \text{ Ns/m}$ , there is sufficient gap between the parametric instability regions (90–125.7 rad/s) and stability threshold (151.9 rad/s). In this case, the rotor speed reaches the desired steady-state value  $\Omega = V_i/k_m$  for  $V_i \leq 45.1 \text{ V}$ . For the supply voltage range  $V_i = 45.1$  to 69.8 V, the rotor speed is captured at the lower stability threshold of parametric instability zone  $u_1$ , i.e. at the average speed of 90 rad/s. The system escapes from the parametric instability for  $V_i \geq 69.9 \text{ V}$  (see Fig. 29), reaches the desired steady-state value  $\Omega = V_i/k_m$  and the whirl amplitudes reduces (see Fig. 30).

**Fig. 29** Rotor speed response during capture at and escape through parametric instability for the rotor with  $c = 100$  Ns/m and material damping

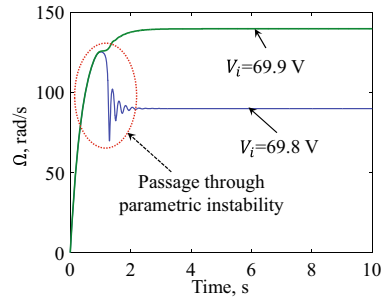
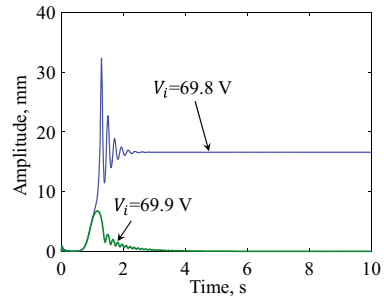


**Fig. 30** Rotor whirl amplitudes during capture at and escape through parametric instability for the rotor with  $c = 100$  Ns/m and material damping



On further increasing the supply voltage, at  $V_i = 75.9$  V, the rotor speed gets stuck at 151.9 rad/s (near threshold value of permanent instability  $\Omega_{th}$ ) with large bounded amplitudes of vibration. Hence, on reaching the stability threshold for  $V_i \geq 75.9$ , there is a permanent capture of rotor speed at average speed of 151.9 rad/s and the whirl amplitude continues to increase with any further increase in voltage, as shown for two such supply voltages in Figs. 31 and 32. Note that in Fig. 32, the whirl amplitude appears unsteady because of the simultaneous presence of synchronous and asynchronous whirls.

This permanent capture at stability threshold is termed as *the Sommerfeld effect of third kind*. It has been discussed previously in various articles [19, 48–51, 77,

**Fig. 31** Rotor speed response during capture at stability threshold for the rotor with material damping

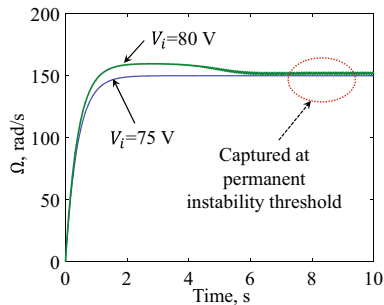
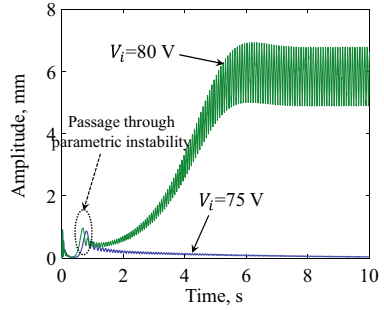


**Fig. 32** Rotor whirl amplitudes during capture at stability threshold for the rotor with material damping



78]. Note that permanent capture at the stability threshold does not give steady whirl amplitude. In fact, there is a synchronous whirl and an asynchronous whirl present at the same time. In rotor dynamic systems, various means have been proposed to increase the stable operating speed regions, such as squeeze film dampers, impact dampers, and visco-elastic supports, all of which attempt to increase the effective external damping in the system. However, effective external damping cannot be increased arbitrarily in a system because it is also related to the vibration isolation capacity of the foundation and the energy efficiency of the non-ideal motor, as has been recently described in [79].

## References

1. El-Badawy, A.A.: Behavioral investigation of a nonlinear nonideal vibrating system. *J. Vib. Control* **13**(2), 203–217 (2007). ISSN 1077–5463. <https://doi.org/10.1177/1077546307073674>
2. Kononenko, V.O.: *Vibrating Systems with Limited Excitation* [in Russian]. Nauka, Moscow (1964)
3. Nayfeh, A., Mook, D.: *Nonlinear Oscillations*. Wiley-Interscience, NY (1979)
4. Sommerfeld, A.: Beiträge Zum Dynamischen Ausbau Der Festigkeitslehre. *Physikal Zeitschr* **3**, 266–286 (1902)
5. Eckert, M.: The Sommerfeld effect: theory and history of a remarkable resonance phenomenon. *Europ. J. Phys.* **17**(5), 285–289 (1996)
6. Kononenko, V.O.: *Vibrating Systems with Limited Excitation*, English Translation from Russian. (Ilife Books) (1969)
7. Timoshenko, S.: *Vibration Problems in Engineering*. Van Nostrand, Princeton, NJ (1961)
8. Blekhman, I.I.: *Vibrational Mechanics: Nonlinear Dynamic Effects, General Approach, Applications*. World Scientific, Singapore (2000)
9. Alifov, A.A., Frolov, K.V.: *Interaction of Non-linear Oscillatory Systems with Energy Sources*. Taylor & Francis, London (1990)
10. Hübner, W.: Die Wechsetwirkung zwischen Schwinger und Antrieb bei Schwingungen. *Ingenieur-Archive* **34**, 411–422 (1965)
11. Rand, R.H., Kinsey, R.J., Mingori, D.L.: Dynamics of spinup through resonance. *Int. J. Non-Linear Mech.* **27**(3), 489–502 (1992)
12. Ryzhik, A., Amer, T., Duckstein, H., Sperling, L.: Zum Sommerfeldeffect beim selbsttätigen Auswuchten in einer Ebene. *Tech. Mech.* **21**(4), 297–312 (2001)
13. Yamanaka, H., Murakami, S.: Optimum designs of operating curves for rotating shaft systems with limited power supplier. In: Chung, H. (ed.), *Current Topics in Structural Mechanics*, pp. 181–185 (1989)
14. Christ, H.: Stationärer und Instatioärer Betrieb Eines Federnd Gelagerten, Unwuchtigen Motors, Ph.D. Thesis, Universität Karlsruhe (1966)
15. Frolov, K.V., Krasnopol'skaya, T.S.: Sommerfeld effect in systems without internal damping. *Prikladnaya Mekhanika* **23**(12), 19–24 (1987)
16. Dimentberg, M.F., McGovern, L., Norton, R.L., Chapdelaine, J., Harrison, R.: Dynamics of an unbalanced shaft interacting with a limited power supply. *Nonlinear Dyn.* **13**, 171–187 (1997)
17. Cveticanin, L.: Dynamics of the non-ideal mechanical systems: a review. *J. Serbian Soc. Comput. Mech.* **4**(2), 75–86 (2010)
18. Samantaray, A.K., Dasgupta, S., Bhattacharyya, R.: Sommerfeld effect in rotationally symmetric planar dynamical systems. *Int. J. Eng. Sci.* **48**(1), 21–36 (2010)
19. Dasgupta, S.S., Samantaray, A.K., Bhattacharyya, R.: Stability of an internally damped non-ideal flexible spinning shaft. *Int. J. Non-linear Mech.* **45**(3), 286–293 (2010)
20. Dimentberg, M.F.: Vibration of a rotating shaft with randomly varying internal damping. *J. Sound Vib.* **285**(3), 759–765 (2005). <https://doi.org/10.1016/j.jsv.2004.11.025>
21. Kovriguine, D.A.: Synchronization and sommerfeld effect as typical resonant patterns. *Arch. Appl. Mech.* **82**(5), 591–604 (2012)
22. Hu, W.H., Thöns, S., Rohrmann, R.G., Said, S., Rücker, W.: Vibration-based structural health monitoring of a wind turbine system. Part I: Reson. Phenomenon. *Eng. Struct.* **89**, 260–272 (2015)
23. Blekhman, I.I., Kremer, E.: Vibrational resistance to vehicle motion due to road unevenness. *J. Sound Vib.* **405**, 306–313 (2017)
24. Sinha, A., Bharti, S.K., Samantaray, A.K., Chakraborty, G., Bhattacharyya, R.: Sommerfeld effect in an oscillator with a reciprocating mass. *Nonlinear Dyn.* **93**(3), 1719–1739 (2018)
25. Balthazar, J.M., Mook, D.T., Weber, H.I., Fenili, A., Belato, D., de Mattos, M.C., Wieczorek, S.: On vibrating systems with a limited power supply and their applications to engineering sciences. In: Honig, C.S. (ed.) *49th Brazilian Seminar of Mathematical Analysis*, pp. 137–277. State University of Campinas, Campinas, SP, Brazil (1999)

26. Balthazar, J.M., Mook, D.T.: Brasil, R.M.L.R.F., Weber, H.I., Fenili, A., Belato, D., Felix, J.L.P., Recent results on vibrating problems with limited power supply. In: Awrejcewicz, J., Brabski, J., Nowakowski, J. (eds.) Sixth Conference on Dynamical Systems Theory and Applications, pp. 27–50. Lodz, Poland (2001)
27. Balthazar, J.M., Mook, D.T., Brasil, R.M.L.R.F., Fenili, A., Belato, D., Felix, J.L.P., Weber, H.I.: Recent results on vibrating problems with limited power supply. *Meccanica* **330**(7), 1–9 (2002)
28. Balthazar, J.M., Brasil, R.M.L.R.F., Garzeri, F.J.: On non-ideal simple portal frame structural model: experimental results under a non-ideal excitation. *Appl. Mech. Mater.* **1–2**, 51–58 (2004)
29. Dantas, M.J.H., Balthazar, J.M.: On the appearance of a Hopf bifurcation in a non-ideal mechanical problem. *Mech. Res. Commun.* **30**(5), 493–503 (2003)
30. Bolla, M.R., Balthazar, J.M., Felix, J.L.P., Mook, D.T.: On an approximate analytical solution to a nonlinear vibrating problem, excited by a nonideal motor. *Nonlinear Dyn.* **50**(4), 841–847 (2007)
31. numerical and analytical approaches: Felix, J.L.P., Balthazar, J.M., Brasil, R.M.L.R.F. Comments on nonlinear dynamics of a non-ideal duffing-rayleigh oscillator. *J. Sound Vib.* **319**, 1136–1149 (2009)
32. Bharti, S.K., Samantaray, A.K.: Resonant capture and Sommerfeld effect due to torsional vibrations in a double Cardan joint driveline. *Commun. Nonlinear Sci. Numer. Simul.* **97**, 105728 (2021)
33. Taylor, H.D.: Critical-speed behavior of unsymmetrical shafts. *J. Appl. Mech.* **7**(2), 71–79 (1940)
34. Dimentberg, F.M.: *Flexural Vibrations of Rotating Shaft*. Butterworths, London (1961)
35. Brosens, P.J., Crandall, S.H.: Whirling of unsymmetrical rotors. *Trans. ASME. J. Appl. Mech.* **28**(3), 355–362 (1961)
36. Yamamoto, T., Ota, H.: On the unstable vibrations of the shaft carrying an unsymmetrical rotor. *J. Appl. Mech.* **31**(3), 515–522 (1964)
37. Yamamoto, T., Yasuda, K.: Unstable Vibrations of an unsymmetrical rotor supported by flexible bearing pedestals. *Bullet. JSME* **15**(87), 1063–1073 (1972)
38. Ikeda, T., Murakami, S.: Dynamic response and stability of a rotating asymmetric shaft mounted on a flexible base. *Nonlinear Dyn.* **20**(1), 1–19 (1999)
39. Srinath, R., Sarkar, A., Sekhar, A.S.: Instability of asymmetric shaft system. *J. Sound Vib.* **362**, 276–291 (2016)
40. Foote, W.R., Poritsky, H., Slade, J.J.: Critical speeds of a rotor with unequal shaft flexibilities, mounted in bearings of unequal flexibility—I. *J. Appl. Mech.* **10**, A77–A84 (1943)
41. Messal, E.E., Bonthron, R.J.: Subharmonic rotor instability due to elastic asymmetry. *J. Eng. Indus.* **94**(1), 185–192 (1972)
42. Ardayfio, D., Frohrib, D.A.: Instabilities of an asymmetric rotor with asymmetric shaft mounted on symmetric elastic supports. *Trans. ASME J. Eng. Indus.* **98**(4), 1161–1165 (1976)
43. Lee, C.W.: *Vibration Analysis of Rotors*. Springer Science & Business Media, 21 (1993)
44. Boru, F.E.: *Numerical and Experimental Response and Stability Investigations of Anisotropic Rotor-Bearing Systems*. Kassel University press GmbH (2010)
45. Bharti, S.K., Sinha, A., Samantaray, A.K., Bhattacharyya, R.: The Sommerfeld effect of second kind: passage through parametric instability in a rotor with non-circular shaft and anisotropic flexible supports. *Nonlinear Dyn.* **100**, 3171–3197 (2020)
46. Samantaray, A.K., Bhattacharyya, R., Mukherjee, A.: An investigation into the physics behind the stabilizing effects of two-phase lubricants in journal bearings. *J. Vib. and Control* **12**(4), 425–442 (2006)
47. Samantaray, A.K., Mukherjee, A., Bhattacharyya, R.: Some studies on rotors with polynomial type nonlinear external and internal damping. *Int. J. Non-linear Mech.* **41**, 1007–1015 (2006)
48. Samantaray, A.K., Dasgupta, S.S., Bhattacharyya, R.: Bond graph modeling of an internally damped nonideal flexible spinning shaft. *J. Dyn. Syst. Measur. Control* **132**(6), 061502 (2010)
49. Samantaray, A.K., A note on internal damping induced self-excited vibration in a rotor by considering source loading of a DC motor drive, *Int. J. Non-Linear Mech.* **43**(9), 1012–1017 (2008)

50. Samantaray, A.K.: Steady state dynamics of a non-ideal rotor with internal damping and gyroscopic effects. *Nonlinear Dyn.* **56**(4), 443–451 (2009)
51. Mukherjee, A., Karmakar, R., Samantaray, A.K.: Modelling of basic induction motors and source loading in rotor-motor systems with regenerative force field. *Simul. Pract. Theory* **7**(5), 563–576 (1999)
52. Kirk, R.G., Gunter, E.J.: The effect of support flexibility and damping on the synchronous response of a single-mass flexible rotor. *J. Eng. Indus. Trans. ASME* **94**, 221–232 (1972)
53. Gunter, E. J.: The influence of internal friction on the stability of high speed rotors. *J. Eng. Indus. Trans. ASME Ser. B* **89**(4), 683–688 (1967)
54. Vance, J.M., *Rotordynamics of Turbomachinery*. New York, Wiley (1988)
55. Genta, G.: *Dynamics of Rotating Systems*. Springer (2005)
56. Greenhill, Lyn, M., Guillermo, A.: Cornejo.: critical speeds resulting from unbalance excitation of backward whirl modes. *Design Eng. Techn. Conf.* **3**, part 3, ASME (1995)
57. Muszynska, A.: Forward and backward precession of a vertical anisotropically supported rotor. *J. Sound Vib.* **192**(1), 207–222 (1996)
58. Bharti, S.K., Bisoi, A., Sinha, A., Samantaray, A.K., Bhattacharyya, R.: Sommerfeld effect at forward and backward critical speeds in a rigid rotor shaft system with anisotropic supports. *J. Sound Vib.* **442**, 330–349 (2019)
59. Karthikeyan, M., Bisoi, A., Samantaray, A.K., Bhattacharyya, R.: Sommerfeld effect characterization in rotors with non-ideal drive from ideal drive response and power balance. *Mech. Mach.* **91**, 269–288 (2015)
60. Bisoi, A., Samantaray, A.K., Bhattacharyya, R.: Sommerfeld effect in a two-disk rotor dynamic system at various unbalance conditions. *Meccanica* **53**(4), 681–701 (2018)
61. Porter, B.: A theoretical analysis of the torsional oscillation of a system incorporating a Hooke's joint. *J. Mech. Eng. Sci.* **3**(4), 324–329 (1961)
62. Porter, B., Gregory, R.W.: Non-linear torsional oscillation of a system incorporating a Hooke's joint. *J. Mecha. Eng. Sci.* **5**(2), 191–200 (1963)
63. Porter, B.: Non-linear torsional oscillation of a two-degree-of-freedom system incorporating a Hooke joint. *Proc. R. Soc. Lond. Ser. A* **277**(1368), 92–106 (1964)
64. Asokanthan, S.F., Hwang, M.C.: Torsional instabilities in a system incorporating a Hooke's joint. *J. Vib. Acoust.* **118**(3), 368–374 (1996)
65. Asokanthan, S.F., Meehan, P.A.: Non-linear vibration of a torsional system driven by a Hooke's joint. *J. Sound Vib.* **233**(2), 297–310 (2000)
66. Bulut, G.: Dynamic stability analysis of torsional vibrations of a shaft system connected by a Hooke's joint through a continuous system model. *J. Sound Vib.* **333**(16), 3691–3701 (2014)
67. De Smidt, H.A., Wang, K.W., Smith, E.C.: Multi-harmonic adaptive vibration control of AMB-driveline systems with non-constant velocity flexible couplings. *Int. Design Eng. Techn. Conf. Comput. Inform. Eng. Conf.* **37033**, 1995–2005 (2003)
68. Yao, W., DeSmidt, H.: Nonlinear coupled torsion/lateral vibration and Sommerfeld behavior in a double U-joint driveshaft. *J. Vib. Acoust.* **143**(3), 031011 (2021)
69. Lima, R., Soize, C., Sampaio, R.: Robust design optimization with an uncertain model of a nonlinear vibro-impact electro-mechanical system. *Commun. Nonlinear Sci. Numer. Simul.* **23**(1–3), 263–273 (2015)
70. Lima, R., Sampaio, R.: Two parametric excited nonlinear systems due to electromechanical coupling. *J. Braz. Soc. Mech. Sci. Eng.* **38**(3), 931–943 (2016)
71. Tsuchida, M., Guilherme, K.L., Balthazar, J.M., Silva G.N., Cheshancov, B.I.: On regular and irregular vibrations of a non-ideal system with two degree of freedom. 1:1 resonance. *J. Sound Vib.* **260**, 949–960 (2003)
72. Tsuchida, M., Guilherme, K.L., Balthazar, J.M.: On chaotic vibrations of a non-ideal system with two degrees of freedom: 1:2 resonance and Sommerfeld effect. *J. Sound Vib.* **282**, 1201–1207 (2005)
73. Quinn, D.D.: Resonant dynamics in a rotordynamic system with nonlinear inertial coupling and shaft anisotropy. *Nonlinear Dynam.* **57**(4), 623–633 (2009)

74. Song, Z., Chen, Z., Li, W., Chai, Y.: Parametric instability analysis of a rotating shaft subjected to a periodic axial force by using discrete singular convolution method. *Meccanica* **52**(4–5), 1159–1173 (2017)
75. Bones, J.A., Hannam, R.G.: Whirling of shafts with asymmetric stiffness. *J. Mech. Eng. Sci.* **8**(4), 437–447 (1966)
76. Genta, G.: On a persistent misunderstanding of the role of hysteretic damping in rotordynamics. *J. Vib. Acoust. Trans. ASME* **126**(3), 459–461 (2004)
77. Wettergren, H.L., Olsson, K.O.: Dynamic instability of a rotating asymmetric shaft with internal viscous damping supported in anisotropic bearings. *J. Sound Vib.* **195**(1), 75–84 (1996)
78. Sinha, A., Bharti, S.K., Bhattacharyya, R., Samantaray, A.K.: Discussion on A novel approach to study effects of asymmetric stiffness on parametric instabilities of multi-rotor-system, Jain et al. *J. Sound Vib.* **413**(2018) 159–172, *J. Sound Vib.* **442**(3), 268–280 (2019)
79. Samantaray, A.K.: Efficiency considerations for Sommerfeld effect attenuation. *Proceedings of the Institution of Mechanical Engineers, Part C: Journal of Mechanical Engineering Science*, 0954406221991584 (2021)

# Nonlinear Modal Analysis of Vibrating Systems with Limited Power Supply



V. Piccirillo , A. M. Tuset , Jose Manoel Balthazar ,  
and A. G. Martinez 

**Abstract** Nonlinear modal analysis is a powerful technique that allows a better understanding of the nonlinear dynamic behavior of mathematical models with few degrees of freedom. Nonlinear modes have emerged as a natural extension of linear modes for systems with large oscillation amplitudes. This chapter applies the technique of nonlinear normal modes analysis in a nonlinear Duffing oscillator driven by a limited (non-ideal) power source. Results show that the use of nonlinear modal analysis allows the description of the complex behavior of the system, resulting from the nonlinearities considered.

## 1 Introduction

It is known that nonlinearities in the dynamical systems may make it exhibits unexpected responses. The dynamic responses of a nonlinear system excited by an external energy source are very rich, being able to show, for example, interactions near resonance regions, and many other interesting phenomena.

The nonlinear normal modes (NNMs) [1, 2] is a promising approach that can be used in nonlinear systems because it allows the decoupling of the system. Therefore, from an engineering point of view, this decoupling is efficient in reduces the engineering structures in oscillators with a single degree of freedom (1-DOF). Besides, all the information related to the dynamics of the non-linear system can be found

---

V. Piccirillo (✉) · A. M. Tuset  
UTFPR, Federal University of Technology, Ponta Grossa, PR, Brazil  
e-mail: [piccirillo@utfpr.edu.br](mailto:piccirillo@utfpr.edu.br)

A. M. Tuset  
e-mail: [tuset@utfpr.edu.br](mailto:tuset@utfpr.edu.br)

J. M. Balthazar  
UNESP, Sao Paulo State University, Bauru, SP, Brazil

A. G. Martinez  
UFPR, Federal University of Parana, Curitiba, PR, Brazil  
e-mail: [agm@ufpr.br](mailto:agm@ufpr.br)



in these oscillators. The nonlinear normal modes theory for strong nonlinearities in conservative or damped autonomous systems was developed by Shaw and Pierre [3]. They built this theory based on the center manifold theory and geometric aspects of a dynamical system. The nonlinear normal modes allow the decoupling of the equations of motion of a dynamical system taking into account both the displacement and the velocity of a chosen set of coordinates. These coordinates are called master coordinates, while the rest of them, consisting of a modal surface, are classified as slave coordinates. This approach can be applied only to autonomous nonlinear systems.

In nonautonomous equations of motion, the time variable is considered as an additional coordinate, which makes the formulation of the NNMs very challenging for this kind of system. To deal with this problem [4], uses a numerical technique based on a Galerkin type scheme with the time as a new coordinate, therefore allowing, determinate the NNMs for each instant of time.

In this chapter, the Nonlinear Normal Modes (NNMs) of oscillators driven by a limited power supply under resonant conditions, and with strongly nonlinearity are formulated for resonant regions. This formulation should allow the reduction of the problem without any loss in the dynamics of the original system.

## 2 The Vibratory System

The equations of motion of a coupled oscillators can be written as follows

$$m\ddot{X} + kX + f_S(X) + f_D(X, \dot{X}) = f_e(\omega\tau) \quad (1)$$

where  $X$  is the displacement vector,  $m$  is the mass matrix,  $k$  is the stiffness matrix related to the linear part,  $f_S(X)$  is a matrix related to the nonlinear stiffness,  $f_D(X, \dot{X})$  is a matrix related to the damping that can be linear or not and the system is excited by an external force vector  $f_e(\omega\tau)$ .

Note that in this equation there are terms dependent on displacement, velocity, as well as the time variable. As pointed out by Warminski [5] a linear procedure of decoupling of the equations can only be applied if the system is weakly nonlinear or linear with little damping. Therefore, a decoupling procedure for a more general dynamical system (apart from the characteristics mentioned before) is complicated. Thus, the decoupling of Eq. (1) occurs in some specific cases.

The nonautonomous system analyzed in this chapter is a two-degree of freedom oscillator nonideal oscillator with Duffing nonlinearity elements and with small viscous damping. The methodology adopted here considers responses near resonant regions. A new version of Eq. (1) can be obtained by assuming the following transformation,

$$X = uY \quad (2)$$

where  $u$  is a linear modal vector and  $Y$  is a vector of normal coordinates. Substituting, Eq. (2) into (1) and multiplying the equation by  $u^T$  (matrix transpose of  $u$ ) we have,

$$M\ddot{Y} + KY = \epsilon \left[ \tilde{F}(Y, \dot{Y}) + \tilde{Q}\cos(\omega\tau) \right] \tag{3}$$

where  $M = \text{diag}[M_j] = u^T m u$ ,  $K = \text{diag}[M_i \omega_{0j}^2] = u^T k u$ , and  $\omega_{0j}^2$  correspond to the  $j$ th natural frequency of a linear mode. A small parameter  $\epsilon$  is used to group all nonlinear terms related to structural and/or damping as a function of  $\tilde{F}(Y, \dot{Y})$  and the excitation in terms of  $\tilde{Q}\cos(\omega\tau)$ . If the parameter  $\epsilon$  is equal to zero, then the set of decoupled linear equations can be solved independently. However, in our case, the presence of nonlinearities cannot be ruled out, and therefore the system is coupled and the normal nonlinear modes need to be introduced.

### 3 Modeling the Nonideal System

In order to model a nonideal system, consider a two degree of freedom oscillator as described in Fig. 1. It consists of two masses  $m_i (i = 1, 2)$  connected by a nonlinear spring described by the function  $f_i(x_i) (i = 1, 2)$  and linear dampers  $c_i (i = 1, 2)$ , and the oscillators are coupled by a linear spring  $k_{12}$ . In addition, let us consider that the first oscillator is driven by a motor with limited power source.

The equations of motion of the model shown in Fig. 1 are described by the following system of differential equations

$$\begin{aligned} M\ddot{x}_1 + c_1\dot{x}_1 + f_1(x_1) + k_{12}(x_1 - x_2) &= m_0r(\dot{\varphi}^2\sin\varphi - \ddot{\varphi}^2\cos\varphi) \\ m_2\ddot{x}_2 + c_2\dot{x}_2 + f_2(x_2) - k_{12}(x_1 - x_2) &= 0 \end{aligned} \tag{4}$$

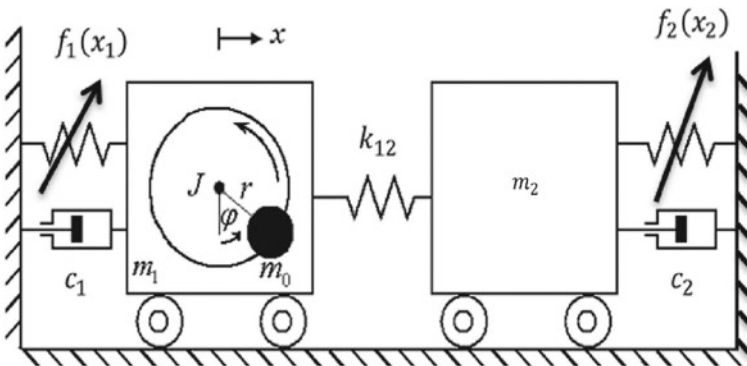


Fig. 1 Two degree of freedom oscillator driven by limited power source

$$J\ddot{\varphi} = \Gamma(\varphi) + m_0 r \ddot{x}_1 \cos\varphi$$

The nonlinear stiffness are functions of the Duffing type, represented by  $f_1(x_1) = k_1 x_1 + \gamma_1 x_1^3$  and  $f_2(x_2) = k_2 x_2 + \gamma_2 x_2^3$ . The physical parameters shown in Fig. 1 are:  $m_0$  unbalance mass;  $M = m_0 + m_1$  total mass of vibrating parts;  $J$  inertia moment of rotor;  $r$  is the eccentricity of mass  $m_0$ ;  $\varphi$  is the angular displacement of the rotor (motor shafts).

Note that Eq. (4) is an autonomous and nonlinear equation, containing cubic nonlinearities. The functions  $m_0 r \dot{\varphi}^2 \sin\varphi$  and  $m_0 r \ddot{\varphi}^2 \cos\varphi$  are the inertia functions produced by the motor and the function  $m_0 r \ddot{x}_1 \cos\varphi$  represents the moment of this force of inertia.

## 4 The Nonlinear Normal Modes Formulation

The normal nonlinear modes are formulated from observations of the response of the physical system [6]. In order to formulate the approach of the nonlinear normal modes, we will focus only on a neighborhood of the primary resonance region.

In contrast to the purely linear system approach, we define the modes of vibration as a function of amplitude. Specifically, one of the modal coefficients is considered to be arbitrary, and the second is expressed as a function of the amplitude. Therefore, the coefficient  $u_1$  is taken to be constant and for convenience this value is equal to 1 ( $u_1 = 1$ ), while the second is a function of the amplitude:  $u_2 = u_2(a)$ , where  $a$  denotes the amplitude function.

For the modal coefficient  $u_{2j}(a)$ , the modal solution takes the following form:

$$X_1 = Y_j \tag{5}$$

$$X_2 = u_{2j}(a)Y_j \tag{6}$$

where  $j = 1, 2$  corresponds to the first and second modes respectively and  $Y_j = a \cos(\omega_{0j} \tau)$  is a time periodic function. Observe that  $\omega_{0j}$  corresponds to the  $j$ th natural frequency of the nonlinear system. According to the definition given in the literature, coordinate  $X_1$  (the displacement) is called the “master coordinate” while  $X_2$  is known as the “slave coordinate”, and is functionally related to the previous one.

This formulation of normal modes for the conservative nonlinear system will be applied to the system Eq. (4).

## 5 Vibration of the Nonideal System

In order to transform the generalized coordinate system into normal coordinates, we will assume that when the considered nonlinear system is conservative within the main resonance, the modes of vibration are sufficiently close to the normal nonlinear modes formulated in the previous section.

By replacing (5) in the set of original Eq. (4) and then multiplying the first equation by  $u_{1j}$  (in this case equal 1) and the second by  $u_{2j}$  ( $j = 1, 2$ ), and then adding the two equations turns out that,

$$(M + m_2 u_{2j}^2) \ddot{Y}_j + [k_1 + u_{2j}^2 k_2 + (1 - u_{2j})^2 k_{12}] Y_j + (\gamma_1 + \gamma_2 u_{2j}^4) Y_j^3 = F_j(\dot{Y}_j, \varphi, \dot{\varphi}, \ddot{\varphi}) \quad (7)$$

where  $F_j(\dot{Y}_j, \varphi, \dot{\varphi}, \ddot{\varphi}) = m_0 r (\dot{\varphi}^2 \sin \varphi - \ddot{\varphi}^2 \cos \varphi) - (c_1 + c_2 u_{2j}^2) \dot{Y}_j$ ,  $j = 1, 2$ .

Taking into account that the system is conservative, is valid that  $F_j(\dot{Y}_j, \varphi, \dot{\varphi}, \ddot{\varphi}) = 0$  and substituting the periodic solution  $Y_j = a \cos(\omega_{0j} \tau)$  in (7), we obtain the relation that represents the natural frequency of the nonlinear system,

$$\omega_{0j}^2 = \frac{1}{(M + m_2 u_{2j}^2)} \left[ k_1 + u_{2j}^2 k_2 + (1 - u_{2j})^2 k_{12} + \frac{3}{4} a^2 (\gamma_1 + \gamma_2 u_{2j}^4) \right] \quad (8)$$

It follows that the equations of motion can be written in terms of nonlinear normal coordinates,

$$M_j(a) \ddot{Y}_j + M_j(a) \omega_{0j}^2(a) Y_j = F_j(\dot{Y}_j, \varphi, \dot{\varphi}, \ddot{\varphi}), \quad j = 1, 2 \quad (9)$$

where  $M_j(a) = M + m_2 u_{2j}^2$  is the modal mass of the system for the first and second vibration modes for  $j = 1, 2$ , respectively.

## 6 Analytical Solution for the Nonideal System

Due to their nonlinear nature, analytical solutions of the system of Eq. (9) can be determined by applying approximation methods. The method of averaging [7], is a well-known perturbation method used to find an approximate solution for nonlinear dynamical systems. In this method, a small parameter  $\epsilon$  is introduced to take into account the nonlinear terms of the problem. Then Eq. (9) can be written in the form,

$$M_j(a) \ddot{Y}_j + M_j(a) \omega_{0j}^2(a) Y_j = \epsilon \tilde{F}_j(\dot{Y}_j, \varphi, \dot{\varphi}, \ddot{\varphi}), \quad j = 1, 2 \quad (10)$$

where,  $F_j = \epsilon \tilde{F}_j$

According to the formulation presented in Sect. 4, it is assumed that the system response is periodic. The previous approach considered the case of primary resonance. In this case, the average angular velocity of the direct current engine, varies close to the natural frequency of the system, that is,  $\dot{\varphi} \approx \omega_{0j}$ .

Imposing  $\epsilon = 0$  (unperturbed problem) in Eq. (10), we obtain that the solution is given by,

$$Y_j = a_j \cos(\varphi + \beta_j) \quad (11)$$

Using the method of the variation of parameters, we have that,

$$\dot{Y}_j = -a_j \omega_{0j} \sin(\varphi + \beta_j) \quad (12)$$

where  $a$ ,  $\varphi$  and  $\beta$  are functions of time  $\tau$ .

When considering displacements close to the resonance region, it is convenient to introduce a tuning parameter  $\sigma$  as follows:

$$\dot{\varphi} = \Omega \quad (13)$$

where

$$\Omega = \omega_{0j} + \epsilon \sigma \quad (14)$$

The first-order derivative of  $Y_j$  in (11) is,

$$\dot{Y}_j = \dot{a}_j \cos(\varphi + \beta_j) - a_j \sin(\varphi + \beta_j) (\Omega + \dot{\beta}_j) \quad (15)$$

Comparing the Eqs. (12) and (15) we have,

$$\dot{a}_j \cos(\varphi + \beta_j) - a_j \dot{\beta}_j \sin(\varphi + \beta_j) = a_j (\Omega - \omega_{0j}) \sin(\varphi + \beta_j) \quad (16)$$

differentiating Eq. (12) we have,

$$\ddot{Y}_j = -\dot{a}_j \omega_{0j} \sin(\varphi + \beta_j) - a_j \dot{\beta}_j \omega_{0j} \cos(\varphi + \beta_j) - a_j \Omega \omega_{0j} \cos(\varphi + \beta_j) \quad (17)$$

After replacing Eqs. (11), (13) and (17) in Eq. (9), we have:

$$\begin{aligned}
 & -M_j(a)[\dot{a}_j\omega_0j\sin(\varphi + \beta_j) + a_j\dot{\beta}_j\omega_0j\cos(\varphi + \beta_j) + a_j\Omega\omega_0j\cos(\varphi + \beta_j)] + M_j(a)\omega_0^2a_j\cos(\varphi + \beta_j) \\
 & = \epsilon[\hat{r}_1(\hat{\Omega}\cos\varphi - \Omega^2\sin\varphi) + va_j\omega_0j\sin(\varphi + \beta_j) - \Psi a_j^3\cos^3(\varphi + \beta_j)]
 \end{aligned} \tag{18}$$

and

$$\dot{\Omega} = \epsilon[\hat{\Gamma}(\Omega) - \hat{r}_2(\dot{a}_j\omega_0j\sin(\varphi + \beta_j) + a_j\Omega\omega_0j\cos(\varphi + \beta_j) + a_j\dot{\beta}_j\omega_0j\cos(\varphi + \beta_j))\cos\varphi] \tag{19}$$

where  $v = c_1 + c_2u_{2j}^2$  and  $\Psi = \gamma_1 + \gamma_2u_{2j}^4$ .

Using trigonometric identities, it is possible to isolate the variables  $\dot{a}$ ,  $\dot{\beta}$  and  $\dot{\Omega}$  from Eqs. (18) and (19),

$$\dot{a}_j = -\frac{\epsilon}{M_j(a)\omega_0j}[\hat{r}_1(\hat{\Omega}\cos\varphi - \Omega^2\sin\varphi) + va_j\omega_0j\sin(\varphi + \beta_j) - \Psi a_j^3\cos^3(\varphi + \beta_j)]\sin(\varphi + \beta_j) \tag{20}$$

$$\dot{\beta}_j = -\epsilon\sigma - \frac{\epsilon}{a_jM_j(a)\omega_0j}[\hat{r}_1(\hat{\Omega}\cos\varphi - \Omega^2\sin\varphi) + va_j\omega_0j\sin(\varphi + \beta_j) - \Psi a_j^3\cos^3(\varphi + \beta_j)]\cos(\varphi + \beta_j) \tag{21}$$

Note that Eqs. (20) and (21) are equivalent to system (4), without making any approximations so far. As a simplification we will neglect all  $O(\epsilon)$  terms that appear in Eqs. (19) through (21). Then,

$$\dot{\Omega} = \epsilon[\hat{\Gamma}(\Omega) - \hat{r}_2a_j\Omega\omega_0^2j\cos(\varphi + \beta_j)\cos\varphi] \tag{22}$$

$$\dot{a}_j = -\frac{\epsilon}{M_j(a)\omega_0j}[\hat{r}_1\omega_0^2j\sin\varphi - va_j\omega_0j\sin(\varphi + \beta_j) + \Psi a_j^3\cos^3(\varphi + \beta_j)]\sin(\varphi + \beta_j) \tag{23}$$

$$\dot{\beta}_j = -\frac{\epsilon}{a_jM_j(a)\omega_0j}[a_jM_j(a)\omega_0j\sigma - \hat{r}_1(\hat{\Omega}\cos\varphi - \Omega^2\sin\varphi) + va_j\omega_0j\sin(\varphi + \beta_j) + \Psi a_j^3\cos^3(\varphi + \beta_j)]\cos(\varphi + \beta_j) \tag{24}$$

Another simplification that can be considered here is that  $a_j$ ,  $\Omega$  and  $\beta_j$  remain constant over a cycle. Thus, by integrating the last three equations on this cycle, by averaging, we obtain the following result:

$$\dot{\Omega} = \epsilon\left[\hat{\Gamma}(\Omega) - \frac{1}{2}\hat{r}_2a_j\omega_0^2j\cos\beta_j\right] \tag{25}$$

$$\dot{a}_j = \epsilon\left[\frac{\hat{r}_1\omega_0j}{2M_j(a)}\cos\beta_j - va_j\right] \tag{26}$$

$$\dot{\beta}_j = -\epsilon\left[\sigma + \frac{\hat{r}_1\omega_0j}{2a_jM_j(a)}\sin\beta_j - \frac{3\Psi}{8M_j(a)\omega_0j}a_j^2\right] \tag{27}$$

Now substituting  $F_j = \epsilon \tilde{F}_j$  into the above equations, it follows that,

$$\dot{\Omega} = \Gamma(\Omega) - \frac{1}{2}r_2a_j\omega_{0j}^2\cos\beta_j \quad (28)$$

$$\dot{a}_j = \frac{r_1\omega_{0j}}{2M_j(a)}\cos\beta_j - \nu a_j \quad (29)$$

$$\dot{\beta}_j = \frac{3\Psi}{8M_j(a)\omega_{0j}}a_j^2 - (\Omega - \omega_{0j}) - \frac{\hat{r}_1\omega_{0j}}{2a_jM_j(a)}\sin\beta_j \quad (30)$$

In order to obtain the equilibrium points, we have that  $\dot{\Omega} = \dot{a}_j = \dot{\beta}_j = 0$ , therefore,

$$\Gamma(\Omega) - A\cos\beta_j = 0 \quad (31)$$

$$B\cos\beta_j - \nu a_j = 0 \quad (32)$$

$$Ca_j^2 - (\Omega - \omega_{0j}) - \frac{\hat{r}_1\omega_{0j}}{2a_jM_j(a)}\sin\beta_j = 0 \quad (33)$$

where  $A = \frac{1}{2}r_2a_j\omega_{0j}^2$ ,  $B = \frac{r_1\omega_{0j}}{2M_j(a)}$ ,  $C = \frac{3\Psi}{8M_j(a)\omega_{0j}}$ .

From Eqs. (31) and (32) we have  $\cos^2\beta_j = \frac{\nu}{AB}\Gamma(\Omega)$ . Rewriting Eq. (33) in terms of  $\sigma = \Omega - \omega_{0j}$ , we obtain  $B\sin(\beta) = Ca_j(a_j^2 - \sigma)$ . Using fundamental trigonometric identity, we have:

$$\frac{\nu}{AB}\Gamma(\Omega) + \left[\frac{a_j}{B}(Ca_j(a_j^2 - \sigma))\right]^2 - 1 = 0 \quad (34)$$

Therefore

$$\frac{C^2}{B^2}a_j^6 - 2\frac{C}{B^2}a_j^4 + \frac{\sigma^2}{B^2}a_j^2 + \frac{\nu}{AB}\Gamma(\Omega) - 1 = 0 \quad (35)$$

Note that in this polynomial the terms of odd degree are absent, so it can be rewritten as a third-degree polynomial in  $a_j^2$ . We can have 3 real roots or just one real and two other complex conjugates.

The existence of more than one real root, corresponds to a ‘‘multivalued’’ amplitude and indicates the entrance into a region of instability, that is, the presence of an unstable solution.

### 7 Numerical Results

In this section, some numerical results are presented for the data of the nonlinear model. Considering  $M = 1$ ;  $m_2 = 2$ ;  $k_1 = 1$ ;  $k_2 = 1$ ;  $k_{12} = 0, 3$ ;  $\gamma_1 = 0.1$ ;  $\gamma_2 = 0.1$ . In this case, the coefficients of the modal matrix are,

$$u = \begin{bmatrix} u_{11} & u_{12} \\ u_{21} & u_{22} \end{bmatrix}$$

where  $u_{11} = 1$ ,  $u_{21} = 2.3770$ ,  $u_{12} = 1$ ,  $u_{22} = 0.21035$  and the corresponding natural frequencies to the linear system are  $\omega_{01} = 0.766091$ ,  $\omega_{02} = 1.16752$ .

Considering Eq. 8, which constitutes the relation between the coefficient  $u_2$  ( $u_{21}$  and  $u_{22}$ ) and the amplitude of vibration, the nonlinear modal curve can be evaluated as a function of the amplitude. Figure 2 shows a comparison of such coefficient of vibration between the linear and nonlinear cases. For the linear system, this coefficient is independent of the amplitude (vertical line). However, as might be expected, the nonlinear vibration mode corresponds to the linear modes, when the amplitude value is equal to zero, i.e.,  $a = 0$ . For non-zero amplitude values, in the nonlinear case, it is possible to observe a variation of these coefficients.

Figure 3 shows the comparison between the natural frequencies for the two modes of vibration (linear and nonlinear cases) given by the non-ideal system studied here, considering free vibration. Dashed lines show that natural frequencies, of the two linear modes of vibration, do not change in the presence of a variation in the amplitude of vibration. On the other hand, the solid lines representing the two non-linear vibration modes, vary as the system exhibits vibration.

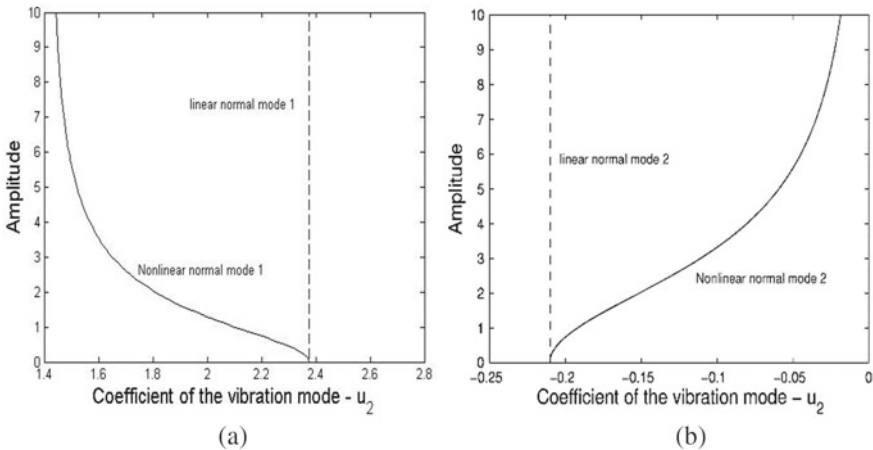
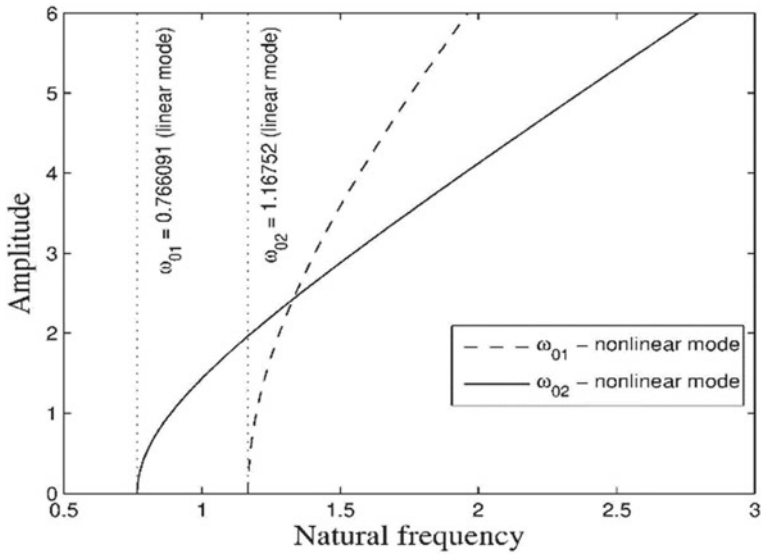


Fig. 2 Amplitude versus vibration modes **a** first mode, **b** second mode





**Fig. 3** Amplitude versus natural frequency of vibration

Figures 4 and 5 shows the responses, analytically determined in normal coordinates, of the coupled oscillators for the non-ideal system. Using the nonlinear transformation given by Eq. (5) we have that the initial conditions of the problem in terms of the modal coordinates are:  $Y_1(0) = 10$ ;  $\dot{Y}_1(0) = 0$ ;  $Y_2(0) = 10$ ;  $\dot{Y}_2(0) = 0$ .

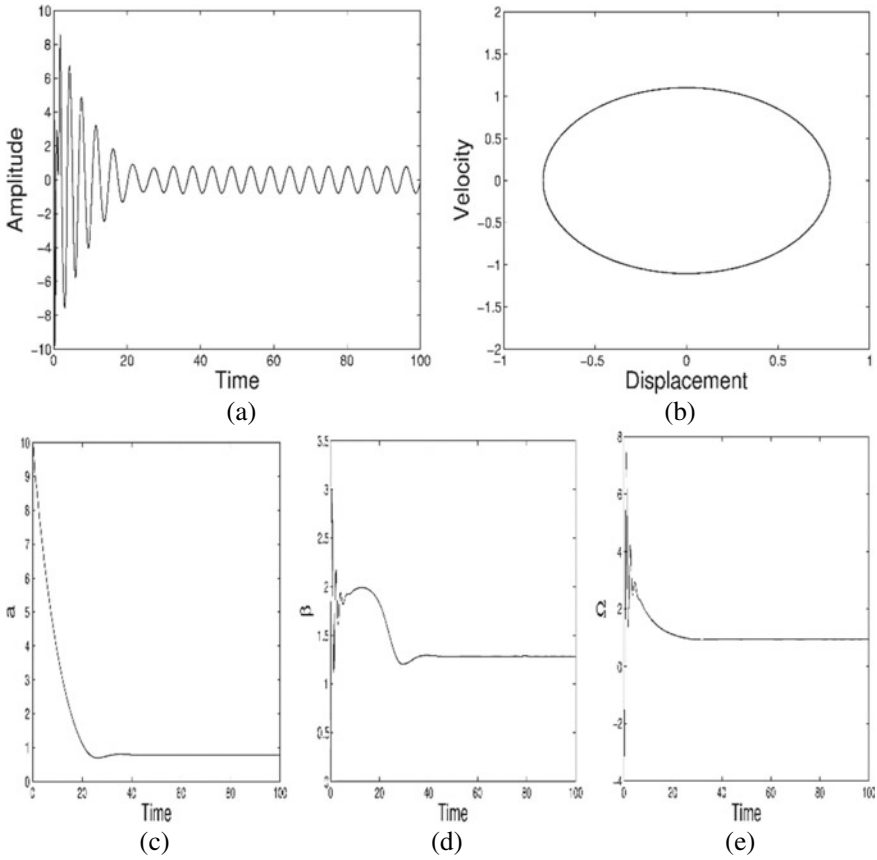


**Fig. 4** Vibration in modal coordinates for the first mode: **a** Amplitude versus time, **b** Phase plane, **c** Modulation of the amplitude, **d** Modulation of the phase, **e** History of the rotational velocity of the motor

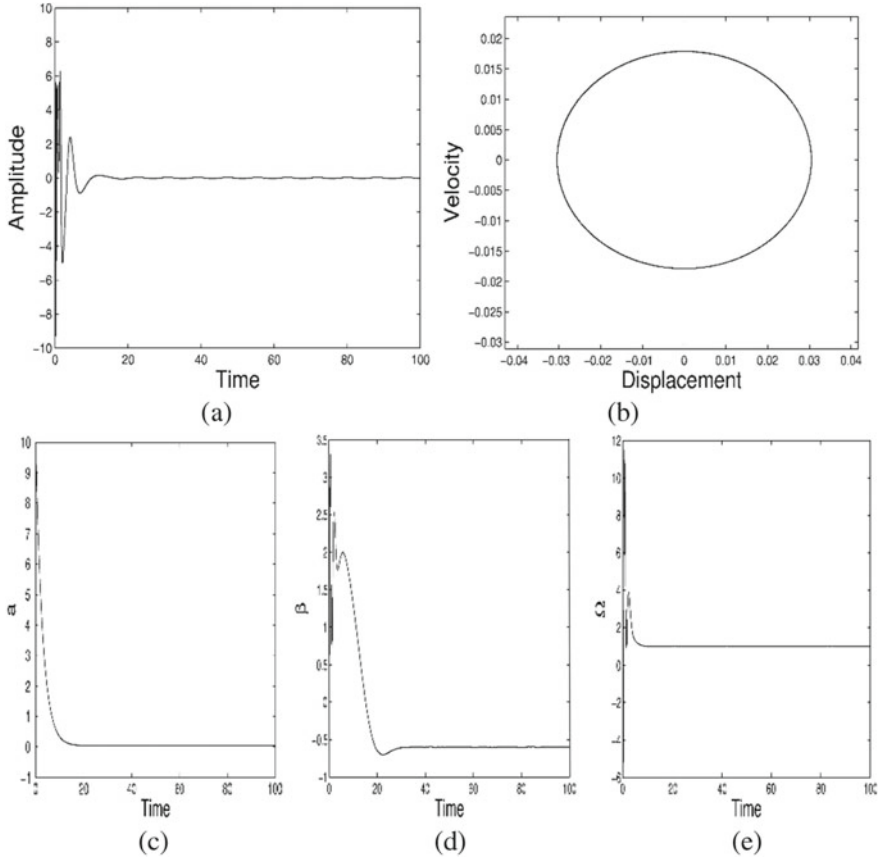


**Fig. 5** Vibration in modal coordinates for the second mode: **a** Amplitude versus time, **b** Phase plane, **c** Modulation of the amplitude, **d** Modulation of the phase, **e** History of the rotational velocity of the motor

## References

1. Rosenberg, R.M.: Normal modes of non-linear dual-mode systems. *J. Appl. Mech. Ser. E* **27**(2), 263–268 (1960)
2. Vakakis, A.F.: Non-linear normal modes (NNMs) and their applications in vibration theory: an overview. *Mech. Syst. Signal Process.* **11**(1), 3–22 (1997)
3. Shaw, S.W., Pierre, C.: Normal modes for non-linear vibratory systems. *J. Sound Vib.* **164**(1), 85–124 (1993)
4. Jiang, D., Pierre, C., Shaw, S.W.: Nonlinear normal modes for vibratory systems under harmonic excitation. *J. Sound Vib.* **288**, 791–812 (2005)
5. Warminski, J.: Nonlinear vibration modes of parametrically coupled self-excited oscillators. *Mach. Dyn. Problems* **32**(4), 107–118 (2008)
6. Szabelski, K., Warminski, J.: Vibrations of a non-linear self-excited system with two degrees of freedom under external and parametric excitation. *Nonlinear Dyn.* **14**, 23–36 (1997)
7. Nayfeh, A.H., Mook, D.T.: *Nonlinear Oscillations*. Wiley, New York (1979)

# Resonance Dynamics of the Non-ideal System Having the Pendulum as Absorber of Elastic Vibrations



Y. O. Lebedenko , Y. V. Mikhlin , and M. A. Pinsky 

**Abstract** The resonance behavior of the 3-DOF system with a limited power supply (non-ideal system) having the pendulum-type absorber is analyzed by the multiple scales method. Comparison of the obtained analytical solution with corresponding numerical simulation demonstrates a good exactness of the analytical construction. It is shown that amplitudes of the elastic sub-system resonance vibrations can be essentially reduced by some choosing of the system parameters.

**Keywords** Non-ideal system · Resonance · Pendulum absorber

## 1 Introduction

The system with a limited power supply (or non-ideal system, NIS) is characterized by interaction of source of energy and elastic sub-system which is under action of the source. For the non-ideal systems the external applied excitation depends on displacements of the excited elastic sub-system. The most interesting effect appearing in such systems is the Sommerfeld effect [1], when in the elastic sub-system it is appeared the stable resonance regime with large amplitudes, and the big part of the vibration energy passes from the energy source to these resonance vibrations. Resonance dynamics of the non-ideal systems was first analytically described by V.O. Kononenko [2]. Then investigations on the subject were continued as by Kononenko [3], as well by other authors [4–7]. Reviews on numerous studies of the NIS dynamics can be found in papers [8, 9] and in the book [10]. We can note that different kinds of the NIS behavior were considered, including forced and parametric vibrations, self-oscillations, transient, including transfer to chaotic vibrations, interaction of the NIS with the energy supplies of the different physical characters, etc.

It is known that nonlinear vibration absorbers permit to reduce essentially amplitudes of the resonance elastic vibrations. Reduction of the vibration amplitudes and

---

Y. O. Lebedenko · Y. V. Mikhlin (✉)

National Technical University “Kharkiv Polytechnic Institute”, Kharkiv 61002, Ukraine

M. A. Pinsky

University of Nevada Reno, Reno, NV 89557, USA

elimination or reduction of the Sommerfeld effect in NIS coupled with different type nonlinear absorbers and dampers, are studied in [11–13].

In the paper the resonance behavior of the 3-DOF non-ideal system having the pendulum-type absorber is considered by the multiple scales method. The basic model is presented in Sect. 2. Then the construction of the system solution in the region of the first resonance is presented in Sect. 3. Numerical simulation is shown in Sect. 4. Besides, it is shown in the Sect. 4 that amplitudes of the elastic sub-system resonance vibrations in the system can be reduced by changing some system parameters.

## 2 The Basic Model

The non-ideal system under consideration contains the limited power supply (or the motor), the elastic sub-system with the Duffing type nonlinear elastic characteristic, which vibrations take place under the motor excitation. Besides, the system contains the pendulum as absorber. Models under consideration are shown in Fig. 1. The motor (source of energy) acts to the elastic sub-system having a mass  $M$  by the crank shaft of the radius  $r$ . The pendulum having a mass  $m$  is attached to the elastic sub-system. Here  $L$  is the driving moment of the source of energy.

Kinetic and potential energies of the system without the driving moment are the following:

$$\begin{aligned} T &= \frac{1}{2}I\dot{\varphi}^2 + \frac{1}{2}M\dot{x}^2 + \frac{1}{2}m\left[(\dot{x} + l\dot{\theta} \cos \theta)^2 + l^2\dot{\theta}^2 \sin^2 \theta\right]; \\ V &= \frac{1}{2}c_0x^2 + \frac{1}{2}c_1(x - r \sin \varphi)^2 + mgl(1 - \cos \theta). \end{aligned} \quad (1)$$

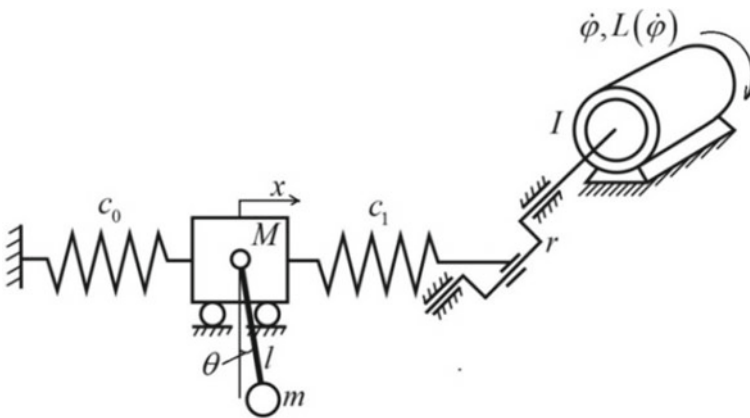


**Fig. 1** The non-ideal systems with the pendulum absorber

The small parameter  $\varepsilon$  in relations (1) characterizes a smallness of the absorber mass with respect to the mass of elastic part of the system. Using the Lagrange equations, one obtains the following equations of motion:

$$\begin{cases} (M + m)\ddot{x} + (c_0 + c_1)x = c_1 r \sin \varphi - ml(\ddot{\theta} \cos \theta - \dot{\theta}^2 \sin \theta); \\ I\ddot{\varphi} = a - b\dot{\varphi} + c_1 r(x - r \sin \varphi) \cos \varphi; \\ ml(l\ddot{\theta} + g \sin \theta + \ddot{x} \cos \theta) = 0. \end{cases} \quad (2)$$

In relations (1) and Eq. (2)  $I$  is a moment of inertia of rotating masses;  $(c_0 + c_1)$  is a stiffness of the elastic sub-system having the mass  $M$ ,  $L = a - b\dot{\varphi}$  is the driving moment of the source of energy, that is the motor characteristic. We can see from the Eq. (2) that the moment  $c_1 r x \cos \varphi$  is such part of the motor excitation, which depends on the elastic sub-system vibrations.

### 3 Construction of the Analytical Solution

To describe the system behavior in the neighborhood of the resonance some asymptotic approach, namely the multiple scales method [14] is used. To apply the method one has the following transformations. First of all, we use expansions of the functions  $\cos \theta$  and  $\sin \theta$  in the system (2) to the Maclaurin series, and save terms up to third degree. The small parameter  $\varepsilon$  introduced in the equations of motion characterizes a smallness of the absorber mass with respect to the mass of elastic part of the system,  $m \rightarrow \varepsilon m$ , and a smallness of vibration components in variability in time of angle  $\varphi$  velocity with respect to the main constant component. The small terms  $\varepsilon h \dot{x}$  and  $\varepsilon h \dot{\theta}$  describe a dissipation which is proportional to velocities of variables. Considering a region of the resonance between frequencies of the motor rotation and the elastic sub-system vibrations, we introduce the small detuning as  $\varepsilon \Delta = \omega^2 - \dot{\varphi}^2$ , where  $(c_0 + c_1)/M = \omega^2$ . We also suppose that in a region of the resonance the external excitation to the elastic sub-system is small. The relatively not large nonlinear response of the elastic sub-system is presented by the term  $\varepsilon \tau x^3$ . It is included to the first equation of the system (2). Thus, the equations of motion (2) are transformed to the following equations, containing the small parameter:

$$\begin{cases} (M + \varepsilon m)\ddot{x} + \omega^2 Mx + \varepsilon h \dot{x} + \varepsilon \tau x^3 = \varepsilon c_1 r \sin \varphi - \varepsilon ml \begin{pmatrix} \ddot{\theta} \left(1 - \frac{1}{2}\theta^2\right) \\ -\left(\theta - \frac{\theta^3}{6}\right) \dot{\theta}^2 \end{pmatrix} \\ I\ddot{\varphi} = \varepsilon(a - b\dot{\varphi} + c_1 r(x - r \sin \varphi) \cos \varphi) \\ \varepsilon ml \left( l\ddot{\theta} + g \left(\theta - \frac{\theta^3}{6}\right) + \ddot{x} \left(1 - \frac{1}{2}\theta^2\right) \right) + \varepsilon h \dot{\theta} = 0 \end{cases} \quad (3)$$

Later the following notations will be used:

$$\frac{a}{I\Omega^2} = K, \frac{b}{I\Omega} = N, \frac{c_1 r}{I\Omega^2} = q \quad (4)$$

According to the multiple scales method one uses the following presentations for the unknown variables:

$$\begin{aligned} x(t, \varepsilon) &= x(t, \varepsilon t, \varepsilon^2 t, \dots; \varepsilon); \quad \varphi(t, \varepsilon) = \varphi(t, \varepsilon t, \varepsilon^2 t, \dots; \varepsilon); \\ \theta(t, \varepsilon) &= \theta(t, \varepsilon t, \varepsilon^2 t, \dots; \varepsilon) \end{aligned} \quad (5)$$

Besides, the next transformations are also used:

$$\begin{aligned} \frac{d}{dt} &= \frac{\partial}{\partial T_0} + \varepsilon \frac{\partial}{\partial T_1} + \varepsilon^2 \frac{\partial}{\partial T_2} + \dots \\ \frac{d^2}{dt^2} &= \frac{\partial^2}{\partial T_0^2} + 2\varepsilon \frac{\partial}{\partial T_0} \frac{\partial}{\partial T_1} + \varepsilon^2 \left( \frac{\partial^2}{\partial T_1^2} + 2 \frac{\partial}{\partial T_0} \frac{\partial}{\partial T_2} \right) + \dots \end{aligned} \quad (6)$$

Here  $T_0 = \omega t$ ;  $T_1 = \varepsilon t$ , etc. Solutions for variables  $x$ ,  $\varphi$  and  $\theta$  are presented as the following power series by the small parameter:

$$x = x_0 + \varepsilon x_1 + \varepsilon^2 x_2 + \dots, \quad \varphi = \varphi_0 + \varepsilon \varphi_1 + \varepsilon^2 \varphi_2 + \dots, \quad \theta = \theta_0 + \varepsilon \theta_1 + \varepsilon^2 \theta_2 + \dots \quad (7)$$

Substituting the expansions (5)–(7) to the system (3) one extracts terms of the zero and first power by the small parameter. As a result, the following system of differential equations can be obtained:

$$\varepsilon^0 : \frac{\partial^2 x_0}{\partial T_0^2} + \Omega^2 x_0 = 0 \quad (8)$$

$$\frac{\partial^2 \varphi_0}{\partial T_0^2} = 0 \quad (9)$$

$$\begin{aligned} \varepsilon^1 : & 2M \frac{\partial^2 x_0}{\partial T_0 \partial T_1} + M \frac{\partial^2 x_1}{\partial T_0^2} + m \frac{\partial^2 x_0}{\partial T_0^2} + \Delta M x_0 + \\ & + M \Omega^2 x_1 + h \frac{\partial x_0}{\partial T_0} + r \tau x_0^3 = c_1 r \sin(\Omega T_0) - \\ & - ml \frac{\partial^2 \theta_0}{\partial T_0^2} + \frac{1}{2} ml \frac{\partial^2 \theta_0}{\partial T_0^2} \cdot \theta_0^2 + ml \theta_0 \left( \frac{\partial \theta_0}{\partial T_0} \right)^2 - ml \frac{\theta_0^3}{6} \cdot \left( \frac{\partial \theta_0}{\partial T_0} \right)^2 \end{aligned} \quad (10)$$

$$2 \frac{\partial^2 \varphi_0}{\partial T_0 \partial T_1} + \frac{\partial^2 \varphi_1}{\partial T_0^2} = K - N \frac{\partial \varphi_0}{\partial T_0} + q x_0 \cos \varphi_0 - 0.5 q r \sin 2\varphi_0 \quad (11)$$

$$l \frac{\partial^2 \theta_0}{\partial T_0^2} + g \theta_0 - g \frac{\theta_0^3}{6} + \frac{\partial^2 x_0}{\partial T_0^2} - \frac{\theta_0^2}{2} \frac{\partial^2 x_0}{\partial T_0^2} + (h/ml) \frac{\partial \theta_0}{\partial T_0} = 0 \quad (12)$$

One has the solution of the Eqs. (8) and (9) as

$$\begin{cases} x_0 = A \cos(\Omega T_0) + B \sin(\Omega T_0) \\ \varphi_0 = \Omega T_0 \end{cases} \quad (13)$$

We assume that in the resonance under consideration between frequencies of the motor rotation and the elastic sub-system vibrations, amplitudes of the pendulum vibrations are not large. Thus, one assumes that in the system (12) all terms having a power more than one, have an order of the small parameter  $\varepsilon$ . Hence one has from the Eq. (12) that

$$\theta_0 = C \cos \Omega T_0 + D \sin \Omega T_0, \text{ where } C = \frac{A\Omega^2}{g - l\Omega^2}, D = \frac{B\Omega^2}{g - l\Omega^2} \quad (14)$$

The solution of the zero approximation by the small parameter is substituted to the Eq. (10). To avoid an appearance the secular terms in solution, coefficients at  $\sin(\Omega T_0)$ ,  $\cos(\Omega T_0)$  in the right side of the equation are equated to zero. As a result one obtains so-called modulation equations in the following form:

$$2 \frac{\partial A}{\partial T_1} \Omega + \mu B \Omega^2 - \Delta B + \frac{hA\Omega}{M} - \frac{3\tau A^2 B}{4M} - \frac{3\tau B^3}{4M} + \sigma + \mu l D \Omega^2 = 0 \quad (15)$$

$$-2 \frac{\partial B}{\partial T_1} \Omega + \mu A \Omega^2 - \Delta A - \frac{hB\Omega}{M} - \frac{3\tau AB^2}{4M} - \frac{3\tau A^3}{4M} + \mu l C \Omega^2 = 0 \quad (16)$$

$$\left( \mu = \frac{m}{M}, \sigma = \frac{c_1 r}{M} \right)$$

Then, to avoid an appearance of the secular terms in solution of the Eq. (11), one has the following relation:

$$2 \frac{\partial \Omega}{\partial T_1} + N \Omega^2 = K + \frac{qA}{2}, \quad (17)$$

where  $K, N, q$  are determined by the relations (4). The Eqs. (14) and (15) represent a dependence of functions  $A$  and  $B$  on the excitation frequency  $\Omega$ . The Eq. (16) is the so-called “system characteristic”. Together all three Eqs. (15)–(17) give values of the variables  $A, B$  and  $\Omega$  corresponding to the resonance state under consideration.

Considering the stationary solution we assume that values  $A, B$  and  $\Omega$  are constant. In this case the Eqs. (15)–(17) are converted to the system of nonlinear algebraic equations with respect to these values, which is solved by the numerical Newton method in the pocket Matlab. Thus, the constant values  $A_0, B_0, \Omega_0$  for the stationary regime can be obtained. In particular, we have from the Eq. (17) that

$$\Omega_0 = \pm \sqrt{\frac{2a + c_1 r A_0}{2b}} \quad (18)$$



Note that in the resonance region the frequencies  $\Omega$  and  $\omega$  differ for the value of the order of the small parameter  $\varepsilon$ . Thus, if we change in the coefficients  $K$ ,  $N$  the variable frequency  $\Omega$  for  $\omega$ , we can find the following solution of the Eq. (17):

$$\Omega = \Omega_0 + \rho e^{-0.5NT_1} \quad (19)$$

Here the constant  $\rho$  is determined by the initial value of  $\Omega$ . The last relation presents a tending of the motor frequency to the stationary value  $\Omega_0$  with an increase of time.

#### 4 Numerical Simulation. Influence of the System Parameters to Resonance Dynamics of the System

Here we consider an influence of the system parameters to the elastic vibration amplitudes in the resonance region. Namely, a change of the parameter of the driving moment  $a$ , the pendulum mass  $m$  and the parameter of the nonlinearity in elastic force  $\tau$  is considered. Simultaneously the obtained analytical solution is compared with numerical simulation which is realized for the basic system (2) by use of the Runge–Kutta method of the 4-th order. Note that an increase of the pendulum length  $l$  leads to the insignificant decrease of the elastic vibration amplitude, thus, results corresponding to change of the parameter are not presented here.

Based on the numerical simulation we can conclude that amplitudes of the resonance elastic vibrations can be essentially reduced when the mass  $m$  and the parameter  $\tau$  increase. Some change of the parameter  $a$ , permits to reduce essentially the elastic vibration amplitude. Note that values of the parameter  $a$  are chosen near the value corresponding to maximal resonance amplitudes. We can note that only a small part of obtained numerical results are presented.

In Fig. 2 the analytical and numerical solutions are shown for the following parameters:  $a = 0.3815$ ,  $l = 0.5$ ,  $\tau = 0.05$  when the pendulum mass  $m$  is changing. In Fig. 2a the parameter  $m = 0.04$  (here  $A_0 = 0.506$ ,  $B_0 = -0.836$ ), and in Fig. 2b the parameter  $m = 0.1$  (here  $A_0 = -0.07$ ,  $B_0 = 0.489$ ). We can see here the noticeable decrease of the resonance vibration amplitude with increase of the absorber mass. In Fig. 3 the analytical and numerical solutions are presented for the following parameters:  $l = 1$ ,  $a = 0.3728$ ,  $m = 0.05$  when the parameter of nonlinearity  $\tau$  is changing. Figure 3a represents calculations made for  $\tau = 0.01$ , and in Fig. 3b the parameter  $\tau = 0.03$ . In Fig. 4 the analytical and numerical solutions are shown for the following parameters:  $m = 0.05$ ,  $l = 1$ ,  $\tau = 0.05$  when the parameter  $a$  is changing. In Fig. 4a the calculations are made for  $a = 0.3728$ , and in Fig. 4b the parameter  $a = 0.3778$ . We can see the essential decrease of the resonance vibration amplitude for considered change of the parameters  $\tau$  and  $a$ , where such effect is observed even for insignificant change of the parameter characterizing the driving moment  $a$ . Note that in all presented variants the admissible coincidence of the analytical solution

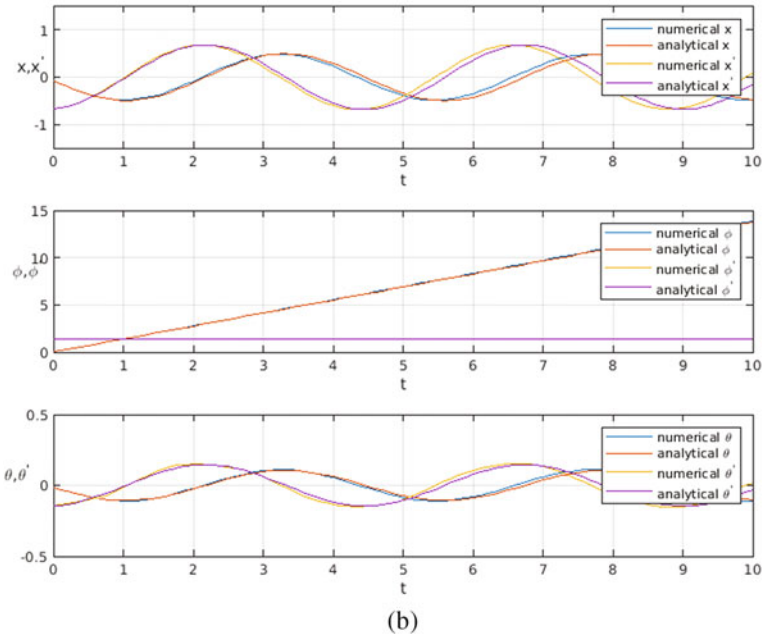
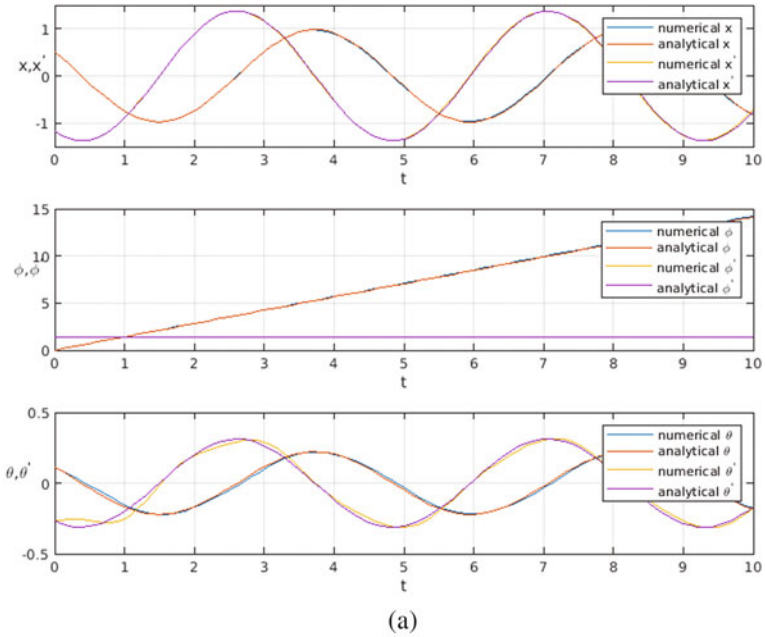


**Fig. 2** Change of the variables  $x$ ,  $\varphi$ ,  $\theta$  in time for different values of the pendulum mass  $m$

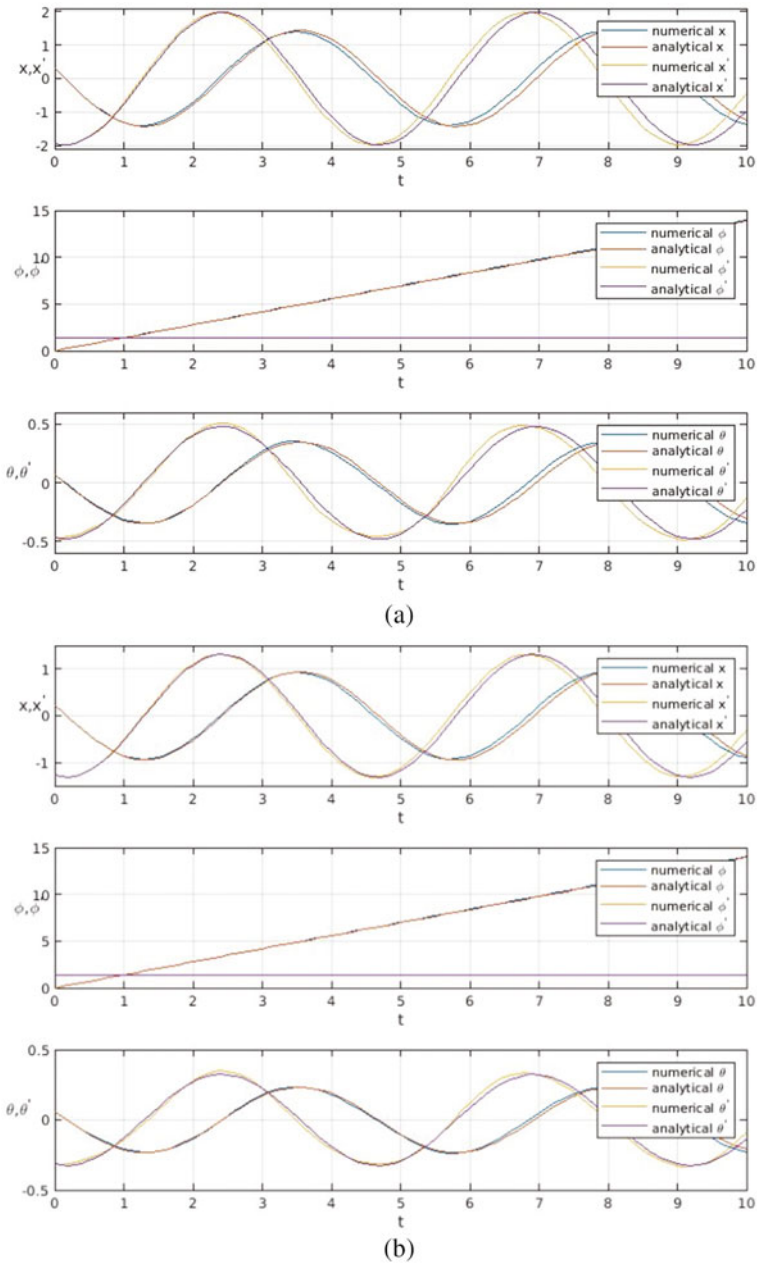


**Fig. 3** Change of the variables  $x$ ,  $\varphi$ ,  $\theta$  in time for different values of the parameter of nonlinearity  $\tau$

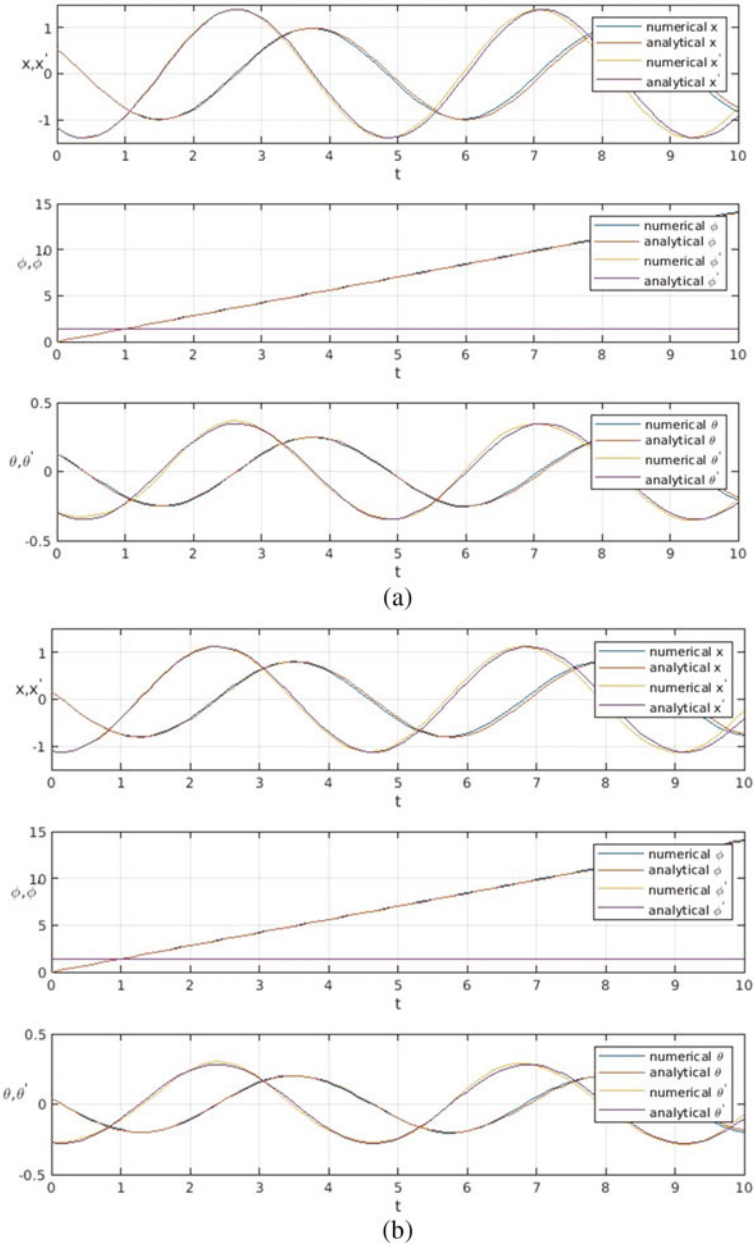


**Fig. 4** Change of the variables  $x$ ,  $\phi$ ,  $\theta$  in time for different values of the parameter  $\alpha$

and the numerical simulations is observed. Here the numerical solution is calculated with initial values obtained from the approximate analytical solution.

## 5 Conclusion

In the paper the system with a limited power supply (or non-ideal system) having the pendulum as absorber, is considered. The analytical solution in the region of the first resonance is obtained by the multiple scales method. Numerical simulation shows a good exactness of the analytical results. It is shown that an essential reduction of the system resonance vibration amplitudes can be obtained by choose of the system parameters, namely, of the pendulum mass  $m$ , the parameter  $\tau$  characterizing the nonlinear response of the elastic sub-system, and the parameter of the driving moment  $a$ . We suppose that the presented results can help in the future as in more precise analysis of the steady states of the non-ideal system, as well in analysis of transient in such systems.

**Acknowledgements** This study is supported in part by the grant of the Ministry of Education and Science of Ukraine M2137, UDK 539.3, № ДП 0118U002045.

## References

1. Sommerfeld, A.: Beitrage zum dynamischen ausbau der festigkeitslehe. *Physikal Zeitschr* **3**, 266–286 (1902)
2. Kononenko, V.O.: *Vibrating Systems with Limited Power Supply*. Illife Books, London (1969)
3. Kononenko, V.O., Kovalchuk, P.S.: Dynamic interaction of mechanisms generating oscillations in nonlinear systems. *Mech. Solids (USSR)* **8**, 48–56 (1973). (in Russian)
4. Goloskokov, E.G., Filippov, A.P.: *Unsteady oscillations of deformable systems*. Naukova dumka, Kyiv (1977) (in Russian)
5. Alifov, A.A., Frolov, K.V.: *Interaction of Nonlinear Oscillating Systems*. Taylor & Francis Inc., London (1990)
6. Palacios Felix, J.L., Balthazar, J.M., Dantas, M.J.H.: On energy pumping, synchronization and beat phenomenon in a non-ideal structure coupled to an essentially nonlinear oscillator. *Nonlinear Dyn* **56**(1–2), 1–11 (2009)
7. Mikhlin, Yu., Onizhuk, A., Awrejcewicz, J.: Resonance behavior of the system with a limited power supply having the Mises girder as absorber. *Nonlinear Dyn.* **99**(1), 519–536 (2020)
8. Eckert, M.: The Sommerfeld effect: theory and history of a remarkable resonance phenomenon. *European J. Phys.* **17**(5), 285–289 (1996)
9. Balthazar, J.M., et al.: An overview on the appearance of the Sommerfeld effect and saturation phenomenon in non-ideal vibrating systems (NIS) in macro and mems scales. *Nonlinear Dyn.* **93**(1), 19–40 (2018)
10. Cveticanin, L., Zukovic, M., Balthazar, J.M.: *Dynamics of Mechanical Systems with Non-Ideal Excitation*. Springer, Cham (2018)
11. Felix, J.L.P., Balthazar, J.M., Dantas, M.J.H.: On energy pumping, synchronization and beat phenomenon in a non-ideal structure coupled to an essentially nonlinear oscillator. *Nonlinear Dyn.* **56**(1–2), 1–11 (2009)

12. Felix, J.L.P., Balthazar, J.M.: Comments on a nonlinear and non-ideal electromechanical damping vibration absorber, Sommerfeld effect and energy transfer. *Nonlinear Dyn.* **55**(1), 1–11 (2009)
13. de Souza, et al.: Impact dampers for controlling chaos in systems with limited power supply. *J. Sound and Vibration* **279**(3–5), 955–967 (2005)
14. Nayfeh, A.H., Mook, D.T.: *Nonlinear Oscillations*. Wiley, NY (1979)

# On a Vehicular Suspension for a Non-ideal and Nonlinear Orchard Tower Sprayer Through an Inverted Pendulum Using Reologic Magneto (MR)



R. N. Silva , J. L. P. Felix , Jose Manoel Balthazar, A. M. Tusset , M. A. Ribeiro , W. B. Lenz , and A. Cunha 

**Abstract** In this paper, analysis of the nonlinear dynamics responses of a structure equipped with a vehicle suspension that uses a fluid with magneto rheological characteristics to control the possible instability and chaotic motion. It is a spray orchards of tower type, with an unbalanced electric motor (Non-ideal) located at the top of the tower representing the concentrated mass of their fans, which represents the real system the best way possible. The simulations show that the MR suspension reduce the amplitude of oscillations of all the masses of the system, being the most important the mass of the cart and fans. The influence of the non- ideal motor is important to check the influence of a possible imbalance of fans.

**Keywords** Spray orchards type tower · Nonlinear dynamics · Non-ideal system · Vehicle suspension · Magneto- Rheological fluid damper

## 1 Theoretical Mathematical Model of the Tower-Type Orchard Sprayer

The study of the [6, 8] nonlinear dynamics of an agricultural tower pulverizer, coupled with a vehicle suspension, that is subject to random excitations due to soil irregularities, modeled as an inverted double pendulum over a moving suspension, with three degrees of freedom (one translation and two rotations). To take into account the random loadings, a parametric probabilistic approach was employed, where the external force was assumed to be a harmonic random process with random amplitude and frequency. The probability distribution of these random [8] parameters was

---

R. N. Silva (✉) · J. M. Balthazar · A. M. Tusset · M. A. Ribeiro · W. B. Lenz  
Federal Technological University of Paraná, Campus Ponta Grossa, PR, Brazil

J. M. Balthazar  
Faculty of Mechanical Engineering of Bauru, São Paulo State University, Bauru, SP, Brazil

A. Cunha  
Institute of Mathematics and Statistics, Rio de Janeiro State University, Rio de Janeiro, RJ, Brazil

J. L. P. Felix  
Federal University of Southern Frontier -UFFS, Cerro Largo, RS, Brazil

constructed based on the known information through the maximum entropy principle. The results of numerical simulation show that large discrepancies in the system response can be seen when one compares the mean of the stochastic model with the nominal (deterministic) model. It is also noted that these responses are subject to a high level of uncertainty. Furthermore, an analysis of the system response probability distributions [6, 8] shows that they present asymmetries with respect to mean and unimodal behavior.

Some considerations were taken to arrive at the theoretical model. Initially, the simplifications [14, 15] will be considered. Where, initially, all the masses (truck, axle, wheel and tower with its eight fans) are concentrated in their centers of gravity. One of the main simplifications to be considered is that the operation of the sprayer will take place in short periods of time, because if long periods are taken the mass of the reservoir tank will have its center of gravity shifted, due to the fact that the sprayer starts the work with the reservoir full of defensive liquid and it is discharging during the spraying operation, until it finishes empty. Therefore, the mass of the reservoir tank is considered constant.

Once this is done, the reservoir mass and the chassis mass are grouped into a single invariant center of gravity  $m_2$ . All the concentrated masses of the eight fans are replaced by a single mass which, added to the motor mass, results in  $m_3$ , and the unbalanced mass of the direct current electric motor is  $m_0$ , located at the top of the tower. The tower, in turn, is represented by a negligible mass element of length  $L_2$ . The pivot point of the tower is represented by a point  $P$ , located at a distance  $L_1$  above the trailer's center of gravity. This same junction  $P$  is represented by an elastic element  $k_t$  and damping  $c_t$  torsional and linear.

Starting from the premise that, when the system rotates around the point of concentrated mass  $m_2$ , the left and right tires have the same displacement, in opposite directions; thus, it is considered that the system only presents a translational movement in the vertical direction. Therefore, the theoretical system can be considered as being of  $\frac{1}{4}$  of a vehicle or quarter-car, taking into account the displacement of only one of the wheels. This wheel is then represented by an element of mass  $m_l$  with linear stiffness  $k_1$ . And a vehicle-type MR damper, represented by  $F$ , is coupled to the system, in parallel to the viscous spring-damper suspension  $k_2$  and  $c$ , respectively, according to the Bounc-Wen model.

An X-Y coordinate system is adopted, with X at ground level and Y passing through the center of mass of truck  $m_2$ . The tower will then have an angular offset  $\phi_1$ . It is the angular displacement of the unbalanced mass is  $\phi_2$ . Excitements resulting from irregularities presented by the soil of the orchards cause displacements in the tires represented by  $ye_1$ ; mathematically  $ye_1$  represents an excitation source that can be of the harmonic, transient, etc. type.

However, it is observed that in the simplification presented the model presented has four degrees of freedom, with only the mass of the fans concentrated at the top of the tower, called  $m_2$  in the figure, and without taking in considering the mass of the wheels. Finally, the next simplification will be to add the unbalanced mass engine at the top of the tower and also the mass of a wheel, thus transforming the model



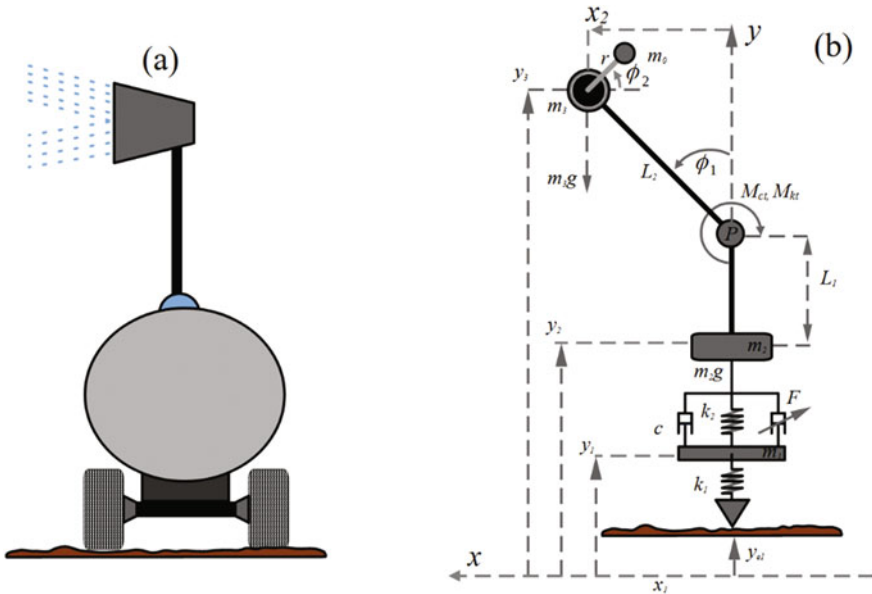


**Fig. 1** Theoretical mathematical model of the turret sprayer. **a** trailer and tower coupled and **b** scheme of forces applied

into a ¼ vehicle (Quarter-car). Finally, all the simplifications mentioned above are represented in a theoretical scheme presented in the following figure, Fig. 1.

The differential equations of motion are obtained from the Method of Energies and Conservative Forces, which is employed using the so-called Euler–Lagrange Equations.

## 2 Euler–Lagrange Energy Method

Euler–Lagrange equation is defined as:

$$\frac{d}{dt} \left( \frac{\partial L}{\partial \dot{q}_j} \right) - \frac{\partial L}{\partial q_j} = Q_j \tag{1}$$

with  $j = 1, 2, 3, \dots$ . Where  $L = T_T - V_T$ , called Lagrangian where  $T_T$  represents the total kinetic energy of the system,  $V_T$  is the work of conservative forces (potential energy of the chassis, tower and unbalanced motor masses, and the potential energy of the elastic elements). And  $Q$  is the work of all non-conservative forces (such as the energy dissipated by the damping elements).

## 2.1 Total Kinetic Energy of the System

The total kinetic energy of the  $T_T$  system is the sum of the kinetic energy portions of the trailer, the tower, the unbalanced mass of the engine, and the tire, which are represented by  $T_c$ ,  $T_t$ ,  $T_o$  and  $T_p$  respectively.  $T_T$  is then defined as:

$$T_T = T_p + T_c + T_t + T_o \quad (2)$$

Where:

$$T_p = \frac{1}{2}m_1V_1^2 = \frac{1}{2}m_1(\dot{x}_1^2 + \dot{y}_1^2) \quad (3)$$

$$T_c = \frac{1}{2}m_2V_2^2 = \frac{1}{2}m_2(\dot{x}_1^2 + \dot{y}_2^2) \quad (4)$$

$$T_t = \frac{1}{2}(m_3)V_3^2 = \frac{1}{2}(m_3)(\dot{x}_2^2 + \dot{y}_3^2) + \frac{1}{2}m_3L_2^2\dot{\phi}_1^2 \quad (5)$$

With  $m_3 = M + m$ , where  $M$  represents the concentrated mass of the fans and  $m$  the mass of the motor. The term  $m_3L_2^2$  in Eq. 5 represents the moment of inertia of the tower.

$$T_o = \frac{1}{2}m_0(\dot{x}_0^2 + \dot{y}_0^2) + \frac{1}{2}m_0r^2\dot{\phi}_2^2 \quad (6)$$

The horizontal and vertical positions of the  $m_3$  tower mass are given as follows, respectively: The horizontal position is:

$$\begin{aligned} x_2 &= L_2\sin\phi_1 - x_1 \\ x_2 &= L_2\sin\phi_1 - x_1 \end{aligned} \quad (7)$$

and its first and second derivatives, respectively in time:

$$\begin{aligned} \dot{x}_2 &= L_2\dot{\phi}_1\cos\phi_1 - \dot{x}_1 \\ \ddot{x}_2 &= \ddot{x}_1L_2\ddot{\phi}_1\cos\phi_1 - L_2\dot{\phi}_1^2\sin\phi_1 \end{aligned}$$

The vertical position is:

$$y_3 = y_2 + L_1 + L_2\cos\phi_1 \quad (8)$$

and its first and second derivatives, respectively in time:

$$\dot{y}_3 = \dot{y}_2 + L_1 + L_2\dot{\phi}_1\sin\phi_1$$

$$\ddot{y}_3 = \ddot{y}_2 - L_2\ddot{\phi}_1\sin\phi_1 - L_2\dot{\phi}_1^2\cos\phi_1$$

The horizontal and vertical positions of the unbalanced mass  $m_0$  can be described as follows:

$$x_0 = L_2\sin\phi_1 - r\cos\phi_2 \quad (9)$$

$$y_0 = L_2\cos\phi_1 - r\sin\phi_2 + L_1 + y_2 \quad (10)$$

With its derivatives  $\dot{x}_0$  and  $\dot{y}_0$  in time given by:

$$\dot{x}_0 = \dot{\phi}_1 L_2 \cos\phi_1 + \dot{\phi}_2 r \sin\phi_2$$

$$\dot{y}_0 = -\dot{\phi}_1 L_2 \sin\phi_1 + \dot{\phi}_2 r \cos\phi_2 + \dot{y}_2$$

representing the coordinates of the angular velocity of the unbalanced mass  $m_0$ .

In this way, substituting Eqs. 3–6 in Eq. 2, we obtain:

$$T_t = \frac{1}{2}m_1(\dot{x}_1^2 + \dot{y}_1^2) + \frac{1}{2}m_2(\dot{x}_2^2 + \dot{y}_2^2) + \frac{1}{2}m_3(\dot{x}_3^2 + \dot{y}_3^2) + \frac{1}{2}m_3L_2^2\dot{\phi}_1^2 + \frac{1}{2}m_0(\dot{x}_0^2 + \dot{y}_0^2) + \frac{1}{2}m_0r^2\dot{\phi}_2^2 \quad (11)$$

with respect to time of Eqs. 7 and 8 in the previous Eq. 11, we have:

$$\begin{aligned} T_t &= \frac{1}{2}m_1\dot{x}_1^2 + \frac{1}{2}m_1\dot{y}_1^2 + \frac{1}{2}m_2\dot{x}_2^2 + \frac{1}{2}m_2\dot{y}_2^2 + \\ &\frac{1}{2}m_0(\dot{x}_0^2 + \dot{y}_0^2) + \frac{1}{2}m_3L_2^2\dot{\phi}_1^2 + \frac{1}{2}m_0r^2\dot{\phi}_2^2 \\ &\frac{1}{2}m_3(\dot{x}_1 + L_2\dot{\phi}_1\cos\phi_1)^2 + \frac{1}{2}m_3(\dot{y}_2 - L_2\dot{\phi}_1\sin\phi_1)^2 + \end{aligned} \quad (12)$$

And now the first time derivatives of Eqs. 9 and 10 in Eq. 12, you get:

$$\begin{aligned} T_T &= \frac{1}{2}m_1\dot{x}_1^2 + \frac{1}{2}m_1\dot{y}_1^2 + \frac{1}{2}m_2\dot{x}_2^2 + \frac{1}{2}m_2\dot{y}_2^2 \\ &+ \frac{1}{2}m_3(\dot{x}_1 + L_2\dot{\phi}_1\cos\phi_1)^2 + \frac{1}{2}m_3(\dot{y}_2 - L_2\dot{\phi}_1\sin\phi_1)^2 + \\ &\frac{1}{2}m_0(\dot{\phi}_1 L_2 \cos\phi_1 + \dot{\phi}_2 r \sin\phi_2)^2 + \frac{1}{2}m_3L_2^2\dot{\phi}_1^2 + \frac{1}{2}m_0r^2\dot{\phi}_2^2 \\ &\frac{1}{2}m_0(-\dot{\phi}_1 L_2 \sin\phi_1 + \dot{\phi}_2 r \cos\phi_2 + \dot{y}_2)^2 \end{aligned} \quad (13)$$

$$T_T = \frac{1}{2}m_3\dot{x}_1^2 + \frac{1}{2}m_3\dot{y}_2^2 - m_3\dot{x}_1L_2\dot{\phi}_1\cos\phi_1 - m_3\dot{y}_2L_2\dot{\phi}_1\sin\phi_1 +$$

$$\begin{aligned}
& \frac{1}{2}m_3L_2^2\dot{\phi}_1^2(\cos^2\phi_1 + \sin^2\phi_1) + \frac{1}{2}m_0\dot{\phi}_1^2L_2^2(\cos^2\phi_1 + \sin^2\phi_1) + \\
& \frac{1}{2}m_0\dot{\phi}_2^2r^2(\cos^2\phi_2 + \sin^2\phi_2) - \\
& m_0\dot{\phi}_1\dot{\phi}_2L_2r(\cos\phi_2\sin\phi_1 - \cos\phi_1\sin\phi_2) + \\
& \frac{1}{2}m_0\dot{y}_2^2 - m_0\dot{y}_2\dot{\phi}_1L_2\sin\phi_1 + m_0\dot{y}_2\dot{\phi}_2r\cos\phi_2 + \\
& \frac{1}{2}m_1\dot{x}_1^2 + \frac{1}{2}m_1\dot{y}_1^2 + \frac{1}{2}m_2\dot{x}_1^2 + \frac{1}{2}m_2\dot{y}_2^2 + \frac{1}{2}m_3L_2^2\dot{\phi}_1^2 + \frac{1}{2}m_0r^2\dot{\phi}_2^2 \quad (13b)
\end{aligned}$$

The lateral displacement of the trailer's center of gravity,  $x_1$ , limited by the tires, is very small compared to the magnitudes of the other displacements. Thus, it will be assumed that  $x_1$  is constant [13]. So: if constant, then: if  $x_1 \cong \text{constant}$ , then:  $\dot{x}_1 \cong \ddot{x}_1 \cong 0$ .

In this way, making use of the trigonometric identities below:

$$\sin^2\phi_2 + \cos^2\phi_2 = 1$$

$$\cos\phi_2\cos\phi_1 + \sin\phi_1\sin\phi_2 = \cos(\phi_2 - \phi_1)$$

we have the following equation for the total kinetic energy of the system:

$$\begin{aligned}
T_T = & \frac{1}{2}m_3\dot{y}_2^2 - m_3\dot{y}_1L_2\dot{\phi}_1\sin\phi_1 + \frac{1}{2}m_3L_2^2\dot{\phi}_1^2 + \frac{1}{2}m_0\dot{\phi}_1^2L_2^2 \\
& + \frac{1}{2}m_0r^2\dot{\phi}_2^2 - m_0\dot{\phi}_1\dot{\phi}_2L_2r\cos(\phi_2 - \phi_1) + \frac{1}{2}m_0\dot{y}_2^2 - \\
& m_0\dot{y}_2\dot{\phi}_1L_2\sin\phi_1 + m_0\dot{y}_2\dot{\phi}_2r\cos\phi_2 + \frac{1}{2}m_1\dot{y}_1^2 + \frac{1}{2}m_2\dot{y}_2^2 + \\
& \frac{1}{2}m_3L_2^2\dot{\phi}_1^2 + \frac{1}{2}m_0r^2\dot{\phi}_2^2 \quad (14)
\end{aligned}$$

$$\begin{aligned}
T_T = & \frac{1}{2}(m_2 + m_3 + m_0)\dot{y}_2^2 - (m_3 + m_0)L_2\dot{y}_2\dot{\phi}_1\sin\phi_1 + \\
& m_3L_2^2\dot{\phi}_1^2 + m_0r^2\dot{\phi}_2^2 + m_0\dot{y}_2\dot{\phi}_2r\cos\phi_2 - \\
& m_0r\dot{\phi}_1\dot{\phi}_2L_2\cos(\phi_2 - \phi_1) + \frac{1}{2}m_1\dot{y}_1^2 + \frac{1}{2}m_0L_2^2\dot{\phi}_1^2 \quad (14a)
\end{aligned}$$

## 2.2 Total Potential Energy of the System

The total potential energy of the system or the work of the conservative forces of the  $V_T$  system is given by the sum of the potential energy portions of the elastic elements of the  $K_1$ ,  $K_2$  and  $K_T$  system, as follows:

$$V_T = E_{Pk1} + E_{Pk2} + E_{PkT} \quad (15)$$

The previous potential energy equation can then be rewritten as follows:

$$V_T = \frac{1}{2}K_1(\Delta y_{K_1})^2 + \frac{1}{2}K_2(\Delta y_{K_2})^2 + \frac{1}{2}K_T(\Delta y_{K_T})^2 \quad (16)$$

Replacing the appropriate displacements, Eqs. 8 and 10, we obtain the following equation:

$$V_T = \frac{1}{2}K_1(y_1 - y_{e1})^2 + \frac{1}{2}K_2(y_2 - y_1)^2 + \frac{1}{2}K_T\phi_1^2 \quad (17)$$

$$V_T = \frac{1}{2}K_1(y_1^2 - 2y_1y_{e1} + y_{e1}^2)^2 + \frac{1}{2}K_2(y_1^2 - 2y_1y_2 + y_2^2)^2 + \frac{1}{2}K_T\phi_1^2 \quad (17a)$$

From the previous equation (Eq. 17a), the effect of gravity as a conservative force was disregarded, due to its little influence on the response of the system.

### 2.3 Work of Non-Conserved Forces

The work of the non-conserved forces or total damping of the  $Q$  system represents the total energy dissipated by the damping elements, and is given by the sum of the energy dissipated by the suspension damper ( $F_c$ ) and by the junction damper torsional ( $F_{c_T}$ ), in addition to the energy dissipated by the damper with MR ( $F$ ), as follows:

$$Q = F_c + F_{c_T} + F \quad (18)$$

So the previous equation is rewritten as follows:

$$Q = C(\Delta \dot{y}_C) + C_T(\Delta \dot{y}_{C_T}) + F \quad (19)$$

where the terms  $\Delta \dot{y}_C$  and  $\Delta \dot{y}_{C_T}$  represent the deformation velocities of the damping elements, respectively. And they are given as follows:

$$\Delta \dot{y}_C = \dot{y}_2 - \dot{y}_1 \quad (20)$$

$$\Delta \dot{y}_{C_T} = \dot{\phi}_1 \quad (21)$$

The strength of the MR damper is mathematically represented by the Bounce-Wen model. And then, replacing Eqs. 20 and 21 in 19, you can rewrite the expression for  $Q$  as follows:

$$Q = C(\dot{y}_2 - \dot{y}_1) + C_T(\dot{\phi}_1) + \alpha z \quad (22)$$

where  $V_a$  is the supply voltage,  $i_a$  is the supply current,  $\Phi$  is the magnetic flux and  $\varphi$  is the angular position of the motor [12].

$$L_a \frac{di_a}{dt} + R_a i_a + E_b = V_a \quad (23)$$

where  $E_b$  is the counter-electromotive force between the motor armature terminals given by:

$E_b = k_E \frac{d\phi_2}{dt}$  where  $k_E$  is the motor voltage constant and  $\phi_2$  the motor angular position. Also according to [12], to study the interaction between the tower and the motor, the direct current motor is considered in a simplified way, and therefore the torque generated by the motor can be expressed as follows:

$$M_m = \hat{a} - \hat{b}\dot{\phi}_2 \quad (24)$$

where parameter  $\hat{a}$  is related to the electrical voltage applied to the direct current motor and  $\hat{b}$  related to the type of motor used, both defined as follows, respectively:

$$\hat{a} = \frac{k_m V_a}{R_a} \quad (25)$$

$$\hat{b} = \frac{k_m k_b}{R_a} \quad (26)$$

where  $R_a$  is the motor electrical resistance,  $k_b$  the motor voltage constant,  $V_a$  the input voltage applied to the motor armature,  $k_m$  is the motor torque constant.

Then, replacing Eq. 24, rewrite Eq. 22 as follows:

$$Q = C(\dot{y}_2 - \dot{y}_1) + C_T(\dot{\phi}_1) + \alpha z + \hat{a} - \hat{b}\dot{\phi}_2 \quad (27)$$

## 2.4 Application of the Euler–Lagrange Equation

The Lagrangian of the system under study is calculated by the difference between the total kinetic energy, the total potential energy and the dissipation energy of the system, is  $L = T_T - V_T$ . The Lagrangian is then obtained through the difference between Eqs. 7, 10 which results in [5]

$$\begin{aligned}
L = & \frac{1}{2}(m_2 + m_3 + m_0)\dot{y}_2^2 - (m_3 + m_0)L_2\dot{y}_2\dot{\phi}_1\sin\phi_1 \\
& + m_3L_2^2\dot{\phi}_1^2 + m_0r^2\dot{\phi}_2^2 - m_0\dot{y}_2\dot{\phi}_2r\cos\phi_2 - \\
& m_0r\dot{\phi}_1\dot{\phi}_2L_2\cos(\phi_2 - \phi_1) + \frac{1}{2}m_1\dot{y}_1^2 + \frac{1}{2}m_0L_2^2\dot{\phi}_1^2 - \\
& \frac{1}{2}K_1(y_1^2 - 2y_1y_{e1} + y_{e1}^2)^2 + \frac{1}{2}K_2(y_1^2 - 2y_1y_2 + y_1^2)^2 + \frac{1}{2}K_T\phi_1^2 \quad (28)
\end{aligned}$$

For the application of the Lagrange Equation, the generalized coordinates of the system in question must be determined. For the system of the present work, the following generalized coordinates are defined:  $y_1$ ,  $y_2$ ,  $\phi_1$  and  $\phi_2$ , so according to the Lagrange Equation, the Lagrangian (Eq. 16) must be derived in relation to these generalized coordinates.

But, once the equations of kinetic, potential and dissipation energies are deduced, the Hamilton Principle can be used for each one of the generalized coordinates. As will be shown below: For the  $y_1$  coordinate, vertical displacement of the tire:

$$\begin{aligned}
\frac{d}{dt}\left(\frac{\partial L}{\partial \dot{y}_1}\right) - \left(\frac{\partial L}{\partial y_1}\right) &= Q_1 \\
\frac{d}{dt}\left(\frac{\partial T_T}{\partial \dot{y}_1} - \frac{\partial V_T}{\partial y_1}\right) - \left(\frac{\partial T_T}{\partial y_1} - \frac{\partial V_T}{\partial y_1}\right) &= Q_1 \quad (29)
\end{aligned}$$

But:  $\frac{\partial V_T}{\partial \dot{y}_1} = 0$  e  $\frac{\partial T_T}{\partial y_1} = 0$  so the previous equation looks like this:

$$\frac{d}{dt}\left(\frac{\partial T_T}{\partial \dot{y}_1}\right) + \frac{\partial V_T}{\partial y_1} = Q_1$$

$$m_1\ddot{y}_1 = -K_1(y_1 - y_{e1}) + K_2(y_2 - y_1) + C(\dot{y}_2 - \dot{y}_1) - \delta z \quad (30)$$

where  $z$  is the evolutionary variable given by:

$$\dot{z} = -\gamma|\dot{y}_2 - \dot{y}_1|z|z|^{n-1}z - \beta(\dot{y}_2 - \dot{y}_1)|z|^n + \lambda(\dot{y}_2 - \dot{y}_1)$$

More details on the evolutionary variable  $z$  [5].

And  $y_{e1}$  is considered to be an excitation of the harmonic type and given as follows  $y_{e1} = A\cos(\omega t)$ , where  $A$  is the amplitude that represents the irregularities of the ground surface.

For the  $y_2$  coordinate, vertical displacement of the chassis:

$$\begin{aligned}
\frac{d}{dt}\left(\frac{\partial L}{\partial \dot{y}_2}\right) - \left(\frac{\partial L}{\partial y_2}\right) &= Q_2 \\
\frac{d}{dt}\left(\frac{\partial T_T}{\partial \dot{y}_2} - \frac{\partial V_T}{\partial y_2}\right) - \left(\frac{\partial T_T}{\partial y_2} - \frac{\partial V_T}{\partial y_2}\right) &= Q_2 \quad (31)
\end{aligned}$$

But:  $\frac{\partial V_T}{\partial \dot{y}_2} = 0$  e  $\frac{\partial T_T}{\partial y_2} = 0$  so the previous equation looks like this:

$$\frac{d}{dt} \left( \frac{\partial T_T}{\partial \dot{y}_2} \right) + \frac{\partial V_T}{\partial y_2} = Q_2$$

$$\begin{aligned} & (m_2 + m_3 + m_0) \ddot{y}_2 - (m_3 + m_0) L_2 \ddot{\phi}_1 \sin \phi_1 + m_0 r \ddot{\phi}_2 \cos \phi_2 \\ & = (m_3 + m_0) L_2 \dot{\phi}_1^2 \cos \phi_1 + m_0 r \dot{\phi}_2^2 \sin \phi_2 + K_2 (y_2 - y_1) + \\ & C (\dot{y}_1 - \dot{y}_2) - \delta z \end{aligned} \quad (32)$$

Similarly, the Hamilton Principle is used for the  $\phi_1$  coordinate, angular displacement of the tower:

$$\begin{aligned} \frac{d}{dt} \left( \frac{\partial L}{\partial \dot{\phi}_1} \right) - \left( \frac{\partial L}{\partial \phi_1} \right) &= Q_3 \\ \frac{d}{dt} \left( \frac{\partial T_T}{\partial \dot{\phi}_1} - \frac{\partial V_T}{\partial \dot{\phi}_1} \right) - \left( \frac{\partial T_T}{\partial \phi_1} - \frac{\partial V_T}{\partial \phi_1} \right) &= Q_3 \end{aligned} \quad (33)$$

But:  $\frac{\partial V_T}{\partial \phi_1} = 0$  so the previous equation looks like this:

$$\begin{aligned} \frac{d}{dt} \left( \frac{\partial T_T}{\partial \dot{\phi}_1} \right) - \frac{\partial T_T}{\partial \phi_1} + \frac{\partial V_T}{\partial \phi_1} &= Q_3 \\ - (m_3 + m_0) \ddot{y}_2 L_2 \sin \phi_1 + 2m_3 L_2^2 \ddot{\phi}_1 + m_0 L_2^2 \ddot{\phi}_1 - \\ m_0 r L_2 \ddot{\phi}_2 \cos(\phi_2 - \phi_1) &= -m_0 r L_2 \dot{\phi}_2 \sin(\phi_2 - \phi_1) (\dot{\phi}_2 - \dot{\phi}_1) - \\ m_0 r L_2 \dot{\phi}_2 \dot{\phi}_1 \sin(\phi_2 - \phi_1) - K_T \phi_1 - C_T \dot{\phi}_1 \end{aligned} \quad (34)$$

And now, using Hamilton's Principle for the  $\phi_2$  coordinate, angular displacement of the unbalanced mass, we have:

$$\begin{aligned} \frac{d}{dt} \left( \frac{\partial L}{\partial \dot{\phi}_2} \right) - \left( \frac{\partial L}{\partial \phi_2} \right) &= Q_4 \\ \frac{d}{dt} \left( \frac{\partial T_T}{\partial \dot{\phi}_2} - \frac{\partial V_T}{\partial \dot{\phi}_2} \right) - \left( \frac{\partial T_T}{\partial \phi_2} - \frac{\partial V_T}{\partial \phi_2} \right) &= Q_4 \end{aligned} \quad (35)$$

But:  $\frac{\partial V_T}{\partial \phi_2} = 0$  so the previous equation looks like this:

$$\begin{aligned} \frac{d}{dt} \left( \frac{\partial T_T}{\partial \dot{\phi}_2} \right) - \frac{\partial T_T}{\partial \phi_2} + \frac{\partial V_T}{\partial \phi_2} &= Q_4 \\ 2m_0 r^2 \ddot{\phi}_2 + m_0 r \ddot{y}_2 \cos \phi_2 - m_0 r L_2 \ddot{\phi}_1 \cos(\phi_2 - \phi_1) \\ &= -m_0 r L_2 \dot{\phi}_1 \sin(\phi_2 - \phi_1) (\dot{\phi}_2 - \dot{\phi}_1) + \\ m_0 r L_2 \dot{\phi}_1 \dot{\phi}_2 \sin(\phi_2 - \phi_1) &+ (\hat{a} - \hat{b} \dot{\phi}_2) \end{aligned} \quad (36)$$

So the system of differential equations that define the movements of the system under

$$\begin{aligned} m_1 \ddot{y}_1 &= -K_1 (y_1 - y_{e1}) + K_2 (y_2 - y_1) + C (\dot{y}_2 - \dot{y}_1) - \delta z \\ (m_2 + m_3 + m_0) \ddot{y}_2 &- (m_3 + m_0) L_2 \ddot{\phi}_1 \sin \phi_1 + m_0 r \ddot{\phi}_2 \cos \phi_2 \end{aligned}$$



$$\begin{aligned}
&= (m_3 + m_0)L_2\dot{\phi}_1^2\cos\phi_1 + \\
&m_0r\dot{\phi}_2^2\sin\phi_2 + K_2(y_2 - y_1) + C(\dot{y}_1 - \dot{y}_2) - \delta z \\
&\quad - (m_3 + m_0)\ddot{y}_2L_2\sin\phi_1 + 2m_3L_2^2\ddot{\phi}_1 + m_0L_2^2\ddot{\phi}_1 \\
&\quad - m_0rL_2\ddot{\phi}_2\cos(\phi_2 - \phi_1) = - \\
&m_0rL_2\dot{\phi}_2\sin(\phi_2 - \phi_1)(\dot{\phi}_2 - \dot{\phi}_1) \\
&\quad - m_0rL_2\dot{\phi}_2\dot{\phi}_1\sin(\phi_2 - \phi_1) - K_T\phi_1 - C_T\dot{\phi}_1 \\
&2m_0r^2\ddot{\phi}_2 + m_0r\ddot{y}_2\cos\phi_2 - m_0rL_2\ddot{\phi}_1\cos(\phi_2 - \phi_1) \\
&= -m_0rL_2\dot{\phi}_1\sin(\phi_2 - \phi_1)(\dot{\phi}_2 - \dot{\phi}_1) + \\
&m_0rL_2\dot{\phi}_1\dot{\phi}_2\sin(\phi_2 - \phi_1) + \left(\hat{a} - \hat{b}\dot{\phi}_2\right) \tag{37}
\end{aligned}$$

When the turret plus the non-ideal unbalanced motor are considered as a simple pendulum, then the angle  $\phi_1$  is considered small compared to  $\phi_2$ . Therefore, the following relation is valid [13].

$$\begin{cases} \sin\phi_1 \cong \phi_1 \\ \cos\phi_1 \cong 1 \end{cases}$$

Thus, the system of equations presented above (Eq. 37) is rewritten as follows:

$$\begin{aligned}
&m_1\ddot{y}_1 \\
&= -K_1(y_1 - y_{e1}) + K_2(y_2 - y_1) + C(\dot{y}_2 - \dot{y}_1) - \delta z \\
&(m_2 + m_3 + m_0)\ddot{y}_2 - (m_3 + m_0)L_2\ddot{\phi}_1\phi_1 + m_0r\ddot{\phi}_2\cos\phi_2 \\
&= (m_3 + m_0)L_2\dot{\phi}_1^2 + \\
&m_0r\dot{\phi}_2^2\sin\phi_2 + K_2(y_2 - y_1) + C(\dot{y}_1 - \dot{y}_2) - \delta z \\
&\quad - (m_3 + m_0)\ddot{y}_2L_2\phi_1 + 2m_3L_2^2\ddot{\phi}_1 + m_0L_2^2\ddot{\phi}_1 \\
&\quad - m_0rL_2\ddot{\phi}_2\cos(\phi_2 - \phi_1) = - \\
&m_0rL_2\dot{\phi}_2\sin(\phi_2 - \phi_1)(\dot{\phi}_2 - \dot{\phi}_1) \\
&\quad - m_0rL_2\dot{\phi}_2\dot{\phi}_1\sin(\phi_2 - \phi_1) - K_T\phi_1 - C_T\dot{\phi}_1 \\
&2m_0r^2\ddot{\phi}_2 + m_0r\ddot{y}_2\cos\phi_2 - m_0rL_2\ddot{\phi}_1\cos(\phi_2 - \phi_1) \\
&= -m_0rL_2\dot{\phi}_1\sin(\phi_2 - \phi_1)(\dot{\phi}_2 - \dot{\phi}_1) + \\
&m_0rL_2\dot{\phi}_1\dot{\phi}_2\sin(\phi_2 - \phi_1) + \left(\hat{a} - \hat{b}\dot{\phi}_2\right) \tag{38}
\end{aligned}$$

The previous system of equations (Eq. 38) is rewritten as follows:

$$\begin{aligned}
\ddot{y}_1 &= -q_1(y_1 - y_{e1}) + q_2(y_2 - y_1) + p_1(\dot{y}_2 - \dot{y}_1) - \mu z \\
&(1 + \alpha_1 + \alpha)\ddot{y}_2 - (\alpha_1 + \alpha)\ddot{\phi}_1\phi_1 + \alpha r\ddot{\phi}_2\cos\phi_2 \\
&= (\alpha_1 + \alpha)L_2\dot{\phi}_1^2 + \\
&\alpha r\dot{\phi}_2^2\sin\phi_2 + q_3(y_2 - y_1) + p_2(y_1' - y_2') - \mu_1 z
\end{aligned}$$

$$\begin{aligned}
& -\frac{m_3 + m_0}{2m_3L_2}\ddot{y}_2\phi_1 + \left(1 + \frac{m_0}{2m_3}\right)\ddot{\phi}_1 - \frac{m_0r}{2m_3L_2}\ddot{\phi}_2 \cos(\phi_2 - \phi_1) = - \\
& \frac{m_0r}{2m_3L_2}\dot{\phi}_2 \sin(\phi_2 - \phi_1)(\dot{\phi}_2 - \dot{\phi}_1) \\
& - \frac{m_0r}{2m_3L_2}\dot{\phi}_2\dot{\phi}_1 \sin(\phi_2 - \phi_1) - q_4\phi_1 - p_3\dot{\phi}_1 \\
& \frac{1}{2r}\ddot{y}_2\cos\phi_2 + \ddot{\phi}_2 - \frac{m_0L_2}{2r}\ddot{\phi}_1\cos(\phi_2 - \phi_1) \\
& = \frac{L_2}{2r}\dot{\phi}_1 \sin(\phi_2 - \phi_1)(\dot{\phi}_2 - \dot{\phi}_1) + \\
& \frac{L_2}{2r}\dot{\phi}_1\dot{\phi}_2 \sin(\phi_2 - \phi_1) + a - b\dot{\phi}_2
\end{aligned} \tag{39}$$

The parameters considered in the previous system are listed below:

$$\begin{aligned}
q_1 &= \frac{K_1}{m_1}, q_2 = \frac{K_2}{m_1}, q_3 = \frac{K_2}{m_1}, q_3 = \frac{K_2}{m_2}, p_1 = \frac{C}{m_1}, p_2 = \frac{C}{m_1}, p_3 = \frac{C_T}{m_3L_2^2}, \alpha = \frac{m_0}{m_2}\alpha_1 = \frac{m_3}{m_2}, \\
\alpha_2 &= \frac{m_0}{m_3}, \zeta = \frac{r}{L_2}, \mu = \frac{\delta}{m_1L_2}, \mu_1 = \frac{\delta}{m_2L_2}, a = \frac{\hat{a}}{m_0r^2}, b = \frac{\hat{b}}{m_0r^2}.
\end{aligned}$$

The system of equations is then rewritten, making use of a change of variables employing the following state variables:

$$u_1 = y_1, u_2 = y_1', u_3 = y_2, u_4 = y_2', u_5 = \phi_1, u_6 = \phi_1', u_7 = \phi_2, u_8 = \phi_2', e_{u_9} = z.$$

Which results in a new system of equations:

$$\begin{cases} E_1y_2 - E_2\phi_1 + E_3\phi_2 = f_2 \\ -E_4y_2 + E_5\phi_1 + E_6\phi_2 = f_3 \\ E_7y_2 - E_8\phi_1 + E_9\phi_2 = f_4 \end{cases} \tag{40}$$

Where do you have:

$$\begin{aligned}
f_1 &= -q_1[u_1 - A \cos(\omega t)] + q_2(u_3 - u_1) + p_1(u_4 - u_2) - \mu_1z - u_5) - q_4u_5 - p_3u_6 \\
f_2 &= (\alpha_1 + \alpha)L_2u_6^2 + \alpha ru_8^2 \sin u_7 - q_3(u_3 - u_1) - p_2(u_4 - u_2) + \mu_1z \\
f_3 &= -\frac{m_0r}{2m_3L_2}u_8 \sin(u_7 - u_5)(u_8 - u_6) - \frac{m_0r}{2m_3L_2}u_6u_8 \sin(u_7 \\
f_4 &= -\frac{L_2}{2r}u_6 \sin(u_7 - u_5)(u_8 - u_6) + \frac{L_2}{2r}u_6u_8 \sin(u_7 - u_5) + \alpha - bu_8
\end{aligned}$$

And also:

$$\begin{aligned}
E_1 &= 1 + \alpha_1 + \alpha E_2 = (\alpha_1 + \alpha_2)L_2u_5 E_3 = ar \cos(\alpha_7) E_4 = \frac{m_3+m_0}{2m_3L_2}u_5 E_5 = 1 + \frac{m_0}{2m_3} \\
E_6 &= \frac{m_0r}{2m_3L_2} \cos(u_7 - u_5) E_7 = \frac{1}{2r} \cos(u_7) E_8 = \frac{m_0L_2}{2r} \cos(u_7 - u_5) E_9 = 1
\end{aligned}$$

So, rewriting the system in matrix form, you have:

$$\begin{bmatrix} E_1 & -E_2 & E_3 \\ -E_4 & E_5 & -E_6 \\ E_7 & -E_8 & E_9 \end{bmatrix} \begin{bmatrix} y_2'' \\ \phi_1'' \\ \phi_2'' \end{bmatrix} = \begin{bmatrix} f_2 \\ f_3 \\ f_4 \end{bmatrix}$$

$$\begin{bmatrix} y_2'' \\ \phi_1'' \\ \phi_2'' \end{bmatrix} = \begin{bmatrix} f_2 \\ f_3 \\ f_4 \end{bmatrix} \begin{bmatrix} E_1 & -E_2 & E_3 \\ -E_4 & E_5 & -E_6 \\ E_7 & -E_8 & E_9 \end{bmatrix}^{-1} \tag{41}$$

Finally, solving the inverse matrix and making the necessary multiplication of this answer in the system of equations above, we have the system of second order linear differential equations that govern the dynamics of the system under study, presented below:

$$\begin{aligned} y_1 &= f_1 \\ y_2 &= 1/\Delta[(E_5E_9 - E_6E_8)f_2 + (E_2E_9 - E_3E_8)f_3 + (E_2E_6 - E_3E_5)f_4] \\ \phi_1 &= 1/\Delta[(E_4E_9 - E_6E_7)f_2 + (E_1E_9 - E_3E_7)f_3 + (E_1E_6 - E_3E_4)f_4] \\ \phi_2 &= 1/\Delta[(E_4E_8 - E_5E_7)f_2 + (E_1E_8 - E_2E_7)f_3 + (E_1E_5 - E_2E_4)f_4] \\ z' &= -\gamma|u_4 - u_2|u_9|u_9|^{n-1} - \beta(u_4 - u_2)|u_9|^n + \lambda(u_4 - u_2) \end{aligned} \tag{42}$$

The parameter  $\Delta$  of the previous equation (Eq. 42) is given by:

$$\Delta = E_1E_5E_9 - E_1E_6E_8 - E_2E_4E_9 + E_2E_6E_7 + E_3E_4E_8 - E_3E_5E_7$$

Making now, the right sides of the equations of  $y_2''$ ,  $\phi_1''$  and  $\phi_2''$  of the previous system (Eq. 42) equal to  $f_5$ ,  $f_6$  and  $f_7$ , respectively, and also the equation of  $z$  equal to  $f_8$  as follows:

$$f_8 = -\gamma|u_4 - u_2|u_9|u_9|^{n-1} - \beta(u_4 - u_2)|u_9|^n + \lambda(u_4 - u_2) \tag{43}$$

You can write the derivatives of system 42 as follows:

$$\begin{aligned} u_1' &= u_2 \\ u_2' &= f_1 \\ u_3' &= u_4 \\ u_4' &= f_5 \\ u_5' &= u_6 \\ u_6' &= f_6 \\ u_7' &= u_8 \\ u_8' &= f_7 \\ u_9' &= f_8 \end{aligned} \tag{44}$$

### 3 Results

#### 3.1 System Responses in Time Domain

Time and phase domain responses will be presented for the following system components: wheel mass, trailer mass, mass concentrated at the top of the tower and unbalanced engine mass, respectively. The values considered for the dimensionless parameters of the system are those shown in Table 1, for a time interval of  $0 \leq t \leq 100$  and the initial conditions were considered as being null.

The following table (Table 2) shows the values considered for the MR damper parameters.

Figure 2 shows the behavior of the displacements of the wheel in (a), the trailer in (b), the turret in (c) and the angular velocity of the unbalanced mass of the engine in (d), under suspension action with MR, in red compared to the MR shockless response in black. It can be seen that with the addition of the suspension with MR it significantly reduces the range of motion of each component of the system, having a lesser influence, in relation to the other components, on the displacement of the wheel, as expected. It is verified that the greatest influence is on the displacement of the trailer, which satisfies the proposed objectives, since the proposal is the reduction of the amplitudes of the trailer and the tower.

**Table 1** Values for dimensionless parameters for the non-suspension system with MR

Parameter	Value	Parameter	Value
q1	77.5	$\alpha 1$	0.247
q2	6.016	b	1.3
q3	1.11	$\mu$	500
q4	5.395	$\mu 1$	92.307
p1	1.306	$\alpha$	$7.69 \times 10^{-4}$
p2	0.241	p3	0.108

**Table 2** Values assigned to the parameters related to the MR damper

Parameter	Value
$\gamma$ (1/m2)	800
$\beta$ (1/m2)	1,000,000
$\lambda$	1.0
n	2.0

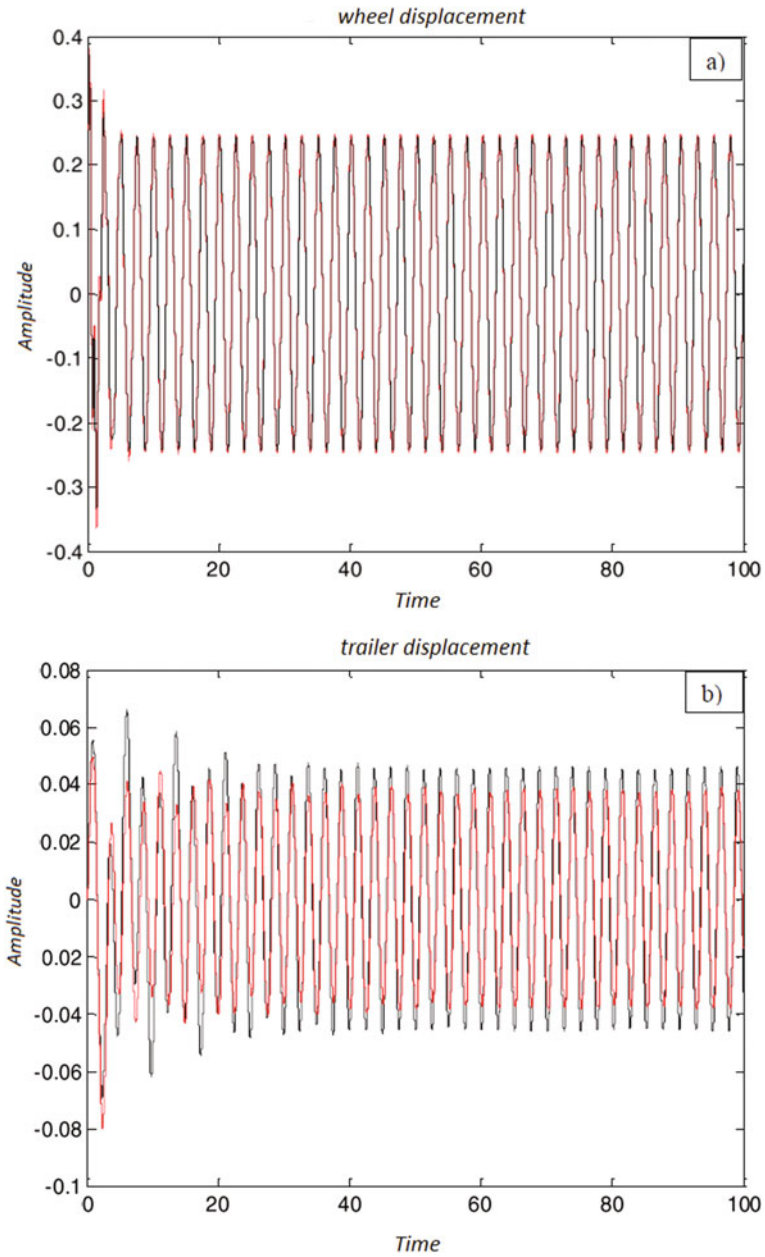


**Fig. 2** displacements of the wheel in (a), the trailer in (b), the turret in (c) and the angular velocity of the unbalanced mass of the engine in (d)

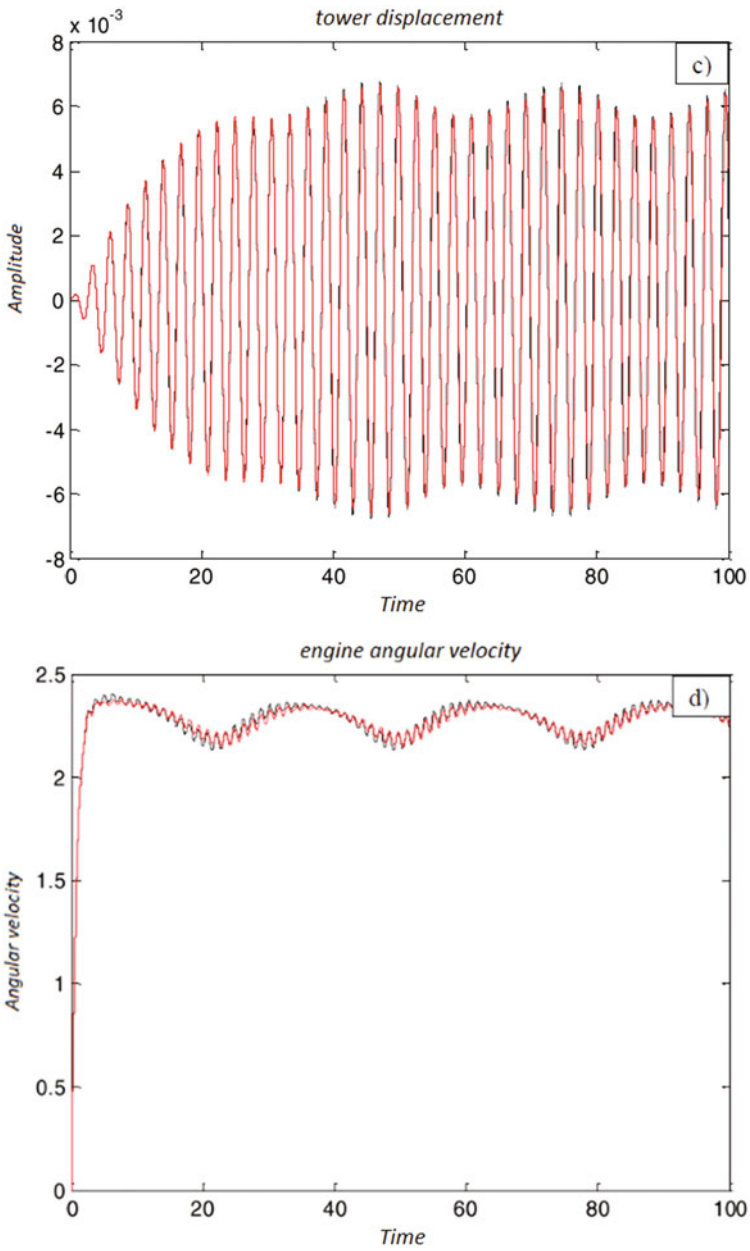
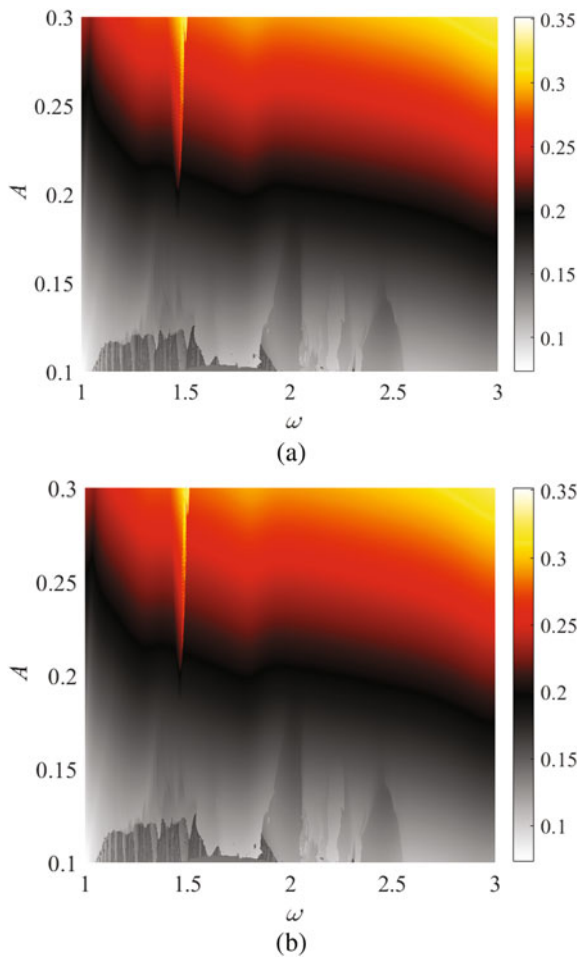


Fig. 2 (continued)

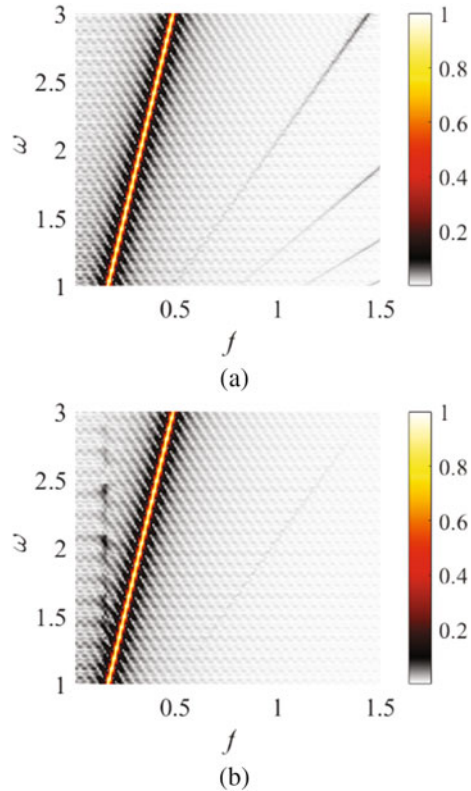
### 3.2 Analyze the Influence of the External Force Applied on the Structure Described

We analyze the influence of the external force applied on the structure described by Eq. (42) considering amplitude  $A$  in the interval  $[0.1: 0.3]$  and frequency  $\omega$  in the interval  $[1, 2]$ . For this we use the 4th order Runge–Kutta method with an integration step  $h = 0.001$  and a total integration time  $t = 106[s]$ . We also consider a transient time of 40% of the total time and considering the initial conditions  $\times 0 = [0, 0, 0, 0, 0, 0, 0, 0]$ . Figure 3a represents the maximum amplitude of the displacement of the trailer and Fig. 3b of the tower that supports the motor for spraying, both are described by the set of Eq. 42. Thus, the yellow regions represent the maximum amplitude and the light gray region represents the minimum amplitude for the structure.

**Fig. 3** Representation of the maximum amplitude considering Eq. (42). **a** trailer displacement and **b** turret displacement



**Fig. 4** Representation of the FFT for the parameter  $\omega$  as Eq. (42). **a** trailer displacement and **b** turret displacement



Another analysis performed was the oscillation frequency and thus we obtain the fast Fourier transforms (FFT) with the variation of the amplitude of the external force ( $\omega$ ), in which we can observe a characteristic frequency of the Eq. (42) referring to the trailer and the tower. Figure 4. (a) represents the FFT sweeping the parameter  $\omega$  in the interval  $[1, 2]$  of the trailer displacement, in which we can observe a natural frequency of the system in yellow and in gray scale are very low secondary frequencies. In Fig. 4b represents the variation  $\omega$  for the same interval, however, for the tower displacement, in yellow it represents the dominant frequency of the system and in gray, low amplitude secondary frequencies.

Therefore, we delimited the maximum amplitude regions for the displacement of the sprayer system truck and tower considering the external force applied to the system. This external force in Eq. (42) represents possible irregularities in the terrain where the spraying vehicle moves, as high displacements in the structure compromise the spraying application. The analysis of the frequency of for the parameter  $\omega$  showed that there is a natural frequency for both the truck and the tower vibration, which showed a behavior of possible periodicity, such frequencies are between 0.1 and 0.5 [Hz]. Thus, Fig. 5a–c represent the time series of the trailer displacement for  $\omega = 2.936$  [Hz] and considering  $A = [0.0, 0.16, 0.5]$ , respectively.



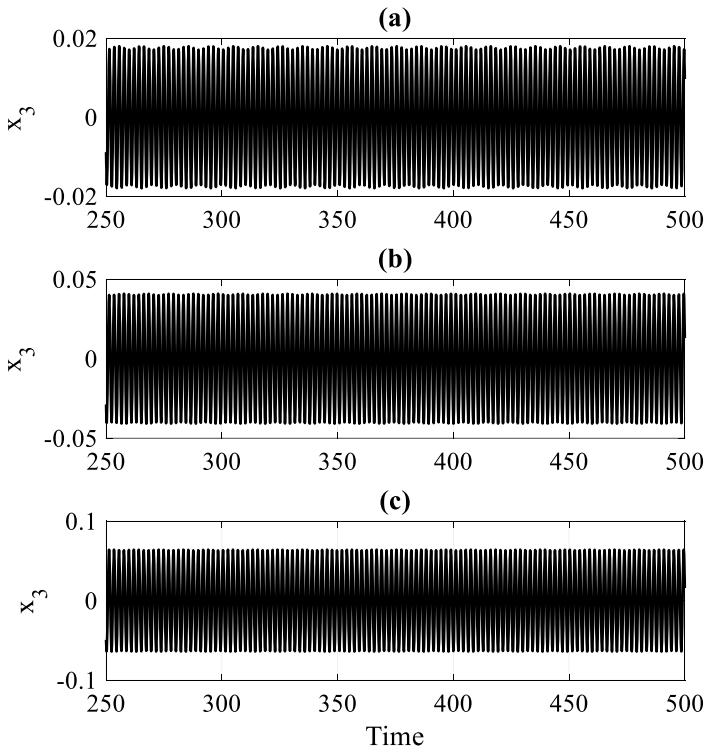


**Fig. 5** Time series of the trailer displacement **a**  $A = 0.0$ , **b**  $A = 1.6$  and **c**  $A = 0.5$

Thus, Figs. 6a–c represent the time series of the trailer displacement for  $\omega = 2.936$  [Hz] and considering  $A = [0.0, 0.16, 0.5]$ , respectively.

### 3.3 Calculation of Resulting Vibrations with and Without MR

Thus, we calculated the vibrations resulting from the absence of the MR actuation in Eq. (42), considering the same constants of the previous case, that is, the same constants of the MR system actuation in the vehicle system. Fig. 7a represent the maximum amplitude of the tower and (7b) represent the maximum amplitude of the trailer with the variation of the parameters of the external force of the system. Colors from white to black represent the minimum to medium span and from black to yellow the medium to maximum span.

We also calculated the variation of the control parameter (a) for the system with and without MR application. Thus, Fig. 8a represents the behavior of the tower vibrations with the MR and Fig. 8b without the MR acting on the system with the variation of the parameter  $a = [3, 7]$ . It can be observed that there are peaks of

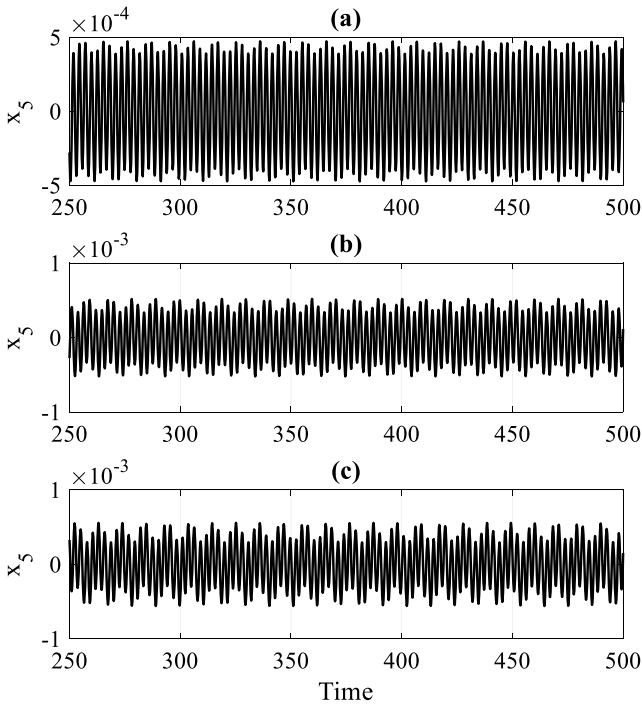


**Fig. 6** Time series of tower displacement **a**  $A = 0.0$ , **b**  $A = 1.6$  and **c**  $A = 0.5$

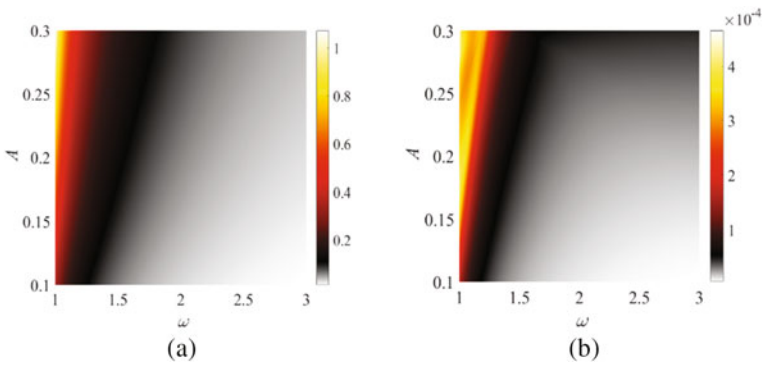


**Fig. 7** Representation of maximum amplitude as a function of external force parameters. **a** turret and **b** cart

maximum amplitude  $a = 5.329$  and  $a = 7.691$  for the system containing the MR and for the system with the MR there is a decay of the amplitude, however, it remains in a range from 0.04625 to 0.04616.

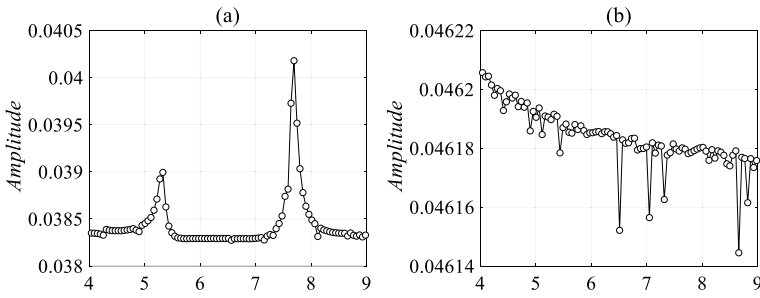


**Fig. 8** Representation of the maximum amplitude with the variation of the tower control parameter. **a** with the application of the MR and **b** without the application of the MR

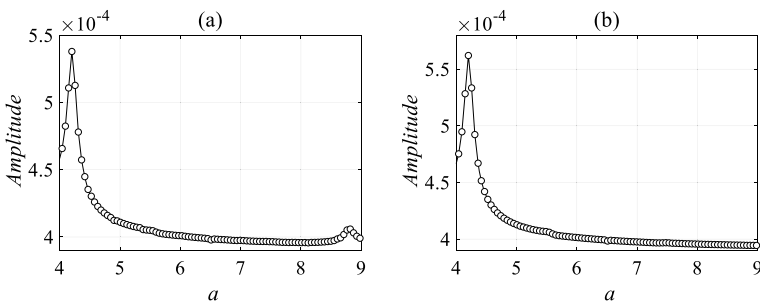


**Fig. 9** Representation of the maximum amplitude with the variation of the trailer control parameter. **a** with the application of the MR and **b** without the application of the MR.

And figs. a and fig. B. Represents the behavior of the control parameter (a) for the trailer with and without the MR application, respectively (Fig. 9).

We can observe that there is a peak with maximum amplitude for the value of  $a = 4.2$  in both cases with and without the MR, however, there is the appearance of a peak with amplitude at  $a = 8.8$ .

### 4 Conclusion

In this work, a vehicular suspension with Magneto Rheological (MR) was used, plus the addition of an unbalanced electric motor on top of the tower of a Quarter-car model that represents the structure of an orchard sprayer, in order to reduce vertical movements. mainly of the trailer or chassis, and also the angular movements of the turret. The use of the MR damper proved to be efficient for the main purpose for which it was used: to reduce the oscillation amplitudes of both the trailer or chassis ( $m_2$ ) and the tower ( $m_3$ ). It is clearly seen that there were reductions in amplitude, however in some components of the system, this reduction was minimal, as can be

seen, for the wheel, and also for the tower. This fact can be justified due to the shock absorber with MR being strongly influenced by an external electric current, which was considered to be constant in this work. The analysis of the unbalanced electric motor showed that the  $m_3$  mass amplitudes are strongly influenced by a possible unbalance of the sprayer fan blades.

## References

1. Balthazar, J.M. et.al.: *Vibration Engineering and Technology of Machinery*. Part of the Mechanisms and Machine Science book series (Mechan. Machine Science), vol. 95. Springer
2. Bombard, A.J.F., Joekes, I., Knobel, M.: *Evaluation of a Magneto-Rheological Fluid in a Prototype Damper*. Society of Automotive Engineers, Magneto-Rheometer and Magnetometer (2000)
3. Soize, C.: Stochastic modeling of uncertainties in computational structural dynamics—recent theoretical advances. *J. Sound Vib.* **332**, 2379–2395 (2013)
4. Carlson, J. D.: *Controlling Vibration with Magnetorheological Fluid Damping*. Lord Corporation. Disponível em: <http://www.sensorsmag.com/sensors/electric-magnetic/controlling-vibration-with-magnetorheological-fluid-damping-999>. Acesso em: 10 set. 2013 (2002)
5. Cézár, É.S.: *Control System Methodology For A Vehicle Suspension With Rheological Magnet (Mr) For A Tower-Type Sprayer* (2014). Thesis (Master's degree), Federal University of Pampa
6. Cunha Jr, A., Felix, J. L. P., Balthazar, J. M.: Quantification of parametric uncertainties induced by irregular soil loading in orchard tower sprayer nonlinear dynamics. *J. Sound Vibrat. JCR*, **408**, 252–269 (2017)
7. Cunha Jr, Nasser, R., Sampaio, R., Lopes, H., Breitman, K.: Uncertainty quantification through Monte Carlo method in a cloud computing setting. *Comput. Phys. Commun.* **185**, 1355–1363 (2014)
8. Cunha Jr, A., Felix, J.L.P., Balthazar, J.M.: On the nonlinear dynamics of an inverted double pendulum over a vehicle suspension subjected to random excitations. HAL Id: hal-01473586 <https://hal.archives-ouvertes.fr/hal-01473586>. Submitted on 22 Feb 2017
9. Jansen, L.M., Dyke, S.J.: Semi-active control strategies for MR dampers: A comparative study. *ASCE J. Eng. Mech.* **126**(8), 795–803 (2000)
10. Kciuk, M., Turczyn, R.: Properties and application of magnetorheological fluids. *J. Achieve. Mater. Manuf. Eng.* **18**, 127–130 (2006)
11. Kim, J.-H., Oh, J.-H.: Development of an above knee prosthesis using MR Damper and leg simulator. *International Conference on Robotics & Automation*, pp. 3686- 3691 (2001)
12. Palacios Felix, J. L.: *Teoria de Sistemas Vibratórios Aporticados Não Lineares e Não Ideais*, p. 205. Tese (Doutorado em Engenharia Mecânica)-Universidade Estadual de Campinas, Faculdade Engenharia Mecânica, Campinas (2002)
13. Sartori, S. Jr., Balthazar, J. M., Pontes, B. R.: Nonlinear dynamics of an orchard tower sprayer based on a double inverted pendulum model. 19<sup>th</sup> International Congress of Mechanical Engineering, Brasilia (2007)
14. Sartori, S. Jr.: *Mathematical modeling and dynamic analysis of the tower of an orchard sprayer*, p. 150. Dissertation (Masters in Mechanical Engineering) – São Paulo State University “Júlio de Mesquita Filho”, Bauru (2008)
15. Sartori, S. Jr., Balthazar, J. M., Pontes, B. R.: Non-linear dynamics of a tower orchard sprayer based on an inverted pendulum model. *Biosystems Engineering*, pp. 417–426 (2009)
16. Spencer Jr, B. F., Dyke, S. J., Sain, M. K., Carlson, J. D.: Phenomenological model for magnetorheological dampers. *J. Eng. Mech.* **123**, 230–238 (1997)

17. Tuset, A. M.: Optimal Control Applied in a Non-Linear Vehicle Suspension Model Controlled by Magneto-Rheological Damper, p. 156. Thesis (Doctorate in Engineering)–Federal University of Rio Grande do Sul, PROMEC, Porto Alegre (2008)
18. Tuset, A. M., Balthazar, J. M., Felix, J. L. P.: On elimination of chaotic behavior in a non-ideal portal frame structural system, using both passive and active controls. *J. Vibration Control* (2012)

# On the Use of Synchrosqueezing Transform for Chaos and Nonlinear Dynamics Analysis in Fractional-Order Systems



M. Varanis , C. Oliveira , M. A. Ribeiro , W. B. Lenz , A. M. Tusset , and Jose Manoel Balthazar 

**Abstract** In this paper, the behavior of an electromechanical device for power production is investigated. The device consists of a motor containing an unbalanced mass, which has been coupled with a system containing piezoelectric material that produces an electric current. Thus, the average power produced in the piezoelectric material subjected to the vibrations of the motor and the fractional dynamics of the system will be analyzed. For this analysis, the parameter of the fractional derivative operator and the parameter  $F$  for controlling the system are observed. Bifurcation diagrams and time–frequency analysis method based on synchrosqueezing transform are used, and the range of the fractional derivative operator parameter near 1, which modifies the dynamics of the system, is also determined.

**Keywords** Fractional calculus · Nonlinear dynamics · Synchrosqueezing transform

## 1 Introduction

With the technological advances in recent years, the great demand for energy consumption has allowed researchers to discover mechanisms that produce energy in a clean and renewable way. Thus, many works on these mechanisms have been explored. Examples of these works are those in [1–3] that explore high-degree-of-freedom mechanisms that convert mechanical energy from applied external forces into electrical energy.

Several works such as [3, 4] explore the dynamics of mechanisms for energy production. However, they propose control designs to suppress the chaotic motions.

---

M. Varanis (✉) · C. Oliveira

Faculdade de Engenharia, Universidade Federal da Grande Dourados, Dourados, MS, Brazil  
e-mail: [marcusvaranis@ufgd.edu.br](mailto:marcusvaranis@ufgd.edu.br)

M. A. Ribeiro · W. B. Lenz · A. M. Tusset · J. M. Balthazar

Universidade Tecnológica Federal Do Paraná-Campus Ponta Grossa, Ponta Grossa, Brazil

J. M. Balthazar

Faculty of Mechanical Engineering of Bauru, São Paulo State University, Bauru, SP, Brazil

Many fractional derivative operators are used to analyze the behavior of electromechanical structures, an example is the flexibility behavior of microbeams in MEMS systems. Examples of fractional derivative operators applied for dynamic analysis are Riemann–Liouville and Grunwald Letnikov [5, 6].

In recent years, new techniques for time–frequency analysis have been proposed, one emerging technique is the synchrosqueezed transform. Known limitations, such as tradeoffs between time and frequency resolution, can be overcome by alternative techniques that extract instantaneous modal components, as presented in the synchrosqueezed transform. EMD decomposition of a signal into components that are well separated in the time–frequency plane, allowing reconstruction of these components [7]. In particular the work presented in [8], provides an overview of time–frequency reassignment and synchronization techniques used in multicomponent signals, covering the theoretical background and applications, furthermore it tries to explain how synchrosqueezing can be seen as a special case of mode enable reassignment reconstruction. Methods based on synchrosqueezing transform are actually an extension of CWT that incorporates elements of empirical mode decomposition and frequency reassignment techniques. This new tool produces a better-defined time–frequency representation, allowing the identification of instantaneous frequencies to highlight individual components.

Synchrosqueezing Wavelet Transform (SWT) is a time–frequency analysis method [8]. The anti-noise capability and time–frequency resolution of SWT are improved based on the wavelet transform (CWT). SWT maintains the advantages of EMD and CWT. SWT is adaptive like EMD and does not depend on the original wavelet; the mode mixing problem is significantly improved. Classical time–frequency analysis methods have been widely used in nonlinear dynamics and chaos applications [5, 7, 9–12], currently a series of applications based on synchrosqueezing have been proposed [13–17].

Therefore, will be made a fractional dynamics analysis of the model proposed by [18, 19] considering Caputo’s fractional derivative operator. However, with a coupled piezoelectric in the system for the average power output and the exploration of the proposed fractional mathematical model numerically.

## 2 Mathematical Background

### 2.1 Mathematical Model

The mathematical model is based on the one proposed by [20] and the Fig. 1 shows the mechanism for application the Caputo Operator derivative.

The Eq (1) describe the motor movement and its vertical displacement of the mass, thus:

$$\ddot{x}(M + m) + c\dot{x} - md(\dot{\phi}\sin(\phi) + \dot{\phi}^2\cos(\phi)) + k_1x + k_2x^3$$

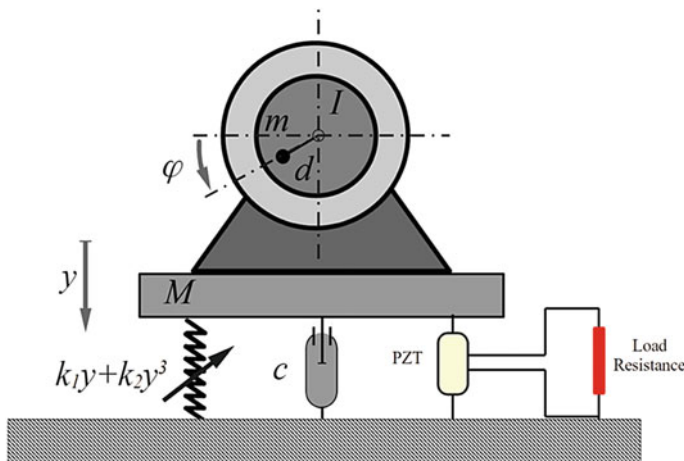


Fig. 1 Scheme of the structure with piezoceramic material coupled

$$\begin{aligned}
 & + \theta(1 + \theta_n|x|)q = (M + m)g \\
 & \ddot{\phi}(J + md^2) - md \ddot{x} \sin(\phi) + mgd \sin(\phi) = \Gamma(\dot{\phi})
 \end{aligned} \tag{1}$$

$$\rho \dot{q} - \theta(1 + \theta_n|y|)q + q = 0$$

where  $M$  mass is connected to a fixed basemet by a non-linear spring and a linear viscous damper (damping coefficient  $c$ ). The nonlinear spring stiffness is given by  $k_1x + k_2x^3$ , where  $x$  denotes the structure displacement with respect to some equilibrium position in the absolute reference frame. The motion of the structure is due to an in-board non-ideal motor driving an unbalanced rotor. Denoted by  $\phi$  the angular displacement of the rotor unbalance, and model it as a particle of mass  $m$  and radial distance  $d$  from the rotating axis. The moment of inertia of the rotating part is  $J$ . For the resonant case the structure has an influence on the motor input or output. The forcing function is dependent of the system it acts on, and the source is of non-ideal type. And  $q$  is electrical current and  $\theta$  is the linear and  $\theta_n$  the nonlinear part.

Considering the following change in variables:

$$\begin{aligned}
 p &= \frac{\omega}{\Omega}, \omega^2 = \frac{k_1}{M+m}, \gamma = \frac{k_3}{(M+m)\Omega^6}, \zeta = \frac{c}{(M+m)\Omega}, \mu = \frac{md\Omega^2}{(M+m)g}, \eta = \frac{gmd}{(I+md^2)\Omega^2}, \\
 F &= \frac{M_0}{(I+md^2)\Omega^2}, \Gamma(\dot{\phi}) = M_0\left(1 - \frac{\dot{\phi}}{\Omega}\right), x \rightarrow y = \frac{\Omega^2}{g}x \text{ and } t \rightarrow \tau = \Omega t.
 \end{aligned}$$

Therefore, we rewrite Eq. (1):

$$\begin{aligned}
 \ddot{y} + \zeta \dot{y} - p^2 y + \gamma y^3 &= 1 + \mu(\ddot{\phi} \sin(\phi) + \dot{\phi}^2 \cos(\phi)) - \theta(1 + \theta_n|y|)q \\
 \ddot{\phi} &= \eta \ddot{y} \sin(\phi) - \eta \sin(\phi) + F(1 - \dot{\phi})
 \end{aligned} \tag{2}$$



$$\dot{q} = \frac{1}{\rho}[\theta(1 + \theta_n|y|)q - q]$$

In this way, considering  $y = x_1$ ,  $\dot{y} = x_2$ ,  $\phi = x_3$ ,  $\dot{\phi} = x_4$  and  $q = x_5$ , the system of first order differential equations is obtained:

$$\begin{aligned} \dot{x}_1 &= x_2 \\ \dot{x}_2 &= \frac{1}{1 - \mu\eta\sin^2(y_3)}(-\zeta y_2 - p y_1 - \gamma y_1^3 + 1 + \mu \sin(y_3)) \\ &\quad (\mu y_4^2 \cos(y_3) - \eta \sin(y_3) + F(1 - y_4)) - \theta(1 + \theta_n|x_1|)x_5 \\ \dot{x}_3 &= x_4 \\ \dot{x}_4 &= \frac{\eta \sin(y_3)}{1 - \mu\eta\sin^2(y_3)}(-\zeta y_2 - p y_1 - \gamma y_1^3 + 1 + \mu y_4^2 \cos(y_3) \\ &\quad + \mu \sin(y_3)(-\eta \sin(y_3) + F(1 - y_4))) - \eta \sin(y_3) + F(1 - y_4) \\ \dot{x}_5 &= \frac{1}{\rho}[\theta(1 + \theta_n|x_1|)x_5 - x_5] \end{aligned} \quad (3)$$

The Caputo operator is defined as follows [11–18]:

$${}_a^C D^q f(t) = \frac{1}{\Gamma(q - n)} \int_a^t \frac{f^{(n)}(\tau) d\tau}{(t - \tau)^{q+1-n}} \quad (4)$$

where  $n - 1 < q < n$ , in our considerations  $n = 1$ , thus,  $0 < q < 1$  and  $\Gamma(\cdot)$  is defined as the gamma function. Therefore, rewrite the System of Differential Equations considering the Caputo operator for analyses:

$$\begin{aligned} {}_a^C D^q x_1 &= x_2 \\ {}_a^C D^q x_2 &= \frac{1}{1 - \mu\eta\sin^2(y_3)}(-\zeta y_2 - p y_1 - \gamma y_1^3 + 1 \\ &\quad + \mu \sin(y_3)(\mu y_4^2 \cos(y_3) - \eta \sin(y_3) + F(1 - y_4))) \\ &\quad - \theta(1 + \theta_n|x_1|)x_5 \\ {}_a^C D^q x_3 &= x_4 \\ {}_a^C D^q x_4 &= \frac{\eta \sin(y_3)}{1 - \mu\eta\sin^2(y_3)}(-\zeta y_2 - p y_1 - \gamma y_1^3 + 1 \\ &\quad + \mu y_4^2 \cos(y_3) + \mu \sin(y_3)(-\eta \sin(y_3) + F(1 - y_4))) \\ &\quad - \eta \sin(y_3) + F(1 - y_4) \\ {}_a^C D^q x_5 &= \frac{1}{\rho}[\theta(1 + \theta_n|x_1|)x_5 - x_5] \end{aligned} \quad (5)$$

## 2.2 Synchrosqueezed Transform

STFT and CWT are the main approaches to simultaneously decompose a signal into time and frequency components. Known limitations, such as tradeoffs between time and frequency resolution, can be overcome by alternative techniques that extract instantaneous modal components. EMD aims to decompose a signal into components that are well separated in the time–frequency plane, allowing reconstruction of these components. On the other hand, a recently proposed method called the synchrosqueezing transform (SST) is an extension of the wavelet transform that incorporates elements of empirical mode decomposition and frequency reassignment techniques. This new tool produces a well-defined time–frequency representation, allowing the identification of instantaneous frequencies in non-stationary signals to highlight individual components.

SST was initially proposed in the wavelet case [8] and then later extended to the STFT case [7, 8]. In fact, it corresponds to a nonlinear operator that bounces the time–frequency representation of a signal, combining the localization and scattering properties of the Reassignment Methods with the invertibility property of linear time–frequency representations.

## 2.3 Synchrosqueezing Wavelet Transform

The Synchrosqueezing Wavelet Transform calculation consists of three steps. The first step is to calculate the CWT. In the second step, a preliminary frequency  $\omega(a, b)$  is obtained from the oscillatory behavior of  $W_x(a, b)$  at  $a$ , so that:

$$\omega(a, b) = -i(W_x(a, b))^{-1} \frac{\partial}{\partial a} W_x(a, b) \tag{6}$$

In the third step the transformation from the time scale plane to the time–frequency plane is performed. Each value of  $W_x(a, b)$  is assigned again to  $(a, \omega)$ . Where  $\omega$  denotes the frequency that is closest to the preliminary frequency of the original (discrete) point  $\omega(a, b)$ . This operation is presented in Eq. (7):

$$T(a, \omega_1) = (\Delta\omega)^{-1} \sum_{b_k: |\omega(a, b_k) - \omega_1| \leq \Delta\omega/2} W_x(a, b_k) b_k^{-3/2} \Delta b \tag{7}$$

In Eq. (7)  $\Delta\omega$  denotes the width of each frequency  $b$  in  $\Delta\omega = \omega_{l+1} - \omega_l$  and equivalently for  $\Delta b$ . SWT can obtain a high-resolution time–frequency spectrum by compressing (reassigning) the CWT result. However, when the amplitude of the high-frequency components of a signal is low, it is difficult to identify the components in the CWT spectrum or the SST spectrum that is based on the CWT result. In contrast to CWT, the SWT transform is able to more efficiently display the high frequency, low amplitude components of a signal and perform a lossless inverse transformation.

Originally proposed in the wavelet case, the SST has been similarly extended to the STFT context, known as the Fourier-based synchrosqueezing transform (FSST). A long study and in-depth formulation on STFT, CWT and FSST can be seen in [21–24].

### 3 Numerical Results and Discussion

For the numerical analysis, using the following initial conditions  $x_0 = [0,0,0,0]$  and for analysis corresponds to  $q = [0.978- 1]$ . Thus, we analyzed the behavior of fractional dynamics for values close to 1, which we could observe some chaotic windows in the system. The parameters is:  $\eta = 0.05$ ,  $\mu = 8.737$ ,  $p = 1.0$ ,  $\gamma = 9.0$ ,  $\theta = 0.1$ ,  $\theta_n = 0.5$ ,  $\zeta = 0.2$ ,  $\theta = 0.1$  and  $\theta_n = 0.5$  [20].

The numerical method for solving the Eq. (5) is composed of the initial value problem and the variational system and Adams–Bashforth–Moulton scheme for fractional differential equations [20–24], with a  $h = 0.001$  and a time of  $10^5$  [s] considering 40% of total time with transient time. Utiliza-se métodos de análise tempo-frequência para caracterizar a dinâmica caótica do sistema, ente eles CWT e métodos baseados em synchrosqueezing transform, em especial, Fourier-based synchrosqueezing transform e synchrosqueezing wavelet transform [4, 9, 14].

Therefore, Fig. 2 shows the behavior of the bifurcation diagrams of the systems, and considering  $F = [23., 46.6, 70]$ , we can observe the emergence of chaotic windows with the variation of the parameter of the fractional derivative.

Figure 2a observes the chaotic windows at  $q = [0.9790:0.9793]$ ,  $[0.9816, 0.9822]$ ,  $[0.9871, 0.9873]$ ,  $[0.9887, 0.9936]$  and  $q = [0.995; 1.0]$  with parameter  $F = 23.3$ . According to [9] for  $F = 23.3$  and  $q = 1$ , which results in the conventional derivative operator, so the system exhibits chaotic regime. This happens for  $q = 1$  at  $F = 46.6$  and 70 has a chaotic behavior which corroborates the data collected by [9], where for systems with the entire derivative operator the system is in a chaotic regime. In Fig. 2b with  $F = 46.6$  has the following chaotic windows  $q = [0.978, 0.9783]$ ,  $q = [0.9875, 0.9876]$ ,  $q = [0.9937, 0.9941]$ ,  $q = [0.9946, 0.9952]$  and  $q = [0.9976;1]$  and in Fig. 2c  $q = [0.978; 0.9737]$ ,  $q = [0.9871; 0.9875]$ ,  $q = [0.9919; 0.992]$ ,  $q = [0.9921; 0.9928]$ ,  $q = [0.9942; 0.996]$  and  $q = [0.9983; 1]$ . In Fig. 2c with  $F = 70$  has the following chaotic windows  $q = [0.978, 0.9783]$ ,  $q = [0.9875, 0.9876]$ ,  $q = [0.9937, 0.9941]$ ,  $q = [0.9946, 0.9952]$  and  $q = [0.9976;1]$  and in Fig. 3c  $q = [0.978; 0.9737]$ ,  $q = [0.9871; 0.9875]$ ,  $q = [0.9919; 0.992]$ ,  $q = [0.9921; 0.9928]$ ,  $q = [0.9942; 0.996]$  and  $q = [0.9983; 1]$ . Thus, through the bifurcation diagrams we can observe the correspondence of the intervals in which the chaotic behavior of the subintervals contained in the interval  $q = [0.978, 1.0]$ .

Next in Fig. 3 is presented the time–frequency analysis of the system for  $F = 23$  and  $q = 0.98$ . In Fig. 3a the phase diagram is presented. Already in Fig. 3b is presented the response of the system in the frequency domain to CWT and it is possible to identify the periodicity of the system, as well as to identify the dominant frequency and the multiple frequencies, typical of systems with cubic nonlinearity,

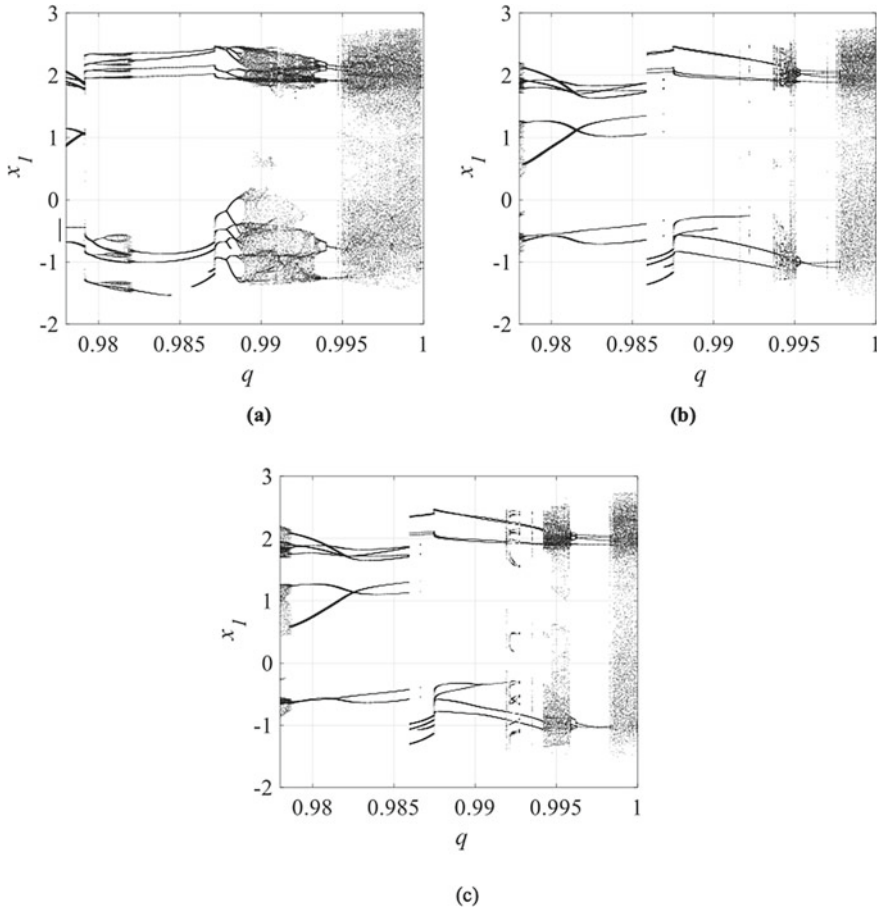


Fig. 2 Bifurcation diagram for  $q = [0.978, 1.0]$ : **a**  $F = 23.3$ , **b**  $F = 46.6$  and **c**  $F = 70$

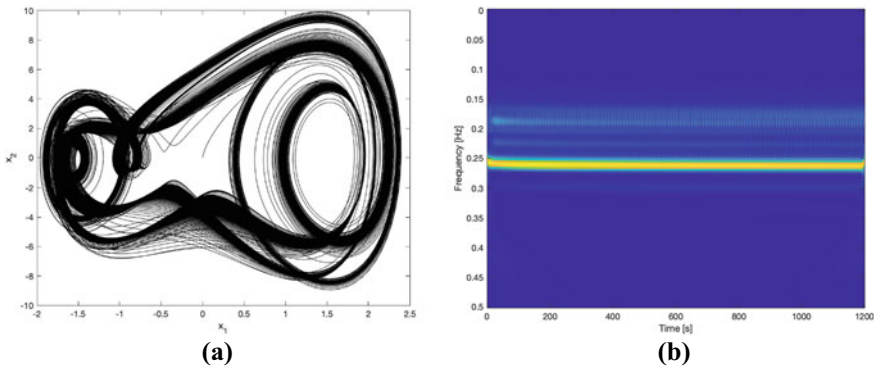


Fig. 3  $F = 23$ ,  $q = 0.98$ : **a** Phase diagram, **b** CWT

but there is still an energy dispersion in the time–frequency plane, which does not make the analysis suitable for application. Meyer’s wavelet [4] was used in the CWT analysis.

In Fig. 4 the time–frequency analysis of the system ( $F = 23$  and  $q = 0.98$ ) using synchrosqueezing transform based methods is presented. In Fig. 4a the system response is analyzed using the Fourier-based synchrosqueezing transform (FSST), it is possible to characterize the periodicity of the system, as well as identify the dominant frequency and the multiple frequencies, but the method presents low resolution in the time–frequency plane. In Fig. 4b is presented the system response in the frequency domain using SWT, in this case it is possible, quite clearly, to identify the periodicity of the system, as well as to identify the dominant frequency and the multiple frequencies and notice that the energy dispersion in the time–frequency plane is very small.

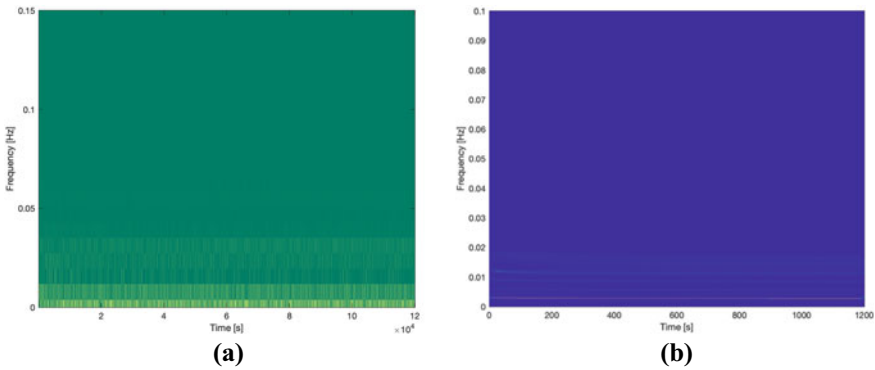


Fig. 4  $F = 23, q = 0,98$ : a S-SFT, b SWT

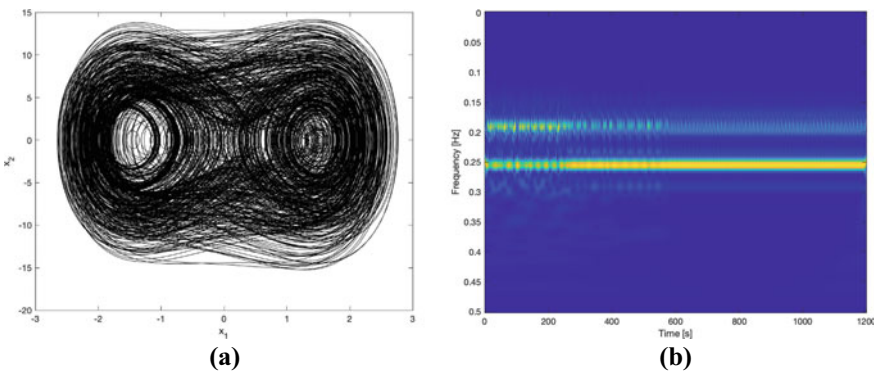
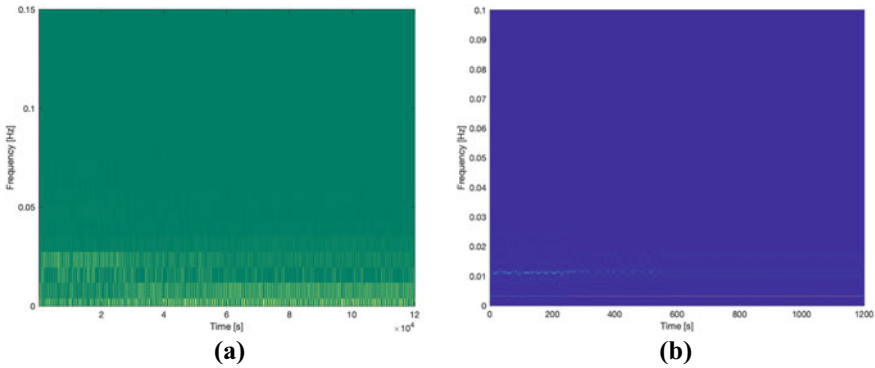


Fig. 5  $F = 23, q = 1$ : a Phase diagram, b CWT



**Fig. 6**  $F = 23, q = 1$ : **a** S-SFT, **b** SWT

In Fig. 5 is presented the time–frequency analysis of the system for  $F = 23$  and  $q = 1$ , for these parameters the system exhibits chaotic dynamics, as shown in the bifurcation diagram (Fig. 2a). In Fig. 5a the phase diagram of the system is presented. In Fig. 5b the response of the system in the frequency domain to CWT is presented, it is still possible to identify the dominant frequency, but the response presents a large scattering and abrupt change in the frequency spectrum, typical characteristic of chaotic systems [4, 14].

Figure 6 presents the time–frequency analysis of the system ( $F = 23$  and  $q = 1$ ) using synchrosqueezing transform based methods. The system response is analyzed using FSST (Fig. 6a), it is noted that there was large scattering and abrupt change in the frequency spectrum, but due to low resolution and large energy dispersion in the time–frequency plane, it is not possible to characterize the chaotic dynamics of the system. In Fig. 6b is presented the response of the system in the frequency domain using SWT, in this case it is possible to identify the dominant frequency and the response presents a large scattering and abrupt change in the frequency spectrum, but the energy dispersion in the time–frequency plane is very small, which makes the technique quite accurate and appropriate.

Next in Fig. 7 is presented the time–frequency analysis of the system for  $F = 46.6$  and  $q = 0.985$ . Again, the phase space is presented (Fig. 7a) and the CWT response of the system in the frequency domain (Fig. 7b). The response via CWT allows the periodicity of the system to be identified, as well as easily identifying the dominant frequency and multiple frequencies.

In Fig. 8 the time–frequency analysis of the system ( $F = 46.6$  and  $q = 0.985$ ) using synchrosqueezing transform based methods is presented. The response of the system using FSST is presented in Fig. 8a, the large energy dispersion and low resolution in the time–frequency plane do not allow to characterize the periodicity of the system, also the dominant frequency and multiple frequencies cannot be identified with the necessary clarity. In Fig. 8b the response of the system ( $F = 23$  and  $q = 0.98$ ) in the frequency domain using SWT is presented, in this case it is possible to identify the periodicity of the system, as well as to identify the dominant frequency and the multiple frequencies.

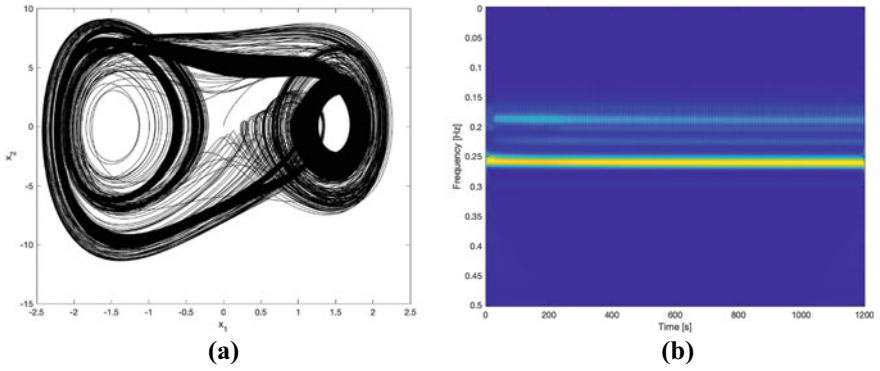


Fig. 7  $F = 46.6, q = 0.985$ : a Phase diagram, b CWT

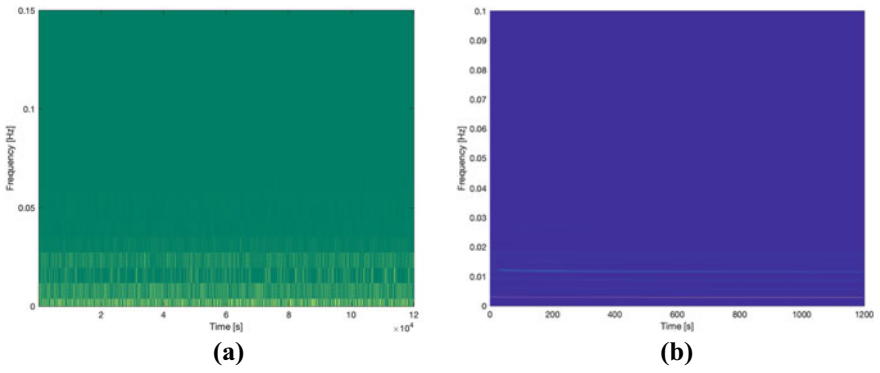


Fig. 8  $F = 46.6, q = 0.985$ : a S-SFT, b SWT

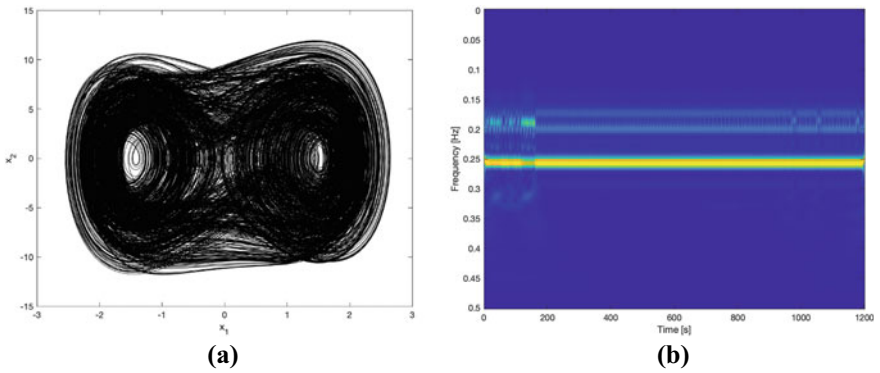
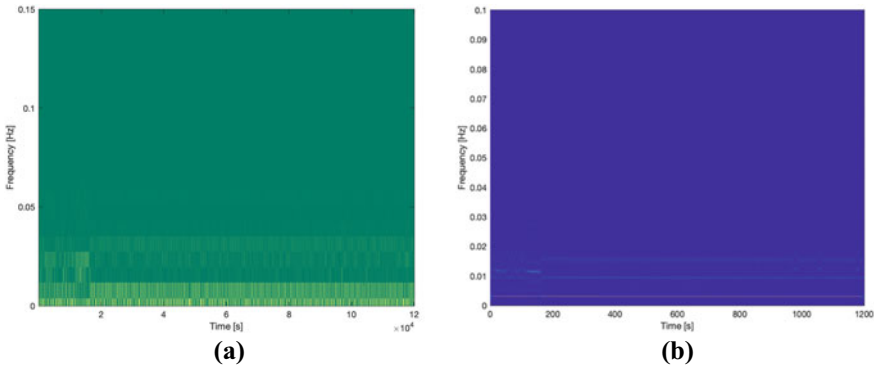


Fig. 9  $F = 46.6, q = 1$ : a Phase diagram, b CWT



**Fig. 10**  $F = 46,6, q = 0,995$ : **a** FSST, **b** SWT

Figure 9 presents the time–frequency analysis of the system for  $F = 46.6$  and  $q = 1$ , for these parameters the system exhibits chaotic dynamics as presented in the bifurcation diagram (Fig. 2b). In Fig. 9a the phase diagram of the system is presented. In Fig. 9b is presented the response of the system in the frequency domain to CWT, one can clearly identify the dominant frequency, but the response presents a large scattering and abrupt change at the beginning of the frequency spectrum, indicating chaos in the system.

In Fig. 10a the response of the system using FSST is presented, it can be seen that there was a large scattering and abrupt change in the frequency spectrum, but due to low resolution and large energy dispersion in the time–frequency plane, it is not possible to clearly characterize the chaotic dynamics of the system. The SWT analysis (Fig. 10b) shows that it is possible to identify the dominant frequency and a large scattering and abrupt change in the frequency spectrum at the beginning of the response, again the low energy dispersion allows the characterization of the chaotic dynamics of the system.

Next in Fig. 11 is presented the time–frequency analysis of the system for  $F = 70$  and  $q = 0.995$ . Again, the phase space is presented (Fig. 11a) and the system response in the frequency domain to CWT (Fig. 11b). The response via CWT allows, as in the previous cases, the periodicity of the system to be identified, as well as easily identifying the dominant frequency and multiple frequencies. The same occurs with analysis via FSST (Fig. 12c) and SWT (Fig. 12d).

Finally, Fig. 13 presents the time–frequency analysis of the system for  $F = 70$  and  $q = 0.999$ . The phase space (Fig. 13a) shows the rich dynamics of the system and the response of the system in the frequency domain to CWT (Fig. 13b) characterizing the chaotic dynamics in the system. In (Fig. 14a) shows the response of the system with the use of FSST, it is noted that there was large scattering and abrupt change in the frequency spectrum, as in previous cases, it is not possible to clearly characterize the chaotic dynamics of the system. The analysis using SWT (Fig. 14b), shows that it is possible to identify the dominant frequency and a large scattering and abrupt change in the frequency spectrum, in order to characterize the chaotic dynamics of the system.



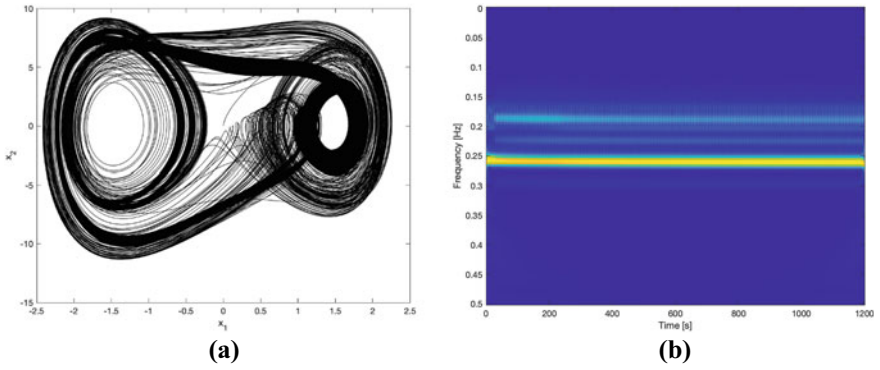


Fig. 11  $F = 70$ ,  $q = 0.995$ : **a** Phase diagram, **b** STFT

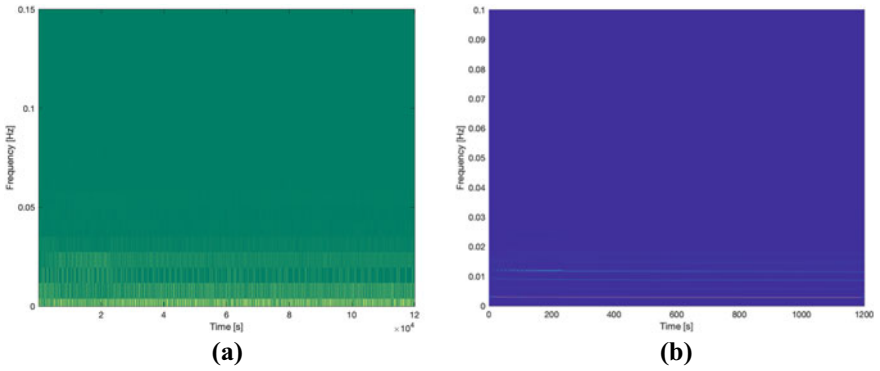


Fig. 12  $F = 70$ ,  $q = 0.985$ : **a** S-SFT, **b** SWT

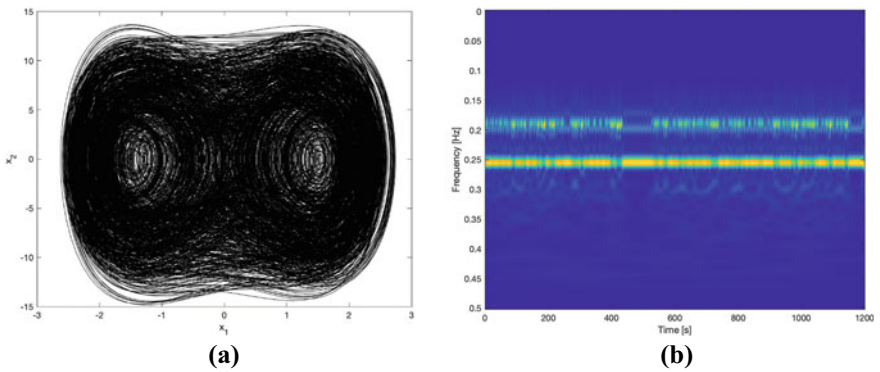
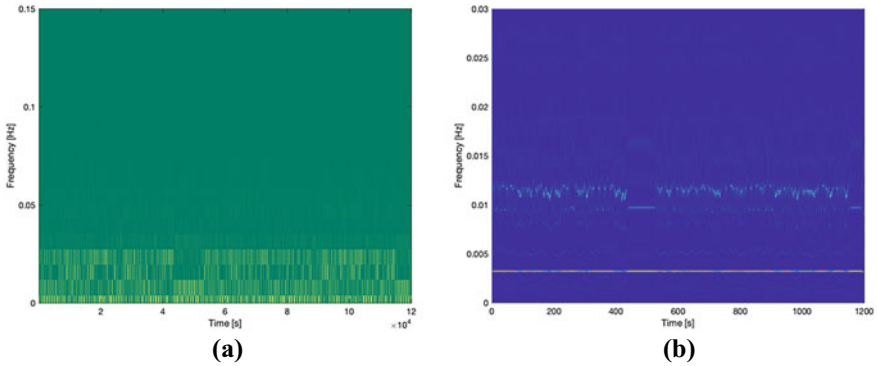


Fig. 13  $F = 70$ ,  $q = 0.999$ : **a** Phase diagram, **b** CWT



**Fig. 14**  $F = 70, q = 0,999$ : **a** S-SFT, **b** SWT

### 4 Conclusion

The fractional model for energy harvesting presented in the interval  $q = [0.958, 1]$  a chaotic behavior for the structure with Caputo’s fractional derivative operator. Thus, bifurcation diagrams and synchrosqueezing-based transform were used to analyze the location of these windows, for a set of  $F$  parameters and characterize the chaotic dynamics of the system. Therefore, it was determined for values close to  $q = 1$ , regions that exhibited chaotic and periodic behavior. These regions are confirmed in the bifurcation diagrams, CWT and SWT. The analysis of the fractional dynamics of the system not only corroborates the generalization of the mathematical model in a numerical form, but also in the behavior with the Caputo fractional derivative operator. CWT-based techniques show good resolution in the time–frequency plane, but CWT still overshadows other components when there are high concentrations of energy at some signal frequency. Applications of wavelet transform-based techniques to nonlinear systems have demonstrated the ability of this technique to monitor signal frequency variations and detect short-term transients with excellent time–frequency localization, far exceeding the limitations presented by Fourier transform-based techniques such as STFT.

Finally, the results obtained using the synchrosqueezed wavelet transform were excellent, showing very good time–frequency resolution and minimal energy dispersion, proving adequate to characterize the chaotic dynamics of the system.

## References

1. Ribeiro, M. A., Balthazar, J. M., Lenz, W. B., Rocha, R. T., Tusset, A. M.: Numerical exploratory analysis of dynamics and control of an atomic force microscopy in tapping mode with fractional order. *Shock and Vib.* 2020 (2020)
2. Tusset, A. M., Balthazar, J. M., Ribeiro, M. A., Lenz, W. B., Rocha, R. T.: Chaos control of an atomic force microscopy model in fractional-order. *Eur Phys J Spec Top* 1–12 (2021)
3. Tusset, A.M., Ribeiro, M.A., Lenz, W.B., Rocha, R.T., Balthazar, J.M.: Time delayed feedback control applied in an atomic force microscopy (AFM) model in fractional-order. *J. Vib. Eng. Technol.* **8**(2), 327–335 (2020)
4. Varanis, M. V., Tusset, A. M., Balthazar, J. M., Litak, G., Oliveira, C., Rocha, R. T., Piccirillo, V.: Dynamics and control of periodic and non-periodic behavior of Duffing vibrating system with fractional damping and excited by a non-ideal motor. *J. Frankl. Inst.* **357**(4), 2067–2082 (2020)
5. Iliuk, I., Balthazar, J.M., Tusset, A.M., Piqueira, J.R.C., de Pontes, B.R., Felix, J.L.P., et al.: A non-ideal portal frame energy harvester controlled using a pendulum. *Eur. Phys. J. Spec. Top.* **222**, 1575–1586 (2013)
6. Iliuk, I., Balthazar, J.M., Tusset, A.M., Piqueira, J.R., de Pontes, B.R., Felix, J.L., et al.: A non-ideal portal frame energy harvester controlled using a pendulum. *Eur. Phys. J. Spec. Top.* **222**(7), 1575–1586 (2013)
7. Varanis, M., Silva, A. L., Balthazar, J. M., Pederiva, R.: A tutorial review on time-frequency analysis of non-stationary vibration signals with nonlinear dynamics applications. *Braz. J. Phys.* 1–19 (2021)
8. Daubechies, I., Lu, J., Wu, H.T.: Synchrosqueezed wavelet transforms: an empirical mode decomposition-like tool. *Appl. Comput. Harmon. Anal.* **30**(2), 243–261 (2011)
9. Varanis, M., Balthazar, J.M., Silva, A., Mereles, A.G., Pederiva, R.: Remarks on the sommerfeld effect characterization in the wavelet domain. *J. Vib. Control* **25**(1), 98–108 (2019)
10. Li, Y., Sun, R., Yin, K., Xu, Y., Chai, B., Xiao, L.: Forecasting of landslide displacements using a chaos theory based wavelet analysis-Volterra filter model. *Sci. Rep.* **9**(1), 1–19 (2019)
11. Mao, J., Zhang, X., Li, J.: Wind power forecasting based on chaos and wavelet packet theory. In 2018 13th IEEE Conference on Industrial Electronics and Applications (ICIEA) (pp. 1604–1608). IEEE (2018)
12. Cattani, C.: A review on harmonic wavelets and their fractional extension. *J. Adv. Eng. Comput* **2**(4), 224–238 (2018)
13. Hu, J., Liu, B., Yu, M.: A novel method of realizing stochastic chaotic secure communication by synchrosqueezed wavelet transform: the finite-time case. *IEEE Access* (2021)
14. Varanis, M., Norenberg, J.P.C., Rocha, R.T., Oliveira, C., Balthazar, J.M., Tusset, A.M.: A comparison of time-frequency methods for nonlinear dynamics and chaos analysis in an energy harvesting model. *Braz. J. Phys.* **50**(3), 235–244 (2020)
15. He, K., Li, Q., Yang, Q.: Characteristic analysis of welding crack acoustic emission signals using synchrosqueezed wavelet transform. *J. Test. Eval.* **46**(6), 2679–2691 (2018)
16. Hasan, F.S.: Chaotic signals denoising using empirical mode decomposition inspired by multivariate denoising. *Int. J. Electr. Comput. Eng.* **10**, 1352–1358 (2020)
17. Alugongo, A. A. (2021). Experimental study of the impact of the fluid forces on disturbances induced by the rotor-stator rubbing (Part II). In 2021 IEEE 12th International Conference on Mechanical and Intelligent Manufacturing Technologies (ICMIMT), pp. 133–138. IEEE (2021)
18. Iliuk, I., Brasil, R.M.L.R.F., Balthazar, J.M., Tusset, A.M., Piccirillo, V., Piqueira, J.R.C.: Potential application in energy harvesting of intermodal energy exchange in a frame: FEM analysis. *Int. J. Struct. Stab. Dyn.* **14**(8), 1440027 (2014)
19. Iliuk, I., Balthazar, J.M., Tusset, A.M., Piqueira, J.R., de Pontes, B.R., Felix, J.L., et al.: Application of passive control to energy harvester efficiency using a nonideal portal frame structural support system. *J. Intell. Mater. Syst. Struct.* **25**(4), 417–429 (2014)

20. Gonçalves, A., Ribeiro, M. A., Gunha, J. V., Somer, A., Zanuto, V. S., Astrath, N. G., Novatski, A.: A generalized Drude–Lorentz model for refractive index behavior of tellurite glasses. *J. Mater. Sci. Mater. Electron.* **30**(18), 16949–16955 (2019)
21. Flandrin, P., Auger, F., Chassande-Mottin, E. (2018). Time-frequency reassignment: from principles to algorithms. In *Applications in time-frequency signal processing*, pp. 179–204. CRC Press
22. Flandrin, P.: *Explorations in Time-Frequency Analysis*. Cambridge University Press (2018)
23. Fourer, D., Auger, F., Czarnecki, K., Meignen, S., Flandrin, P.: Chirp rate and instantaneous frequency estimation: application to recursive vertical synchrosqueezing. *IEEE Signal Process. Lett.* **24**(11), 1724–1728 (2017)
24. Addison, P.S.: *The illustrated wavelet transform handbook: introductory theory and applications in science, engineering, medicine and finance*. CRC Press (2017)

# On the Stability and Long-Term Behaviour of Structural Systems Excited by Nonideal Power Sources



Javier González-Carbajal , Daniel García-Vallejo ,  
and Jaime Domínguez 

**Abstract** This chapter investigates the problem of an unbalanced motor attached to a fixed frame by means of a nonlinear spring and a linear damper. The proposed mathematical model is simple enough to allow for an analytical treatment of the equations, while sufficiently complex to preserve the main nonlinear phenomena that can be observed in real unbalanced rotating machinery. The primary focus is on the bidirectional interaction that in general exists between the excitation provided by the motor and the response of the vibrating structure. By combining various mathematical tools (Averaging, Singular Perturbation Theory, classification of Hopf bifurcations, Poincaré-Bendixson Theorem), the long-term behaviour of the system is investigated in detail. The analytical results are verified numerically. It should be noted that the study presented in this Chapter was originally published in [1, 2].

**Keywords** Nonideal excitation · Stability · Bifurcation analysis · Limit cycles · Unbalanced motors

## 1 Introduction

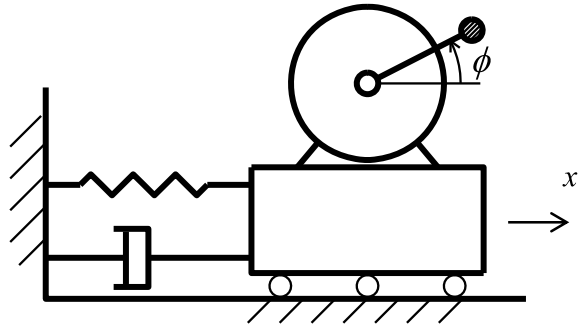
The motion of unbalanced rotors constitutes one of the most common vibration sources in mechanical engineering [3, 4]. Vibrations due to unbalance may occur in any kind of rotating systems, such as turbines, flywheels, blowers or fans [5]. Actually, in practice, rotors can never be completely balanced because of manufacturing errors such as porosity in casting, non-uniform density of the material, manufacturing tolerances, etc. [6]. Even a subsequent balancing process will never be perfect due to the tolerances of the balancing machines.

Usually, rotor unbalance has a harmful effect on rotating machinery, since vibration may damage critical parts of the machine, such as bearings, seals, gears and couplings [6]. However, there are applications where unbalanced rotors are used to generate a desired vibration. Some examples are the feeding, conveying and screening

---

J. González-Carbajal (✉) · D. García-Vallejo · J. Domínguez  
Faculty of Engineering of Seville, Department of Mechanical Engineering and Manufacturing,  
C/ Camino de los Descubrimientos S/N, 41092 Seville, Spain  
e-mail: [jgcarbajal@us.es](mailto:jgcarbajal@us.es)

**Fig. 1** Simple 2-DOF model of a structure excited by an unbalanced motor



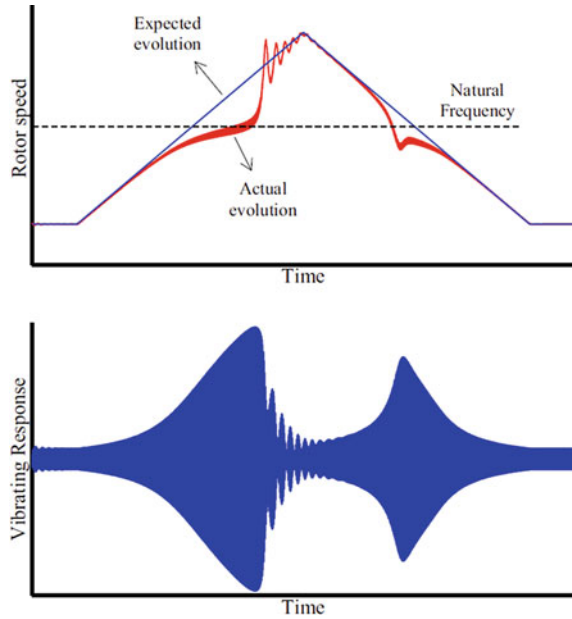
of bulk materials, or the vibrocompaction of quartz agglomerates, which makes use of unbalanced motors to compact a quartz-resin mixture. Actually, our interest in this vibrocompaction process has been the motivation for the presented study.

A simple model to analyse the dynamic response of a structure to the excitation produced by an unbalanced motor is sketched in Fig. 1. The simplest approach to this problem consists in assuming the rotor speed to be either constant or a prescribed function of time. In the constant speed case, the centrifugal force on the unbalance produces a harmonic excitation on the vibrating system, whose amplitude grows with the square of the rotating speed and whose frequency coincides with the rotating speed [5, 7].

Note that, with this approach, it is implicitly being assumed that the rotational motion of the motor is independent of the vibration of the structure. This property is what defines an ideal excitation: it remains unaffected by the vibrating system response. Thus, the amplitude and frequency of an ideal excitation are known a priori, before solving the vibration problem. Obviously, this notion of ideality is applicable to any kind of excitation, and not only to the one produced by an unbalanced motor.

The ideality assumption is valid, with good approximation, in many real problems. However, there are situations where it is not. In 1904, Sommerfeld [8], whose pioneering work inspired many subsequent investigations, found experimentally kinds of behaviour that could not be explained upon the ideality hypothesis. He mounted an unbalanced electric motor on an elastically supported table and monitored the input power as well as the frequency and amplitude of the response [9]. The experiment consisted in increasing continuously the power input in order to make the rotor speed pass through the resonance frequency of the table, and then conduct the inverse process by decreasing the input power. The results obtained by Sommerfeld are qualitatively depicted in Fig. 2. When the rotor speed was close to resonance, an increment of the input power produced only a very slight increase of the rotor speed, while the oscillation amplitude increased considerably. This means that, in this part of the experiment, the increasing input power was not making the motor rotate faster, but was giving rise to larger oscillations. With further increasing of the input power, the rotor speed jumped abruptly to a frequency above resonance and, at the same time, the vibration amplitude jumped to a much smaller quantity than measured in the resonance region. When the process was reversed, by decreasing the motor input

**Fig. 2** Sommerfeld effect



power, a jump phenomenon in the resonance region was also observed (see Fig. 2). However, this jump was found to be different from the one occurring for increasing rotor speed. This anomalous behaviour is usually referred to as ‘The Sommerfeld Effect’.

In 1969 [10], Kononenko published a book entirely devoted to the study of nonideal excitations. He considered different configurations of vibrating systems excited by nonideal motors and applied the Averaging Method to the equations of motion. By taking into account the two-way interaction between the motor and the vibrating structure, he was able to explain the nonlinear phenomena found by Sommerfeld. According to Kononenko, the Sommerfeld effect is produced by the torque on the rotor due to vibration of the unbalanced mass.

Rand et al. [11] reported the detrimental effect of a nonideal energy source in dual spin spacecrafts, which could endanger a particular manoeuvre of the spacecraft once placed in orbit.

Although most studies use averaging procedures to obtain approximate solutions to the equations of motion, Blekhman [12] proposed an alternative approach, based on the method of ‘Direct Separation of Motions’.

Several authors, like El-Badawi [13] and Bolla et al. [14], analysed models where the vibrating system included an intrinsic cubic nonlinearity, in addition to the nonlinearity associated to the nonideal coupling between exciter and structure.

Balthazar et al. [15] published an extensive exposition of the state of the art concerning nonideal excitations.

The contents of this chapter are organized as follows. The analytical developments needed to understand the long-term behaviour of the system are presented in Sect. 2. Section 3 contains the results of a number of significant simulations with a twofold purpose: investigate some bifurcations of limit cycles that are too complex for an analytical treatment and serve as a numerical validation of the analytical procedures of Sect. 2. Finally, Sect. 4 presents the major conclusions of the study.

## 2 Analytical Approach

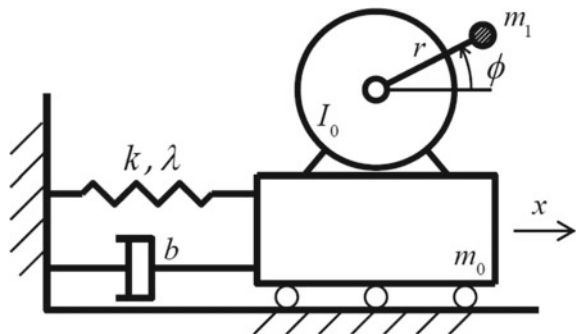
In this section, several analytical techniques are used to investigate the dynamics of a 2-DOF system consisting in an unbalanced motor attached to the fixed frame by a nonlinear spring and a linear damper.

### 2.1 Problem Statement and Assumptions

Consider the system depicted in Fig. 3. It consists in an unbalanced motor attached to a fixed frame by a nonlinear spring—whose force has linear and cubic components—and a linear damper. The cubic component of the spring gives the possibility to model a nonlinear behaviour for the structure supporting the motor [16]. The effect of gravity can be shown to have no relevance [17] and, therefore, it will not be included in the model.

Variable  $x$  stands for the linear motion,  $\phi$  is the angle of the rotor,  $m_1$  is the unbalanced mass with eccentricity  $r$ ,  $m_0$  is the rest of the vibrating mass,  $I_0$  is the rotor inertia (without including the unbalance),  $b$  is the viscous damping coefficient and  $k$  and  $\lambda$  are, respectively, the linear and cubic coefficients of the spring. The equations of motion for the coupled 2-DOF system are [13]

Fig. 3 Model





$$\begin{aligned} m\ddot{x} + b\dot{x} + kx + \lambda x^3 &= m_1 r (\dot{\phi}^2 \cos \phi + \ddot{\phi} \sin \phi) \\ I\ddot{\phi} &= L_m(\dot{\phi}) + m_1 r \ddot{x} \sin \phi, \end{aligned} \quad (1)$$

where  $m = m_0 + m_1$ ,  $I = I_0 + m_1 r^2$  and an overdot represents differentiation with respect to time,  $t$ .

Function  $L_m(\dot{\phi})$  is the driving torque produced by the motor—given by its torque-speed curve, also known as static characteristic—minus the losses torque due to friction at the bearings, windage, etc. We assume this net torque to be a linear function of the rotor speed:

$$L_m(\dot{\phi}) = A + D\dot{\phi}. \quad (2)$$

Although  $L_m(\dot{\phi})$  includes the damping of rotational motion, we will usually refer to it shortly as ‘the motor characteristic’.

As will be seen later, it is convenient for the purpose of this chapter to write the driving torque in an alternative way. Then, denoting by  $\omega_n$  the linear natural frequency of the oscillator, given by  $\omega_n = \sqrt{k/m}$ , the motor torque can be written as

$$L_m(\dot{\phi}) = C + D(\dot{\phi} - \omega_n), \quad (3)$$

where  $C$  represents the driving torque at resonance ( $L_m(\omega_n) = C$ ). From Eqs. (2) and (3), the relation between constants  $A$  and  $C$  can be directly deduced:

$$C = A + D\omega_n. \quad (4)$$

Along the whole chapter, the motor characteristic will be written as (3) or (4), depending on the situation. It should be kept in mind that these two expressions are totally equivalent. The important point is that the driving torque is assumed to follow a linear relation with the rotor speed. It is further assumed that  $D < 0$ —the driving torque decreases with the rotor speed—, as is usual for most kinds of motor. This assumption will prove to be of major importance.

As an example, the static characteristic of an induction motor is depicted in Fig. 4. Note that such a motor is usually designed to work on the region  $\dot{\phi} > \omega_{peak}$ , where the curve could be reasonably approximated by a straight line with negative slope. The simplified motor characteristic given at (3) is represented in Fig. 5.

In the second of Eq. (1), which imposes the equilibrium of the rotor, the last term is of great significance, since it accounts for the torque on the rotor caused by linear motion of the system. Its physical interpretation can be readily understood with the aid of Fig. 6. Due to displacement  $x(t)$ , a horizontal inertial force acts on the unbalanced mass and generates a torque with respect to the rotor axis. This particular term of the equations of motion is what makes the excitation nonideal, for it takes into account how vibration influences rotation. If this torque due to vibration did

**Fig. 4** Typical static characteristic for an asynchronous motor

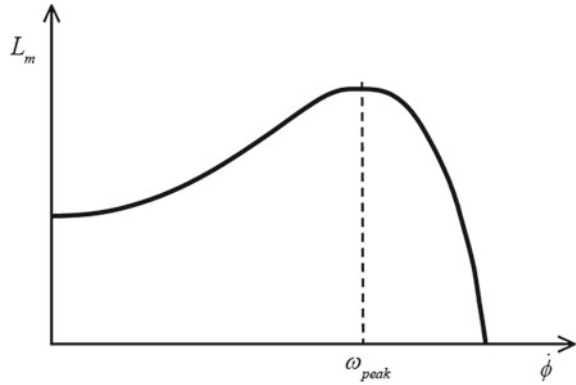


**Fig. 5** Static characteristic corresponding to Eq. (3)

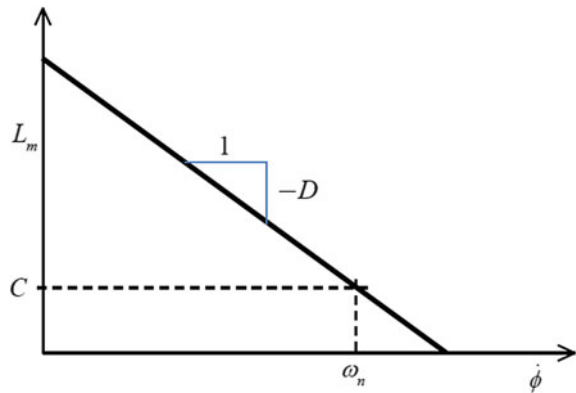
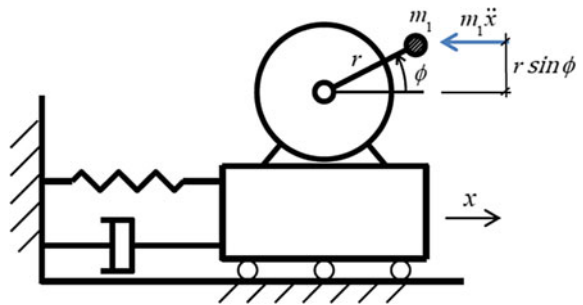


**Fig. 6** Torque on the rotor due to vibration



not exist –or if it was negligible–, the rotor equilibrium equation would reduce to  $I\ddot{\phi} = L_m(\dot{\phi})$ , and it could be solved for  $\phi(t)$  regardless of the linear motion. Then, this solution  $\phi(t)$  could be introduced in the first of Eq. (1) as a prescribed excitation.

By defining

$$\begin{aligned} R_m &= m_1/m, & R_I &= m_1 r^2/I, & \xi &= \frac{b}{2\sqrt{km}}, & \alpha &= \frac{R_I R_m}{2\xi} \\ c &= \frac{C}{I\omega_n^2}, & d &= \frac{D}{I\omega_n}, & \tau &= \omega_n t, & u &= \frac{x}{r} \frac{2\xi}{R_m}, & \rho &= \frac{\lambda r^2}{k} \left( \frac{R_m}{2\xi} \right)^2, \end{aligned} \quad (5)$$

the equations of motion can be written in a more convenient dimensionless form

$$\begin{aligned} \ddot{u} + u &= -2\xi\dot{u} - \rho u^3 + 2\xi(\dot{\phi}^2 \cos \phi + \ddot{\phi} \sin \phi) \\ \ddot{\phi} &= c + d(\dot{\phi} - 1) + \alpha \ddot{u} \sin \phi, \end{aligned} \quad (6)$$

where a dot now represents differentiation with respect to dimensionless time,  $\tau$ .

In order to apply perturbation techniques to system (6), some assumptions on the order of magnitude of the system parameters have to be made. Thus, we assume the damping, the unbalance and the nonlinearity to be small. This is expressed by making the corresponding coefficients proportional to a sufficiently small, positive and dimensionless parameter  $\epsilon$ :

$$\xi = \epsilon \xi_0, \quad \alpha = \epsilon \alpha_0, \quad \rho = \epsilon \rho_0, \quad (7)$$

where parameters with subscript '0' are  $\epsilon$ -independent. It is also assumed that the torque generated by the motor at resonance ( $\dot{\phi} = 1$ ) is sufficiently small:

$$c = \epsilon c_0 \quad (8)$$

Finally, the slope of the motor characteristic is assumed to be of the order of unity, i.e. independent of  $\epsilon$ :

$$d = d_0 \quad (9)$$

This last statement deserves some attention. Two possible assumptions with respect to the order of magnitude of parameter  $d$  are particularly relevant:  $d = d_0$  (*large slope* of the motor characteristic) and  $d = \epsilon d_0$  (*small slope* of the motor characteristic). It will be seen in Sect. 2.4 that the particular choice made in this chapter (*large slope*) implies that the slope of the motor torque curve is comparable to the slope of the curve representing the torque on the rotor due to vibration. On the other hand, the assumption of *small slope* of the motor characteristic corresponds to a situation where the motor torque is nearly constant around the resonance region of the system. Both the required mathematical approach and the dynamics exhibited by the system are very different depending on whether the slope of the motor characteristic is large or small. References [18, 19] are examples of investigations based on the assumption of *small slope* of the motor characteristic, while [9, 10, 12, 14, 17] correspond to the assumption of *large slope*.

Taking the proposed scaling (7)–(9) into account and dropping the subscript ‘0’ for convenience, system (1) takes the form

$$\begin{aligned} \ddot{u} + u &= \epsilon[-2\xi\dot{u} - \rho u^3 + 2\xi(\dot{\phi}^2 \cos \phi + \ddot{\phi} \sin \phi)] \\ \dot{\phi} &= d(\dot{\phi} - 1) + \epsilon[c + \alpha\ddot{u} \sin \phi]. \end{aligned} \quad (10)$$

## 2.2 First Order Averaging

Before turning to the treatment of (10), a specific averaging technique is developed in this section. The reader might wonder why there is a need to develop any new averaging procedures, instead of relying on the well-established averaging theorems for dynamical systems that can be found, for example, in [18]. The reason is that averaging theorems are usually valid for systems where the state variables can be split-up into two groups: a set of slow variables and one or more fast rotating phases over which the averaging is performed. It will be seen in Sect. 2.3 that the system under study does not take this form, but has one additional non-angular fast variable that makes conventional averaging theorems not applicable.

In order to make the procedure as general as possible, consider a system of the form

$$\left\{ \begin{array}{l} \dot{\mathbf{x}} = \epsilon[\mathbf{A}\mathbf{y} + \mathbf{X}(\mathbf{x}, \phi)] + O(\epsilon^2) \\ \dot{\mathbf{y}} = \mathbf{B}\mathbf{y} + \mathbf{Y}(\mathbf{x}, \phi) + O(\epsilon) \\ \dot{\phi} = \Omega + O(\epsilon) \end{array} \right\}, \quad \begin{array}{l} \mathbf{x} \in D \subset \mathbb{R}^n \\ \mathbf{y} \in R \subset \mathbb{R}^m \\ \phi \in S^1, \end{array} \quad (11)$$

where  $\mathbf{A}$  and  $\mathbf{B}$  are matrices of constant coefficients and  $\Omega$  is a scalar constant, bounded away from zero. It will be shown in the next section that system (10) can be written in the form (11).

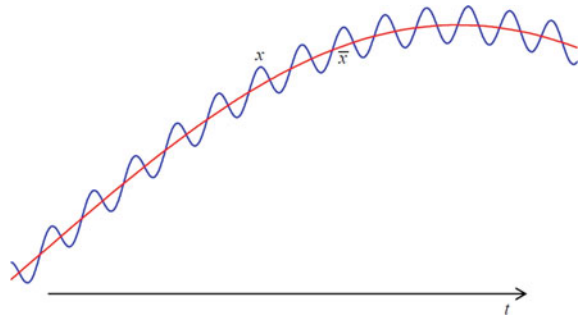
First, we define the averaged variables as

$$\bar{\mathbf{x}}(t) \equiv \frac{1}{T} \int_{t-T/2}^{t+T/2} \mathbf{x}(s) ds, \quad \bar{\mathbf{y}}(t) \equiv \frac{1}{T} \int_{t-T/2}^{t+T/2} \mathbf{y}(s) ds \quad (12)$$

where  $T = 2\pi/\Omega$ . As illustrated in Fig. 7, the effect of the operator defined in (12) is to smooth out the short-term fluctuations of each variable, while retaining the long-term behavior.

Suppose we are interested in the evolution of the averaged variables  $\bar{\mathbf{x}}(t)$  and  $\bar{\mathbf{y}}(t)$ . Then, we can average the first two equations in (11), which yields

**Fig. 7** Definition of the averaged variables



$$\left\{ \begin{array}{l} \dot{\bar{\mathbf{x}}} = \epsilon \left[ \mathbf{A}\bar{\mathbf{y}} + \frac{1}{T} \int_{t-T/2}^{t+T/2} \mathbf{X}(\mathbf{x}(s), \phi(s)) ds \right] + O(\epsilon^2) \\ \dot{\bar{\mathbf{y}}} = \mathbf{B}\bar{\mathbf{y}} + \frac{1}{T} \int_{t-T/2}^{t+T/2} \mathbf{Y}(\mathbf{x}(s), \phi(s)) ds + O(\epsilon) \end{array} \right\}, \quad (13)$$

where it has been used that the average, as defined in (12), is a linear operator (the average of the sum is the sum of the averages).

The next step consists in transforming the integrals in (13). Since the process is exactly the same for both integrals, we only focus on the first of them.

First, we can write

$$\frac{1}{T} \int_{t-T/2}^{t+T/2} \mathbf{X}(\mathbf{x}(s), \phi(s)) ds = \frac{1}{T} \int_{t-T/2}^{t+T/2} \mathbf{X}(\mathbf{x}(t), \phi(s)) ds + O(\epsilon), \quad (14)$$

where it has been used the property that, in one period  $T$ ,  $\mathbf{x}(t)$  can only change by  $O(\epsilon)$ , according to (11). Thus, we can write  $\mathbf{x}(s) = \mathbf{x}(t) + O(\epsilon)$ . Changing the integration variable from  $s$  to  $\phi$  yields

$$\frac{1}{T} \int_{t-T/2}^{t+T/2} \mathbf{X}(\mathbf{x}(t), \phi(s)) ds + O(\epsilon) = \frac{1}{2\pi} \int_{\phi(t-T/2)}^{\phi(t+T/2)} \mathbf{X}(\mathbf{x}(t), \phi) d\phi + O(\epsilon), \quad (15)$$

where the last of relations (11) has been used ( $d\phi = \Omega ds + O(\epsilon)$ ). The integration limits can also be transformed by using again  $\dot{\phi} = \Omega + O(\epsilon)$ :

$$\frac{1}{2\pi} \int_{\phi(t-T/2)}^{\phi(t+T/2)} \mathbf{X}(\mathbf{x}(t), \phi) d\phi + O(\epsilon) = \frac{1}{2\pi} \int_{\phi(t)-\pi}^{\phi(t)+\pi} \mathbf{X}(\mathbf{x}(t), \phi) d\phi + O(\epsilon). \quad (16)$$

Finally, as function  $X$  is  $2\pi$ -periodic in  $\phi$ , we can write

$$\frac{1}{2\pi} \int_{\phi(t)-\pi}^{\phi(t)+\pi} X(\mathbf{x}(t), \phi) d\phi + O(\epsilon) = \frac{1}{2\pi} \int_0^{2\pi} X(\mathbf{x}(t), \phi) d\phi + O(\epsilon). \quad (17)$$

Thus, system (13) can be rewritten as

$$\left\{ \begin{aligned} \dot{\bar{\mathbf{x}}} &= \epsilon [A\bar{\mathbf{y}} + \bar{X}(\bar{\mathbf{x}})] + O(\epsilon^2) \\ \dot{\bar{\mathbf{y}}} &= B\bar{\mathbf{y}} + \bar{Y}(\bar{\mathbf{x}}) + O(\epsilon) \end{aligned} \right\}, \quad (18)$$

where

$$\bar{X}(\cdot) \equiv \frac{1}{2\pi} \int_0^{2\pi} X(\cdot, \phi) d\phi, \quad \bar{Y}(\cdot) \equiv \frac{1}{2\pi} \int_0^{2\pi} Y(\cdot, \phi) d\phi \quad (19)$$

We have been able to derive an autonomous system for the averaged variables, where the fast angle no longer appears –except in the higher order terms of (18). Note that the proposed approach exploits a particular property of system (11), namely the fact that the vector of fast variables  $\mathbf{y}$  only appears linearly on the r.h.s. of the equations. This feature, together with the linearity of the averaging operator, allows applying an averaging technique to system (11), despite it containing fast variables (in addition to the fast rotating phase  $\phi$ ).

Finally, it is convenient to remark the difference between the original and averaged variables. From Eq. (11), variations of  $\mathbf{x}$  and  $\mathbf{y}$  in one period  $T$  are  $O(\epsilon)$  and  $O(1)$ , respectively. Therefore, we can write

$$\mathbf{x}(t) = \bar{\mathbf{x}}(t) + O(\epsilon), \quad \mathbf{y}(t) = \bar{\mathbf{y}}(t) + O(1). \quad (20)$$

### 2.3 Perturbation Approach: Derivation of the Reduced System

Going back to the mechanical system under study, Eq. (10) constitute an autonomous dynamical system of dimension 4, with state variables  $\{u, \dot{u}, \phi, \dot{\phi}\}$ . A perturbation approach is proposed in this section, whereby (10) is transformed into an approximate 2D system.

First, it is convenient to perform a change of variables, from  $\{u, \dot{u}\}$  to polar coordinates [18]:

$$\begin{aligned} u &= a \cos(\phi + \beta) \\ \dot{u} &= -a \sin(\phi + \beta). \end{aligned} \quad (21)$$

This step does not include any approximation, since it consists in just replacing the pair of variables  $\{u(\tau), \dot{u}(\tau)\}$  with the pair of amplitude-phase variables  $\{a(\tau), \beta(\tau)\}$ .

By differentiating the first of relations (21) we obtain

$$\dot{u} = \dot{a} \cos(\phi + \beta) - a(\dot{\phi} + \dot{\beta}) \sin(\phi + \beta). \quad (22)$$

Comparing (22) with the second of relations (21) yields

$$\dot{a} \cos(\phi + \beta) - a(\dot{\phi} - 1 + \dot{\beta}) \sin(\phi + \beta) = 0. \quad (23)$$

On the other hand, if (21) is introduced into the first of Eq. (10), we have

$$\begin{aligned} & -\dot{a} \sin(\phi + \beta) - a(\dot{\phi} - 1 + \dot{\beta}) \cos(\phi + \beta) = \\ & = \epsilon [2\xi a \sin(\phi + \beta) - \rho a^3 \cos^3(\phi + \beta) + 2\xi(\dot{\phi}^2 \cos \phi + \ddot{\phi} \sin \phi)] \end{aligned} \quad (24)$$

Equations (23) and (24) together form a linear system for  $\dot{a}$  and  $\dot{\beta}$  that can be readily solved:

$$\begin{aligned} \dot{a} &= -\epsilon \sin(\phi + \beta) [2\xi a \sin(\phi + \beta) - \rho a^3 \cos^3(\phi + \beta) + 2\xi(\dot{\phi}^2 \cos \phi + \ddot{\phi} \sin \phi)] \\ \dot{\beta} &= 1 - \dot{\phi} - \epsilon \frac{\cos(\phi + \beta)}{a} [2\xi a \sin(\phi + \beta) - \rho a^3 \cos^3(\phi + \beta) + 2\xi(\dot{\phi}^2 \cos \phi + \ddot{\phi} \sin \phi)] \end{aligned} \quad (25)$$

It is also suitable to define a new variable for the rotor speed:

$$\Omega \equiv \dot{\phi}. \quad (26)$$

Then, the dynamical system, written in terms of the new variables, becomes

$$\left\{ \begin{array}{l} \dot{a} = -\epsilon \sin(\phi + \beta) F_1(a, \beta, \phi, \Omega) + O(\epsilon^2) \\ \dot{\beta} = 1 - \Omega - \epsilon \frac{\cos(\phi + \beta)}{a} F_1(a, \beta, \phi, \Omega) + O(\epsilon^2) \\ \dot{\Omega} = d(\Omega - 1) + \epsilon(c - \alpha a \sin \phi \cos(\phi + \beta)) + O(\epsilon^2) \\ \dot{\phi} = \Omega, \end{array} \right. \quad (27)$$

where

$$F_1 = 2\xi a \sin(\phi + \beta) - \rho a^3 \cos^3(\phi + \beta) + 2\xi[\Omega^2 \cos \phi + d(\Omega - 1) \sin \phi]. \quad (28)$$

A new 4D autonomous dynamical system (27) has been derived, with state variables  $\{a, \beta, \phi, \Omega\}$ , which is fully equivalent to (10).

Consider now a general set of initial conditions  $\{a_0, \beta_0, \phi_0, \Omega_0\}$  and let us investigate how the variables evolve with time. In the next subsections, it will be shown that the dynamics of (27) is composed of three consecutive stages of time, with different qualitative behaviours.

### First stage

For the moment, consider only the evolution equations for variables  $\beta$  and  $\Omega$ , which can be written as

$$\begin{cases} \dot{\beta} = 1 - \Omega + O(\epsilon) \\ \dot{\Omega} = d(\Omega - 1) + O(\epsilon) \end{cases}. \quad (29)$$

It is clear that, to first order of approximation, the evolution of  $\beta$  and  $\Omega$  only depends on  $\Omega$ . This first order approximation corresponds to neglecting the  $O(\epsilon)$  terms in (29).

$$\begin{cases} \dot{\beta} = 1 - \Omega \\ \dot{\Omega} = d(\Omega - 1) \end{cases}. \quad (30)$$

The relation between exact system (29) and (30) is established by the Regular Perturbation Theory [18], which assures that solutions of (30) are  $O(\epsilon)$ -approximations to solutions of (29), for  $\tau = O(1)$ . Thus, we proceed to solve system (30):

$$\begin{cases} \beta = \beta_0^* + \frac{1-\Omega_0}{d} e^{d\tau} \\ \Omega = 1 + [\Omega_0 - 1] e^{d\tau} \end{cases}, \quad (31)$$

with

$$\beta_0^* \equiv \beta_0 + \frac{\Omega_0 - 1}{d}. \quad (32)$$

It is clear from (31) that both variables tend exponentially to constant values:

$$\beta \rightarrow \beta_0^*, \quad \Omega \rightarrow 1. \quad (33)$$

This is due to the assumption  $d < 0$  (otherwise, the exponentials in (31) would be divergent). Taking into account the approximation made when transforming (29) into (30), it can be stated that, after a time interval  $\tau = O(1)$ , we have

$$\beta = \beta_0^* + O(\epsilon), \quad \Omega = 1 + O(\epsilon). \quad (34)$$

Once  $\beta$  and  $\Omega$  are at an  $O(\epsilon)$ -distance from  $\beta_0^*$  and 1, respectively, the first stage of the motion is over. Note that, during this stage, the rotor speed evolves monotonically towards the resonance region.



During this first phase, variable  $a$  remains nearly constant. Since  $\dot{a} = O(\epsilon)$ —see (27), variable  $a$  needs a time length  $\tau = O(1/\epsilon)$  to evolve significantly. Thus, at the end of the first stage, we have

$$a = a_0 + O(\epsilon). \tag{35}$$

In summary, the first stage corresponds to a time length  $\tau = O(1)$ . It starts at  $\tau = 0$  and it ends when  $\beta$  and  $\Omega$  have reached an  $O(\epsilon)$ –distance to  $\beta_0^*$  and 1, respectively.

**Second stage**

At the beginning of the second stage, the rotor speed is already in the vicinity of resonance. Consequently, it can be naturally expanded as

$$\Omega = 1 + \epsilon\sigma. \tag{36}$$

A new variable  $\sigma$  has been introduced in (36), which will be very widely used throughout the chapter. Notice that  $\sigma$  is a detuning coordinate, which measures how much the rotor speed deviates from the system natural frequency.

If system (27) is written using variable  $\sigma$  instead of  $\Omega$ , it becomes

$$\left\{ \begin{array}{l} \dot{a} = -\epsilon \sin(\phi + \beta) F_2(a, \beta, \phi) + O(\epsilon^2) \\ \dot{\beta} = -\epsilon\sigma - \epsilon \frac{\cos(\phi + \beta)}{a} F_2(a, \beta, \phi) + O(\epsilon^2) \\ \dot{\sigma} = c + d\sigma - \alpha a \sin \phi \cos(\phi + \beta) + O(\epsilon) \\ \dot{\phi} = 1 + \epsilon\sigma \end{array} \right\}, \tag{37}$$

where

$$F_2 = 2\xi a \sin(\phi + \beta) - \rho a^3 \cos^3(\phi + \beta) + 2\xi \cos \phi. \tag{38}$$

Notice that the closeness between the rotor speed and the natural frequency of the system has transformed  $\beta$  into a slow variable. Note also that system (37) is of the form (11), with  $\{a, \beta\}$  playing the role of vector  $\mathbf{x}$  and  $\sigma$  that of vector  $\mathbf{y}$ . Therefore, the averaging technique presented in Sect. 2.2 can be readily applied to (37), in order to obtain the evolution of the averaged variables.

The averaged system, which in the general case is given by (18), takes in the present case the form

$$\left\{ \begin{array}{l} \dot{\bar{a}} = -\epsilon\xi(\bar{a} + \sin \bar{\beta}) + O(\epsilon^2) \\ \dot{\bar{\beta}} = -\epsilon\left(\bar{\sigma} + \xi \frac{\cos \bar{\beta}}{\bar{a}} - \frac{3}{8}\rho\bar{a}^2\right) + O(\epsilon^2) \\ \dot{\bar{\sigma}} = c + d\bar{\sigma} + \frac{\alpha}{2}\bar{a} \sin \bar{\beta} + O(\epsilon) \end{array} \right\}, \tag{39}$$

where the averaged variables  $\{\bar{a}, \bar{\beta}, \bar{\sigma}\}$  are defined as in (12). System (39) has dimension 3, since variable  $\phi$  no longer appears.

It is convenient to highlight the relation between the original and the averaged variables. Particularizing the general expression (20) to the system under analysis, we find

$$\begin{aligned} a &= \bar{a} + O(\epsilon) \\ \beta &= \bar{\beta} + O(\epsilon) \\ \sigma &= \bar{\sigma} + O(1). \end{aligned} \quad (40)$$

Observe that, even with an  $O(1)$  error in  $\sigma$ , the rotor speed is still known with  $O(\epsilon)$  precision, according to (36). From now on, the overbars will be omitted, unless otherwise stated.

The task now is to investigate system (39). As pointed out before, this is a fast-slow system, with two slow variables  $a$  and  $\beta$  and one fast variable  $\sigma$ . This difference in the time scales allows exploiting the Singular Perturbation Theory [20–22].

According to the SPT, a system with the form of (39) displays two qualitatively different behaviors at two sequential time scales, which correspond to the second and third stages of the original system (27). With the aim of studying the first of them –second stage of (27), consider a time interval  $\tau = O(1)$  for system (39). Since  $a$  and  $\beta$  evolve with rate  $O(\epsilon)$ , it is clear that we have

$$\begin{aligned} a &= a_0 + O(\epsilon) \\ \beta &= \beta_0^* + O(\epsilon) \\ \dot{\sigma} &= c + d\sigma + \frac{\alpha}{2}a_0 \sin \beta_0^* + O(\epsilon), \end{aligned} \quad (41)$$

where we have taken into account that, at the beginning of stage 2,  $a = a_0 + O(\epsilon)$  and  $\beta = \beta_0^* + O(\epsilon)$ .

Then, the only variable that changes considerably during this stage is  $\sigma$ . From a direct analysis of the last of Eq. (41), it can be deduced that  $\sigma$  tends exponentially to the following value

$$\sigma \rightarrow -\frac{c}{d} - \frac{\alpha}{2d}a_0 \sin \beta_0^*, \quad (42)$$

which is the only fixed point for the last of Eq. (41). The assumption  $d < 0$  guarantees that the fixed point is globally attracting.

Expression (42), generalized to any values of  $a$  and  $\beta$ , gives what is called ‘the Slow Manifold’:

$$\sigma^*(a, \beta) = -\frac{c}{d} - \frac{\alpha}{2d}a \sin \beta. \quad (43)$$

Thus, (42) can be rewritten as

$$\sigma \rightarrow \sigma^*(a_0, \beta_0^*). \tag{44}$$

Thereby, at this stage, the slow variables remain almost constant, while the fast variable evolves until reaching the vicinity of the slow manifold.

Summing up, the second stage corresponds to a time length  $\tau = O(1)$ , just as the first one. It ends once variable  $\sigma$  has reached an  $O(\epsilon)$ -distance to  $\sigma^*(a_0, \beta_0^*)$ . During this phase of the motion,  $a$  and  $\beta$  do not change significantly.

**Third stage**

The third stage of the original system (27)—which is the second stage of the averaged system (39)—occurs at a time scale  $\tau = O(1/\epsilon)$ . This can be easily understood by noticing that, once the system is near the slow manifold, variable  $\sigma$  becomes slow (introducing (43) in (39) leads to  $\dot{\sigma} = O(\epsilon)$ ). Therefore, near the slow manifold, all variables are slow and, as a consequence, the system natural time scale is  $\tau = O(1/\epsilon)$ .

Obviously it still needs to be proved that, once the system is near the slow manifold, it remains in its neighborhood for all subsequent time. In other words, we have to verify that the manifold is always attracting. Although the proof is beyond the scope of this book and will not be displayed here, it can be shown that the attractiveness of the slow manifold is guaranteed as long as  $d < 0$ .

By introducing the expression of the slow manifold in (39), the equations corresponding to the third phase of the motion are obtained:

$$\left\{ \begin{array}{l} \dot{a} = -\epsilon \xi(a + \sin \beta) + O(\epsilon^2) \\ \dot{\beta} = -\epsilon \left( \sigma^*(a, \beta) + \xi \frac{\cos \beta}{a} - \frac{3}{8} \rho a^2 \right) + O(\epsilon^2) \\ \sigma = \sigma^*(a, \beta) + O(\epsilon). \end{array} \right\} \tag{45}$$

As usual, higher order terms in (45) can be eliminated, giving rise to an  $O(\epsilon)$  approximation for a time length  $\tau = O(1/\epsilon)$ :

$$\left\{ \begin{array}{l} \dot{a} = -\epsilon \xi(a + \sin \beta) \\ \dot{\beta} = -\epsilon \left( \sigma^*(a, \beta) + \xi \frac{\cos \beta}{a} - \frac{3}{8} \rho a^2 \right) \\ \sigma = \sigma^*(a, \beta). \end{array} \right\} \tag{46}$$

It is convenient to observe that, although (46) contains three equations, only two of them are differential equations. Thus, (46) represents a 2D autonomous dynamical system. The evolution of  $a$  and  $\beta$  no longer depends on  $\sigma$ , once  $\sigma$  is written as a function of  $a$  and  $\beta$ . The last equation is written with the only purpose of tracking the evolution of variable  $\sigma$ .

In summary, the third stage corresponds to a time length  $\tau = O(1/\epsilon)$ . At this phase of the motion, the averaged system evolves along the slow manifold given by (43). Variables  $a$ ,  $\beta$  and  $\sigma$  obey Eq. (46), with  $O(\epsilon)$  precision.

Figure 8 shows a schematic representation of the three different stages of the system dynamics, summing up the results obtained in the present section. Note that,

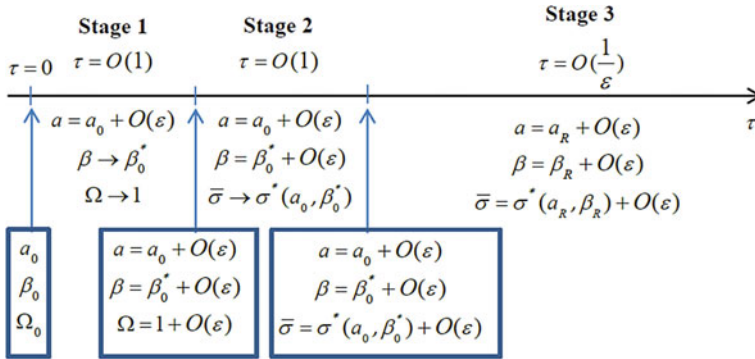


**Fig. 8** Overview of the system dynamics, with  $\{a_R, \beta_R\}$  being the solution of system (46) with appropriate initial conditions

in Fig. 8, the use of overbars for the averaged variables is recovered. The most relevant result is that, once the initial transient corresponding to the first two stages has finished, the evolution of variables  $a$  and  $\beta$  is governed by Eq. (46)—within an  $O(\epsilon)$  error—.

From Fig. 8, it is clear that suitable initial conditions for system (46) are  $\{a_0, \beta_0^*\}$ . Recalling definition (32), this can be written as  $\{a_0, \beta_0 + (\Omega_0 - 1)/d\}$ , where  $\{a_0, \beta_0, \phi_0, \Omega_0\}$  is the set of initial conditions for system (27).

However, we may be interested in a particular set of initial conditions for system (10), given as  $\{u_0, \dot{u}_0, \phi_0, \dot{\phi}_0\}$ . It is, then, convenient, to express the initial conditions for (46) as functions of the initial conditions for (10):

$$\begin{aligned}
 a_0 &= \sqrt{u_0^2 + \dot{u}_0^2} \\
 \beta_0^* &= \tan^{-1}\left(\frac{-\dot{u}_0}{u_0}\right) - \phi_0 + \frac{\dot{\phi}_0 - 1}{d},
 \end{aligned}
 \tag{47}$$

as can be readily deduced from relations (21), (26) and (32).

Recapitulating, we have been able to eliminate from the formulation variable  $\phi$  by Averaging, and variable  $\sigma$  by applying the Singular Perturbation Theory.

### 2.4 Analysis of the Reduced System

This section focuses on the behaviour of system (46), once it has been shown to capture, with  $O(\epsilon)$  precision, the dynamics of the original system (10) during the third stage of the motion.

Firstly, it is useful to make a comparison between the system under study and its ideal counterpart, where the rotor speed is constant. Clearly, for this ideal case, the equation of motion of the system shown in Fig. 3 is given by

$$m\ddot{x} + b\dot{x} + kx + \lambda x^3 = m_1 r \dot{\phi}^2 \cos \phi, \quad (48)$$

with  $\dot{\phi}$  fixed. Equation (48) describes a Duffing oscillator, subjected to harmonic excitation. This is a very well-known problem, which has been widely studied in the literature [9, 19, 23, 24]. Under the assumptions of small damping, small nonlinearity, small unbalance and near-resonant excitation ( $\dot{\phi} = 1 + \epsilon \sigma_0$ ), the Averaging Method can be applied to system (48), leading to

$$\left\{ \begin{array}{l} \dot{a} = -\epsilon \xi (a + \sin \beta) \\ \dot{\beta} = -\epsilon \left( \sigma_0 + \xi \frac{\cos \beta}{a} - \frac{3}{8} \rho a^2 \right) \end{array} \right\}, \quad (49)$$

where all the parameters and variables are defined as in Sects. 2.1 and 2.3. It is easy to verify that system (49) is exactly the same as (46), with the only difference of replacing  $\sigma^*(a, \beta)$  by the constant value  $\sigma_0$ . This is a clear illustration of the concept of nonideal excitation. In the ideal case, the rotor speed appears in Eq. (49) as a constant value  $\sigma_0$ , externally imposed by the motor. However, in the nonideal case, the rotor speed enters Eq. (46) as a function of the system vibratory motion,  $\sigma^*(a, \beta)$ .

It is also important to observe that an ideal motor displays a vertical static characteristic, corresponding to the limit case  $d \rightarrow -\infty$ . The motor is, then, able to generate any torque for the same rotor speed. This suggests the idea that a real motor with a static characteristic of very large slope (in absolute value) is more likely to behave in an ideal manner than another one with a smaller slope.

### Fixed points

Going back to the objective of analyzing system (46), it is first convenient to look for its fixed points,  $\{a_{eq}, \beta_{eq}, \sigma_{eq}\}$ :

$$\begin{aligned} a_{eq} &= -\sin \beta_{eq} \\ \sigma^*(a_{eq}, \beta_{eq}) &= \frac{3}{8} \rho a_{eq}^2 - \xi \frac{\cos \beta_{eq}}{a_{eq}} \\ \sigma_{eq} &= \sigma^*(a_{eq}, \beta_{eq}). \end{aligned} \quad (50)$$

From the first of Eq. (50), we have

$$\cos \beta_{eq} = -z \sqrt{1 - a_{eq}^2}, \quad z = \pm 1. \quad (51)$$

Combining (43), (50) and (51) yields

$$-\frac{c}{d} + \frac{\alpha}{2d} a_{eq}^2 = \frac{3}{8} \rho a_{eq}^2 + z \xi \frac{\sqrt{1 - a_{eq}^2}}{a_{eq}}. \quad (52)$$

Solutions of (52), for both values of  $z$ , give  $a_{eq}$  for all the fixed points of (46). This can be done analytically, but the expressions become cumbersome and difficult to interpret. An alternative procedure is proposed, which leads to the fixed points of (46) in a graphical way. To this end, the last of Eq. (46) can be rewritten as

$$c + d\sigma = -\frac{\alpha}{2}a \sin \beta, \quad (53)$$

where definition (43) has been used. Now, recall the last of Eq. (39), which governs the evolution of the rotor speed for the averaged system:

$$\dot{\sigma} = c + d\sigma + \frac{\alpha}{2}a \sin \beta + O(\epsilon). \quad (54)$$

In the light of (54), (53) can be interpreted as an equilibrium between two torques on the rotor. The left hand term in (53) represents the driving torque produced by the motor, while the right hand term represents the resisting torque due to vibration. Thus, the fact that the averaged system is on the slow manifold—which is expressed in Eq. (53)—can be understood as a torque equilibrium condition.

Equation (53), particularized for the fixed point  $\{a_{eq}, \beta_{eq}, \sigma_{eq}\}$ , takes the form

$$c + d\sigma_{eq} = \frac{\alpha}{2}a_{eq}^2, \quad (55)$$

where (50) has been used. We now define the following functions:

$$\begin{aligned} T_m(\sigma) &\equiv c + d\sigma \\ T_v(a) &\equiv \frac{\alpha}{2}a^2. \end{aligned} \quad (56)$$

Clearly, according to the comments below Eq. (54),  $T_m$  represents the driving torque produced by the motor, while  $T_v$  corresponds to the resisting torque due to vibration. Then, (55) can be rewritten as

$$T_m(\sigma_{eq}) = T_v(a_{eq}), \quad (57)$$

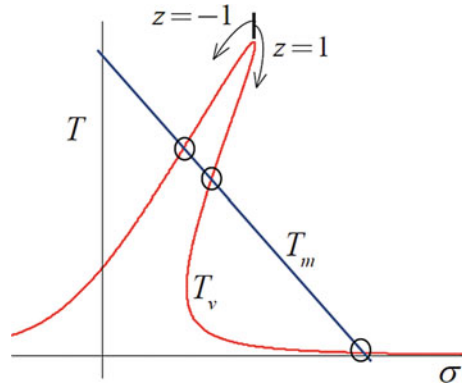
which is the torque equilibrium condition, particularized for the fixed point.

In order to solve (57) in a graphical way, it would be desirable to write both torques explicitly in terms of  $\sigma_{eq}$ . However, this would in turn need explicitly writing  $a_{eq}$  in terms of  $\sigma_{eq}$ , which produces long and complicated expressions. Thus, an implicit procedure for the graphical representation is proposed. Combining (50) and (51) results in

$$\sigma_{eq} = \sigma_v(z, a_{eq}), \quad (58)$$

where function  $\sigma_v(z, a)$  is defined as

**Fig. 9** Fixed points of system (46)



$$\sigma_v(z, a) \equiv \frac{3}{8} \rho a^2 + z \xi \frac{\sqrt{1 - a^2}}{a}. \tag{59}$$

The proposed representation can be constructed as follows: first, graph  $T_m$  versus  $\sigma$  according to (56). Then, graph on the same plot the parametric curve given by  $\{\sigma_v(z, a), T_v(a)\}$ , for  $z = \pm 1$  and  $a \in (0, 1]$ . The fact that  $a$  is strictly positive comes from the definition of  $a$  as the radius of a polar coordinate transformation –see (21)–(20). On the other hand  $a_{eq}$  cannot be greater than 1, according to the first of Eq. (50).

The above procedure gives rise to a plot like that shown in Fig. 9. Considering Eq. (57), the fixed points can be found as the intersections of the two torque curves. In the particular case displayed in Fig. 9, there are three equilibrium points, marked with circles. Note that the curve associated to the vibration torque is composed of two branches, which collide at the maximum of the curve. They correspond to the two possible values of parameter  $z$ , as specified in Fig. 9.

We note that the ‘Sommerfed effect’, which was described in the introduction, can be readily explained by using Fig. 9. For such an explanation, the interested reader can refer to [9, 10, 12, 17].

**Stability Analysis**

Once the fixed points of the reduced system have been obtained, it is convenient to investigate their stability. For a 2D system, this reduces to calculating the trace and determinant of the jacobian matrix, evaluated at the equilibrium point of interest:

$$\mathbf{J}_{eq} = \epsilon \begin{bmatrix} -\xi & z \xi R_{eq} \\ \left(-\frac{\alpha}{2d} + \frac{3\rho}{4}\right) a_{eq} - \frac{z \xi R_{eq}}{a_{eq}^2} & -\frac{z \alpha a_{eq} R_{eq}}{2d} - \xi \end{bmatrix}, \tag{60}$$

where  $R_{eq}$  stands for  $\sqrt{1 - a_{eq}^2}$ .

The conditions for a fixed point to be asymptotically stable are

$$\mathbf{C1.} \quad \text{tr}(J_{eq}) < 0 \tag{61}$$

$$\mathbf{C2.} \quad \det(J_{eq}) > 0. \tag{62}$$

After some algebra, these conditions can be expressed as

$$\mathbf{C1.} \quad \frac{z\alpha a_{eq} R_{eq}}{4d} + \xi > 0 \tag{63}$$

$$\mathbf{C2.} \quad \left\{ \begin{array}{l} \frac{1}{\eta} - \frac{1}{d} < 0, \quad \text{if } z = 1 \\ \frac{1}{\eta} - \frac{1}{d} > 0, \quad \text{if } z = -1 \end{array} \right\}, \tag{64}$$

where  $\eta$  denotes the slope of the  $T_v$  curve at the considered equilibrium point (see Figs. 10 and 11), and has the expression

$$\frac{1}{\eta} = -\frac{z\xi}{\alpha a_{eq}^3 R_{eq}} + \frac{3\rho}{4\alpha}, \tag{65}$$

as can be deduced from (56), (59).

Conditions (63) and (64) are now applied to evaluate stability regions in different scenarios. The procedure is as follows. Consider parameters  $\alpha, \xi, \rho$  fixed, so that

**Fig. 10** Stability regions for  $z = -1$ .  $S$  and  $U$  label the stable and unstable regions, respectively. **a**  $\eta > 0$ , **b**  $\eta < 0$

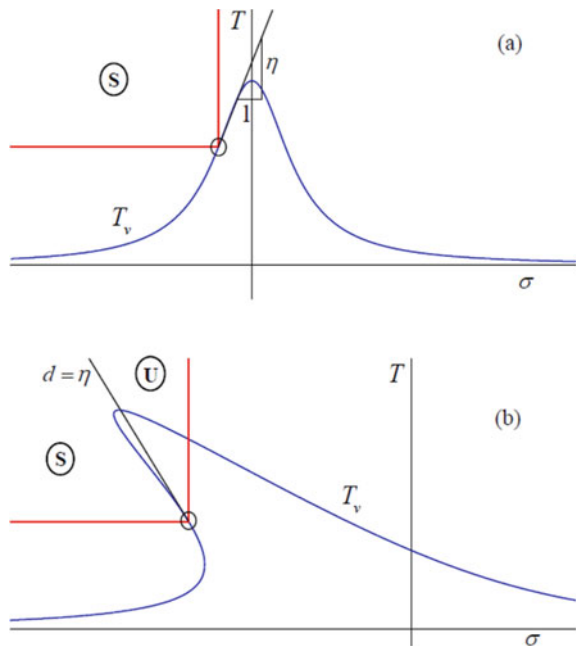
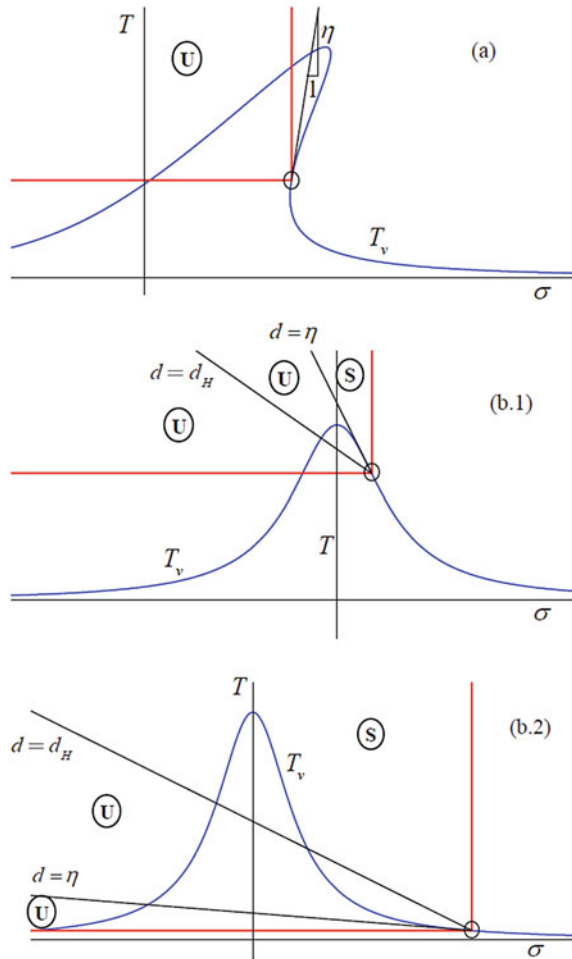




**Fig. 11** Stability regions for  $z = 1$ .  $S$  and  $U$  label the stable and unstable regions, respectively. **a**  $\eta > 0$ , (b.1)  $\eta < d_H < 0$ , (b.2)  $d_H < \eta < 0$



the  $T_v$  curve –see Fig. 9– is fixed too. Consider a pair of values  $(c, d)$  that gives a particular curve  $T_m(\sigma)$ . The intersections between the two curves represent the equilibrium points of the system. Select one of them –if there are more than one– and let parameters  $(c, d)$  vary in such a way that the selected equilibrium point remains an equilibrium point. In other words, let parameters  $(c, d)$  vary so as to make the curve  $T_m(\sigma)$  rotate around the selected equilibrium point, satisfying restriction  $d < 0$ . Finally, use conditions (63) and (64) to analyze how the stability of the fixed point is affected by the slope  $d$  of the motor characteristic.

Figure 10 displays the outcome of applying the above procedure for a fixed point located at the left branch of the vibration torque ( $z = -1$ ). Two scenarios are considered, depending on the sign of slope  $\eta$ , evaluated at the fixed point under consideration. It is observed that a change of stability occurs when both torque

curves become tangent ( $d = \eta$ ). This can be shown to correspond to a transcritical bifurcation. Note that, in Fig. 10, the motor curve corresponding to  $d = \eta$  has been directly labeled as  $d = \eta$ , instead of  $T_m(d = \eta)$ . This shortened notation will be widely used in the figures of the document.

Figure 11 shows analogous results for a fixed point located at the right branch of the vibration torque curve ( $z = 1$ ). The system behavior is richer in this case, since stability may change in two different ways, depending on the comparison  $\eta \lesseqgtr d_H$  where  $d_H$  is defined below.

We define critical slope  $d_H$  as the value of  $d$  that makes  $tr(J_{eq}) = 0$ . Recall that the stability condition  $tr(J_{eq}) < 0$  was written as (63). Therefore,  $d_H$  takes the form

$$d_H(\alpha, \xi, a_{eq}) = -\frac{\alpha a_{eq} R_{eq}}{4\xi}. \tag{66}$$

Below, the different possibilities for  $z = 1$  are considered.

- If  $\eta > 0$  (Fig. 11a), condition **C2** is never fulfilled, so the fixed point is unstable regardless the value of slope  $d$ .
- If  $\eta < d_H < 0$  (Fig. 11b.1), the critical condition –i.e. the one that produces the stability change– is **C2**. In this case, a transcritical bifurcation can be shown to occur when both torque curves are tangent ( $d = \eta$ ). Note that this result is analogous to that obtained for the left branch (Fig. 10).
- If  $d_H < \eta < 0$  (Fig. 11b.2), the critical condition is **C1**. In this case, the stability change occurs at  $d = d_H$  through a Hopf bifurcation, after which parameter  $d_H$  was named.

To better understand the nature of the different bifurcations, notice the following correspondence between conditions **C1** and **C2**, and the eigenvalues of  $J_{eq}$ , according to (61), (62):

- **C1** is the critical condition  $\rightarrow \left\{ \begin{array}{l} tr(J_{eq}) = 0 \\ det(J_{eq}) > 0 \end{array} \right\}$  both eigenvalues of  $J_{eq}$ , being complex conjugates, cross the imaginary axis.
- **C2** is the critical condition  $\rightarrow \left\{ \begin{array}{l} tr(J_{eq}) < 0 \\ det(J_{eq}) = 0 \end{array} \right\}$  a single, real eigenvalue of  $J_{eq}$  crosses the imaginary axis.

It is worth stressing that most of the literature on nonideal excitations maintains that stability changes when the torque curves become tangent [9, 10, 12, 17]. This is consistent with our results, with the important exception of case  $z = 1, d_H < \eta < 0$  (Fig. 11b.2). Thus, one of the major findings presented in this chapter consists in having found a case where the usual rule of thumb for stability is not valid. In this scenario, the stable region is in fact smaller than predicted by usual theories (see Fig. 11b.2). Not taking this into account may be dangerous in real applications, since it could lead to unexpected instabilities.

Finally, the conditions for the existence of a Hopf bifurcation in the linear case ( $\rho = 0$ ) are investigated in more detail. As stated above, a Hopf bifurcation exists if

$$z = 1, \quad d_H < \eta < 0. \tag{67}$$

By substituting expression (65) and (66) into (67), for  $\rho = 0$ , we have

$$z = 1, \quad -\frac{\alpha a_{eq} R_{eq}}{4\xi} < -\frac{\alpha a_{eq}^3 R_{eq}}{\xi} < 0. \tag{68}$$

Simplifying (68) yields

$$z = 1, \quad a_{eq} < 0.5. \tag{69}$$

Therefore, if the system under study has no structural nonlinearity ( $\rho = 0$ ), it is particularly easy to predict the existence of a Hopf bifurcation, by simply checking condition (69).

### 2.5 Classification of the Hopf Bifurcations

Clearly, it would be of great interest to characterize the Hopf bifurcation encountered in last section as subcritical or supercritical. In the former case, an unstable limit cycle coexists with the stable fixed point, while in the latter case there is a stable limit cycle coexisting with the unstable fixed point, as represented in Fig. 12.

Characterizing the bifurcations requires several transformations of system (46) that are detailed below.

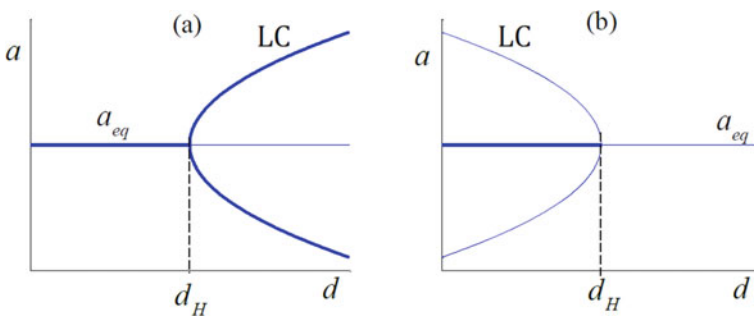


**Fig. 12** Classification of Hopf bifurcations. **a** Supercritical **b** Subcritical. Thick (thin) lines represent stable (unstable) solutions

**Transformation to Cartesian Coordinates**

We assume the system parameters are such that there exists a fixed point on the right branch of curve  $T_v$  ( $z = 1$ ), satisfying condition (67) and, thereby, undergoing a Hopf bifurcation. By defining change of variables

$$\begin{cases} \tilde{x} = a \cos \beta \\ \tilde{y} = a \sin \beta \end{cases}, \tag{70}$$

system (46), particularized for the bifurcation point ( $d = d_H$ ), can be rewritten as

$$\begin{cases} \dot{\tilde{x}} = -\epsilon \left[ \xi \tilde{x} + \frac{c}{d_H} \tilde{y} + \frac{\alpha}{2d_H} \tilde{y}^2 + \frac{3}{8} \rho \tilde{y} (\tilde{x}^2 + \tilde{y}^2) \right] \\ \dot{\tilde{y}} = \epsilon \left[ -\xi \tilde{y} - \frac{c}{d_H} \tilde{x} + \frac{\alpha}{2d_H} \tilde{x} \tilde{y} + \frac{3}{8} \rho \tilde{x} (\tilde{x}^2 + \tilde{y}^2) \right] \end{cases}. \tag{71}$$

**Displacement of the origin**

In order to characterize the bifurcation, it is convenient to locate the origin of the coordinate system at the fixed point under investigation. Then, we define change of variables

$$\begin{cases} x = \tilde{x} - a_{eq} \cos \beta_{eq} \\ y = \tilde{y} - a_{eq} \sin \beta_{eq} \end{cases}. \tag{72}$$

Using the new coordinates, system (71) takes the form

$$\begin{cases} \dot{x} = \epsilon \left[ -\left[ \xi + \frac{3}{4} \rho a^3 R \right] x - \left[ \frac{3}{4} \rho a^4 + \xi \left( \frac{R}{a} - \frac{R}{a} \right) \right] y + \frac{3}{8} \rho a^2 x^2 + \left[ \frac{2\xi}{aR} + \frac{9}{8} \rho a^2 \right] y^2 + \frac{3}{4} \rho a R x y - \frac{3}{8} \rho y [x^2 + y^2] \right] \\ \dot{y} = \epsilon \left[ \left[ \frac{3}{4} \rho a^2 R^2 - \xi \frac{R}{a} \right] x + \left[ \xi + \frac{3}{4} \rho a^3 R \right] y - \frac{9}{8} \rho a R x^2 - \frac{3}{4} \rho a R y^2 - \left[ \frac{2\xi}{aR} + \frac{3}{4} \rho a^2 \right] x y + \frac{3}{8} \rho x [x^2 + y^2] \right] \end{cases}. \tag{73}$$

where  $a_{eq}$  and  $R_{eq}$  are shortly written as  $a$  and  $R$ , respectively, in order to make the expression more manageable. This abbreviated notation will also be used in the Appendix. Note that system (73) is of the form

$$\begin{bmatrix} \dot{x} \\ \dot{y} \end{bmatrix} = \epsilon \left( A \begin{bmatrix} x \\ y \end{bmatrix} + \mathbf{h}(x, y) \right) \tag{74}$$

where matrix  $A$  is given by

$$A = \begin{bmatrix} -\left( \xi + \frac{3}{4} \rho a^3 R_{eq} \right) & -\left[ \frac{3}{4} \rho a^4 + \xi \left( \frac{2a_{eq}}{R_{eq}} - \frac{R_{eq}}{a_{eq}} \right) \right] \\ \frac{3}{4} \rho a_{eq}^2 R_{eq}^2 - \xi \frac{R_{eq}}{a_{eq}} & \xi + \frac{3}{4} \rho a_{eq}^3 R_{eq} \end{bmatrix} \tag{75}$$

and vector  $\mathbf{h}(x, y)$  contains the nonlinear terms of the system.

### Transformation to the real eigenbasis of matrix $\mathbf{A}$

A new change of variables, using the real eigenbasis of matrix  $\mathbf{A}$ , is defined:

$$\begin{bmatrix} x \\ y \end{bmatrix} = \mathbf{T} \begin{bmatrix} z_1 \\ z_2 \end{bmatrix}, \quad (76)$$

where the columns of matrix  $\mathbf{T}$  are the real and imaginary parts of the complex conjugate eigenvectors of  $\mathbf{A}$ , denoted by  $\mathbf{v}_{1,2}$ :

$$\mathbf{v}_{1,2} = \begin{bmatrix} c_1 \\ c_2 \end{bmatrix} \pm i \begin{bmatrix} \omega_0 \\ 0 \end{bmatrix} \rightarrow \mathbf{T} = \begin{bmatrix} c_1 & \omega_0 \\ c_2 & 0 \end{bmatrix}, \quad (77)$$

with

$$\begin{aligned} c_1 &= \xi + \frac{3}{4} \rho a_{eq}^3 R_{eq} \\ c_2 &= \xi \frac{R_{eq}}{a_{eq}} - \frac{3}{4} \rho a_{eq}^2 R_{eq}^2 \\ \omega_0 &= \sqrt{\left(\frac{1-4a_{eq}^2}{a_{eq}^2}\right) \xi^2 - \frac{3}{4} \rho \xi a_{eq} R_{eq}}. \end{aligned} \quad (78)$$

System (73), written in terms of the new variables, takes the form

$$\begin{bmatrix} \dot{z}_1 \\ \dot{z}_2 \end{bmatrix} = \epsilon \left( \begin{bmatrix} 0 & -\omega_0 \\ \omega_0 & 0 \end{bmatrix} \begin{bmatrix} z_1 \\ z_2 \end{bmatrix} + \begin{bmatrix} f(z_1, z_2) \\ g(z_1, z_2) \end{bmatrix} \right), \quad (79)$$

where functions  $f$  and  $g$ , containing the nonlinear terms of the system, can be written as Taylor series:

$$\begin{aligned} f(z_1, z_2) &= \sum_{i+j=2}^3 \frac{1}{i!j!} f_{ij} z_1^i z_2^j \\ g(z_1, z_2) &= \sum_{i+j=2}^3 \frac{1}{i!j!} g_{ij} z_1^i z_2^j \end{aligned} \quad (80)$$

Coefficients  $f_{ij}$  and  $g_{ij}$  are specified in the Appendix.

### Transformation to normal form

The final step to characterize the bifurcation includes transformation in complex form, near-identity transformation and transformation in polar coordinates [25]. This is a standard procedure whose details can be found in [26, 27]. After these last transformations, system (79) can be written in its Normal Form

$$\dot{r} = \epsilon \delta r^3, \tag{81}$$

which governs the radial dynamics at the bifurcation. As shown in [27], coefficient  $\delta$  can be computed as

$$16\delta = \left\{ \begin{array}{l} f_{30} + f_{12} + g_{21} + g_{03} \\ + \frac{1}{\omega_0} [f_{11}(f_{20} + f_{02}) - g_{11}(g_{20} + g_{02})] \\ + \frac{1}{\omega_0} [f_{02}g_{02} - f_{20}g_{20}] \end{array} \right\}. \tag{82}$$

In summary, we can say that, after a large number of variable transformations, system (46) can be written as (81), from which we deduce that the bifurcation is supercritical (subcritical) if  $\delta < 0$  ( $\delta > 0$ ).

Despite the fact that coefficients  $f_{ij}$  and  $g_{ij}$  are of rather complicated form, we find –with the aid of the symbolic computation toolbox in Matlab– that the condition for supercriticality or subcriticality can be expressed in a surprisingly simple manner:

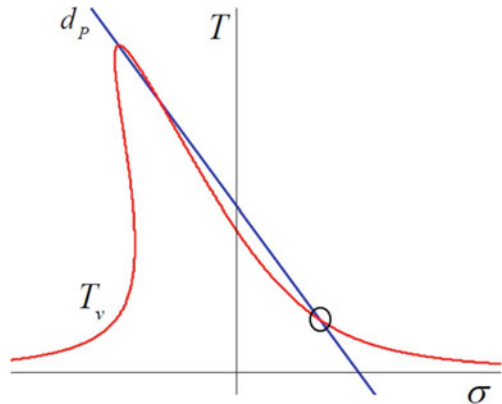
$$\begin{aligned} \text{Supercritical} &\Rightarrow \delta < 0 \Rightarrow \rho < -\frac{8\xi}{3a_{eq}R_{eq}} \\ \text{Subcritical} &\Rightarrow \delta > 0 \Rightarrow \rho > -\frac{8\xi}{3a_{eq}R_{eq}} \end{aligned} \tag{83}$$

From (83), it is clear that a nonlinearity of the softening type ( $\rho < 0$ ) is needed to have a supercritical bifurcation.

It is also worth noting that conditions (83) admit a very clear graphical interpretation. Consider a curve  $T_m$  which intersects  $T_v$  at the equilibrium point under consideration and also at the peak of curve  $T_v$ . Let  $d_P$  denote the slope of this particular motor characteristic, as depicted in Fig. 13.

In order to obtain  $d_P$ , the coordinates of the two points defining the straight line are defined below. First, the highest peak of curve  $T_v$  can be shown to correspond to  $a = 1$ . Substituting this condition into (56) and (59) yields

**Fig. 13** Definition of slope  $d_P$



$$\sigma = \frac{3}{8}\rho, \quad T = \frac{\alpha}{2} \tag{84}$$

On the other hand, the  $(\sigma, T)$  coordinates of the equilibrium point under study are directly given in (56) and (59):

$$\sigma = \frac{3}{8}\rho a_{eq}^2 + \xi \frac{R_{eq}}{a_{eq}}, \quad T = \frac{\alpha}{2} a_{eq}^2 \tag{85}$$

Then, from (84) and (85), the expression of  $d_P$  can be readily obtained:

$$\frac{1}{d_P} = \frac{3\rho}{4\alpha} - \frac{2\xi}{\alpha a_{eq} R_{eq}}, \tag{86}$$

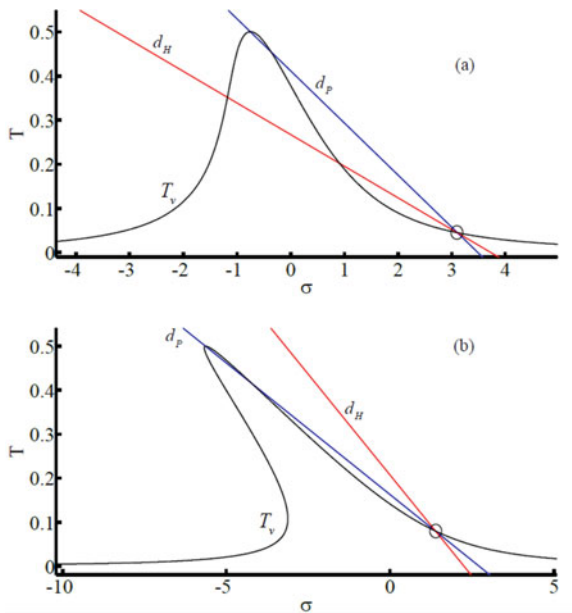
By comparing (86) and (66) conditions (83) can be expressed as

$$\text{Supercritical} \Rightarrow d_H < d_P \tag{87}$$

$$\text{Subcritical} \Rightarrow d_H > d_P.$$

This last manner of characterizing the bifurcation is certainly appealing from a graphical point of view, since the essential information about the bifurcation can be directly observed from the torque–speed curves, as shown in Fig. 14 for two particular examples.

**Fig. 14** Examples of **a** subcritical and **b** supercritical bifurcations. **a**  $\xi = 1, \alpha = 1, \rho = -2, a_{eq} = 0.3$  **b**  $\xi = 1, \alpha = 1, \rho = -15, a_{eq} = 0.4$



## 2.6 *Conditions Under Which All System Trajectories are Attracted Towards a Limit Cycle*

In Sect. 2.5, a simple condition has been obtained to ascertain whether the Hopf bifurcation under study is subcritical or supercritical, which in turn allows predicting the kind of limit cycle generated by the bifurcation (see Fig. 12). Although this distinction is relevant, it is based on a local analysis and, consequently, it only gives local information about the system behaviour. This is so in two senses: the analysis of Sect. 2.5 provides insight into the system dynamics.

- for values of  $d$  close enough to  $d_H$  (results are local in the parameter space) and
- for trajectories close enough to the investigated fixed point (results are local in the phase plane).

In view of the aforementioned limitations, this section addresses a new global result that complements those of Sect. 2.5. First, let us briefly recall the Poincaré-Bendixson theorem, which is an essential result from the global theory of nonlinear systems [28]. The theorem can be stated, in short terms, as follows.

Consider a 2D dynamical system and a closed, bounded region  $R$  of the phase plane that does not contains any equilibrium points. Then, every trajectory that is confined in  $R$  –it starts in  $R$  and remains in  $R$  for all future time– is a closed orbit or spirals towards a closed orbit as  $t \rightarrow \infty$ . For a more rigorous and detailed exposition of the theorem, see [28].

Let us show that, under certain circumstances, the P-B theorem can be used to prove that all trajectories of the system under study are attracted towards a limit cycle.

First, it can be easily deduced from (46) that

$$a > 1 \Rightarrow \dot{a} < 0. \tag{88}$$

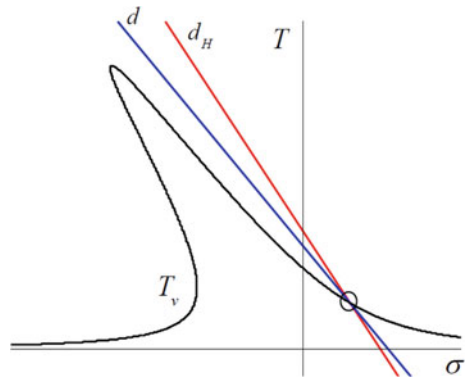
Let  $a$  and  $\beta$  represent polar coordinates on the phase plane, according to (70), and let  $D$  denote a circle centred at the origin of the phase plane with a radius slightly greater than 1, say 1.01. From (88), it can be said that every trajectory starting outside region  $D$  will enter  $D$  and remain inside for all subsequent time. Obviously, trajectories starting inside  $D$  will also remain inside forever. This kind of behavior would present  $D$  as a suitable candidate for the role of region  $R$  in the P-B theorem, if it were not for the presence of fixed points inside  $D$ .

Consider now the following particular situation:

$$\left\{ \begin{array}{l} \text{The system has only one fixed point} \\ z = 1, \quad d_H < d < \eta < 0 \end{array} \right\}, \tag{89}$$



**Fig. 15** Schematic view of the torque curves corresponding to conditions (89)



whose torque curves are depicted in Fig. 15. We suppose that the only fixed point of the system is on the right branch of curve  $T_v$  and undergoes a Hopf bifurcation. It is also assumed that the actual slope of the motor characteristic is  $d > d_H$  and, therefore, the equilibrium is unstable.

First, let us prove that the fixed point is a repeller. Since the equilibrium is already known to be unstable, we only need to prove that it is not a saddle. Let  $J_{eq}$  be the jacobian matrix of system (46), evaluated at the equilibrium point. Taking into account that a saddle point has two real eigenvalues  $\lambda_1, \lambda_2$  with different signs, we can state

$$\text{If } \det(J_{eq}) = \lambda_1 \lambda_2 > 0, \text{ then the equilibrium is not a saddle.} \quad (90)$$

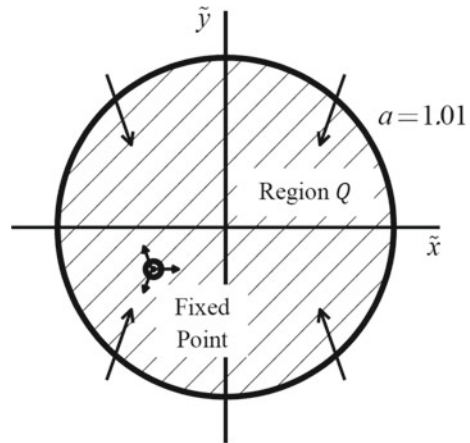
With some simple algebra, it can be shown that, for  $z = 1$ , condition  $\det(J_{eq}) > 0$  can be written as  $d < \eta$ . Then, it is clear that, for a fixed point satisfying (89), we have  $\det(J_{eq}) > 0$ . Thus, the equilibrium is a repeller.

A new region  $Q$  is now defined as  $D$  minus a circle of infinitesimal radius around the equilibrium point. From the above considerations –all trajectories enter  $D$  and the fixed point is a repeller–, it is clear that the flow on the boundary of  $Q$  is directed inwards, as depicted in Fig. 16.

In summary, a closed, bounded region  $Q$  of the phase plane has been obtained, which contains no fixed points and such that all trajectories of the system enter  $Q$  and remain inside forever. Then, all conditions of the P-B theorem are fulfilled, and it can be assured that any trajectory of the system is attracted towards a closed orbit as  $t \rightarrow \infty$ , if it is not a closed orbit itself.

Finally, it should be noted that, although the P-B theorem does not guarantee that all trajectories tend to the same closed orbit, all the numerical experiments conducted show the presence of only one stable limit cycle, namely that created by the Hopf bifurcation. This suggests that, for a system verifying (89), all the system dynamics is attracted towards a unique limit cycle.

**Fig. 16** Flow on the boundary of region  $Q$  (dashed), under conditions (89)



## 2.7 Discussion

### Time validity

A crucial point in any perturbation analysis is the time scale for which the obtained approximate solution is valid. It has been shown in Sect. 2.3 that the solution given by the reduced system is valid, at least, for a time scale  $\tau = O(1/\epsilon)$ —see Fig. 8—.

However, the situation is even better than that. From the Averaging Theory, it is known [18], that the asymptotic approximations attained through averaging are valid for all time, whenever they are attracted by a stable fixed point or a stable limit cycle. In the latter case, the uniform validity holds for all variables except the angular one, i.e. the variable measuring the flow on the limit cycle. As will be seen later, all the numerical solutions obtained in this chapter fulfil the above condition of attraction.

### Comparison with other authors' results

In this subsection, the presented approach and results are compared to some proposed by other authors.

First of all, as far as the authors know, there has been no attempt in the literature to use the SPT for the analysis of nonideally excited systems. Thus, the analytical procedure addressed in this Chapter appears to be a novel approach to the problem.

On the other hand, the possibility of a Hopf bifurcation on the right branch of the vibration torque curve (Fig. 11b.2) has been addressed. An important implication of this result is that the stability of the stationary solutions near resonance does not only depends on the comparison between the slopes of the two torque curves ( $\eta \lesssim d$ ), as commonly stated in the literature [9, 10, 12, 17]. Let us try to explain this divergence in the results.

Kononenko’s book [10] is one of the most relevant references in the subject. He considered several linear and nonlinear systems excited by nonideal motors. By using the averaging method, he was able to analytically investigate the stationary motions of the motor and their stability. His approach was as follows. Considering the rotor speed to be in the vicinity of resonance, he expanded it as

$$\dot{\phi} = 1 + \Delta, \quad \Delta = \epsilon\sigma. \tag{91}$$

Thus, he found equations of motion of the form

$$\left\{ \begin{array}{l} \dot{a} = O(\epsilon) \\ \dot{\beta} = -\epsilon\sigma + O(\epsilon) \\ \dot{\Delta} = O(\epsilon) \\ \dot{\phi} = 1 + \Delta \\ \Delta = \epsilon\sigma \end{array} \right\}, \tag{92}$$

which is a system analogous to (37). Then, he averaged (92) over the fast angle  $\phi$ , obtaining an averaged system of the form

$$\left\{ \begin{array}{l} \dot{\bar{a}} = O(\epsilon) \\ \dot{\bar{\beta}} = -\epsilon\bar{\sigma} + O(\epsilon) \\ \dot{\bar{\Delta}} = O(\epsilon) \\ \bar{\Delta} = \epsilon\bar{\sigma} \end{array} \right\}. \tag{93}$$

This averaged system is completely analogous to system (39), obtained in the present chapter. The only difference lies in the fact that Kononenko used the evolution equation for  $\bar{\Delta}$ , instead of that for  $\bar{\sigma}$ . This has an important consequence. From (39), it is clear that  $\bar{\sigma}$  is a fast variable, while  $\bar{a}$  and  $\bar{\beta}$  are slow. This property was exploited in Sect. 2.3 to obtain a reduced 2D system (46), by using the SPT. The analysis of the fixed points of this reduced system and their stability has revealed the possibility of Hopf bifurcations, and conditions for their appearance have been derived in Sect. 2.4. However, the form of the averaged Eq. (93), used by Kononenko, doesn’t evidence so clearly the fact that  $\bar{\sigma}$  is a fast variable. Then, instead of taking advantage of this separation in the time scales through the SPT, he directly investigated system (93), which did not allow him to obtain analytical conditions for the existence of Hopf bifurcations.

While several authors followed Kononenko’s approach [9, 17], Blekhman proposed a completely different one, based on the ‘method of direct separation of motions’ [12]. With this procedure, he came to the conclusion that the system dynamics is governed by equation

$$I\ddot{\phi} = L_m(\dot{\phi}) + V(\phi) \tag{94}$$

where dimensional variables have been used. In (94),  $V(\dot{\phi})$  represents the torque on the rotor due to vibration. Based on this equation, Blekhman deduced the same result as Kononenko regarding the stability of stationary solutions, namely, that stability changes when the driving torque curve and the vibration torque curve are tangent.

It is worth noting that Blekhman's approach is not applicable under the assumptions of the present chapter. The reason is that, in general, the torque on the rotor due to vibration depends on the linear motion of the system, as observed in the second of Eq. (1). This feature is maintained in the averaged system (39) obtained in this Chapter, where the vibration torque appears as a function of  $a$ ,  $\beta$ .

On the contrary, in [12], the vibration torque is written as a function of the rotor speed—see (94), which implies neglecting the dynamics associated to variables  $a$  and  $\beta$ . This would only be valid if the rotor speed was a much slower variable than those associated to the linear vibration ( $a$ ,  $\beta$ ). To better understand this point, suppose that, in system (1), the rotor inertia was  $O(1/\epsilon)$ , with the rest of the parameters being  $O(1)$ . Then, writing  $I = \tilde{I}/\epsilon$ , system (1) would take the form

$$\left\{ \begin{array}{l} m\ddot{x} + b\dot{x} + kx + \lambda x^3 = m_1 r \dot{\phi}^2 \cos \phi + O(\epsilon) \\ \tilde{I}\ddot{\phi} = \epsilon[A + D\dot{\phi} + m_1 r \ddot{x} \sin \phi] \end{array} \right\}. \quad (95)$$

With this particular scaling of the parameters, Blekhman's approach would be valid because the dynamics of linear motion would be much faster than that of the rotor speed. Then, as predicted by the SPT, the variables associated to the linear motion would be slaved to the rotor speed. This would in turn allow writing the vibration torque as a function of the rotor speed, as in (94).

As pointed out above, the assumptions of the present chapter (7)–(9) are not compatible with the results in [12], because the required difference in the time scales of the different variables is not satisfied. This can be observed in the averaged system (39), where we find  $\{\dot{a} = O(\epsilon), \dot{\beta} = O(\epsilon), \dot{\sigma} = O(1)\}$ .

More recently, Bolla et al. [14] used the Multiple Scales method to solve the same problem studied in this Chapter, under the same assumptions. However, after obtaining system (39), they conducted the stability analysis considering only the first two equations in (39) and taking  $\sigma$  as a fixed parameter. As explained at the beginning of Sect. 2.4, this corresponds to studying the ideal case, where the rotor speed is externally imposed. Consequently, they did not find the Hopf bifurcations that have been identified within this work. In fact, Bolla et al. explicitly stated the impossibility of Hopf bifurcations: 'This fact eliminates the possibility of a pair eigenvalue pure imaginary, so this eliminates Hopf bifurcation kind'. Thus, the present Chapter can be envisaged as an extension of [14], where new bifurcations are encountered due to the nonideal interaction between motor and vibrating system.

### 3 Numerical Simulations

This section presents two main purposes. First, a numerical investigation of the reduced system (46) is conducted in order to analyse the global bifurcations of limit cycles. While Sect. 2.5 studies how the Hopf bifurcations give rise to the appearance of limit cycles, Sect. 3.1 gives some insight about the dynamical mechanisms whereby the limit cycles are destroyed. A second subsection is presented where, by comparing numerical solutions of the original and reduced systems (10) and (46), respectively the proposed approach is validated. The objective is to demonstrate that the conclusions attained for the reduced system are also valid for the original system.

#### 3.1 Global Bifurcations of the Limit Cycles

In Sect. 3.1, the creation of limit cycle oscillations (LCOs) through Hopf bifurcations has been investigated. Now, the opposite question is examined: once a limit cycle is born, does it exist for every  $d > d_H$  in the supercritical case –for every  $d < d_H$  in the subcritical case–, or is it destroyed at any point? In the latter case, it would also be interesting to know the dynamical mechanism which makes the limit cycle disappear.

The aim of this Section is to analyse the global dynamics of the system, tracking the evolution of the limit cycles in order to find out how they are destroyed –if they are destroyed at all–. Since this task is in general too difficult to be carried out analytically, we resort to numerical computation.

##### The Subcritical Case

Consider the following set of dimensionless parameters:

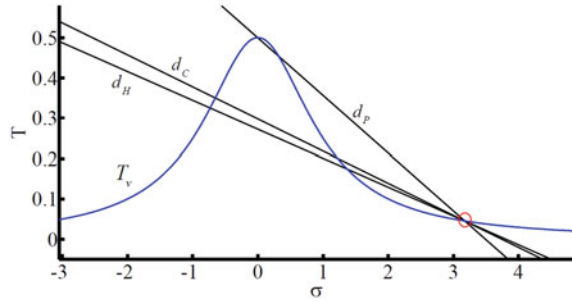
$$\xi = 1, \quad \alpha = 1, \quad \rho = 0, \quad a_{eq} = 0.3, \quad z = 1, \tag{96}$$

which might be associated to dimensional parameters

$$\left\{ \begin{array}{l} m = 1 \text{ kg} \\ k = 1 \text{ N/m} \\ b = 0.002 \text{ N s/m} \\ m_1 = 0.001 \text{ kg} \\ \lambda = 0 \text{ N/m}^3 \\ r = 0.1 \text{ m} \\ I = 5 \cdot 10^{-3} \text{ m}^2 \text{ kg} \end{array} \right\}, \tag{97}$$

with  $\epsilon = 0.001$ . Obviously, (97) is only one of the many possible sets of dimensional parameters giving rise to (96).

**Fig. 17** Torque curves corresponding to parameters (96)



By using Eqs. (66) and (86), slopes  $d_H$  and  $d_P$  can be obtained, as depicted in Fig. 17.

$$d_H = -0.0715, \quad d_P = -0.1431 \tag{98}$$

According to criterion (87), the Hopf bifurcation is found to be subcritical. Thus, as represented in Fig. 12, an unstable limit cycle is known to exist for  $d < d_H$ , within a certain neighborhood of  $d_H$ . We are interested in tracking the evolution of this limit cycle as slope  $d$  decreases. By numerically integrating system (46), using embedded Runge-Kutta formulae of orders 4 and 5, for different values of  $d$ , the limit cycle is found to disappear at  $d = d_C$  –see Fig. 17, with

$$d_C = -0.0795 \tag{99}$$

The dynamical mechanism whereby the limit cycle is destroyed, which turns out to be a homoclinic bifurcation [26], is shown in Figs. 18 and 19. Let us follow the evolution of the phase portrait. From Fig. 18a, b, the Hopf bifurcation takes place: the focus becomes stable, while an unstable limit cycle is born around it. In Fig. 19a, the cycle has swelled considerably and passes close to saddle point  $S$ . The homoclinic bifurcation occurs when the cycle touches the saddle point ( $d = d_C$ ), becoming a homoclinic orbit. In Fig. 19b, we have  $d < d_C$  and the loop has been destroyed.

It is worth noting that, when the unstable limit cycle exists –namely, for  $d_C < d < d_H$ –, it acts as a frontier between the domains of attraction of the two stable equilibrium points of the system –see Figs. 18b, 19a.

Many other cases exhibiting a subcritical bifurcation, which are not shown here, have also been numerically solved. In all of them, the unstable limit cycle has been found to disappear through a homoclinic bifurcation.

**The Supercritical Case**

Consider the following set of dimensionless parameters:

$$\xi = 1, \quad \alpha = 2, \quad \rho = -10, \quad a_{eq} = 0.5, \quad z = 1, \tag{100}$$

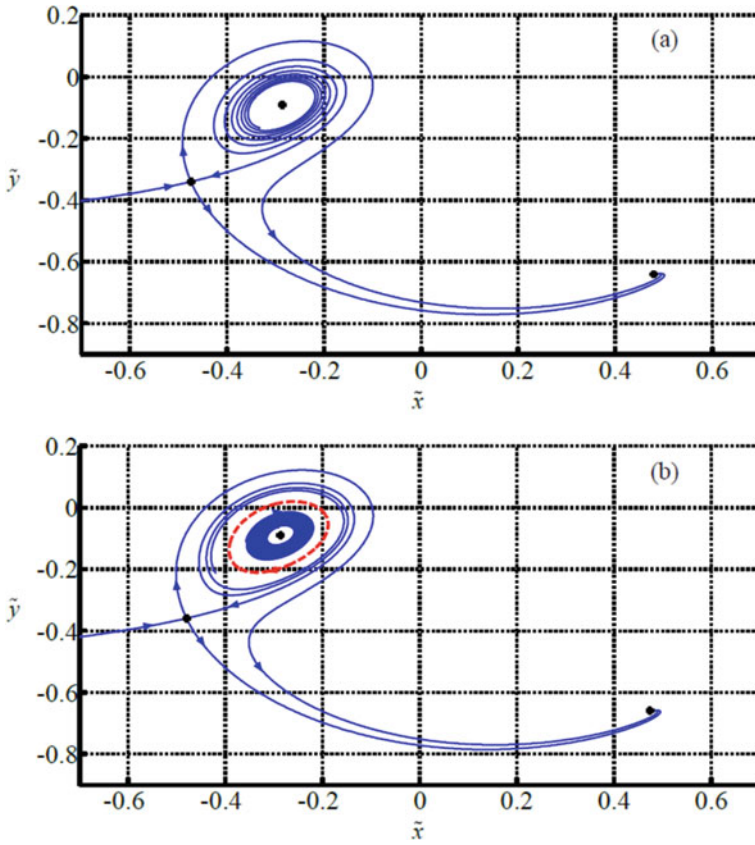


**Fig. 18** Phase portraits corresponding to parameters (96). The fixed points are marked with dots. The dashed loop represents the unstable limit cycle **a**  $d = -0.070$ , **b**  $d = -0.073$

which might be associated to dimensional parameters

$$\left\{ \begin{array}{l} m = 1 \text{ kg} \\ k = 1 \text{ N/m} \\ b = 0.002 \text{ Ns/m} \\ m_1 = 0.001 \text{ kg} \\ \lambda = -4 \text{ N/m}^3 \\ r = 0.1 \text{ m} \\ I = 2.5 \cdot 10^{-3} \text{ m}^2 \text{ kg} \end{array} \right\}, \tag{101}$$

with  $\epsilon = 0.001$ . Equations (66) and (86) yield the values of slopes  $d_H$  and  $d_P$ , depicted in Fig. 20.

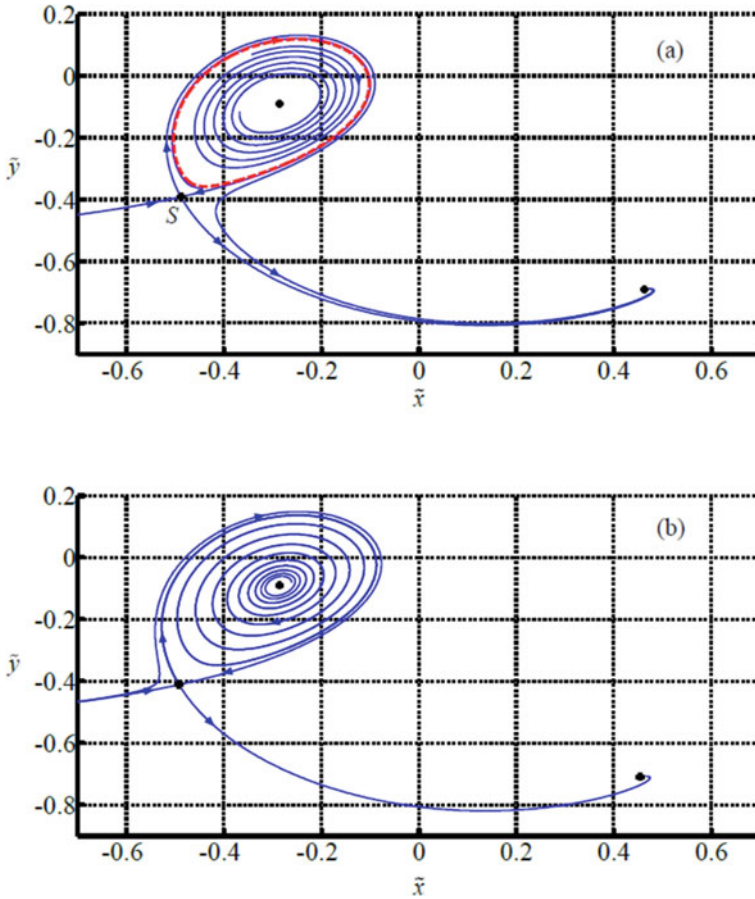
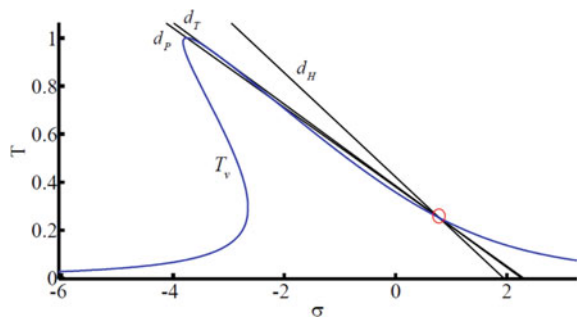


**Fig. 19** Phase portraits corresponding to parameters (96). The fixed points are marked with dots. The dashed loop represents the unstable limit cycle **a**  $d = -0.078$ , **b**  $d = -0.081$

**Fig. 20** Torque curves corresponding to parameters (100)





$$d_H = -0.2165, \quad d_P = -0.1650 \quad (102)$$

Criterion (87) allows characterizing the bifurcation as supercritical. Then, as represented in Fig. 12, it can be assured that a stable limit cycle encircles the unstable equilibrium for  $d > d_H$ , within a certain neighborhood of  $d_H$ . As a matter of fact, the results of Sect. 2.6 can be used here to investigate the range of slopes  $d$  for which the limit cycle exists.

Consider the curve  $T_m$  which intersects  $T_v$  at the fixed point under study and is tangent to curve  $T_v$  at some other point close to the peak. Let  $d_T$  stand for the slope of that particular torque curve, as displayed in Fig. 20. Then, it is straightforward to show that, for  $d_H < d < d_T$ , conditions (89) are fulfilled and, consequently, it can be assured that all system trajectories tend to a periodic orbit. In the case under analysis, we have

$$d_T = -0.1697 \quad (103)$$

Note that the Poincaré-Bendixson Theorem gives sufficient, but not necessary, conditions for the existence of a stable periodic orbit. Thus, it cannot be deduced from the Theorem whether the limit cycle survives or not when  $d > d_T$ . To the end of answering this question, we resort again to a numerical resolution of system (46), for increasing values of  $d$ . The results are displayed in Figs. 21 and 22.

Let us track the evolution of the phase portrait. In Fig. 21a we have  $d < d_H$  and all system trajectories are attracted towards the only fixed point of the system. It may seem from Fig. 21a that trajectories are actually attracted towards a limit cycle surrounding the fixed point. The reason for this false impression is that the attraction of the fixed point is very weak, as it is close to becoming unstable ( $d$  is close to  $d_H$ ). Hence the required time for trajectories to approach the equilibrium is extremely long.

Figure 21b corresponds to  $d_H < d < d_T$ . The Hopf bifurcation has occurred and, therefore, the focus has lost its stability at the same time that a stable limit cycle has appeared around it. Note that, in Fig. 21b, conditions (89) hold. Consequently, all system trajectories are attracted towards a periodic orbit. Actually, Fig. 21b can be observed as a particular example of the general picture shown in Fig. 16.

The numerical results mentioned above are only useful to confirm the analytical developments of previous sections. By contrast, Fig. 22 does provide new information about the global dynamics of the system. It shows that the stable limit cycle is destroyed through a saddle-node homoclinic bifurcation [26], which occurs at  $d = d_T$ . This means that the cycle disappears exactly when conditions (89) are not fulfilled anymore. The mechanism is as follows. At  $d = d_T$  a new fixed point, which immediately splits into a saddle and a node, is created through a saddle-node bifurcation. This new equilibrium appears precisely on the limit cycle, transforming it into a homoclinic orbit. What is found at  $d > d_T$ , as observed in Fig. 22, is that the limit cycle has been replaced by a couple of heteroclinic orbits connecting the saddle and the node.

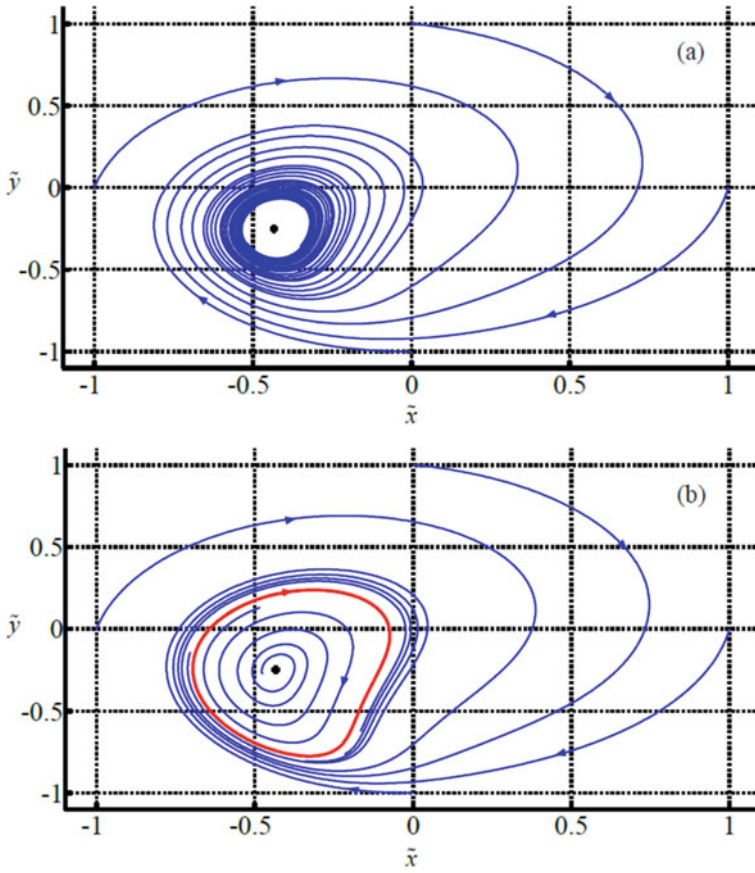
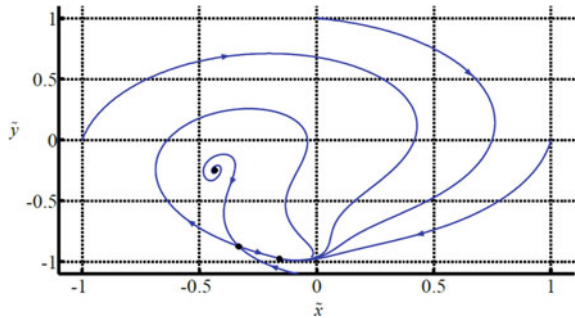


**Fig. 21** Phase portraits corresponding to parameters (100). The fixed points are marked with dots. The solid loop represents the stable limit cycle. **a**  $d = -0.22$ , **b**  $d = -0.19$

**Fig. 22** Phase portraits corresponding to parameters (100), for  $d = -0.169$ . The fixed points are marked with dots



It has been shown that, for the particular set of parameters (100), conditions (89) are necessary and sufficient for the existence of a stable limit cycle. Thus, the periodic orbit never coexists with any other attractor of the system. Nevertheless, it should be stressed that this is not always the case. In fact, cases have also been found where the stable limit cycle is destroyed through a homoclinic bifurcation, just like in the subcritical case. In these situations, the global bifurcation occurs at certain slope  $d_C > d_T$  and, therefore, the limit cycle coexists with a stable equilibrium for  $d_T < d < d_C$ .

As an example, consider a case with  $d_H$  satisfying  $d_T < d_H < d_P$ . Clearly, according to (87), the Hopf bifurcation is supercritical. However, it is not possible for the limit cycle to be destroyed through a saddle-node homoclinic bifurcation, because the saddle and the node are created before the limit cycle. In fact, in these cases, the closed orbit has been found to die in the same way as the unstable limit cycle shown in Fig. 19., i.e. through a homoclinic bifurcation due to the presence of a saddle point.

In summary, the simulations carried out suggest that, while unstable limit cycles are destroyed by homoclinic bifurcations, the stable ones can disappear either through homoclinic bifurcations or saddle-node homoclinic bifurcations.

### 3.2 Numerical Validation of Analytical Results

#### A Subcritical Case

Consider again the set of parameters given at (96), which gives rise to a subcritical Hopf bifurcation, as depicted in Figs. 18 and 19. Two different scenarios are studied, corresponding to the following slopes of the motor characteristic:

$$d_1 = -0.078, \quad d_2 = -0.070. \quad (104)$$

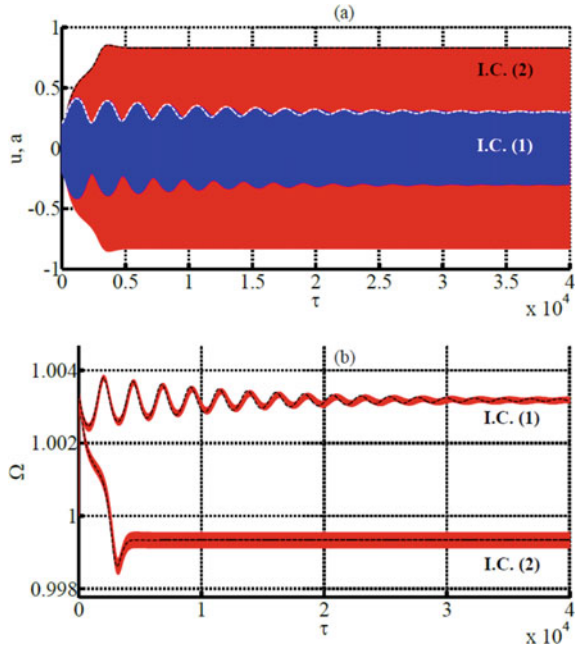
By comparing (104) with Figs. 18 and 19, it can be verified that, for  $d = d_1$ , the system has a stable focus surrounded by an unstable limit cycle, while, at  $d = d_2$ , the focus has become unstable through a Hopf bifurcation. As pointed out in Sect. 3.1, the unstable limit cycle for  $d = d_1$  is the boundary which separates the basins of attraction of the two attracting fixed points present in the system—see Fig. 19a.

For  $d = d_1$ , two sets of initial conditions, I.C. (1) and I.C. (2), are selected, outside and inside the limit cycle, respectively:

$$\text{I.C.}(1) \left\{ \begin{array}{l} a_0 = 0.2 \\ \beta_0^* = -2.8 \end{array} \right\}, \quad \text{I.C.}(2) \left\{ \begin{array}{l} a_0 = 0.1 \\ \beta_0^* = -2.8 \end{array} \right\}. \quad (105)$$

Then, by using relations (47), corresponding initial conditions for the original system can be computed:

**Fig. 23** Comparison of numerical solutions of the original (solid line) and reduced (dashed line) systems for parameters (96),  $\epsilon = 10^{-3}$  and  $d = d_1 = -0.078$ . **a** Displacements **b** Rotor Speed



$$\text{I.C. (1)} \begin{Bmatrix} u_0 = 0.2 \\ \dot{u}_0 = 0 \\ \phi_0 = 2.8 \\ \dot{\phi}_0 = 1 \end{Bmatrix}, \quad \text{I.C. (2)} \begin{Bmatrix} u_0 = 0.1 \\ \dot{u}_0 = 0 \\ \phi_0 = 2.8 \\ \dot{\phi}_0 = 1 \end{Bmatrix}. \quad (106)$$

Note that this step has not a unique solution, because different sets of original initial conditions can produce the same reduced initial conditions.

The obtained numerical solutions are shown in Fig. 23, for  $\epsilon = 10^{-3}$ . A good agreement between solutions of both systems is observed. Clearly, the two considered sets of initial conditions lead the system to different attractors.

It is convenient to make here an observation about the size of parameter  $\epsilon$ . The procedure used in Sect. 2 to transform the original system into a simpler reduced system is based on perturbation methods. These techniques are useful for dynamical systems containing a small parameter  $\epsilon$ , and they explain how such systems behave for a sufficiently small  $\epsilon$ . This means that the smaller  $\epsilon$  is, the more accurate perturbation predictions are. Figure 23 shows that, for the case under consideration, a value of  $\epsilon = 10^{-3}$  gives a remarkable accordance between solutions of the original and reduced system. As an illustrative example, the same numerical computation is done, for initial conditions I.C. (2) and  $\epsilon = 10^{-2}$ . This larger  $\epsilon$  gives rise to a less accurate prediction, as displayed in Fig. 24. The required  $\epsilon$  to have an accurate result depends on the case under study. For instance, in the following simulation (Fig. 25), it was

**Fig. 24** Comparison of numerical solutions of the original (solid line) and reduced (dashed line) systems for parameters (96), initial conditions I. C. (2),  $\epsilon = 10^{-2}$  and  $d = d_1 = -0.078$ . **a** Displacements **b** Rotor Speed

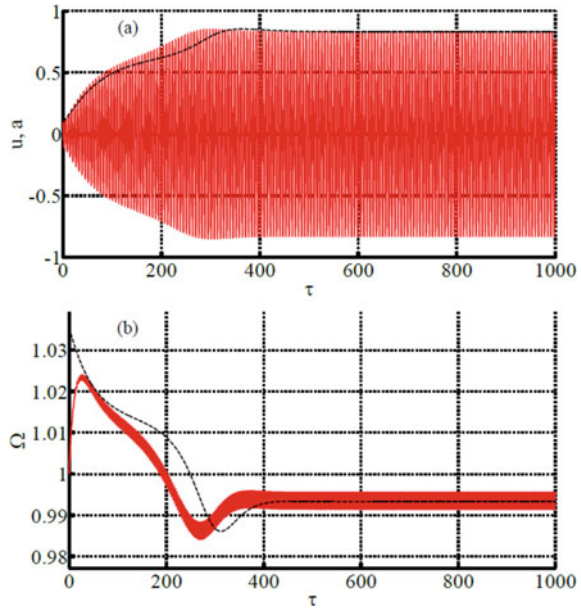
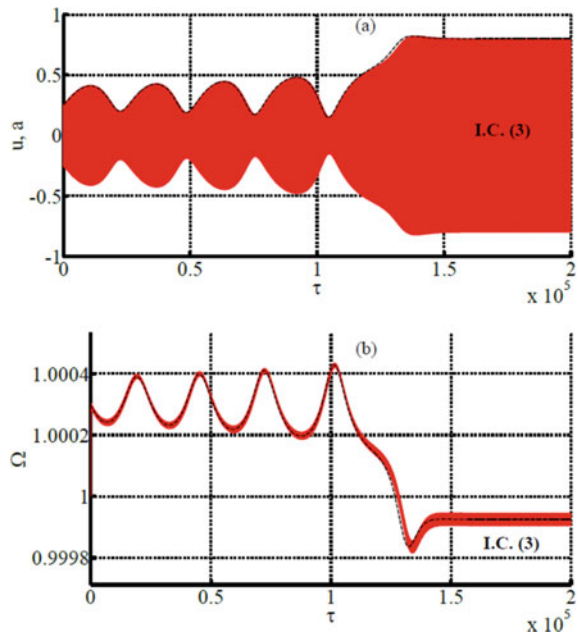


**Fig. 25** Comparison of numerical solutions of the original (solid line) and reduced (dashed line) systems for parameters (96),  $\epsilon = 10^{-4}$  and  $d = d_2 = -0.070$ . **a** Displacements **b** Rotor speed



necessary to take  $\epsilon = 10^{-4}$  for a good matching between solutions of the exact and approximate systems. However, in the majority of simulations conducted within this work,  $\epsilon = 10^{-3}$  proved to be small enough.

Consider now the case  $d = d_2$  where, according to Fig. 18a, the focus is unstable and there is a unique attracting fixed point in the system. Initial conditions

$$\text{I.C.}(3) \left\{ \begin{array}{l} a_0 = 0.25 \\ \beta_0^* = -2.65 \end{array} \right\} \quad (107)$$

are selected for the reduced system, from which corresponding initial conditions for the original system can be obtained:

$$\text{I.C.}(3) \left\{ \begin{array}{l} u_0 = 0.25 \\ \dot{u}_0 = 0 \\ \phi_0 = 2.65 \\ \dot{\phi}_0 = 1 \end{array} \right\}. \quad (108)$$

The original and reduced systems are numerically solved with  $\epsilon = 10^{-4}$  and initial conditions (108) and (107) respectively. The results are displayed in Fig. 25, where it is clearly observed how the system moves away from the unstable focus, as the oscillation amplitude increases, until it is attracted to the stable node.

### A Supercritical Case

In order to observe limit cycle oscillations in the original system, we need to consider a case where a supercritical Hopf bifurcation occurs, giving birth to a stable limit cycle. Thus, consider again the set of parameters given at (100) and a motor characteristic with slope  $d = -0.19$ , which corresponds to the phase portrait exhibited in Fig. 21b. With these parameters, the original system of Eq. (10) is numerically solved for  $\epsilon = 10^{-3}$  and initial conditions

$$\left\{ \begin{array}{l} u_0 = 0.1 \\ \dot{u}_0 = 0 \\ \phi_0 = 0 \\ \dot{\phi}_0 = 0 \end{array} \right\}. \quad (109)$$

The reduced system (46) is numerically integrated as well for comparison. The associated initial conditions for the reduced system can be computed with the aid of relations (47):

$$\left\{ \begin{array}{l} a_0 = 0.1 \\ \beta_0^* = 5.263 \end{array} \right\}. \quad (110)$$

With these sets of initial conditions, the obtained results for both systems are represented in Figs. 26 and 27, exhibiting very good agreement.

It is worth stressing that, as depicted in Figs. 26 and 27, a new kind of behaviour has been found for the mechanical system under study, which consists in a vibratory motion of the structure with slowly oscillating amplitude, due to the nonideal interaction between exciter and vibrating system. The periodic solutions of the averaged system correspond to quasiperiodic solutions of the original one.

This type of motion had not been addressed before, to the authors' knowledge, in the literature about nonideal excitations. Note that the LCOs give rise, in this case, to very large variations of the amplitude. Thus, the effect of the studied instability may be of great importance in real applications.

**Fig. 26** Comparison of displacements obtained by numerical resolution of the original (solid line) and reduced (dashed line) systems for parameters (100),  $\epsilon = 10^{-3}$  and  $d = -0.19$

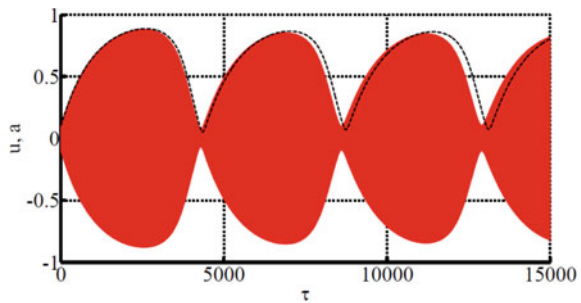
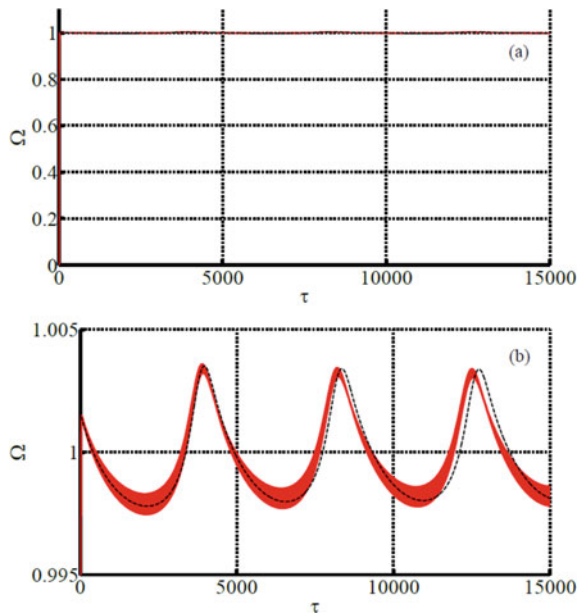


**Fig. 27** Comparison of the rotor speed obtained by numerical resolution of the original (solid line) and reduced (dashed line) systems for parameters (100),  $\epsilon = 10^{-3}$  and  $d = -0.19$  **a** Full view **b** Close-up around resonance



## 4 Summary and Conclusions

The present chapter contains a detailed analytical and numerical investigation of the dynamics of a 2-DOF mechanical system, consisting in an unbalanced motor connected to a fixed frame through a nonlinear spring and a linear damper. This model intends to constitute a simplified representation of a general unbalanced rotating machine, with the purpose of analyzing the kinds of nonlinear behavior that might be found in real applications.

In addition to the nonlinearity of the spring, a peculiar type of nonlinearity appears if the excitation is nonideal, i.e. if there is a significant bidirectional interaction between the system vibration and the rotation of the motor. The combination of these two types of nonlinearity gives rise to a rich dynamic behavior that can be studied analytically and numerically.

The main contributions presented in this chapter are summarized below.

- A novel analytical approach to the problem, which combines an averaging procedure with the Singular Perturbation Theory (SPT), has been proposed. It is worth stressing that, although both the SPT and the Averaging Method are actually classical in nonlinear dynamics, they had not been used together before in the context of nonideal excitations. Thanks to this novel combination of perturbation techniques, the original 4D system is transformed into a reduced 2D system, much easier to analyse.
- The conditions for stability of equilibria of the reduced system have been analytically derived. Transcritical and Hopf bifurcations have been found. The Hopf bifurcation is particularly relevant, for it gives rise to a smaller stable region than predicted by conventional theories. Consequently, not taking it into account may be perilous for real applications, since unexpected instabilities could occur.
- The Hopf bifurcations have been analytically investigated, in order to characterize them as subcritical or supercritical. A very simple criterion, with clear graphical interpretation, has been obtained to distinguish both types of bifurcations.
- The Poincaré-Bendixson Theorem has been used to find conditions under which all trajectories in the averaged system are attracted towards a periodic orbit, corresponding to a quasiperiodic solution of the original system.
- The global bifurcations destroying the stable and unstable limit cycles have been numerically investigated. These simulations suggest that unstable LCOs are destroyed through homoclinic bifurcations, while stable LCOs can be destroyed either through homoclinic bifurcations or through saddle-node homoclinic bifurcations.
- When an unstable limit cycle exists, the system exhibits two stable equilibrium points, whose domains of attraction are clearly delimited by the periodic orbit.
- The presence of LCOs in the problem under study has been confirmed by numerically solving the original system of equations. An excellent agreement between the solutions of the original and reduced systems has been found. In addition, numerical results show that LCOs can produce very significant variations in the



vibration amplitude, which suggests that the addressed instability might be of great relevance in real applications.

- All the analytical developments presented here have been validated by comparing numerical solutions of the original and reduced systems. In particular, the Hopf bifurcation existence has been numerically proved, not only for the reduced system, but, more importantly, also for the original system of equations.

## Appendix

This section provides the expressions of parameters  $f_{ij}$  and  $g_{ij}$  in Eq. (80). These are simply the coefficients of the nonlinear terms of system (79), which result when system (73) is transformed according to change of variables (76),

$$f_{20} = -\frac{3\rho a R}{4c_2}(3c_1^2 + c_2^2) - 2c_1\left(\frac{2\xi}{aR} + \frac{3}{4}\rho a^2\right) \quad (\text{A.1})$$

$$f_{02} = -\frac{9\rho a R \omega_0^2}{4c_2} \quad (\text{A.2})$$

$$f_{11} = -\frac{3}{4}\rho\omega_0 a\left(a + 3R\frac{c_1}{c_2}\right) - \frac{2\xi\omega_0}{aR} \quad (\text{A.3})$$

$$f_{30} = \frac{9\rho c_1}{4c_2}(c_1^2 + c_2^2) \quad (\text{A.4})$$

$$f_{03} = \frac{9\rho\omega_0^3}{4c_2} \quad (\text{A.5})$$

$$f_{21} = \frac{3\rho\omega_0}{4c_2}(3c_1^2 + c_2^2) \quad (\text{A.6})$$

$$f_{12} = \frac{9c_1\rho\omega_0^2}{4c_2} \quad (\text{A.7})$$

$$g_{20} = \frac{(c_1^2 + c_2^2)}{\omega_0} \left[ \frac{9\rho a}{4} \left( R\frac{c_1}{c_2} + a \right) + \frac{4\xi}{aR} \right] \quad (\text{A.8})$$

$$g_{02} = \frac{3\rho\omega_0 a}{4} \left( a + 3R\frac{c_1}{c_2} \right) \quad (\text{A.9})$$

$$g_{11} = \frac{3}{2}\rho a^2 c_1 + \frac{3\rho a R}{4c_2}(3c_1^2 + c_2^2) + \frac{2\xi c_1}{aR} \quad (\text{A.10})$$

$$g_{30} = -\frac{9\rho}{4\omega_0 c_2} (c_1^2 + c_2^2)^2 \quad (\text{A.11})$$

$$g_{03} = -\frac{9c_1 \rho \omega_0^2}{4c_2} \quad (\text{A.12})$$

$$g_{21} = -\frac{9c_1 \rho}{4c_2} (c_1^2 + c_2^2) \quad (\text{A.13})$$

$$g_{12} = -\frac{3\rho\omega_0}{4c_2} (3c_1^2 + c_2^2), \quad (\text{A.14})$$

where  $a_{eq}$  and  $R_{eq}$  have been shortly written as  $a$  and  $R$ , respectively.

## References

- González-Carbajal, J., Domínguez, J.: Limit cycles in nonlinear vibrating systems excited by a nonideal energy source with a large slope characteristic. *Nonlinear Dyn.* (2017). <https://doi.org/10.1007/s11071-016-3120-7>
- González-Carbajal, J., Domínguez, J.: Nonlinear vibrating systems excited by a nonideal energy source with a large slope Characteristic. *Mech. Syst. Signal Process* (2017)
- Boyaci, A., Lu, D., Schweizer, B.: Stability and bifurcation phenomena of Laval/Jeffcott rotors in semi-floating ring bearings. *Nonlinear Dyn.* **79**, 1535–1561 (2015). <https://doi.org/10.1007/s11071-014-1759-5>
- Yang, J., Gao, Y., Liu, Z., et al.: A method for modeling and analyzing the rotor dynamics of a locomotive turbocharger. *Nonlinear Dyn.* **84**, 287–293 (2016). <https://doi.org/10.1007/s11071-015-2497-z>
- Shabana, A.A.: *Theory of Vibration (An Introduction)* (1996)
- Xu, M., Marangoni, R.D.: Vibration analysis of a motor-flexible coupling-rotor system subject to Misalignment and unbalance, Part I: theoretical model and analysis. *J. Sound Vib.* **176**, 663–679 (1994)
- Thomson, W.T.: *Theory of Vibration with Applications* (1996)
- Sommerfeld, A.: *Naturwissenschaftliche Ergebnisse der Neuren Technischen Mechanik*. Verein Dtsch Ing Zeitschrift **18**, 631–636 (1904). <https://doi.org/10.1109/COC.2000.873973>
- Nayfeh, A.H., Mook, D.T.: *Nonlinear Oscillations*. John Wiley and Sons (1995)
- Kononenko, V.O.: *Vibrating Systems with a Limited Power Supply*. Illife, London (1969)
- Rand, R.H., Kinsey, R.J., Mingori, D.L.: Dynamics of spinup through resonance. *Int. J. Non. Linear Mech.* **27**, 489–502 (1992). [https://doi.org/10.1016/0020-7462\(92\)90015-Y](https://doi.org/10.1016/0020-7462(92)90015-Y)
- Blekhman, I.I.: *Vibrational Mechanics-Nonlinear Dynamic Effects, General Approach*. Singapore (2000)
- El-Badawy, A.A.: Behavioral investigation of a nonlinear nonideal vibrating system. *J. Vib. Control* **13**, 203–217 (2007). <https://doi.org/10.1177/1077546307073674>
- Bolla, M.R., Balthazar, J.M., Felix, J.L.P., Mook, D.T.: On an approximate analytical solution to a nonlinear vibrating problem , excited by a nonideal motor. *Nonlinear Dyn.*, 841–847 (2007). <https://doi.org/10.1007/s11071-007-9232-3>
- Balthazar, J.M., Mook, D.T., Weber, H.I., et al.: An overview on non-Ideal vibrations. *Meccanica* **38**, 613–621 (2003)
- Mettler, E.: *Handbook of Engineering Mechanics*. McGraw-Hill, New York (1962)

17. Dimentberg, M.F., Mcgovern, L., Norton, R.L. et al.: Dynamics of an unbalanced shaft interacting with a limited power Supply. *Nonlinear Dyn.*, 171–187 (1997). <https://doi.org/10.1023/a:1008205012232>
18. Sanders, J.A., Verhulst, F., Murdock, J.: *Averaging Methods in Nonlinear Dynamical Systems*. Springer, New York (2007)
19. Fidlin, A.: *Nonlinear Oscillations in Mechanical Engineering*. Springer-Verlag, Berlin, Heidelberg (2006)
20. Hunter, J.K.: *Asymptotic analysis and singular perturbation theory*. Dep. Math. Univ. Calif. Davis (2004)
21. Lesne, A.: *Multi-scale approaches*. Lab Phys la Matière Condens Univ Pierre Marie Curie (2006)
22. Verhulst, F., Bakri, T.: The dynamics of slow manifolds. *J. Indones Math. Soc.*, 1–16 (2006)
23. Brennan, M.J., Kovacic, I., Carrella, A., Waters, T.P.: On the jump-up and jump-down frequencies of the Duffing oscillator. *J. Sound Vib.* **318**, 1250–1261 (2008). <https://doi.org/10.1016/j.jsv.2008.04.032>
24. Thomsen, J.J.: *Vibrations and Stability*. Heidelberg, New York, Berlin (2003)
25. Habib, G., Kerschen, G.: Suppression of limit cycle oscillations using the nonlinear tuned vibration absorber. *Proc. R Soc.* (2015)
26. Kuznetsov, Y.A.: *Elements of Applied Bifurcation Theory*. Second Edition, New York (1998)
27. Guckenheimer, J., Holmes, P.: *Nonlinear Oscillations, Dynamical Systems, and Bifurcations of Vector Fields*. Springer, New York, New York, NY (1983)
28. Perko, L.: *Differential Equations and Dynamical Systems*, 3rd edn. Springer, New York (2001)

# **Nonlinear Dynamics of RNIS, Control of RNIS and Harvester Energy of RNIS**

# Nonlinear Control Applied in Jump Attenuation of a Non-ideal System



A. M. Tuset , A. Kossoski , A. M. Bueno , Jose Manoel Balthazar ,  
J. L. P. Felix , A. Cunha Jr , and R. H. Avanço 

**Abstract** This work proposes the attenuation of the Sommerfeld effect (jump phenomenon) present in a non-ideal oscillator through the use of different nonlinear controllers. The non-ideal system is composed of a beam-like mechanical structure excited by a limited power supply, in this case an unbalanced direct current motor. Two different control techniques are considered. The first controller has its feedback gain obtained through the SDRE (State-Dependent Riccati Equation) technique in conjunction with a feedforward gain. The second controller is based in the SMC (Sliding Mode Control) technique. Numerical simulations show that the two proposed control strategies are effective in suppressing the jump phenomenon, and thus keeping the structure vibration of the studied system at desirable levels.

**Keywords** Non-ideal system · SDRE control · Sliding Mode Control · Sommerfeld effect

---

A. M. Tuset (✉)  
Federal University of Technology, Paraná, Brazil

A. Kossoski · A. M. Bueno · J. M. Balthazar  
Sao Paulo State University, São Paulo, Brazil  
e-mail: [atila.bueno@unesp.br](mailto:atila.bueno@unesp.br)

J. L. P. Felix  
Federal University of Pampa, Rio Grande do Sul, Brazil  
e-mail: [jorge.felix@unipampa.edu.br](mailto:jorge.felix@unipampa.edu.br)

A. Cunha Jr  
Rio de Janeiro State University, Rio de Janeiro, Brazil  
e-mail: [americo.cunha@uerj.br](mailto:americo.cunha@uerj.br)

R. H. Avanço  
Federal University of Maranhão, Maranhão, Brazil

## 1 Introduction

The Sommerfeld effect is a resonance phenomenon that arises from the interaction between a non-ideal energy source with the mechanical structure. The energy source influences the mechanical structure, which in turn influences and exchanges energy with the source, in a two-way effect. The nomenclature of non-ideal energy source comes from the fact that the power supply provides limited energy to the system, thus being a characteristic of all real energy sources [1–6].

The first researcher who studied this phenomenon was Arnould Sommerfeld in 1902 [7]. Through a simple experiment, which consisted of an unbalanced DC electric motor fixed on a table, Sommerfeld realized that as the motor rotational speed approached the critical speed of the mechanical structure, the increase in voltage no longer corresponded to the increase in motor speed, but the vibration amplitudes continued to increase. This behavior was not expected, as direct current motors have their angular speed directly proportional to the armature voltage. Moreover, this behavior quickly changes when the system reaches a critical point, where the vibration amplitudes suddenly drop to low levels and the motor speed increases return to the values corresponding to the applied voltage, thus generating a jump phenomenon in the vibration amplitude graphs in relation to the motor angular velocity [2, 4, 8–10].

Some works have proposed methodologies to suppress the jump effect, because this effect if is unwanted as it represents a loss of system energy, as well as resulting in an amplification of the mechanical vibrations. Reference [11] proposed to include a friction element in a non-ideal structural system to eliminate the Sommerfeld effect. In [4] is considered a semi-active control using a magnetorheological damper for reducing the resonance vibrations of a non-ideal structure in an active way. Reference [12] considered a shape-memory alloy to attenuate the vibration and Sommerfeld effect of a non-ideal type oscillator. In [13] is considered a snap-through truss absorber for attenuation of the jump phenomenon in an oscillator under excitation of an electric motor with an eccentricity and limited power.

In this work is proposed the use of an active control in order to attenuate the Sommerfeld effect and the vibration amplitudes of a non-ideal mechanical oscillator. The NIS studied is composed of a beam and an unbalanced electric motor with limited power supply. For the active control of the system are considered two techniques. The first being a controller that uses a portion of feedback gain and another portion of feedforward gain and the second controller is based in the sliding mode control technique.

## 2 Mathematical Model

Figure 1a shows the mechanical part of the non-ideal system. In this figure,  $m_1$  is the mass of the cart with the motor,  $m_2$  is the motor unbalance mass,  $r$  is the length of the unbalance axis and  $\varphi$  is the position angle of the motor shaft.  $k$  and  $c$  represent

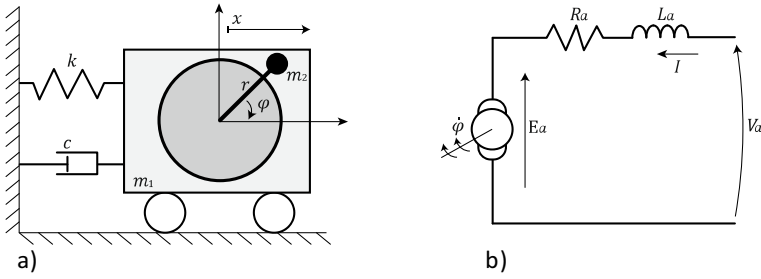


**Fig. 1** a Non-ideal mechanical system (NIS). b electrical schematic representation of the DC motor

the stiffness and damping of the mechanical structure, respectively. Motor unbalance will cause vibration, with displacement  $x$  [4, 9, 14, 15].

The mathematical model that represents the dynamics of the system shown in Fig. 1 is developed using Lagrange’s energy method, where the Lagrange’s function is expressed as:

$$L = E_k - E_p \tag{1}$$

where  $E_k$  is the kinetic energy, and  $E_p$  is the potential energy. The equations of motion can be obtained through the Euler–Lagrange equation, given by:

$$\frac{d}{dt} \left( \frac{\partial L}{\partial \dot{Q}_i} \right) - \frac{\partial L}{\partial Q_i} = \mathcal{T}_i \tag{2}$$

where  $i = 1, 2, \dots, N$ .  $N$  is the number of degrees-of-freedom,  $\mathcal{T}_i$ ’s are the non-conservatives forces,  $Q_i$ ’s are the generalized coordinates, being that  $Q_1 = x$ , and  $Q_2 = \varphi$ .

The kinetic energy is given by:

$$E_k = \frac{1}{2} m_1 \dot{x}^2 + \frac{1}{2} J \dot{\varphi}^2 + \frac{1}{2} m_2 ((\dot{x} - \dot{\varphi} r \sin(\varphi))^2 + (\dot{\varphi} r \cos(\varphi))^2) \tag{3}$$

where:  $J$  is the moment of inertia,  $\dot{\varphi}$  is the rotational speed,  $m_2$  is the unbalanced mass.

The potential energy is given by:

$$E_p = \frac{1}{2} k x^2 \tag{4}$$

The non-conservatives forces are given by:

$$\mathcal{T}_1 = -c \dot{x} \tag{5}$$

Substituting Eqs. (3), (4) into Eq. (1), and substituting the result accounting for Eq. (5) into Eq. (2), we obtain:

$$\begin{aligned} M\ddot{x} + c\dot{x} + kx &= mr(\dot{\varphi}^2 \sin(\varphi) + \ddot{\varphi} \cos(\varphi)) \\ (J + mr^2)\ddot{\varphi} &= mrx \cos(\varphi) + T_e \end{aligned} \quad (6)$$

where:  $M = m_1 + m_2$

The electrical part, shown in Fig. 1b, refers to the circuit of a direct current motor. In this circuit,  $V_a$  is the applied armature voltage,  $I$  is the armature current.  $R_a$  and  $L_a$  are the resistance and inductance of the armature, respectively.  $E_A$  is the counter-electromotive force (CEMF) and in the case of constant flux can be directly related to the rotational speed of the motor as  $E_a = k_e \dot{\varphi}$ , where  $k_e$  is the electrical constant. Using the Kirchhoff's circuit laws will have:

$$V_a = R_a I + L_a \dot{I} + E_a \quad (7)$$

This is the voltage equation for the armature circuit of a DC motor. To obtain the motor torque equation, it is necessary to analyze its mechanical structure, where the torque experienced by the motor windings  $T_e$  can be directly related to the armature current as  $T_e = k_t I$ , where  $k_t$  is the torque constant. The equation of motion for a DC motor is given by:

$$T_e = J\ddot{\varphi} + b\dot{\varphi} + T_l \quad (8)$$

where:  $J$  is the inertia,  $b$  is the coefficient of viscous friction and  $T_l$  is the load torque. In this paper  $T_l$  will be neglected.

Coupling the elements of inertia, as well as relating the displacement of the mechanical structure to the angular displacement of the motor, it is possible to obtain the following set of equations, this being the set of dynamic nonlinear equations for the non-ideal system shown in Fig. 1.

$$\begin{aligned} M\ddot{x} + c\dot{x} + kx &= mr(\dot{\varphi}^2 \sin(\varphi) + \ddot{\varphi} \cos(\varphi)) \\ (J + mr^2)\ddot{\varphi} &= mrx \cos(\varphi) + k_t I \\ L_a \dot{I} &= R_a I - k_e I + V_a \end{aligned} \quad (9)$$

Equation (9) can be written in state-space notation as follows:

$$\begin{aligned} \dot{x}_1 &= x_2 \\ \dot{x}_2 &= \Delta(\alpha_1 x_5 \cos(x_3) - \alpha_2 x_4^2 \sin(x_3) - \alpha_3 x_2 - \alpha_4 x_1) \\ \dot{x}_3 &= x_4 \\ \dot{x}_4 &= \Delta(-\beta_1 x_4^2 \sin(x_3) \cos(x_3) - \beta_2 x_2 \cos(x_3) - b_3 x_1 \cos(x_3) + \beta_4 x_5) \end{aligned}$$



$$\dot{x}_5 = -c_1x_5 - c_2x_4 + c_3 \tag{10}$$

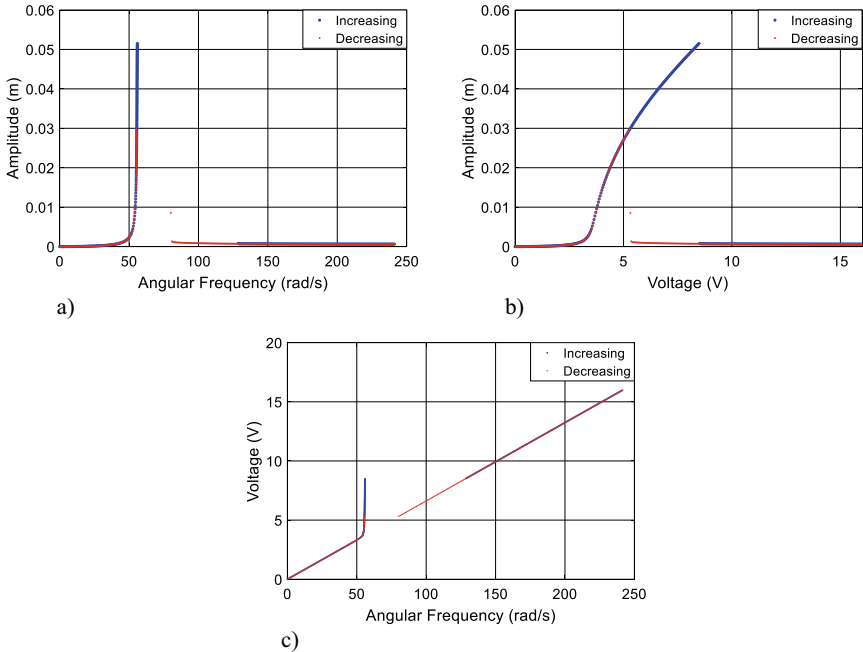
where:  $x_1 = x, x_2 = \dot{x}, x_3 = \varphi, x_4 = \dot{\varphi}, x_5 = I, \alpha_1 = k_tmr, \alpha_2 = m^2r^3 + Jmr, \alpha_3 = cmr^2 + cJ, \alpha_4 = kmr^2 + kJ, \alpha_5 = Mmr^2 + JM, \beta_1 = m^2r^2, \beta_2 = cmr, \beta_3 = kmr, \beta_4 = Mk_t, c_1 = \frac{R_a}{L_a}, c_2 = \frac{k_e}{L_a}, c_3 = \frac{V}{L_a}$  and  $\Delta = \frac{1}{-\beta_1 \cos(x_3)^2 + \alpha_5}$ .

### 3 Numerical Simulations

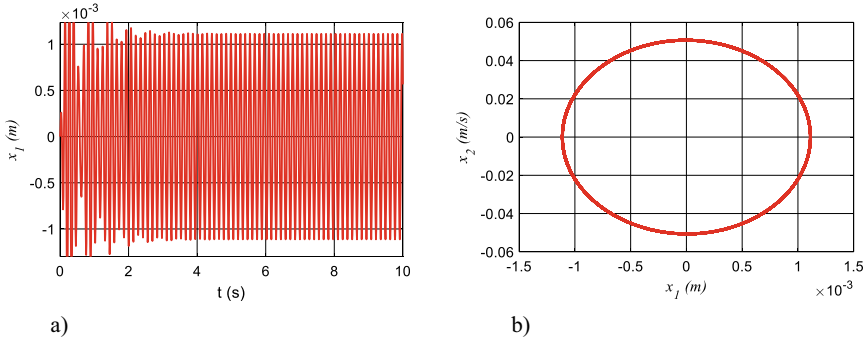
The numerical simulations are carried out accounting for the following parameters:  $m_1 = 0.13, m_2 = 0.005, k = 399, c = 0.077, t = 0.015, R_a = 51, J = 9 \times 10^{-7}, J = 2.82 \times 10^{-6}, L_a = 0.004, k_t = 0.0663$  and  $k_m = 0.0663$ .

Figure 2 shows the results for the jump phenomenon according to the motor shaft angular frequency and the voltage applied to the armature.

Considering the process of increasing the electrical voltage (V), the jump phenomenon occurs when the motor reaches 56 rad/s and 8.5 V. After this point, if the voltage increase is maintained, the system returns to the linear and normal operation expected. Due to the effect of the coupling between the motor and the



**Fig. 2** Jump phenomenon. **a** Frequency response diagram. **b** Jump phenomenon due to the applied voltage in the DC motor. **c** Angular frequency response by voltage



**Fig. 3** Dynamics of the systems considering  $x_1$ . **a** Time history. **b** Phase plane for  $x_1$  versus  $x_2$

mechanical structure, the system has its operation weakened and it is realized that between 3.5 and 8.5 V all the increase of voltage in the motor serves almost solely to increase the amplitudes of vibration and not the rotation of the motor. This disruption of the direct relationship between electrical voltage and motor rotation can be clearly seen in Fig. 2c. The effect of converting electrical energy into mechanical vibration can also be observed during the process of decreasing the electrical voltage. However, as this is a non-linear system and that it depends on its initial conditions, the Sommerfeld effect of the voltage decrease process occurs at a different point than that of the increasing voltage process, in this case occurring when the motor reaches 55.5 rad/s and 5.3 V. This conversion of electrical energy into mechanical vibration energy is one of the biggest problems of this type of system, being responsible for reducing the efficiency of the electric motor, as well as reducing the angular frequencies available for the project.

In Fig. 3 it is possible to observe the behavior of the system (11), considering a voltage of 3 V applied to the DC motor.

As can be seen in Fig. 3, when the motor is powered with 3 V, the vibrations of the structure are low, showing a periodic behavior with a unit period after the transient period.

Considering the behavior of  $x_1$  shown in Fig. 3, the following displacement equation for  $x_1$  can be determined:

$$\begin{aligned} \tilde{x}_1 &= 0.001113 \sin(44.88t) \\ \tilde{x}_2 &= 0.05 \cos(44.88t) \end{aligned} \tag{11}$$

### 3.1 Nonlinear Control Project

Considering that the objective is to eliminate the Sommerfeld effect observed in  $x_1$ , the following control signal ( $U$ ) can be introduced in Eq. (10) [9, 14, 16, 17]:

$$\begin{aligned}
 \dot{x}_1 &= x_2 \\
 \dot{x}_2 &= \Delta(\alpha_1 x_5 \cos(x_3) - \alpha_2 x_4^2 \sin(x_3) - \alpha_3 x_2 - \alpha_4 x_1) + U \\
 \dot{x}_3 &= x_4 \\
 \dot{x}_4 &= \Delta(-\beta_1 x_4^2 \sin(x_3) \cos(x_3) - \beta_2 x_2 \cos(x_3) - b_3 x_1 \cos(x_3) + \beta_4 x_5) \\
 \dot{x}_5 &= -c_1 x_5 - c_2 x_4 + c_3
 \end{aligned} \tag{12}$$

Since the objective of the control signal ( $U$ ) is to control the displacement of  $x_1$ , the control design can be obtained by considering only the first two equations of (12). In addition, the states  $x_3$ ,  $x_4$  and  $x_5$  will be considered disturbances in the system [9].

$$\begin{aligned}
 \dot{x}_1 &= x_2 \\
 \dot{x}_2 &= \Delta(\alpha_1 x_5 \cos(x_3) - \alpha_2 x_4^2 \sin(x_3) - \alpha_3 x_2 - \alpha_4 x_1) + U
 \end{aligned} \tag{13}$$

### 3.2 Proposed SDRE Control

The vector control  $U$  for the Optimal Linear feedback control consists of two parts:  $U = \tilde{u} + u$ , where  $u$  is the optimal feedback control and  $\tilde{u}$  is the feedforward control gain, the last one responsible for maintaining the system in the desired trajectory. The feedforward gain is given by:

$$\tilde{u} = -\Delta(\alpha_1 x_5 \cos(x_3) - \alpha_2 x_4^2 \sin(x_3) - \alpha_3 \tilde{x}_2 - \alpha_4 \tilde{x}_1) \tag{14}$$

Substituting Eq. (14) into Eq. (13), and defining the deviation of the desired trajectory as:

$$e = \begin{bmatrix} x_1 - \tilde{x}_1 \\ x_2 - \tilde{x}_2 \end{bmatrix} \tag{15}$$

where  $\tilde{x}_1$  and  $\tilde{x}_2$  are the trajectories desired. The system can be represented in the following form:

$$\begin{aligned}
 \dot{e}_1 &= e_2 \\
 \dot{e}_2 &= -\Delta\alpha_3 e_2 - \Delta\alpha_4 e_1 + u
 \end{aligned} \tag{16}$$

Or in matrix form as:

$$\mathbf{P} = \mathbf{Ae} + \mathbf{Bu} \quad (17)$$

The control  $\mathbf{u}$  is optimal and it transfers the nonlinear system of Eq. (16) from any initial state to the final state  $\mathbf{e}(\infty) = 0$ .

Minimizing the cost functional to:

$$J = \int_0^{\infty} (\mathbf{e}^T \mathbf{Qe} + \mathbf{u}^T \mathbf{Ru}) dt \quad (18)$$

the control  $\mathbf{u}$  can be found solving the following equation:

$$\mathbf{u} = -\mathbf{R}^{-1} \mathbf{B}^T \mathbf{Pe} \quad (19)$$

Being  $\mathbf{P}$  a symmetric matrix, the Algebraic Riccati Equation is developed, denoted by:

$$\mathbf{PA} + \mathbf{A}^T \mathbf{P} - \mathbf{PBR}^{-1} \mathbf{B}^T \mathbf{P} + \mathbf{Q} = \mathbf{0} \quad (20)$$

The matrices  $\mathbf{A}$  and  $\mathbf{B}$  may be represented by:

$$\mathbf{A} = \begin{bmatrix} 0 & 1 \\ -\Delta\alpha_4 & -\Delta\alpha_3 \end{bmatrix}, \mathbf{B} = \begin{bmatrix} 0 \\ 1 \end{bmatrix} \text{ and by definition: } \mathbf{Q} = 10^4 \begin{bmatrix} 10^3 & 0 \\ 0 & 1 \end{bmatrix} \text{ and } \mathbf{R} = 10^{-4}.$$

In Figs. 4, it is observed the jump phenomenon suppression using the proposed control  $U = \tilde{u} + u$ , considering  $\tilde{x}_1$  and  $\tilde{x}_2$  obtained in the Eq. (11).

As can be seen in the results presented in Fig. 4, using the proposed control ( $U = \tilde{u} + u$ ), it is possible to eliminate the jump effect, keeping the displacements in the desired amplitude and frequency.

### 3.3 Proposed Sliding Mode Control

For the sliding mode control, the sliding surface is generally given by [18, 19]:

$$s = e_2 + \lambda e_1 \quad (21)$$

The existence of the sliding mode requires the following conditions to be satisfied:

$$\begin{aligned} s &= e_2 + \lambda e_1 \\ \dot{s} &= \dot{e}_2 + \lambda \dot{e}_1 \end{aligned} \quad (22)$$

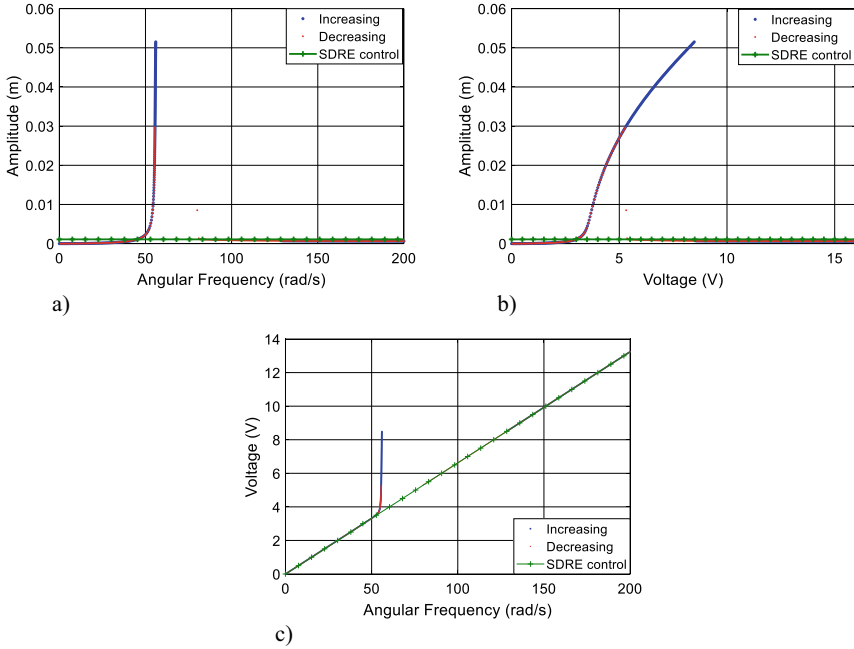


**Fig. 4** Jump phenomenon suppression by SDRE control. **a** Frequency response diagram. **b** Jump phenomenon due to the applied voltage in the DC motor. **c** Angular frequency response by voltage

where  $\lambda$  represents a real number.

Equation (21) defines the output of the sliding mode control, while the reaching law is given by [18, 19]:

$$U = \begin{cases} U_{\max} & \text{if } \frac{s}{\mu} < -1 \\ -U_{\max} & \text{if } \frac{s}{\mu} > 1 \\ K_{smc}s & \text{if } -1 < \frac{s}{\mu} < 1 \end{cases} \quad (23)$$

where  $\mu$  is the layer thickness of the control,  $K_{smc}$  is a proportional gain, and  $U_{\max}$  is related to the saturation value. The parameters  $\mu$  and  $K_{smc}$  are positive constants [18, 19].

In Figs. 5, it is observed the jump phenomenon suppression using the Proposed sliding mode control for parameters:  $\mu = 10^{-3}$ ,  $K_{smc} = 10^3$  and  $U_{\max} = 100$ .

It can be seen in Fig. 5 that the proposed control using the sliding mode control was also efficient in suppressing the jump effect, keeping the displacements in the desired amplitude and frequency.

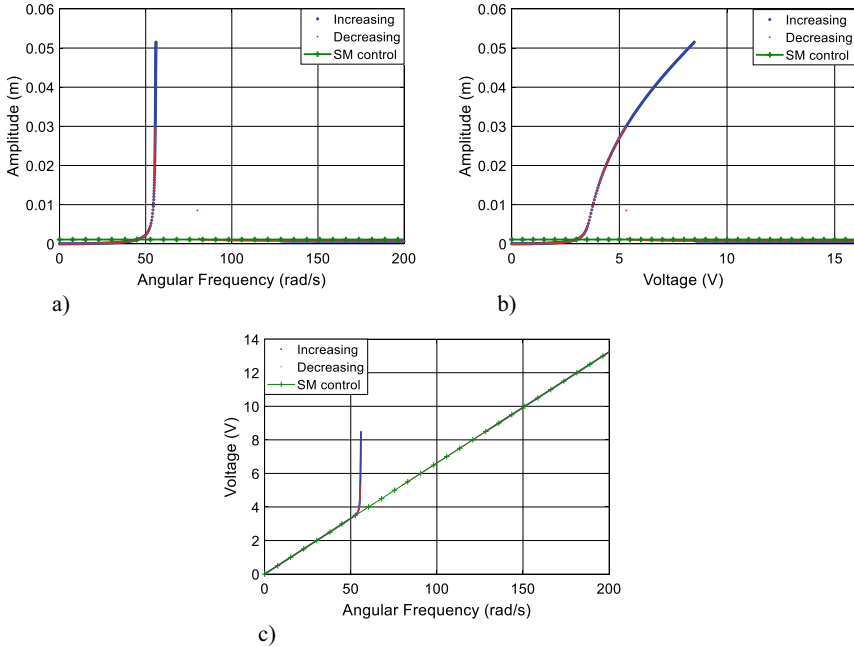


**Fig. 5** Jump phenomenon suppression by Sliding Mode control. **a** Frequency response diagram. **b** Jump phenomenon due to the applied voltage in the DC motor. **c** Angular frequency response by voltage

## 4 Conclusions

This work presented two control techniques for suppression of the Sommerfeld effect of a non-ideal system, i.e., a system where the excitation source is influenced by its own performance, losing energy in the process that serves only to amplify the vibration amplitudes.

The numerical results showed that both the SDRE and SMC controls are efficient in suppressing the jump effect, keeping the vibration amplitudes at desired levels as well as the motor voltage.

## References

1. Kononenko, V.O.: *Vibrating System of Limited Power Supply*. Illife Books, London (1969)
2. Nayfeh, A.H., Mook, D.T.: *Nonlinear Oscillations*. Wiley-Interscience, New York (1979)
3. Krasnopolskaya, T.S.: Chaos in acoustic subspace raised by the Sommerfeld-Kononenko effect. *Meccanica* **41**, 299–310 (2006)
4. Piccirillo, V., Tuset, A.M., Balthazar, J.M.: Dynamical jump attenuation in a non-ideal system through magneto rheological damper. *J. Theor. Appl. Mech.* **53**, 595–604 (2014)

5. Gonçalves, P.J.P., Silveira, M., Petronio, E.A., Pontes, B.R., Balthazar, J.M.: Double resonance capture of a two-degree-of-freedom oscillator coupled to a non-ideal motor. *Meccanica* **51**, 2203–2214 (2016)
6. Balthazar J. M., Tusset A. M., Brasil R. M. L. R. F., Felix J. L. P., Rocha R. T., Janzen, F. C., Nabarrete, A., Oliveira C.: An overview on the appearance of the Sommerfeld effect and saturation phenomenon in non-ideal vibrating systems (NIS) in macro and MEMS scales. *Nonlinear Dyn.* **93**, 19–40 (2018)
7. Sommerfeld, A.: Beiträge zum dynamischen ausbau der festigkeitslehre. *Phys. Z.* **3**, 266–286 (1902)
8. Tusset, A.M., Balthazar, J.M.: On the chaotic suppression of both ideal and non-ideal duffing based vibrating systems, using a magnetorheological damper. *Differ. Equ. Dyn. Syst.* **21**, 105–121 (2013)
9. Tusset A.M., Piccirillo V., Balthazar J.M., Brasil M.R.L.F.: On suppression of chaotic motions of a portal frame structure under non-ideal loading using a magneto-rheological damper. *J. Theoret. Appl. Mech.*, 653–664 (2015)
10. Awrejcewicz, J., Starosta, R., Sypniewska-Kaminska, G.: Decomposition of governing equations in the analysis of resonant response of a nonlinear and non-ideal vibrating. *Nonlinear Dyn.* **82**, 299–309 (2015)
11. Felix, J.L.P., Balthazar, J.M., Brasil, R.M.L.R.F., Pontes, B.R.: On lugre friction model to mitigate Nonideal vibrations. *ASME. J. Comput. Nonlinear Dynam.* **4**, 034503 (2009)
12. Kossoski, A., Tusset, A.M., Janzen, F.C., Rocha, R.T., Balthazar, J.M., Brasil, R.M.L.R.F., Nabarrete, A.: Jump attenuation in a non-ideal system using shape memory element. *Matec Web Conf.* **148**, 03003–03003–4 (2018)
13. De Godoy, W.R., Balthazar, J.M., Pontes, B.R., Felix, J.L., Tusset, A.M.: A note on non-linear phenomena in a non-ideal oscillator, with a snap-through truss absorber, including parameter uncertainties. *Proc. Inst. Mech. Eng. Part K: J. Multi-body Dyn.* **227**, 76–86 (2013)
14. Tusset, A.M., Balthazar, J.M., Rocha, R.T., Ribeiro, M.A., Lenz, W.B., Janzen, F.C.: Time-Delayed Feedback Control Applied in a Nonideal System with Chaotic Behavior. *Nonlinear Dynamics and Control*. 1ed.: Springer International Publishing, Vol. 1, pp. 237–244 (2020)
15. Kossoski, A., Tusset, A.M., Janzen, F.C., Ribeiro, M.A., Balthazar, J.M.: Attenuation of the Vibration in a Non-ideal Excited Flexible Electromechanical System Using a Shape Memory Alloy Actuator. *Mechanisms and Machine Science*. 1ed.: Springer International Publishing, Vol. 95, pp. 431–444 (2021)
16. Tusset, A.M., Balthazar, J.M., Chavarette, F.R., Felix, J.L.P.: On energy transfer phenomena, in a nonlinear ideal and nonideal essential vibrating systems, coupled to a (MR) magnetorheological damper. *Nonlinear Dyn.* **69**, 1859–1880 (2012)
17. Tusset, A.M., Balthazar, J.M., Felix, J.L.P.: On elimination of chaotic behavior in a non-ideal portal frame structural system, using both passive and active controls. *J. Vib. Control* **19**, 803–813 (2013)
18. Bassinello, D.G., Tusset, A.M., Rocha, R.T., Balthazar, J.M.: Dynamical analysis and control of a chaotic microelectromechanical resonator model. *Shock. Vib.* **50**, 1–10 (2018)
19. Piccirillo, V., Goes, L.C.S., Balthazar, J.M., Tusset, A.M.: Deflection control of an aeroelastic system utilizing an antagonistic shape memory alloy actuator. *Meccanica* **53**, 727–745 (2017)

# Chaos Control in a Nonideal Vibrating Systems



A. M. Tuset , V. Piccirillo , S. L. T. de Souza , A. M. Batista ,  
Jose Manoel Balthazar , R. M. L. R. F. Brasil , C. Oliveira ,  
and M. Varanis 

**Abstract** This paper presents two control techniques for a non-ideal system with chaotic behavior. To place and maintain the system in a periodic orbit, the techniques of Time Delayed Feedback Control and Continuous-Delay Control with Saturation are considered. The non-ideal system presented is composed of a mass-spring-damper system, with cubic stiffness, and an external excitation from a power limited DC electric motor driven by an unbalanced rotating mass that provides the non-ideal excitation. To suppress the chaotic behavior, additional damping is considered for the mechanical system, and the damping force is estimated by the proposed control strategies. Dynamic analysis of the system is performed by various techniques, including bifurcation diagrams, phase portraits, power spectral densities, and 0–1 test. Numerical simulations demonstrate the effectiveness of the control strategies leading the system to a stable periodical orbit.

---

A. M. Tuset (✉) · V. Piccirillo  
Federal University of Technology-Paraná, Curitiba, Brazil

V. Piccirillo  
e-mail: [piccirillo@utfpr.edu.br](mailto:piccirillo@utfpr.edu.br)

S. L. T. de Souza  
Federal University of São João del-Rei-Minas Gerais, Gerais, Brazil

A. M. Batista  
State University of Ponta Grossa- Paraná, Ponta Grossa, Brazil

J. M. Balthazar  
Sao Paulo State University-São Paulo, São Paulo, Brazil

R. M. L. R. F. Brasil  
Federal University of ABC-São Paulo, São Paulo, Brazil

C. Oliveira · M. Varanis  
Federal University of Grande Dourados-Dourados, Dourados, Brazil  
e-mail: [clivaldooliveira@ufgd.edu.br](mailto:clivaldooliveira@ufgd.edu.br)

M. Varanis  
e-mail: [marcusvaranis@ufgd.edu.br](mailto:marcusvaranis@ufgd.edu.br)



## 1 Introduction

The study of vibrating systems for the case where the external excitation is influenced by the system response has attracted many researchers, because its problem is a great challenge in both theoretical and practical engineering. When the excitation is influenced by the system response or for which the power supply is limited it is a non-ideal system [1]. Usually, these systems are considered when motors are coupled to structures that need excitation power levels similar to the power capacity of these motors [1–3].

In many cases, the non-ideal nonlinearities of the system can lead the system to the jump effect (Sommerfeld effect) [1, 4, 5], or to chaotic behavior [6], as observed in this work. These behaviors are undesirable in most cases, as they can cause data to the system [7], being necessary to suppress them.

In this paper, control, and dynamic analysis of a nonideal system are applied and investigated. The 0–1 test is used to investigate the chaotic behavior of the system. To suppress the chaotic motion, the Time Delayed Feedback Control (TDFC) and Continuous-Delay Control with Saturation (DCSC) are applied.

The TDFC is originally proposed by Pyragas [8], who considered a continuous control input that stabilizes a chaotic oscillation under the difference between the velocity current output and the previous velocity one [8–10], and successfully applied in nonideal system [9].

The DCSC is proposed in [11], to control a non-ideal system with chaotic behavior, and successfully applied to nonideal systems [12, 13].

The 0–1 test is originally proposed by [14]. The method consider a time series data, based on the statistical properties of a single variable, and analysing its spectral and statistical properties by considering the asymptotic properties of a Brownian motion [14–18].

## 2 Mathematical Model

The system presented in Fig. 1, represents a nonideal oscillator, and consists of a structure of mass  $m_l$  connected to a damper and to a nonlinear spring with a nonlinear cubic stiffness. The proposed system is excited by a nonideal DC motor characterized by the moment of inertia  $J_M$  and the unbalanced mass  $m_o$  with eccentricity  $r$ . The physical schematics of the DC motor is shown in Fig. 1b. [6, 7, 9, 19, 20].

The equations of motion of the non-ideal system are given by [6, 9]

$$\begin{aligned}
 m_l \ddot{x} + \mu \dot{x} - k_1 x + k_2 x^3 &= m_o r (\dot{\phi}^2 \sin \phi - \ddot{\phi} \cos \phi) \\
 (J + m_o r^2) \ddot{\phi} &= C_M \Phi I - m_o r \ddot{x} \cos \phi \\
 \dot{I}_m &= -\frac{R_t}{L_t} I_m - \frac{C_E \Phi}{L_t} \dot{\phi} + \frac{U_m}{L_t}
 \end{aligned} \tag{1}$$

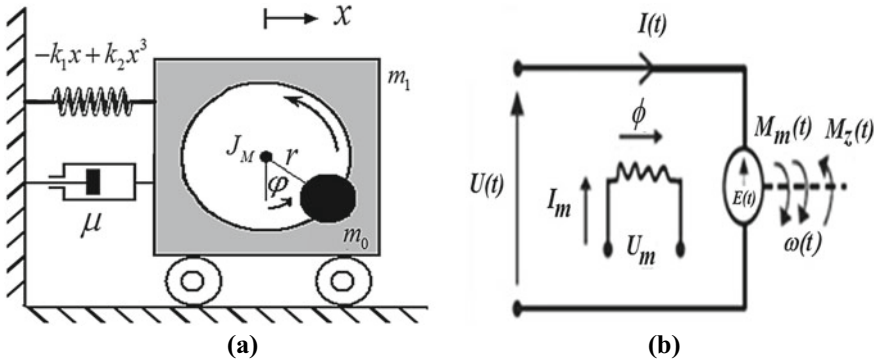


Fig. 1 a Non-ideal oscillator and b the DC motor in the electrical schematics

where  $C_M$ ,  $C_E$  are mechanical and electrical constants, respectively. The magnetic flux is represented by  $\Phi$  and  $\omega(t)$  is the angular velocity of the rotor. It is assumed that the external exciting current  $I_m$  and voltage  $U_m$  are constants and then the magnetic flux  $\Phi$  is constant.

The dimensionless mathematical model represented in state-space notation, for the system (1) can be expressed by the following system of equations [9]:

$$\begin{cases} \dot{x}_1 = x_2 \\ \dot{x}_2 = A(w_1(x_4^2 \sin x_3 - p_3 x_5 \cos x_3) - \beta x_2 + x_1 - \delta x_1^3) \\ \dot{x}_3 = x_4 \\ \dot{x}_4 = A(p_3 x_5 - w_2 w_1 x_4^2 \sin x_3 \cos x_3 + w_2 \beta w \cos x_3 - w_2 \cos x_3 (x_1 - \delta x_1^3)) \\ \dot{x}_5 = -p_1 x_5 - p_2 x_4 + \nu \end{cases} \tag{2}$$

where  $x_1 = x$ ,  $x_2 = \dot{x}_1$ ,  $x_3 = \varphi$ ,  $x_4 = \dot{\varphi}$  and  $x_5 = I$ , and the dimensionless parameters are denoted by

$$\omega_0^2 = \frac{k_1}{m_1 + m_0}, \beta = \frac{\mu}{m_1 \omega_0}, \delta = \frac{k_2}{k_1} x_0^2, w_1 = \frac{m_0 r}{m_1 x_0}, w_2 = \frac{m_0 r x_0}{(J + m_0 r^2)}, p_1 = \frac{R_t}{L_t I_0 \omega_0}, \nu = \frac{U_m}{L_t I_0 \omega_0}, p_2 = \frac{C_E \Phi}{L_t I_0}, p_3 = \frac{C_M \Phi I_0}{(J + m_0 r^2) \omega_0^2} \text{ and } A = \frac{1}{1 - w_1 w_2 (\cos x_3)^2}.$$

### 3 Numerical Results

For numerical simulation is considered the parameters:  $\delta = 0.1$ ,  $w_1 = 0.2$ ,  $w_2 = 0.3$ ,  $p_1 = 0.3$ ,  $p_2 = 3$ ,  $p_3 = 0.15$ ,  $\beta = 0.0337$ ,  $\omega_0 = 46.4$  and  $2 \leq \nu \leq 7$ , along with the initial conditions:  $x_i(0) = 0$ , where  $i = 1:5$  [9]. Where the integration step is considered by  $h = 0.001$ .

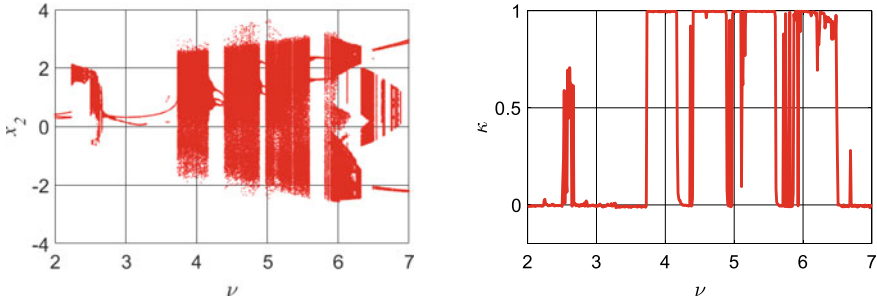


**Fig. 2** a Bifurcation diagram. b 0–1 test

In Fig. 2 one can observe the Bifurcation diagram and 0–1 test, for the system (2) considering:  $2 \leq \nu \leq 7$ .

As can be seen in Fig. 2a for certain values of ( $\nu$ ) the system (2) has periodic or chaotic behavior. Considering the results of the 0–1 test presented in Fig. 2b, one can observe that the system is chaotic for values of ( $\kappa$ ) close to 1 and periodic for values of ( $\kappa$ ) close to zero [21, 22].

In Fig. 2 one can observe the chaotic behavior of the system (2) for  $\nu = 5.4$  ( $\kappa = 1$ ).

As can be seen in Fig. 2 the system (2) without control has a chaotic behavior.

## 4 Chaos Control

To eliminate the chaotic behavior presented by the system, the proposed control techniques are introduced as a control signal  $U$ , given by:

$$\begin{cases} \dot{x}_1 = x_2 \\ \dot{x}_2 = A(w_1(x_4^2 \sin x_3 - p_3 x_5 \cos x_3) - \beta x_2 + x_1 - \delta x_1^3) + U \\ \dot{x}_3 = x_4 \\ \dot{x}_4 = A(p_3 x_5 - w_2 w_1 x_4^2 \sin x_3 \cos x_3 + w_2 \beta w \cos x_3 - w_2 \cos x_3 (x_1 - \delta x_1^3)) \\ \dot{x}_5 = -p_1 x_5 - p_2 x_4 + \nu \end{cases} \tag{3}$$

### 4.1 Chaos Control by Time Delayed Feedback Control

The TDF control, was originally suggested by the author of [8], being obtained by the difference between the past and current velocity for a given sampling time [8, 9]. Thus, assuming that the oscillation speed ( $x_2$ ) can be measured, the TDF control signal  $U_{TDFc}$  is given as:

$$U_{TDFc} = k_{TDFc}[x_2(\tau - T) - x_2(\tau)] \tag{4}$$

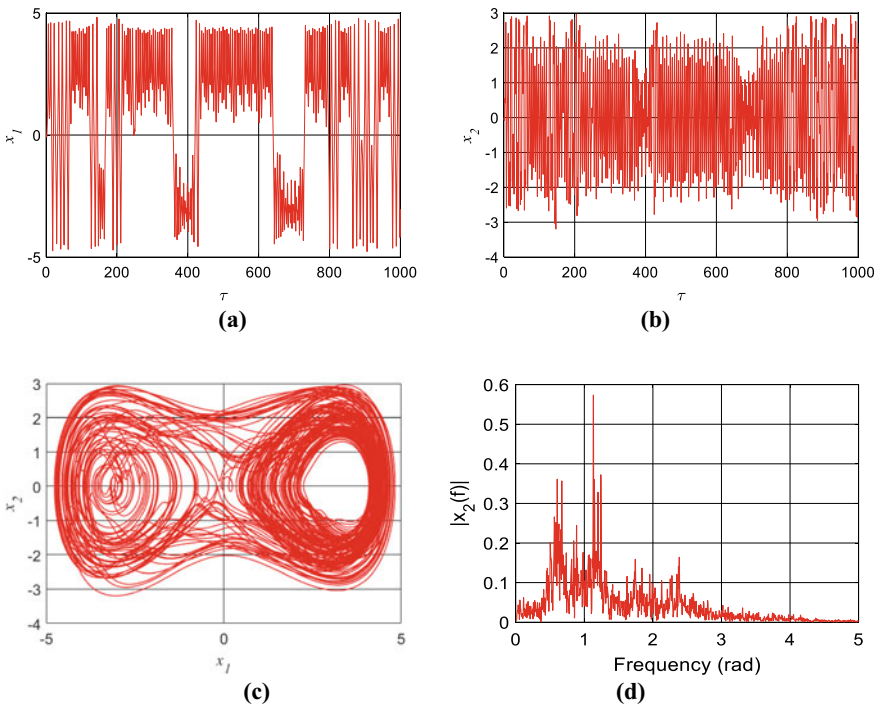
where  $T$  is the time delay and  $k_{TDFc}$  the feedback gain.

Figure 4 shows the 0–1 test for different feedback gain intervals of the  $0 \leq k_{TDFc} \leq 10$ , with fixed  $T = 1.133$ .

As can be seen in Fig. 4 for gains of ( $k_{TDFc} \geq 0.1$ ), the control (4) takes the system (3) to a periodic behavior, considering that ( $U = U_{TDFc}$ ).

In Fig. 5 we can observe the system (3) with TDF control ( $U = U_{TDFc}$ ) and parameters:  $k_{TDFc} = 0.3$  and  $T = 1.133$ .

As can be seen in Fig. 5 the TDF controlled the system to a chaotic behavior for a periodic with a small control signal (Fig. 3d).



**Fig. 3** **a** Time history of the states  $x_1$ . **b** Time history of the states  $x_2$ . **c** Phase diagram to  $x_1$  versus  $x_2$ . **d** Power spectral density (FFT) to  $x_2$

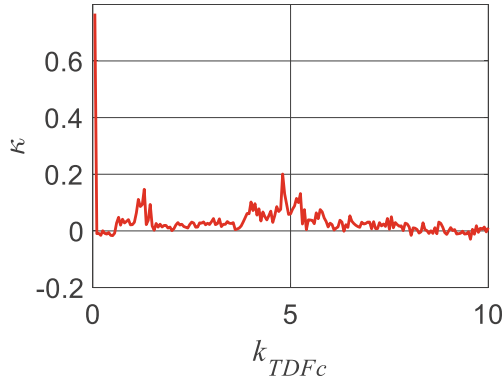


Fig. 4 0–1 test for  $0 \leq k_{TDFc} \leq 10$  and  $T = 1.133$

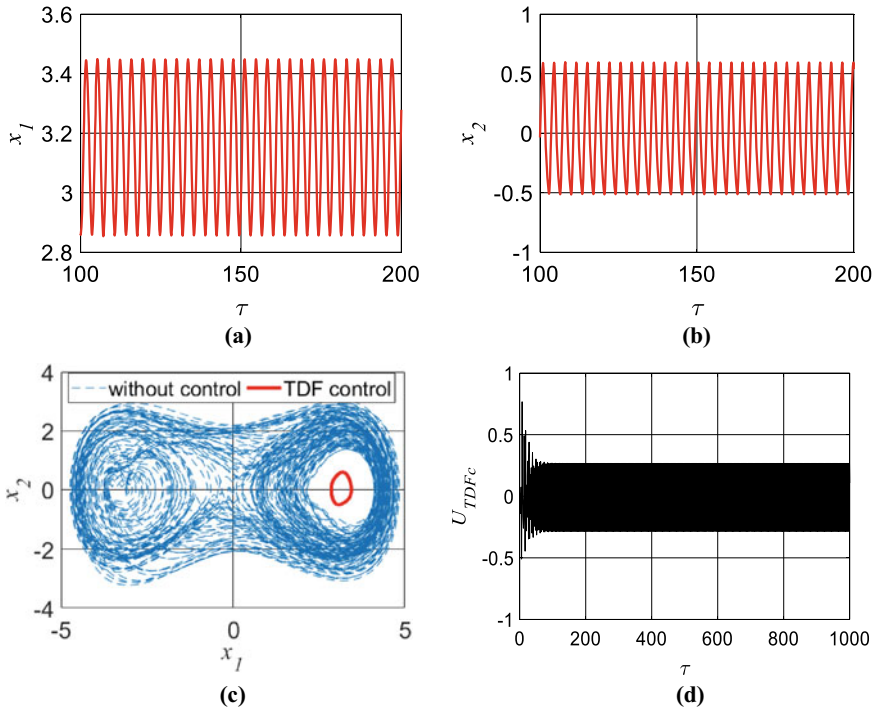
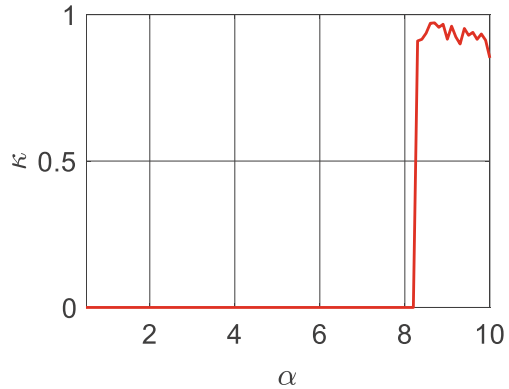


Fig. 5 **a** Time history of the states  $x_1$ . **b** Time history of the states  $x_2$ . **c** Phase diagram to  $x_1$  versus  $x_2$ . **d** Signal control  $U_{TDFc}$

**Fig. 6** 0–1 test for  $0.5 \leq \alpha \leq 10$  and  $\beta = 1$



### 4.2 Suppression of Chaotic Behaviour by Continuous-Delay Control with Saturation

The Continuous-Delay Control with Saturation (CDCS), was proposed by [11] to control a non-ideal system with chaotic behavior, and successfully used in other nonideal mechanical systems [12, 13].

The Continuous-Delay Control with Saturation signal ( $U_{CDCS}$ ) is given as [12, 13]:

$$U_{CDCS} = \alpha \tanh(\beta x_2) \tag{5}$$

where  $\alpha$  and  $\beta$  are positive constant.

Figure 6 shows the 0–1 test for system (3) with ( $U = -U_{CDCS}$ ) and different f gain intervals of the  $0.5 \leq \alpha \leq 10$ , with fixed  $\beta = 1$ .

As can be seen in Fig. 4 for gains of ( $0.5 \leq \alpha \leq 8.2$ ), the control (5) takes the system (3) to a periodic behavior, considering that ( $U = -U_{CDCS}$ ).

In Fig. 7 we can observe the system (3) with continuous-delay control with saturation ( $U = -U_{CDCS}$ ) and parameters:  $\alpha = 0.5$  and  $\beta = 1$ .

As can be seen in Fig. 7 the CDCS control drove the system to a chaotic behavior for a periodic with a small control signal (Fig. 7d).

## 5 Conclusions

To control the chaos of the non-ideal system presented in Eq. (2), Time Delayed Feedback Control and the Continuous-Delay Control with Saturation are considered to be projected and applied. The efficiency of two techniques was demonstrated through numerical simulations in order to eliminate the chaotic behavior of the system, and it was efficient to maintain the amplitude of the non-ideal systems in the periodic

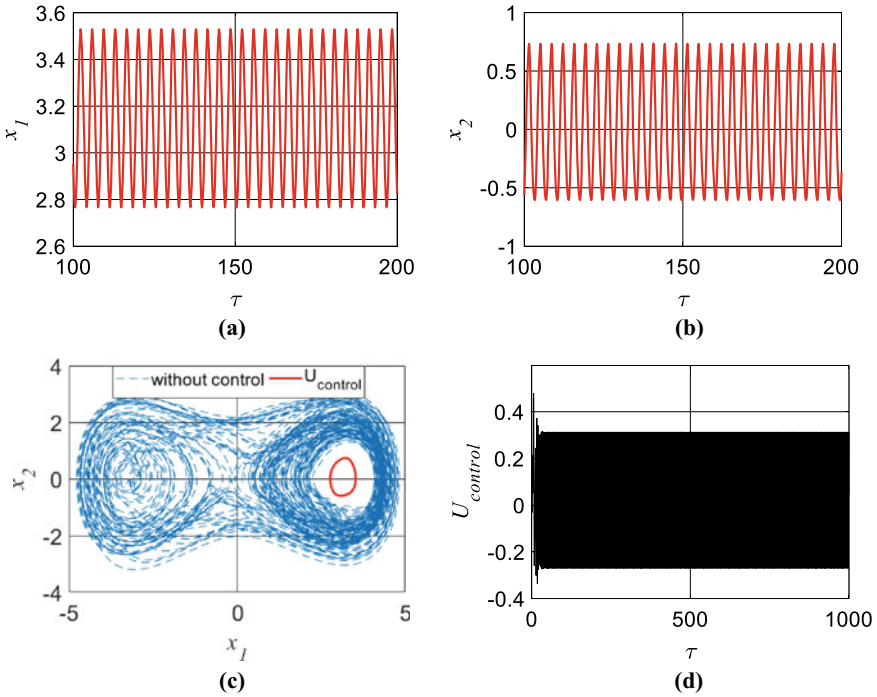


**Fig. 7** **a** Time history of the states  $x_1$ . **b** Time history of the states  $x_2$ . **c** Phase diagram to  $x_1$  versus  $x_2$ . **d** Signal control  $U_{CDCS}$

orbit. As can be seen in Figs. 5c and 7c, both controls took the system to the same orbit with practically the same control signal, as can be seen in Figs. 5d and 7d.

## Appendix

### A.1. The 0–1 Test Method

The 0–1 test consists of estimating a single parameter  $\kappa$  by [17]:

$$\kappa = \frac{\text{cov}(Y, M(\bar{c}))}{\sqrt{\text{var}(Y)\text{var}(M(\bar{c}))}} \tag{A1}$$

where:  $\bar{c} \in (0, \pi)$ ,  $M(\bar{c}) = [M(1, \bar{c}), M(2, \bar{c}), \dots, M(n_{max}\bar{c})]$  and  $Y = [1, 2, \dots, n_{max}]$ .

If  $\kappa$  is close to 0 the system is periodic. On the other hand, if  $\kappa$  is close to 1 the system is chaotic. The test utilizes a system variable  $x(j)$ , where two new coordinates  $(p, q)$  are defined as follows [18]:

$$p(n, \bar{c}) = \sum_{j=0}^n x(j) \cos(j\bar{c}) \quad (\text{A2})$$

$$q(n, \bar{c}) = \sum_{j=0}^n x(j) \sin(j\bar{c}) \quad (\text{A3})$$

The mean square displacement of the new variables  $p(n, \bar{c})$  and  $q(n, \bar{c})$  is given by [18]:

$$M(n, c) = \lim_{n \rightarrow \infty} \frac{1}{N} \sum_{j=1}^N [(p(j+n, \bar{c}) - p(j, \bar{c}))^2 \dots + (q(j+n, \bar{c}) - q(j, \bar{c}))^2] \quad (\text{A4})$$

where  $n = 1, 2, \dots, N$ .

## References

1. Kononenko, V.O.: *Vibrating System of Limited Power Supply*. Illife Books, London (1969)
2. Tusset, A.M., Balthazar, J.M., Chavarette, F.R., Felix, J.L.P.: On energy transfer phenomena, in a nonlinear ideal and nonideal essential vibrating systems, coupled to a (MR) magneto-rheological damper. *Nonlinear Dyn.* **69**, 1859–1880 (2012)
3. Balthazar, J.M., Tusset, A.M., Brasil, R.M.L.R.F., Felix, J.L.P., Rocha, R.T., Janzen, F.C., Nabarrete, A., Oliveira, C.: An overview on the appearance of the Sommerfeld effect and saturation phenomenon in non-ideal vibrating systems (NIS) in macro and MEMS scales. *Nonlinear Dyn.* **93**, 19–40 (2018)
4. Nayfeh, A.H., Mook, D.T.: *Nonlinear Oscillations*. Wiley-Interscience, New York (1979)
5. Krasnopolskaya, T.S.: Chaos in acoustic subspace raised by the Sommerfeld-Kononenko effect. *Meccanica* **41**, 299–310 (2006)
6. Piccirillo, V., Tusset, A.M., Balthazar, J.M.: Dynamical jump attenuation in a non-ideal system through magneto rheological damper. *J. Theor. Appl. Mech.* **53**, 595–604 (2014)
7. Tusset, A.M., Piccirillo, V., Balthazar, J.M., Brasil, M.R.L.F.: On suppression of chaotic motions of a portal frame structure under non-ideal loading using a magneto-rheological damper. *J. Theoret. Appl. Mech.*, 653–664 (2015)
8. Pyragas, K.: Continuous control of chaos by self-controlling feedback. *Phys. Lett. A.* **170**, 421–428 (1992)
9. Tusset, A.M., Balthazar, J.M., Rocha, R.T., Ribeiro, M.A., Lenz, W.B., Janzen, F.C.: Time-Delayed Feedback Control Applied in a Nonideal System with Chaotic Behavior. *Nonlinear Dynamics and Control*. 1ed.: Springer International Publishing, vol. 1, pp. 237–244 (2020)
10. Tusset, A.M., Ribeiro, M.A., Lenz, W.B., Rocha, R.T., Balthazar, J.M.: Time delayed feedback control applied in an atomic force microscopy (AFM) model in fractional-order. *J. Vib. Eng. Technol.* **8**, 327–335 (2020)
11. Controlling chaotic oscillators by altering their energy: Tereshko, V., Chacón R, P. V. *Phys Lett A* **320**, 408–416 (2004)
12. Zukovic, M., Cveticanin, L.: Chaotic responses in a stable duffing system of non-ideal type. *J. Vib. Control* **13**, 751–767 (2007)



13. Arbex, H.C., Balthazar, J.M., Pontes Jr, B.R., Brasil, M.R.L.F., Felix, J.L., Tusset, A.M., Bueno, A.M.: On nonlinear dynamics behavior and control of a new model of a magnetically levitated vibrating system, excited by an unbalanced DC motor of limited power supply. *J. Brazilian Soc. Mech. Sci. Eng.*, 1139–1150 (2014)
14. Gottwald, G.A., Melbourne, I.: A new test for chaos in deterministic systems. *Proc. Royal Soc. A Math. Phys. Eng. Sci.* **460**, 603–611 (2004)
15. Gottwald, G.A., Melbourne, I.: Testing for chaos in deterministic systems with noise. *Physica D* **212**, 100–110 (2005)
16. Bernardini, D., Rega, G., Litak, G., Syta, A.: Identification of regular and chaotic isothermal trajectories of a shape memory oscillator using the 0–1 test. *Proc. Inst. Mech. Eng. Part K: J. Multi-body Dyn.* **227**, 17–22 (2013)
17. Bernardini, D., Litak, G.: An overview of 0–1 test for chaos. *J. Braz. Soc. Mech. Sci. Eng.* **38**, 1433–1450 (2016)
18. Litak, G., Syta, A., Wiercigroch, M.: Identification of chaos in a cutting process by the 0–1 test. *Chaos Solitons Fractals* **40**, 2095–2101 (2009)
19. Tusset, A.M., Balthazar, J.M., Felix, J.L.P.: On elimination of chaotic behavior in a non-ideal portal frame structural system, using both passive and active controls. *J. Vib. Control* **19**, 803–813 (2013)
20. Tusset, A.M., Balthazar, J.M.: On the chaotic suppression of both ideal and non-ideal duffing based vibrating systems, using a magnetorheological damper. *Differ. Equ. Dyn. Syst.* **21**, 105–121 (2013)
21. Litak, G., Bernardini, D., Syta, A., Rega, G., Rysak, A.: Analysis of chaotic non-isothermal solutions of thermomechanical shape memory oscillators. *Europ. Phys. J. Spec. Topics* **222**, 1637–1647 (2013)
22. Tusset, A.M., Balthazar, J.M., Ribeiro, M.A., Lenz, W.B., Rocha, R.T.: Chaos control of an atomic force microscopy model in fractional-order. *Europ. Phys. J. Spec. Topics* **1**, 1–12 (2021)

# Nonlinear Control of Rotating Flexible Structures Considering Aerodynamic Effects and Non-ideal Interactions



André Fenili 

**Abstract** The mathematical modelling and control of a nonlinear system comprising of a rotating flexible beam-like structure driven by a non-ideal DC motor and interacting with a surrounding quiescent fluid is investigated here. The flexible structure is mathematically modeled considering linear curvature and clamped-free boundary conditions. This structure has an angle of attack which is considered constant in this work. Nonlinearities resulting from the coupling between the angular velocity of the rotating axis and the transversal vibration of the beam are considered. The interaction between the structure and the fluid is considered through the inclusion in the mathematical model of the system of a drag force and of a lift force acting along the beam length. These forces are considered velocity dependent nonlinear external excitations. In the mathematical model investigated here, the direct current (DC) motor, responsible for the angular displacement, interacts with the structure being moved and this structure interacts with the DC motor, characterizing what is conventionally called a non-ideal system. It is one of the objectives of this research to investigate the degree of this interaction. The system studied here is a nonlinear underactuated system. In order to eliminate the vibration on the flexible structure and at the same time to control the velocity of the rotating axis one considers here the nonlinear control technique named partial feedback linearization.

**Keywords** Rotating flexible structures · Nonlinear systems · Nonlinear control · Non ideal systems · Drag force · Lift force

---

A. Fenili (✉)

Center for Engineering, Modeling and Applied Social Sciences (CECS), Federal University of ABC (UFABC), Instrumentation, Automation and Robotics Engineering / Aerospace Engineering / Mechanical Engineering, Avenida Dos Estados, 5001 / Bairro Santa Terezinha - Bloco B - Sala 936 Campus Santo André, Santo André, SP 09210-580, Brazil  
e-mail: [andre.fenili@ufabc.edu.br](mailto:andre.fenili@ufabc.edu.br)

## 1 Introduction

The mathematical modeling, dynamics and control of nonlinear rotating flexible beam-like structures compose an area of continuing interest to researchers and scientists around the world due to the wide range of application of such structures in research areas as distinct as aerospace, naval and oceanic engineering. The main objective of these studies is, in general, the design of more lightweight and faster structures. For the purposes for which they are intended, it is essential that the designer takes into account the stability of these complex structures, as well as the control or reduction of their mechanical vibrations.

The inclusion of the aerodynamic drag and lift effects (in a simple—as in this work—or in a more complex manner) in the mathematical model of such flexible rotating structures incorporates the interaction between these structures and the surrounding fluid. This interaction can significantly alter the control performance and efficiency. But this type of interaction, despite being present in real systems and despite its importance, is not the main subject of this work.

The main interaction discussed in this work involves the energy transference between the actuator (sometimes identified as the energy source) and the system on which it is acting (the flexible structure) through an ideal and a non ideal system approach [1, 2]. In dealing with these kind of rotating structures, the interaction between the angular displacement and velocity of the rotating axis and the deflection of the structure can be very important in some cases, as in high angular speed maneuvers [3–5]. In fact, in the case where a linear model is assumed for the curvature of the flexible structure, the governing equation of motion of the beam is nonlinear due only to the presence of terms that represent its interaction with the rotating axis. On the other hand, and since terms associated with the beam also appear in the mathematical model related to the motor shaft, the angular displacement and velocity that are driving the beam are not known as long as the beam equations are not integrated. In other words, the whole set is integrated at the same time.

Because of its mechanical characteristics these structures are vulnerable to any external or internal disturbances. The undesired oscillations along the structure must be eliminated with some appropriate vibration control design. In the discussion presented here, in addition to the elimination of vibration in the structure, one wants also the angular velocity of the rotating axis to be kept constant, which asks for another control action.

The flexible structures like the one presented here belong to a class of systems named continuous or distributed parameter systems. In order to actuate along these structures one must use specific devices such as piezoelectric actuators [6, 7]. The forces developed in these actuators, in order to realize its tasks, must follow some control law.

Besides all the particularities and difficulties commented above, the system investigated here is also underactuated [8], what means that it belongs to a class of dynamical systems which are characterized by the fact that they have fewer actuators than the number of degrees of freedom. The underactuation condition in the

problem investigated here comes from the ascension degree of freedom, which is not controlled.

This class of systems asks for a specific class of nonlinear control methods. The nonlinear control technique for underactuated nonlinear systems used in this work is the partial feedback linearization [9, 10].

The part of the dynamics corresponding to the actuated degrees of freedom is linearized by nonlinear feedback. The part related to the degrees of freedom which are not controlled is not linearized and constitutes what is called the zero dynamics, whose analysis is crucial to the understanding of the response of the overall system [11, 12].

## 2 The Geometric Model

The geometric model of the system investigated in this work is presented in Fig. 1.

This system comprises a rigid cylindrical body connected to a flexible beam-like structure in rotation about Z axis and the whole set is interacting with a quiescent fluid. The fluid effect on this structure is represented in this work by the drag,  $D(x, t)$  and the lift,  $L(x, t)$ , forces. These forces are not represented on the figure.

The drag and lift forces, as considered in this work, are functions of the velocities  $\dot{v}(x, t)$  and  $\dot{\theta}(t)$ . The lift is also a function of the vertical velocity  $\dot{s}(t)$ . The model for the lift uses strip theory, and no tridimensional effects are included.

In Fig. 1, the inertial axis is represented by XYZ and the moving axis (attached to the system and rotating with it) is represented by xyz.

## 3 The Mathematical Model

The governing equations of motion for the system depicted in Fig. 1 are obtained through the energy method [13, 14]. The application of this method requires knowledge of the kinetic, potential and strain energies stored in the system (hub and flexible structure) during the time evolution.

The total kinetic energy,  $T$ , of the system is given by:

$$\begin{aligned}
 T = & \frac{1}{2}m_{\text{hub}}\dot{s}^2 + \frac{1}{2}I_{\text{hub}}\dot{\theta}^2 + \frac{1}{2} \int_0^L \rho A [\dot{\theta}^2 (r+x)^2 - 2\dot{\theta}(r+x)\dot{v} \sin \alpha \\
 & + \dot{v}^2 + v^2 \sin^2 \alpha \dot{\theta}^2 + 2\dot{v} \cos \alpha \dot{s} + \dot{s}^2] dx
 \end{aligned}
 \tag{1}$$

In Eq. (1) (and Fig. 1),  $\theta(t)$  represents the angular displacement of the hub axis,  $s(t)$  represents the vertical displacement of the system,  $r$  represents the radius of the hub,  $\alpha$  represents the angle of attack of the beam,  $v(x, t)$  represents the transversal

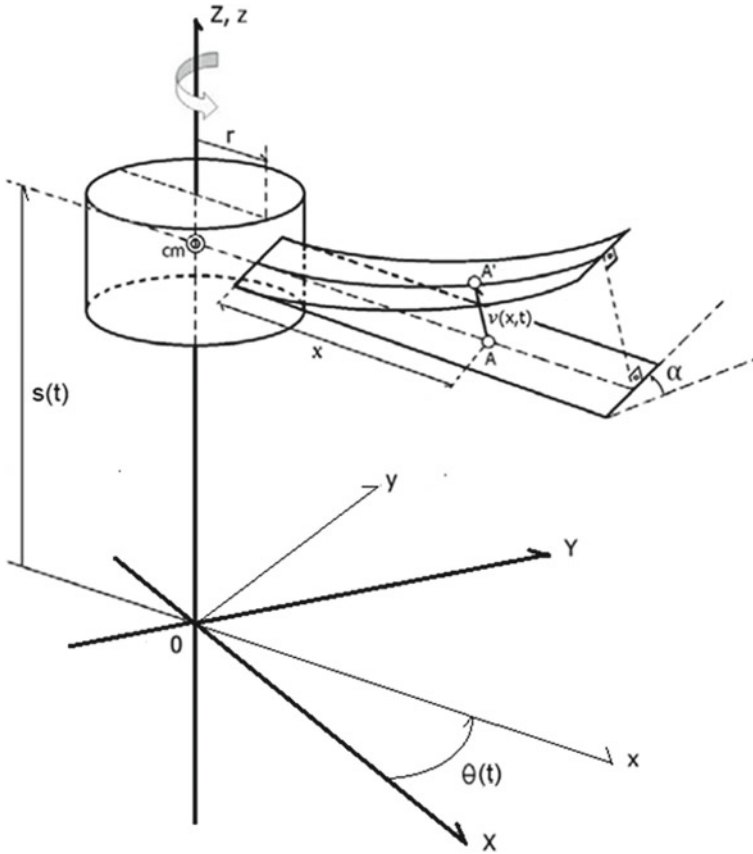


**Fig. 1** The rotating flexible beam system interacting with a fluid

displacement of the beam,  $\rho$  represents the density of the material that composes the beam,  $A$  represents the beam cross section area and  $L$  represents the non-deflected length of the beam.

Linear curvature is assumed in this work for the flexible structure [2, 15, 16]. The total potential + strain energy,  $V$ , of the system is given by:

$$V = m_{hub}gs + \frac{1}{2} \int_0^L \rho Ag(s + v \cos \alpha)dx + \frac{1}{2} \int_0^L EIv''^2 dx \tag{2}$$

where  $E$  represents the Young's modulus of the material of which the beam is made, and  $I$  represents the moment of inertia of the cross-sectional area of the beam.

The lagrangian,  $L$ , therefore, is given by:

$$L = T - V \tag{3}$$

or:

$$L = \frac{1}{2} m_{hub} \dot{s}^2 + \frac{1}{2} I_{hub} \dot{\theta}^2 - m_{hub} g s + \frac{1}{2} \int_0^L \rho A [\dot{\theta}^2 (r+x)^2 - 2\dot{\theta}(r+x)\dot{v} \sin \alpha + \dot{v}^2 + v^2 \sin^2 \alpha \dot{\theta}^2 + 2\dot{v} \cos \alpha \dot{s} + \dot{s}^2 - 2g(s + v \cos \alpha) - \frac{EI}{\rho A} v''^2] dx \tag{4}$$

The drag effect is inserted into the Hamiltonian formalism as the work done by the non-conservative generalized drag force,  $D$ , which is given at any cross section by [17]:

$$D_{sec} = \frac{1}{2} \rho_f S C_D U^2 \tag{5}$$

In Eq. (5),  $\rho_f$  represents the density of the fluid,  $S = c \sin \beta_f$  represents the section orthographic projection of the beam,  $c$  is the beam cross sectional width (mean chord),  $U$  is the modulus of the fluid velocity as seen by the beam cross section, with:

$$U^2 = [\dot{\theta}(r+x) - \dot{v} \sin \alpha]^2 + [\dot{v} \cos \alpha + \dot{s}]^2 \tag{6}$$

and  $C_D$  represents the nondimensional drag coefficient. The parameter  $\beta_f$  is the angle of attack as seen by the beam cross section and is given by:

$$\beta_f(x, t) = \alpha - \tan^{-1} \left( \frac{\dot{v} \cos \alpha + \dot{s}}{\dot{\theta}(r+x) - \dot{v} \sin \alpha} \right) \tag{7}$$

This angle varies with the cross section position,  $x$ , along the beam and time. Assuming that the horizontal velocity is much larger than the vertical velocity, it is possible to consider  $\beta_f = \alpha$ . In this case, the sectional lift is in the vertical direction ( $z$  direction) and the sectional drag is in the horizontal direction ( $y$  direction).

The external force normal to the flow, the lift force, is also inserted into the Hamiltonian formalism as a work done by a non-conservative generalized lift force,  $L$ .

Let a cross section of the beam at a distance  $x$  from the hub. The lift generated by this beam section is given by [17]:

$$L_{sec} = \frac{1}{2} \rho_f U^2 c C_L \tag{8}$$

where  $C_L$  represents the nondimensional lift coefficient.

For further details on the assumptions that are made with relation to the drag and lift forces see [17, 18].

The virtual work generated by the cross sectional lift and drag forces is given by:

$$\begin{aligned} \delta W_{\text{sec}} = & (L_{\text{sec}} + D_{\text{sec}}) \{v \sin \alpha \delta \theta \mathbf{i} + [(r+x)\delta \theta - \delta v \sin \alpha] \mathbf{j} \\ & + [\delta v \cos \alpha + \delta s] \mathbf{k}\} \end{aligned} \quad (9)$$

Using Eqs. (5) and (8), the total virtual work due to the lift and drag forces is obtained by the integration of Eq. (9) along the beam, resulting:

$$\begin{aligned} \delta W_{\text{fluid}} = & \frac{1}{2} \rho_f c \int_0^L \{[\dot{\theta}(r+x) - \dot{v} \sin \alpha]^2 + (\dot{v} \cos \alpha + \dot{s})^2\} C_L (\delta v \cos \alpha + \delta s) dx \\ & - \frac{1}{2} \rho_f S C_D \int_0^L \{[\dot{\theta}(r+x) - \dot{v} \sin \alpha]^2 + (\dot{v} \cos \alpha + \dot{s})^2\} [(r+x)\delta \theta - \delta v \sin \alpha] dx \end{aligned} \quad (10)$$

The torque applied to the axis of the cylinder is not considered at this point. It will be discussed later when the DC motor equations are introduced. The analysis of the mechanical part of the DC motor provides the governing equation of motion for the variable  $\theta$ .

The extended Hamilton's Principle can be given for a mechanical system as [13]:

$$\int_{t_1}^{t_2} (\delta W + \delta L) dt = 0 \quad (11)$$

where  $W$  is the total work done by external forces (or loads) on the bodies,  $t_1$  and  $t_2$  are the initial and final times and  $L$  is the lagrangian of the system. In this work, the external forces are the result of the interaction between the structure and the fluid and Eq. (11) can be written as:

$$\int_{t_1}^{t_2} (\delta W_{\text{fluid}} + \delta L) dt = 0 \quad (12)$$

Substituting Eqs. (4) and (10) into Eq. (12) results the governing equations of motion for the variables  $s(t)$  and  $v(x, t)$ , respectively, as given by:

$$(m_{\text{hub}} + \rho A L) \ddot{s} + \rho A \cos \alpha \int_0^L \ddot{v} dx - (m_{\text{hub}} - \rho A L) g = F_s \quad (13)$$

$$\begin{aligned} \ddot{v} + (r+x) \sin \alpha \ddot{\theta} + \cos \alpha \ddot{s} - v \sin^2 \alpha \dot{\theta}^2 \\ + \rho A g \cos \alpha + \frac{EI}{\rho A} v^{iv} = f_v \end{aligned} \quad (14)$$

where  $F_s$  and  $f_v$  are given by:

$$F_s = \frac{\rho c}{2} \int_0^L C_L \{ [\dot{\theta}(r+x) - \dot{v} \sin \alpha]^2 + [\dot{v} \cos \alpha + \dot{s}]^2 \} dx \tag{15}$$

$$f_v = \frac{\rho c}{2} \{ [\dot{\theta}(r+x) - \dot{v} \sin \alpha]^2 + [\dot{v} \cos \alpha + \dot{s}]^2 \} [C_L \cos \alpha + \frac{1}{2} k \sin \alpha] \tag{16}$$

where the proportionality constant  $k$  is given by:

$$k = \rho_f S C_D.$$

The boundary conditions for the beam can be obtained as a subproduct of the application of the extended Hamilton’s Principle and are given to a clamped-free beam by:

$$v(0, t) = 0$$

$$v'(0, t) = 0$$

$$v''(L, t) = 0$$

$$v'''(L, t) = 0$$

### 3.1 Applying the Simpson’s Rule

Consider the method for numerical approximation of definite integrals named Simpson’s rule as given by [19]:

$$\int_a^b f(x) dx \approx \frac{h}{3} (f(x_0) + 4f(x_1) + 2f(x_2) + 4f(x_3) + 2f(x_4) + \dots + 4f(x_{n-1}) + f(x_n)) \tag{17}$$

The beam is divided in 8 elements (or 9 nodes). The element size is  $h$ . Expanding  $\int_0^L \ddot{v} dx$  in Eq. 13 using the Simpson’s rule as defined in Eq. (17) results:



$$\int_0^L \ddot{v} \, dx = \frac{h}{3} (\ddot{v}_1 + 4\ddot{v}_2 + 2\ddot{v}_3 + 4\ddot{v}_4 + 2\ddot{v}_5 + 4\ddot{v}_6 + 2\ddot{v}_7 + 4\ddot{v}_8 + \ddot{v}_9) \quad (18)$$

Expanding the term  $\int_0^L C_L(\alpha) \{[\dot{\theta}(r+x) - \dot{v} \sin \alpha]^2 + [\dot{v} \cos \alpha + \dot{s}]^2\} dx$  in Eq. 15 results:

$$\begin{aligned} & \int_0^L C_L [r^2 \dot{\theta}^2 + 2rx \dot{\theta}^2 + x^2 \dot{\theta}^2 + \dot{v}^2 + \dot{s}^2 - 2\dot{v} \dot{\theta}(r+x) \sin \alpha + 2\dot{v} \dot{s} \cos \alpha] dx \\ &= (r^2 \dot{\theta}^2 + \dot{s}^2) \int_0^L C_L dx + 2r \dot{\theta}^2 \int_0^L C_L x dx + \dot{\theta}^2 \int_0^L C_L x^2 dx + \int_0^L C_L \dot{v}^2 dx - 2r \dot{\theta} \int_0^L C_L \dot{v} \sin \alpha dx \\ & \quad - 2\dot{\theta} \int_0^L C_L \dot{v} x \sin \alpha dx + 2\dot{s} \int_0^L C_L \dot{v} \cos \alpha dx \end{aligned} \quad (19)$$

Using the Simpson's rule in Eq. (19) (and again considering that the beam is divided in 8 elements (or 9 nodes)), each term in this equation can be rewritten as:

$$\begin{aligned} (r^2 \dot{\theta}^2 + \dot{s}^2) \int_0^L C_L dx &= (r^2 \dot{\theta}^2 + \dot{s}^2) \frac{h}{3} (C_{L1} + 4C_{L2} + 2C_{L3} + 4C_{L4} + 2C_{L5} + 4C_{L6} + 2C_{L7} + 4C_{L8} + C_{L9}) \\ 2r \dot{\theta}^2 \int_0^L C_L x dx &= 2r \dot{\theta}^2 \frac{h}{3} (x_1 C_{L1} + 4x_2 C_{L2} + 2x_3 C_{L3} + 4x_4 C_{L4} + 2x_5 C_{L5} + 4x_6 C_{L6} + 2x_7 C_{L7} \\ & \quad + 4x_8 C_{L8} + x_9 C_{L9}) \\ &= 2r \dot{\theta}^2 \frac{h}{3} ((0)C_{L1} + 4(h)C_{L2} + 2(2h)C_{L3} + 4(3h)C_{L4} + 2(4h)C_{L5} + 4(5h)C_{L6} \\ & \quad + 2(6h)C_{L7} + 4(7h)C_{L8} + (8h)C_{L9}) \\ &= r \dot{\theta}^2 \frac{h^2}{3} (8C_{L2} + 8C_{L3} + 24C_{L4} + 16C_{L5} + 40C_{L6} + 24C_{L7} + 56C_{L8} + 16C_{L9}) \\ \dot{\theta}^2 \int_0^L C_L x^2 dx &= \dot{\theta}^2 \frac{h}{3} (x_1^2 C_{L1} + 4x_2^2 C_{L2} + 2x_3^2 C_{L3} + 4x_4^2 C_{L4} + 2x_5^2 C_{L5} + 4x_6^2 C_{L6} + 2x_7^2 C_{L7} \\ & \quad + 4x_8^2 C_{L8} + x_9^2 C_{L9}) \\ &= \dot{\theta}^2 \frac{h}{3} ((0)^2 C_{L1} + 4(h)^2 C_{L2} + 2(2h)^2 C_{L3} + 4(3h)^2 C_{L4} + 2(4h)^2 C_{L5} + 4(5h)^2 C_{L6} \\ & \quad + 2(6h)^2 C_{L7} + 4(7h)^2 C_{L8} + (8h)^2 C_{L9}) \\ &= \dot{\theta}^2 \frac{h^3}{3} (4C_{L2} + 8C_{L3} + 36C_{L4} + 32C_{L5} + 100C_{L6} + 72C_{L7} + 196C_{L8} + 64C_{L9}) \\ \int_0^L C_L \dot{v}^2 dx &= \frac{h}{3} (C_{L1} \dot{v}_1^2 + 4C_{L2} \dot{v}_2^2 + 2C_{L3} \dot{v}_3^2 + 4C_{L4} \dot{v}_4^2 + 2C_{L5} \dot{v}_5^2 + 4C_{L6} \dot{v}_6^2 + 2C_{L7} \dot{v}_7^2 + 4C_{L8} \dot{v}_8^2 + C_{L9} \dot{v}_9^2) \end{aligned}$$

$$\begin{aligned}
-2r\dot{\theta} \int_0^L C_L \dot{v} \sin \alpha dx &= -r\dot{\theta} \frac{h}{3} (2C_{L1} \dot{v}_1 \sin \alpha_1 + 8C_{L2} \dot{v}_2 \sin \alpha_2 + 4C_{L3} \dot{v}_3 \sin \alpha_3 + 8C_{L4} \dot{v}_4 \sin \alpha_4 \\
&\quad + 4C_{L5} \dot{v}_5 \sin \alpha_5 + 8C_{L6} \dot{v}_6 \sin \alpha_6 + 4C_{L7} \dot{v}_7 \sin \alpha_7 + 8C_{L8} \dot{v}_8 \sin \alpha_8 + 2C_{L9} \dot{v}_9 \sin \alpha_9) \\
-2\dot{\theta} \int_0^L C_L \dot{v} x \sin \alpha dx &= -\dot{\theta} \frac{h^2}{3} (8C_{L2} \dot{v}_2 \sin \alpha_2 + 8C_{L3} \dot{v}_3 \sin \alpha_3 + 24C_{L4} \dot{v}_4 \sin \alpha_4 + 16C_{L5} \dot{v}_5 \sin \alpha_5 \\
&\quad + 40C_{L6} \dot{v}_6 \sin \alpha_6 + 24C_{L7} \dot{v}_7 \sin \alpha_7 + 56C_{L8} \dot{v}_8 \sin \alpha_8 + 16C_{L9} \dot{v}_9 \sin \alpha_9) \\
2\dot{s} \int_0^L C_L \dot{v} \cos \alpha dx &= \dot{s} \frac{h}{3} (2C_{L1} \dot{v}_1 \cos \alpha_1 + 8C_{L2} \dot{v}_2 \cos \alpha_2 + 4C_{L3} \dot{v}_3 \cos \alpha_3 + 8C_{L4} \dot{v}_4 \cos \alpha_4 \\
&\quad + 4C_{L5} \dot{v}_5 \cos \alpha_5 + 8C_{L6} \dot{v}_6 \cos \alpha_6 + 4C_{L7} \dot{v}_7 \cos \alpha_7 + 8C_{L8} \dot{v}_8 \cos \alpha_8 + 2C_{L9} \dot{v}_9 \cos \alpha_9)
\end{aligned}$$

In the terms above, for example, one has  $C_{L1} = C_{L1}(\alpha_1)$  where  $\alpha_1 = \alpha(x_1)$  represents the angle of attack at position  $x_1$  (and so on).

Substituting all these terms in the first governing equation of motion—Eq. 13—and considering  $\dot{v}_1 = \ddot{v}_1 = 0$  results (the second governing equation of motion is not altered at this step):

$$\begin{aligned}
(m_{\text{hub}} + \rho AL)\ddot{s} + \frac{\rho Ah \cos \alpha}{3} (\ddot{v}_1 + 4\ddot{v}_2 + 2\ddot{v}_3 + 4\ddot{v}_4 + 2\ddot{v}_5 + 4\ddot{v}_6 + 2\ddot{v}_7 + 4\ddot{v}_8 \\
+ \ddot{v}_9) - (m_{\text{hub}} - \rho AL)g &= \frac{\rho c}{2} \left[ \frac{(r^2 \dot{\theta}^2 + \dot{s}^2)h}{3} (C_{L1} + 4C_{L2} + 2C_{L3} + 4C_{L4} + 2C_{L5} \right. \\
&\quad + 4C_{L6} + 2C_{L7} + 4C_{L8} + C_{L9}) + \frac{r^2 \dot{\theta}^2}{3} (8C_{L2} + 8C_{L3} + 24C_{L4} + 16C_{L5} + 40C_{L6} + 24C_{L7} \\
&\quad + 56C_{L8} + 16C_{L9}) + \frac{h^3 \dot{\theta}^2}{3} (4C_{L2} + 8C_{L3} + 36C_{L4} + 32C_{L5} + 100C_{L6} + 72C_{L7} + 196C_{L8} \\
&\quad + 64C_{L9}) + \frac{h}{3} (C_{L1} \dot{v}_1^2 + 4C_{L2} \dot{v}_2^2 + 2C_{L3} \dot{v}_3^2 + 4C_{L4} \dot{v}_4^2 + 2C_{L5} \dot{v}_5^2 + 4C_{L6} \dot{v}_6^2 + 2C_{L7} \dot{v}_7^2 \\
&\quad + 4C_{L8} \dot{v}_8^2 + C_{L9} \dot{v}_9^2) - \frac{r\dot{\theta}}{3} (2C_{L1} \dot{v}_1 \sin \alpha_1 + 8C_{L2} \dot{v}_2 \sin \alpha_2 + 4C_{L3} \dot{v}_3 \sin \alpha_3 + 8C_{L4} \dot{v}_4 \sin \alpha_4 \\
&\quad + 4C_{L5} \dot{v}_5 \sin \alpha_5 + 8C_{L6} \dot{v}_6 \sin \alpha_6 + 4C_{L7} \dot{v}_7 \sin \alpha_7 + 8C_{L8} \dot{v}_8 \sin \alpha_8 + 2C_{L9} \dot{v}_9 \sin \alpha_9) \\
&\quad - \frac{h^2 \dot{\theta}}{3} (8C_{L2} \dot{v}_2 \sin \alpha_2 + 8C_{L3} \dot{v}_3 \sin \alpha_3 + 24C_{L4} \dot{v}_4 \sin \alpha_4 + 16C_{L5} \dot{v}_5 \sin \alpha_5 + 40C_{L6} \dot{v}_6 \sin \alpha_6 \\
&\quad + 24C_{L7} \dot{v}_7 \sin \alpha_7 + 56C_{L8} \dot{v}_8 \sin \alpha_8 + 16C_{L9} \dot{v}_9 \sin \alpha_9) + \frac{h\dot{s}}{3} (2C_{L1} \dot{v}_1 \cos \alpha_1 \\
&\quad + 8C_{L2} \dot{v}_2 \cos \alpha_2 + 4C_{L3} \dot{v}_3 \cos \alpha_3 + 8C_{L4} \dot{v}_4 \cos \alpha_4 + 4C_{L5} \dot{v}_5 \cos \alpha_5 + 8C_{L6} \dot{v}_6 \cos \alpha_6 \\
&\quad \left. + 4C_{L7} \dot{v}_7 \cos \alpha_7 + 8C_{L8} \dot{v}_8 \cos \alpha_8 + 2C_{L9} \dot{v}_9 \cos \alpha_9) \right]
\end{aligned}$$

or:

$$\begin{aligned}
\Delta_1 \ddot{s} + \Delta_2 \ddot{v}_2 + \Delta_3 \ddot{v}_3 + \Delta_2 \ddot{v}_4 + \Delta_3 \ddot{v}_5 + \Delta_2 \ddot{v}_6 + \Delta_3 \ddot{v}_7 + \Delta_2 \ddot{v}_8 + \Delta_4 \ddot{v}_9 - \Delta_5 \\
= \beta_1 \dot{\theta}^2 + \beta_{21} \dot{s}^2 + \beta_{22} \dot{v}_2^2 + \beta_{23} \dot{v}_3^2 + \beta_{24} \dot{v}_4^2 + \beta_{25} \dot{v}_5^2 + \beta_{26} \dot{v}_6^2 + \beta_{27} \dot{v}_7^2 + \beta_{28} \dot{v}_8^2 + \beta_{29} \dot{v}_9^2 - \beta_2 \dot{\theta} \dot{v}_2 \\
- \beta_3 \dot{\theta} \dot{v}_3 - \beta_4 \dot{\theta} \dot{v}_4 - \beta_5 \dot{\theta} \dot{v}_5 - \beta_6 \dot{\theta} \dot{v}_6 - \beta_7 \dot{\theta} \dot{v}_7 - \beta_8 \dot{\theta} \dot{v}_8 - \beta_9 \dot{\theta} \dot{v}_9 + \beta_{13} \dot{s} \dot{v}_2 + \beta_{14} \dot{s} \dot{v}_3 \\
+ \beta_{15} \dot{s} \dot{v}_4 + \beta_{16} \dot{s} \dot{v}_5 + \beta_{17} \dot{s} \dot{v}_6 + \beta_{18} \dot{s} \dot{v}_7 + \beta_{19} \dot{s} \dot{v}_8 + \beta_{20} \dot{s} \dot{v}_9
\end{aligned} \tag{20}$$

where:

$$\Delta_1 = m_{\text{hub}} + \rho AL$$

$$\Delta_2 = \frac{4\rho Ah \cos \alpha}{3}$$

$$\Delta_3 = \frac{2\rho Ah \cos \alpha}{3}$$

$$\Delta_4 = \frac{\rho Ah \cos \alpha}{3}$$

$$\Delta_5 = (m_{\text{hub}} - \rho AL)g$$

$$\beta_1 = \frac{\rho c}{2} \left( \frac{\beta_{10} r^2 h + \beta_{11} r h^2 + \beta_{12} h^3}{3} \right)$$

$$\beta_2 = \frac{8\rho c}{6} (r h + h^2) C_{L2} \sin \alpha_2$$

$$\beta_3 = \frac{4\rho c}{6} (r h + 2h^2) C_{L3} \sin \alpha_3$$

$$\beta_4 = \frac{8\rho c}{6} (r h + 3h^2) C_{L4} \sin \alpha_4$$

$$\beta_5 = \frac{4\rho c}{6} (r h + 4h^2) C_{L5} \sin \alpha_5$$

$$\beta_6 = \frac{8\rho c}{6} (r h + 5h^2) C_{L6} \sin \alpha_6$$

$$\beta_7 = \frac{4\rho c}{6} (r h + 6h^2) C_{L7} \sin \alpha_7$$

$$\beta_8 = \frac{8\rho c}{6} (r h + 7h^2) C_{L8} \sin \alpha_8$$

$$\beta_9 = \frac{2\rho c}{6} (r h + 8h^2) C_{L9} \sin \alpha_9$$

$$\beta_{10} = \frac{\rho c}{2} (C_{L1} + 4C_{L2} + 2C_{L3} + 4C_{L4} + 2C_{L5} + 4C_{L6} + 2C_{L7} + 4C_{L8} + C_{L9})$$

$$\beta_{11} = \frac{\rho c}{2} (8C_{L2} + 8C_{L3} + 24C_{L4} + 16C_{L5} + 40C_{L6} + 24C_{L7} + 56C_{L8} + 16C_{L9})$$

$$\beta_{12} = \frac{\rho c}{2}(4C_{L2} + 8C_{L3} + 36C_{L4} + 32C_{L5} + 100C_{L6} + 72C_{L7} + 196C_{L8} + 64C_{L9})$$

$$\beta_{13} = \frac{8\rho c}{6}hC_{L2} \cos \alpha_2$$

$$\beta_{14} = \frac{4\rho c}{6}hC_{L3} \cos \alpha_3$$

$$\beta_{15} = \frac{8\rho c}{6}hC_{L4} \cos \alpha_4$$

$$\beta_{16} = \frac{4\rho c}{6}hC_{L5} \cos \alpha_5$$

$$\beta_{17} = \frac{8\rho c}{6}hC_{L6} \cos \alpha_6$$

$$\beta_{18} = \frac{4\rho c}{6}hC_{L7} \cos \alpha_7$$

$$\beta_{19} = \frac{8\rho c}{6}hC_{L8} \cos \alpha_8$$

$$\beta_{20} = \frac{2\rho c}{6}hC_{L9} \cos \alpha_9$$

$$\beta_{21} = \frac{\rho c}{6}\beta_{10}h$$

$$\beta_{22} = \frac{4\rho c}{6}hC_{L2}$$

$$\beta_{23} = \frac{2\rho c}{6}hC_{L3}$$

$$\beta_{24} = \frac{4\rho c}{6}hC_{L4}$$

$$\beta_{25} = \frac{2\rho c}{6}hC_{L5}$$

$$\beta_{26} = \frac{4\rho c}{6}hC_{L6}$$

$$\beta_{27} = \frac{2\rho c}{6}hC_{L7}$$

$$\beta_{28} = \frac{4\rho c}{6}hC_{L8}$$

$$\beta_{29} = \frac{\rho c}{6} h C_{L9}$$

In Eq. (20), for example,  $\ddot{v}_1$  means  $\frac{d^2 v_1}{dt^2}$  at the point whose space coordinate is  $x_1$  (it is a total derivative and not a partial derivative). And so on.

The next step is the application of the finite difference method into the governing equation of motion given by Eq. 14.

### 3.2 Applying the Finite Difference Method

Making explicit the derivatives of  $v$  in Eq. 14 and expanding  $f_v$  in Eq. 16 results:

$$\begin{aligned} \frac{\partial^2 v}{\partial t^2} + (r+x) \sin \alpha \ddot{\theta} + \cos \alpha \ddot{s} - v \sin^2 \alpha \dot{\theta}^2 + \rho A g \cos \alpha + \frac{EI}{\rho A} \frac{\partial^4 v}{\partial x^4} &= \frac{\rho c}{2} \{ [\dot{\theta}(r+x) - \frac{\partial v}{\partial t} \sin \alpha]^2 \\ + [\frac{\partial v}{\partial t} \cos \alpha + \dot{s}]^2 \} [C_L \cos \alpha + \frac{1}{2} k \sin \alpha] \end{aligned} \tag{21}$$

Consider Fig. 2.

The general formula for the central difference using 5 points is given by [20]:

$$\frac{\partial^4 v(x_i, t)}{\partial x^4} = \frac{v(x_i + 2h, t) - 4v(x_i + h, t) + 6v(x_i, t) - 4v(x_i - h, t) + v(x_i - 2h, t)}{h^4} \tag{22}$$

For points 3 to 7 one has, respectively (remembering that  $v_1 = 0$ ):

$$\frac{\partial^4 v(x_3, t)}{\partial x^4} = \frac{v(x_3 + 2h, t) - 4v(x_3 + h, t) + 6v(x_3, t) - 4v(x_3 - h, t) + v(x_3 - 2h, t)}{h^4}$$

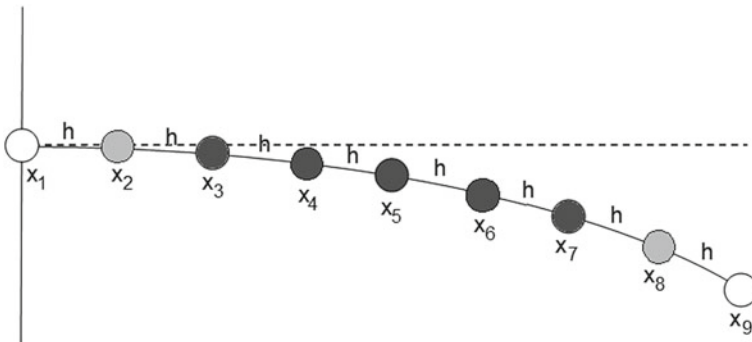


Fig. 2 Discretization of a clamped-free beam

$$= \frac{v_5 - 4v_4 + 6v_3 - 4v_2 + v_1}{h^4} = \frac{v_5 - 4v_4 + 6v_3 - 4v_2}{h^4} = \frac{\partial^4 v_3}{\partial x^4} \quad (23)$$

$$\begin{aligned} \frac{\partial^4 v(x_4, t)}{\partial x^4} &= \frac{v(x_4 + 2h, t) - 4v(x_4 + h, t) + 6v(x_4, t) - 4v(x_4 - h, t) + v(x_4 - 2h, t)}{h^4} \\ &= \frac{v_6 - 4v_5 + 6v_4 - 4v_3 + v_2}{h^4} = \frac{\partial^4 v_4}{\partial x^4} \end{aligned} \quad (24)$$

$$\begin{aligned} \frac{\partial^4 v(x_5, t)}{\partial x^4} &= \frac{v(x_5 + 2h, t) - 4v(x_5 + h, t) + 6v(x_5, t) - 4v(x_5 - h, t) + v(x_5 - 2h, t)}{h^4} \\ &= \frac{v_7 - 4v_6 + 6v_5 - 4v_4 + v_3}{h^4} = \frac{\partial^4 v_5}{\partial x^4} \end{aligned} \quad (25)$$

$$\begin{aligned} \frac{\partial^4 v(x_6, t)}{\partial x^4} &= \frac{v(x_6 + 2h, t) - 4v(x_6 + h, t) + 6v(x_6, t) - 4v(x_6 - h, t) + v(x_6 - 2h, t)}{h^4} \\ &= \frac{v_8 - 4v_7 + 6v_6 - 4v_5 + v_4}{h^4} = \frac{\partial^4 v_6}{\partial x^4} \end{aligned} \quad (26)$$

$$\begin{aligned} \frac{\partial^4 v(x_7, t)}{\partial x^4} &= \frac{v(x_7 + 2h, t) - 4v(x_7 + h, t) + 6v(x_7, t) - 4v(x_7 - h, t) + v(x_7 - 2h, t)}{h^4} \\ &= \frac{v_9 - 4v_8 + 6v_7 - 4v_6 + v_5}{h^4} = \frac{\partial^4 v_7}{\partial x^4} \end{aligned} \quad (27)$$

As the structure is clamped at point 1, for this point one always has:

$$v(x_1, t) = v_1 = 0 \quad (28)$$

It means that it is not necessary to solve an equation for this variable.

For point 2, applying the general formula one has:

$$\frac{\partial^4 v(x_2, t)}{\partial x^4} = \frac{v(x_2 + 2h, t) - 4v(x_2 + h, t) + 6v(x_2, t) - 4v(x_2 - h, t) + v(x_2 - 2h, t)}{h^4} \quad (29)$$

The point  $x_2 - 2h$  is outside the beam. However, for point  $x_1$  it is known that  $v'(x_1, t) = 0$  (since the beam is clamped at this point). Using the central difference formula and considering three points, it can be written that:

$$\frac{\partial v(x_1, t)}{\partial x} = \frac{v(x_1 + h, t) - v(x_1 - h, t)}{2h} = \frac{v(x_1 + h, t) - v(x_2 - 2h, t)}{2h} = 0 \quad (30)$$

Therefore:

$$v(x_1 + h, t) = v(x_2 - 2h, t) \quad (31)$$

Substituting Eq. (31) into Eq. (29) results:

$$\begin{aligned}\frac{\partial^4 v(x_2, t)}{\partial x^4} &= \frac{v(x_2 + 2h, t) - 4v(x_2 + h, t) + 6v(x_2, t) - 4v(x_2 - h, t) + v(x_1 + h, t)}{h^4} \\ &= \frac{v_4 - 4v_3 + 7v_2 - 4v_1}{h^4} = \frac{v_4 - 4v_3 + 7v_2}{h^4} = \frac{\partial^4 v_2}{\partial x^4}\end{aligned}\quad (32)$$

For point 8, applying the general formula one has:

$$\frac{\partial^4 v(x_8, t)}{\partial x^4} = \frac{v(x_8 + 2h, t) - 4v(x_8 + h, t) + 6v(x_8, t) - 4v(x_8 - h, t) + v(x_8 - 2h, t)}{h^4}\quad (33)$$

The point  $x_8 + 2h$  is outside the beam. However, for point  $x_9$  it is known that  $v''(x_9, t) = 0$  (since the beam is free at this point). Using the central difference formula and considering three points, it can be written that:

$$\frac{\partial^2 v(x_9, t)}{\partial x^2} = \frac{v(x_9 + h, t) - 2v(x_9, t) + v(x_9 - h, t)}{h^2} = 0\quad (34)$$

or:

$$\frac{\partial^2 v(x_9, t)}{\partial x^2} = \frac{v(x_8 + 2h, t) - 2v(x_9, t) + v(x_9 - h, t)}{h^2} = 0\quad (35)$$

Therefore:

$$v(x_8 + 2h, t) = 2v(x_9, t) - v(x_9 - h, t)\quad (36)$$

Substituting Eq. (36) into Eq. (33) results:

$$\begin{aligned}\frac{\partial^4 v(x_8, t)}{\partial x^4} &= \frac{2v(x_9, t) - v(x_9 - h, t) - 4v(x_8 + h, t) + 6v(x_8, t) - 4v(x_8 - h, t) + v(x_8 - 2h, t)}{h^4} \\ &= \frac{-2v_9 + 5v_8 - 4v_7 + v_6}{h^4} = \frac{\partial^4 v_8}{\partial x^4}\end{aligned}\quad (37)$$

For point 9, applying the general formula one has:

$$\frac{\partial^4 v(x_9, t)}{\partial x^4} = \frac{v(x_9 + 2h, t) - 4v(x_9 + h, t) + 6v(x_9, t) - 4v(x_9 - h, t) + v(x_9 - 2h, t)}{h^4}\quad (38)$$

The points  $x_9 + h$  and  $x_9 + 2h$  are outside the beam. However, from Eq. (36) one has:

$$v(x_8 + 2h, t) = 2v(x_9, t) - v(x_9 - h, t) = v(x_9 + h, t)\quad (39)$$

From the problem in question (free end), it is also known that:

$$\frac{\partial^3 v(x_9, t)}{\partial x^3} = 0$$

or, using the central difference formula considering 5 points:

$$\frac{\partial^3 v(x_9, t)}{\partial x^3} = \frac{v(x_9 + 2h, t) - 2v(x_9 + h, t) + 2v(x_9 - h, t) - v(x_9 - 2h, t)}{2h^3} = 0$$

Therefore:

$$v(x_9 + 2h, t) = 2v(x_9 + h, t) - 2v(x_9 - h, t) + v(x_9 - 2h, t) \quad (40)$$

Substituting Eq. (39) into Eq. (40) results:

$$v(x_9 + 2h, t) = 4v(x_9, t) - 4v(x_9 - h, t) + v(x_9 - 2h, t) \quad (41)$$

Substituting Eq. (39) and Eq. (41) into Eq. (38) results:

$$\frac{\partial^4 v(x_9, t)}{\partial x^4} = \frac{2v(x_9, t) - 4v(x_9 - h, t) + 2v(x_9 - 2h, t)}{h^4} = \frac{2v_9 - 4v_8 + 2v_7}{h^4} = \frac{\partial^4 v_9}{\partial x^4} \quad (42)$$

So, finally, Eq. 21 can be rewritten for nodes 2 through 9 as (and considering that  $x_2 = h, x_3 = 2 h, x_4 = 3 h, \dots$ ):

$$\begin{aligned} \ddot{v}_2 + (r + h) \sin \alpha_2 \ddot{\theta} + \cos \alpha_2 \ddot{s} - v_2 \sin^2 \alpha_2 \dot{\theta}^2 + \rho A g \cos \alpha_2 \\ + \frac{EI}{\rho A h^4} (v_4 - 4v_3 + 7v_2) = \frac{\rho c}{2} \{[\dot{\theta}(r + h) - \dot{v}_2 \sin \alpha_2]^2 \\ + [\dot{v}_2 \cos \alpha_2 + \dot{s}]^2\} [C_{L2} \cos \alpha_2 + \frac{1}{2} k \sin \alpha_2] \end{aligned} \quad (43)$$

$$\begin{aligned} \ddot{v}_3 + (r + 2h) \sin \alpha_3 \ddot{\theta} + \cos \alpha_3 \ddot{s} - v_3 \sin^2 \alpha_3 \dot{\theta}^2 + \rho A g \cos \alpha_3 + \frac{EI}{\rho A h^4} (v_5 - 4v_4 + 6v_3 \\ - 4v_2) = \frac{\rho c}{2} \{[\dot{\theta}(r + 2h) - \dot{v}_3 \sin \alpha_3]^2 + [\dot{v}_3 \cos \alpha_3 + \dot{s}]^2\} [C_{L3} \cos \alpha_3 + \frac{1}{2} k \sin \alpha_3] \end{aligned} \quad (44)$$

$$\begin{aligned} \ddot{v}_4 + (r + 3h) \sin \alpha_4 \ddot{\theta} + \cos \alpha_4 \ddot{s} - v_4 \sin^2 \alpha_4 \dot{\theta}^2 + \rho A g \cos \alpha_4 + \frac{EI}{\rho A h^4} (v_6 - 4v_5 + 6v_4 - 4v_3 \\ + v_2) = \frac{\rho c}{2} \{[\dot{\theta}(r + 3h) - \dot{v}_4 \sin \alpha_4]^2 + [\dot{v}_4 \cos \alpha_4 + \dot{s}]^2\} [C_{L4} \cos \alpha_4 + \frac{1}{2} k \sin \alpha_4] \end{aligned} \quad (45)$$

$$\begin{aligned} \ddot{v}_5 + (r + 4h) \sin \alpha_5 \ddot{\theta} + \cos \alpha_5 \ddot{s} - v_5 \sin^2 \alpha_5 \dot{\theta}^2 + \rho A g \cos \alpha_5 + \frac{EI}{\rho A h^4} (v_7 - 4v_6 + 6v_5 - 4v_4 \\ + v_3) = \frac{\rho c}{2} \{[\dot{\theta}(r + 4h) - \dot{v}_5 \sin \alpha_5]^2 + [\dot{v}_5 \cos \alpha_5 + \dot{s}]^2\} [C_{L5} \cos \alpha_5 + \frac{1}{2} k \sin \alpha_5] \end{aligned} \quad (46)$$



$$\begin{aligned} \ddot{v}_6 + (r + 5h) \sin \alpha_6 \ddot{\theta} + \cos \alpha_6 \ddot{s} - v_6 \sin^2 \alpha_6 \dot{\theta}^2 + \rho A g \cos \alpha_6 + \frac{EI}{\rho A h^4} (v_8 - 4v_7 + 6v_6 - 4v_5 \\ + v_4) = \frac{\rho c}{2} \{[\dot{\theta}(r + 5h) - \dot{v}_6 \sin \alpha_6]^2 + [\dot{v}_6 \cos \alpha_6 + \dot{s}]^2\} [C_{L6} \cos \alpha_6 + \frac{1}{2} k \sin \alpha_6] \end{aligned} \quad (47)$$

$$\begin{aligned} \ddot{v}_7 + (r + 6h) \sin \alpha_7 \ddot{\theta} + \cos \alpha_7 \ddot{s} - v_7 \sin^2 \alpha_7 \dot{\theta}^2 + \rho A g \cos \alpha_7 + \frac{EI}{\rho A h^4} (v_9 - 4v_8 + 6v_7 - 4v_6 \\ + v_5) = \frac{\rho c}{2} \{[\dot{\theta}(r + 6h) - \dot{v}_7 \sin \alpha_7]^2 + [\dot{v}_7 \cos \alpha_7 + \dot{s}]^2\} [C_{L7} \cos \alpha_7 + \frac{1}{2} k \sin \alpha_7] \end{aligned} \quad (48)$$

$$\begin{aligned} \ddot{v}_8 + (r + 7h) \sin \alpha_8 \ddot{\theta} + \cos \alpha_8 \ddot{s} - v_8 \sin^2 \alpha_8 \dot{\theta}^2 + \rho A g \cos \alpha_8 + \frac{EI}{\rho A h^4} (-2v_9 + 5v_8 - 4v_7 \\ + v_6) = \frac{\rho c}{2} \{[\dot{\theta}(r + 7h) - \dot{v}_8 \sin \alpha_8]^2 + [\dot{v}_8 \cos \alpha_8 + \dot{s}]^2\} [C_{L8} \cos \alpha_8 + \frac{1}{2} k \sin \alpha_8] \end{aligned} \quad (49)$$

$$\begin{aligned} \ddot{v}_9 + (r + 8h) \sin \alpha_9 \ddot{\theta} + \cos \alpha_9 \ddot{s} - v_9 \sin^2 \alpha_9 \dot{\theta}^2 + \rho A g \cos \alpha_9 + \frac{EI}{\rho A h^4} (2v_9 - 4v_8 + 2v_7) \\ = \frac{\rho c}{2} \{[\dot{\theta}(r + 8h) - \dot{v}_9 \sin \alpha_9]^2 + [\dot{v}_9 \cos \alpha_9 + \dot{s}]^2\} [C_{L9} \cos \alpha_9 + \frac{1}{2} k \sin \alpha_9] \end{aligned} \quad (50)$$

Equations (43) to (50) can be rewritten as:

$$\begin{aligned} \ddot{v}_2 + (r + h) \sin \alpha_2 \ddot{\theta} + \cos \alpha_2 \ddot{s} - C_2 (r + h)^2 \dot{\theta}^2 - C_2 \dot{v}_2^2 - C_2 \dot{s}^2 + 2C_2 (r + h) \sin \alpha_2 \dot{\theta} \dot{v}_2 \\ - 2C_2 \cos \alpha_2 \dot{s} \dot{v}_2 - \sin^2 \alpha_2 v_2 \dot{\theta}^2 + \frac{EI}{\rho A h^4} (v_4 - 4v_3 + 7v_2) = -\rho A g \cos \alpha_2 \end{aligned} \quad (51)$$

$$\begin{aligned} \ddot{v}_3 + (r + 2h) \sin \alpha_3 \ddot{\theta} + \cos \alpha_3 \ddot{s} - C_3 (r + 2h)^2 \dot{\theta}^2 - C_3 \dot{v}_3^2 - C_3 \dot{s}^2 + 2C_3 (r + 2h) \sin \alpha_3 \dot{\theta} \dot{v}_3 \\ - 2C_3 \cos \alpha_3 \dot{s} \dot{v}_3 - \sin^2 \alpha_3 v_3 \dot{\theta}^2 + \frac{EI}{\rho A h^4} (v_5 - 4v_4 + 6v_3 - 4v_2) = -\rho A g \cos \alpha_3 \end{aligned} \quad (52)$$

$$\begin{aligned} \ddot{v}_4 + (r + 3h) \sin \alpha_4 \ddot{\theta} + \cos \alpha_4 \ddot{s} - C_4 (r + 3h)^2 \dot{\theta}^2 - C_4 \dot{v}_4^2 - C_4 \dot{s}^2 + 2C_4 (r + 3h) \sin \alpha_4 \dot{\theta} \dot{v}_4 \\ - 2C_4 \cos \alpha_4 \dot{s} \dot{v}_4 - \sin^2 \alpha_4 v_4 \dot{\theta}^2 + \frac{EI}{\rho A h^4} (v_6 - 4v_5 + 6v_4 - 4v_3 + v_2) = -\rho A g \cos \alpha_4 \end{aligned} \quad (53)$$

$$\begin{aligned} \ddot{v}_5 + (r + 4h) \sin \alpha_5 \ddot{\theta} + \cos \alpha_5 \ddot{s} - C_5 (r + 4h)^2 \dot{\theta}^2 - C_5 \dot{v}_5^2 - C_5 \dot{s}^2 + 2C_5 (r + 4h) \sin \alpha_5 \dot{\theta} \dot{v}_5 \\ - 2C_5 \cos \alpha_5 \dot{s} \dot{v}_5 - \sin^2 \alpha_5 v_5 \dot{\theta}^2 + \frac{EI}{\rho A h^4} (v_7 - 4v_6 + 6v_5 - 4v_4 + v_3) = -\rho A g \cos \alpha_5 \end{aligned} \quad (54)$$

$$\begin{aligned} \ddot{v}_6 + (r + 5h) \sin \alpha_6 \ddot{\theta} + \cos \alpha_6 \ddot{s} - C_6 (r + 5h)^2 \dot{\theta}^2 - C_6 \dot{v}_6^2 - C_6 \dot{s}^2 + 2C_6 (r + 5h) \sin \alpha_6 \dot{\theta} \dot{v}_6 \\ - 2C_6 \cos \alpha_6 \dot{s} \dot{v}_6 - \sin^2 \alpha_6 v_6 \dot{\theta}^2 + \frac{EI}{\rho A h^4} (v_8 - 4v_7 + 6v_6 - 4v_5 + v_4) = -\rho A g \cos \alpha_6 \end{aligned} \quad (55)$$

$$\begin{aligned} \ddot{v}_7 + (r + 6h) \sin \alpha_7 \ddot{\theta} + \cos \alpha_7 \ddot{s} - C_7 (r + 6h)^2 \dot{\theta}^2 - C_7 \dot{v}_7^2 - C_7 \dot{s}^2 + 2C_7 (r + 6h) \sin \alpha_7 \dot{\theta} \dot{v}_7 \\ - 2C_7 \cos \alpha_7 \dot{s} \dot{v}_7 - \sin^2 \alpha_7 v_7 \dot{\theta}^2 + \frac{EI}{\rho A h^4} (v_9 - 4v_8 + 6v_7 - 4v_6 + v_5) = -\rho A g \cos \alpha_7 \end{aligned} \quad (56)$$

$$\begin{aligned} \ddot{v}_8 + (r + 7h) \sin \alpha_8 \ddot{\theta} + \cos \alpha_8 \ddot{s} - C_8 (r + 7h)^2 \dot{\theta}^2 - C_8 \dot{v}_8^2 - C_8 \dot{s}^2 + 2C_8 (r + 7h) \sin \alpha_8 \dot{\theta} \dot{v}_8 \\ - 2C_8 \cos \alpha_8 \dot{s} \dot{v}_8 - \sin^2 \alpha_8 v_8 \dot{\theta}^2 + \frac{EI}{\rho A h^4} (-2v_9 + 5v_8 - 4v_7 + v_6) = -\rho A g \cos \alpha_8 \end{aligned} \quad (57)$$

$$\begin{aligned} \ddot{v}_9 + (r + 8h) \sin \alpha_9 \ddot{\theta} + \cos \alpha_9 \ddot{s} - C_9 (r + 8h)^2 \dot{\theta}^2 - C_9 \dot{v}_9^2 - C_9 \dot{s}^2 + 2C_9 (r + 8h) \sin \alpha_9 \dot{\theta} \dot{v}_9 \\ - 2C_9 \cos \alpha_9 \dot{s} \dot{v}_9 - \sin^2 \alpha_9 v_9 \dot{\theta}^2 + \frac{EI}{\rho A h^4} (2v_9 - 4v_8 + 2v_7) = -\rho A g \cos \alpha_9 \end{aligned} \quad (58)$$

where:

$$C_2 = \frac{\rho c}{2} \left( C_{L2} \cos \alpha_2 + \frac{1}{2} k \sin \alpha_2 \right)$$

$$C_3 = \frac{\rho c}{2} \left( C_{L3} \cos \alpha_3 + \frac{1}{2} k \sin \alpha_3 \right)$$

$$C_4 = \frac{\rho c}{2} \left( C_{L4} \cos \alpha_4 + \frac{1}{2} k \sin \alpha_4 \right)$$

$$C_5 = \frac{\rho c}{2} \left( C_{L5} \cos \alpha_5 + \frac{1}{2} k \sin \alpha_5 \right)$$

$$C_6 = \frac{\rho c}{2} \left( C_{L6} \cos \alpha_6 + \frac{1}{2} k \sin \alpha_6 \right)$$

$$C_7 = \frac{\rho c}{2} \left( C_{L7} \cos \alpha_7 + \frac{1}{2} k \sin \alpha_7 \right)$$

$$C_8 = \frac{\rho c}{2} \left( C_{L8} \cos \alpha_8 + \frac{1}{2} k \sin \alpha_8 \right)$$

$$C_9 = \frac{\rho c}{2} \left( C_{L9} \cos \alpha_9 + \frac{1}{2} k \sin \alpha_9 \right)$$

## 4 The Non-ideal DC Motor

The difference between the mathematical models of an ideal and of a non-ideal dynamical system is given by the choice of the actuator-structure coupling model, e.g., it depends on the way the torque  $\tau$  is modeled [1, 2].

In the case the motor axis is sufficiently short, in order that one can consider it sufficiently rigid, the total torque,  $\tau$ , acting on this axis can be written as:

$$\tau = -M + I_{\text{axis}} \ddot{\theta} \quad (59)$$

In Eq. (59),  $M$  is the flexure moment of the beam, acting on the motor axis. Using this equation, the mechanical equation of the DC motor becomes:

$$(I_{\text{axis}} + I_m N_g^2) \ddot{\theta} + (c_m N_g^2) \dot{\theta} - (N_g K_t) i_a = M \quad (60)$$

The moment  $M$  can be represented by the assumption of linear curvature model as:

$$M = EI v''(x_1, x) = EI v_1''(t)$$

Using the central difference formula and considering three points, it can be written:

$$\frac{\partial^2 v(x_1, t)}{\partial x^2} = \frac{v(x_1 + h, t) - 2v(x_1, t) + v(x_1 - h, t)}{h^2} = \frac{v_2 - 2v_1 + v(x_1 - h, t)}{h^2} = v_1''(t)$$

Using Eqs. (30) and (31) one can write:

$$v(x_1 - h, t) = v(x_2 - 2h, t) = v(x_1 + h, t)$$

Therefore:

$$v_1''(t) = \frac{2v_2 - 2v_1}{h^2}$$

And, finally:

$$M = \frac{2EI}{h^2} (v_2 - v_1) = \left( \frac{2EI}{h^2} \right) v_2 \quad (61)$$

The equations of motion for the slewing flexible structure considering an ideal ( $\beta = 0$ ) and a nonideal ( $\beta = 1$ ) power source are given by Eqs. (20) and (51) to (58) and by the electrical and mechanical direct current motor governing equations of motion given respectively by:

$$L_m \frac{di_a}{dt} + R_a i_a + N_g K_b \dot{\theta} = U \quad (62)$$

$$(I_{axis} + I_m N_g^2) \ddot{\theta} + (c_m N_g^2) \dot{\theta} - (N_g K_t) i_a = \beta \left( \frac{2EI}{h^2} \right) v_2 \quad (63)$$

The electrical time constant  $\frac{L_m}{R_a}$  is often neglected since it is at least one order in magnitude smaller than the mechanical time constant  $\frac{I_{axis} + I_m N_g^2}{c_m N_g^2}$ . By neglecting the term  $L_m \frac{di_a}{dt}$  in Eq. (62), one can write:

$$i_a = \frac{U - N_g K_b \dot{\theta}}{R_a} \quad (64)$$

Substituting Eq. (64) into Eq. (63), the governing equation of motion of the electric motor is simplified to:

$$(I_{axis} + I_m N_g^2) \ddot{\theta} + \left( c_m N_g^2 + \frac{N_g^2 K_t K_b}{R_a} \right) \dot{\theta} = \left( \frac{N_g K_t}{R_a} \right) U + \beta \left( \frac{2EI}{h^2} \right) v_2 \quad (65)$$

### 5 The Piezoelectric Actuator

A more detailed discussion about these actuators, their mathematical modeling and incorporation into the governing equations of motion of the rotating flexible structure is not part of the scope of this work. For this work, the idea that the addition of piezoelectric actuators acting along the flexible structure adds external forces on the right side of Eq. (14) is sufficient.

Adding the piezoelectric actuation in Eq. (14) results [21, 22]:

$$\ddot{v} + (r + x) \sin \alpha \ddot{\theta} + \cos \alpha \ddot{s} - v \sin^2 \alpha \dot{\theta}^2 + \rho A g \cos \alpha + \frac{EI}{\rho A} v^{iv} = f_v + \frac{\partial^2 M_{piezo}(x, t)}{\partial x^2} \quad (66)$$

ou, equivalently:

$$\ddot{v} + (r + x) \sin \alpha \ddot{\theta} + \cos \alpha \ddot{s} - v \sin^2 \alpha \dot{\theta}^2 + \rho A g \cos \alpha + \frac{EI}{\rho A} v^{iv} = f_v + q_{piezo}(x, t) \quad (67)$$

where  $M_{piezo}(x, t)$  in Eq. (66) represents the bending moment applied by the piezoelectric actuator to the beam and  $q_{piezo}(x, t)$  in Eq. (67) represents the force applied by the piezoelectric actuator to the beam. The external force  $q_{piezo}(x, t)$  is also the control force to be applied along the flexible structure.

In Eqs. (43) to (50) (or Eqs. (51) to (58)), related to each one of the discretized nodes, one must add on the right side the external forces  $q_{piezo, i}(x_i, t)$  where  $i = 2$  to 9 or, equivalently,  $q_{piezo, i}(t)$ . This external force applied to each node is related to the vibration control of the flexible structure and is connected to an ideal DC motor. The equations for the ideal motor are not considered here in the numerical integration of the governing equations of motion.

### 6 Nonlinear Control: Partial Feedback Linearization

The main ideas developed in this subchapter are based on several papers which deal with a very assorted class of underactuated mechanical systems [10, 23–25].

The stability and control analysis of the underactuated system investigated here start with the definition of two classes of variables: collocated variables (or the actuated variables) and non-collocated variables (or the unactuated variables), which are represented respectively by the vectors  $q_1$  and  $q_2$ .

In matrix form, the complete set of governing equations of motion can be written as:

$$\begin{bmatrix} M_{11} & M_{12} \\ M_{21} & M_{22} \end{bmatrix} \begin{Bmatrix} \ddot{q}_1 \\ \ddot{q}_2 \end{Bmatrix} + \begin{Bmatrix} h_1 \\ h_2 \end{Bmatrix} + \begin{Bmatrix} 0_1 \\ 0_2 \end{Bmatrix} + \begin{Bmatrix} \ell_1 \\ \ell_2 \end{Bmatrix} = \begin{Bmatrix} t \\ 0 \end{Bmatrix} \quad (68)$$

In Eq. (68), Coriolis and centrifugal terms are collected into the vector functions  $\mathbf{h}_1$  and  $\mathbf{h}_2$ , gravitational terms are collected into the vector functions  $\varphi_1$  and  $\varphi_2$ , the linear terms are collected into the vector functions  $\ell_1$  and  $\ell_2$  and the input generalized forces produced by the actuators on the actuated variables are collected into the vector function  $\boldsymbol{\tau}$ .

The matrix Eq. (68) can be rewritten as:

$$\mathbf{M}_{11}\ddot{\mathbf{q}}_1 + \mathbf{M}_{12}\ddot{\mathbf{q}}_2 + \mathbf{h}_1 + \mathbf{0}_1 + \ell_1 = \boldsymbol{\tau} \quad (69)$$

$$\mathbf{M}_{21}\ddot{\mathbf{q}}_1 + \mathbf{M}_{22}\ddot{\mathbf{q}}_2 + \mathbf{h}_2 + \mathbf{0}_2 + \ell_2 = \mathbf{0} \quad (70)$$

The unactuated states,  $\mathbf{q}_2$ , can be determined from Eq. (70) according to:

$$\ddot{\mathbf{q}}_2 = -\mathbf{M}_{22}^{-1}(\mathbf{M}_{21}\ddot{\mathbf{q}}_1 + \mathbf{h}_2 + \mathbf{0}_2 + \ell_2) \quad (71)$$

Substituting  $\ddot{\mathbf{q}}_2$  as given by Eq. (71) into Eq. (69) results:

$$\bar{\mathbf{M}}_{11}\ddot{\mathbf{q}}_1 + \bar{\mathbf{h}}_1 + \bar{\mathbf{0}}_1 + \bar{\ell}_1 = \boldsymbol{\tau} \quad (72)$$

where:

$$\bar{\mathbf{M}}_{11} = \mathbf{M}_{11} - \mathbf{M}_{12}\mathbf{M}_{22}^{-1}\mathbf{M}_{21}$$

$$\bar{\mathbf{h}}_1 = \mathbf{h}_1 - \mathbf{M}_{12}\mathbf{M}_{22}^{-1}\mathbf{h}_2$$

$$\bar{\mathbf{0}}_1 = \mathbf{0}_1 - \mathbf{M}_{12}\mathbf{M}_{22}^{-1}\mathbf{0}_2$$

$$\bar{\ell}_1 = \ell_1 - \mathbf{M}_{12}\mathbf{M}_{22}^{-1}\ell_2$$

Equation (72) can be rewritten in order to isolate  $\ddot{\mathbf{q}}_1$  according to:

$$\ddot{\mathbf{q}}_1 = \bar{\mathbf{M}}_{11}^{-1}(\boldsymbol{\tau} - \bar{\mathbf{h}}_1 - \bar{\mathbf{0}}_1 - \bar{\ell}_1) \quad (73)$$

or:

$$\ddot{\mathbf{q}}_1 = \bar{\mathbf{M}}_{11}^{-1}(\boldsymbol{\tau} - \bar{\mathbf{h}}_1 - \bar{\mathbf{0}}_1) - \bar{\mathbf{M}}_{11}^{-1}\bar{\ell}_1$$

or, finally:

$$\ddot{\mathbf{q}}_1 + \bar{\mathbf{M}}_{11}^{-1}\bar{\ell}_1 = \bar{\mathbf{M}}_{11}^{-1}(\boldsymbol{\tau} - \bar{\mathbf{h}}_1 - \bar{\mathbf{0}}_1) \quad (74)$$

In Eq. (74), matrix  $\overline{\mathbf{M}}_{11}^{-1}$  is constant (that is, it has elements that do not vary over time, since the angle of attack  $\alpha$  is considered constant in this work). In this way, all the linear terms on the set of governing equations of motion and that represent important couplings for the problem in question are kept. The left side of Eq. (74) is linear.

Consider the actuated states,  $\mathbf{q}_1$ , as the system outputs. Let the control signal  $\tau$  be defined as:

$$\tau = \overline{\mathbf{M}}_{11} \mathbf{v}_a + \overline{\mathbf{h}}_1 + \overline{\mathbf{0}}_1 \tag{75}$$

where  $\mathbf{v}_a$  is an additional control input (yet to be defined).

Substituting Eq. (75) into Eq. (74), the equation of motion related to the actuated dynamics becomes:

$$\ddot{\mathbf{q}}_1 + \overline{\mathbf{M}}_{11}^{-1} \overline{\ell}_1 = \mathbf{v}_a \tag{76}$$

Considering Eq. (76) and substituting  $\ddot{\mathbf{q}}_1$  as given by this equation into Eq. (70), the complete set of governing equations of motion (related to both collocated and non-collocated variables) is now written as:

$$\ddot{\mathbf{q}}_1 + \overline{\mathbf{M}}_{11}^{-1} \overline{\ell}_1 = \mathbf{v}_a \tag{77}$$

$$\mathbf{M}_{22} \ddot{\mathbf{q}}_2 + \mathbf{h}_2 + \mathbf{0}_2 + \ell_2 - \mathbf{M}_{21} \overline{\mathbf{M}}_{11}^{-1} \overline{\ell}_1 = -\mathbf{M}_{21} \mathbf{v}_a \tag{78}$$

$$\mathbf{y}_1 = \mathbf{q}_1 \tag{79}$$

Equation (78) represents the dynamics of the unactuated degrees of freedom and Eq. (79) is the output equation.

The new controller  $\mathbf{v}_a$  in Eqs. (77) and (78) must be designed to drive the actuated variables:

$$\mathbf{q}_1 = \{ \theta \ v_2 \ v_3 \ v_4 \ v_5 \ v_6 \ v_7 \ v_8 \ v_9 \}^T \tag{80}$$

to the desired final values (or reference values):

$$\mathbf{q}_1^d = \{ \theta^d \ v_2^d \ v_3^d \ v_4^d \ v_5^d \ v_6^d \ v_7^d \ v_8^d \ v_9^d \}^T \tag{81}$$

In order to reach the desired values given by Eq. (81) and (if possible) to keep the unactuated states stabilized, the additional control input  $\mathbf{v}_a$  is obtained in this work using the optimal control technique named Linear Quadratic Regulator (LQR) according to [26]:

$$\begin{aligned} \mathbf{v}_a &= -\mathbf{R}^{-1}\mathbf{B}^T\mathbf{P}(\mathbf{q}_1 - \mathbf{q}_1^d) \\ &= \{v_{a1} \ v_{a2} \ v_{a3} \ v_{a4} \ v_{a5} \ v_{a6} \ v_{a7} \ v_{a8} \ v_{a9}\} \end{aligned} \quad (82)$$

where  $\mathbf{P}$  is the solution of the Riccati equation:

$$\mathbf{P}\mathbf{A} + \mathbf{A}^T\mathbf{P} + \mathbf{Q} - \mathbf{P}\mathbf{B}\mathbf{R}^{-1}\mathbf{B}^T\mathbf{P} = \mathbf{0} \quad (83)$$

$\mathbf{Q}$  and  $\mathbf{R}$  are weighting matrices that satisfy the positivedefiniteness condition  $\mathbf{Q} > 0$  and  $\mathbf{R} > 0$ ,  $\mathbf{A}$  and  $\mathbf{B}$  are matricesobtained when the system is written in the state space form:

$$\dot{\mathbf{x}} = \mathbf{A}\mathbf{x} + \mathbf{B}\mathbf{u} \quad (84)$$

$\mathbf{x}$  is the state vector (not including the states related to variable  $s$ ) and  $\mathbf{u}$  is the vector of control forces and torques in the state space form.

For underactuated mechanical systems, after the governing equations of motion related to the actuated degrees of freedom are linearized through partial feedback linearization, the remaining equation(s) related to the unactuated degree(s) of freedom is(are) nonlinear and is(are) called internal dynamics [10]. The internal dynamics for the problem under investigation here is given by Eq. (78).

The stability of the internal dynamics must be investigated. If the internal dynamics is stable (in this stage of the analysis, the stability of the equations related to the actuated variables was already checked), the whole system is stable. This stability of the internal dynamics is checked through the analysis of the zero dynamics, which is the set of governing equations that remains when one considers all the actuated degrees of freedom and its time derivatives equal to zero (the actuated states converged to the desired values) in the internal dynamics [10].

## 7 The Complete Set of Governing Equations of Motion Considering the Nonlinear Control

Considering the developments presented in Sect. 3, 4 and 5, the complete set of governing equations of motion for the mechanical system presented in Fig. 1 is finally given by:

$$(\mathbf{I}_{\text{axis}} + \mathbf{I}_m \mathbf{N}_g^2) \ddot{\theta} + \left( c_m \mathbf{N}_g^2 + \frac{\mathbf{N}_g^2 \mathbf{K}_t \mathbf{K}_b}{\mathbf{R}_a} \right) \dot{\theta} = \left( \frac{\mathbf{N}_g \mathbf{K}_t}{\mathbf{R}_a} \right) \mathbf{U} + \beta \left( \frac{2EI}{h^2} \right) \mathbf{v}_2 \quad (85)$$

$$\begin{aligned} &\Delta_1 \ddot{s} + \Delta_2 \ddot{v}_2 + \Delta_3 \ddot{v}_3 + \Delta_2 \ddot{v}_4 + \Delta_3 \ddot{v}_5 + \Delta_2 \ddot{v}_6 + \Delta_3 \ddot{v}_7 + \Delta_2 \ddot{v}_8 + \Delta_4 \ddot{v}_9 - \Delta_5 \\ &= \beta_1 \dot{\theta}^2 + \beta_{21} \dot{s}^2 + \beta_{22} \dot{v}_2^2 + \beta_{23} \dot{v}_3^2 + \beta_{24} \dot{v}_4^2 + \beta_{25} \dot{v}_5^2 + \beta_{26} \dot{v}_6^2 + \beta_{27} \dot{v}_7^2 + \beta_{28} \dot{v}_8^2 + \beta_{29} \dot{v}_9^2 - \beta_2 \dot{\theta} \dot{v}_2 \\ &\quad - \beta_3 \dot{\theta} \dot{v}_3 - \beta_4 \dot{\theta} \dot{v}_4 - \beta_5 \dot{\theta} \dot{v}_5 - \beta_6 \dot{\theta} \dot{v}_6 - \beta_7 \dot{\theta} \dot{v}_7 - \beta_8 \dot{\theta} \dot{v}_8 - \beta_9 \dot{\theta} \dot{v}_9 + \beta_{13} \dot{s} \dot{v}_2 + \beta_{14} \dot{s} \dot{v}_3 + \beta_{15} \dot{s} \dot{v}_4 \end{aligned}$$

$$+ \beta_{16}\dot{s}\dot{v}_5 + \beta_{17}\dot{s}\dot{v}_6 + \beta_{18}\dot{s}\dot{v}_7 + \beta_{19}\dot{s}\dot{v}_8 + \beta_{20}\dot{s}\dot{v}_9 \quad (86)$$

$$\ddot{v}_2 + (r+h)\sin\alpha_2\ddot{\theta} + \cos\alpha_2\ddot{s} - C_2(r+h)^2\dot{\theta}^2 - C_2v_2^2 - C_2\dot{s}^2 + 2C_2(r+h)\sin\alpha_2\dot{\theta}\dot{v}_2 \\ - 2C_2\cos\alpha_2\dot{s}\dot{v}_2 - \sin^2\alpha_2v_2\dot{\theta}^2 + \frac{EI}{\rho Ah^4}(v_4 - 4v_3 + 7v_2) = -\rho Ag\cos\alpha_2 + q_{piezo,2} \quad (87)$$

$$\ddot{v}_3 + (r+2h)\sin\alpha_3\ddot{\theta} + \cos\alpha_3\ddot{s} - C_3(r+2h)^2\dot{\theta}^2 - C_3v_3^2 - C_3\dot{s}^2 + 2C_3(r+2h)\sin\alpha_3\dot{\theta}\dot{v}_3 \\ - 2C_3\cos\alpha_3\dot{s}\dot{v}_3 - \sin^2\alpha_3v_3\dot{\theta}^2 + \frac{EI}{\rho Ah^4}(v_5 - 4v_4 + 6v_3 - 4v_2) = -\rho Ag\cos\alpha_3 + q_{piezo,3} \quad (88)$$

$$\ddot{v}_4 + (r+3h)\sin\alpha_4\ddot{\theta} + \cos\alpha_4\ddot{s} - C_4(r+3h)^2\dot{\theta}^2 - C_4v_4^2 - C_4\dot{s}^2 + 2C_4(r+3h)\sin\alpha_4\dot{\theta}\dot{v}_4 \\ - 2C_4\cos\alpha_4\dot{s}\dot{v}_4 - \sin^2\alpha_4v_4\dot{\theta}^2 + \frac{EI}{\rho Ah^4}(v_6 - 4v_5 + 6v_4 - 4v_3 + v_2) = -\rho Ag\cos\alpha_4 + q_{piezo,4} \quad (89)$$

$$\ddot{v}_5 + (r+4h)\sin\alpha_5\ddot{\theta} + \cos\alpha_5\ddot{s} - C_5(r+4h)^2\dot{\theta}^2 - C_5v_5^2 - C_5\dot{s}^2 + 2C_5(r+4h)\sin\alpha_5\dot{\theta}\dot{v}_5 \\ - 2C_5\cos\alpha_5\dot{s}\dot{v}_5 - \sin^2\alpha_5v_5\dot{\theta}^2 + \frac{EI}{\rho Ah^4}(v_7 - 4v_6 + 6v_5 - 4v_4 + v_3) = -\rho Ag\cos\alpha_5 + q_{piezo,5} \quad (90)$$

$$\ddot{v}_6 + (r+5h)\sin\alpha_6\ddot{\theta} + \cos\alpha_6\ddot{s} - C_6(r+5h)^2\dot{\theta}^2 - C_6v_6^2 - C_6\dot{s}^2 + 2C_6(r+5h)\sin\alpha_6\dot{\theta}\dot{v}_6 \\ - 2C_6\cos\alpha_6\dot{s}\dot{v}_6 - \sin^2\alpha_6v_6\dot{\theta}^2 + \frac{EI}{\rho Ah^4}(v_8 - 4v_7 + 6v_6 - 4v_5 + v_4) = -\rho Ag\cos\alpha_6 + q_{piezo,6} \quad (91)$$

$$\ddot{v}_7 + (r+6h)\sin\alpha_7\ddot{\theta} + \cos\alpha_7\ddot{s} - C_7(r+6h)^2\dot{\theta}^2 - C_7v_7^2 - C_7\dot{s}^2 + 2C_7(r+6h)\sin\alpha_7\dot{\theta}\dot{v}_7 \\ - 2C_7\cos\alpha_7\dot{s}\dot{v}_7 - \sin^2\alpha_7v_7\dot{\theta}^2 + \frac{EI}{\rho Ah^4}(v_9 - 4v_8 + 6v_7 - 4v_6 + v_5) = -\rho Ag\cos\alpha_7 + q_{piezo,7} \quad (92)$$

$$\ddot{v}_8 + (r+7h)\sin\alpha_8\ddot{\theta} + \cos\alpha_8\ddot{s} - C_8(r+7h)^2\dot{\theta}^2 - C_8v_8^2 - C_8\dot{s}^2 + 2C_8(r+7h)\sin\alpha_8\dot{\theta}\dot{v}_8 \\ - 2C_8\cos\alpha_8\dot{s}\dot{v}_8 - \sin^2\alpha_8v_8\dot{\theta}^2 + \frac{EI}{\rho Ah^4}(-2v_9 + 5v_8 - 4v_7 + v_6) = -\rho Ag\cos\alpha_8 + q_{piezo,8} \quad (93)$$

$$\ddot{v}_9 + (r+8h)\sin\alpha_9\ddot{\theta} + \cos\alpha_9\ddot{s} - C_9(r+8h)^2\dot{\theta}^2 - C_9v_9^2 - C_9\dot{s}^2 + 2C_9(r+8h)\sin\alpha_9\dot{\theta}\dot{v}_9 \\ - 2C_9\cos\alpha_9\dot{s}\dot{v}_9 - \sin^2\alpha_9v_9\dot{\theta}^2 + \frac{EI}{\rho Ah^4}(2v_9 - 4v_8 + 2v_7) = -\rho Ag\cos\alpha_9 + q_{piezo,9} \quad (94)$$

Writing Eqs. (85) to (94) in matrix form results:

$$\begin{bmatrix} \mathbf{I}_{axis} + \mathbf{I}_m N_g^2 & 0 & 0 & 0 & 0 & 0 & 0 & 0 & 0 & 0 \\ 0 & \Delta_1 & \Delta_2 & \Delta_3 & \Delta_2 & \Delta_3 & \Delta_2 & \Delta_3 & \Delta_2 & \Delta_4 \end{bmatrix} \begin{bmatrix} \ddot{\theta} \\ \ddot{s} \\ \ddot{v}_2 \\ \ddot{v}_3 \\ \ddot{v}_4 \\ \ddot{v}_5 \\ \ddot{v}_6 \\ \ddot{v}_7 \\ \ddot{v}_8 \\ \ddot{v}_9 \end{bmatrix} + \begin{bmatrix} 0 \\ f_1 \\ f_2 \\ f_3 \\ f_4 \\ f_5 \\ f_6 \\ f_7 \\ f_8 \\ f_{19} \end{bmatrix} + \begin{bmatrix} 0 \\ -\Delta_5 \\ (\rho A \cos \alpha_2)g \\ (\rho A \cos \alpha_3)g \\ (\rho A \cos \alpha_4)g \\ (\rho A \cos \alpha_5)g \\ (\rho A \cos \alpha_6)g \\ (\rho A \cos \alpha_7)g \\ (\rho A \cos \alpha_8)g \\ (\rho A \cos \alpha_9)g \end{bmatrix} + \begin{bmatrix} \ell_{1a} \\ 0 \\ \ell_{1b} \\ \ell_{1c} \\ \ell_{1d} \\ \ell_{1e} \\ \ell_{1f} \\ \ell_{1g} \\ \ell_{1h} \\ \ell_{1i} \end{bmatrix}$$



$$= \begin{bmatrix} \frac{N_g K_t}{R_a} & 0 & 0 & 0 & 0 & 0 & 0 & 0 & 0 \\ 0 & 0 & 0 & 0 & 0 & 0 & 0 & 0 & 0 \\ 0 & 0 & 1 & 0 & 0 & 0 & 0 & 0 & 0 \\ 0 & 0 & 0 & 1 & 0 & 0 & 0 & 0 & 0 \\ 0 & 0 & 0 & 0 & 1 & 0 & 0 & 0 & 0 \\ 0 & 0 & 0 & 0 & 0 & 1 & 0 & 0 & 0 \\ 0 & 0 & 0 & 0 & 0 & 0 & 1 & 0 & 0 \\ 0 & 0 & 0 & 0 & 0 & 0 & 0 & 1 & 0 \\ 0 & 0 & 0 & 0 & 0 & 0 & 0 & 0 & 1 \end{bmatrix} \begin{pmatrix} U \\ 0 \\ q_{piezo,2} \\ q_{piezo,3} \\ q_{piezo,4} \\ q_{piezo,5} \\ q_{piezo,6} \\ q_{piezo,7} \\ q_{piezo,8} \\ q_{piezo,9} \end{pmatrix} \tag{95}$$

where:

$$f_1 = \beta_1 \dot{\theta}^2 + \beta_{21} \dot{s}^2 + \beta_{22} \dot{v}_2^2 + \beta_{23} \dot{v}_3^2 + \beta_{24} \dot{v}_4^2 + \beta_{25} \dot{v}_5^2 + \beta_{26} \dot{v}_6^2 + \beta_{27} \dot{v}_7^2 + \beta_{28} \dot{v}_8^2 + \beta_{29} \dot{v}_9^2 - \beta_2 \dot{\theta} \dot{v}_2 - \beta_3 \dot{\theta} \dot{v}_3 - \beta_4 \dot{\theta} \dot{v}_4 - \beta_5 \dot{\theta} \dot{v}_5 - \beta_6 \dot{\theta} \dot{v}_6 - \beta_7 \dot{\theta} \dot{v}_7 - \beta_8 \dot{\theta} \dot{v}_8 - \beta_9 \dot{\theta} \dot{v}_9 + \beta_{13} \dot{s} \dot{v}_2 + \beta_{14} \dot{s} \dot{v}_3 + \beta_{15} \dot{s} \dot{v}_4 + \beta_{16} \dot{s} \dot{v}_5 + \beta_{17} \dot{s} \dot{v}_6 + \beta_{18} \dot{s} \dot{v}_7 + \beta_{19} \dot{s} \dot{v}_8 + \beta_{20} \dot{s} \dot{v}_9 \tag{96}$$

$$f_2 = -C_2(r+h)^2 \dot{\theta}^2 - C_2 \dot{v}_2^2 - C_2 \dot{s}^2 + 2C_2(r+h) \sin \alpha_2 \dot{\theta} \dot{v}_2 - 2C_2 \cos \alpha_2 \dot{s} \dot{v}_2 - \sin^2 \alpha_2 v_2 \dot{\theta}^2 \tag{97}$$

$$f_3 = -C_3(r+2h)^2 \dot{\theta}^2 - C_3 \dot{v}_3^2 - C_3 \dot{s}^2 + 2C_3(r+2h) \sin \alpha_3 \dot{\theta} \dot{v}_3 - 2C_3 \cos \alpha_3 \dot{s} \dot{v}_3 - \sin^2 \alpha_3 v_3 \dot{\theta}^2 \tag{98}$$

$$f_4 = -C_4(r+3h)^2 \dot{\theta}^2 - C_4 \dot{v}_4^2 - C_4 \dot{s}^2 + 2C_4(r+3h) \sin \alpha_4 \dot{\theta} \dot{v}_4 - 2C_4 \cos \alpha_4 \dot{s} \dot{v}_4 - \sin^2 \alpha_4 v_4 \dot{\theta}^2 \tag{99}$$

$$f_5 = -C_5(r+4h)^2 \dot{\theta}^2 - C_5 \dot{v}_5^2 - C_5 \dot{s}^2 + 2C_5(r+4h) \sin \alpha_5 \dot{\theta} \dot{v}_5 - 2C_5 \cos \alpha_5 \dot{s} \dot{v}_5 - \sin^2 \alpha_5 v_5 \dot{\theta}^2 \tag{100}$$

$$f_6 = -C_2(r+5h)^2 \dot{\theta}^2 - C_6 \dot{v}_6^2 - C_6 \dot{s}^2 + 2C_6(r+5h) \sin \alpha_6 \dot{\theta} \dot{v}_6 - 2C_6 \cos \alpha_6 \dot{s} \dot{v}_6 - \sin^2 \alpha_6 v_6 \dot{\theta}^2 \tag{101}$$

$$f_7 = -C_7(r+6h)^2 \dot{\theta}^2 - C_7 \dot{v}_7^2 - C_7 \dot{s}^2 + 2C_7(r+6h) \sin \alpha_7 \dot{\theta} \dot{v}_7 - 2C_7 \cos \alpha_7 \dot{s} \dot{v}_7 - \sin^2 \alpha_7 v_7 \dot{\theta}^2 \tag{102}$$

$$f_8 = -C_8(r+7h)^2 \dot{\theta}^2 - C_8 \dot{v}_8^2 - C_8 \dot{s}^2 + 2C_8(r+7h) \sin \alpha_8 \dot{\theta} \dot{v}_8 - 2C_8 \cos \alpha_8 \dot{s} \dot{v}_8 - \sin^2 \alpha_8 v_8 \dot{\theta}^2 \tag{103}$$

$$f_9 = -C_9(r+8h)^2 \dot{\theta}^2 - C_9 \dot{v}_9^2 - C_9 \dot{s}^2 + 2C_9(r+8h) \sin \alpha_9 \dot{\theta} \dot{v}_9 - 2C_9 \cos \alpha_9 \dot{s} \dot{v}_9 - \sin^2 \alpha_9 v_9 \dot{\theta}^2 \tag{104}$$

$$\ell_{1a} = \left( c_m N_g^2 + \frac{N_g^2 K_t K_b}{R_a} \right) \dot{\theta} + \beta \left( \frac{2EI}{h^2} \right) v_2 \tag{105}$$

$$\ell_{1b} = \frac{EI}{\rho A h^4} (v_4 - 4v_3 + 7v_2) \tag{106}$$

$$\ell_{1c} = \frac{EI}{\rho A h^4} (v_5 - 4v_4 + 6v_3 - 4v_2) \tag{107}$$

$$\ell_{1d} = \frac{EI}{\rho Ah^4} (v_6 - 4v_5 + 6v_4 - 4v_3 + v_2) \tag{108}$$

$$\ell_{1e} = \frac{EI}{\rho Ah^4} (v_7 - 4v_6 + 6v_5 - 4v_4 + v_3) \tag{109}$$

$$\ell_{1f} = \frac{EI}{\rho Ah^4} (v_8 - 4v_7 + 6v_6 - 4v_5 + v_4) \tag{110}$$

$$\ell_{1g} = \frac{EI}{\rho Ah^4} (v_9 - 4v_8 + 6v_7 - 4v_6 + v_5) \tag{111}$$

$$\ell_{1h} = \frac{EI}{\rho Ah^4} (-2v_9 + 5v_8 - 4v_7 + v_6) \tag{112}$$

$$\ell_{1i} = \frac{EI}{\rho Ah^4} (2v_9 - 4v_8 + 2v_7) \tag{113}$$

In order to write the governing equations in the matrix form shown in Eq. (68), Eq. (95) is rewritten as:

$$\begin{bmatrix}
 I_{axis} + I_m N_g^2 & 0 & 0 & 0 & 0 & 0 & 0 & 0 & 0 & 0 \\
 (r+h) \sin \alpha_2 & 1 & 0 & 0 & 0 & 0 & 0 & 0 & 0 & \cos \alpha_2 \\
 (r+2h) \sin \alpha_3 & 0 & 1 & 0 & 0 & 0 & 0 & 0 & 0 & \cos \alpha_3 \\
 (r+3h) \sin \alpha_4 & 0 & 0 & 1 & 0 & 0 & 0 & 0 & 0 & \cos \alpha_4 \\
 (r+4h) \sin \alpha_5 & 0 & 0 & 0 & 1 & 0 & 0 & 0 & 0 & \cos \alpha_5 \\
 (r+5h) \sin \alpha_6 & 0 & 0 & 0 & 0 & 1 & 0 & 0 & 0 & \cos \alpha_6 \\
 (r+6h) \sin \alpha_7 & 0 & 0 & 0 & 0 & 0 & 1 & 0 & 0 & \cos \alpha_7 \\
 (r+7h) \sin \alpha_8 & 0 & 0 & 0 & 0 & 0 & 0 & 1 & 0 & \cos \alpha_8 \\
 (r+8h) \sin \alpha_9 & 0 & 0 & 0 & 0 & 0 & 0 & 0 & 1 & \cos \alpha_9 \\
 0 & \Delta_2 & \Delta_3 & \Delta_2 & \Delta_3 & \Delta_2 & \Delta_3 & \Delta_2 & \Delta_4 & \Delta_1
 \end{bmatrix}
 \begin{bmatrix}
 \ddot{\theta} \\
 \ddot{v}_2 \\
 \ddot{v}_3 \\
 \ddot{v}_4 \\
 \ddot{v}_5 \\
 \ddot{v}_6 \\
 \ddot{v}_7 \\
 \ddot{v}_8 \\
 \ddot{v}_9 \\
 \ddot{s}
 \end{bmatrix}
 +
 \begin{bmatrix}
 0 \\
 f_2 \\
 f_3 \\
 f_4 \\
 f_5 \\
 f_6 \\
 f_7 \\
 f_8 \\
 f_9 \\
 f_1
 \end{bmatrix}
 +
 \begin{bmatrix}
 0 \\
 (\rho A \cos \alpha_2)g \\
 (\rho A \cos \alpha_3)g \\
 (\rho A \cos \alpha_4)g \\
 (\rho A \cos \alpha_5)g \\
 (\rho A \cos \alpha_6)g \\
 (\rho A \cos \alpha_7)g \\
 (\rho A \cos \alpha_8)g \\
 (\rho A \cos \alpha_9)g \\
 -\Delta_5
 \end{bmatrix}
 +
 \begin{bmatrix}
 \ell_{1a} \\
 \ell_{1b} \\
 \ell_{1c} \\
 \ell_{1d} \\
 \ell_{1e} \\
 \ell_{1f} \\
 \ell_{1g} \\
 \ell_{1h} \\
 \ell_{1i} \\
 0
 \end{bmatrix}
 \tag{114}$$

$$=
 \begin{bmatrix}
 \frac{N_g K_t}{R_a} & 0 & 0 & 0 & 0 & 0 & 0 & 0 & 0 & 0 \\
 0 & 1 & 0 & 0 & 0 & 0 & 0 & 0 & 0 & 0 \\
 0 & 0 & 1 & 0 & 0 & 0 & 0 & 0 & 0 & 0 \\
 0 & 0 & 0 & 1 & 0 & 0 & 0 & 0 & 0 & 0 \\
 0 & 0 & 0 & 0 & 1 & 0 & 0 & 0 & 0 & 0 \\
 0 & 0 & 0 & 0 & 0 & 1 & 0 & 0 & 0 & 0 \\
 0 & 0 & 0 & 0 & 0 & 0 & 1 & 0 & 0 & 0 \\
 0 & 0 & 0 & 0 & 0 & 0 & 0 & 1 & 0 & 0 \\
 0 & 0 & 0 & 0 & 0 & 0 & 0 & 0 & 1 & 0 \\
 0 & 0 & 0 & 0 & 0 & 0 & 0 & 0 & 0 & 1
 \end{bmatrix}
 \begin{bmatrix}
 U \\
 q_{piezo,2} \\
 q_{piezo,3} \\
 q_{piezo,4} \\
 q_{piezo,5} \\
 q_{piezo,6} \\
 q_{piezo,7} \\
 q_{piezo,8} \\
 q_{piezo,9} \\
 0
 \end{bmatrix}$$

Based on Eq. (68) and Eq. (114), one can write:

$$\mathbf{M}_{11} = \begin{bmatrix} \mathbf{I}_{\text{axis}} + \mathbf{I}_m N_g^2 & 0 & 0 & 0 & 0 & 0 & 0 & 0 & 0 \\ (r+h) \sin \alpha_2 & 1 & 0 & 0 & 0 & 0 & 0 & 0 & 0 \\ (r+2h) \sin \alpha_3 & 0 & 1 & 0 & 0 & 0 & 0 & 0 & 0 \\ (r+3h) \sin \alpha_4 & 0 & 0 & 1 & 0 & 0 & 0 & 0 & 0 \\ (r+4h) \sin \alpha_5 & 0 & 0 & 0 & 1 & 0 & 0 & 0 & 0 \\ (r+5h) \sin \alpha_6 & 0 & 0 & 0 & 0 & 1 & 0 & 0 & 0 \\ (r+6h) \sin \alpha_7 & 0 & 0 & 0 & 0 & 0 & 1 & 0 & 0 \\ (r+7h) \sin \alpha_8 & 0 & 0 & 0 & 0 & 0 & 0 & 1 & 0 \\ (r+8h) \sin \alpha_9 & 0 & 0 & 0 & 0 & 0 & 0 & 0 & 1 \end{bmatrix}$$

$$\mathbf{M}_{12} = [0 \cos \alpha_2 \cos \alpha_3 \cos \alpha_4 \cos \alpha_5 \cos \alpha_6 \cos \alpha_7 \cos \alpha_8 \cos \alpha_9]^T$$

$$\mathbf{M}_{21} = [0 \Delta_2 \Delta_3 \Delta_2 \Delta_3 \Delta_2 \Delta_3 \Delta_2 \Delta_4]$$

$$\mathbf{M}_{22} = [\Delta_1]$$

$$\mathbf{h}_1 = \{0 f_2 f_3 f_4 f_5 f_6 f_7 f_8 f_9\}^T$$

$$\mathbf{h}_2 = \{f_1\}$$

$$\mathbf{0}_1 = \rho A g \{0 \cos \alpha_2 \cos \alpha_3 \cos \alpha_4 \cos \alpha_5 \cos \alpha_6 \cos \alpha_7 \cos \alpha_8 \cos \alpha_9\}^T$$

$$\mathbf{0}_2 = \{-\Delta_5\}$$

$$\ell_1 = \{\ell_{1a} \ell_{1b} \ell_{1c} \ell_{1d} \ell_{1e} \ell_{1f} \ell_{1g} \ell_{1h} \ell_{1i}\}^T$$

$$\ell_2 = \{0\}$$

$$\boldsymbol{\tau} = \left\{ \left( \frac{N_g K_t}{R_a} \right) U \mathbf{q}_{\text{piezo},2} \mathbf{q}_{\text{piezo},3} \mathbf{q}_{\text{piezo},4} \mathbf{q}_{\text{piezo},5} \mathbf{q}_{\text{piezo},6} \mathbf{q}_{\text{piezo},7} \mathbf{q}_{\text{piezo},8} \mathbf{q}_{\text{piezo},9} \right\}^T$$

Expanding  $\overline{\mathbf{M}}_{11}$  one obtains:



And let the inverse of  $\overline{\mathbf{M}}_{11}$  be given by:

$$\overline{\mathbf{M}}_{11}^{-1} = \begin{bmatrix} m_1 & 0 & 0 & 0 & 0 & 0 & 0 & 0 & 0 & 0 \\ m_{10} & m_{11} & m_{12} & m_{13} & m_{14} & m_{15} & m_{16} & m_{17} & m_{18} & \\ m_{19} & m_{20} & m_{21} & m_{22} & m_{23} & m_{24} & m_{25} & m_{26} & m_{27} & \\ m_{28} & m_{29} & m_{30} & m_{31} & m_{32} & m_{33} & m_{34} & m_{35} & m_{36} & \\ m_{37} & m_{38} & m_{39} & m_{40} & m_{41} & m_{42} & m_{43} & m_{44} & m_{45} & \\ m_{46} & m_{47} & m_{48} & m_{49} & m_{50} & m_{51} & m_{52} & m_{53} & m_{54} & \\ m_{55} & m_{56} & m_{57} & m_{58} & m_{59} & m_{60} & m_{61} & m_{62} & m_{63} & \\ m_{64} & m_{65} & m_{66} & m_{67} & m_{68} & m_{69} & m_{70} & m_{71} & m_{72} & \\ m_{73} & m_{74} & m_{75} & m_{76} & m_{77} & m_{78} & m_{79} & m_{80} & m_{81} & \end{bmatrix}$$

The elements of matrix  $\overline{\mathbf{M}}_{11}^{-1}$  are quite complex to be obtained analytically. These quantities must be obtained numerically. In this article, this matrix is constant and only needs to be calculated once.

Expanding Eqs. (77) and (78), the governing equations motion in closed-loop form (for the actuated variables) result:

$$\ddot{\theta} + \vartheta_1 \dot{\theta} + (\beta \vartheta_{10}) v_2 = v_{a1} \tag{115}$$

$$\begin{aligned} \ddot{v}_2 + \vartheta_2 \dot{\theta} + (\beta \vartheta_{11} + \vartheta_{19}) v_2 + \vartheta_{27} v_3 + \vartheta_{35} v_4 + \vartheta_{43} v_5 \\ + \vartheta_{51} v_6 + \vartheta_{59} v_7 + \vartheta_{67} v_8 + \vartheta_{75} v_9 = v_{a2} \end{aligned} \tag{116}$$

$$\begin{aligned} \ddot{v}_3 + \vartheta_3 \dot{\theta} + (\beta \vartheta_{12} + \vartheta_{20}) v_2 + \vartheta_{28} v_3 + \vartheta_{36} v_4 + \vartheta_{44} v_5 \\ + \vartheta_{52} v_6 + \vartheta_{60} v_7 + \vartheta_{68} v_8 + \vartheta_{76} v_9 = v_{a3} \end{aligned} \tag{117}$$

$$\begin{aligned} \ddot{v}_4 + \vartheta_4 \dot{\theta} + (\beta \vartheta_{13} + \vartheta_{21}) v_2 + \vartheta_{29} v_3 + \vartheta_{37} v_4 + \vartheta_{45} v_5 \\ + \vartheta_{53} v_6 + \vartheta_{61} v_7 + \vartheta_{69} v_8 + \vartheta_{77} v_9 = v_{a4} \end{aligned} \tag{118}$$

$$\begin{aligned} \ddot{v}_5 + \vartheta_5 \dot{\theta} + (\beta \vartheta_{14} + \vartheta_{22}) v_2 + \vartheta_{30} v_3 + \vartheta_{38} v_4 + \vartheta_{46} v_5 \\ + \vartheta_{54} v_6 + \vartheta_{62} v_7 + \vartheta_{70} v_8 + \vartheta_{78} v_9 = v_{a5} \end{aligned} \tag{119}$$

$$\ddot{v}_6 + \vartheta_6 \dot{\theta} + (\beta \vartheta_{15} + \vartheta_{23})v_2 + \vartheta_{31}v_3 + \vartheta_{39}v_4 + \vartheta_{47}v_5 + \vartheta_{55}v_6 + \vartheta_{63}v_7 + \vartheta_{71}v_8 + \vartheta_{79}v_9 = v_{a6} \tag{120}$$

$$\ddot{v}_7 + \vartheta_7 \dot{\theta} + (\beta \vartheta_{16} + \vartheta_{24})v_2 + \vartheta_{32}v_3 + \vartheta_{40}v_4 + \vartheta_{48}v_5 + \vartheta_{56}v_6 + \vartheta_{64}v_7 + \vartheta_{72}v_8 + \vartheta_{80}v_9 = v_{a7} \tag{121}$$

$$\ddot{v}_8 + \vartheta_8 \dot{\theta} + (\beta \vartheta_{17} + \vartheta_{25})v_2 + \vartheta_{33}v_3 + \vartheta_{41}v_4 + \vartheta_{49}v_5 + \vartheta_{57}v_6 + \vartheta_{65}v_7 + \vartheta_{73}v_8 + \vartheta_{81}v_9 = v_{a8} \tag{122}$$

$$\ddot{v}_9 + \vartheta_9 \dot{\theta} + (\beta \vartheta_{18} + \vartheta_{26})v_2 + \vartheta_{34}v_3 + \vartheta_{42}v_4 + \vartheta_{50}v_5 + \vartheta_{58}v_6 + \vartheta_{66}v_7 + \vartheta_{74}v_8 + \vartheta_{82}v_9 = v_{a9} \tag{123}$$

$$\begin{aligned} \Delta_1 \ddot{s} + f_1 - \Delta_5 - \sigma_1 \ell_{1a} - \sigma_2 \ell_{1b} - \sigma_3 \ell_{1c} - \sigma_4 \ell_{1d} - \sigma_5 \ell_{1e} \\ - \sigma_6 \ell_{1f} - \sigma_7 \ell_{1g} - \sigma_8 \ell_{1h} - \sigma_9 \ell_{1i} = -\Delta_2 v_{a2} - \Delta_3 v_{a3} - \Delta_2 v_{a4} - \Delta_3 v_{a5} \\ - \Delta_2 v_{a6} - \Delta_3 v_{a7} - \Delta_3 v_{a7} - \Delta_2 v_{a8} - \Delta_4 v_{a9} \end{aligned} \tag{124}$$

where:

$\vartheta_1 = m_1 \left( c_m N_g^2 + \frac{N_g^2 K_t K_b}{R_a} \right)$	$\vartheta_2 = m_{10} \left( c_m N_g^2 + \frac{N_g^2 K_t K_b}{R_a} \right)$	$\vartheta_3 = m_{19} \left( c_m N_g^2 + \frac{N_g^2 K_t K_b}{R_a} \right)$
$\vartheta_4 = m_{28} \left( c_m N_g^2 + \frac{N_g^2 K_t K_b}{R_a} \right)$	$\vartheta_5 = m_{37} \left( c_m N_g^2 + \frac{N_g^2 K_t K_b}{R_a} \right)$	$\vartheta_6 = m_{46} \left( c_m N_g^2 + \frac{N_g^2 K_t K_b}{R_a} \right)$
$\vartheta_7 = m_{55} \left( c_m N_g^2 + \frac{N_g^2 K_t K_b}{R_a} \right)$	$\vartheta_8 = m_{64} \left( c_m N_g^2 + \frac{N_g^2 K_t K_b}{R_a} \right)$	$\vartheta_9 = m_{73} \left( c_m N_g^2 + \frac{N_g^2 K_t K_b}{R_a} \right)$

$\phi_{10} = \frac{2m_1 EI}{h^2}$	$\phi_{11} = \frac{2m_0 EI}{h^2}$	$\phi_{12} = \frac{2m_0 EI}{h^2}$	$\phi_{13} = \frac{2m_0 EI}{h^2}$	$\phi_{14} = \frac{2m_0 EI}{h^2}$
$\phi_{15} = \frac{2m_0 EI}{h^2}$	$\phi_{16} = \frac{2m_0 EI}{h^2}$	$\phi_{17} = \frac{2m_0 EI}{h^2}$	$\phi_{18} = \frac{2m_0 EI}{h^2}$	
$\phi_{19} = \frac{EI}{\rho Ah^4} (7m_{11} - 4m_{12} + m_3)$	$\phi_{20} = \frac{EI}{\rho Ah^4} (7m_{20} - 4m_{21} + m_{22})$			$\phi_{21} = \frac{EI}{\rho Ah^4} (7m_{29} - 4m_{30} + m_{31})$
$\phi_{22} = \frac{EI}{\rho Ah^4} (7m_{38} - 4m_{39} + m_4)$	$\phi_{23} = \frac{EI}{\rho Ah^4} (7m_{47} - 4m_{48} + m_{49})$			$\phi_{24} = \frac{EI}{\rho Ah^4} (7m_{56} - 4m_{57} + m_{58})$
$\phi_{25} = \frac{EI}{\rho Ah^4} (7m_{65} - 4m_{66} + m_{67})$	$\phi_{26} = \frac{EI}{\rho Ah^4} (7m_{74} - 4m_{75} + m_{76})$			
$\phi_{27} = \frac{EI}{\rho Ah^4} (6m_{12} - 4m_{11} - 4m_{13} + m_{14})$		$\phi_{28} = \frac{EI}{\rho Ah^4} (6m_{21} - 4m_{20} - 4m_{22} + m_{23})$		
$\phi_{29} = \frac{EI}{\rho Ah^4} (6m_{30} - 4m_{29} - 4m_{31} + m_{32})$		$\phi_{30} = \frac{EI}{\rho Ah^4} (6m_{39} - 4m_{38} - 4m_{40} + m_{41})$		
$\phi_{31} = \frac{EI}{\rho Ah^4} (6m_{48} - 4m_{47} - 4m_{49} + m_{50})$		$\phi_{32} = \frac{EI}{\rho Ah^4} (6m_{57} - 4m_{56} - 4m_{58} + m_{59})$		
$\phi_{33} = \frac{EI}{\rho Ah^4} (6m_{66} - 4m_{65} - 4m_{67} + m_{68})$		$\phi_{34} = \frac{EI}{\rho Ah^4} (6m_{75} - 4m_{74} - 4m_{76} + m_{77})$		
$\phi_{35} = \frac{EI}{\rho Ah^4} (m_{11} - 4m_{12} + 6m_{13} - 4m_{14} + m_{15})$		$\phi_{36} = \frac{EI}{\rho Ah^4} (m_{20} - 4m_{21} + 6m_{22} - 4m_{23} + m_{24})$		
$\phi_{37} = \frac{EI}{\rho Ah^4} (m_{29} - 4m_{30} + 6m_{31} - 4m_{32} + m_{33})$		$\phi_{38} = \frac{EI}{\rho Ah^4} (m_{38} - 4m_{39} + 6m_{40} - 4m_{41} + m_{42})$		
$\phi_{39} = \frac{EI}{\rho Ah^4} (m_{47} - 4m_{48} + 6m_{49} - 4m_{50} + m_{51})$		$\phi_{40} = \frac{EI}{\rho Ah^4} (m_{56} - 4m_{57} + 6m_{58} - 4m_{59} + m_{60})$		
$\phi_{41} = \frac{EI}{\rho Ah^4} (m_{65} - 4m_{66} + 6m_{67} - 4m_{68} + m_{69})$		$\phi_{42} = \frac{EI}{\rho Ah^4} (m_{74} - 4m_{75} + 6m_{76} - 4m_{77} + m_{78})$		
$\phi_{43} = \frac{EI}{\rho Ah^4} (m_{12} - 4m_{13} + 6m_{14} - 4m_{15} + m_{16})$		$\phi_{44} = \frac{EI}{\rho Ah^4} (m_{21} - 4m_{22} + 6m_{23} - 4m_{24} + m_{25})$		
$\phi_{45} = \frac{EI}{\rho Ah^4} (m_{30} - 4m_{31} + 6m_{32} - 4m_{33} + m_{34})$		$\phi_{46} = \frac{EI}{\rho Ah^4} (m_{39} - 4m_{40} + 6m_{41} - 4m_{42} + m_{43})$		
$\phi_{47} = \frac{EI}{\rho Ah^4} (m_{48} - 4m_{49} + 6m_{50} - 4m_{51} + m_{52})$		$\phi_{48} = \frac{EI}{\rho Ah^4} (m_{57} - 4m_{58} + 6m_{59} - 4m_{60} + m_{61})$		
$\phi_{49} = \frac{EI}{\rho Ah^4} (m_{66} - 4m_{67} + 6m_{68} - 4m_{69} + m_{70})$		$\phi_{50} = \frac{EI}{\rho Ah^4} (m_{75} - 4m_{76} + 6m_{77} - 4m_{78} + m_{79})$		
$\phi_{51} = \frac{EI}{\rho Ah^4} (m_{13} - 4m_{14} + 6m_{15} - 4m_{16} + m_{17})$		$\phi_{52} = \frac{EI}{\rho Ah^4} (m_{22} - 4m_{23} + 6m_{24} - 4m_{25} + m_{26})$		
$\phi_{53} = \frac{EI}{\rho Ah^4} (m_{31} - 4m_{32} + 6m_{33} - 4m_{34} + m_{35})$		$\phi_{54} = \frac{EI}{\rho Ah^4} (m_{40} - 4m_{41} + 6m_{42} - 4m_{43} + m_{44})$		
$\phi_{55} = \frac{EI}{\rho Ah^4} (m_{49} - 4m_{50} + 6m_{51} - 4m_{52} + m_{53})$		$\phi_{56} = \frac{EI}{\rho Ah^4} (m_{58} - 4m_{59} + 6m_{60} - 4m_{61} + m_{62})$		

(continued)

(continued)

$\phi_{10} = \frac{2m_1 EI}{h^2}$	$\phi_{11} = \frac{2m_{10} EI}{h^2}$	$\phi_{12} = \frac{2m_{19} EI}{h^2}$	$\phi_{13} = \frac{2m_{28} EI}{h^2}$	$\phi_{14} = \frac{2m_{37} EI}{h^2}$
$\phi_{57} = \frac{EI}{\rho A h^4} (m_{67} - 4m_{68} + 6m_{69} - 4m_{70} + m_{71})$			$\phi_{58} = \frac{EI}{\rho A h^4} (m_{76} - 4m_{77} + 6m_{78} - 4m_{79} + m_{80})$	
$\phi_{59} = \frac{EI}{\rho A h^4} (m_{14} - 4m_{15} + 6m_{16} - 4m_{17} + 2m_{18})$			$\phi_{60} = \frac{EI}{\rho A h^4} (m_{23} - 4m_{24} + 6m_{25} - 4m_{26} + 2m_{27})$	
$\phi_{61} = \frac{EI}{\rho A h^4} (m_{32} - 4m_{33} + 6m_{34} - 4m_{35} + 2m_{36})$			$\phi_{62} = \frac{EI}{\rho A h^4} (m_{41} - 4m_{42} + 6m_{43} - 4m_{44} + 2m_{45})$	
$\phi_{63} = \frac{EI}{\rho A h^4} (m_{50} - 4m_{51} + 6m_{52} - 4m_{53} + 2m_{54})$			$\phi_{64} = \frac{EI}{\rho A h^4} (m_{59} - 4m_{60} + 6m_{61} - 4m_{62} + 2m_{63})$	
$\phi_{65} = \frac{EI}{\rho A h^4} (m_{68} - 4m_{69} + 6m_{70} - 4m_{71} + 2m_{72})$			$\phi_{66} = \frac{EI}{\rho A h^4} (m_{77} - 4m_{78} + 6m_{79} - 4m_{80} + 2m_{81})$	
$\phi_{67} = \frac{EI}{\rho A h^4} (m_{15} - 4m_{16} + 5m_{17} - 4m_{18})$			$\phi_{68} = \frac{EI}{\rho A h^4} (m_{24} - 4m_{25} + 5m_{26} - 4m_{27})$	
$\phi_{69} = \frac{EI}{\rho A h^4} (m_{33} - 4m_{34} + 5m_{35} - 4m_{36})$			$\phi_{70} = \frac{EI}{\rho A h^4} (m_{42} - 4m_{43} + 5m_{44} - 4m_{45})$	
$\phi_{71} = \frac{EI}{\rho A h^4} (m_{51} - 4m_{52} + 5m_{53} - 4m_{54})$			$\phi_{72} = \frac{EI}{\rho A h^4} (m_{60} - 4m_{61} + 5m_{62} - 4m_{63})$	
$\phi_{73} = \frac{EI}{\rho A h^4} (m_{69} - 4m_{70} + 5m_{71} - 4m_{72})$			$\phi_{74} = \frac{EI}{\rho A h^4} (m_{78} - 4m_{79} + 5m_{80} - 4m_{81})$	
$\phi_{75} = \frac{EI}{\rho A h^4} (m_{16} - 2m_{17} + 2m_{18})$			$\phi_{76} = \frac{EI}{\rho A h^4} (m_{25} - 2m_{26} + 2m_{27})$	
$\phi_{77} = \frac{EI}{\rho A h^4} (m_{34} - 2m_{35} + 2m_{36})$			$\phi_{78} = \frac{EI}{\rho A h^4} (m_{43} - 2m_{44} + 2m_{45})$	
$\phi_{79} = \frac{EI}{\rho A h^4} (m_{52} - 2m_{53} + 2m_{54})$			$\phi_{80} = \frac{EI}{\rho A h^4} (m_{61} - 2m_{62} + 2m_{63})$	
$\phi_{81} = \frac{EI}{\rho A h^4} (m_{70} - 2m_{71} + 2m_{72})$			$\phi_{82} = \frac{EI}{\rho A h^4} (m_{79} - 2m_{80} + 2m_{81})$	



$$\sigma_1 = \Delta_2 m_{10} + \Delta_3 m_{19} + \Delta_2 m_{28} + \Delta_3 m_{37} + \Delta_2 m_{46} + \Delta_3 m_{55} + \Delta_2 m_{64} + \Delta_4 m_{73}$$

$$\sigma_2 = \Delta_2 m_{11} + \Delta_3 m_{20} + \Delta_2 m_{29} + \Delta_3 m_{38} + \Delta_2 m_{47} + \Delta_3 m_{56} + \Delta_2 m_{65} + \Delta_4 m_{74}$$

$$\sigma_3 = \Delta_2 m_{12} + \Delta_3 m_{21} + \Delta_2 m_{30} + \Delta_3 m_{39} + \Delta_2 m_{48} + \Delta_3 m_{57} + \Delta_2 m_{66} + \Delta_4 m_{75}$$

$$\sigma_4 = \Delta_2 m_{13} + \Delta_3 m_{22} + \Delta_2 m_{31} + \Delta_3 m_{40} + \Delta_2 m_{49} + \Delta_3 m_{58} + \Delta_2 m_{67} + \Delta_4 m_{76}$$

$$\sigma_5 = \Delta_2 m_{14} + \Delta_3 m_{23} + \Delta_2 m_{32} + \Delta_3 m_{41} + \Delta_2 m_{50} + \Delta_3 m_{59} + \Delta_2 m_{68} + \Delta_4 m_{77}$$

$$\sigma_6 = \Delta_2 m_{15} + \Delta_3 m_{24} + \Delta_2 m_{33} + \Delta_3 m_{42} + \Delta_2 m_{51} + \Delta_3 m_{60} + \Delta_2 m_{69} + \Delta_4 m_{78}$$

$$\sigma_7 = \Delta_2 m_{16} + \Delta_3 m_{25} + \Delta_2 m_{34} + \Delta_3 m_{43} + \Delta_2 m_{52} + \Delta_3 m_{61} + \Delta_2 m_{70} + \Delta_4 m_{79}$$

$$\sigma_8 = \Delta_2 m_{17} + \Delta_3 m_{26} + \Delta_2 m_{35} + \Delta_3 m_{44} + \Delta_2 m_{53} + \Delta_3 m_{62} + \Delta_2 m_{71} + \Delta_4 m_{80}$$

$$\sigma_9 = \Delta_2 m_{18} + \Delta_3 m_{27} + \Delta_2 m_{36} + \Delta_3 m_{45} + \Delta_2 m_{54} + \Delta_3 m_{63} + \Delta_2 m_{72} + \Delta_4 m_{81}$$

Let the state variables be given by:

$x_1 = \theta$	$x_2 = \dot{\theta}$	$x_3 = v_2$	$x_4 = \dot{v}_2$
$x_5 = v_3$	$x_6 = \dot{v}_3$	$x_7 = v_4$	$x_8 = \dot{v}_4$
$x_9 = v_5$	$x_{10} = \dot{v}_5$	$x_{11} = v_6$	$x_{12} = \dot{v}_6$
$x_{13} = v_7$	$x_{14} = \dot{v}_7$	$x_{15} = v_8$	$x_{16} = \dot{v}_8$
$x_{17} = v_9$	$x_{18} = \dot{v}_9$	$x_{19} = s$	$x_{20} = \dot{s}$

Considering these new variables, Eqs. (115)–(123) are written in state space form as:

$$\dot{x}_1 = x_2 \quad (125)$$

$$\dot{x}_2 = v_{a1} - \vartheta_1 x_2 - (\beta \vartheta_{10}) x_3 \quad (126)$$

$$\dot{x}_3 = x_4 \quad (127)$$

$$\dot{x}_4 = v_{a2} - \vartheta_2 x_2 - (\beta \vartheta_{11} + \vartheta_{19}) x_3 - \vartheta_{27} x_5 - \vartheta_{35} x_7 - \vartheta_{43} x_9 - \vartheta_{51} x_{11} - \vartheta_{59} x_{13}$$

$$- \vartheta_{67}x_{15} - \vartheta_{75}x_{17} \quad (128)$$

$$\dot{x}_5 = x_6 \quad (129)$$

$$\begin{aligned} \dot{x}_6 = & v_{a3} - \vartheta_3x_2 - (\beta\vartheta_{12} + \vartheta_{20})x_3 - \vartheta_{28}x_5 - \vartheta_{36}x_7 - \vartheta_{44}x_9 - \vartheta_{52}x_{11} - \vartheta_{60}x_{13} \\ & - \vartheta_{68}x_{15} - \vartheta_{76}x_{17} \end{aligned} \quad (130)$$

$$\dot{x}_7 = x_8 \quad (131)$$

$$\begin{aligned} \dot{x}_8 = & v_{a4} - \vartheta_4x_2 - (\beta\vartheta_{13} + \vartheta_{21})x_3 - \vartheta_{29}x_5 - \vartheta_{37}x_7 - \vartheta_{45}x_9 - \vartheta_{53}x_{11} - \vartheta_{61}x_{13} \\ & - \vartheta_{69}x_{15} - \vartheta_{77}x_{17} \end{aligned} \quad (132)$$

$$\dot{x}_9 = x_{10} \quad (133)$$

$$\begin{aligned} \dot{x}_{10} = & v_{a5} - \vartheta_5x_2 - (\beta\vartheta_{14} + \vartheta_{22})x_3 - \vartheta_{30}x_5 - \vartheta_{38}x_7 - \vartheta_{46}x_9 - \vartheta_{54}x_{11} - \vartheta_{62}x_{13} \\ & - \vartheta_{70}x_{15} - \vartheta_{78}x_{17} \end{aligned} \quad (134)$$

$$\dot{x}_{11} = x_{12} \quad (135)$$

$$\begin{aligned} \dot{x}_{12} = & v_{a6} - \vartheta_6x_2 - (\beta\vartheta_{15} + \vartheta_{23})x_3 - \vartheta_{31}x_5 - \vartheta_{39}x_7 - \vartheta_{47}x_9 - \vartheta_{55}x_{11} - \vartheta_{63}x_{13} \\ & - \vartheta_{71}x_{15} - \vartheta_{79}x_{17} \end{aligned} \quad (136)$$

$$\dot{x}_{13} = x_{14} \quad (137)$$

$$\begin{aligned} \dot{x}_{14} = & v_{a7} - \vartheta_7x_2 - (\beta\vartheta_{16} + \vartheta_{24})x_3 - \vartheta_{32}x_5 - \vartheta_{40}x_7 - \vartheta_{48}x_9 - \vartheta_{56}x_{11} - \vartheta_{64}x_{13} \\ & - \vartheta_{72}x_{15} - \vartheta_{80}x_{17} \end{aligned} \quad (138)$$

$$\dot{x}_{15} = x_{16} \quad (139)$$

$$\begin{aligned} \dot{x}_{16} = & v_{a8} - \vartheta_8x_2 - (\beta\vartheta_{17} + \vartheta_{25})x_3 - \vartheta_{33}x_5 - \vartheta_{41}x_7 - \vartheta_{49}x_9 - \vartheta_{57}x_{11} - \vartheta_{65}x_{13} \\ & - \vartheta_{73}x_{15} - \vartheta_{81}x_{17} \end{aligned} \quad (140)$$

$$\dot{x}_{17} = x_{18} \quad (141)$$

$$\begin{aligned} \dot{x}_{18} = & v_{a9} - \vartheta_9x_2 - (\beta\vartheta_{18} + \vartheta_{26})x_3 - \vartheta_{34}x_5 - \vartheta_{42}x_7 - \vartheta_{50}x_9 - \vartheta_{58}x_{11} - \vartheta_{66}x_{13} \\ & - \vartheta_{74}x_{15} - \vartheta_{82}x_{17} \end{aligned} \quad (142)$$



$$\mathbf{x} = \{ x_1 \ x_2 \ x_3 \ x_4 \ x_5 \ x_6 \ x_7 \ x_8 \ x_9 \ x_{10} \ x_{11} \ x_{12} \ x_{13} \ x_{14} \ x_{15} \ x_{16} \ x_{17} \ x_{18} \}^T$$

$$\dot{\mathbf{x}} = \{ \dot{x}_1 \ \dot{x}_2 \ \dot{x}_3 \ \dot{x}_4 \ \dot{x}_5 \ \dot{x}_6 \ \dot{x}_7 \ \dot{x}_8 \ \dot{x}_9 \ \dot{x}_{10} \ \dot{x}_{11} \ \dot{x}_{12} \ \dot{x}_{13} \ \dot{x}_{14} \ \dot{x}_{15} \ \dot{x}_{16} \ \dot{x}_{17} \ \dot{x}_{18} \}^T$$

$$\mathbf{u} = \{ v_{a1} \ v_{a2} \ v_{a3} \ v_{a4} \ v_{a5} \ v_{a6} \ v_{a7} \ v_{a8} \ v_{a9} \}$$

and the LQR weighting matrices are given by:

$$\mathbf{Q} = \begin{bmatrix} Q_1 & 0 & 0 & 0 & 0 & 0 & 0 & 0 & 0 & 0 & 0 & 0 & 0 & 0 & 0 & 0 & 0 & 0 \\ 0 & Q_2 & 0 & 0 & 0 & 0 & 0 & 0 & 0 & 0 & 0 & 0 & 0 & 0 & 0 & 0 & 0 & 0 \\ 0 & 0 & Q_3 & 0 & 0 & 0 & 0 & 0 & 0 & 0 & 0 & 0 & 0 & 0 & 0 & 0 & 0 & 0 \\ 0 & 0 & 0 & Q_4 & 0 & 0 & 0 & 0 & 0 & 0 & 0 & 0 & 0 & 0 & 0 & 0 & 0 & 0 \\ 0 & 0 & 0 & 0 & Q_5 & 0 & 0 & 0 & 0 & 0 & 0 & 0 & 0 & 0 & 0 & 0 & 0 & 0 \\ 0 & 0 & 0 & 0 & 0 & Q_6 & 0 & 0 & 0 & 0 & 0 & 0 & 0 & 0 & 0 & 0 & 0 & 0 \\ 0 & 0 & 0 & 0 & 0 & 0 & Q_7 & 0 & 0 & 0 & 0 & 0 & 0 & 0 & 0 & 0 & 0 & 0 \\ 0 & 0 & 0 & 0 & 0 & 0 & 0 & Q_8 & 0 & 0 & 0 & 0 & 0 & 0 & 0 & 0 & 0 & 0 \\ 0 & 0 & 0 & 0 & 0 & 0 & 0 & 0 & Q_9 & 0 & 0 & 0 & 0 & 0 & 0 & 0 & 0 & 0 \\ 0 & 0 & 0 & 0 & 0 & 0 & 0 & 0 & 0 & Q_{10} & 0 & 0 & 0 & 0 & 0 & 0 & 0 & 0 \\ 0 & 0 & 0 & 0 & 0 & 0 & 0 & 0 & 0 & 0 & Q_{11} & 0 & 0 & 0 & 0 & 0 & 0 & 0 \\ 0 & 0 & 0 & 0 & 0 & 0 & 0 & 0 & 0 & 0 & 0 & Q_{12} & 0 & 0 & 0 & 0 & 0 & 0 \\ 0 & 0 & 0 & 0 & 0 & 0 & 0 & 0 & 0 & 0 & 0 & 0 & Q_{13} & 0 & 0 & 0 & 0 & 0 \\ 0 & 0 & 0 & 0 & 0 & 0 & 0 & 0 & 0 & 0 & 0 & 0 & 0 & Q_{14} & 0 & 0 & 0 & 0 \\ 0 & 0 & 0 & 0 & 0 & 0 & 0 & 0 & 0 & 0 & 0 & 0 & 0 & 0 & Q_{15} & 0 & 0 & 0 \\ 0 & 0 & 0 & 0 & 0 & 0 & 0 & 0 & 0 & 0 & 0 & 0 & 0 & 0 & 0 & Q_{16} & 0 & 0 \\ 0 & 0 & 0 & 0 & 0 & 0 & 0 & 0 & 0 & 0 & 0 & 0 & 0 & 0 & 0 & 0 & Q_{17} & 0 \\ 0 & 0 & 0 & 0 & 0 & 0 & 0 & 0 & 0 & 0 & 0 & 0 & 0 & 0 & 0 & 0 & 0 & Q_{18} \end{bmatrix}$$

$$\mathbf{R} = \begin{bmatrix} R_1 & 0 & 0 & 0 & 0 & 0 & 0 & 0 & 0 \\ 0 & R_2 & 0 & 0 & 0 & 0 & 0 & 0 & 0 \\ 0 & 0 & R_3 & 0 & 0 & 0 & 0 & 0 & 0 \\ 0 & 0 & 0 & R_4 & 0 & 0 & 0 & 0 & 0 \\ 0 & 0 & 0 & 0 & R_5 & 0 & 0 & 0 & 0 \\ 0 & 0 & 0 & 0 & 0 & R_6 & 0 & 0 & 0 \\ 0 & 0 & 0 & 0 & 0 & 0 & R_7 & 0 & 0 \\ 0 & 0 & 0 & 0 & 0 & 0 & 0 & R_8 & 0 \\ 0 & 0 & 0 & 0 & 0 & 0 & 0 & 0 & R_9 \end{bmatrix}$$

In the problem investigated here, one of the actuated degrees of freedom ( $\theta$ ) and its time derivative ( $\dot{\theta}$ ) are not equal to zero. The governing equation of motion for the analysis of the zero dynamics is obtained by manipulating the internal dynamics given by Eq. (124) and results:

$$\ddot{s} + \sigma_{10}\dot{s}^2 + \sigma_{11}\dot{\theta}^2 - \sigma_{12}\dot{\theta} + \sigma_{13}g = 0 \quad (144)$$

where:

$$\begin{aligned} \sigma_{10} &= \frac{\beta_{21}}{\rho AL + m_{\text{hub}}} \\ \sigma_{11} &= \frac{\beta_1}{\rho AL + m_{\text{hub}}} \\ \sigma_{12} &= \frac{\sigma_1}{\rho AL + m_{\text{hub}}} \left( c_m N_g^2 + \frac{N_g^2 K_t K_b}{R_a} \right) \\ \sigma_{13} &= \frac{\rho AL - m_{\text{hub}}}{\rho AL + m_{\text{hub}}} \end{aligned}$$

In Eq. (144), the third, fourth and fifth terms are constant and will be collected in the constant parameter  $\sigma_{14}$ . For this reason, let:

$$\sigma_{14} = \sigma_{11}\dot{\theta}^2 - \sigma_{12}\dot{\theta} + \sigma_{13}g$$

Then, Eq. (144) is rewritten as:

$$\ddot{s} + \sigma_{10}\dot{s}^2 + \sigma_{14} = 0 \quad (145)$$

Writing Eq. (145) in state space form results:

$$\dot{x}_{19} = x_{20} \quad (146)$$

$$\dot{x}_{20} = -\sigma_{10}x_{20}^2 - \sigma_{14} \quad (147)$$

The stability of Eqs. (146) and (147) is verified through numerical simulations.

## 8 Numerical Simulations and Discussions

The problem of flexible rotary wings rotating at high speeds and interacting with a fluid (as in the case of mathematical modeling of helicopters) is a very complex problem. This one is not yet a work that intends to discuss issues of aerodynamics and aeroelasticity associated with these systems. The expressions for  $C_D$  and  $C_L$  are presented here just to complete the reasoning. The aim here is to present the simplest (and sufficiently representative) expressions for these coefficients just so

that their values are not imposed in a table. Here, only the geometric angle of attack is considered ( $\alpha$ ; the angle between the free stream and the chord line).

Therefore, for a finite and symmetrical wing-like structure, the lift coefficient and the drag coefficient considered in this work are given, respectively, by:

$$C_L = \frac{2 \pi \sin (\alpha + \beta_h)}{1 + \frac{2}{AR}}$$

$$C_D = C_{D\infty} + \frac{C_L^2}{\pi AR}$$

where  $AR = \frac{b^2}{A_p}$  represents the aspect ratio of the wing,  $\beta_h$  represents a parameter (angle) associated to unsymmetric airfoils,  $C_{D\infty}$  represents the drag of the infinite-span airfoil,  $b$  represents the span of the wing (the longest distance between the plane’s wing tips) and  $A_p$  represents the planform area (the body area as seen from above; suitable for wide, flat bodies such as wings and hydrofoils).

In this work, the airfoil is symmetric ( $\beta_h = 0^\circ$ ) and the flexible wing-like structure is rectangular. Considering this:  $A_p = \frac{b}{2}c = Lc$  and  $AR = \frac{(\frac{b}{2})^2}{A_p} = \frac{L^2}{A_p} = \frac{L}{c}$ . It is also considered, for simplicity, that  $C_{D\infty}$  is negligible.

The parameters values used in the numerical simulations are presented in Table 1.

The objective of the numerical simulation presented here (and the objective of this work as well) is to discuss the significant difference between the ideal system approach for the system investigated in this work and the non-ideal (more realistic) system approach for this same system.

**Table 1** Parameters values used in the numerical simulations

Parameter	Nomenclature	Value
Mass density (beam)	$\rho$	2700 kg/m <sup>3</sup>
Elastic modulus (beam)	$E$	0.700*10 <sup>11</sup> Pa
Beam length	$L$	1.500 m
Beam tickness	$h_b$	0.001 m
Beam width	$w$	0.080 m
Gravitational acceleration	$g$	9.810 m/s <sup>2</sup>
Radius of the hub	$r$	0.100 m
Density of the fluid	$\rho_f$	1.184 kg/m <sup>3</sup>
Mean chord (beam cross sectional width)	$c$	0.080 m
Angle of attack	$\alpha$	1°
Nondimensional lift coefficient	$C_L$	$C_L = 2 \pi \sin(\alpha) \left( \frac{L}{L+2c} \right) = 0.099$
Nondimensional drag coefficient	$C_D$	$C_D = C_L^2 \left( \frac{c}{\pi L} \right) = 1.664 * 10^{-4}$
Span	$b$	3.000 m (=2L)



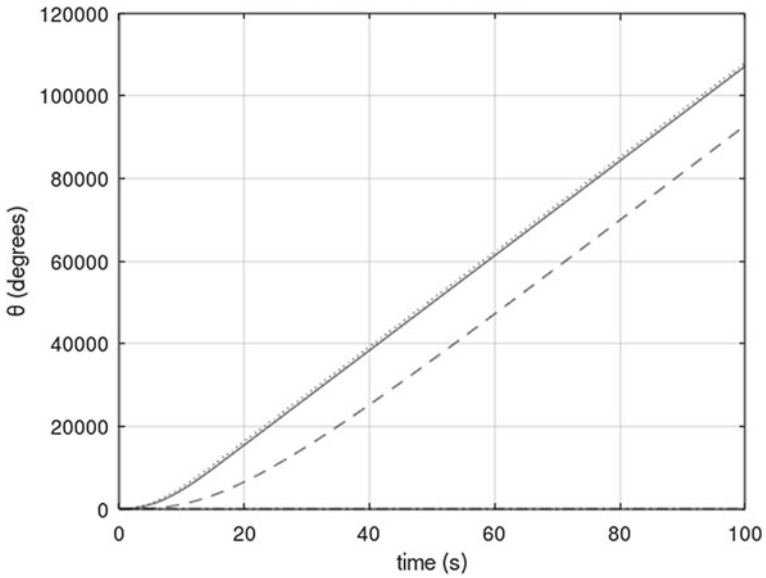


Fig. 3 Angular displacement: (.....) reference, (- - -) ideal approach and (—) non-ideal approach

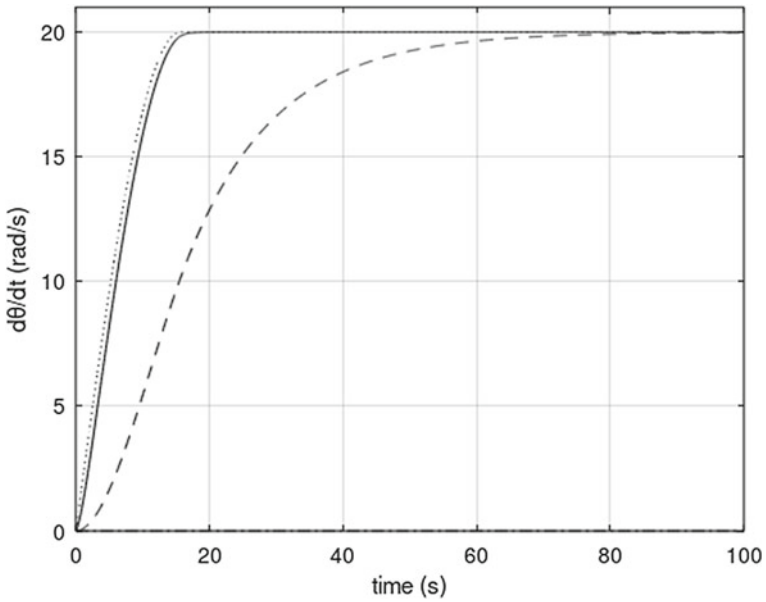
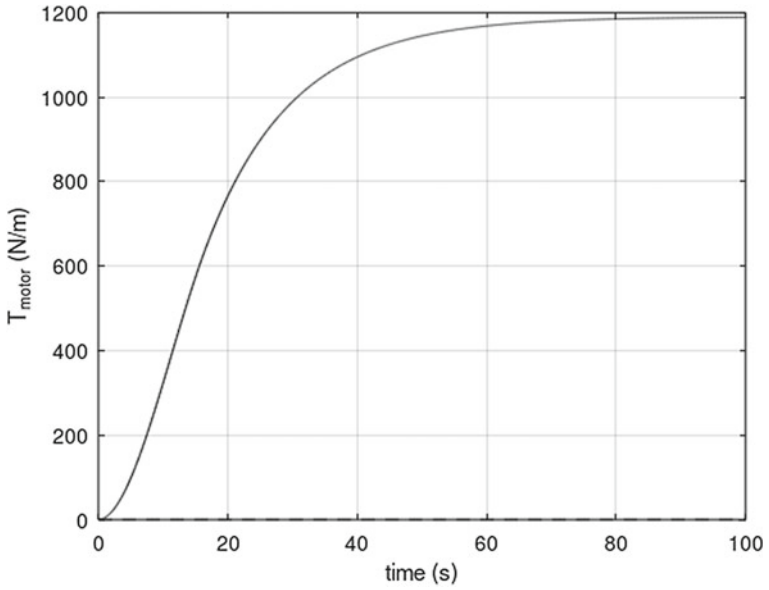
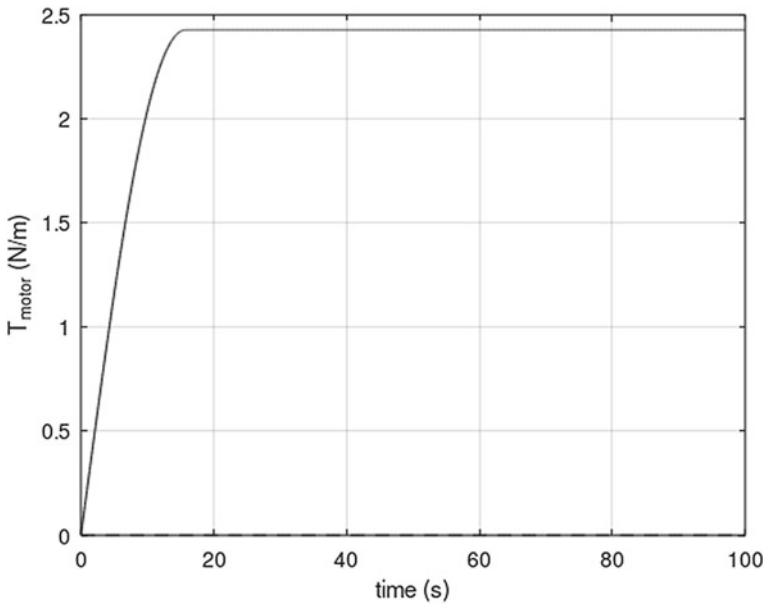


Fig. 4 Angular velocity: (.....) reference, (- - -) ideal approach and (—) non-ideal approach





**Fig. 5** Control torque generated by the direct current motor: ideal approach



**Fig. 6** Control torque generated by the direct current motor: non-ideal approach

approach is considered. And even so, as observed in the previous paragraph, the motor control torque in the non-ideal approach proves to be more efficient. In the non-ideal approach, part of the energy stored in the beam (due to the angular displacement and velocity provided by the motor) flows back to the dc motor through the coupling terms involving the beam variables and the motor variables present in the motor equation (which characterizes the system as non-ideal) and helps the control action. It is clear the amount of error one may commit in the case the wrong approach is considered. For the same task, the ideal system approach will ask for a much larger motor (actuator).

Figures 7 and 8 present the control forces generated on the piezoelectric actuators considering the ideal approach (Fig. 7) and the non-ideal approach (Fig. 8). Again, the control forces required for the non-ideal approach are in general smaller than those required when considering the ideal approach. In this case, the differences are significant but not as dissimilar as in the case of motor control torques.

Figures 9 and 10 present a comparison between the beam deflection (through its nodes) for each approach. It is clear again that the non-ideal approach predicts a much smaller amplitude of vibration than the ideal approach. As stated before, in fact, part of the energy in the beam flows back to the dc motor. Figures 11 and 12 present similar results for the velocities along the beam.

Figures 13 and 14 present the results for the zero dynamics for this problem. The variable  $s$  and its first time derivative are related to the unactuated variables. Figure 14

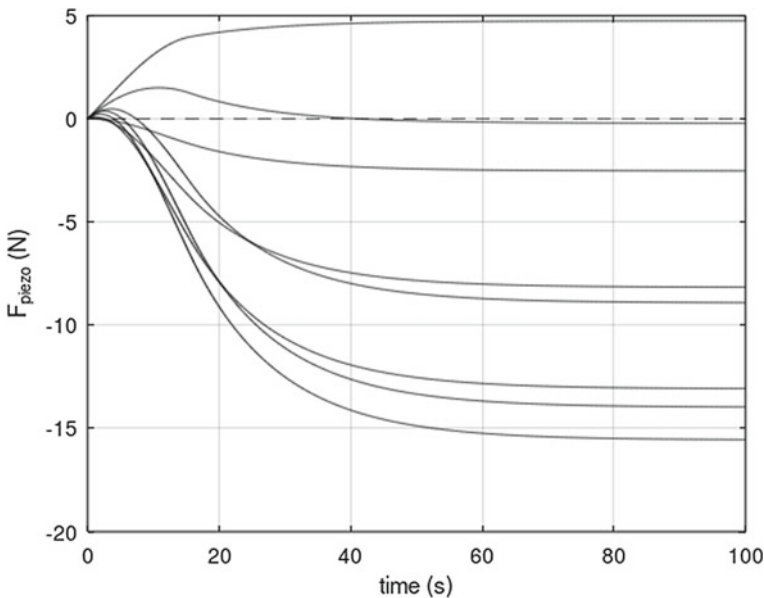


Fig. 7 Control forces generated on the piezoelectric actuators: ideal approach

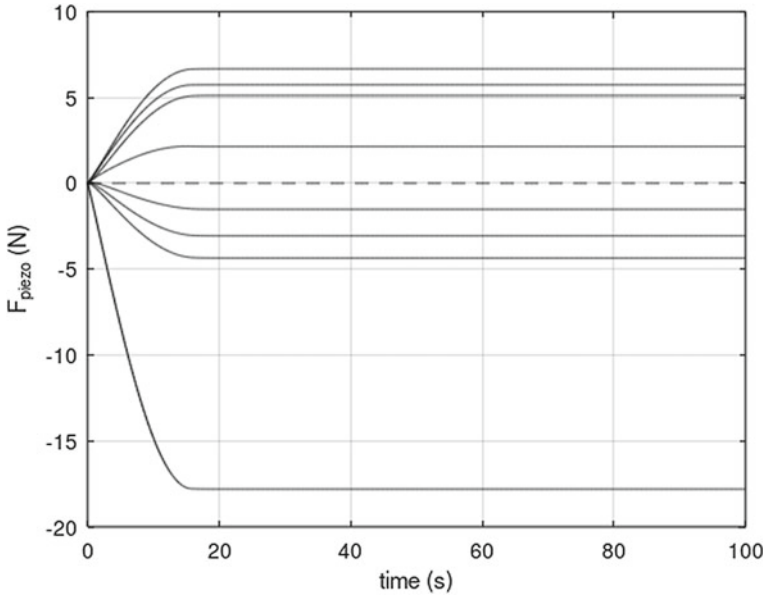


Fig. 8 Control forces generated on the piezoelectric actuators: non-ideal approach

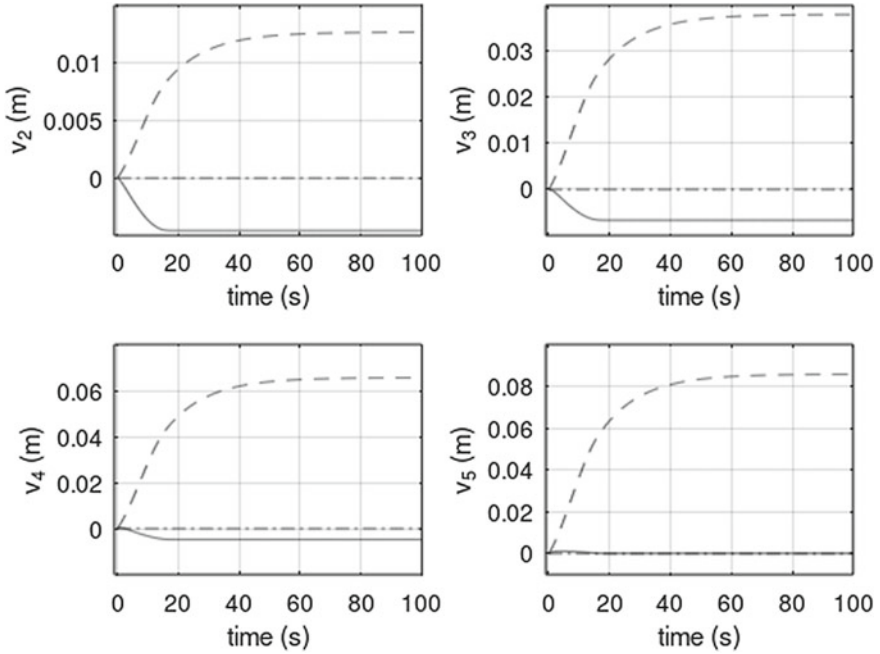
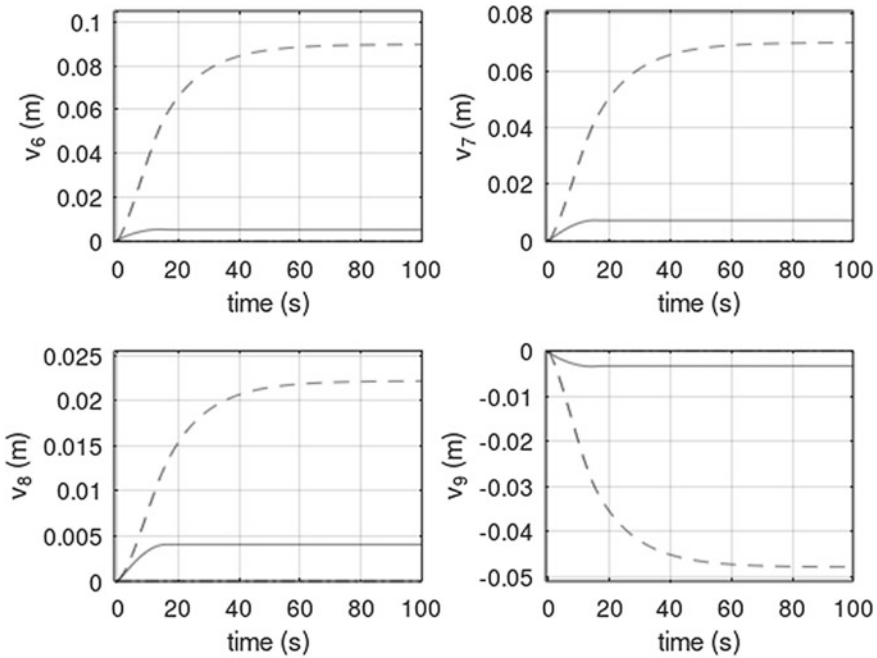


Fig. 9 Displacement of beam nodes 2 to 5: (- - -) ideal approach and (—) non-ideal approach



**Fig. 10** Displacement of beam nodes 6 to 9: (---) ideal approach and (—) non-ideal approach

shows that the ascension velocity naturally converges to a specific constant value and, therefore, according to Fig. 13, the vertical displacement continues linearly forever.

The situation in which the system reaches a certain height and interrupts its ascension, causing the ascension velocity to converge to zero (a movement called hovering) is not considered in this work.

## 9 Conclusions

A mathematical model for a mechanical system consisting of a rotating flexible beam-like structure under the influence of aerodynamic drag and lift forces is derived using extended Hamilton’s principle. The resulting system of coupled nonlinear governing equations of motion is analyzed in closed loop under two assumptions: ideal and non-ideal energy source interactions. The choice between one approach or another significantly alters the results obtained by the numerical integration of the governing equations of motion and depends on the understanding and knowledge about the mathematical modeling of these systems.

The results presented here prove that indeed the ideal and the non-ideal approaches produce totally different results. The response amplitudes for the non-ideal approach are always smaller when compared to the response amplitudes presented in the ideal

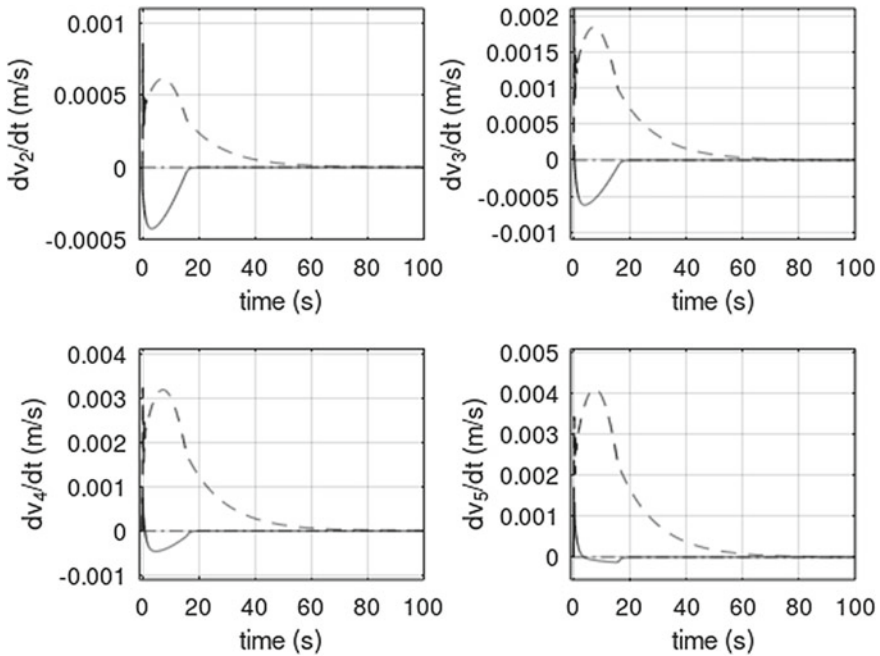


**Fig. 11** Velocity of beam nodes 2 to 5: (---) ideal approach and (—) non-ideal approach

approach. In the non-ideal approach, part of the energy stored in the flexible structure is allowed to flow back to the energy source (dc motor) while, in the ideal approach, all the energy accumulated on the flexible structure is contained in the structure, increasing the vibration amplitudes and the efforts necessary for the control actions.

The nonlinear control technique named Partial Feedback Linearization complemented by a linear control method named Linear Quadratic Regulator is used in order to eliminate the vibration on the flexible structure while controlling the angular velocity of the system in order to keep it constant. The control laws command the torque on the dc motor axis and the forces on the piezoelectric actuators located along the beam-like structure. Despite the differences in magnitude, the linear and nonlinear control laws employed here are effective for both the ideal and the non-ideal cases. For the non-ideal case, however, the forces and torque magnitudes are smaller and the control action is more efficient.

The system investigated here is underactuated. In the study of these systems, it is important to analyze the behavior of the non-actuated states (internal dynamics). The analysis of the zero dynamics associated with the system investigated here shows that the uncontrolled variables do not present a behavior that will compromise the behavior of the controlled variables over time.

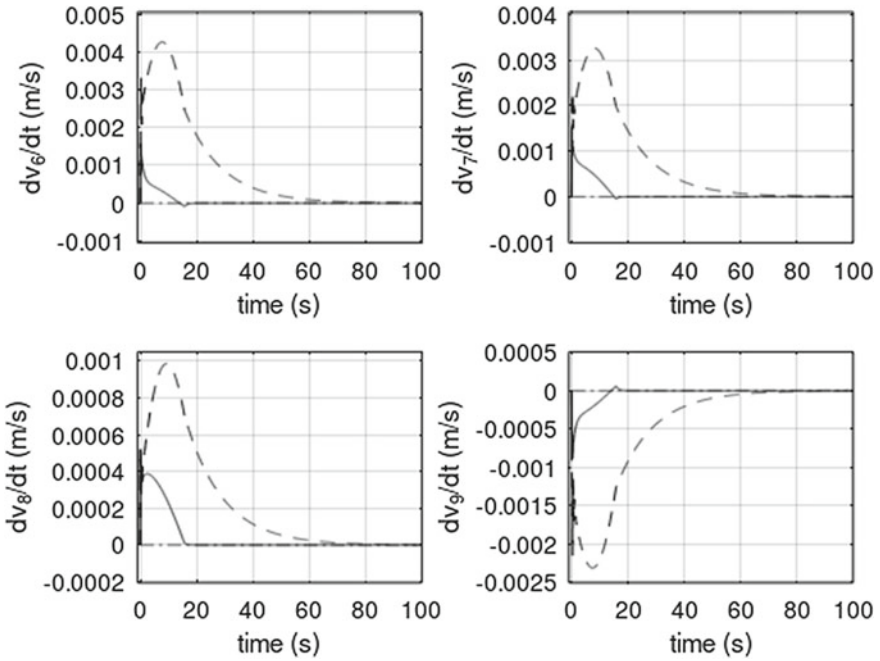


Fig. 12 Velocity of beam nodes 6 to 9: (- -) ideal approach and (—) non-ideal approach

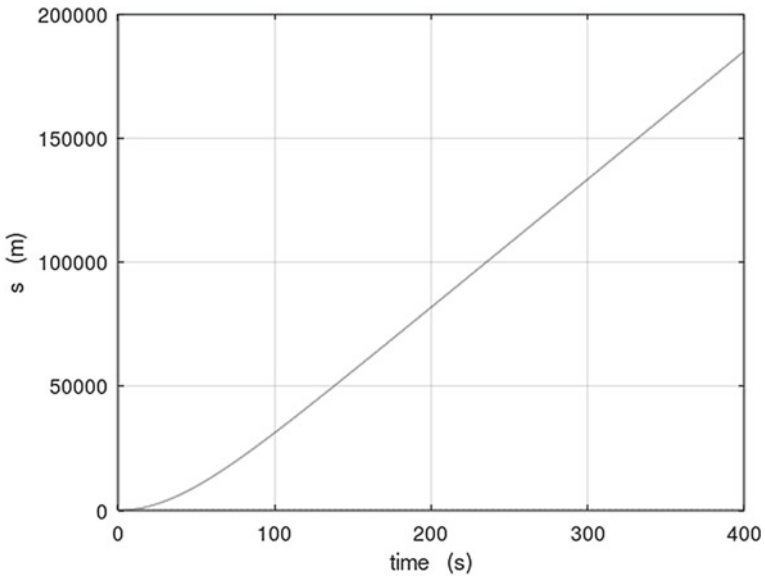
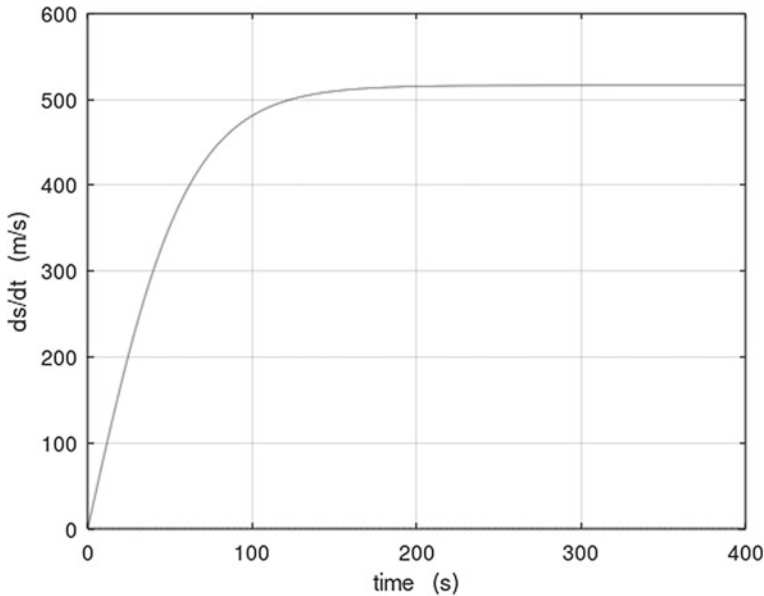


Fig. 13 Zero dynamics: vertical displacement (ideal and non-ideal approaches give the same result)



**Fig. 14** Zero dynamics: vertical velocity (ideal and non-ideal approaches give the same result)

## References

1. Kononenko, V.O.: *Vibrating Systems with a Limited Power Supply*. Iliffe Books Ltd. (1969)
2. Fenili A.: *Mathematical modeling and analysis of the ideal and nonideal behavior of slewing flexible structures*. Ph.D. thesis, University of Campinas (UNICAMP), Faculty of Mechanical Engineering. Campinas/São Paulo. Brazil. In Portuguese (2000)
3. Telli, S., Kopmaz, O.: On the mathematical modelling of beams rotating about a fixed axis. *Mathemat. Comput. Appl.* **9**(3), 333–347 (2004)
4. Low, K.H.: Vibration analysis of a tip-loaded beam attached to a rotating joint. *Comput. Struct.* **52**(5), 955–968 (1994)
5. Putter, S., Manor, H.: Natural frequencies of radial rotating beams. *J. Sound Vib.* **56**(2), 175–185 (1978)
6. Zhang, J., He, L., Wang, E.: Active vibration control of piezoelectric intelligent structures. *J. Comput.* **5**(3), 401–409 (2010)
7. Yousefi-Koma, A.: *Active vibration control of smart structures using Piezoelements*. Ph.D. thesis, Department of Mechanical and Aerospace Engineering, Carleton University. Ottawa/Ontario. Canada (1997)
8. Spong, M.W.: Under-actuated mechanical systems, Book chapter of “Control Problems in Robotics and Automation,” B. Siciliano and K.P. Valavanis (Eds), *Lecture Notes in Control and Information Sciences*, Springer-Verlag, London, Great Britain (1998)
9. Arisoy, A., Gokasan, M., Bogosyan, O.: Partial feedback linearization control of a single flexible link robot manipulator. *Proceedings of 2nd International Conference on Recent Advances in Space Technologies, 2005 (RAST 2005)*, 9–11 June 2005, Istanbul, Turkey. <https://doi.org/10.1109/RAST.2005.1512577>
10. Spong, M.W.: Partial feedback linearization of underactuated mechanical systems. *IEEE/RSJ/GI International Conference on Intelligent Robots and Systems*, Munich, Germany, pp. 314–321, 12–16 September 1994

11. Jiffri, S., Paoletti, P., Cooper, J.E., Mottershead, J.E.: Feedback linearization for nonlinear vibration problems. *Shock Vib.* (2014), Article ID 106531. <https://doi.org/10.1155/2014/106531>
12. Mahmud, M.R., Pota, H.: Robust partial feedback linearized controller design for standalone hybrid PV-BES system. *Electronics* **10**, 772 (2021). <https://doi.org/10.3390/electronics10070772>
13. Lanczos, C.: *The Variational Principles of Mechanics*. Dover publications, Toronto (1970)
14. Meirovitch, L.: *Analytical Methods in Vibrations*. Macmillan Publishing Co., Inc, New York (1967)
15. Popov, E.P.: *Introdução à Mecânica dos Sólidos*, Editora Edgar Blücher Ltda (1978)
16. Sah, J.J., Mayne, R.W.: Modeling of a slewing motor-beam system. *Proceedings of the International Computers in Engineering Conference*, Boston, pp. 481–486 (1990)
17. White, F.M.: “*Fluid Mechanics*”, Seventh Edition, McGraw-Hill series in mechanical engineering, The McGraw-Hill Companies, Inc. (2009)
18. Fenili, A., Francisco, C.P.F., Burr, K.P.: Mathematical modelling of a rotating nonlinear flexible beam-like wing. *Presentations of the 11th International Congress on Vibration Problems (ICOVP2013)*, Lisbon, Portugal, September 9–12 (2013)
19. Abramowitz, M., Stegun, I.A.: *Handbook of Mathematical Functions: With Formulas, Graphs, and Mathematical Tables*”, 9th ed., Dover Publications (1965)
20. LeVeque, R.J.: *Finite difference methods for ordinary and partial differential equations: steady-state and time-dependent problems*. Soc. Indus. Appl. Math. (2007). ISBN: 978–0–89871–629–0
21. Yousefi-Koma, A.: (1997) *Active Vibration Control of Smart Structures Using Piezoelements*. Ph.D. thesis, Department of Mechanical and Aerospace Engineering, Carleton University. Ottawa / Ontario. Canada
22. Beache, K.V.A., Fenili, A.: Active vibration control of a smart beam under rotation. *Proceedings of the XXXVII Iberian Latin-American Congress on Computational Methods in Engineering (CILAMCE 2016)*, Brasília, DF, Brazil, November 6–9, 2016
23. Tuan, L.A., Kim, G.H., Lee, S.G.: Partial feedback linearization control of the three dimensional overhead crane. *8th IEEE International Conference on Automation Science and Engineering*, 20–24 August 2012a, Seoul, Korea
24. Tuan, L.A., Kim, G.H., Kim, M.Y., Lee, S.G.: Partial feedback linearization control of overhead cranes with varying cable lengths. *Int. J. Precision Eng. Manuf.* **13**(4), 501–507 (2012). <https://doi.org/10.1007/s12541-012-0065-8>
25. Lee, S.G., Tuan, L.A., Moon, S.C.: Partial feedback linearization and sliding mode techniques for 2D crane control. *Trans. Inst. Meas. Control.* (2014). <https://doi.org/10.1177/0142331213492369>
26. Elgerd, O.I.: *Control Systems Theory*. McGraw-Hill Book Company (1967)



# Control of the Dynamics of Mechanical Structures Supporting DC Motors with Limited Power Supply



A. A. Nanha Djanan, B. R. Nana Nbandjo, and P. Wofo

**Abstract** The present Chapter presents on its entirety the dynamics of mechanical structures such as beam and rectangular plate when they are subjected to one or more DC motors with limited power supply. Attention is paid on the various applications of such study in civil and mechanical engineering. To deal with this topic, we developed two main approaches with the purpose to give a good insight on vibration control and stability of the studied system. The first step consists on the use of some electric transducers and tuned mass damper to reduce the amplitudes of vibration of a plate. An adequate choice of the physical parameters of the control device enhances the efficiency of the control strategy. A stability analysis using the Routh-Hurwitz criteria confirms the pertinence of the control strategy. The second method is rather based on the synchronization with and without delay between the external sources (DC motors) working on the structure. Here, the physical parameters of the structure enable to present the phase and anti-phase or rapid and late synchronization phenomena between the motors. This difference of phase or the input delay between the motors and the voltage applied on the motors lead to situations where the amplitude vibrations of the mechanical structure are considerably reduced.

**Keywords** Nonlinear dynamics · Mechanical structures · Non ideal sources · DC motors · Electric transducers · Tuned mass damper · Routh-Hurwitz criteria · Self-synchronization

## 1 Introduction

The study of thin plate vibrations displays a rich and complex dynamics that ranges from linear to strongly nonlinear regimes when increasing the vibration amplitude with respect to the thickness. A plate is a continuous system, and thus, in the language of Mechanical Engineering, it possesses an infinite number of degrees of freedom. Truncating the degrees of freedom from an infinite number to a finite one can lead

---

A. A. N. Djanan · B. R. N. Nbandjo (✉) · P. Wofo  
Laboratory of Modeling and Simulation in Engineering, Biomimetics and Prototypes, Faculty of Sciences, University of Yaoundé I, PO Box 812, Yaoundé, Cameroon

nonetheless to a faithful reproduction of the dynamics. When a rectangular plate vibrates in a weakly nonlinear regime, modal couplings produce amplitude dependent vibrations, internal resonances, instabilities, jumps and bifurcations. In the case where it vibrates in a strongly nonlinear regime, the most appropriate description of the dynamics is given in terms of the statistical properties of the system, because of the large number of interacting degrees-of-freedom.

The range of applications of plates is quite large, thus thin vibrating structures are found very often in musical instruments. For example, plates are fundamental components of the piano and the guitar, serving as soundboards; they have been extensively used as analog reverb units before the advent of digital systems. Instruments such as bells, gongs or cymbals are, roughly speaking, curved plates. In old theatres, large metallic plates were used at times to simulate the powerful sounds of thunders and storms.

The scientific interest of studying mechanical structures such as rectangular plates is really broad, and comprises domains that are apparently very different. Many applications are found in common engineering problems, such as panel flutter in aeronautics, energy harvesting of fluttering flexible plates, piezoelectric and laminated plates, and others.

Several engineering structures such as buildings, airplanes wings, helicopter blades, bridges are usually subjected to various types of vibrations. These vibrations may result from wind gusts, high speeding cars, rotating machines and some environmental disturbances. The dynamic response of mechanical and civil structures prone to high-amplitude motions is often undesirable and dangerous. These vibrations often lead to material fatigue, structural damage and failure, deterioration of system performance, and increased noise level.

Frequently we encounter in civil and mechanical engineering situations where a rectangular plate is excited by one or more DC motors leading to high amplitude of vibration. However, there are two principal types of rotating machines, each of them is composed by a fixed part called stator and another one mobile around a fixed axes named rotor. These motors can be powered either by direct current (DC motors) or by alternative current (AC motors). In DC motors, the rotational speed is proportional to the applied voltage and the normal method of speed control is by varying the input voltage. This speed is however also inversely proportional to the flux in the air gap. This means that the speed increases as the flux provided by the coils decreases.

Analysis of the response of structures subjected to non-ideal excitations is of fundamental importance for their implementation in industry and civil engineering. For such an analysis to be able to predict the realistic behavior of a structure during an actual non-ideal motion, certain information is necessary. First, the nature of the Non-ideal excitation must be specified, and secondly the mechanical behavior of the structure (thin plate) should be modeled within a reasonable accuracy. Since 1956, there exist numerous analytical and numerical techniques for the modeling and dynamics predictions of linear and nonlinear thin plate. Platforms, quay, flagstone and bridges are some examples of rectangular thin plates currently present in our environment (Ashour 2001, Shafic 1999). The mastery of this dynamics helps to prevent some catastrophe and disaster during the construction or the functioning of

such structures. Among the perturbations which can cause mechanical vibration in structure, one can note wind, rotating machines, static and moving charges. In the case of rotating machines which can be divided in two principals groups, AC and DC motors one can note some situations currently encountered in civil and mechanical engineering. Usually, these motors are mounted on structure in industry to function alone or in series. In this last case, the synchronization phenomenon can probably appear between them when they are coupled. This phenomenon has been well studied in the last decades.

Sometimes DC motors are capable of limited power supply and in a situation where they are fixed on a mechanical structure, the system is named a non ideal one because the excitation source will be influenced by the response of the main system [1]. In industry we note the presence of some electrical machines mounted on elastic structure and during their works they will certainly interact. This interaction may be profitable or not to the firm, in the last case one has to take some care to avoid damage. Thus, it is well recommend to study the vibration control theory to predict some unpredictable behaviors.

The second section will be devoted to the presentation of the generalities on interaction of DC motors with limited power supply with mechanical structures. Section 3 deals with mathematical formalism for the vibration control of a rectangular plate where both techniques are presented. The fourth section presents recent results on the topic and the last section concludes the chapter.

## **2 Generalities on Interaction of DC Motor with Limited Power Supply and Mechanical Structures**

In the manufacturing process in industry, it is common to have a DC motor resting on a mechanical structure. However, motors will inevitably induce vibrations to the structure. Depending on the running speed of the motor, we may face a situation where the resulting vibrations of the mechanical structure will influence that of the DC motor which initially acts as an exciter. In the literature, it is known that when the excitation of a vibrating system is not influenced by its response, it is said to be an ideal excitation or an ideal source of energy. On the other hand, when the excitation is influenced by the response of the system, it is said to be non-ideal one.

The behavior of ideal vibrating systems is well known in the current literature [2, 3] but there are few results on non ideal ones. Laval is probably the first one to work with non-ideal problems. He built, in 1889, a one single-stage turbine and demonstrated that in the case of rapid passage through resonance with enough power; the maximum vibration amplitude may be reduced significantly compared with that obtained in the steady state resonant vibration. Balthazar [1] and his research group present the progress of this kind of problem. It is also known for non ideal systems that sometimes the passage through resonance requires more input power than the dynamical system driven has available. The consequence is the so-called Sommerfeld Effect which

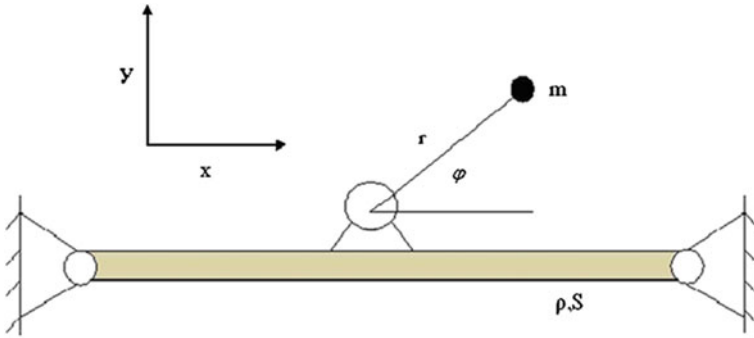


Fig. 1 A DC motor mounted on a hinged-hinged beam

means that the dynamical system cannot pass the resonance or requires an intensive interaction between the dynamical system and the motor to do it. Kononenko [4] has devoted an entire text to this subject. Nayfeh and Mook [5] gave a comprehensive and complete review of different approaches to the problem up to 1979. More recently, De Mattos [6] presented experimental results of the vibrations excited by a rotating mass at the end of a cantilever beam. They observed that the extent of the associated jump could be increased by increasing the unbalanced mass. Also, they observed that, in some cases, the amplitude and frequency of the motion became and remained modulated. Contrary to their counterpart, non-ideal vibrating systems have one more degree of freedom.

As application of such systems, one can have a mechanical structure (beam, rectangular plate, etc....) supporting an unbalanced direct-current (DC) motor with limited power supply. A sample of schematic presentation of non ideal system is given in Fig. 1, where the DC motor is mounted on a hinged-hinged beam.

The general form of dynamical equations of a non ideal system is presented as follow:

$$\left\{ \begin{array}{l} \text{Dynamic Equation of the supporting structure} = \text{Interaction terms} \\ J \frac{d^2\varphi}{dt^2} + F \left( \frac{d\varphi}{dt} \right) = \text{Other Interaction terms} \end{array} \right.$$

where  $J$ ,  $H$  and  $\left(\frac{d\varphi}{dt}\right)$  represent respectively the inertia moment of the rotating mass, the driving torque of the DC motor and the angular velocity of the rotor. The previous equations can take into account damping and the resisting torque of the motor. Others details will depend on the particular problem studied the properties of the supported structure and the characteristics of the used rotor.

Another characteristic of non ideal excitation is that it is always limited in two senses:

- The characteristic curves of the energy source (DC source)

- The dependence of the motion of the dynamical system on the motion of the energy source, that is, the coupling between the governing equations of motion of the dynamical system and the energy source

### **3 Mathematical Formalism of the Vibration Control of Rectangular Plate**

The present section gives some information about the different control approaches which could be used to control the vibration amplitude of a rectangular plate, beginning by the use of some electric transducers in Sect. 3.1. Section 3.2 used the coupling between DC sources and the plate. Each section gives some details about the mathematical formalism used. The equations of motion of a rectangular plate submitted to a non ideal excitation can be derived following the Hamilton's principle. This principle is based on the knowledge of the kinetic, the elastic potential and the external energy of the system under consideration.

#### ***3.1 Rectangular Plate Connected to an Electric Transducer as Controller***

The active control is based on the use of secondary sources of noise or vibrations which by superposition with the primary sources leads to a minimize signal. For this control strategy, the actuator applies a force on a structure using for their functioning an external energy source [7] (Bravo 2000, Ottersten 2003, Tchokuegno 2003, Le 2009, Deng 2012, Jamula 2012, Yan 2013). This control method uses two main strategies. The first consists to identify the perturbation creating the excitation and to cancel it by adding another source of excitation inverse to it. The second one consists of identifying the response of the structure instead of the excitation, thus it needs the modeling of the dynamics behavior of the structure. One can use smart materials like piezoelectric, ceramics or electric transducers as device to reduce the amplitude of vibration of mechanical structures. Today, we have some new control techniques like opto-electromechanical control, saturation control [3], magnetorheological control [8].

In the case of electric transducers, we have to add another differential equation to the one obtained without the transducer. Thus the system will have a new degree of freedom, which can be the electric charge or the electric current of the studied system. The dynamical equation of the plate will have an additional term related to the coupling with the electric transducer; this term is usually connected to the control parameter of the system. Its variation leads to appreciate the control of the amplitude of vibration in considered structure. The dynamical equation of the controller have too a term coupled to the mechanical structure which is responsible to the energy balance between the external source and the controller.

Sometimes the form of the coupling terms leads to some phenomenon as saturation one [9]. When we display analytically the dynamical equation of the system, one can denote the influence of these terms in the energy transfer between the external excitation and the absorber.

The usual form of the dynamic equation of a rectangular plate supporting a DC motor with limited power supply connected to an electric transducer is given as follow:

$$\left\{ \begin{array}{l} \text{Dynamic equation of the structure} = \text{Interactions terms} + \text{Coupling term} \\ J \frac{d^2\varphi}{dt} + L \left( \frac{d\varphi}{dt} \right) = \text{Other interaction terms} \\ \text{Dynamic equation of the controller} = \text{Another Coupling term} \end{array} \right.$$

where  $J$ ,  $L$  and  $\left(\frac{d\varphi}{dt}\right)$  represent respectively the inertia moment of the rotating mass, the driving torque of the DC motor and the angular velocity of the rotor.

The obtained dynamical equations are explored by taking into account the boundary conditions of the plate. The solutions of the PDE of the system are supposed to be a superposition of a spatial and a temporal term expressed as follow:

Inserting this solution in the PDE and using the orthogonal properties of the spatial function, one obtains the normalized equation in the first mode denoted modal equation of the system. This modal equation can be analyzed by a number of different methods such as the asymptotic methods, the multiples scales method and the method of normal forms.

### 3.2 DC Motors Mounted on a Rectangular Plate

In this subsection, we present mechanical systems, with rotating parts, which are typical in engineering applications and subject of intensive studies. Problem of scientific interest, which among others occurs in those systems, is the phenomenon of synchronization of different rotating parts. Such situations are currently encountered in industry where on the same mechanical structure are mounted two or more DC motors with limited power supply. This is usually done in order to increase the output, to avoid human physical effort and to realize easily some tasks. The coupling between the external sources is assured by the rectangular plate where they are fixed.

Balthazar et al. [10] investigated the self-synchronization of a vibrating system composed of two rotating unbalanced motors with limited power supply, mounted on a simple portal frame. Their obtained results lead to conclude that we can denote self-synchronization and absence of synchronization between the two motors for specific characteristics. This phenomenon has been studied before in the literature in other ideal problems, distinct from the present one by [11, 12], among others.

In seventeenth century Huygens reported his discovery of tendency of two pendulums (of the clocks) coupled through elastic structure (beam) to synchronize [13].

It was the first observation, which has an application in physics, of phenomenon of coupled harmonic oscillators. Kanunnikov and Lamper prove that accurate antiphase motion of pendulums with different masses cannot occur. Pogromsky created a controller which solves the synchronization problem. Pendulums reach required level of energy and move synchronously in opposite directions. More recently, others works have been implemented in the same sense. Between them, we can note those of Czolczynski et al. [14, 15] who studied the synchronization phenomenon appearing between a numbers of rotating pendulums mounted on a horizontal beam which can roll on the parallel surface. They showed that after the initial transient, different states of pendulums synchronization occurs. Additionally, it is shown in [16], that two motors mounted on the same plate can enter into synchronization with a phase difference equal to  $0$ ,  $\pi$  or  $2\pi$  depending on the physical characteristics of the motors and the plate, and that a reduction of vibration in a plate is obtained when the motors phase difference is equal to  $\pi$ .

The number of the PDE describing the dynamic of a rectangular plate supporting some DC motors with limited power supply depends on the number of non ideal sources fixed on the plate. Their usual form is obtained by using the Hamilton principle and is given as follow:

$$\left\{ \begin{array}{l} \text{Dynamic equation of the structure} = \text{Interactions term (equal to} \\ \text{the number of DC sources)} \\ J_i \frac{d^2 \phi_i}{dt^2} + L_i \left( \frac{d \phi_i}{dt} \right) = \text{Other interaction terms} \end{array} \right.$$

where  $J_i$ ,  $L_i$  and  $\left( \frac{d \phi_i}{dt} \right)$  represent respectively the inertia moment of the rotating mass, the driving torque and the angular velocity of the rotor of each DC motor.

## 4 Recent Results

The present section is devoted to the recent published results on the vibration control of rectangular plate supporting some DC motors. The presented results are obtained by the authors on the use of electric transducers and tuned mass damper as controller device where we paid an attention on the stability analysis of the controlled system and self-synchronization with and without delay of the DC sources mounted on the rectangular plate.

## **4.1 *Electromechanical Control of Vibration on a Plate Submitted to a Non-ideal Excitation***

Nonlinear vibration of rectangular plates has been investigated by a number of authors [17]. Subjected to various types of excitation they can lead to high amplitude of vibration which is not always necessary for the human being.

The topic of vibration control is one of the most relevant in the civil and mechanical engineering domain. However, the attenuation of vibration remains a problem of primary importance in many engineering fields. In the past, the reduction of the amplitude of vibration in a mechanical system was pursued by increasing the stiffness and the mass of the structure with respect to the initial scheme in order to increase the damping effect. To deal with vibrations in mechanical structure, various configurations of devices have been proposed until now. Thus, in the literature we can note that they are range from simple archaic solutions to more modern one using new techniques of vibration control. The new one presents the advantage that they are less costly and more effective. Moreover, some control techniques used electric transducers such as electromechanical devices to come through natural vibration in mechanical structures. However in 2006, Kitio Kwuimy et al. showed the optimization of the electromechanical control of a beam submitted to transversal and axial loads.

In this subsection, we present an electromechanical device used to control the vibration of a rectangular plate submitted to a DC motor with an unbalanced mass acting on a particular surface of the plate. After the modeling of the studied system, we analyze analytically and numerically the condition for the effectiveness of the control strategy. The reader should keep in their mind that in our previous works [9, 18], the dynamics of a beam was studied. There, we have used an electrostatic device as a controller coupled with the notion of saturation to determine the effect of control on the vibration amplitude.

### **4.1.1 Presentation of the Device and Mathematical Modeling of the Studied Problem**

The studied system consists of a mechanical structure represent here by a rectangular plate with edges simply supported, on which a DC motor with an unbalanced mass is fixed. In order to perform the modeling of the studied system, the surface on which the motor is fixed is taken into account through the step function. The acting force provided by the mechanical part of the electromechanical system acts under the plate by various stings regularly spaced and connected to the plate. Figure 2 presents an overview of the studied system.

The angular displacement of the motor is denoted by  $\varphi$ . The DC motor is composed by a rotor with a moment of inertia  $J$  which carries an unbalanced mass  $m_0$  situated at a distance  $r$  from the axis. In order to pursue the theoretical study, the driving torque



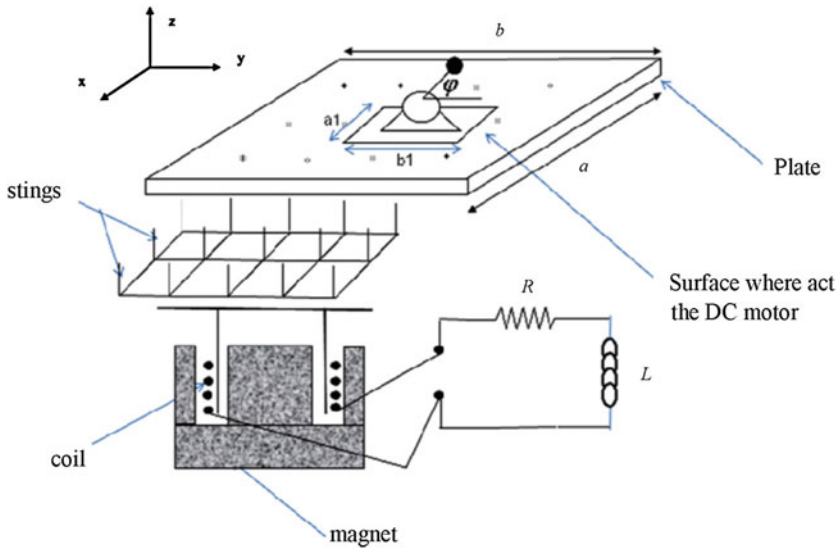


**Fig. 2** An overview of the system under control (the top of figure is composed by a rectangular plate where is resting a DC motor and the bottom is composed by a RL circuit with a magnet connected to the structure by stings)

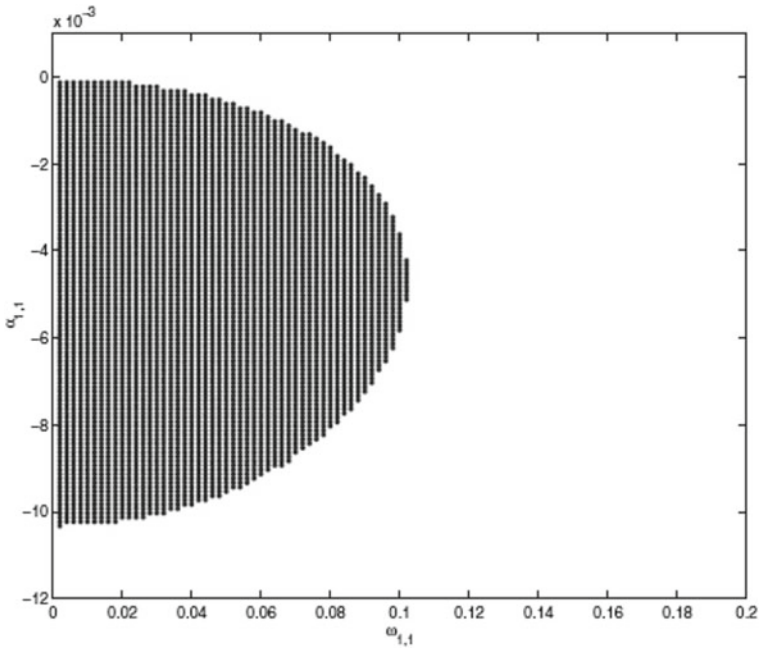


**Fig. 3** Stability card of the controlled system around the chosen fixed point

characteristic of the motor is considered to be a type frame 284. This indication is a reference which is well known either by the manufacturer or the experimenters.

The dynamical equations of motions are derived using the Hamilton Principle where is taken into account the total potential energy of the controlled system, the kinetic energy of the system and the sum of the non conservative forces.

According to the Hamilton Principle we obtained the coupled partial differential equations of the motion for the plate under control (of length a, wide b and thickness h) with the DC motor are given as follows:

$$\begin{aligned}
 & \left( \rho h + \frac{m_0}{ab} \right) \frac{\partial^2 W}{\partial t^2} + \lambda \frac{\partial W}{\partial t} + D \left[ \frac{\partial^4 W}{\partial x^4} + 2 \frac{\partial^2 W}{\partial x^2} \frac{\partial^2 W}{\partial y^2} + \frac{\partial^4 W}{\partial y^4} \right] \\
 & = \frac{m_0 r}{a_1 b_1} (\dot{\varphi}^2 \sin \varphi - \ddot{\varphi} \cos \varphi) [H(x - x_0) - H(x - x'_0)] \\
 & \quad \times [H(y - y_0) - H(y - y'_0)] - \frac{l_b B}{NM} \sum_{i=1}^N \sum_{j=1}^M I \delta(x - x_i) \delta(y - y_i) \\
 & \quad [(J + m_0 r^2) \ddot{\varphi} - L(\dot{\varphi}) + m_0 r g \cos \varphi] + \frac{m_0 r}{2} \frac{\partial^2 W}{\partial t^2} \cos \varphi = 0 \\
 & \quad L \left( (1 + \zeta) - \zeta \tanh^2 \left( \frac{I}{I_0} \right) \right) \frac{\partial I}{\partial t} + RI = l_b B \sum_{i=1}^N \sum_{j=1}^M \frac{\partial W}{\partial t} \delta(x - x_i) \delta(y - y_i)
 \end{aligned} \tag{1}$$

where  $W$ ,  $\rho$ ,  $D$  and  $h$  are respectively transversal displacement, density, flexural rigidity and thickness of the plate,  $L(\varphi)$  is the difference between the generated and frictional torque of the motor,  $\lambda$  is the damping coefficient,  $r$  and  $m_0$  are the eccentricity and the mass of the unbalanced shaft of the electric motor,  $g$  the intensity of the gravity field.  $B$ ,  $L$ ,  $l_b$ ,  $\zeta$  and  $R$  are respectively the magnetic field, inductance, length, saturation parameter of the coil and resistance of the electric circuit.  $a_1 = x'_0 - x_0$  and  $b_1 = y'_0 - y_0$  the position of the electric motor on the plate, where  $x_0$ ,  $x'_0$ ,  $y_0$ ,  $y'_0$  are coordinates of the boundary of the surface occupy by the DC motor respectively in  $x$  and  $y$  directions,  $I$  the electric current.  $H$ ,  $\delta$  are respectively the Heaviside and Dirac delta functions.  $x_i$  and  $y_j$  are the coordinates of the stings acting under the plate. The characteristic curve of the energy source (DC motor) is considered as a straight line (for more details see Warminski [19]): In this case the constant  $u_1$  and  $u_2$  refer respectively to the voltage and a physical characteristic of the corresponding motor.

$$L(\dot{\varphi}) = u_1 - u_2 \dot{\varphi} \tag{2}$$

In this case the constants  $u_1$  and  $u_2$  refer respectively to the voltage and a physical characteristic of the corresponding motor.

Taking in account the boundary conditions of the plate (simply supported one) and according to the orthogonality of the eigenfunctions (Peeters, 2010), the following modal equations are derived as:

$$\begin{aligned}
& \left( \rho h + \frac{m_0}{ab} \right) \ddot{Y}_{n,m}(t) + \lambda \dot{Y}_{n,m}(t) + D \left[ \left( \frac{n\pi}{a} \right)^2 + \left( \frac{m\pi}{b} \right)^2 \right]^2 Y_{n,m}(t) \\
& = \frac{4m_0 r}{\pi^2 a_1 b_1} \left( \dot{\varphi}^2 \sin \varphi - \ddot{\varphi} \cos \varphi \right) \left[ \cos \left( \frac{n\pi}{a} x_0 \right) - \cos \left( \frac{n\pi}{a} x'_0 \right) \right] \\
& \times \left[ \cos \left( \frac{m\pi}{b} y_0 \right) - \cos \left( \frac{m\pi}{b} y'_0 \right) \right] - \frac{4l_b B}{abNM} I \sum_{i=1}^N \sum_{j=1}^M \sin \left( \frac{n\pi}{a} x_i \right) \sin \left( \frac{m\pi}{b} y_j \right) \\
& \left[ \left( J + m_0 r^2 \right) \ddot{\varphi} - L(\dot{\varphi}) + m_0 r g \cos \varphi \right] + \frac{\pi^2 m_0 r}{8(1 - \cos(n\pi))(1 - \cos(m\pi))} \ddot{Y}_{n,m}(t) \cos \varphi = 0 \\
& L \left( (1 + \zeta) - \zeta \tanh^2 \left( \frac{I}{I_0} \right) \right) \frac{dI}{dt} + RI = l_b B \dot{Y}_{nm}(t) \sum_{i=1}^N \sum_{j=1}^M \sin \left( \frac{n\pi}{a} x_i \right) \sin \left( \frac{m\pi}{b} y_j \right)
\end{aligned} \tag{3}$$

Where

$$\dot{Y}_{n,m}(t) = \frac{dY_{n,m}}{dt}, \quad \dot{\varphi} = \frac{d\varphi}{dt}, \quad \ddot{\varphi} = \frac{d^2\varphi}{dt^2}, \quad \ddot{Y}_{n,m} = \frac{d^2Y_{n,m}}{dt^2},$$

For the n and m mode in each direction we derive the normalized equations:

$$\begin{aligned}
& \ddot{U}_{n,m}(t) + \gamma \dot{U}_{n,m}(t) + \omega_{n,m}^2 U_{n,m}(t) = \frac{4m_0 r}{a\pi^2 a_1 b_1 (\rho h + (m_0/ab))} \left( \dot{\varphi}^2 \sin \varphi - \ddot{\varphi} \cos \varphi \right) \\
& \times \left[ \cos \left( \frac{n\pi}{a} x_0 \right) - \cos \left( \frac{n\pi}{a} x'_0 \right) \right] \\
& \times \left[ \cos \left( \frac{m\pi}{b} y_0 \right) - \cos \left( \frac{m\pi}{b} y'_0 \right) \right] - \frac{4l_b B I_0 \omega_0^2}{a^2 b N M (\rho h + (m_0/ab))} V_{n,m} \\
& \times \sum_{i=1}^N \sum_{j=1}^M \sin \left( \frac{n\pi}{a} x_i \right) \sin \left( \frac{m\pi}{b} y_j \right) \\
& \ddot{\varphi} = L'(\dot{\varphi}) + \chi \cos \varphi + \sigma_{n,m} \ddot{U}_{n,m}(t) \cos \varphi \\
& \left( 1 - \varepsilon \tanh^2(V_{n,m}) \right) \frac{dV_{n,m}}{dt} + \omega_\varepsilon V_{n,m}(t) = \frac{al_b B}{I_0 L} \dot{U}_{nm}(t) \sum_{i=1}^N \sum_{j=1}^M \sin \left( \frac{n\pi}{a} x_i \right) \sin \left( \frac{m\pi}{b} y_j \right)
\end{aligned} \tag{4}$$

with the dimensionless variables given by:  $V_{nm} = (I/I_0)$ ;  $U_{nm} = (Y_{nm}/a)$ ;  $\tau = (t/\omega_0)$ ;

Here  $I_0$ ,  $v$ ,  $N$  and  $M$  are respectively the characteristic current of the electrical circuit, Poisson ratio, number of stings acting in x and y direction respectively.

### 4.1.2 Performance of the Control Strategy

#### (a) *Stability analysis of the controlled system*

Instead of reinforcing the structure, active control strategies could destabilize the structure due to the forces acting on the system. It is therefore primordial to focus on the stability of the system in autonomous case. Thus, the Jacobian matrix related to the dynamics equations is extracted and explored. Four fixed points are derived from the dynamics equations with a condition but only two are physically possible [20]. The characteristic polynomial is derived from this Jacobian and according to the Routh–Hurwitz criterion [21], the system is stable if some conditions are satisfied. In order to get the real domain where the controlled system will be stable in the space parameter, we display the following diagram, where the region with dark points is the stable region of the controlled system. The stability card obtained is validated by carrying out the eigenvalues of the Jacobian matrix of the controlled system in the both regions [20].

#### (b) *Effect of the control on the amplitude of vibration of the plate*

The equations of motion of the system under control are solved analytically by using the harmonic balance method. After some algebraic analytical manipulation, we obtained strongly non-linear and coupled amplitude equations. A good accordance between our analytical results with the numerical one is observed since it is quite impossible to plot separately the amplitude of the structure, angular velocity and the current as function of the motor velocity (see [20] for more details).

To show the effect of the control strategy used, we display in Fig. 4 the evolution of amplitude when the control is on and off. We observed from this figure that the amplitude response of the plate is well reduced for these set of parameters.

By increasing the number of stings acting under the plate in each direction, we observe in Fig. 5 that the amplitude response of the plate is more and more reduced.

The effect of the saturation parameters of the inductance has been explored and we can observe that the reduction of amplitude may lead to the production of an important quantity of energy in the electromechanical device. It is also proved [20] that the amplitude of vibration of the plate decreases as the number of the stings increases and as the intensity of the magnetic field increases.

## 4.2 *Vibration Control a Rectangular Plate Submitted to a Non-ideal Excitation with a TLCD*

### 4.2.1 **Description of the Control Device and Mathematical Modeling of the Studied Problem**

The schematic of the studied system consists on simply supported edges rectangular plate under the excitation of an unbalanced DC motor with limited power supply

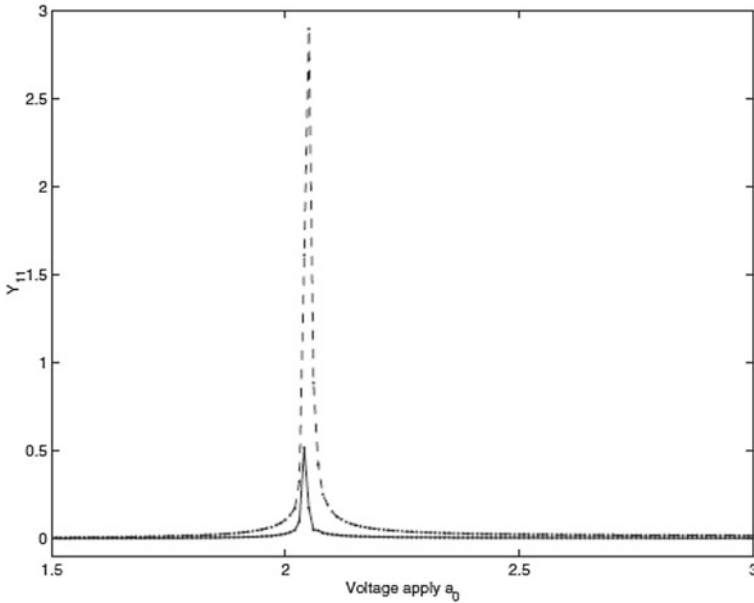


**Fig. 4** Amplitude curve of the plate when the control is off (points with dashed line) and on (points with line) for  $N = 5$  and  $M = 3$

coupled with a TLCD. Both the motor and the damper are fixed to the plate. The plate and the DC motor system form a non-ideal system, meaning that the excitation created by the DC motor is influenced by the response of the supporting structure and that the applied voltage has a limited power supply.

The present device is different from the others commonly seen in the literature [3] in the sense that the orifice is placed vertically. Once the system is excited by the motor, there arise transversal vibrations of the plate. As a result, the liquid inside the columns of TLCD starts vibrating by passing through the vertical orifice and try to stabilize the plate. This allows us to distinguish the vertical column  $L_v$  to the horizontal column  $L_h$  as shown in Fig. 6.

The dynamic equations of the system are obtained by combining the kinetic, potential and external energies of the plate, the motor, and the TLCD. Then after determining the respective derivatives and substituting in the Lagrangian equations, we get the following system of equations:

$$\begin{cases} \left[ \rho_p h + \frac{m_0}{a_0 b_0} (H(x - x_1) - H(x - x_2))(H(y - y_1) - H(y - y_2)) + \frac{\rho_c L}{a_1 b_1} (H(x - x'_1) - H(x - x'_2))(H(y - y'_1) - H(y - y'_2)) \right] \ddot{W}_s \\ \frac{\lambda}{ab} \ddot{W}_s + D \left[ \frac{\partial^4 W_s}{\partial x^4} + 2 \frac{\partial^4 W_s}{\partial x^2 \partial y^2} + \frac{\partial^4 W_s}{\partial y^4} \right] = \frac{m_0 r_0}{a_0 b_0} (\ddot{\varphi} \sin \varphi + \dot{\varphi}^2 \cos \varphi) (H(x - x_1) - H(x - x_2))(H(y - y_1) - H(y - y_2)) \\ - \frac{\rho_c \lambda}{a_1 b_1} (2\dot{W}_f^2 + 2W_f \ddot{W}_f) (H(x - x'_1) - H(x - x'_2))(H(y - y'_1) - H(y - y'_2)) \\ (J + m_0 r^2) \ddot{\varphi} - \frac{1}{2} m_0 r \ddot{W}_s \sin \varphi - \frac{1}{2} m_0 g r \cos \varphi = \hat{a} - b \dot{\varphi} \\ 2L_v \ddot{W}_f + \frac{1}{2L} \xi |\dot{W}_f| \dot{W}_f + g W_f = -2W_f \ddot{W}_s \end{cases} \tag{5}$$

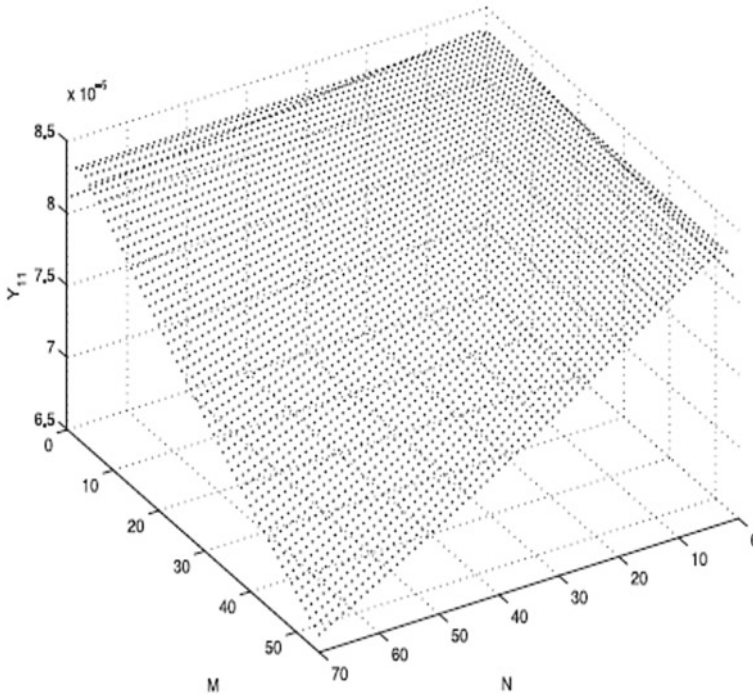


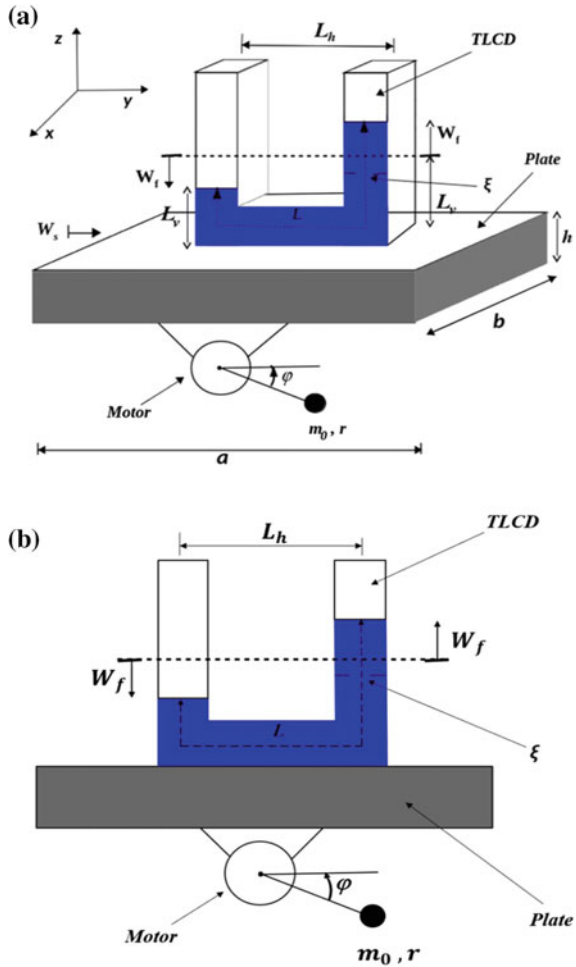
**Fig. 5** Maximum amplitude of the plate as function of the number of stings acting in each direction

with  $L_v$  and  $L_h$  the vertical and horizontal length of the liquid inside the tube,  $\rho_c$  the density of the fluid inside the columns of the TLCD,  $a_1 = x_2 - x_1$  and  $b_1 = y_2 - y_1$  are the dimensions occupied by the TLCD along the  $x$ - and  $y$ -axes of the plate, respectively, with  $x_1, x_2, y_1,$  and  $y_2$  the coordinates of the boundaries of the areas occupied by the TLCD, respectively, in the  $x$  and  $y$  directions.  $A_v$  and  $A_h$  are the cross-sectional areas, respectively, of the vertical and the horizontal columns of the tube, and  $H$  represents the Heaviside function. The movement of the system is characterized by two generalized coordinates  $W_f$  and  $W_s$ , respectively, the response of the liquid damper (TLCD) and the response of the plate in the transversal motion. The plate has the following dimensions: the length  $a$ , the width  $b$ , and the thickness  $h$ . Concerning the motor, a mass  $m_0$  is fixed on the shaft of the rotor with an eccentricity  $r$ .

**4.2.2 Optimization of the Control Strategy**

Taking into account the boundary conditions of the plate and the Galerking approach we displayed the orthogonality of the obtained spaced function and we derived the following algebraic modal dimensionless equations:

**Fig. 6** Rectangular plate supporting an unbalanced DC motor and a TLCD: **a** perspective view and **b** front view



$$\begin{cases} \ddot{T}_{nm} + \lambda \dot{T}_{nm} + \omega_{nm}^2 T_{nm} = \alpha_0 (\ddot{\varphi} \sin \varphi + \dot{\varphi}^2 \cos \varphi) - \alpha_1 (2\dot{Z}_f^2 + 2Z_f \ddot{Z}_f) \\ \ddot{\varphi} - \beta_0 \ddot{T}_{nm} \sin \varphi - g_0 \cos \varphi = u_1 - v_1 \dot{\varphi} \\ \ddot{Z}_f + \frac{1}{4L} \xi |\dot{Z}_f| \dot{Z}_f + g_1 Z_f = -\beta_1 Z_f \ddot{T}_{nm} \end{cases} \quad (6)$$

This system of ODE's has been displayed analytically and numerically to perform the control strategy used (Feulefack 2021). Thus, it has been proved that some physical parameters of the studied system have a great effect on the vibration control of the rectangular plate.

Modeling of the studied system here takes more details into account such as the spaces occupied by the DC motor and TLCD under and over the rectangular plate respectively. Physical and mechanical parameters used for numerical simulations are chosen according to a common situation in civil or mechanical engineering.

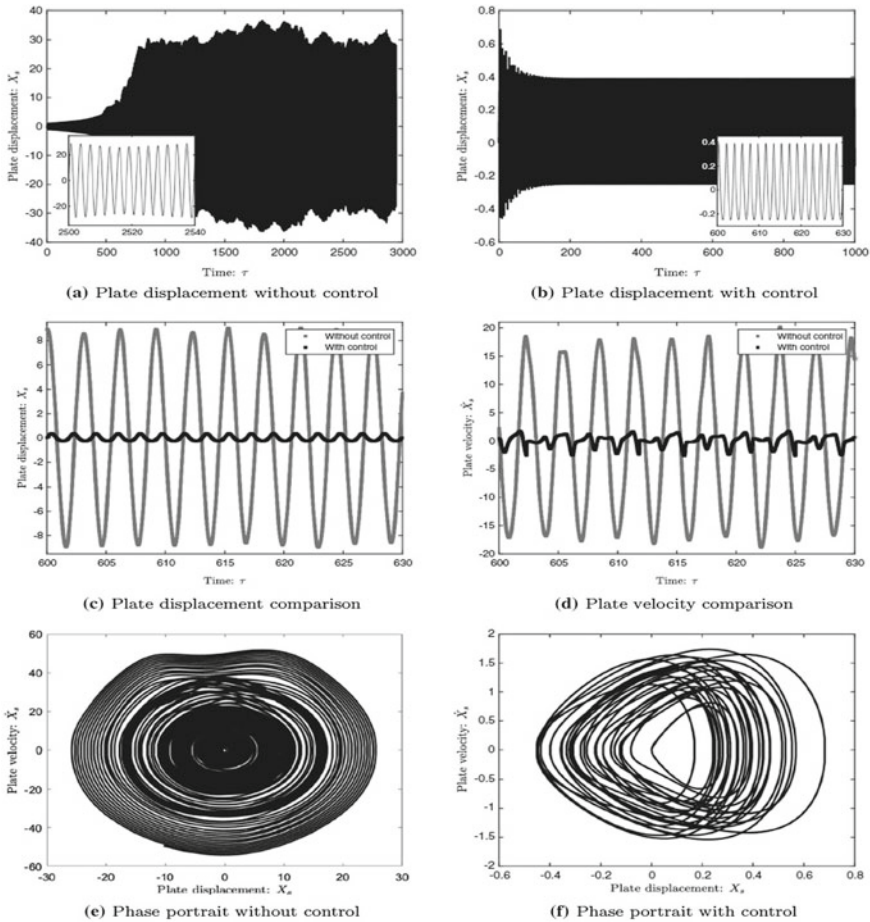


**Fig. 7** Numerical results of the responses of the rectangular plate and phase diagrams with and without TLCD device obtained with the parameters' values  $u_1 = 2.1$ ;  $\alpha_0 = 0.42$ ;  $\alpha_1 = 0.201$ ;  $g_0 = 7.9$ ;  $g_1 = 1$ ;  $\beta_0 = 0.1$ ;  $\lambda_1 = 0.001$ ;  $\xi = 0.6$ ;  $\omega_1 = 2$ ;  $\beta_1 = 1.25$ ; and  $v_1 = 0.02$

Accordance observed between numerical and analytical results lead to conclude that one can predict the influence of some physical or mechanical parameters of the system on the plate amplitude of vibration. Consequently, the results obtained will, therefore, encourage engineers to use a TLCD concept as a control system for tall buildings and structures due to its multiple advantages.



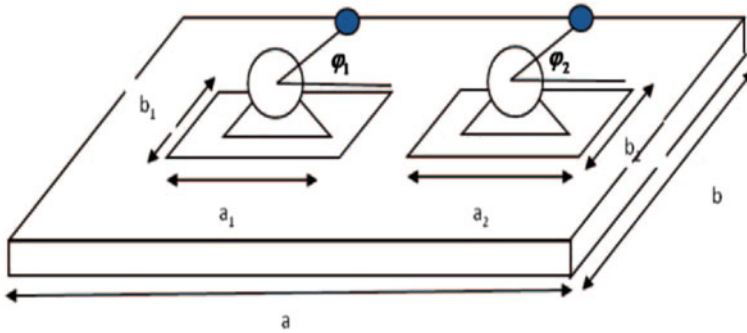


Fig. 8 Rectangular plate supporting two DC motors

### 4.3 Self-synchronization of DC Motors on a Rectangular Plate and Reduction of Vibration

In industry, several rotating machines inevitably exhibit nonlinear behaviors when they are mounted on flexible structures. In general, the excitation of this type of vibrating system is considered to be always a limited power supply since the response of the structure influences the rotating moving of the motors [1, 9]. The Mathematical formalism leading to the modeling of a non-ideal system includes an additional equation compared to that of the corresponding ideal system, to describe the interaction between the energy source and the rest of the system.

In order to optimize the output in industry or to carry out many tasks at the same time, synchronization or desynchronization of machines can be necessary to optimize the production. Thus, it may be possible for two or more machines having each a motor to self-synchronize. Balthazar et al. [1, 22] investigated the self-synchronization of a vibrating system composed of two rotating unbalanced motors with limited power supply mounted on a simple portal frame. They reached to the conclusion that we can denote self-synchronization and absence of synchronization between the two motors for specific characteristics.

The results presented here are divided in two parts where the first one is devoted to the synchronization of two DC motors supported by the same plate and on the analysis of plate vibration control when the motors enter into synchronization. The second one focuses on the synchronization of three DC motors supported by the same plate when they are rotating in the same or in the opposite direction. The plate vibration control analysis is studied when the motors enter into synchronization or not. Using numerical simulation, one can show the influence of the main frequency structure on synchronization, and the impact of rotating direction of the DC motors on the plate displacement.

### 4.3.1 Self-synchronization of Two DC Motors Mounted on a Rectangular Plate

(a) *Description of the model*

The studied system consists of a rectangular plate with simply supported edges, on which two DC motors with an unbalanced mass are fixed. The surface on which the motors are fixed is taken into account by considering the area  $a_1b_1$  and  $a_2b_2$ .

The angular displacements of the motors are denoted  $\varphi_1$  and  $\varphi_2$ . The rotors have respectively the inertia moment  $J_1, J_2$  and carry the same unbalanced mass  $m_0$  at a distance  $r$  from their axis. The physical characteristics of the motors such as the characteristic driving torque of the motor for each is assumed to be well known, either from the manufacturer or from experiments [10].

According to the Hamilton principle, the PDE describing the dynamics of the system is given as follow:

$$\sum_i \left( \rho h + \frac{m_1+m_2}{ab} \right) \frac{\partial^2 w}{\partial t^2} + \lambda \frac{\partial w}{\partial t} + D \left[ \frac{\partial^4 w}{\partial x^4} + 2 \frac{\partial^4 w}{\partial x^2 \partial y^2} + \frac{\partial^4 w}{\partial y^4} \right] =$$

$$1^2 \frac{-m_i r_i}{a_i b_i} \left( \dot{\varphi}_i^2 \sin \varphi_i - \ddot{\varphi}_i \cos \varphi_i \right) [H(x - x_i) - H(x - x'_i)] [H(y - y_i) - H(y - y'_i)]$$

$$\ddot{\varphi}_i = \frac{-m_i r_i}{2(J+m_i r_i^2)} \frac{\partial^2 w}{\partial t^2} \cos \varphi_i - \frac{m_i r_i g}{(J+m_i r_i^2)} \cos \varphi_i + L_i(\dot{\varphi}_i)$$
(7)

Taking in account the boundary conditions of the plate (simply supported one), and using the orthogonality of the eigenfunctions obtained, the following normalized modal equations are derived as:

$$\ddot{y} + \delta \dot{y} + \omega^2 y = \alpha_1 (\dot{\varphi}_1^2 \sin \varphi_1 - \ddot{\varphi}_1 \cos \varphi_1) + \alpha'_1 (\dot{\varphi}_2^2 \sin \varphi_2 - \ddot{\varphi}_2 \cos \varphi_2)$$

$$\ddot{\varphi}_1 = \beta_1 \ddot{y} \cos \varphi_1 + \varepsilon_1 \cos \varphi_1 + \tilde{L}_1(\dot{\varphi}_1)$$

$$\ddot{\varphi}_2 = \beta_2 \ddot{y} \cos \varphi_2 + \varepsilon_2 \cos \varphi_2 + \tilde{L}_2(\dot{\varphi}_2)$$

wherey represent the normalized plate amplitude.

Considering the two non ideal sources acting on the structure and taking into account their physical characteristics, we can distinguish four situations for which the dynamics can be explored:

- . 1st case:  $a_{01} = a_{02}, b_{01} = b_{02}$ , meaning that the DC motors are identical and have the same applied voltages.
- . 2nd case:  $a_{01} \neq a_{02}, b_{01} \neq b_{02}$ , meaning that the DC motors are different and have different applied voltages.
- . 3rd case:  $a_{01} = a_{02}, b_{01} \neq b_{02}$ , meaning that the DC motors have the same applied voltages and are different.
- . 4th case:  $a_{01} \neq a_{02}, b_{01} = b_{02}$ , meaning that the DC motors are identical and have different applied voltages.

We assume first that the both non ideal sources are identical with the same source of voltage apply, that the both non ideal sources have a source voltage, Fig. 9 shows

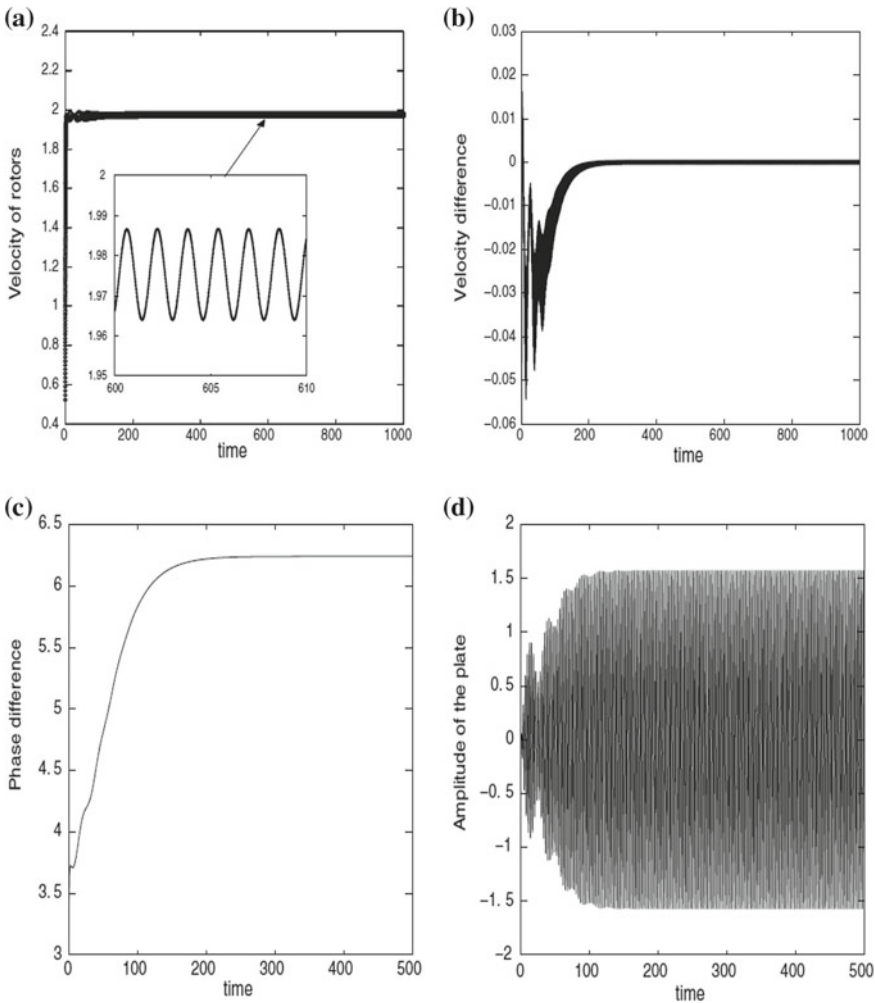


**Fig. 9** Self-synchronization of the non ideal sources with  $b_{01} = b_{02} = 1.624$  and  $a_{01} = 3.209$ ,  $a_{02} = 3.207$

the (a) variation of the velocity, (b) velocity difference, (c) phase difference between the two motors (d) and plate amplitude as a function of the time.

Observation of these curves let appears that curves that the two DC motors enter into synchronization in the first case mentioned above with a phase difference of  $\Delta\varphi=2\pi$ . This synchronization appears with time because of the energy transfer between the two rotors (Kapitaniak 2012). This synchronization phenomenon appears with time because of the energy transfer between the two rotors (Kapitaniak 2012). It is also found that the amplitude of vibration of the plate increases.

Still in the first case, one notice that for some values of the frequencies, the phases difference can be equal to  $\pi$ ,  $2\pi$  or equal to 0 (see Fig. 10).

However, there is a domain where the phase difference is different to the previous values (see Fig. 10). This domain is situated between the domains where the phase differences are  $\pi$  and  $2\pi$  or 0. In this domain we note high amplitude of vibration in the plate [16]. On the base of these results, we can note that self-synchronization of non ideal sources may lead to reduction of amplitude vibration of the plate when they have a phase difference  $\Delta\varphi = \pi$ .

Due to the fact that, the frequency of the structure  $\omega$  is a parameter which contributes to get synchronization with phase difference of  $\pi$  or  $2\pi$ , the density of the structure and its thickness are parameters that can be chosen to reduce the amplitude of the plate. For instance, with two identical DC motors, a concrete plate having the following characteristics:

- . Dimensions: 800 mm  $\times$  600 mm  $\times$  4 mm;
- . Density: 2500 kg/m<sup>3</sup>;
- . Young modulus:  $3.0 \times 10^{10}$  N.m<sup>-2</sup>;
- . Poisson ratio: 0.20.

leads to a structure frequency of  $\omega = 2.21$  when the thickness is  $h = 4$  mm, meaning that we can get self-synchronization with  $\Delta\varphi = 2\pi$ . and when the thickness is  $h = 1.4$  mm we have  $\omega = 0.77$  leading to self-synchronization with  $\Delta\varphi = \pi$ . With a thickness of  $h = 2.4$  mm, the phase difference is between]  $\pi$ ,  $2\pi$  [.

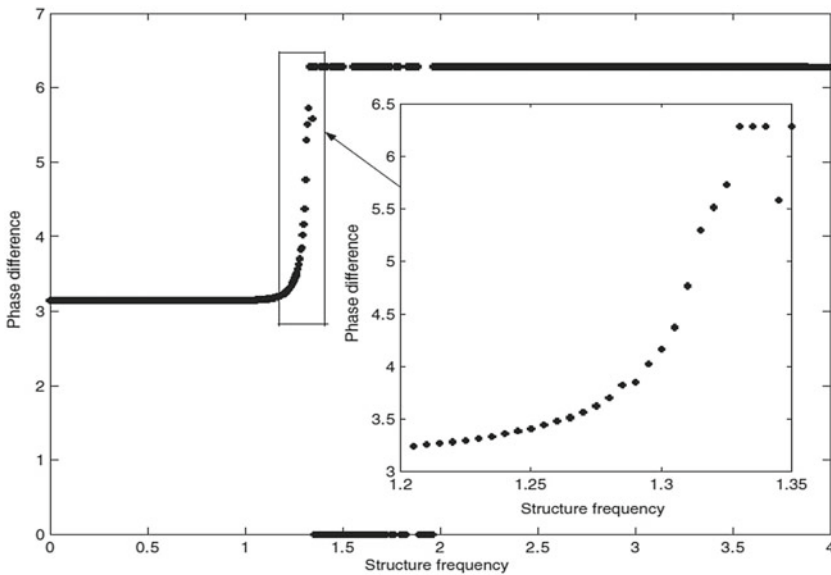


**Fig. 10** Phase difference between the DC sources as function of frequency structure for identical sources

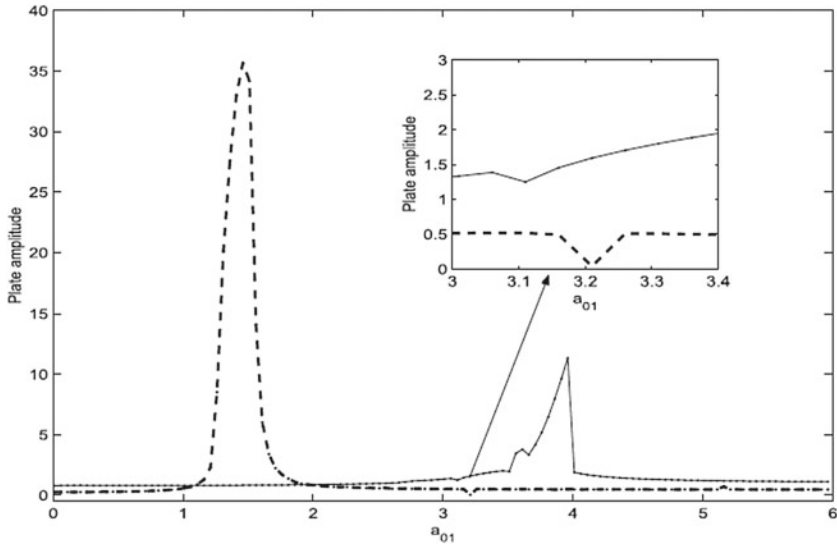


**Fig. 11** Amplitude of the plate for  $\Delta\varphi = \pi$  (dash lines)  $\omega = 0.78$ ,  $\Delta\varphi = 2\pi$  (solid lines)  $\omega = 2.21$

(b) *Influences of voltage sources on amplitude vibration of the plate for different motor*

For identical motors ( $b_{01} = b_{02}$ ), we display in Fig. 11 the amplitude of vibration of the plate when the voltage applied to one DC source varies and for the other one we fix as  $a_{02} = 3.201$ . Observation of this curve shows that the transition to the resonance leads to less amplitude of vibration when the two DC sources are synchronized with a phase difference of  $2\pi$  or  $0$  compared to the synchronization with phase difference of  $\pi$ . In the region where we have  $\omega = 0.78$  and  $\omega = 1.3$  (synchronization with  $\Delta\varphi = \pi$  and self-synchronization with  $\Delta\varphi \in ]\pi, 2\pi[$ ) Figs. 12 and 13 show a global view of the plate amplitude in a 3D plot for identical DC motors ( $b_{01} = b_{02}$ ), while each applied voltage is varied. The associated color bars showing different regions, indicating values of the amplitude vibration of the plate as it increases from minimum (blue) to maximum (brown) are clearly identified. The blue color denotes regions in space parameters ( $a_{01}, a_{02}$ ) where the amplitude vibration of the plate is less than amplitude in the region where we have brown color. Through the diagonal ( $a_{01} = a_{02}$ ), we note less amplitude of vibration in the plate whether in resonant regions or not. Figure 13 Amplitude of the plate as function of  $a_{01}$  and  $a_{02}$  for  $\omega = 1.3$  and identical motor. a: Space representation in 3D; b projection in the plan

(iii) *Influences of voltage sources on amplitude vibration of the plate for different motor*

When the two non ideal sources are different ( $b_{01} \neq b_{02}$ ), we represent the amplitude vibration of the plate when varying the voltage applied to one DC motor and setting the other at  $a_{02} = 3.201$ . The curves in Fig. 14 are obtained with two values of

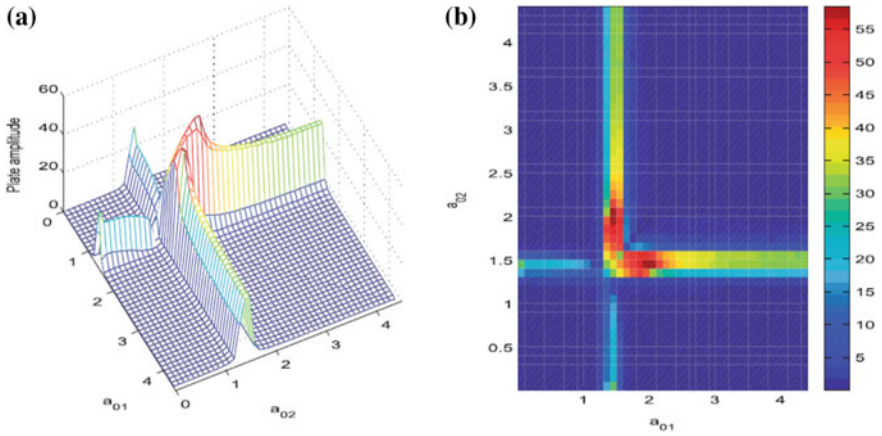


**Fig. 12** Amplitude of the plate as function of  $a_{01}$  and  $a_{02}$  for  $\omega = 0.78$  and identical motor. **a** Space representation in 3D; **b** projection in the plan

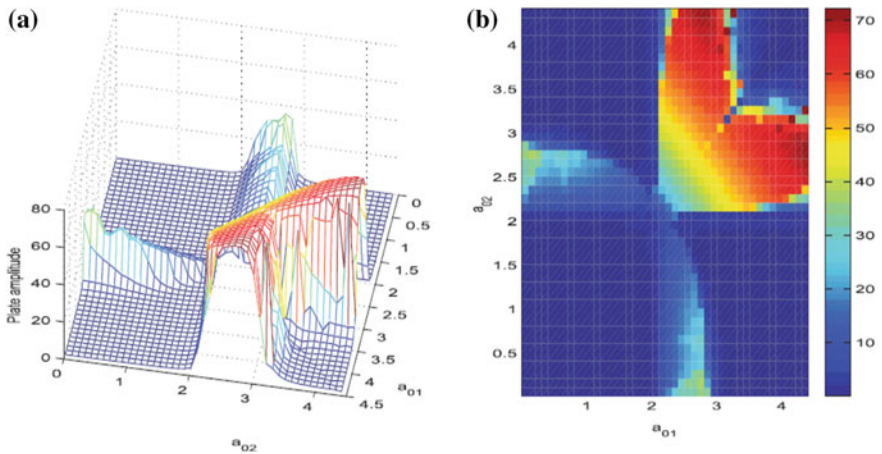


**Fig. 13** Amplitude of the plate as function of  $a_{01}$  and  $a_{02}$  for  $\omega = 1.3$  and identical motor. **a**: Space representation in 3D; **b** projection in the plan

structure frequency ( $\omega = 0.78, \omega = 2.5$ ). We note that, the amplitude of vibration in the structure is reduced for  $\omega = 2.5$  compare with the value  $\omega = 0.78$  at the resonance.

Comparison between the both figures let appears that the amplitude of vibration of the plate is more reduced when the frequency structure is increasing. Thus for different DC motors, plate thickness and his density are parameters to be chosen carefully so as to avoid high amplitude of vibration in the structure. It is also important to know the physical characteristics of one motor which will self-synchronize (in phase or in antiphase) with a different one whose characteristics are well known [16].

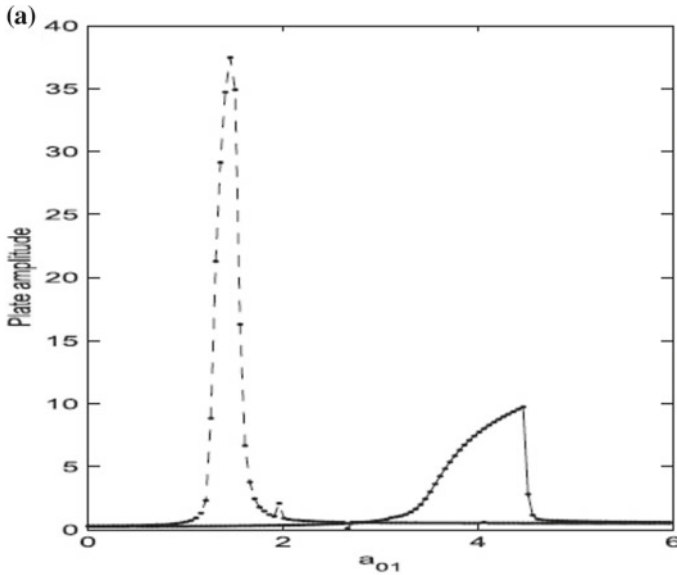


**Fig. 14** Plate amplitude as function of voltage apply to one DC motor  $\mathbf{a}$   $\omega = 0.78$  dashed curve with stars and  $\omega = 2.5$  solid lines with points

### 4.3.2 Self-synchronization of Three DC Motors Mounted on a Rectangular Plate

(a) Description of the studied system

Here, the studied system consists of a rectangular plate with simply supported edges, on which three DC motors with an unbalanced mass are fixed and are capable to rotate in the same or in the opposite direction. The surface on which the motors are fixed is taken into account by considering the area  $a_1b_1$ ,  $a_2b_2$  and  $a_3b_3$ . A schematic of the set-up is shown in Fig. 15. The rotors have each the moment of inertia  $J_i$  carrying an unbalanced mass  $m_i$  at a distance  $r$  from their axis. The angular displacements of the motors are denoted  $\varphi_i$ . The characteristic driving torque of the motor for each given power level is assumed to be well known, either from the manufacturer or from experiments [19].

On the base of the Hamilton principle, the obtained PDE describe the dynamics of the system is similar to the one obtained in the case of two DC motors but the number of PDE correspond to the number of DC motors mounted on the plate. The main structure equation has additional external term equal to the number of the DC sources mounted on the structure.

The rotating opposite direction of the DC sources is taken in account in the characteristics equations by taken negative the voltage apply to the DC sources. This characteristics curve of the energy source is assumed to be a straight line as in

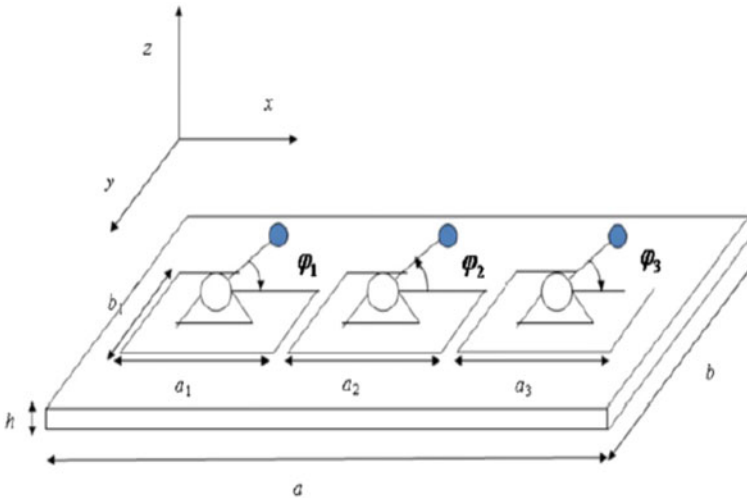


**Fig. 15** Schematic of a rectangular plate supporting three DC motors rotating in opposite direction

Warminski [19]. The boundary condition of the studied plate is a simply supported one.

- (b) Self-synchronization and amplitude vibration of the plate when the DC motors rotate in the same direction

In this subsection, we assume that the non-ideal sources have a same source voltage and the same physical characteristics. It is quite important to note that the values of the coupling terms are different because of different position occupied by the motors on the structure. We denote self-synchronization between the DC sources [23] by observing the behavior of the phase difference between the DC motors as the structure frequency is varied. We note that for small frequency of vibration of the structure the phase difference between motors 2 (DC2) and 3 (DC3) is equal to 0 while the phase difference between motor 1 (DC1) and motor 2 (DC2) is  $\pi$ . When the plate frequency is high there is a perfect synchronization between motor 2 and motor 3 and anti phase synchronization between motor 1 and motor 2 or motor 3.

Through numerical simulation, we observe that by comparing the plate amplitude for small and high value of the frequency, anti-phase synchronization is quite recommended to get small amplitude of vibration of the plate.

Substituting DC motor 2 by another one, we note that for small frequency of the plate, the phase differences  $\phi_2 - \phi_3$  and  $\phi_1 - \phi_2$  are equal to  $4\pi/5$  and represent the half of  $\phi_1 - \phi_3$ , while for high frequency, all the DC motors synchronize in phase. Looking and comparing the plate amplitude, one can note that these amplitudes are small when one motor synchronizes in phase with the others even if one of them is out of phase. It is also possible to substitute a DC motor with another one capable of creating and in-phase synchronization.



As we note that the natural frequency of the structure is a relevant parameter which contributes to get synchronization with phase difference of  $\pi$ ,  $4\pi/5$ ,  $8\pi/5$  or  $2\pi$  we can conclude that the density of the structure and its thickness are parameters that can be well chosen in order to more reduce the amplitude vibration of the plate.

(iii) *Self-synchronization and amplitude vibration of the plate when the DC motors rotate in different directions*

This subsection is related to the situation presented in Fig. 15, however according to the rotating direction of DC motor 2, the control parameter  $a_2$  will be count negatively. Thus, when we considered identical motors ( $b_{01} = b_{02} = b_{03}$ ), we display in Fig. 16 the phase differences between the DC motors while the plate frequency is varied.

The corresponding plate amplitude show low amplitude of vibration for less value of the frequency and high amplitude in the other case. This means that when two of the three DC sources are synchronized in phase the amplitude of vibration is inevitably high even if the structure frequency is high.

By displaying the corresponding plate amplitude, the obtained figures [23], it is shown that for identical motors rotating in the same direction compare to the case of different motors rotating in the opposite direction both obtained for a small value of the structure frequency.

However, it is noted that for a high value of the structure frequency the amplitude of vibration of the plate is identical when the motors are identical or not and rotating in the same direction or in the opposite directions.

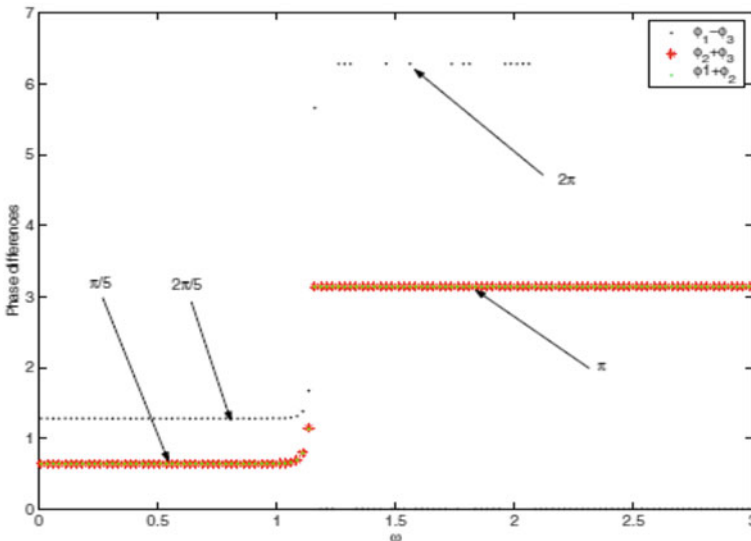


**Fig. 16** Phase difference between DC motors as function of structure frequency, DC1-DC3 (black points), DC2-DC3 (red stars), DC1-DC2 (green points)

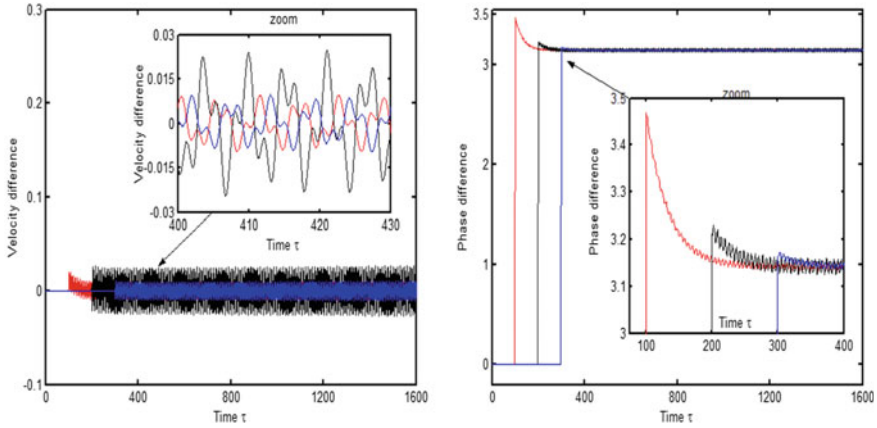


**Fig. 17** Representation of velocity difference (a) and phase difference (b) between the two DC motors as function of dimensionless time computed with  $\alpha_1 = \alpha_2 = 0.201$  when the main frequency of the structure is  $\omega_{11} = 0.873$

In the case where the three non-ideal sources are different ( $b_{01} \neq b_{02} \neq b_{03}$ ), we denote small amplitude of vibration when one of the motors rotate in the opposite direction.

### 4.3.3 Effect of Time Delay of DC Motors on Their Self-synchronization When Mounted on a Rectangular Plate

It has been already proved before that two or three DC motors supported by a rectangular plate can easily enter in a self-synchronized dynamics with different phase differences. However, up to now we do not yet pay enough attention about the effect of the switching delay which could be imposed to one or two DC motors when others are already switch on [24].

The mathematical formalism of such system follows the same rules as presented before thus, we obtained the following dynamical equations:

$$\ddot{Y}_{k,l}(\tau) + 2\delta\dot{Y}_{k,l}(\tau) + \omega_{k,l}^2 Y_{k,l}(\tau) = \alpha_i(\tau - \tau_i)(\dot{\varphi}_i^2 \sin \varphi_i - \ddot{\varphi}_i \cos \varphi_i) + \beta_i(\tau - \tau_i)$$

$$\ddot{\varphi}_i = \sigma_{i,kl}\ddot{Y}_{k,l}(\tau) \cos \varphi_i + \varepsilon_i \cos \varphi_i + \tilde{L}_i(\dot{\varphi}_i)$$

where  $i = 1;2$  or  $3$ ,  $\tau_i$  the functioning delay imposed to the DC motors,  $k$  and  $l$  refer nodal lines along the  $x$ - and the  $y$ - directions, respectively.

#### (a) Case of two DC motors

Here we display a situation where two DC motors are mounted on a rectangular plate and one is switch on with a delay  $\tau_i$  when the second one is already working on the plate. The study is restricted here to the first mode of vibration in each direction of the plate because it has been proven that it is the place of high amplitude of vibration in

the system. Based on numerical simulations done, It is observed that when the second DC motor starts to function with a delay  $\tau_2$ , both DC motors quickly synchronize, the faster for an increased delay. Hence, this leads us to conclude firstly that late switching on of the second motor reduces the time to reach to a synchronous state between DC motors.

However from Fig. 18, we observe that whatever the value of the starting delay imposed to the second DC motor, it doesn't have any effect on the plate amplitude of vibration in the case of the high natural frequency of the plate. Nevertheless, we denote the presence of high amplitude of plate vibration when the phase difference  $\varphi_2 - \varphi_1 = 2\pi$  compared to the situation of an anti-phase ( $\varphi_2 - \varphi_1 = \pi$  obtained with low value of the natural frequency) synchronization between the sources which is in accordance with previous results [16].

**(b) Case of three DC motors**

The situation presented here consists of three motors resting and acting on a rectangular plate. However, the starting delay imposed to the DC motors can be introduced in different ways. To show the impact of the starting delay of the DC motors on the time required for synchronization, we focus our attention on the case where the DC motors are synchronized (identical motor characteristics and same voltage supply). Note that numerical solutions have been provided for the fundamental mode in each direction of the plate and motors rotate in the same direction.

However, when the natural frequency of the plate is  $\omega_{11} = 0.873$ (Fig. 19) the starting time of the third motor affects the time required to achieve synchronization of the three DC motors. Thus, from the start of the third DC motor, the three DC motors are caused to synchronize more sooner. This can be explained by the fact that

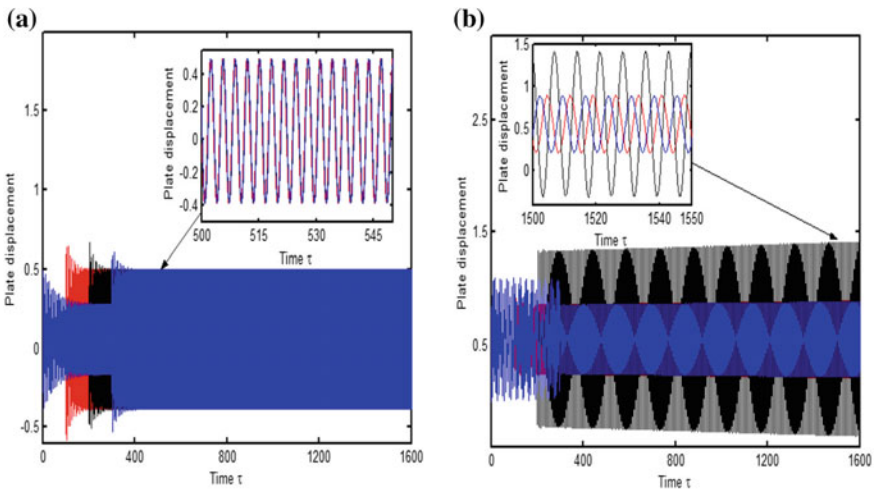


**Fig. 18** Representation of plate amplitude vibration for two values of the main frequency of the plate  $\omega_{11} = 2.73$  (a) and  $\omega_{11} = 0.873$  (b) in view of their comparison

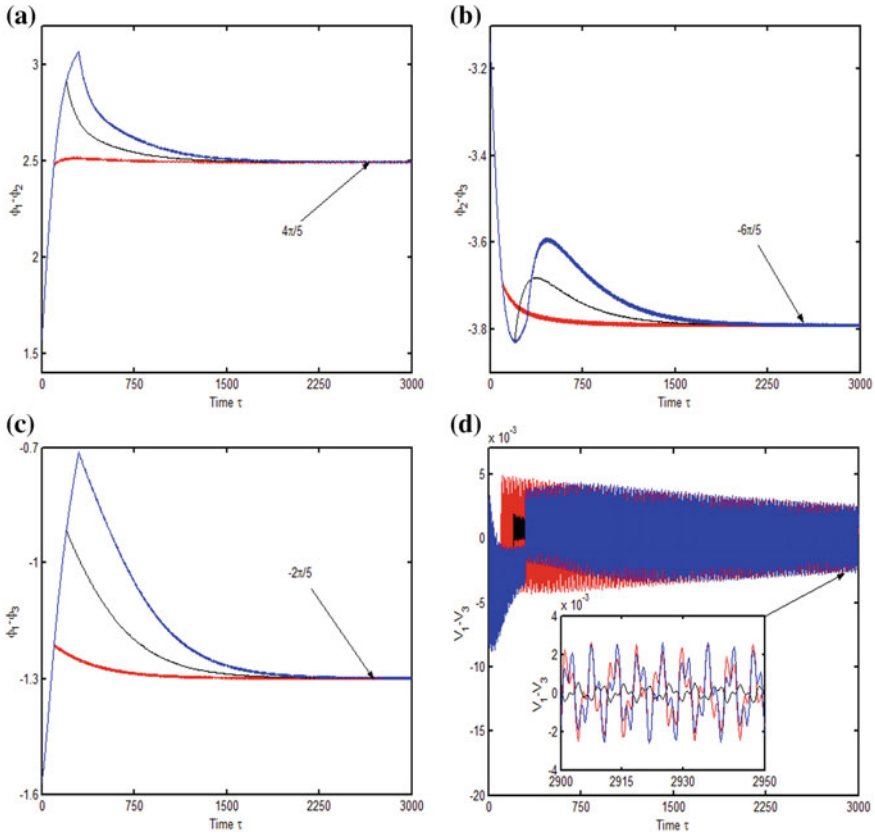


**Fig. 19** Representation of phase difference (a, b, c) between the three motors and velocity difference between the DC1 and DC3 (d) for a main frequency of the structure of  $\omega_{11} = 0.873$ . The first and the second DC motors start at the same moment  $\tau_1 = \tau_2 = 0$  while the third starts with a delay  $\tau_3 = 100$  (red);  $\tau_3 = 200$  (black);  $\tau_3 = 300$  (blue)

the third DC starts when the two others are already synchronized. Thus, we could conclude that the natural frequency of the plate (by its physical and mechanical characteristics) contributes efficiently to the rapid self-synchronization between the DC motors. Moreover, we can denote that energy transfer is quickly realized between the sources for a high of the value natural frequency of the plate.

### 5 Conclusions

In this chapter, the dynamics and vibration control of mechanical structures submitted to the vibrations of rotating machines with limited power supply is treated. Such systems are usually called non ideal systems because they are systems for which the

external source is influenced by the response of main system. This kind of system is regularly encountered in industry, civil and mechanical engineering.

The first section presents a large number of applications of rectangular plate, following by history and some information about rotating machines especially the DC motor. The vibration control problem is approached by the presentation of some control techniques. Some examples/applications and details on the dynamics on non-ideal systems are presented in the following section.

The mathematical formalism of the vibration control of the mechanical structure is presented in two steps. The first one concerns the used of electric transducer and a tuned mass damper as controller device and the second the synchronization phenomenon with and without delay appearing between the external excitation. A brief review of each techniques of control is well presented.

The recent results on the subject are divided in two parts, they concern the electromechanical control of the rectangular plate where we paid an attention on the stability of the control system and the self synchronization of the DC sources mounted on the rectangular plate.

In the first case studied, after modeling of the proposed device, the implementation of the control strategy leads to obtain the condition for which the control is effective, the effect of some control parameters on the reduction of the amplitude are displayed and the stability condition of all the system is established in order to enhance the efficiency of the control strategy used.

In the second set of results, the dynamics of two and three DC sources with limited power supply mounted on a rectangular plate is studied; the sources are capable to rotate in the same or in the opposite direction. The main phenomenon observes is the self-synchronization appearing between the DC sources with time. It is shown that the structure frequency is a relevant factor allowing synchronization between the sources with a phase difference of zero,  $\pi$ ,  $2\pi$ ,  $2\pi/5$ ,  $4\pi/5$ ,  $8\pi/5$ . The effects of the control parameter (voltage apply to the DC sources), physical and mechanical characteristics of the plate are displayed and the impact on the control strategy of the direction of rotation of the sources is also shown. It is conclude that the rectangular plate will less vibrate when the two sources are antiphase synchronizing, or when one of the sources are rotate in the opposite direction than the two others. The phase synchronization will be profitable only in the case of resonance.

This work leads to some prospective works which could be to get vibration control device which do not need more energy for functioning and to evaluate eventually damage on the structure when it is connected to the controlled device during his functioning. In addition, it will be preferable to adapt the DC motors before or during his functioning to the mechanical structure in order to get early energy balance between the both and to avoid early high amplitude of vibration of the system. We can also study the stability of the system, while the DC motors are synchronized on the mechanical structure and look for experimental verification of the synchronization of DC motors fixed on a plate usually encountered in building site.

**Acknowledgements** The first author would like to acknowledge AGNES (African-German Network of Excellence in Science) for the award/support accorded during this work. Part of this work was done during a research visit of Prof. Nana Nbandjo at the University of Kassel in Germany. He is grateful to the ERASMUS+ KA 107 for financial support.

## References

1. Balthazar, J.M., Mook, D.T., Weber, H.I., Brasil, R.M., Fenili, A., Belato, D., Felix, J.L.: An overview on non-ideal vibrations. *Meccanica* **38**, 613–621 (2003)
2. Dimentberg, M., Mc, G.L., Norton, R.L., Chapdelaine, J., Harrison, R.: Dynamics of an unbalanced shaft interacting with a limited power supply. *Nonl. Dyn.* **13**, 171–187 (1997)
3. Felix, J.L.P., Balthazar, J.M., BRASIL, R.M.L.R.: On tuned liquid column dampers mounted on a structural frame under a non-ideal excitation. *J. Sound Vib.* **282**(3–5), 1285–1292 (2005)
4. Kononenko, V.O.: *Vibrating Systems with a Limited Power Supply*. Illife Books, London (1969)
5. Nayfeh, A.H., Mook, D.T.: *Nonlinear Oscillation*. Wiley, New York (1979)
6. De Mattos, M.C., Balthazar, J.M., Wieczork, S., Mook, D.T.: An experimental study of vibrations of non-ideal systems. In: *Proceedings of DETC 97, ASME Design Engineering Technical Conference, Sacramento, CA, CD-ROM* (1997)
7. Nana Nbandjo, BR.: Dynamics and active control with delay of the dynamics of unbounded monostable mechanical structures with  $\phi^6$  potential. Ph.D. Thesis, University of Yaoundé I (2004)
8. Tusset, A.M., Balthazar, J.M., Felix, J.L.P.: On elimination of chaotic behavior in a non-ideal portal frame structural system, using both passive and active controls. *J. Vib. Cont.* **19**(6), 803–813 (2012)
9. Nanha Djanan, A.A., Nana Nbandjo, B.R., Wofo, P.: Control of vibration on a hinged-hinged beam under a non-ideal excitation using RLC circuit with variable capacitance. *Nonl. Dyn.* **63**, 477–489 (2011)
10. Balthazar, J.M., Felix, J.L.P., Brasil, R.M.L.R.F.: Short comments on self-synchronization of two non-ideal sources supported by a flexible portal-frame structure. *J. Vib. Cont.* **10**, 1739–1748 (2004)
11. Bleckhman, II.: *Self-Synchronization in Science and Technology*. ASME Press, New York (1988).
12. Dimentberg, M., Cobb, E., Mensching, J.: Self-synchronization of transient rotations in multiple shaft systems. *J. Vib. Cont.* **7**, 221–232 (2001)
13. Pikovsky, A.S., Rosenblum, M., Kurths, J.: *Synchronization-A Unified Approach to Nonlinear Science*. Cambridge University Press, Cambridge (2001)
14. Czolczynski, K., Perlikowski, P., Stefanski, A., Kapitaniak, T.: Synchronization of pendula rotating in different directions. *Commun. Nonl. Sc. Num. Sim.* **17**(9), 3658–3672 (2012)
15. Czolczynski, K., Perlikowski, P., Stefanski, A., Kapitaniak, T.: Synchronization of slowly rotating pendulums. *Int. J. Bif. Chaos* **22**(5), 1250128 (2012)
16. Nanha Djanan, A.A., Nana Nbandjo, B.R., Wofo, P.: Self-synchronization of two motors on a rectangular plate and reduction of vibration. *J. Vib. Cont.* **21**(11), 2114–2123 (2015)
17. Timoshenko, S.P.: *Théorie de la stabilitéélastique*. Dunod, Paris (1956)
18. Nanha Djanan, A.A.: Dynamic and control of a hinged-hinged beam supporting a DC motor. Master's Degree Thesis, University of Yaoundé I (2010)
19. Warminski, J., Balthazar, J.M., Brasil, R.M.L.R.F.: Vibrations of a non-ideal parametrically and self-excited model. *J. Sound Vib.* **245**, 363–374 (2001)
20. Nanha Djanan, A.A., Nana Nbandjo, B.R., Wofo, P.: Electromechanical control of vibration on a plate submitted to a non-ideal excitation. *Mech. Res. Comm.* **54**, 72–82 (2013)
21. Hayashi, C.: *Nonlinear Oscillations in Physical Systems*. Mc-Graw-Hill, New York (1964)

22. Balthazar, J.M., Felix, J.L.P., Brasil, R.M.L.R.F.: Some comments on the numerical simulation of self-synchronization of four non-ideal exciters. *App. Math. Comput.* **164**, 615–625 (2005)
23. Nanha Djanan, A.A., Nana Nbandjo, B.R., Wofo, P.: Effect of self synchronization of DC motors on the amplitude of vibration of a rectangular plate. *Eur. Phys. J. Special Topics* **223**, 813–825 (2014)
24. Nanha Djanan, A.A., Marburg, S., Nana Nbandjo, B.R.: Appearance of fast or late self synchronization between non-ideal sources mounted on a rectangular plate due to time delay. *Math. Comput. Appl.* **27**, 20 (2022). <https://doi.org/10.3390/mca27020020>
25. Naim, A.O.: Nonlinear control of plate vibrations. Ph.D. Thesis, Virginia Polytechnic Institute and State University (2001)
26. Cveticanin, L.: Dynamics of the non-ideal mechanical systems: a review. *J. Serb. Soc. Comput. Mech.* **4**(2), 75–86 (2010)
27. Felix, J.L.P., Balthazar, J.M., Brasil, R.M.L.R.F.: On saturation control of a non-ideal vibrating portal frame foundation type shear- building. *J. Vib. Cont.* **11**, 121–136 (2005)
28. Feulefack Songong, E., Nanha Djanan, A.A., Nana Nbandjo, B.R.: Vibration absorption of a rectangular plate supporting a DC motor with a TLCD. *Nonlinear Dyn.* **105**, 1357–1372 (2021)
29. Kapitaniak, M., Czolczynski, K., Perlikowski, P., Stefanski, A., Kapitaniak, T.: Synchronization of clocks. *Phy. Rep.* **517**, 1–69 (2012)
30. Kitio Kwuimy, C.A., Nana Nbandjo, B.R., Wofo, P.: Optimization of electromechanical control of beam dynamics: analytical method and finite differences simulation. *J. Sound Vib.* **298**, 180–193 (2006)
31. Naucler, P.: Modeling and control of vibration in mechanical structures. Ph.D. Thesis, Uppsala University (2005)
32. Oueini, S.S.: Techniques for Controlling Structural Vibrations. Virginia Polytechnic Institute and State University (1999)

# Dynamic Analysis and PID Control of a Double Pendulum Arm Excited by a Nonideal Source



A. M. Tuset , P. L. Paula Filho , V. Piccirillo , G. G. Lenzi ,  
Jose Manoel Balthazar , C. Oliveira , and M. Varanis 

**Abstract** In this paper the dynamics of a double pendulum arm coupled through a magnetic field to a nonlinear RLC based shaker circuit is presented and will be studied numerically. This kind of electromechanical system is often found in robotic systems and has important applications in Engineering Sciences. The double pendulum considered is coupled through a magnetic field to an RLC circuit based on nonlinear shaker. The nonlinear response analysis of the system is done by various techniques, including bifurcation diagrams, phase portraits, power spectral densities, and Lyapunov exponents. Numerical simulations show the existence of chaotic and hyperchaotic behavior for some regions of the parameter space. In order to suppress the chaotic motion, a PID control is proposed and analyzed. Numerical simulations show the effectiveness of the proposed control in suppressing the chaotic motion.

**Keywords** Non-ideal systems · Electromechanical system · PID control · Chaos suppression · Hyperchaotic behavior · Chaotic behavior

## 1 Introduction

The growing number of researches considering the dynamical systems with pendulum elements has demonstrated the importance of the theme in applications in Engineering Sciences. In [1–11] the dynamics of the parametrically excited

---

A. M. Tuset (✉) · P. L. P. Filho · V. Piccirillo · G. G. Lenzi  
Federal University of Technology, Paraná, Brazil

V. Piccirillo  
e-mail: [piccirillo@utfpr.edu.br](mailto:piccirillo@utfpr.edu.br)

J. M. Balthazar  
Sao Paulo State University, São Paulo, Brazil

C. Oliveira · M. Varanis  
Federal University of Grande Dourados, Dourados, Brazil  
e-mail: [clivaldooliveira@ufgd.edu.br](mailto:clivaldooliveira@ufgd.edu.br)

M. Varanis  
e-mail: [marcusvaranis@ufgd.edu.br](mailto:marcusvaranis@ufgd.edu.br)



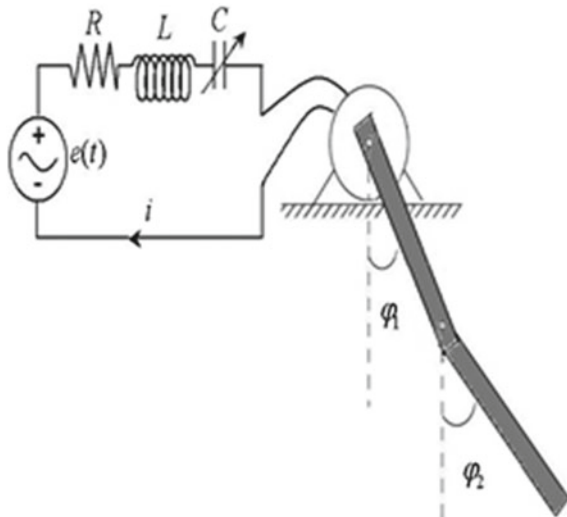
pendulum is studied. In [12–16] the nonideal pendulum autoparametric system was studied, and in [17, 18] the double pendulum autoparametric system with harmonic excitation was studied. The nonlinear dynamics of a triple pendulum is investigated experimentally and numerically in [19–23].

Dynamic systems with pendulum elements can exhibit different types of behavior, ranging from periodic oscillations to chaotic behavior [24–26]. In many cases, periodic behavior may be desirable, avoiding chaotic movement [27]. The suppression of chaotic behavior has received a lot of attention in recent years and various control methods have been proposed to control the chaotic system [28]. In [29] analyzed delayed feedback control. In [28] the Lyapunov function method is applied to design the control. In [30] the nonlinear SDRE control is used to suppress the chaotic behavior of a simple pendulum system with parametric excitation. In [18], SDRE and Saturation control are considered to suppress the chaotic behavior of a double pendulum system. In [31], an MR damper was used as a passive control for the suppression of chaotic behavior in a simple pendulum system with autoparametric excitation. In this paper, a PID control is proposed to suppress the chaotic behavior of the double pendulum arm coupled to a nonlinear shaker.

## 2 Mathematical Model

Figure 1 presents the double pendulum of lengths  $l_1$  and  $l_2$  and masses  $m_1$  and  $m_2$  investigated in the paper.

**Fig. 1** Schematic diagram of the electrical excited pendulum system



In Fig. 1 it is observed that the electrical part of the system consists of a capacitor  $C$ , an inductor  $L$ , a resistor  $R$  and a source of voltage  $e(t)$ , where the pendulum deflection angles  $\varphi_1$  and  $\varphi_2$  are measured from the vertical axis.

The mathematical model for the system presented by Fig. 1 can be expressed by equations [18]:

$$\begin{aligned}
 L\ddot{q} + R\dot{q} + \frac{1}{C_0}q + a_3q^3 + \frac{nB\sigma^2l^2}{2}\dot{\phi}_1 &= v_0 \cos(\Omega t) \\
 (m_1 + m_2)l_1^2\ddot{\phi}_1 + m_2l_1l_2\ddot{\phi}_2 \cos(\phi_1 - \phi_2) \\
 + m_2l_2\dot{\phi}_2^2 \sin(\phi_1 - \phi_2) + (m_1 + m_2)gl_1 \sin \phi_1 &= \\
 - c_1\dot{\phi}_1 - c_2(\dot{\phi}_1 - \dot{\phi}_2) + \frac{nB\sigma^2l^2}{2}\dot{q} \\
 m_2l_2^2\ddot{\phi}_2 + m_2l_1l_2\ddot{\phi}_1 \cos(\phi_1 - \phi_2) \\
 - m_2l_1l_2\dot{\phi}_1^2 \sin(\phi_1 - \phi_2) + m_2gl_2 \sin \phi_2 &= c_2(\dot{\phi}_1 - \dot{\phi}_2) \quad (1)
 \end{aligned}$$

where:  $v_0$  and  $\Omega$  are the amplitude and frequency, respectively,  $C_0$  is the linear value of  $C$ ,  $a_3$  is the nonlinear coefficient depending on the type of the capacitor used,  $c_1$  and  $c_2$  is damping coefficients,  $B$  is magnetic field,  $\sigma$  is the permeability coefficient,  $l$  is length of the conductor and  $n$  is the number of turns per unit length.

The dimensionless mathematical model for the system (1) can be expressed by the following system of equations [18]:

$$\begin{aligned}
 \ddot{x} + \mu\dot{x} + x + kx^3 + b_1\dot{\phi}_1 &= E \cos(\omega\tau) \\
 \ddot{\phi}_1 + \frac{1}{(b+1)a}\ddot{\phi}_2 \cos(\phi_1 - \phi_2) \\
 + \frac{1}{(b+1)a}\dot{\phi}_2^2 \sin(\phi_1 - \phi_2) + \omega_1^2 \sin \phi_1 &= -\mu_1\dot{\phi}_1 \\
 - \frac{\mu_2}{(b+1)a^2}(\dot{\phi}_1 - \dot{\phi}_2) + b_2\dot{x} \\
 \ddot{\phi}_2 + a\ddot{\phi}_1 \cos(\phi_1 - \phi_2) - a\dot{\phi}_1^2 \sin(\phi_1 - \phi_2) + (\omega_2^2 a) \sin \phi_2 &= \mu_2(\dot{\phi}_1 - \dot{\phi}_2) \quad (2)
 \end{aligned}$$

where:  $\tau = \omega_e t$ ,  $x = \frac{q}{Q_0}$ ,  $a = \frac{l_1}{l_2}$ ,  $b = \frac{m_1}{m_2}$ ,  $\mu = \frac{R}{L\omega_e}$ ,  $k = \frac{a_3 Q_0^2}{L\omega_e^2}$ ,  $\omega_e^2 = \frac{1}{LC_0}$ ,  $\omega_2^2 = \frac{g}{l_2\omega_e^2} = \omega^2 a$ ,  $\omega = \frac{\Omega}{\omega_e}$ ,  $E = \frac{v_0}{LQ_0\omega_e}$ ,  $\mu_1 = \frac{c_1}{(m_1+m_2)l_1^2\omega_e}$ ,  $\mu_2 = \frac{c_2}{m_2l_2^2\omega_e}$ ,  $b_1 = \frac{nB\sigma^2l^2}{2LQ_0\omega_e}$  and  $b_2 = \frac{nB\sigma^2l^2Q_0}{2(m_1+m_2)l_1^2\omega_e}$ .

Equation (2) can be rewritten in state space form as follows:

$$\begin{aligned}
 \dot{x}_1 &= x_2 \\
 \dot{x}_2 &= -\mu x_2 - x_1 - kx_1^3 - b_1x_4 + E \cos(\omega\tau) \\
 \dot{x}_3 &= x_4
 \end{aligned}$$

$$\begin{aligned} \dot{x}_4 &= -\frac{1}{(b+1)a} \dot{x}_6 \cos(x_3 - x_5) \\ &\quad - \frac{1}{(b+1)a} x_6^2 \sin(x_3 - x_5) - \omega_1^2 \sin x_3 - \mu_1 x_4 \\ &\quad - \frac{\mu_2}{(b+1)a^2} (x_4 - x_6) + b_2 x_2 \\ \dot{x}_5 &= x_6 \\ \dot{x}_6 &= -a \dot{x}_4 \cos(x_3 - x_5) + a x_4^2 \sin(x_3 - x_5) - (\omega_1^2 a) \sin x_5 + \mu_2 (x_4 - x_6) \end{aligned} \quad (3)$$

### 3 Numerical Simulation

For numerical simulation is considered the parameters:  $E = 1, b = 0.5, \mu = 0.02, \mu_1 = 0.01, \mu_2 = 0.01, k = 0.95, \omega_1 = 1, \omega = 1, b_1 = 0.2$  and  $b_2 = 0.4$ , along with the initial conditions:  $x_i(0) = 0$ , where  $i = 1:6$  [18].

In Fig. 2 one can observe the Bifurcation diagram for the system (3) considering  $0.5 \leq a \leq 1$ .

Analyzing the results obtained in Fig. 2, it can be perceived that the system has a chaotic behavior for a range of values of  $a = \frac{l_1}{l_2}$ , demonstrating that the length of the links interferes directly in the dynamics of the system.

In Fig. 3 the first two most significant Lyapunov exponent of the system (3) considering  $0.5 \leq a \leq 1$  are presented.

Analyzing the results presented in Fig. 3, it can be seen that the system shows chaotic behavior for  $a > 0.55$ . As the system has two positive Lyapunov exponents for  $a > 0.57$ , it can be said that the system has hyperchaotic behavior [32].

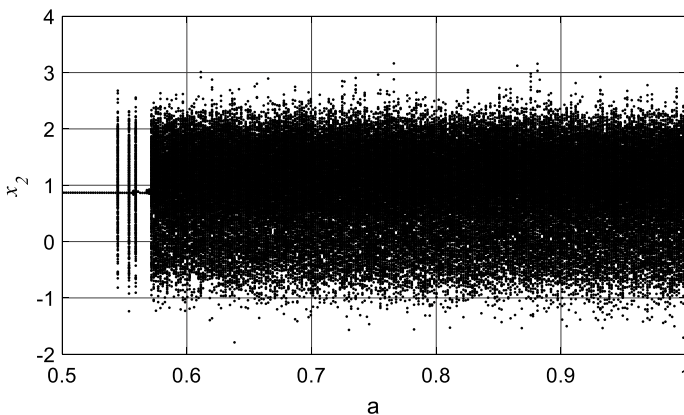


Fig. 2 Bifurcation diagram

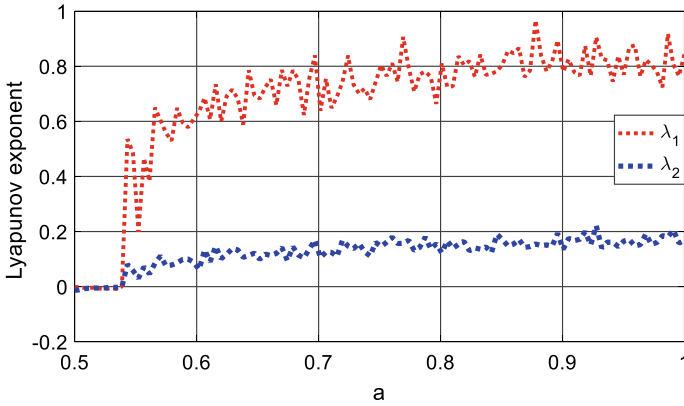


Fig. 3 Most significant Lyapunov exponent

In Fig. 4, 5 and 6 one can observe the time history of the states, for the electrical system, first link and second link, respectively, considering  $a = 0.91$ .

As can be seen from the results presented in Fig. 4, 5 and 6, the system shows a chaotic behavior with variations in the motor voltage and movements of the links.

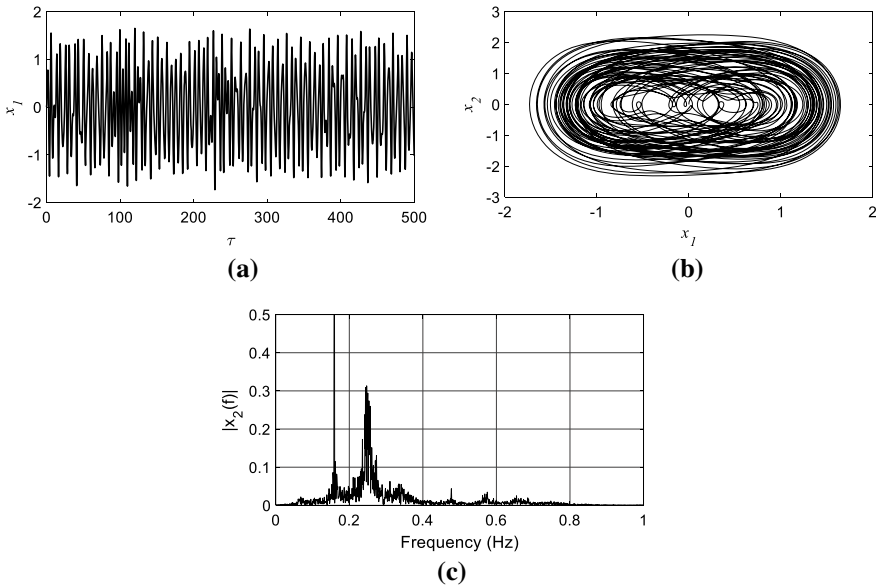
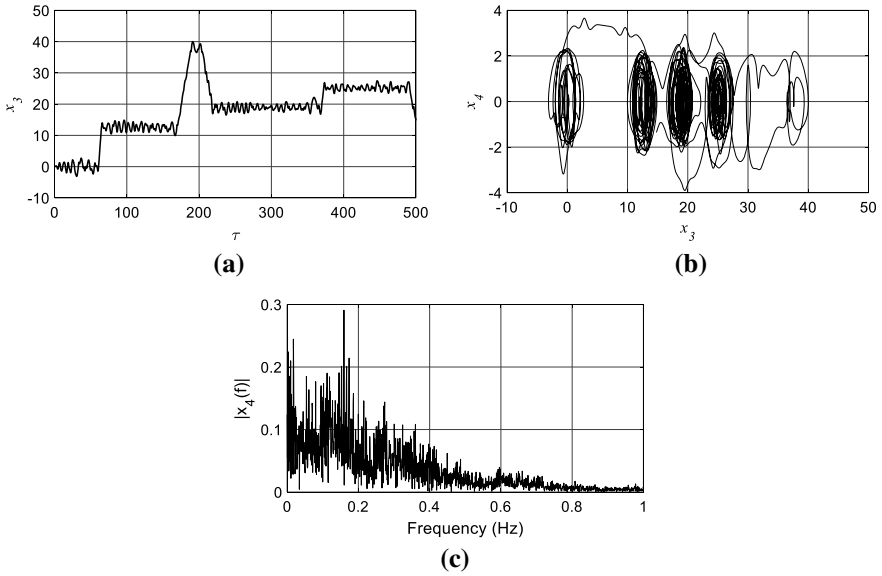
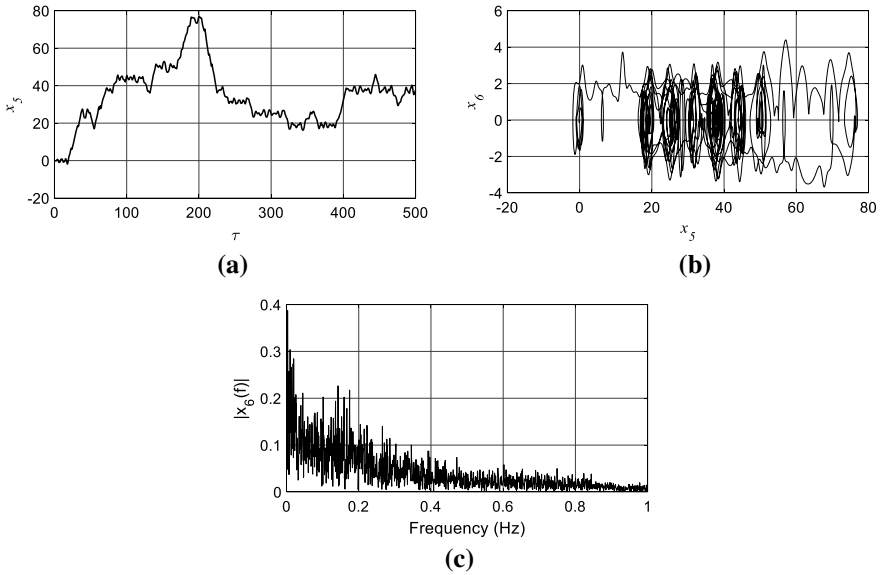


Fig. 4 Electrical system. a Time history of the states  $x_1$ . b Phase diagram to  $x_1$  versus  $x_2$ . c Power Spectral Density for  $x_2$



**Fig. 5** First link. **a** Time history of the states  $x_3$ . **b** Phase diagram to  $x_3$  versus  $x_4$ . **c** Power Spectral Density for  $x_4$



**Fig. 6** Second link. **a** Time history of the states  $x_5$ . **b** Phase diagram to  $x_5$  versus  $x_6$ . **c** Power Spectral Density for  $x_6$

## 4 Proposed PID Control

The designed control systems aim to eliminate the chaotic behavior of the system (3) for  $a = 0.91$  by introducing a control signal ( $u$ ) into system (3), (4) shows the proposed method.

$$\begin{aligned}
 \dot{x}_1 &= x_2 \\
 \dot{x}_2 &= -\mu x_2 - x_1 - kx_1^3 - b_1x_4 + E \cos(\omega\tau) + u_1 \\
 \dot{x}_3 &= x_4 \\
 \dot{x}_4 &= -\frac{1}{(b+1)a} \dot{x}_6 \cos(x_3 - x_5) \\
 &\quad - \frac{1}{(b+1)a} x_6^2 \sin(x_3 - x_5) - \omega_1^2 \sin x_3 - \mu_1 x_4 \\
 &\quad - \frac{\mu_2}{(b+1)a^2} (x_4 - x_6) + b_2 x_2 + u_2 \\
 \dot{x}_5 &= x_6 \\
 \dot{x}_6 &= -a\dot{x}_4 \cos(x_3 - x_5) + ax_4^2 \sin(x_3 - x_5) - (\omega_1^2 a) \sin x_5 + \mu_2(x_4 - x_6) + u_3
 \end{aligned} \tag{4}$$

The PID controller operates according to the following equations [33]:

$$\begin{aligned}
 u_1 &= k_{p1}e_1 + k_{d1}\dot{e}_1 + k_{i1} \int e_1 d\tau \\
 u_2 &= k_{p2}e_2 + k_{d1}\dot{e}_2 + k_{i1} \int e_2 d\tau \\
 u_3 &= k_{p3}e_3 + k_{d1}\dot{e}_3 + k_{i1} \int e_3 d\tau
 \end{aligned} \tag{5}$$

where  $k_{p\_}$  is the proportional gain,  $k_{d\_}$  is the derivative gain and  $k_{i\_}$  is the corresponding integral gain of the control loop, respectively. The errors,  $e_1 = \tilde{x}_1 - x_1$ ,  $e_2 = \tilde{x}_3 - x_3$  and  $e_3 = \tilde{x}_5 - x_5$ , where  $\tilde{x}_-$  represent the desired states.

For numerical simulations, the gains are adjusted using Ziegler-Nichols method, and is considered:  $\tilde{x}_1 = 1.5 \sin(\tau)$ ,  $\tilde{x}_3 = \sin(\tau)$  and  $\tilde{x}_5 = \sin(\tau + \frac{\pi}{2})$ .

### 4.1 Control in Electrical System, and in First and Second Link

Considering the case in which it is possible to control the motor voltage and the torque of the two links, the proposed control (Eq. (4)) can be defined as follows:

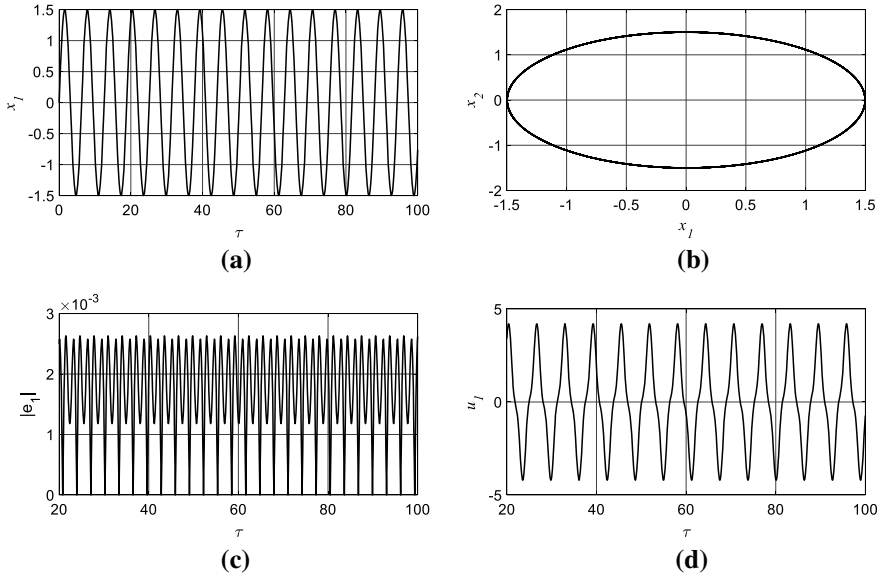


**Fig. 7** Electrical system. **a** Time history of the states  $x_1$ . **b** Phase diagram to  $x_1$  versus  $x_2$ . **c** Absolute error  $e_1$ . **d** Signal of the control  $u_1$

$$\begin{aligned}
 u_1 &= 605.3207e_1 + 62.6759\dot{e}_1 + 1343.5235 \int e_1 d\tau \\
 u_2 &= 4071.7062e_2 + 102.0894\dot{e}_2 + 28487.1399 \int e_2 d\tau \\
 u_3 &= 293.75204e_3 + 33.37143\dot{e}_3 + 554.6683 \int e_3 d\tau
 \end{aligned} \tag{6}$$

In Fig. 7, 8 and 9 one can observe the behavior of the system (4) with the proposed control (Eq. (6)).

### 4.2 Control Only in Electrical System and in First Link

Considering now the case that it is possible to directly control only the electric motor and the first link, using  $u_1$  and  $u_2$ . In this case, we consider that  $u_3 = 0$ . In Fig. 10, 11 and 12 one can observe the behavior of the system (4), considering only the control  $u_1$  and  $u_2$ .

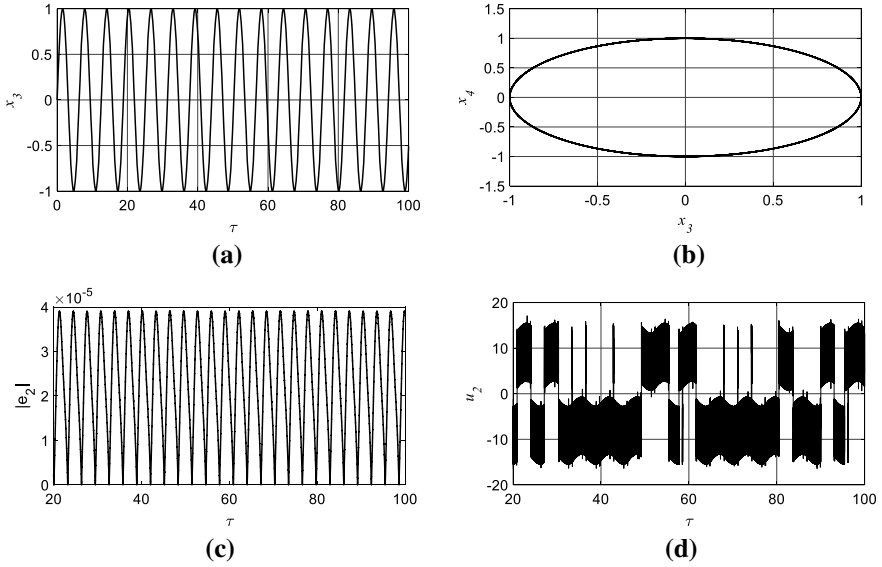


**Fig. 8** First link. **a** Time history of the states  $x_3$ . **b** Phase diagram to  $x_3$  versus  $x_4$ . **c** Absolute error  $e_2$ . **d** Signal of the control  $u_2$

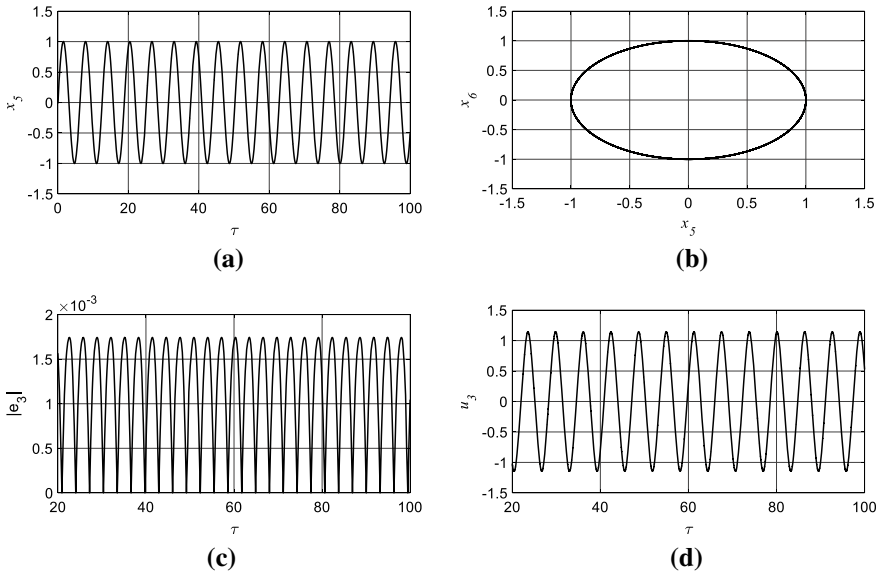


**Fig. 9** Second link. **a** Time history of the states  $x_5$ . **b** Phase diagram to  $x_5$  versus  $x_6$ . **c** Absolute error  $e_3$ . **d** Signal of the control  $u_3$



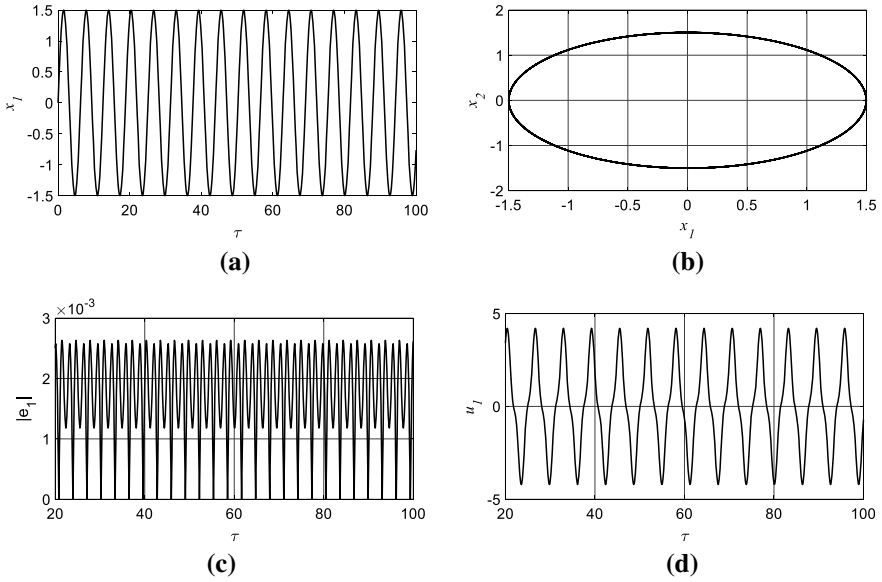


**Fig. 10** Electrical system. **a** Time history of the states  $x_1$ . **b** Phase diagram to  $x_1$  versus  $x_2$ . **c** Absolute error  $e_1$ . **d** Signal of the control  $u_1$

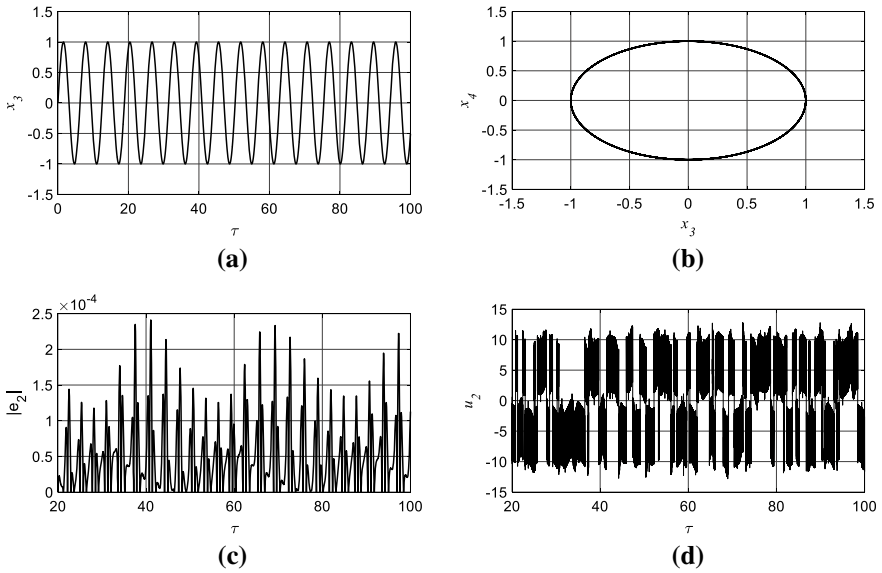


**Fig. 11** First link. **a** Time history of the states  $x_3$ . **b** Phase diagram to  $x_3$  versus  $x_4$ . **c** Absolute error  $e_2$ . **d** Signal of the control  $u_2$

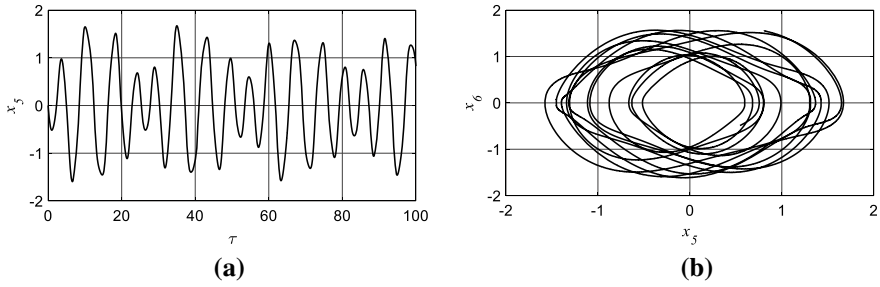


**Fig. 12** Second link. **a** Time history of the states  $x_5$ . **b** Phase diagram to  $x_6$  versus  $x_5$

### 4.3 Control Only in Electrical System

Considering the case that it is only possible to include control in the electric motor. In this case, only  $u_1$  is used, and it is considered that:  $u_2 = u_3 = 0$ . In Fig. 13, 14 and 15 one can observe the behavior of the system (4), considering only the control  $u_1$ .

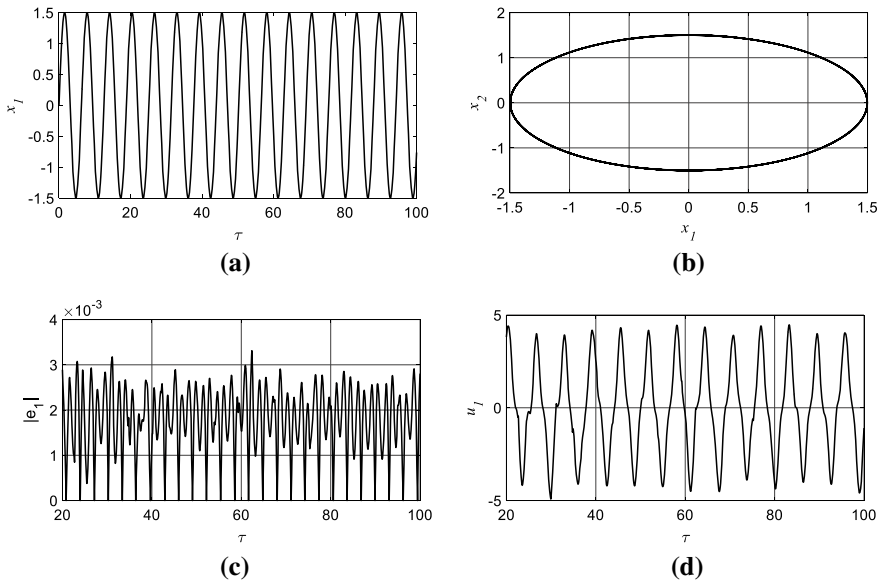


**Fig. 13** Electrical system. **a** Time history of the states  $x_1$ . **b** Phase diagram to  $x_1$  versus  $x_2$ . **c** Absolute error  $e_1$ . **d** Signal of the control  $u_1$

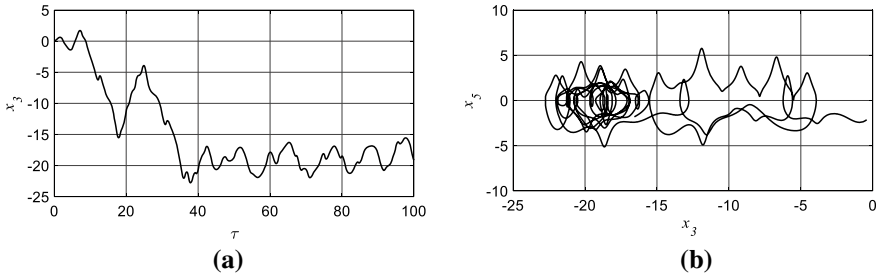


**Fig. 14** First link. **a** Time history of the states  $x_3$ . **b** Phase diagram to  $x_3$  versus  $x_4$

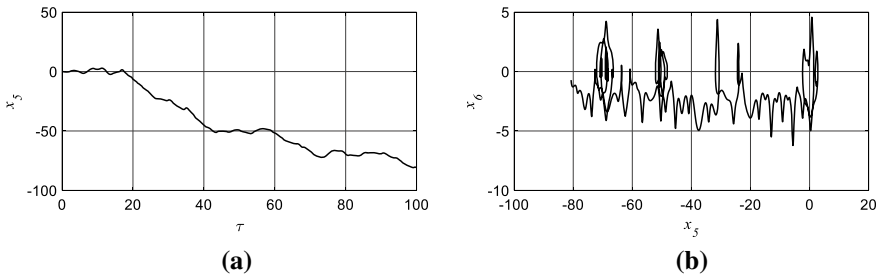


**Fig. 15** First link. **a** Time history of the states  $x_5$ . **b** Phase diagram to  $x_5$  versus  $x_6$

### 5 Final Considerations

In Fig. 16, the absolute errors for  $e_1 = \tilde{x}_1 - x_1$ ,  $e_2 = \tilde{x}_3 - x_3$  and  $e_3 = \tilde{x}_5 - x_5$  are presented, considering the different control strategies considered.

As can be seen from the results presented in Fig. 16, the presented system is of the non-ideal type, as the irregular movements of the elements lead to an increase in the error of the desired voltage ( $\tilde{x}_1 = 1.5 \sin(\tau)$ ). As can be seen in Fig. 16a, the error increases when the system is connected to the motor and does not have the control signal ( $u_2$ ), and remains practically the same when using control on both links ( $x_3$  and  $x_5$ ), or only on the first link ( $x_3$ ).

Analyzing Fig. 13b, it can be seen that the movement of the second link ( $x_5$ ) interferes with the movement of the first link ( $x_3$ ). If the second link is in free movement, the error of the first link increases in relation to the desired one ( $\tilde{x}_3 = \sin(\tau)$ ).

Additionally, it was possible to observe that the relationship in the length of the links is determinant for the dynamic interactions of the presented system. It is possible to observe periodic, chaotic and hyperchaotic behavior for certain values of ( $a = l_1/l_2$ ).

The results presented also demonstrate that for applications where it is desirable to eliminate the chaotic behavior of the system, PID control is a good option.

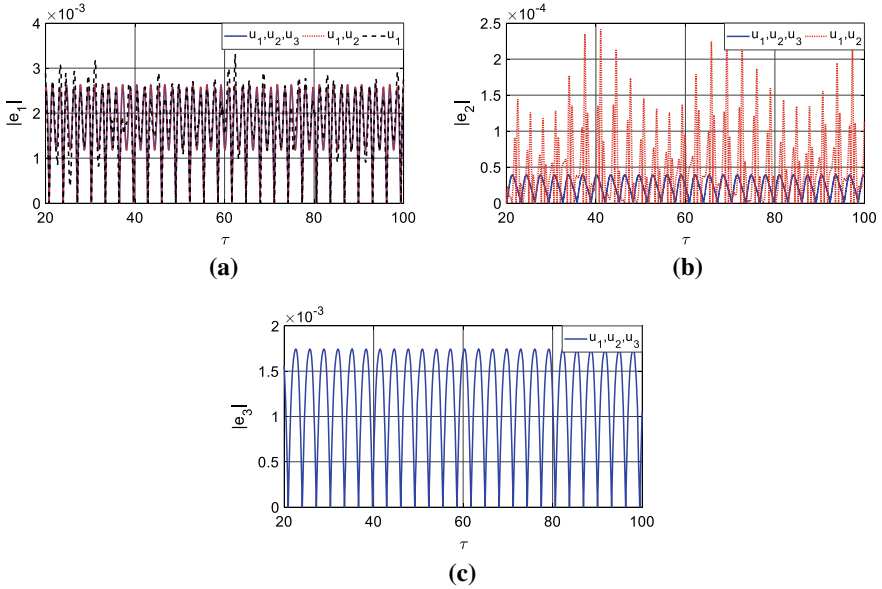


**Fig. 16** a Absolute error  $e_1$ . b Absolute error  $e_2$ . c Absolute error  $e_3$







## References

1. Clifford, M.J., Bishop, S.R.: Rotating periodic orbits of the parametrically excited pendulum. *Phys. Lett. A* **201**(2–3), 191–196 (1995)
2. Clifford, M.J., Bishop, S.R.: Locating oscillatory orbits of the parametrically-excited pendulum. *J. Australian Math. Soc. Ser. B – Appl. Math.* **37**, 309–319 (1996)
3. Lu, C.: Chaotic motions of a parametrically excited pendulum. *Commun. Nonlinear Sci. Numer. Simul.* **11**(7), 861–884 (2006)
4. Lenci, S., Pavlovskaja, E., Rega, G., Wiercigroch, M.: Rotating solutions and stability of parametric pendulum by perturbation method. *J. Sound Vib.* **310**, 243–259 (2008)
5. Lenci, S., Rega, G.: Experimental versus theoretical robustness of rotating solutions in a parametrically excited pendulum: a dynamical integrity perspective. *Physica D* **240**, 814–824 (2011)
6. Nagamine, T., Sato, Y., Koseki, Y.: Stable rotation of a parametrically excited double pendulum. *J. Vib. Control* **13**(2), 111–124 (2007)
7. Masoud, Z., Alhazza, K., Abu-Nada, E., Majeed, M.: A hybrid command-shaper for double-pendulum overhead cranes. *J. Vib. Control* **20**(1), 24–37 (2012)
8. Bridges, T.J., Georgiou, K.V.: A transverse spinning double pendulum. *Chaos, Solitons Fractals* **12**, 131–144 (2001). [https://doi.org/10.1016/S0960-0779\(99\)00180-0](https://doi.org/10.1016/S0960-0779(99)00180-0)
9. Rocha, R.T., Balthazar, J.M., Tusset, A.M., Piccirillo, V.: Using passive control by a pendulum in a portal frame platform with piezoelectric energy harvesting. *J. Vib. Control* **1**, 107754631770938–1 (2017)
10. Janzen, F.C., Tusset, A.M., Balthazar, J.M., Rocha, R.T., De Lima, J.J., Nabarrete, A.: Offshore energy harvesting of a marine floating pendulum platform model. *Latin Am. J. Solids Struct.* **16**, 1–13 (2019)
11. Iliuk, I., Balthazar, J.M., Tusset, A.M., Piqueira, J.R.C., Pontes, B.R., Felix, J.L.P., Bueno, A.M.: A non-ideal portal frame energy harvester controlled using a pendulum. *Eur. Phys. J. Special Topics* **222**, 1575–1586 (2013)

12. Sado, D., Kot, M.: Nonlinear oscillations of a coupled autoparametrical system with ideal and nonideal sources of power. In: *Mathematical Problem in Engineering*, pp. 1–20 (2006)
13. Sado, D., Kot, M.: Chaotic vibration of an autoparametrical system with a non ideal source of power. *J. Theor. Appl. Mech.* **45**(1), 119–131 (2007)
14. Avanço, R.H., Navarro, H.A., Brasil, R.M.L.R., Balthazar, J.M., Bueno, A.M., Tusset, A.M.: Statements on nonlinear dynamics behavior of a pendulum, excited by a crank-shaft-slider mechanism. *Meccanica* **51**, 1301–1320 (2015)
15. Avanço, R.H., Tusset, A.M., Balthazar, J.M., Nabarrete, A., Navarro, H.A.: On nonlinear dynamics behavior of an electro-mechanical pendulum excited by a nonideal motor and a chaos control taking into account parametric errors. *J. Braz. Soc. Mech. Sci. Eng.* **40**, 1–17 (2018)
16. Avanço, R.H., Tusset, A.M., Suetake, M., Navarro, H.A., Balthazar, J.M., Nabarrete, A.: Energy harvesting through pendulum motion and DC generators. *Latin Am. J. Solids Struct.* **16**, 1–12 (2019)
17. Sado, D., Gajos, K.: Analysis of vibration of three degree of freedom dynamical system with double pendulum. *J. Theor. Appl. Mech.* **46**(1), 141–156 (2008)
18. Tusset, A.M., Piccirillo, V., Bueno, A.M., Balthazar, J.M., Sado, D., Felix, J.L.P., Brasil, R.M.L.R.: Chaos control and sensitivity analysis of a double pendulum arm excited by an RLC circuit based nonlinear shaker. *J. Vib. Control* **22**, 3621–3637 (2016)
19. Awrejcewicz, J., Supel, B., Lamarque, C.-H., Kudra, G., Wasilewski, G., Olejnik, P.: Numerical and experimental study of regular and chaotic motion of triple physical pendulum. *Int. J. Bifurc. Chaos* **18**(10), 2883–2915 (2008)
20. Awrejcewicz, J., Kudra, G.: The piston-connecting rod-crankshaft system as triple physical pendulum with impacts. *Int. J. Bifurc. Chaos* **15**(07), 2207–2226 (2005)
21. Awrejcewicz, J., Kudra, G., Lamarque, C.H.: Investigation of triple pendulum with impacts using fundamental solution matrices. *Int. J. Bifurc. Chaos* **14**(12), 4191–4213 (2004)
22. Awrejcewicz, J., Kudra, G., Wasilewski, G.: Experimental and numerical investigation of chaotic regions in the triple physical pendulum. *Nonlinear Dyn* **50**, 755–766 (2007)
23. Awrejcewicz, J., Starosta, R., Sypniewska-Kamińska, G.: Asymptotic analysis of resonances in nonlinear vibrations of the 3-dof pendulum. *Differ Equ Dyn Syst* **21**, 123–140 (2013)
24. Kecik, K., Warminski, J.: Chaos in mechanical pendulum-like system near main parametric resonance. In: *Procedia IUTAM: IUTAM Symposium on 50 Years of Chaos: Applied and Theoretical*, vol. 5, pp. 249–258 (2012)
25. Stachowiak, T., Okada, T.: A numerical analysis of chaos in the double pendulum. *Chaos, Solitons Fractals* **29**, 417–422 (2006)
26. Xu, X., Wiercigroch, M., Cartmell, M.P.: Rotating orbits of a parametrically-excited pendulum. *Chaos, Solitons Fractals* **23**, 1537–1548 (2005)
27. Ge, Z.M., Yang, C.H., Chen, H.H., Lee, S.C.: Non-linear dynamics and chaos control of a physical pendulum with vibrating and rotating support. *J. Sound Vib.* **242**(2), 247–264 (2001)
28. Wang, R., Jing, Z.: Chaos control of chaotic pendulum system. *Chaos, Solitons Fractals* **21**, 201–207 (2004)
29. Yokoi, Y., Hikiyara, T.: Tolerance of start-up control of rotation in parametric pendulum by delayed feedback. *Phys. Lett. A* **375**, 1779–1783 (2011)
30. Tusset, A.M., Bueno, A.M., Dos Santos, J.P.M., Tsuchida, M., Balthazar, J.M.: A non-ideally excited pendulum controlled by SDRE technique. *J. Braz. Soc. Mech. Sci. Eng.* **38**, 2459–2472 (2016)
31. Tusset, A.M., Janzen, F.C., Piccirillo, V., Rocha, R.T., Balthazar, J.M., Litak, G.: On nonlinear dynamics of a parametrically excited pendulum using both active control and passive rotational (MR) damper. *J. Vib. Control* **1**, 107754631771488–12 (2017)
32. Wu, A., Cang, S., Zhang, R., Wang, Z.: Hyperchaos in a conservative system with nonhyperbolic fixed points. *Complexity* **2018**, 1–8 (2018)
33. Tusset, A.M., Piccirillo, V., Janzen, F.C., Lenz, W.B., Lima, J.J., Balthazar, J.M., Brasil, M.R.L.F.: Suppression of vibrations in a nonlinear half-car model using a magneto-rheological damper. *Math. Eng., Sci. Aerospace: Transdiscip. Int. J.* **5**, 427–443 (2014)

# Fractional Dynamics of Harvester with Nonideal Source Excitation



M. A. Ribeiro , W. B. Lenz , A. M. Tusset , Jose Manoel Balthazar ,  
C. Oliveira , and M. Varanis 

**Abstract** In this paper, the behavior of an electromechanical device for energy production is investigated. Such a device consists of a motor containing an unbalanced mass that causes vibrations in a mass, in this device was coupled a system containing piezoelectric material that produces an electric current. Thus, the average power produced in the piezoelectric material subject to the vibrations of the motor and the fractional dynamics analysis of the system considering the Caputo operator is analyzed in this device. For this fractional dynamic analysis, is used the parameter of the fractional derivative operator and the  $F$  parameter for system control, the FFT, bifurcation diagrams, 01-Test, and phase maps of the system were analyzed. Also determine the range of the Caputo fractional derivative operator parameter near 1 in which it modifies the dynamics of the system.

**Keywords** Fractional calculus · Nonlinear dynamics · Nonideal source

## 1 Introduction

With the technological advances in recent years, the great demand for energy consumption has allowed researchers to discover mechanisms that produce energy in a clean and renewable way. Thus, many works on these mechanisms have been explored. Examples of these works are those in [1–3] that explore high-degree-of-freedom mechanisms that convert mechanical energy from applied external forces into electrical energy.

---

M. A. Ribeiro (✉) · W. B. Lenz · A. M. Tusset · J. M. Balthazar  
Universidade Tecnológica Federal Do Paraná-Campus Ponta Grossa, Ponta Grossa, Brazil

J. M. Balthazar  
Faculty of Mechanical Engineering of Bauru, São Paulo State University, Bauru, SP, Brazil

C. Oliveira · M. Varanis  
Universidade Federal de Grande Dourado, Escola de Engenharia, Grande Dourado, MS, Brazil

Thus, many of these mechanisms for producing clean and renewable energy have been explored, such as those using piezoceramic materials. Authors such as [4] explore a device with frame portal geometry with ideal and nonideal external force. Thus, establishing the dynamic behavior and energy production regimes.

Other works such as [5] explore the dynamics of mechanisms for energy production. However, they propose control designs to suppress chaotic movements. Control designs determine the conditions necessary for the system to maintain a periodic orbit that will produce harvest energy.

Other authors [6–10], explore energy production with piezoceramic materials in structures with non-ideal external forces. Thus, they establish the dynamic behavior of these structures and propose new alternatives for clean and renewable energy. In these papers, the authors explore a mechanism with a non-ideal force in a cantilever beam, covered by piezoelectric layers on both sides and a direct current (DC) electric motor connected to the beam and the rotor has an unbalanced mass.

At the attached end, the piezoelectric elements are connected via electrodes to an electrical charge, i.e. load resistor. A direct current (DC) electric motor is connected to the beam with non-linear cubic stiffness and linear damping properties. The rotor has a mass ( $m$ ) to generate the unbalanced oscillatory displacement. Finally, the piezoelectric elements are connected through electrodes to an electrical network, for example, a resistor  $R$ . Therefore, they propose analytical solutions using approximation methods and analyze the Sommerfeld effect that appears in the mathematical model proposed by the authors [11]. Therefore, the generalization of mathematical modeling with fractional calculus corroborates to determine the behavior of the fractional dynamics of the system considering the parameter of the fractional derivative operator. Often, the fractional derivative operator is linked to a property of the system, such as viscoelasticity [12–16].

Many fractional derivative operators are used to analyze the behavior of electromechanical structures, an example is the flexibility behavior of microbeams in MEMS systems [references]. Examples of fractional derivative operators applied for dynamic analysis are Riemann–Liouville and Grünwald–Letnikov [13, 14, 18–20].

Therefore, using a fractional dynamics analysis of the model proposed by [13, 14] considering Caputo's fractional derivative operator. However, coupled a piezoelectric in the system for the average output power. Therefore, the work aims to analyze the fractional dynamic behavior based on the Caputo's fractional derivative operator parameter. For this, was used the FFT to determine the regions of the dominant frequencies, bifurcation diagrams and 0-1 Test [18, 20, 21] for determine the range of the Caputo operator that can generate periodic or chaotic orbits. Another analysis was with the average power generated by the system with the variation of the application of the  $F$  parameter, according to [11] this parameter is defined as the system control parameter. The exploration of the proposed fractional mathematical model is fully numerical.

## 2 Mathematical Modeling

The mathematical model is based on the one proposed by [11] and the Fig. 1 shows the mechanism for application the Caputo Operator derivative.

The Eqs. (1) describe the motor movement and its vertical displacement of the mass, thus:

$$\begin{aligned} \ddot{x}(M + m) + c\dot{x} - md(\dot{\phi}\sin(\phi) + \dot{\phi}^2\cos(\phi)) \\ + k_1x + k_2x^3 + \theta(1 + \theta_n|x|)q = (M + m)g \\ \ddot{\phi}(J + md^2) - md\ddot{x}\sin(\phi) + mgd\sin(\phi) = \Gamma(\dot{\phi}) \end{aligned} \tag{1}$$

$$\rho\dot{q} - \theta(1 + \theta_n|y|)q + q = 0$$

where  $M$  mass is connected to a fixed basement by a non-linear spring and a linear viscous damper (damping coefficient  $c$ ). The nonlinear spring stiffness is given by  $k_1x + k_2x^3$ , where  $x$  denotes the structure displacement with respect to some equilibrium position in the absolute reference frame. The motion of the structure is due to an in-board non-ideal motor driving an unbalanced rotor. Denoted by  $\phi$  the angular displacement of the rotor unbalance, and model it as a particle of mass  $m$  and radial distance  $d$  from the rotating axis. The moment of inertia of the rotating part is  $J$ . For the resonant case the structure has an influence on the motor input or output. The forcing function is dependent of the system it acts on, and the source is of non-ideal type. And  $q$  is electrical current and  $\theta$  is the linear and  $\theta_n$  the nonlinear part.

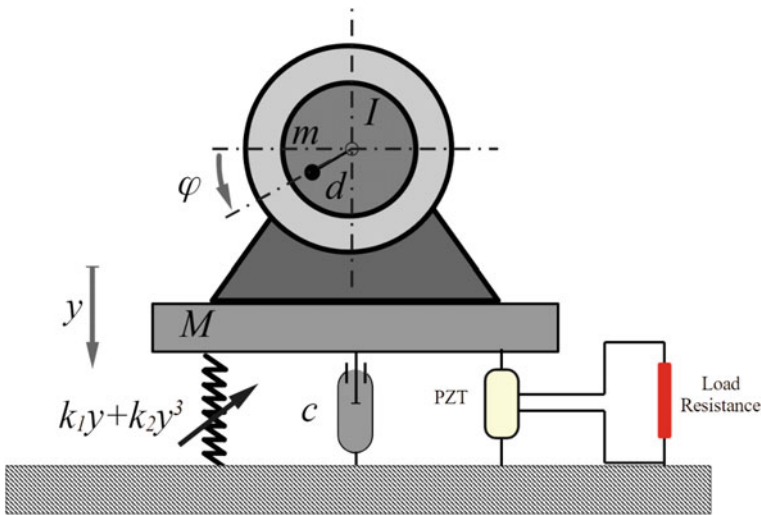


Fig. 1 Scheme of the structure with piezoceramic material coupled



Considering the following change in variables:

$$\begin{aligned}
 p &= \frac{\omega}{\Omega}, \quad \omega^2 = \frac{k_1}{M+m}, \quad \gamma = \frac{k_3}{(M+m)\Omega^6}, \quad \zeta = \frac{c}{(M+m)\Omega}, \quad \mu = \frac{md\Omega^2}{(M+m)g}, \\
 \eta &= \frac{gmd}{(I+md^2)\Omega^2}, \quad F = \frac{M_0}{(I+d^2m)\Omega^2}, \quad \Gamma(\dot{\phi}) = M_0\left(1 - \frac{\dot{\phi}}{\Omega}\right), \\
 x &\rightarrow y = \frac{\Omega^2}{g}x \text{ and } t \rightarrow \tau = \Omega t.
 \end{aligned}$$

Therefore, we rewrite Eqs. (1):

$$\begin{aligned}
 \ddot{y} + \zeta \dot{y} - p^2 y + \gamma y^3 &= 1 + \mu(\ddot{\phi} \sin(\phi) + \dot{\phi}^2 \cos(\phi)) - \theta(1 + \theta_n |y|)q \\
 \ddot{\phi} &= \eta \ddot{y} \sin(\phi) - \eta \sin(\phi) + F(1 - \dot{\phi}) \\
 \dot{q} &= \frac{1}{\rho}[\theta(1 + \theta_n |y|)q - q]
 \end{aligned} \tag{2}$$

In this way, considering  $y = x_1, \dot{y} = x_2, \phi = x_3, \dot{\phi} = x_4$  and  $q = x_5$ , the system of first order differential equations is obtained:

$$\begin{aligned}
 \dot{x}_1 &= x_2 \\
 \dot{x}_2 &= \frac{1}{1 - \mu \eta \sin^2(y_3)}(-\zeta y_2 - p y_1 - \gamma y_1^3 + 1 + \mu \sin(y_3) \\
 &\quad (\mu y_4^2 \cos(y_3) - \eta \sin(y_3) + F(1 - y_4)) - \theta(1 + \theta_n |x_1|)x_5) \\
 \dot{x}_3 &= x_4 \\
 \dot{x}_4 &= \frac{\eta \sin(y_3)}{1 - \mu \eta \sin^2(y_3)}(-\zeta y_2 - p y_1 - \gamma y_1^3 + 1 + \mu y_4^2 \cos(y_3) + \mu \sin(y_3) \\
 &\quad (-\eta \sin(y_3) + F(1 - y_4))) \\
 &\quad - \eta \sin(y_3) + F(1 - y_4) \\
 \dot{x}_5 &= \frac{1}{\rho}[\theta(1 + \theta_n |x_1|)x_5 - x_5]
 \end{aligned} \tag{3}$$

However, we consider the fractional system for our analysis considering the Caputo operator for fractional derivative, the Caputo operator is defined as follows [13–20]:

$${}^C_a D^q f(t) = \frac{1}{\Gamma(q-n)} \int_a^t \frac{f^{(n)}(\tau) d\tau}{(t-\tau)^{q+1-n}} \tag{4}$$

where  $n - 1 < q < n$ , in our considerations  $n = 1$ , thus,  $0 < q < 1$  and  $\Gamma(\cdot)$  is defined as the gamma function. Therefore, rewrite the System of Differential Equations considering the Caputo operator for analyses:

$$\begin{aligned}
 {}^C_a D^q x_1 &= x_2 \\
 {}^C_a D^q x_2 &= \frac{1}{1 - \mu\eta\sin^2(y_3)} (-\zeta y_2 - p y_1 - \gamma y_1^3 + 1 + \mu \sin(y_3) \\
 &\quad (\mu y_4^2 \cos(y_3) - \eta \sin(y_3) + F(1 - y_4)) - \theta(1 + \theta_n |x_1|) x_5) \\
 {}^C_a D^q x_3 &= x_4
 \end{aligned} \tag{5}$$

$$\begin{aligned}
 {}^C_a D^q x_3 &= \frac{\eta \sin(y_3)}{1 - \mu\eta\sin^2(y_3)} (-\zeta y_2 - p y_1 - \gamma y_1^3 + 1 + \mu y_4^2 \cos(y_3) \\
 &\quad + \mu \sin(y_3)(-\eta \sin(y_3) + F(1 - y_4))) \\
 &\quad - \eta \sin(y_3) + F(1 - y_4) \\
 {}^C_a D^q x_5 &= \frac{1}{\rho} [\theta(1 + \theta_n |x_1|) x_5 - x_5]
 \end{aligned}$$

### 3 Numerical Results and Discussion

For the numerical analysis, using the following initial conditions  $x_0 = [0,0,0,0]$  and for analysis corresponds to  $q = [0.978, 1]$  because according to [13–16] values close to  $q = 1$  is conventional derivative operator. Thus, we analyzed the behavior of fractional dynamics for values close to 1, which we could observe some chaotic windows in the system. The parameters is:  $\eta = 0.05, \mu = 8.737, p = 1.0, \gamma = 9.0, \theta = 0.1, \theta_n = 0.5, \zeta = 0.2, \theta = 0.1$  and  $\theta_n = 0.5$  [11].

The numerical method for solving the Eqs. (5) is composed of the initial value problem and the variational system and Adams-Bashforth-Moulton predictor-corrector for fractional differential equations [22–25], with a  $h = 0.001$  and a time of  $10^5$  [s] considering 40% of total time with transient time. Therefore, was analyzed the behavior of Fast Fourier Transforms. In Fig. 2 shows the behavior of the Fourier transforms of Eqs. (5), with the variation of  $q = [0.978, 1]$  and for the following values of  $F = [23.3, 46.6, 70]$ . Can be observed the dominant frequency in the system in the red region where the  $q$  parameter shows more than one dominant frequency of the system, which indicates multiple vibrational periods. It can be observed that values of  $q$  close to 1 the system has overlapping frequencies, thus indicating a chaotic behavior.

Therefore, Fig. 2 shows the behavior of the bifurcation diagrams of the systems, and considering  $F = [23, 46.6, 70]$ , we can observe the emergence of chaotic windows with the variation of the parameter of the fractional derivative.

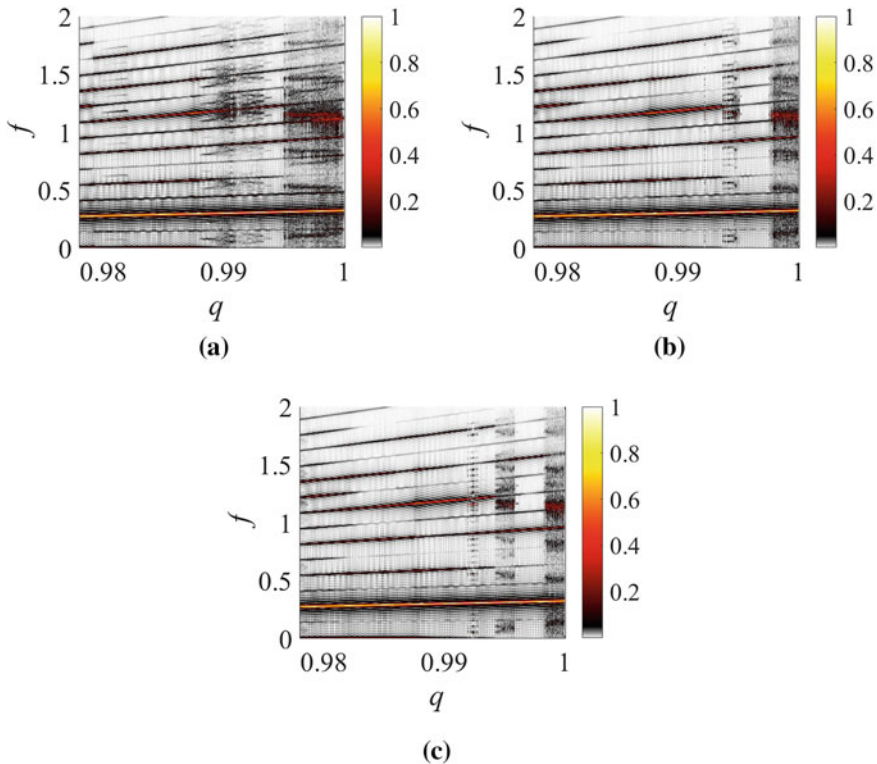


**Fig. 2** FFT for  $q = [0.978, 1.0]$ : **a**  $F = 23.3$ , **b**  $F = 46.6$  and **c**  $F = 70$

In Fig. 2(a) one can observe the chaotic windows at  $q = [0.9790; 0.9793]$ ,  $[0.9816, 0.9822]$ ,  $[0.9871, 0.9873]$ ,  $[0.9887, 0.9936]$  and  $q = [0.995; 1.0]$  with parameter  $F = 23.3$ . According to [11] for  $F = 23.3$  and  $q = 1$  which results in the conventional derivative operator the system is in a chaotic regime. This happens for  $q = 1$  in  $F = 46.6$  and  $70$  has a chaotic behavior which corroborates the data collected by [11], where for systems with the integer derivative operator the system is in a chaotic regime. In Fig. 3(b) with  $F = 46.6$  has the following chaotic windows  $q = [0.978, 0.9783]$ ,  $q = [0.9875, 0.9876]$ ,  $q = [0.9937, 0.9941]$ ,  $q = [0.9946, 0.9952]$  and  $q = [0.9976; 1]$  and in Fig. 3c  $q = [0.978; 0.9737]$ ,  $q = [0.9871; 0.9875]$ ,  $q = [0.9919; 0.992]$ ,  $q = [0.9921; 0.9928]$ ,  $q = [0.9942; 0.996]$  and  $q = [0.9983; 1]$ . In Fig. 4 shows the behavior of 01-Test for the analysis of the fractional system, that is, for values of  $k$  close to zero, the system's periodic behavior is obtained, and for values close to 1, the system's behavior is chaotic [17–21, 23, 25].

Thus, through the bifurcation diagrams and 01-Test we can observe the correspondence of the intervals in which the chaotic behavior of the subintervals contained in the interval  $q = [0.978, 1.0]$ . Due to this correspondence, we build the phase plane ( $x_1$  versus  $x_2$ ), thus we observe the chaotic and periodic behavior that the

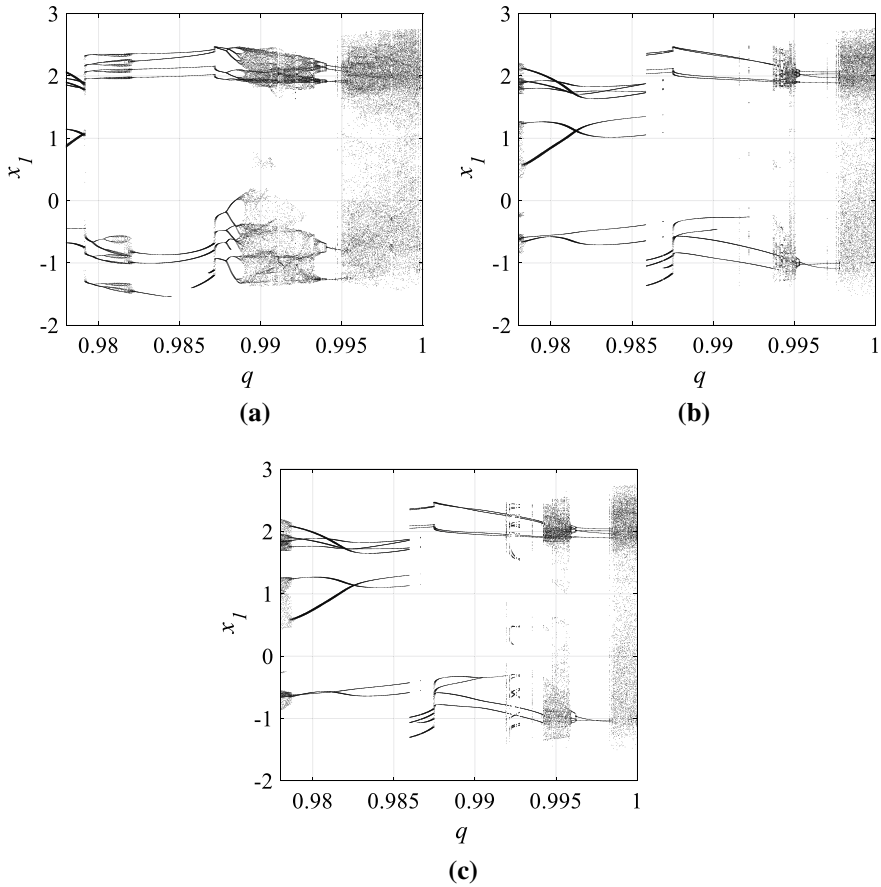


**Fig. 3** Bifurcation diagram for  $q = [0.978, 1.0]$ : **a**  $F = 23.3$ , **b**  $F = 46.6$  and **c**  $F = 70$

system presents, in Fig. 5(a)  $q = 0.98$  periodic behavior, Fig. 5(b)  $q = 0.985$  periodic behavior and Fig. 5(c)  $q = 1.0$  chaotic behavior for a value of  $F = 23.3$ . Figure 5(d)  $q = 0.98$  periodic behavior, Fig. 5(e)  $q = 0.985$  periodic behavior and Fig. 5(f)  $q = 1.0$  chaotic behavior for  $F = 46.6$  and in Fig. 5(g)  $q = 0.98$  periodic behavior, Fig. 5(h)  $q = 0.985$  periodic behavior and Fig. 5(i)  $q = 1.0$  chaotic behavior for a value of  $F = 70.0$ .

We also analyzed the behavior of the harvesting energy of the system produced by the piezoceramic material. According to [6–10], the Harvesting energy, in which calculated from the mechanical component  $V = R\dot{Q}$  and according to the relation for the non-dimensional electric power harvested is determined as follows:

$$P = \rho\dot{q}^2 \tag{6}$$

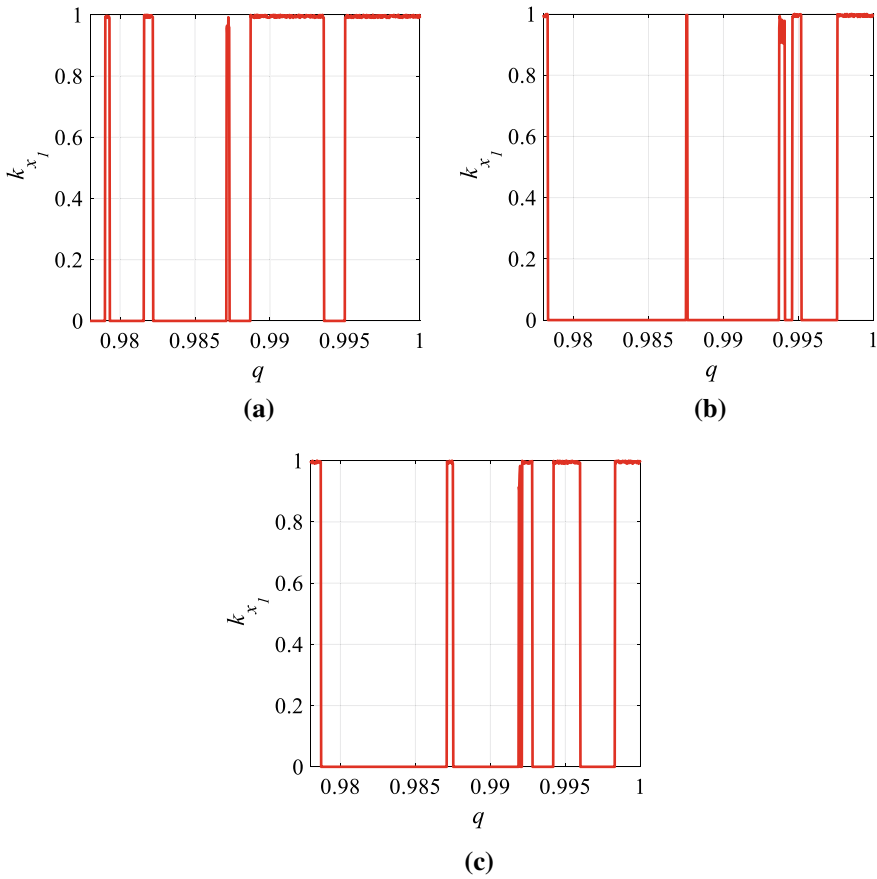


**Fig. 4** 01-Test com  $q = [0.978, 1]$ : **a**  $F = 23.3$ , **b**  $F = 46.6$  and **c**  $F = 70$

where  $\dot{q}$  is the system voltage. However, we determine the average output power of the system:

$$P_{avg} = \frac{1}{T} \int_0^{\tau} P(\tau) d\tau \tag{7}$$

Thus, Fig. 6 show the behavior of the harvesting power considering the parameter  $q$ , we can see that the region in black corresponds to  $P_{avg} < \text{mean}(P_{avg})$  of the system. However, the region between yellow and red corresponds to the calculated maximum power, that is,  $P_{avg} > \text{mean}(P_{avg})$ .

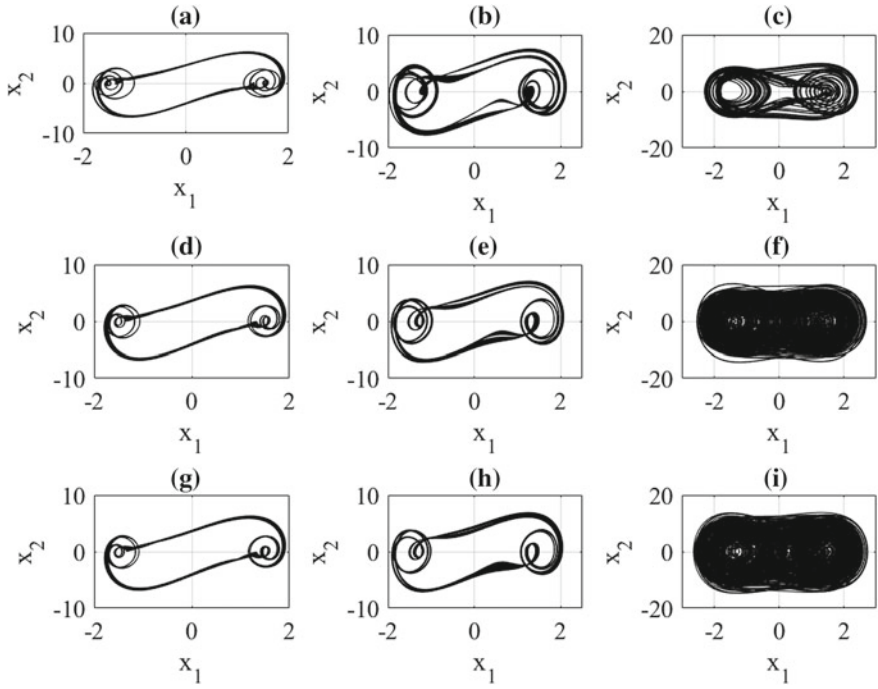


**Fig. 5** Phase Portrait of Eq. (6). (a)  $q=0.98$  and  $F = 23.3$ , (b)  $q=0.985$  and  $F = 23.3$ , (c)  $q=0.98$  and  $F = 1.0$ , (d)  $q=0.98$  and  $F = 23.3$ , (e)  $q=0.985$  and  $F = 23.3$ , (f)  $q=1.0$  and  $F = 23.3$ , (g)  $q=0.98$  and  $F = 46.6$ , (h)  $q=0.985$  and  $F = 46.6$  and (i)  $q=1.00$  and  $F = 46.6$

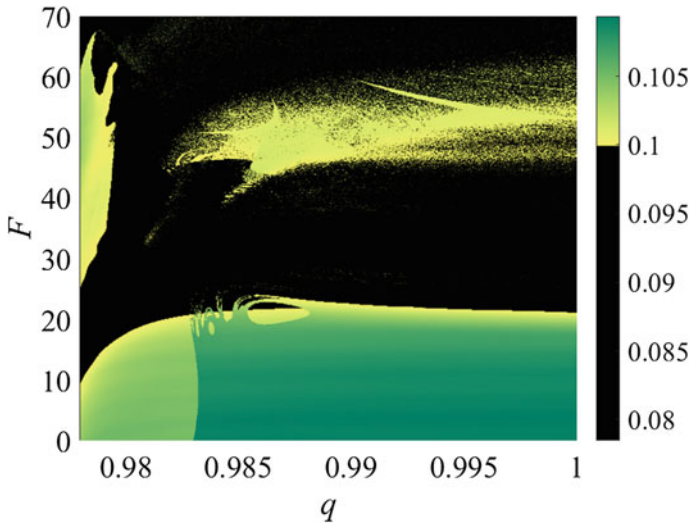


**Fig. 6**  $P_{avg}$  using Eq. (7) for  $q \in [0.978, 1] \times F \in [1, 70]$

## 4 Conclusion

The fractional model for energy harvesting presented in the interval  $q = [0.958, 1]$  a chaotic behavior for the structure with Caputo's fractional derivative operator. Thus, we applied 01-Test and bifurcation diagrams to analyze the location of these windows, for a set of F parameters. Therefore, was determined for values close to  $q = 1$ , regions that presented chaotic and periodical behavior. These regions are confirmed with 01-Test, bifurcation diagrams and the FFT. The analysis of the fractional dynamics of the system not only corroborates the generalization of the mathematical model in a numerical form, but also in the behavior with Caputo's fractional derivative operator.

## References

1. Ribeiro, M.A., Balthazar, J.M., Lenz, W.B., Rocha, R.T., Tusset, A.M.: Numerical exploratory analysis of dynamics and control of an atomic force microscopy in tapping mode with fractional order. *Shock Vib* **2020** (2020)
2. Tusset, A.M., Balthazar, J.M., Ribeiro, M.A., Lenz, W.B., Rocha, R.T.: Chaos control of an atomic force microscopy model in fractional-order. *Eur. Phys. J. Spec. Top.*, 1–12 (2021)
3. Tusset, A.M., Ribeiro, M.A., Lenz, W.B., Rocha, R.T., Balthazar, J.M.: Time delayed feedback control applied in an atomic force microscopy (AFM) model in fractional-order. *J. Vib. Eng. Technol.* **8**(2), 327–335 (2020)
4. Lenz, W.B., Ribeiro, M.A., Rocha, R.T., Balthazar, J.M., Tusset, A.M.: Numerical simulations and control of offshore energy harvesting using piezoelectric materials in a portal frame structure. *Shock Vib.* **2021** (2021)
5. Marin, D., Ribeiro, M.A., Ribeiro, H.V., Lenzi, E.K.: A nonlinear Fokker-Planck equation approach for interacting systems: anomalous diffusion and Tsallis statistics. *Phys. Lett. A* **382**(29), 1903–1907 (2018)
6. Tumolin Rocha, R., Tusset, A., Ribeiro, M. A., Haura Junior, R., Jarzebowska, E., Balthazar, J.M.: On the positioning of a piezoelectric material in the energy harvesting from a non-ideally excited portal frame. *J. Comput. Nonlinear Dyn.*
7. Podlubny, I.: *Fractional differential equations: an introduction to fractional derivatives, fractional differential equations, to methods of their solution and some of their applications.* Elsevier (1998)
8. Hilfer, R. (ed.): *Applications of Fractional Calculus in Physics.* World Scientific (2000)
9. El-Mallawany, R., Ap Ribeiro, M., Lara, L.S., Lenzi, E.K., Alsadig, I.A.A., Novatski, A.: Refractive index behavior of tellurite glasses. *Opt. Mater.* **112**, 110810 (2021)
10. Gonçalves, A., Ribeiro, M. A., Gunha, J.V., Somer, A., Zanuto, V.S., Astrath, N.G., Novatski, A., et al.: A generalized Drude–Lorentz model for refractive index behavior of tellurite glasses. *J. Mater. Sci. Mater. Electron.* **30**(18), 16949–16955 (2019)
11. Iliuk, I., Balthazar, J.M., Tusset, A.M., Felix, J.L.P., de Pontes, B.R, Jr.: On non-ideal and chaotic energy harvester behavior. *Differ. Equ. Dyn. Syst.* **21**(1–2), 93–104 (2013a)
12. Iliuk, I., Balthazar, J.M., Tusset, A.M., Piqueira, J.R.C., de Pontes, B.R., Felix, J.L.P., et al.: A non-ideal portal frame energy harvester controlled using a pendulum. *Eur. Phys. J. Spec. Top.* **222**, 1575–1586 (2013)
13. Iliuk, I., Balthazar, J.M., Tusset, A.M., Piqueira, J.R., de Pontes, B.R., Felix, J.L., et al.: A non-ideal portal frame energy harvester controlled using a pendulum. *Eur. Phys. J. Spec. Top.* **222**(7), 1575–1586 (2013)

14. Iliuk, I., Brasil, R.M.L.R.F., Balthazar, J.M., Tusset, A.M., Piccirillo, V., Piqueira, J.R.C.: Potential application in energy harvesting of intermodal energy exchange in a frame: FEM analysis. *Int. J. Struct. Stab. Dyn.* **14**(8), 1440027 (2014)
15. Iliuk, I., Balthazar, J.M., Tusset, A.M., Piqueira, J.R., de Pontes, B.R., Felix, J.L., et al.: Application of passive control to energy harvester efficiency using a nonideal portal frame structural support system. *J. Intell. Mater. Syst. Struct.* **25**(4), 417–429 (2014)
16. Litak, G., Friswell, M. I., Kwiimy, C.A.K., Adhikari, S., Borowiec, M.: Energy harvesting by two magnetopiezoelectric oscillators with mistuning. *Theor. Appl. Mech. Lett.* **2**(4), 043009 (2012)
17. Litak, G., Friswell, M.I., Adhikari, S.: Regular and chaotic vibration in a piezoelectric energy harvester. *Meccanica* **51**(5), 1017–1025 (2016)
18. Evangelista, L.R., Lenzi, E.K.: *Fractional Diffusion Equations and Anomalous Diffusion*. Cambridge University Press (2018)
19. Sylvain, Z.N., Victor, K.T., Nkamgang, G.B., Kisito, T.P.: Fractional-order analysis of thin magnetostrictive actuators (TMA): analytical solutions, rich dynamics and control. *Int. J. Dyn. Control*, 1–12 (2021)
20. Falconer, I., Gottwald, G.A., Melbourne, I., Wormnes, K.: Application of the 0-1 test for chaos to experimental data. *SIAM J. Appl. Dyn. Syst.* **6**(2), 395–402 (2007)
21. Bernardini, D., Litak, G.: An overview of 0-1 test for chaos. *J. Braz. Soc. Mech. Sci. Eng.* **38**(5), 1433–1450 (2016)
22. Gottwald, G.A., Melbourne, I.: Comment on “Reliability of the 0-1 test for chaos”. *Phys. Rev. E* **77**(2), 028201 (2008)
23. Savi, M.A., Pereira-Pinto, F.H.I., Viola, F.M., de Paula, A.S., Bernardini, D., Litak, G., Rega, G.: Using 0-1 test to diagnose chaos on shape memory alloy dynamical systems. *Chaos Solitons Fractals* **103**, 307–324 (2017)
24. Litak, G., Friswell, M.I., Kwiimy, C.A.K., Adhikari, S., Borowiecki, M.: Energy harvesting by two magnetopiezoelectric oscillators with mistuning. *Theor. Appl. Mech. Lett.* **2**(4), 043009 (2012)
25. Cveticanin, L., Zukovic, M., Balthazar, J.M.: *Dynamics of Mechanical Systems with Non-ideal Excitation*. Springer International Publishing (2018)



# Piezoelectric Energy Harvesting from a Non-ideal Portal Frame System Including Shape Memory Alloy Effect



A. M. Tuset , V. Piccirillo , I. Iliuk , G. G. Lenzi , M. E. K. Fuziki , Jose Manoel Balthazar , G. Litak , and D. Bernardini 

**Abstract** In this work, the investigation of energy harvesting for a U-frame-type (portal frame) structure is presented. The structure is considered as a composite made out of a Shape Memory Alloy (SMA), accounting for a non-ideal DC motor of limited power supply attached to its rigid body. The energy harvesting is carried out using a piezoelectric material (PZT), accounting for a nonlinear electromechanical coupling model. For the behavior of the SMA, a polynomial constitutive model is adopted, which relates the voltage variation to the temperature. Numerical results demonstrate that both PZT and SMA material has a significant influence on energy harvesting. In addition, it is highlighted that the use of SMA makes controlling the vibrations of the structure possible, increasing the harvested energy.

**Keywords** Non-ideal systems · Energy harvesting · Piezoelectric devices · Shape memory alloy

---

A. M. Tuset (✉) · V. Piccirillo · I. Iliuk · G. G. Lenzi  
Federal University of Technology, Paraná, Brazil

V. Piccirillo  
e-mail: [piccirillo@utfpr.edu.br](mailto:piccirillo@utfpr.edu.br)

M. E. K. Fuziki  
State University of Maringá, Maringá, Brazil

J. M. Balthazar  
Sao Paulo State University, São Paulo, Brazil

G. Litak  
Lublin University of Technology, Lublin, Poland  
e-mail: [g.litak@pollub.pl](mailto:g.litak@pollub.pl)

D. Bernardini  
University of Rome Sapienza, Rome, Italia  
e-mail: [davide.bernardini@uniroma1.it](mailto:davide.bernardini@uniroma1.it)

## 1 Introduction

In recent years, the demand for renewable energy sources, more efficient and nonpolluting, has been growing. As kinetic energy is an energy source easily found in the environment, devices that convert kinetic energy into electrical energy have been widely studied, and special attention has been given to devices that use piezoelectric elements as a means of energy transduction [1–3].

Among the vibration sources that constantly produce kinetic energy, it is possible to highlight the systems excited by a DC motor with an unbalanced mass connected to its axis. The aforementioned excitation source is of non-ideal type and is characterized as is because its amplitude and frequency are dependent on the movement of the structure [4]. The non-ideal energy source can induce high levels of vibrations in a structure, which becomes a promising kinetic energy source. Therefore, the piezoelectric energy harvesting is a feasible, low-cost, and efficient way to convert kinetic energy into electrical energy.

Many researchers are paying special attention to energy harvesting from nonlinear and non-ideal vibration systems [5–15]. The main advantage of nonlinear energy harvesters is the conversion of energy over a wider range of frequencies of vibrations [7].

In this work, we investigate the energy harvesting for a U-frame-type (portal frame) structure consisting of a composite material accounting for a Shape Memory Alloy subjected to a non-ideal excitation source. The energy harvesting is obtained by using a piezoelectric material accounting for a nonlinear model of electromechanical coupling [16]. To describe the SMA behavior, a polynomial constitutive model is adopted, which relates the voltage variation to temperature [17–20]. When the SMA is heated to a specific temperature, large contraction forces are induced due to the shape recovery that occurs during the martensitic transformation, changing the stiffness of the structure and its dynamics [21–27].

## 2 Mathematical Model

Figure 1 shows an equivalent physical model to represent the sway motion (1<sup>st</sup> mode) of a portal frame structure composed of a shape memory alloy and a piezoelectric material attached on a column. A DC motor with a limited power supply containing an unbalanced rotating mass into its shaft is fixed on the bottom of the mid-span of the supported beam [7].

The mathematical model that represents the dynamics of the system shown in Fig. 1 is developed using Lagrange's energy method, where the Lagrange's function is expressed as:

$$L = E_k - E_p \quad (1)$$

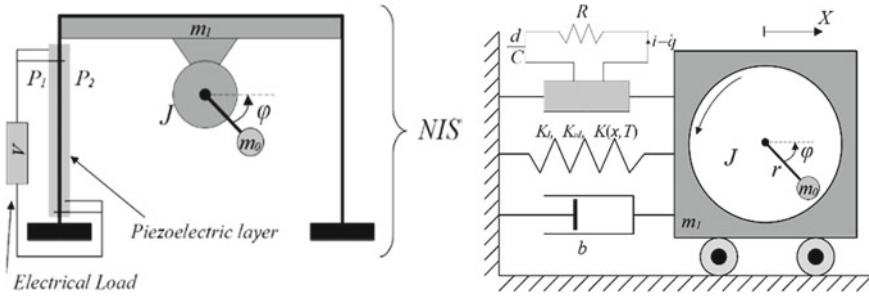


**Fig. 1** Schematic of the non-ideal portal frame energy harvester with SMA material

where  $E_k$  is the kinetic energy, and  $E_p$  is the potential energy. The equations of motion can be obtained through the Euler–Lagrange equation, given by:

$$\frac{d}{dt} \left( \frac{\partial L}{\partial \dot{Q}_i} \right) - \frac{\partial L}{\partial Q_i} = \mathfrak{S}_i \tag{2}$$

where  $i = 1, 2, \dots, N$ .  $N$  is the number of degrees-of-freedom,  $\mathfrak{S}_i$ 's are the non-conservatives forces,  $Q_i$ 's are the generalized coordinates, being that  $Q_1 = X$ ,  $Q_2 = \varphi$  and  $Q_3 = q$ .

The kinetic energy is given by:

$$E_k = \frac{1}{2} M \dot{X}^2 + \frac{1}{2} I \dot{\varphi}^2 + \frac{1}{2} m_0 [\dot{X} - r \dot{\varphi} \sin \varphi]^2 + \frac{1}{2} m_0 [r \dot{\varphi} \cos \varphi]^2 \tag{3}$$

The potential energy is given by:

$$E_p = \frac{1}{2} k_l X^2 + \frac{1}{4} k_{nl} X^4 + m_0 g r \sin \varphi + \frac{1}{2} \bar{a} \Delta T X^2 - \frac{1}{4} \bar{b} X^4 + \frac{1}{6} \bar{e} X^6 - \frac{d(X)}{C} q X + \frac{1}{2C} q^2 \tag{4}$$

The non-conservatives forces are given by:

$$\begin{aligned} \mathfrak{S}_1 &= -c \dot{X} \\ \mathfrak{S}_2 &= V_1 - V_2 \dot{\varphi} \\ \mathfrak{S}_3 &= -R \dot{q} \end{aligned} \tag{5}$$

Substituting Eqs. (3), and (4) into Eq. (1), and substituting the result accounting for Eq. (5) into Eq. (2), we obtain:

$$M \ddot{X} + c \dot{X} + k_l X + k_{nl} X^3 = m_0 r (\ddot{\varphi} \sin \varphi - \dot{\varphi}^2 \cos \varphi) - \frac{d(X)}{C} \dot{q}$$

$$\begin{aligned}
 & -\bar{p}\Delta T X + \bar{b}X^3 - \bar{c}X^5 \\
 (J + m_0r^2)\ddot{\varphi} - m_0r\ddot{X} \cos \varphi &= V_1 - V_2\dot{\varphi} \\
 R\dot{q} - \frac{d(X)}{C}X + \frac{q}{C} &= 0
 \end{aligned}
 \tag{6}$$

where  $M = m_1 + m_0$  is the total mass of the system,  $m_0$  is the eccentric mass of the electric motor shaft,  $m_1$  is the mass of the structure,  $X$  is the vertical displacement of the system,  $c$  is the damping coefficient,  $k_l$  is linear stiffness coefficient,  $k_{nl}$  is nonlinear stiffness coefficient,  $\varphi$  is the angular displacement of the rotor,  $r$  is the eccentricity,  $J$  is the moment of inertia of the rotor,  $\bar{p}$ ,  $\bar{b}$  and  $\bar{c}$  are constants,  $\Delta T = T - T_m$ ,  $T$  is temperature,  $T_m$  is temperature in which the martensitic phase is stable,  $V_1$  and  $V_2$  are parameters of the DC motor,  $d(X)$  is a coupling coefficient between the structure and the PZT material,  $R$  is the electrical resistance,  $C$  is the capacitance, and  $q$  is the electric charge.

Equations (6) can be written in state-space notation as follows:

$$\begin{aligned}
 x'_1 &= x_2 \\
 x'_2 &= \frac{1}{1 - \delta_1\rho_1 \sin(x_3)^2} \left( \begin{aligned} & -\alpha_1x_2 - k_{sma}(a\Delta Tx_1 - bx_1^3 + cx_1^5) \\ & +\theta(1 + \Theta|x_1|)x_5 - \beta_1x_1 - \beta_3x_1^3 \\ & +\delta_1 \sin x_3(-\rho_3x_4 + \rho_2) + \delta_2x_4^2 \cos x_3 \end{aligned} \right) \\
 x'_3 &= x_4 \\
 x'_4 &= \frac{1}{1 - \delta_1\rho_1 \sin(x_3)^2} \left( \begin{aligned} & \rho_1 \sin x_3 \left( \begin{aligned} & -\alpha_1x_2 - k_{sma}(a\Delta Tx_1 - bx_1^3 + cx_1^5) \\ & -\beta_1x_1 - \beta_3x_1^3 + \theta(1 + \Theta|x_1|)x_5 \\ & +\delta_2x_4^2 \cos x_3 \end{aligned} \right) \\ & +\rho_2 - \rho_3x_4 \end{aligned} \right) \\
 x'_5 &= \frac{\theta(1 + \Theta|x_1|)x_1}{\rho} - \frac{x_5}{\rho}
 \end{aligned}
 \tag{7}$$

where  $x_1 = X$ ,  $x_2 = \dot{X}$ ,  $x_3 = \varphi$ ,  $x_4 = \dot{\varphi}$ ,  $x_5 = q$ ,  $\theta(1 + \Theta|x_1|) = d(X)$ ,  $\alpha_1 = \frac{c}{M}$ ,  $k_{sma} = \frac{1}{M}$ ,  $a = \bar{p}$ ;  $b = \bar{b}$ ,  $c = \bar{c}$ ,  $\beta_1 = \frac{k_l}{M}$ ,  $\beta_3 = \frac{k_{nl}}{M}$ ,  $\rho_2 = \frac{V_1}{(J+m_0r^2)}$ ,  $\rho_3 = \frac{V_2}{(J+m_0r^2)}$ ,  $\delta_1 = \delta_2 = \frac{m_0r}{M}$ ,  $\rho_1 = \frac{m_0r}{(J+m_0r^2)}$ , and  $\rho = \frac{1}{CR}$ .

The average power is obtained through

$$P_{avg} = \frac{1}{T} \int_0^T P(\tau) d\tau
 \tag{8}$$

where the instant power is calculated using

$$P = \rho v^2
 \tag{9}$$

### 3 Numerical Simulations

The numerical simulations are carried out accounting for the parameters:  $a = 0.00156987$ ,  $b = 114.367348$ ,  $c = 7232.49136$ ,  $\alpha_1 = 0.1$ ,  $\beta_1 = -1$ ,  $\beta_3 = 0.2$ ,  $\rho_1 = 0.05$ ,  $\rho_2 = 100$ ,  $\rho_3 = 200$ ,  $\delta_1 = 8.373$ ,  $\theta = 0.20$ ,  $\Theta = 0.60$ ,  $\rho = 1.0$ , along with the initial conditions:  $x_i(0) = 0$ , where  $i = 1:5$  [7].

Assuming  $k_{sma}$  as a control parameter for the SMA, the following subsections show the parametrical analysis of the control parameter  $k_{sma}$ , the temperature variation  $\Delta T$ , and the linear piezoelectric coefficient  $\rho$ , discussing their influence in the behavior of the system and in the amount of power available to be harvested.

#### 3.1 Control Parameter $k_{sma}$ Analysis

Here, the influence of the  $k_{sma}$  in the behavior of the system is analyzed. Figure 2 shows the numerical results considering the range of parameters  $k_{sma} = [0.05 : 10]$  and  $\Delta T = 70$ . It is noted that the highest average powers are obtained under a chaotic

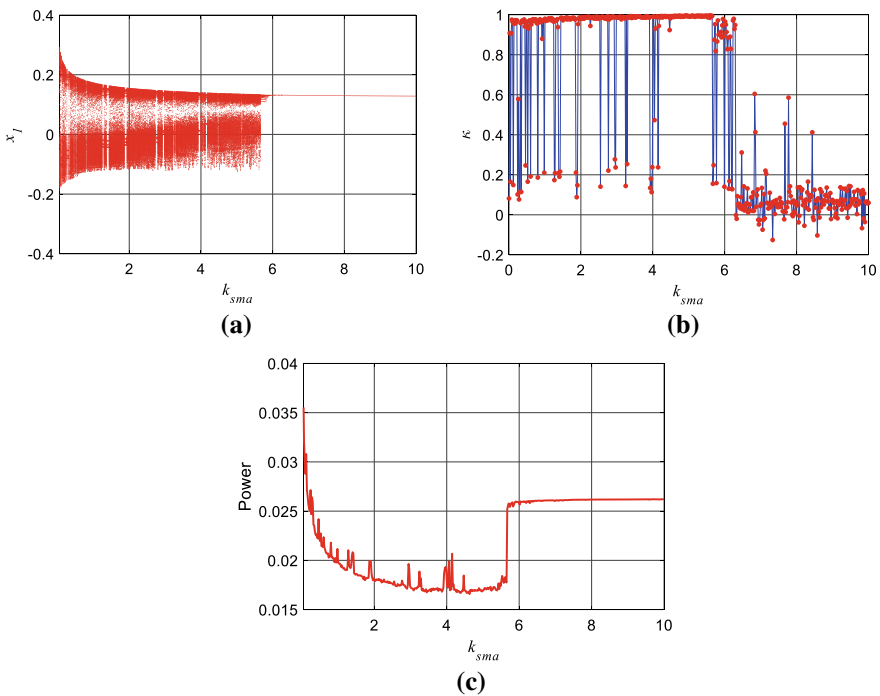
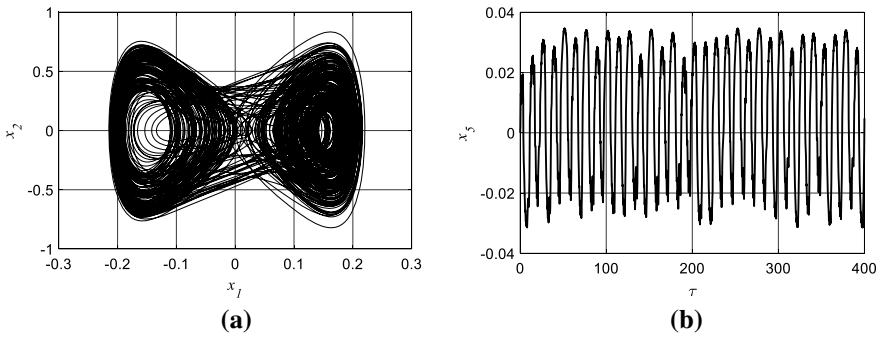


**Fig. 2** Dynamics of de systems for  $k_{sma} = [0.05:10]$  and  $\Delta T = 70$ . **a** Bifurcation Diagram **b** Representation of  $K_c$  (0-1 test). **c** Average power  $P_{avg}$

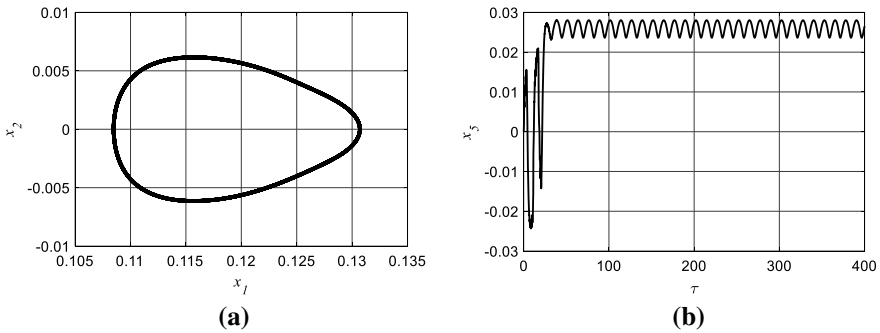
behavior with low  $k_{sma}$  valleys. It is also observed that as  $k_{sma}$  increases, the average power progressively reduces for the system with chaotic behavior until the transition to a periodic behavior (when  $k_{sma} \geq 5.8$ ) with the increase in the average power and stabilizing it at  $P_{avg} = 0.027$ .

Figure 3 shows the phase plane of the system (Fig. 3a) and the time history of the electrical charge (Fig. 3b) accounting for  $k_{sma} = 0.7$  and  $\Delta T = 70$ . It is observed that the system has chaotic behavior, and the generated average power is  $P_{avg} = 0.0203$ .

Figure 4 shows the phase plane of the system (Fig. 4a) and the time history of the electrical charge (Fig. 4b) accounting for  $\Delta T = 70$  and increasing  $k_{sma}$  to  $k_{sma} = 7$ . Note that, in this case, the system shows periodic behavior and also increases the harvested average power to  $P_{avg} = 0.0254$ .



**Fig. 3** Dynamics of the systems for  $k_{sma} = 0.7$  and  $\Delta T = 70$ . **a** Phase plane for  $x_1$  versus  $x_2$ . **b** Time history of the electrical charge  $x_5$



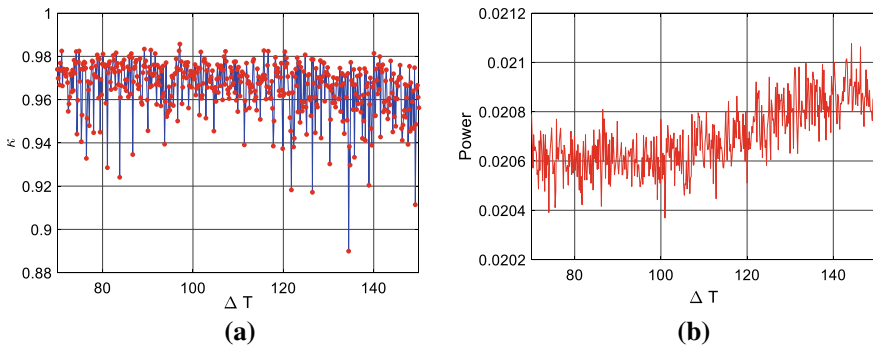
**Fig. 4** Dynamics of de systems for  $k_{sma} = 7$  and  $\Delta T = 70$ . **a** Phase plane for  $x_1$  versus  $x_2$ . **b** Time history of the electrical charge  $x_5$

### 3.2 Temperature Variation $\Delta T$ Analysis

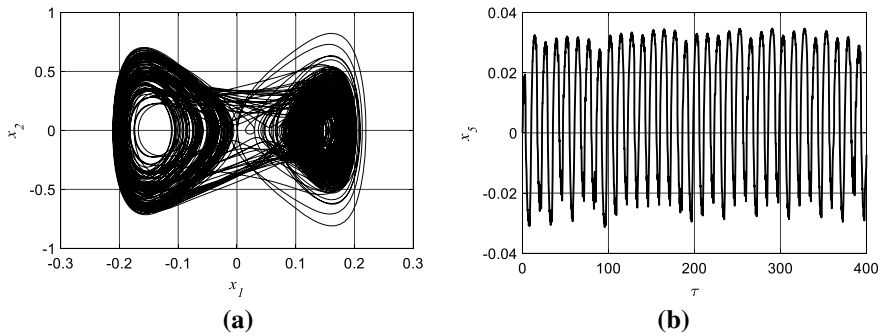
The behavior of the system can also change depending on the variation of temperature of the SMA.

Figure 5 show the 0-1 test (Fig. 5a) and the amount of average power (Fig. 5b) considering  $k_{sma} = 0.7$  and varying the temperature in a range of  $\Delta T = [70 : 150]$ . It is noticed that the system remains in a chaotic regime for the entire range of temperature. However, it is also observed there is an increase of power when the temperature of the SMA increases.

Figure 6 show the phase plane of the system (Fig. 6a) and the time history of the electrical charge (Fig. 6b) accounting for  $k_{sma} = 0.7$  and  $\Delta T = 131.1$ . Note that the system has chaotic behavior, and the generated average power is  $P_{avg} = 0.0211$ .



**Fig. 5** a 0-1 test and b average power varying the temperature within the range of  $\Delta T = [70 : 150]$  and considering  $k_{sma} = 0.7$



**Fig. 6** Dynamic of de systems for  $k_{sma} = 0.7$  and  $\Delta T = 131.1$ . a Phase plane for  $x_1$  versus  $x_2$ . b Time history of the electrical charge  $x_5$

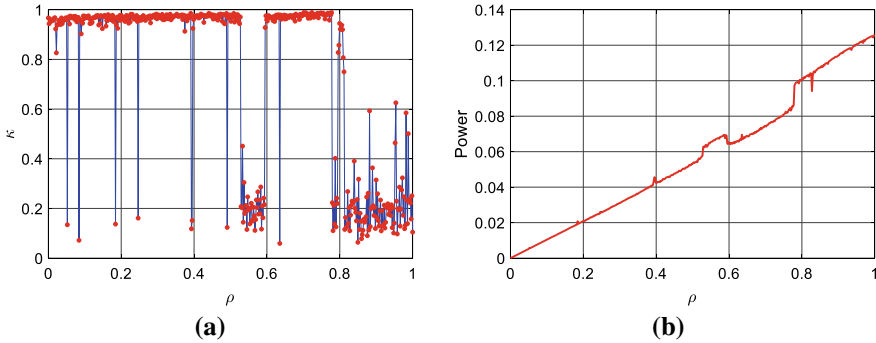


**Fig. 7** **a** 0-1 test and **b** average power varying the linear piezoelectric coefficient within the range of  $\rho = [0.05: 1]$  and considering  $k_{sma} = 0.7$  and  $\Delta T = 131.1$

### 3.3 Linear Piezoelectric Coefficient $\rho$ Analysis

The linear piezoelectric coefficient has the most influence over the possible energy that piezoelectric material can harvest. This coefficient represents the strain coefficient of different piezoelectric materials. Hence, the higher is the coefficient, the higher the energy harvesting is expected. However, it can directly affect the behavior of the system as well.

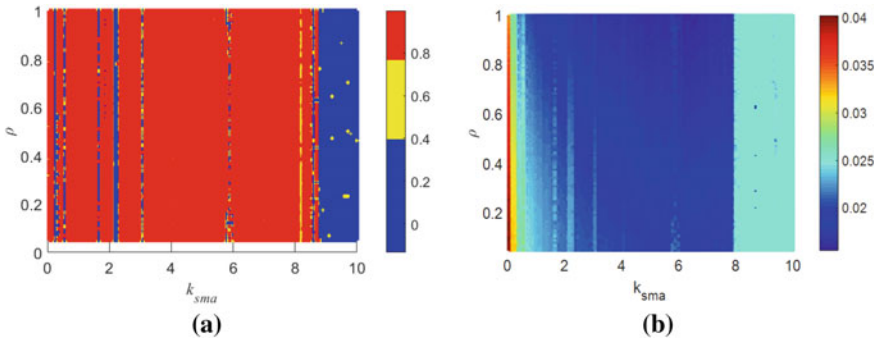
Figure 7 show the 0-1 test (Fig. 7a) and the amount of average power (Fig. 7b) considering  $k_{sma} = 0.7$  at a variation of temperature of  $\Delta T = 131.1$ , and varying the linear piezoelectric coefficient in a range of  $\rho = [0.05: 1]$ . It is observed that the PZT parameter ( $\rho$ ) has a greater influence on the average power. It is also important to highlight that, for values between  $\rho = [0.53: 0.59]$ , and  $\rho = [0.82: 1]$ , there may be  $\rho$  values that drive the system to a periodic state (contrasting Fig. 7b with Fig. 7a).

### 3.4 Control Parameter $k_{sma}$ Versus Piezoelectric Coefficient $\rho$

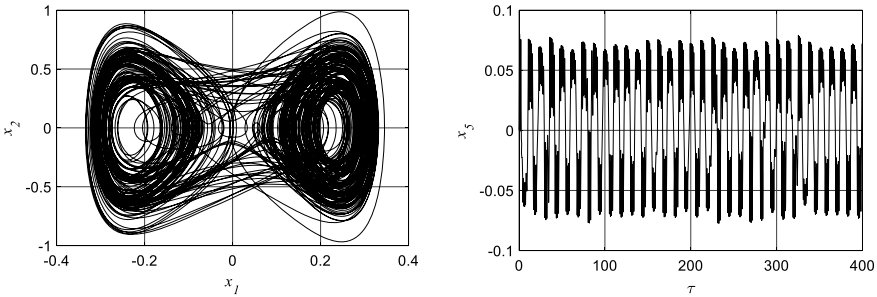
From the previous analyses, it is clear that the parameters  $\rho$  and  $k_{sma}$  are the ones that have the foremost effect on the dynamics of the structure and in the energy harvesting. Therefore, a deep investigation of both parameters is carried out.

Figure 8 show 0-1 test map (Fig. 8a) and the average harvested map (Fig. 8b) power for the variation of both parameters in the ranges  $\rho = [0.05: 1]$ , and  $k_{sma} = [0.05: 10]$  when the variation of temperature is  $\Delta T = 131.1$ . It is observed that for most of the values of  $\rho$  the system presents chaotic behavior ( $K_c \geq 0.8$ ). However, when  $k_{sma} > 8.8$ , periodic behavior is dominant over the dynamics of the system regardless of the values of  $\rho$  ( $K_c < 0.8$ ). In addition, note that the maximum average power is obtained when the values of  $\rho$  and  $k_{sma}$  are minimum.





**Fig. 8** **a** 0-1 test map and **b** average power map for the variation of the  $\rho$  versus  $k_{sma}$  within the ranges of  $\rho = [0.05: 1]$  and  $k_{sma} = [0.05: 10]$ ,  $\Delta T = 131.1$



**Fig. 9** Dynamic of de systems for  $k_{sma} = 0.05$ ,  $\rho = 0.05$ , and  $\Delta T = 131.1$ . **a** Phase plane for  $x_1$  versus  $x_2$ . **b** Time history of the electrical charge  $x_5$

Accounting for the parameters of the system when there is maximum energy harvesting, which are  $\Delta T = 131.1$ ,  $k_{sma} = 0.05$ , and  $\rho = 0.05$ , Fig. 9 show the phase plane of the system (Fig. 9a) and the time history of the electrical charge (Fig. 9b). It is observed that the system is chaotic, and the average power is  $P_{avg} = 0.04$ .

## 4 Conclusions

This work presented the investigation of the energy harvesting for a U-frame-type (portal frame) structure considered a composite material made of an SMA under a non-ideal excitation.

The numerical results demonstrated that the structure with the least of the SMA material and a small piezoelectric component can generate a high amount of power for energy generation. This is observed through Fig. 8b. It is also important to highlight

that the use of SMA showed to be a viable alternative for controlling the chaotic behavior and vibrations of the system, whose results are in agreement with those observed in the cited works.

## Appendix

### The 0-1 Test Method

The 0-1 test consists of estimating a single parameter  $\kappa$  by [28]:

$$\kappa = \frac{\text{cov}(Y, M(\bar{c}))}{\sqrt{\text{var}(Y)\text{var}(M(\bar{c}))}} \quad (10)$$

where:  $\bar{c} \in (0, \pi)$ ,  $M(\bar{c}) = [M(1, \bar{c}), M(2, \bar{c}), \dots, M(n_{max}\bar{c})]$  and  $Y = [1, 2, \dots, n_{max}]$ .

If  $\kappa$  is close to 0 the system is periodic. On the other hand, if  $\kappa$  is close to 1 the system is chaotic. The test utilizes a system variable  $x(j)$ , where two new coordinates ( $p, q$ ) are defined as follows [29]:

$$p(n, \bar{c}) = \sum_{j=0}^n x(j) \cos(j\bar{c}) \quad (11)$$

$$q(n, \bar{c}) = \sum_{j=0}^n x(j) \sin(j\bar{c}) \quad (12)$$

The mean square displacement of the new variables  $p(n, \bar{c})$  and  $q(n, \bar{c})$  is given by [29]:

$$M(n, c) = \lim_{n \rightarrow \infty} \frac{1}{N} \sum_{j=1}^N [(p(j+n, \bar{c}) - p(j, \bar{c}))^2 \dots + (q(j+n, \bar{c}) - q(j, \bar{c}))^2] \quad (13)$$

where  $n = 1, 2, \dots, N$ .

## References

1. Iliuk, I., Brasil, M.R.L.F., Balthazar, J.M., Tusset, A.M., Piqueira, J.R.C.: Potential application in energy harvesting of intermodal energy exchange in a frame: FEM analysis. *Int. J. Struct. Stab. Dyn.*, 1440027 (2014)
2. Lenz, W.B., Ribeiro, M.A., Rocha, R.T., Balthazar, J.M., Tusset, A.M.: Numerical simulations and control of offshore energy harvesting using piezoelectric materials in a portal frame structure. *Shock Vib.* **2021**, 1–11 (2021)
3. Ribeiro, M.A., Tusset, A.M.L., Wagner, B., Balthazar, J.M.: Dynamic analysis of the nonlinear behavior of an ocean buoy for energy harvesting. *Eur. Phys. J. Spec. Top.* **1**, 1–10 (2021)
4. Balthazar, J.M., Tusset, A.M., Brasil, R.M.L.R.F., Felix, J.L.P., Rocha, R.T., Janzen, F.C., Nabarrete, A., Oliveira, C.: An overview on the appearance of the Sommerfeld effect and saturation phenomenon in non-ideal vibrating systems (NIS) in macro and MEMS scales. *Nonlinear Dyn.* **93**, 19–40 (2018)
5. Iliuk, I., Balthazar, J.M., Tusset, A.M., Felix, J.L.P., Pontes, B.R., Jr.: On non-ideal and chaotic energy harvester behavior. *Differ. Equ. Dyn. Syst.* **21**, 93–104 (2013)
6. Iliuk, I., Balthazar, J.M., Tusset, A.M., Piqueira, J.R.C., Pontes, B.R., Jr., Felix, J.L.P., Bueno, A.M.: A non-ideal portal frame energy harvester controlled using a pendulum. *Eur. Phys. J. Spec. Top.* **222**, 1575–1586 (2013)
7. Iliuk, I., Balthazar, J.M., Tusset, A.M., Piqueira, J.R.C., Pontes, B.R., Jr., Felix, J.L.P., Bueno, A.M.: Application of passive control to energy harvester efficiency using a non-ideal portal frame structural support system. *J. Intell. Mater. Syst. Struct.* **25**, 417–429 (2014)
8. Rocha, R.T., Balthazar, J.M., Tusset, A.M., Piccirillo, V., Felix, J.L.P.: Comments on energy harvesting on a 2:1 internal resonance portal frame support structure, using a nonlinear-energy sink as a passive controller. *Int. Rev. Mech. Eng.* **10**, 147–156 (2016)
9. Rocha, R.T., Balthazar, J.M., Tusset, A.M., Piccirillo, V.: Using passive control by a pendulum in a portal frame platform with piezoelectric energy harvesting. *J. Vib. Control* **1**, 107754631770938-1 (2017)
10. Rocha, R.T., Tusset, A.M., Ribeiro, M.A., Lenz, W.B., Balthazar, J.M.: Remarks on energy harvesting of nonlinear charge and voltage piezoelectric models in a two-degrees-of-freedom nonlinear portal frame model. *Proc. Inst. Mech. Eng. Part C J. Mech. Eng. Sci.* **1**, 095440622093999–095440622093999 (2020)
11. Rocha, R.T., Tusset, A.M., Ribeiro, M.A., Haura, R., Jr., Jarzebowska, E., Balthazar, J.M.: On the positioning of a piezoelectric material in the energy harvesting from a non-ideally excited portal frame. *J. Comput. Nonlinear Dyn.* **15**, 121002–121012 (2020)
12. Rocha, R.T., Balthazar, J.M., Tusset, A.M., Piccirillo, V., Felix, J.L.P.: Nonlinear piezoelectric vibration energy harvesting from a portal frame with two-to-one internal resonance. *Meccanica* **52**, 2583–2602 (2017)
13. Varanis, M.V., Tusset, A.M., Balthazar, J.M., Litak, G., Oliveira, C., Rocha, R.T., Nabarrete, A., Piccirillo, V.: Dynamics and control of periodic and non-periodic behavior of Duffing vibrating system with fractional damping and excited by a non-ideal motor. *J. Frankl. Inst. Eng. Appl. Math.* **357**, 2067–2082 (2020)
14. Varanis, M., Norenberg, J.P.C.V., Rocha, R.T., Oliveira, C., Balthazar, J.M., Tusset, A.M.: A Comparison of time-frequency methods for nonlinear dynamics and chaos analysis in an energy harvesting model. *Braz. J. Phys.* **50**, 235–244 (2020)
15. Felix, J.L.P., Balthazar, J.M., Rocha, R.T., Tusset, A.M., Janzen, F.C.: On vibration mitigation and energy harvesting of a non-ideal system with autoparametric vibration absorber system. *Meccanica* **53**, 3177–3188 (2018)
16. Triplett, A., Quinn, D.D.: The effect of nonlinear piezoelectric coupling on vibration-based energy harvesting. *J. Intell. Mater. Syst. Struct.* **20**, 1959–1967 (2009)
17. Savi, M.A., Pacheco, P.M.C.L., Braga, A.M.B.: Chaos in a shape memory two-bars truss. *Int. J. Nonlinear Mech.* **37**, 1387–1395 (2002)

18. Piccirillo, V., Balthazar, J.M., Pontes Jr. B.R., Felix, J.L.P.: Chaos control of a nonlinear oscillator with shape memory alloy using an optimal linear control. Part II: non-ideal energy source. *Nonlinear Dyn.* **56**(3), 243–253 (2009)
19. Janzen, F.C., Tusset, A.M., Piccirillo, V., Balthazar, J.M., Brasil, M.R.L.F.: Motion and vibration control of a slewing flexible structure by SMA actuators and parameter sensitivity analysis. *Eur. Phys. J. Spec. Top.* **224**, 3041–3054 (2015)
20. Lima, J.J., Tusset, A.M., Janzen, F.C., Piccirillo, V., Nascimento, C.B., Balthazar, J.M., Brasil, M.R.L.F.: SDRE applied to position and vibration control of a robot manipulator with a flexible link. *J. Theor. Appl. Mech.* **54**, 1067–1078 (2016)
21. Piccirillo, V., Balthazar, J.M., Tusset, A.M., Bernardini, D., Rega, G.: Nonlinear dynamics of a thermomechanical pseudoelastic oscillator excited by non-ideal energy sources. *Int. J. Nonlinear Mech.* **77**, 12–27 (2015)
22. Piccirillo, V., Balthazar, J.M., Tusset, A.M., Bernardini, D., Rega, G.: Application of a shape memory absorber in vibration suppression. *Appl. Mech. Mater.* **849**, 27–35 (2016)
23. Piccirillo, V., Balthazar, J.M., Tusset, A.M., Bernardini, D., Rega, G.: Characterizing the nonlinear behavior of a pseudoelastic oscillator via the wavelet transform. *Proc. Inst. Mech. Eng. Part C J. Mech. Eng. Sci.* **230**, 120–132 (2016)
24. Bernardini, D., Pence, T.J.: Uniaxial modeling of multivariant shape-memory materials with internal sublooping using dissipation functions. *Meccanica* **40**, 339–364 (2005)
25. Bernardini, D., Rega, G.: Chaos robustness and strength in thermomechanical shape memory oscillators. Part I: a predictive theoretical framework for the pseudoelastic behavior. *Int. J. Bifurc. Chaos* **21**, 2769–2782 (2011)
26. Bernardini, D., Rega, G.: Chaos robustness and strength in thermomechanical shape memory oscillators. Part II: numerical and theoretical evaluation. *Int. J. Bifurc. Chaos* **21**, 2783–2800 (2011)
27. Bernardini, D., Rega, G.: Evaluation of different SMA models performances in the nonlinear dynamics of pseudoelastic oscillators via a comprehensive modeling framework. *Int. J. Mech. Sci.* **130**, 458–475 (2017)
28. Litak, G., Bernardini, D., Syta, A., Rega, G., Rysak, A.: Analysis of chaotic non-isothermal solutions of thermomechanical shape memory oscillators. *Eur. Phys. J. Spec. Top.* **222**, 1637–1647 (2013)
29. Tusset, A.M., Balthazar, J.M., Ribeiro, M.A., Lenz, W.B., Rocha, R.T.: Chaos control of an atomic force microscopy model in fractional-order. *Eur. Phys. J. Spec. Top.* **1**, 1–12 (2021)

# LQR Optimal Control Applied in an Energy Harvesting System with Non-ideal Excitation Operating with Uncertain Parameters



Estevão Fuzaro de Almeida and Fábio Roberto Chavarette

**Abstract** The majority of active control applications in vibrational dynamic systems are utilized to minimize vibrations. The goal of this research, on the other hand, is to employ vibrations to generate electrical energy in such a way that the vibration becomes a desired phenomenon. The change of the physical characteristics of the system was conducted in this work with the goal of enhancing the modeling of complex energy harvesting systems with non-ideal excitation, bringing higher resilience, and bringing them closer to reality. To stabilize the orbits and compare the power generated by the systems with and without control, the optimal control technique via Linear Quadratic Regulator (LQR) is used.

**Keywords** Energy harvesting · Non-ideal excitation · Uncertain parameters · Optimal control · Linear quadratic regulator (LQR)

## 1 Introduction

Energy Harvesting techniques have been created with the goal of providing a sustainable, safe, and efficient source of energy. Tiny temperature gradients, small mass movements, and vibration are among the strategies used to capture energy from nature. Furthermore, Energy Harvesting is a promising alternative for low power electronic devices. In addition, electronic devices are becoming more energy efficient, and some remote sensors can already operate with up to  $100 \mu\text{W}$  [1].

This chapter focuses on vibration-based mechanical energy harvesting systems, considering that luminous energy (from a solar source) and thermal energy may not be accessible at the application site, resulting in an energy shortage, even if minimal [2, 3].

---

E. F. de Almeida (✉)

Department of Mechanical Engineering, São Paulo State University, Ilha Solteira, SP, Brazil  
e-mail: [estevao.fuzaro@unesp.br](mailto:estevao.fuzaro@unesp.br)

F. R. Chavarette

Department of Engineering, Physics and Mathematics, São Paulo State University, Araraquara, SP, Brazil  
e-mail: [fabio.chavarette@unesp.br](mailto:fabio.chavarette@unesp.br)

In addition, vibration-based energy harvesters tend to have low maintenance requirements and, moreover, can be used in environments considered hostile to more technological and complex systems; such environments are commonly chosen for the allocation of these sensors due to the higher amplitude of vibrations and because this type of harvester does not require extensive cabling [4].

The initial types of vibration-based energy harvesters provide efficient responses only when the excitation vibration frequency corresponds with the natural frequency of the excited system, resulting in the phenomenon known as resonance [1, 5–8]. The so-called natural frequency of a body is given by the expression  $\omega = (k/m)^{1/2}$ , where  $k$  is the stiffness of the system and  $m$  is its mass [9]. Thus, resonance occurs when the external excitation frequency ( $\omega$ ) equals the body's natural frequency. Most vibration in the environment, on the other hand, has a large frequency range [1, 10] and behaves randomly, as seen in the vibration of building structures subjected to wind activity [11]. Because of this broad range, the influence of resonance is limited.

Several solutions have been presented in light of the research that has been conducted in the area, with the goal of improving the efficiency of energy capture in vibrational systems, one of which is known as multimodal [12]. The multimodal method offers the use of multiple beams in order to better use the system's natural frequencies of oscillation. The multimodal solution has the effect of keeping the system in extended resonance over a greater range of excitation frequency.

In terms of the system's excitation forms, various studies have been discovered in which periodic excitation sources, i.e., those that repeat throughout time, are utilized. The angular frequency values of these sources are modified for this sort of analysis in order to achieve system resonance and maximum energy capture for the selected parameters. Non-ideal sources, on the other hand, are provided as a novel suggestion for vibrational systems [13]. The essential feature of this sort of excitation is that the source sends energy to the system, and the system's dynamic reaction influences the source's action. Non-ideal systems are those in which the energy source interacts with the system, and the source is referred to as a non-ideal source [14]. Non-ideal sources include brushed DC electric motors, induction motors, drives with dissipative couplings or any type of load-dependent slip, and so on [15, 16].

The usage of controllers is an additional option to what has been presented thus far that tries to improve the efficiency of energy harvesting devices. As stated in the previous works [1, 10], the majority of the vibration in the environment exhibits random behavior, fluctuating throughout a wide frequency band and exhibiting low power. Ideal Control is provided in a recent paper [17] as the most promising option for improving the efficiency of piezoelectricity-based energy harvesting devices through active control.

Furthermore, given that real systems have dimensional limits and are subject to constitutional fluctuations, the application of Uncertain Parameters theory is recommended. Uncertainties are variations in the physical properties of the parts of a dynamic system that cause changes in the natural frequencies of vibration and influence how the non-ideal source behaves. Uncertainties in the modeling of dynamic systems can be taken into consideration using numerous theories available in the

literature, each with its own practical application. The most popular methods for estimating uncertainties are probabilistic formulations, previously determined intervals, and even the theory of possibilities [18–22].

## 2 Objectives

This chapter presents the application of contemporary control theory to an energy harvesting system with piezoelectric-mechanical coupling subjected to non-ideal excitation and operating with Uncertain Parameters using a Linear Quadratic Regulator.

## 3 Methodology

The goal of this chapter is to investigate the energy harvesting system with non-ideal excitation depicted in Fig. 1.

A multimodal mass-spring-damper system is coupled to an energy transducer (piezoelectric ceramics) that endures non-ideal excitation in the energy harvesting system. The system consists of two masses ( $m_1$  and  $m_2$ ) connected by springs ( $k_1$  and  $k_2$ ) and dampers; an unbalancing mass ( $m_0$ ) joined to the shaft of a DC motor by a fixed-length rod ( $r$ ); and a sensor ( $\nu$ ) responsible for converting mechanical energy into electrical energy. The displacements of the masses ( $x_1$  and  $x_2$ ), the angular displacement ( $z$ ) of the non-ideal source, and the voltage collected ( $\nu$ ) by the transducer are the temporal quantities.

The multimodal solution entails the use of multiple beams, which have varied natural frequencies as a result. The stiffness varies with the mass and length of the beam, but the damping remains constant because the material employed in each beam is the same.

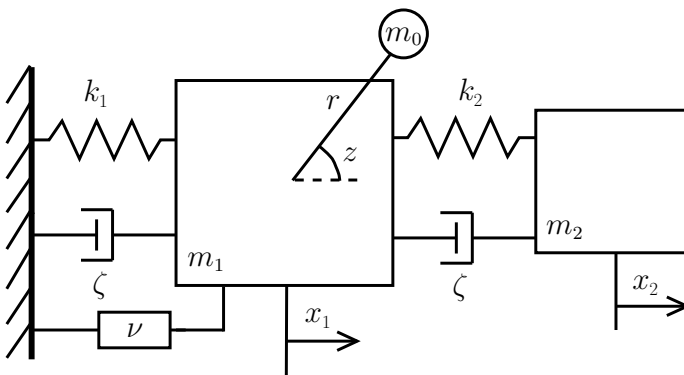


Fig. 1 Energy harvesting model with non-ideal excitation

The non-ideal vibration produced by the unbalanced mass produces changes in the system's behavior. There will be a vibrational reaction, and the piezoelectric ceramic will be distorted, generating an electric current due to the piezoelectric ceramic's physical qualities.

### 3.1 Mathematical Description

A non-dimensional mathematical description of the model shown in Fig. 1 is represented by the system of Eqs. 1 [12, 23].

$$\begin{aligned}
 \ddot{x}_1 + 2\zeta \dot{x}_1 + k_1 x_1 - k_2(x_1 - x_2) - \chi v &= d(\dot{z}^2 \cos z + \ddot{z} \sin z) \\
 \ddot{x}_2 + 2\zeta \dot{x}_2 - k_2(x_1 - x_2) &= 0 \\
 \ddot{z} + b\dot{z} &= r\ddot{x}_1 \sin z + a \\
 \dot{v} + \Lambda v + \kappa(\dot{x}_1 - \dot{x}_2) &= 0
 \end{aligned} \tag{1}$$

where  $\zeta$  is the mass damping factor,  $\chi$  is the piezoelectric-mechanical coupling rate,  $\Lambda$  is the reciprocal of the capacitive loading time constant,  $k_1$  and  $k_2$  are the stiffness rates, and  $\kappa$  is the piezoelectric-electric coupling rate. For the non-ideal source,  $d$  is the eccentricity rate of the unbalanced mass and  $a$  and  $b$  are the rates of net torque resistance by the moment of inertia of the DC motor. The time dependent variables are  $x$  for the displacement of the beam;  $v$  for voltage output rate; and  $z$  for the rate of the angular position of the mass  $m_0$  [12].

A state space is thus defined, presented in the system of Eqs. 2.

$$\begin{aligned}
 \dot{y}_1 &= y_2 \\
 \dot{y}_2 &= \frac{-2\zeta y_2 - k_1 y_1 + k_2(y_1 - y_3) + \chi y_7 + d(y_6^2 \cos y_5 - b y_6 \sin y_5 + a \sin y_5)}{1 - dr \sin^2 y_5} \\
 \dot{y}_3 &= y_4 \\
 \dot{y}_4 &= -2\zeta y_4 + k_2(y_1 - y_3) \\
 \dot{y}_5 &= y_6 \\
 \dot{y}_6 &= \frac{-b y_6 + a + r \sin y_5 [-2\zeta y_2 - k_1 y_1 + k_2(y_1 - y_3) + \chi y_7 + y_6^2 d \cos y_5]}{1 - dr \sin^2 y_5} \\
 \dot{y}_7 &= -\Lambda y_7 - \kappa(y_2 - y_4)
 \end{aligned} \tag{2}$$



### 3.2 Optimal Control—Linear Quadratic Regulator (LQR)

The development of the Optimal Control design is mainly based on previous works [24–29]. A controlled system is governed by Eq. 3, in which  $y \in \mathbf{R}^n$  is a state vector,  $\mathbf{A} \in \mathbf{R}^{n \times n}$  is a parameter matrix (Jacobian matrix),  $\mathbf{B} \in \mathbf{R}^{n \times m}$  is a constant matrix responsible for defining which state variables will be controlled and  $\mathbf{u} \in \mathbf{R}^m$  is the control vector, whose solution has the form presented by Eq. 4, in which  $\mathbf{K}$  is the state feedback vector.

$$\dot{y} = \mathbf{A}y + \mathbf{B}u \quad (3)$$

$$\mathbf{u} = -\mathbf{K}y \quad (4)$$

Substituting Eq. 4 into Eq. 3 gives the new controlled system, and is shown in Eq. 5.

$$\dot{y} = (\mathbf{A} - \mathbf{B}\mathbf{K})y \quad (5)$$

Defining  $\mathbf{A}$ ,  $\mathbf{B}$ ,  $\mathbf{Q}$  and  $\mathbf{R}$  as constant matrices, the positive definite matrix  $\mathbf{P}$  is obtained by solving the nonlinear algebraic Riccati equation, shown in Eq. 6. With  $\mathbf{P}$  obtained, the feedback vector  $\mathbf{K}$  presented in Eq. 7 can be calculated.

$$PA + A^T P - PBR^{-1}B^T P + Q = 0 \quad (6)$$

$$\mathbf{K} = \mathbf{R}^{-1}\mathbf{B}^T\mathbf{P} \quad (7)$$

With the feedback vector  $\mathbf{K}$ , the system can be controlled by the Linear Quadratic Regulator (LQR).

### 3.3 Uncertain Parameters

The uncertain parameters were defined from a deviation of 20% from the mean value. The random function used in MATLAB<sup>®</sup> has variation between 0 and 1, so the Eq. 8 is used in order to get around this computational limitation, where  $\beta$  is the mean parameter to be transformed,  $\beta$  is the uncertain parameter, and  $r(t)$  is the random function with normal distribution. We use modulus over the equation to avoid negative values, as presented below.

$$\beta_u = |0.8 \times \beta + 0.4 \times \beta \times r(t)| \quad (8)$$

### 3.4 Dimensionless Generated Power

The dimensionless power generated in RMS ( $\Phi$ ) is calculated by dividing the output voltage rate squared ( $v^2$ ) by the electrical resistance rate ( $\Psi$ ), as presented by Eq. 9. An electrical resistance rate  $\Psi = 0.1$  was used [12, 23].

$$\Phi = (v_{rms}^2 / \Psi) \tag{9}$$

## 4 Results and Discussion

For all cases, the same initial conditions and the same average parameters were used. Only damping ratio was changed in order to modify the system stability: based on Second Lyapunov Method,  $\zeta = 0.3$  was labeled as stable case and  $\zeta = 0.1 + \text{LQR}$  was labeled as controlled case. In this way, a comparison of the power generated by the systems is encouraged.

### 4.1 Setting Parameters and Initial Conditions

The Table 1 presents the average parameters and Table 2 presents the initial conditions used for the numerical solution of the system. Both the parameters and the initial conditions were chosen arbitrarily.

The next step was to choose the LQR control parameters in such a way that there was the minimum effort just for the systems to undergo translation from an unstable to a stable orbit. The choice of the matrices **Q** and **R**, presented in Eq. 10, were made with the objective of stabilizing the system at the initial instant  $t = t_0$ .

**Table 1** Average parameters

$\chi$	$\kappa$	$\Lambda$	$k_1$	$k_2$	a	b	d	r
1.3	1.07	1.1	0.3	0.2	1.2	0.8	0.5	1

**Table 2** Initial conditions

y1(0)	y2(0)	y3(0)	y4(0)	y5(0)	y6(0)	y7(0)
1.2	0	0.8	0	0	0	0

$$Q = \begin{pmatrix} 0.01 & 0 & 0 & 0 & 0 & 0 & 0 \\ 0 & 0.01 & 0 & 0 & 0 & 0 & 0 \\ 0 & 0 & 0.01 & 0 & 0 & 0 & 0 \\ 0 & 0 & 0 & 0.01 & 0 & 0 & 0 \\ 0 & 0 & 0 & 0 & 0.01 & 0 & 0 \\ 0 & 0 & 0 & 0 & 0 & 0.01 & 0 \\ 0 & 0 & 0 & 0 & 0 & 0 & 0.01 \end{pmatrix}, R = [5] \quad (10)$$

The matrix  $\mathbf{Q}$  has the characteristic of pondering the effects of minimization on the states, and the matrix  $\mathbf{R}$  has the characteristic of pondering the effects of minimization on the input.

The values on the diagonal of  $\mathbf{Q}$  represent the “penalty” that will be used for each of the state variables, in such a way that it dictates how fast it is necessary to reach the desired trajectory during control. The matrix term  $\mathbf{R}$  is related to the energy that will be used in the controller: if  $\mathbf{R}$  is large, it means that the control uses less energy and requires less of the components responsible for the control, if  $\mathbf{R}$  is smaller, it means that the control uses more energy and requires more of the components responsible for the control.

Basically, choosing a large value for  $\mathbf{R}$  means stabilizing the system with less energy. On the other hand, choosing a small value for  $\mathbf{R}$  means that you do not want to penalize the control signal. Similarly, if you choose a small value for  $\mathbf{Q}$ , it means that you try to stabilize the system with as few changes in states as possible, and a large  $\mathbf{Q}$  implies more concern about changes in states. You can choose a large  $\mathbf{R}$  if there is a limit on the controller output signal (for example, if the control signals introduce noise from the sensor or cause saturation of the actuator) and choose a small  $\mathbf{R}$  if a large control signal is not a problem for the system.

## 4.2 Action of Control

The matrix  $\mathbf{A}$  changes at each infinitesimal interval of numerical integration due to the presence of the Uncertain Parameters. The action of control LQR was set for every 1 second: in each step, the controllability matrix of the system is calculated for each input matrix  $\mathbf{B}$ , obtained using a loop-implemented binary counter in order to obtain a combination between zeros and ones. Subsequently, as a definition, all results that corresponded to a rank of the controllability matrix equal to the system dimension ( $n = 7$ ) were obtained, and these cases were classified as controllable. Among these cases, the one with the highest controllability value was chosen and, using LQR function (fed by the matrices  $\mathbf{A}$ ,  $\mathbf{B}$ ,  $\mathbf{Q}$  and  $\mathbf{R}$ ), the gain matrix  $\mathbf{K}$  is calculated, obtaining, finally, the matrix with state feedback ( $\mathbf{A} - \mathbf{BK}$ ).

The system is re-evaluated, taking advantage of the pre-stored values of  $\mathbf{B}$  and  $\mathbf{K}$  and receives new input vectors ( $\mathbf{B}$ ) and, as a consequence, a new gain matrix ( $\mathbf{K}$ ) generating a new state feedback matrix ( $\mathbf{A} - \mathbf{BK}$ ). This progressive control action

during the entire evaluated period guarantees that the system remains stable even if, at some point, the uncertain parameters cause the Jacobian matrix to suffer instability. The choice of control action every 1 second is based directly on minimizing the computational effort during the numerical solution of the system, as could be observed through several tests throughout the simulations.

### 4.3 Phase Planes

Two cases were analyzed using the methods described above: when  $\zeta = 0.3$  (stable case) and when  $\zeta = 0.1$  (unstable case) applying LQR control action.

Figures 2 and 3 show the phase planes for when  $\zeta = 0.3$  for both masses and for the output voltage, respectively.

It can be seen from Fig. 2 that masses present stabilized orbits after the transient period for both the displacement and velocity. Even with the uncertain parameters, the orbit of the velocity displacement remained practically closed, with very minor disturbances due to parameter changes as a function of time. Figure 3 shows the voltage as a stabilized orbit with energy generation due to the AC characteristic, as expected from the energy harvester.

Figures 4 and 5 show the controlled phase planes for when  $\zeta = 0.1$  for both masses and for the output voltage, respectively.

It can be seen from Fig. 4 that mass presents stabilized orbits after the transient period for both the displacement and velocity. The system was already unstable before the inclusion of the uncertain parameters, and the dynamic behavior of the system would be greatly influenced. In this sense, the control action via LQR was

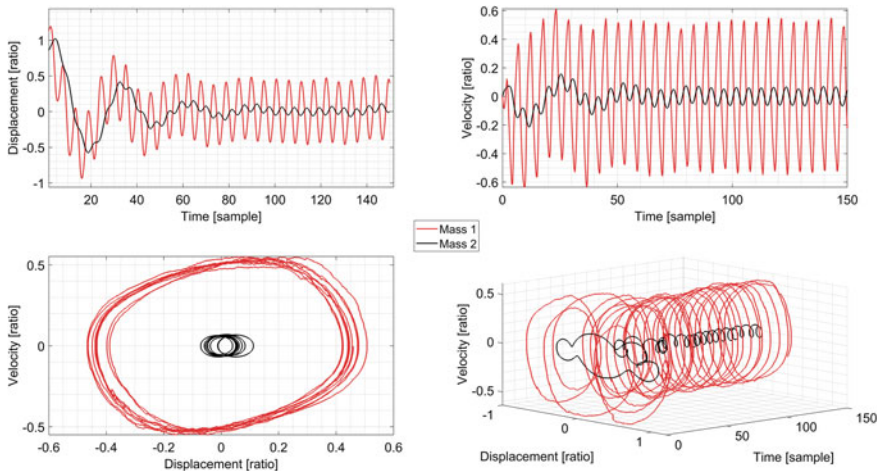


Fig. 2 Phase planes of Mass 1 and Mass 2 when  $\zeta = 0.3$

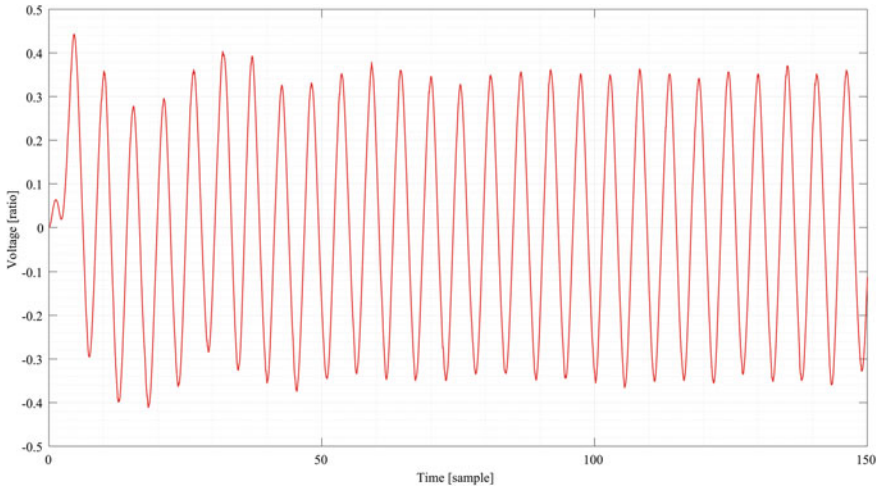


Fig. 3 Phase plane of output voltage when  $\zeta = 0.3$

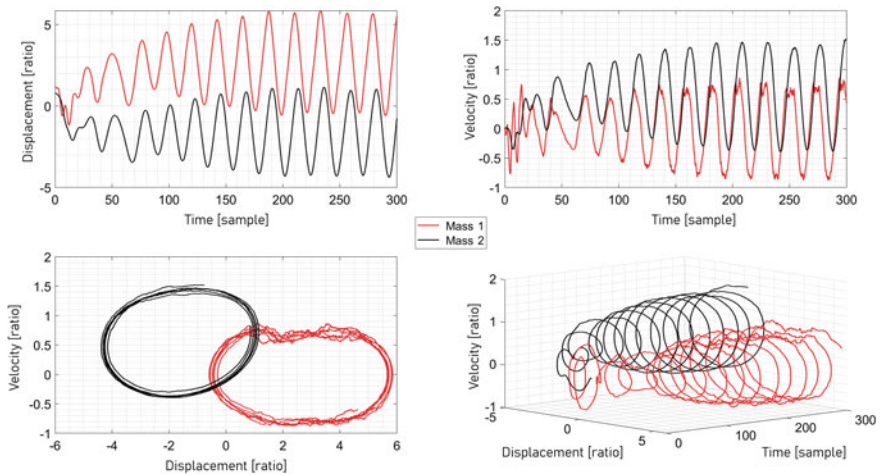
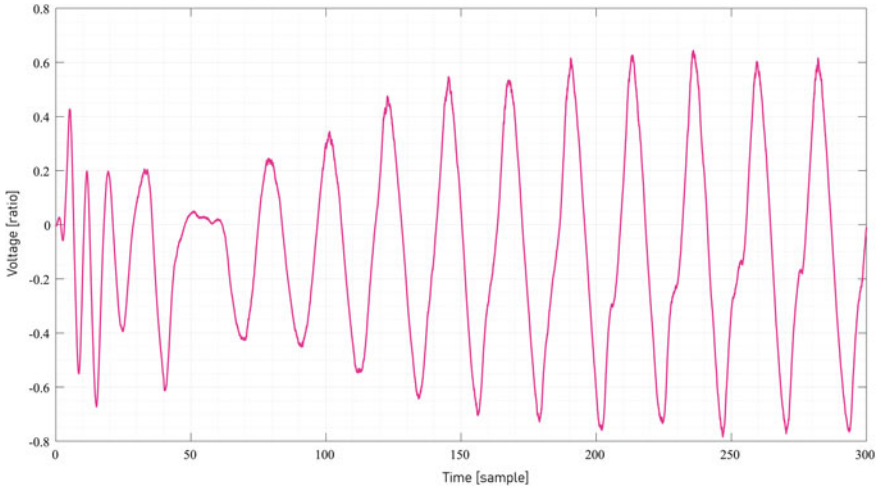


Fig. 4 Controlled phase planes of Mass 1 and Mass 2 when  $\zeta = 0.1$

critical in order to achieve a controlled system that still generates energy. The goal was to stabilize the orbit rather than to bring it to equilibrium. Figure 5 shows the voltage as a stabilized orbit after a large transient period; however, it can be seen that the system generates energy, which was the main objective. It reinforces the effective use of a control action that, while reducing computational effort, is able to stabilize a nonlinear dynamic system.



**Fig. 5** Controlled phase plane of output voltage when  $\zeta = 0.1$

**Table 3.** Dimensionless generated powers

Case	$\zeta$	$\Phi$
Stable	0.3	0.5883
Controlled	0.1	0.7235

Finally, Table 3 presents the generated powers for all the cases studied in this chapter. The dimensionless power generated by the harvesting system is obtained from Eq. 9.

## 5 Conclusions

The addition of uncertain parameters to the energy harvesting system with non-ideal excitation source combined with the application of control increases the computational effort required to simulate the system.

Initially, when it was determined to control only once and based on average parameters and initial conditions, the results achieved were not adequate, owing to the difficulties in regulating systems with uncertain parameters. Because the Jacobian matrix is always changing, it was decided to apply the control technique at each short iteration of  $10^{-5}$  seconds; however, in practice, a controller with such a high actuation frequency does not exist. Finally, it was agreed that the control should be applied every 1 second, which resulted in a significant reduction in processing effort.

It can be concluded that, when using the same parameters and initial conditions varying only the damping rate, which is a critical parameter, the tendency is that unstable systems present an advantage in relation to energy harvesting when

compared to the stable system. But building an unstable system is impossible, given its uncertainty over time. By applying active control on such energy harvesting systems operating with non-ideal sources, it was possible to correct the unstable orbits to stable ones in addition to optimizing the energy harvesting when compared to the stable system. Control will always be beneficial since, in addition to stabilizing the system and permitting its construction, it maximizes energy harvesting in respect to the stable system.

## References

1. Tang, L., Yang, Y., Soh, C.K.: Broadband vibration energy harvesting techniques. In: *Advances in Energy Harvesting Methods*, pp. 17–61. Springer (2013)
2. Youngsman, J.M., Luedeman, T., Morris, D.J., Anderson, M.J., Bahr, D.F.: A model for an extensional mode resonator used as a frequency-adjustable vibration energy harvester. *J. Sound Vib.* **329**(3), 277–288 (2010)
3. Schlichting, A., Fink, E., Garcia, E.: A low-loss hybrid rectification technique for piezoelectric energy harvesting. *Smart Mater. Struct.* **22** (9), 095028 (2013)
4. Challa, V.R., Prasad, M., Shi, Y., Fisher, F.T.: A vibration energy harvesting device with bidirectional resonance frequency tenability. *Smart Mater. Struct.* **17**(1), 015035 (2008)
5. Wu, W.-J., Chen, Y.-Y., Lee, B.-S., He, J.-J., Peng, Y.-T.: Tunable resonant frequency power harvesting devices. In: *Smart Structures and Materials 2006: Damping and Isolation*, vol. 6169, p. 61690A. International Society for Optics and Photonics (2006)
6. Sari, I., Balkan, T., Kulah, H.: An electromagnetic micro power generator for wideband environmental vibrations. *Sens. Actuators A Phys.* **145**, 405–413 (2008)
7. Eichhorn, C., Goldschmidtboeing, F., Porro, Y., Woias, P.: A piezoelectric harvester with an integrated frequency-tuning mechanism. *Power MEMS*, 45–48 (2009)
8. Van Blarigan, L., Danzl, P., Moehlis, J.: A broadband vibrational energy harvester. *Appl. Phys. Lett.* **100**(25), 253904 (2012)
9. Liu, J.-Q., Fang, H.-B., Xu, Z.-Y., Mao, X.-H., Shen, X.-C., Chen, D., Liao, H., Cai, B.-C.: A mems-based piezoelectric power generator array for vibration energy harvesting. *Microelectron. J.* **39**(5), 802–806 (2008)
10. Harné, R.L., Wang, K.: A review of the recent research on vibration energy harvesting via bistable systems. *Smart Mater. Struct.* **22**(2), p. 023001 (2013)
11. Jung, H.-J., Kim, I.-H., Min, D.Y., Sim, S.-H., Koo, J.-H.: A hybrid electro-magnetic energy harvesting device for low frequency vibration. In: *Active and Passive Smart Structures and Integrated Systems 2013*, vol. 8688, p. 86881I. International Society for Optics and Photonics (2013)
12. Ferreira, D.C., Chavarette, F.R., De Almeida, L.R., De Souza, R.S., Lima, L.P.M.: Multimodal energy harvesting efficiency enhancement via linear matrix inequalities control driven. In: *Proceeding Series of the Brazilian Society of Computational and Applied Mathematics*, vol. 4, no. 1 (2016)
13. Kononenko, V.O.: *Vibrating Systems with a Limited Power Supply*. Iliffe (1969)
14. Nayfeh and Mook: *Nonlinear oscillations* (1979)
15. Balthazar, J.M., Mook, D.T., Weber, H.I., Brasil, R.M., Fenili, A., Belato, D., Felix, J.: An overview on non-ideal vibrations. *Meccanica* **38**(6), 613–621 (2003)
16. Cveticanin, L., Zukovic, M., Balthazar, J.M.: *Dynamics of Mechanical Systems with Non-ideal Excitation*. Springer (2018)
17. Wang, Y., Inman, D.J.: A survey of control strategies for simultaneous vibration suppression and energy harvesting via piezoceramics. *J. Intell Mater. Syst. Struct.* **23**(18), 2021–2037 (2012)

18. Chavarette, F.R.: Optimal linear control to parametric uncertainties in a micro electro mechanical system. *Int. J. Pure Appl. Math.* **83**(4), 539–548 (2013)
19. Didier, J., Faverjon, B., Sinou, J.-J.: Analysing the dynamic response of a rotor system under uncertain parameters by polynomial chaos expansion. *J. Vib. Control* **18**(5), 712–732 (2012)
20. Moffat, R.J.: Describing the uncertainties in experimental results. *Exp. Therm. Fluid Sci.* **1**(1), 3–17 (1988)
21. M'oller, B., Beer, M.: *Fuzzy Randomness: Uncertainty in Civil Engineering and Computational Mechanics*. Springer Science & Business Media (2004)
22. Peruzzi, N., Chavarette, F.R., Balthazar, J.M., Tusset, A.M., Peticarrari A.L.P.M., Brasil, R.: The dynamic behavior of a parametrically excited time- periodic mems taking into account parametric errors. *J. Vib. Control* **22**(20), 4101–4110 (2016)
23. Erturk, A., Inman, D.J.: Broadband piezoelectric power generation on high- energy orbits of the bistable duffing oscillator with electromechanical coupling. *J. Sound Vib.* **330**, 2339–2353 (2011)
24. Rafikov, M., Balthazar, J.M.: Optimal pest control problem in population dynamics. *Comput. Appl. Math.* **24**(1), 65–81 (2005)
25. Chavarette, F.R., Balthazar, J.M., Rafikov, M., Hermini, H.A.: On non- linear dynamics and an optimal control synthesis of the action potential of membranes (ideal and non-ideal cases) of the hodgkin–huxley (hh) mathematical model. *Chaos Solitons Fractals* **39**(4), 1651–1666 (2009)
26. Chavarette, F.R., Balthazar, J.M., Peruzzi, N.J., Rafikov, M.: On non- linear dynamics and control designs applied to the ideal and non-ideal variants of the fitzhugh–nagumo (fn) mathematical model. *Commun. Nonlinear Sci. Numer. Simul.* **14**(3), 892–905 (2009)
27. Ferreira, D.C., Chavarette, F.R., Peruzzi, N.J.: Linear matrix inequalities control driven for non-ideal power source energy harvesting. *J. Theor. Appl. Mech.* **53**(3), 605–616 (2015)
28. da Costa Ferreira, D., Chavarette, F.R., Peruzzi, N.J.: Optimal linear control driven for piezoelectric non-linear energy harvesting on non-ideal excitation sourced. In: *Advanced Materials Research*, vol. 971, pp. 1107–1112. rans Tech Publications Ltd. (2014)
29. da Costa Ferreira, D., Chavarette F.R., Peruzzi, N.J.: Non-linear energy harvesting system efficiency comparison from periodic to non-ideal excitation. *Int. J. Pure Appl. Math.* **92**(5), 745–755 (2014)



# A Hybrid PID-LQR Control Applied in Positioning Control of Robotic Manipulators Subject to Excitation from Non-ideal Sources



A. M. Tusset , J. J. De Lima , F. C. Janzen , P. L. Paula Filho ,  
J. A. G. Luz Junior , Jose Manoel Balthazar , and A. Kossoski 

**Abstract** This paper proposes the use of a hybrid controller that combines concepts of the Proportional-Integral-Derivative (PID) controller with the Linear-Quadratic-Regulator (LQR) and a Feedforward gain to control the positioning of a 2 DOF robotic arm with flexible joints. As the joints are flexible, there is in this system a non-ideal coupling between the links of the robotic arm, where the angular movement of one link can generate oscillations that spread and impact the response of the system. The non-ideal excitation source originates from the coupling between the electric motor used to move the link of the robotic arm with the flexible element of the structure. These mechanical oscillations interfere in the positioning of the motor, and thus in the electrical power consumed by the system. In the results section of this work, numerical simulations are used to show the functionality and performance of the proposed controller in the studied system.

**Keywords** Non-ideal systems · Feedforward control · PID control · LQR control · Robotic manipulators

## 1 Introduction

Controlling robotic manipulators with two Degrees of Freedom (DOF) is considered a classical control problem, this being a class of systems that has always attracted the interest of researchers due to the wide industrial use of this type of machine. Thus, one can observe many control strategies proposed for this kind of system [1, 2]. In [3], they proposed a combination of Sliding Mode Control (SMC) and PID

---

A. M. Tusset (✉) · J. J. De Lima · F. C. Janzen · P. L. P. Filho  
Federal University of Technology-Paraná, Paraná, Brazil

F. C. Janzen  
e-mail: [fcjanzen@utfpr.edu.br](mailto:fcjanzen@utfpr.edu.br)

J. A. G. L. Junior · J. M. Balthazar · A. Kossoski  
Sao Paulo State University-São Paulo, São Paulo, Brazil

control. In [4], the authors proposed a controller based on a self-tuning Fuzzy-PID and SMC control. In [5] the authors presented a robust controller to improve the performance of a 2-DOF robotic arm under disturbance. In [2, 6] the authors used adaptive control for robotic arms. In [7–10] the nonlinear SDRE (State-Dependent Riccati Equation) control is implemented. In [11–13] they used a feedforward gain to improve the performance of a SDRE type controller. In [14] the SDRE control is used in association with a feedforward gain for a robotic system with non-ideal excitation.

This work aims to present the control of position and dynamic behavior of a robotic manipulator with 2 DOF driven by DC electric motors and considering flexible joints. We propose the use a hybrid PID-LQR with Feedforward control both meet the positioning objectives and mitigate the effects caused by the non-ideal vibration.

## 2 Mathematical Model

The model of the manipulator with flexible joints with a non-ideal coupling, illustrated in Fig. 1, consists of two rigid links,  $l_1$  and  $l_2$ , and two flexible joints with flexibility coefficient  $k_s$ . The second link is excited by a DC motor.

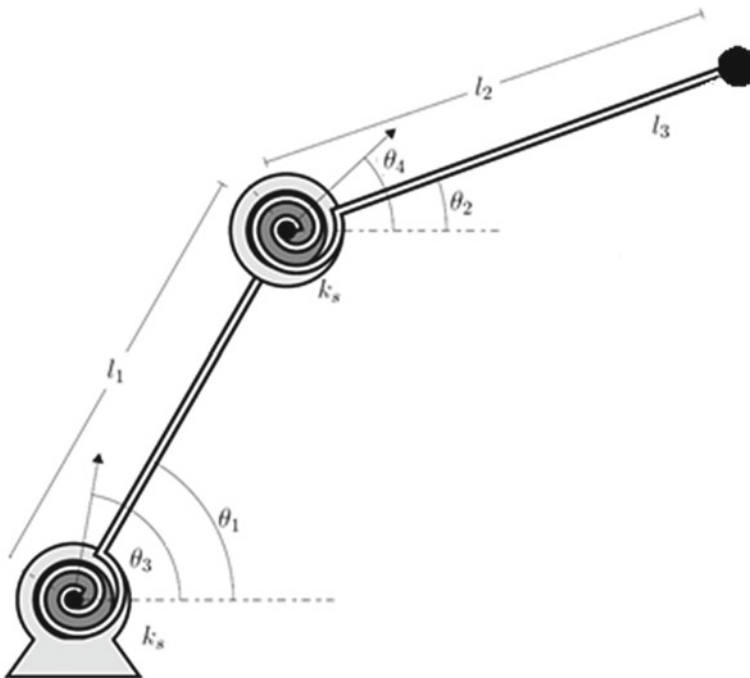


**Fig. 1** Schematic of the manipulator model

The dynamics of the robotic manipulator represented in Fig. 1 can be represented by the following equation [11]:

$$\mathbf{M}\ddot{\boldsymbol{\theta}} + \mathbf{V}\dot{\boldsymbol{\theta}} + k_a\boldsymbol{\theta} + \mathbf{G} = \boldsymbol{\tau} \quad (1)$$

where:  $\mathbf{M}$  is the inertia matrix,  $\mathbf{V}$  is the Coriolis and Centrifugal force matrix,  $k_a$  is the coefficient of friction of the manipulator,  $\mathbf{G}$  is the gravitational matrix and  $\boldsymbol{\tau}$  is the torque. These functions can be represented in the following form:

$$\mathbf{M} = \begin{bmatrix} m_{11} & m_{12} \\ m_{21} & m_{22} \end{bmatrix}, \quad \mathbf{V} = \begin{bmatrix} v_{11} & 0 \\ 0 & v_{22} \end{bmatrix}, \quad \mathbf{G} = \begin{bmatrix} g_{11} \\ g_{21} \end{bmatrix} \text{ and } \boldsymbol{\tau} = \begin{bmatrix} b_s(\dot{\theta}_3 - \dot{\theta}_1) + k(\theta_3 - \theta_1) \\ b_s(\dot{\theta}_4 - \dot{\theta}_2) + k(\theta_4 - \theta_2) \end{bmatrix}.$$

where  $b_s$  is the damping constant,  $k$  is the spring constant, and the other constants are given by:  $v_{11} = -m_2 l_1 l_2 \sin(\theta_2) \dot{\theta}_2$ ;  $v_{21} = -m_2 l_1 l_2 \sin(\theta_2) (2\dot{\theta}_1 + \dot{\theta}_2)$ ,  $g_{11} = -(m_1 + m_2) g l_1 \sin(\theta_1) - m_2 g l_2 \sin(\theta_1 + \theta_2)$ ,  $g_{21} = -m_2 g l_2 \sin(\theta_1 + \theta_2) m_{11} = l_1^2 (m_1 + m_2)$ ,  $m_{21} = m_{12}$ ,  $m_{12} = l_1 l_2 m_2 \cos(\theta_1 - \theta_2)$  and  $m_{22} = l_2^2 m_2$ .

The angular positions of the motor  $\theta_3$  and  $\theta_4$  can be obtained from the following equation [11]:

$$\begin{aligned} J\ddot{\theta}_3 + b_v\dot{\theta}_3 &= k_t i - b_s(\dot{\theta}_3 - \dot{\theta}_1) - k(\theta_3 - \theta_1) \\ J\ddot{\theta}_4 + b_v\dot{\theta}_4 &= k_t i - b_s(\dot{\theta}_4 - \dot{\theta}_2) - k(\theta_4 - \theta_2) \end{aligned} \quad (2)$$

where  $J$  is the motor constant of inertia,  $b_v$  is the rotor damping constant,  $k_t$  is the motor torque constant and  $i$  is the electrical current of the DC motor.

The angular positions of the links  $\theta_1$  and  $\theta_2$  can be obtained from the following equation:

$$\ddot{\boldsymbol{\theta}} = \mathbf{P}(-\mathbf{V}\dot{\boldsymbol{\theta}} - k_a\boldsymbol{\theta} - \mathbf{G} + \boldsymbol{\tau}) \quad (3)$$

where:  $\mathbf{P} = \mathbf{M}^{-1}$ .

Considering the Eqs. (2) and (3), we can obtain the system in the state-space representation:

$$\begin{aligned}
\dot{x}_1 &= x_2 \\
\dot{x}_2 &= -p_{11}kx_1 + \alpha x_2 - p_{12}kx_3 + \beta x_4 + p_{11}kx_5 + p_{11}b_s x_6 + p_{12}kx_7 \\
&\quad + p_{12}b_s x_8 - p_{11}g_1 - p_{12}g_2 \\
\dot{x}_3 &= x_4 \\
\dot{x}_4 &= -p_{21}kx_1 + \gamma x_2 - p_{22}kx_3 + \delta x_4 + p_{21}kx_5 + p_{21}b_s x_6 + p_{22}kx_7 \\
&\quad + p_{22}b_s x_8 - p_{21}g_1 - p_{22}g_2 \\
\dot{x}_5 &= x_6 \\
\dot{x}_6 &= \frac{1}{J}(-kx_1 + b_s x_2 - kx_5 - (b_v + b_s)x_6 + k_t i_1) \\
\dot{x}_7 &= x_8 \\
\dot{x}_8 &= \frac{1}{J}(-kx_3 + b_s x_4 - kx_7 - (b_v + b_s)x_8 + k_t i_2)
\end{aligned} \tag{4}$$

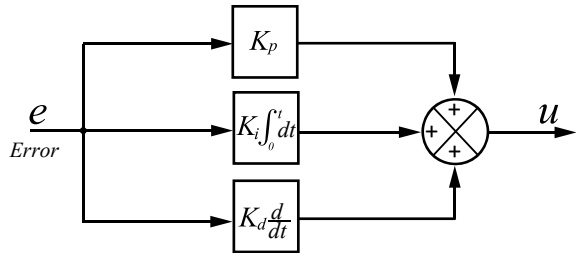
where  $x_1 = \theta_1$ ,  $x_2 = \dot{\theta}_1$ ,  $x_3 = \theta_2$ ,  $x_4 = \dot{\theta}_2$ ,  $x_5 = \theta_3$ ,  $x_6 = \dot{\theta}_3$ ,  $x_7 = \theta_4$ ,  $x_8 = \dot{\theta}_4$ ,  
 $\alpha = -p_{11}(k_a + b_s) - p_{12}c_2$ ,  $\beta = p_{11}c_1 - p_{12}(k_a + b_s)$ ,  $\gamma = -p_{21}(k_a + b_s) - p_{22}c_2$ ,  
 $\delta = -p_{22}(k_a + b_s) - p_{21}c_1$ ,  $p_{11} = \frac{-m_{22}}{-m_{12}m_{21} + m_{11}m_{22}}$ ,  $p_{12} = \frac{-m_{21}}{-m_{12}m_{21} + m_{11}m_{22}}$ ,  $p_{21} = \frac{-m_{12}}{-m_{12}m_{21} + m_{11}m_{22}}$  and  $p_{22} = \frac{-m_{11}}{-m_{12}m_{21} + m_{11}m_{22}}$ .

### 3 Proposed Control

The position control of the motor links and motor shaft is given by the electric current (*i*). Introducing the control of the electric current in the system (4), one will have the following system:

$$\begin{aligned}
\dot{x}_1 &= x_2 \\
\dot{x}_2 &= -p_{11}kx_1 + \alpha x_2 - p_{12}kx_3 + \beta x_4 + p_{11}kx_5 + p_{11}b_s x_6 + p_{12}kx_7 \\
&\quad + p_{12}b_s x_8 - p_{11}g_1 - p_{12}g_2 \\
\dot{x}_3 &= x_4 \\
\dot{x}_4 &= -p_{21}kx_1 + \gamma x_2 - p_{22}kx_3 + \delta x_4 + p_{21}kx_5 + p_{21}b_s x_6 + p_{22}kx_7 \\
&\quad + p_{22}b_s x_8 - p_{21}g_1 - p_{22}g_2 \\
\dot{x}_5 &= x_6 \\
\dot{x}_6 &= \frac{1}{J}(-kx_1 + b_s x_2 - kx_5 - (b_v + b_s)x_6 + k_t U_1) \\
\dot{x}_7 &= x_8 \\
\dot{x}_8 &= \frac{1}{J}(-kx_3 + b_s x_4 - kx_7 - (b_v + b_s)x_8 + k_t U_2)
\end{aligned} \tag{5}$$

**Fig. 2** Block diagram for PID control



where:  $U_i = u_i + \tilde{u}_i$ ,  $u_i$  is the state feedback control, and  $\tilde{u}_i$  is the feedforward control, the last one being composed of terms that depend on the gravitational force  $g$  in the following form [12, 15]:

$$\begin{aligned} \tilde{u}_1 &= p_{11}g_1 + p_{12}g_2 \\ \tilde{u}_2 &= p_{21}g_1 + p_{22}g_2 \end{aligned} \tag{6}$$

The state feedback control is a PID controller, and operates according to the following block diagram (Fig. 2).

Where  $K_p$  is the proportional gain,  $K_d$  is the derivative gain and  $K_i$  is the corresponding integral gain of the control loop, respectively. The errors,  $e_1 = \tilde{x}_1 - x_1$ ,  $e_2 = \tilde{x}_2 - \dot{x}_1$ ,  $e_3 = \tilde{x}_3 - x_3$ ,  $e_4 = \tilde{x}_3 - \dot{x}_3$ ,  $e_5 = \tilde{x}_5 - x_5$ ,  $e_6 = \tilde{x}_5 - \dot{x}_5$ ,  $e_7 = \tilde{x}_7 - x_7$  and  $e_8 = \tilde{x}_7 - \dot{x}_7$ , where  $\tilde{x}_-$  represent the desired states for angular position of the links and the motor shaft.

In this work the LQR control was used to determine the  $K_p$  and  $K_d$  gains, which allows the design of an optimal PD control.

$$\mathbf{K} = \mathbf{R}^{-1}\mathbf{B}^T\mathbf{P} \tag{7}$$

where  $K_p = k_{i,j}$  for  $j = 1, 3, 5, 7, \dots$ ,  $K_d = k_{i,j}$  for  $j = 2, 4, 6, 8, \dots$ , for PD control  $U_i$ . The matrix  $\mathbf{P}$  is obtained by solving the following Riccati equation:

$$\mathbf{A}^T\mathbf{P} + \mathbf{P}\mathbf{A} - \mathbf{P}\mathbf{B}\mathbf{R}^{-1}\mathbf{B}^T\mathbf{P} + \mathbf{Q} = \mathbf{0} \tag{8}$$

The cost function for the control problem for optimal PD control is given by:

$$J = \frac{1}{2} \int_{t_0}^{\infty} (\mathbf{e}^T \mathbf{Q} \mathbf{e} + \mathbf{u}^T \mathbf{R} \mathbf{u}) dt \tag{9}$$

where  $\mathbf{Q}$  and  $\mathbf{R}$  are positive definite matrices.

### 4 Numerical Simulation

The following parameter are used for the numerical simulations [11]:  $m_1 = 1, m_2 = 1, l_1 = 0.8, l_2 = 0.8, g = 9.8, k = 450, b_s = 510, k_a = 6, b_v = 0.02, J = 0.0002, k_t = 0.8$ , along with the initial conditions:  $x_i(0) = 0$ , where  $i = 1:8$ .

Two cases are used in order to analyze the efficiency of the proposed control. In the first case the links are positioned at two fixed points. In the second case, the first link is positioned at a fixed point while the second link is in a rotational movement, representing a motor with unbalanced mass (non-ideal system).

The definite matrices **Q** and **R** and the system matrices **A** and **B** used can be found in the appendix of this paper. The integral gain  $K_i$  is given by: for  $u_1$  ( $K_{i_1} = 2179449.33, K_{i_3} = 224821.58, K_{i_5} = 2280104.28$  and  $K_{i_7} = 21848.79$ ) and for  $u_2$  ( $K_{i_1} = 162457.09, K_{i_3} = 2950790.59, K_{i_5} = 170105.19$  and  $K_{i_7} = 300778.54$ ).

#### 4.1 Position Control for Fixed Points

Considering the desired states:  $\tilde{x}_1 = \tilde{x}_5 = \frac{\pi}{3}, \tilde{x}_3 = \tilde{x}_7 = \frac{\pi}{4}$  and  $\tilde{x}_2 = \tilde{x}_4 = \tilde{x}_6 = \tilde{x}_8 = 0$ . In Fig. 3 we can observe the error in the positioning of the links and the motor shaft considering the case of using only the PD control obtained from the LQR and without using the feedforward control gain and Fig. 4 show the control response with the feedforward control gain.

In Fig. 5 we can observe the error in the positioning of the links and the motor shaft considering the case of using only the PDI control, without using the feedforward control and in Fig. 6 with the feedforward control gain.

Analyzing the numerical results, one can observe that including the feedforward control gain reduced the positioning error of the links and the motor shaft.

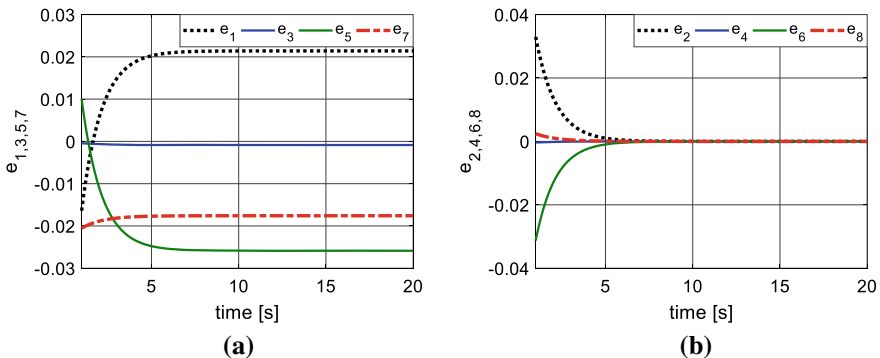


**Fig. 3** Positioning error for PD control without feedforward control. **a** Error for  $\theta_1, \theta_2, \theta_3$  and  $\theta_4$ . **b** Error for  $\theta_1, \theta_2, \theta_3$  and  $\theta_4$

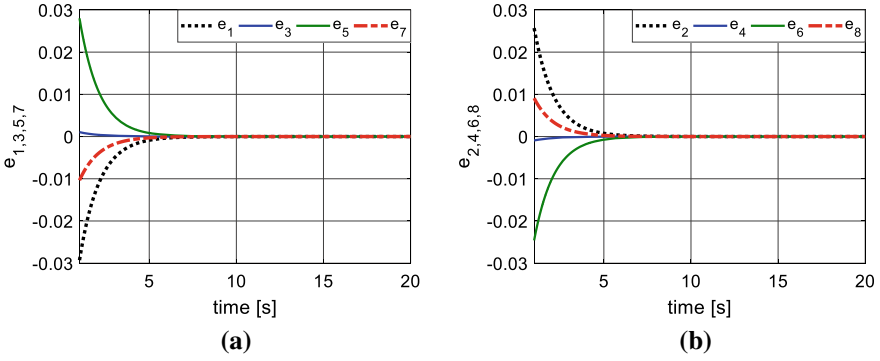


**Fig. 4** Positioning error for PD control with feedforward control. **a** Error for  $\theta_1, \theta_2, \theta_3$  and  $\theta_4$ . **b** Error for  $\dot{\theta}_1, \dot{\theta}_2, \dot{\theta}_3$  and  $\dot{\theta}_4$

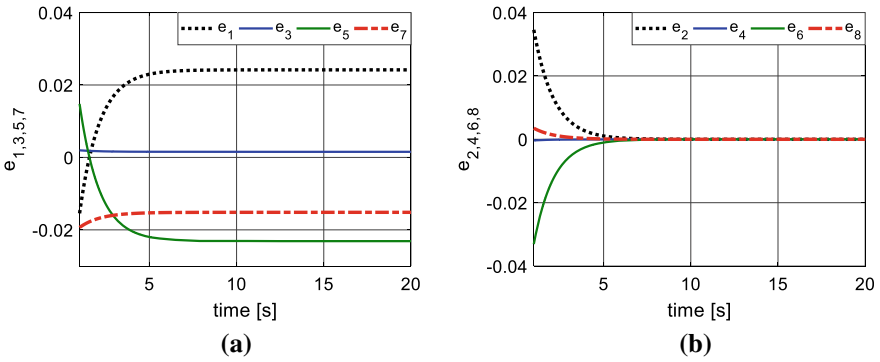


**Fig. 5** Positioning error for PDI control without feedforward control. **a** Error for  $\theta_1, \theta_2, \theta_3$  and  $\theta_4$ . **b** Error for  $\dot{\theta}_1, \dot{\theta}_2, \dot{\theta}_3$  and  $\dot{\theta}_4$

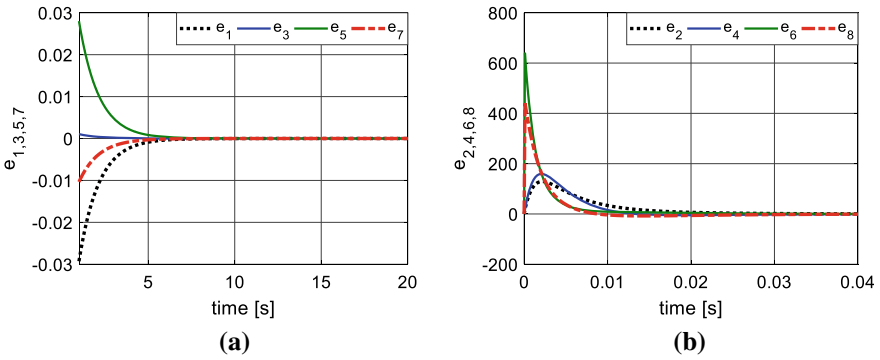


**Fig. 6** Positioning error for PDI control with feedforward control. **a** Error for  $\theta_1, \theta_2, \theta_3$  and  $\theta_4$ . **b** Error for  $\dot{\theta}_1, \dot{\theta}_2, \dot{\theta}_3$  and  $\dot{\theta}_4$

### 4.2 Position Control for a Fixed Points and a Rotational

Considering the desired states:  $\tilde{x}_1 = \tilde{x}_5 = \frac{\pi}{3}, \tilde{x}_3 = \tilde{x}_7 = \sin(t) + t, \tilde{x}_2 = \tilde{x}_6 = 0$  and  $\tilde{x}_4 = \tilde{x}_8 = \cos(t) + 1$ . In Fig. 7 one can observe the error in the positioning of the links and the motor shaft considering the case of using only the PD control obtained from the LQR algorithm, without using the feedforward control, and in Fig. 8 with feedforward control gain.

In Fig. 9 one can observe the error in the positioning of the links and the motor shaft considering the case of using only the PDI control without the feedforward control and in Fig. 10 with the feedforward control gain.

The results show that for the case of position control for the first link in a fixed point and the second in rotational movement, the PD-LQR control without the feedforward control was not efficient, leaving the system unstable. Furthermore, the PID control

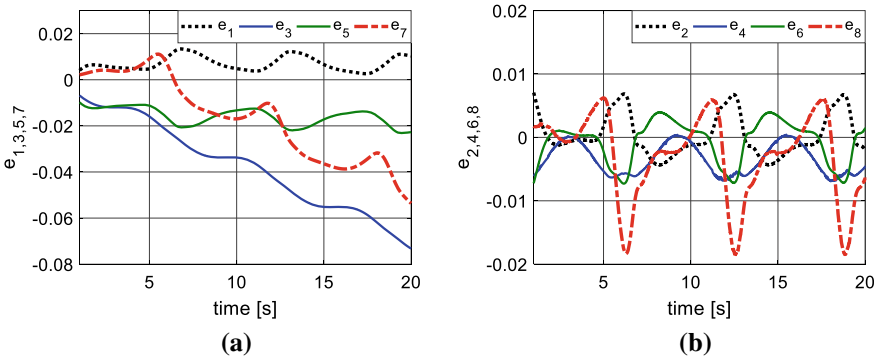


**Fig. 7** Positioning error for PD control without feedforward control. **a** Error for  $\theta_1, \theta_2, \theta_3$  and  $\theta_4$ . **b** Error for  $\dot{\theta}_1, \dot{\theta}_2, \dot{\theta}_3$  and  $\dot{\theta}_4$

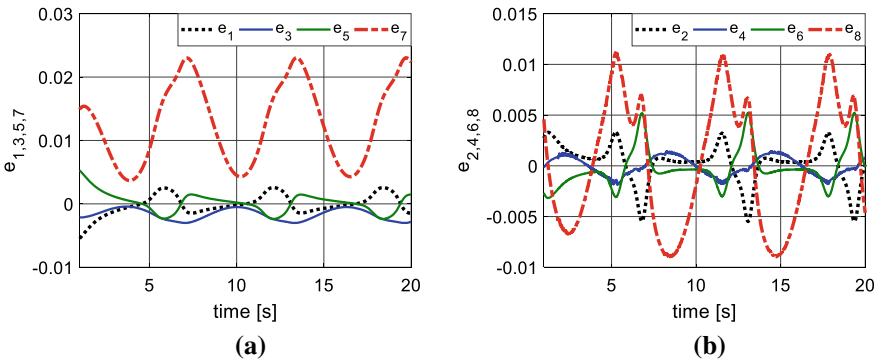


**Fig. 8** Positioning error for PD control with feedforward control. **a** Error for  $\theta_1, \theta_2, \theta_3$  and  $\theta_4$ . **b** Error for  $\dot{\theta}_1, \dot{\theta}_2, \dot{\theta}_3$  and  $\dot{\theta}_4$



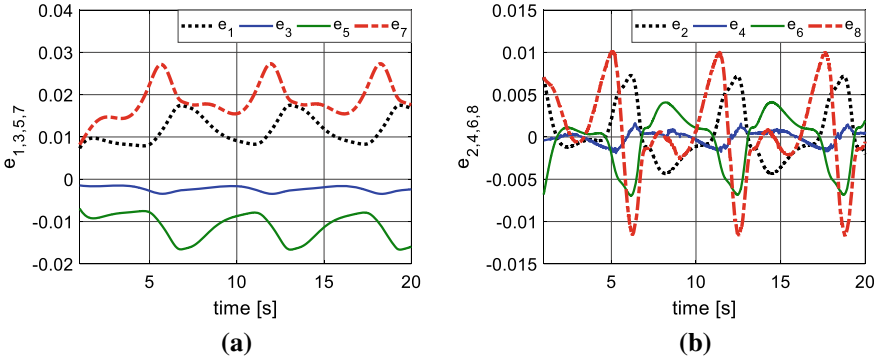


**Fig. 9** Positioning error for PID control without feedforward control. **a** Error for  $\theta_1, \theta_2, \theta_3$  and  $\theta_4$ . **b** Error for  $\dot{\theta}_1, \dot{\theta}_2, \dot{\theta}_3$  and  $\dot{\theta}_4$

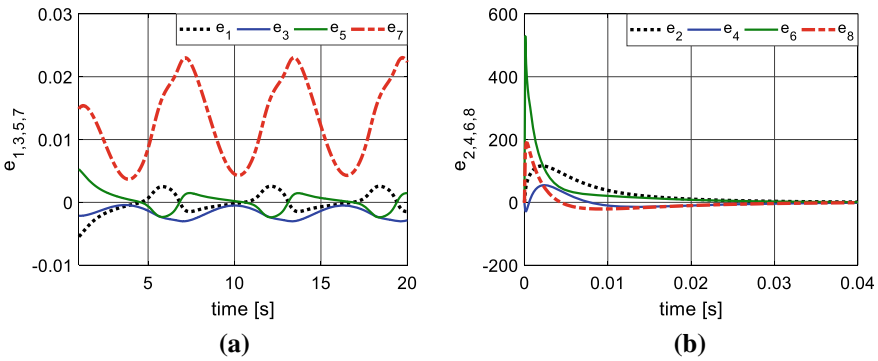


**Fig. 10** Positioning error for PID control with feedforward control. **a** Error for  $\theta_1, \theta_2, \theta_3$  and  $\theta_4$ . **b** Error for  $\dot{\theta}_1, \dot{\theta}_2, \dot{\theta}_3$  and  $\dot{\theta}_4$

versions demonstrated efficiency, controllability and low error, where this last feature is further improved with the inclusion of the feedforward gain.

## 5 Conclusions

The numerical results presented in this paper show that we can consider a robotic arm with flexible joints as a system with non-ideal excitation sources. This behavior was more clear with one link being in rotational movement, a behavior similar to that observed when we couple a motor to the end of the first link. The numerical results showed that the combination of the PID control is the most suitable for cases where the links are subject to rotational movement (vibration), and that the PD and LQR control demonstrates efficiency only when combined with the feedforward gain.

## Appendix

$$\mathbf{Q} = \begin{bmatrix} 10^7 & 0 & 0 & 0 & 0 & 0 & 0 & 0 & 0 \\ 0 & 1 & 0 & 0 & 0 & 0 & 0 & 0 & 0 \\ 0 & 0 & 10^7 & 0 & 0 & 0 & 0 & 0 & 0 \\ 0 & 0 & 0 & 1 & 0 & 0 & 0 & 0 & 0 \\ 0 & 0 & 0 & 0 & 10^7 & 0 & 0 & 0 & 0 \\ 0 & 0 & 0 & 0 & 0 & 1 & 0 & 0 & 0 \\ 0 & 0 & 0 & 0 & 0 & 0 & 10^7 & 0 & 0 \\ 0 & 0 & 0 & 0 & 0 & 0 & 0 & 0 & 1 \end{bmatrix}, \mathbf{B} = \begin{bmatrix} 0 & 0 \\ 0 & 0 \\ 0 & 0 \\ 0 & 0 \\ 0 & 0 \\ \frac{k_f}{J} & 0 \\ 0 & 0 \\ 0 & \frac{k_f}{J} \end{bmatrix},$$

$$\mathbf{A} = \begin{bmatrix} 1 & 0 & 0 & 0 & 0 & 0 & 0 & 0 & 0 \\ -kp_{11} & \alpha & -kp_{12} & \beta & kp_{11} & b_s p_{11} & kp_{12} & b_s p_{12} & \\ 0 & 0 & 1 & 0 & 0 & 0 & 0 & 0 & 0 \\ -kp_{21} & \gamma & -kp_{22} & \delta & kp_{21} & b_s p_{21} & kp_{22} & b_s p_{22} & \\ 0 & 0 & 0 & 0 & 0 & 1 & 0 & 0 & \\ \frac{-k}{J} & \frac{b_s}{J} & 0 & 0 & \frac{-k}{J} & \frac{-(b_s+b_v)}{J} & 0 & 0 & \\ 0 & 0 & 0 & 0 & 0 & 0 & 1 & 0 & \\ 0 & 0 & \frac{-k}{J} & \frac{b_s}{J} & 0 & 0 & \frac{-k}{J} & \frac{-(b_s+b_v)}{J} & \end{bmatrix}$$

$$\mathbf{R} = \begin{bmatrix} 10^{-2} & 0 \\ 0 & 10^{-2} \end{bmatrix},$$

and

$$\mathbf{K} = \begin{bmatrix} 21250.11 & 3008.71 & -21760.09 & -993.00 & 222386.01 & 1.50 & -2111.67 & 0.31 \\ 15721.43 & -925.88 & 289671.93 & 1925.28 & 16458.92 & 0.31 & 30071.57 & 1.70 \end{bmatrix}$$

## References

1. Wang, Y.N., Mai, T.L., Mao, J.X.: Adaptive motion/force control strategy for non-holonomic mobile manipulator robot using recurrent fuzzy wavelet neural networks. *Eng. Appl. Artif. Intell.* **34**, 137–153 (2014)
2. Rad, S.A., Tamizi, M.G., Mirfakhar, A., Masouleh, M.T., Kalhor, A.: Control of a two-DOF parallel robot with unknown parameters using a novel robust adaptive approach. *ISA Trans.* **117**, 70–84 (2021)
3. Zakia, U., Moallem, M., Menon, C.: PID-SMC controller for a 2-DOF planar robot. In: 2019 International Conference on Electrical, Computer and Communication Engineering. IEEE, pp. 1–5 (2019)
4. Van, M., Do, X.P., Mavrouniotis, M.: Self-tuning fuzzy PID-nonsingular fast terminal sliding mode control for robust fault tolerant control of robot manipulators. *ISA Trans.* **1**, 1–12 (2019)
5. Guo, Q., Yu, T., Jiang, D.: Robust H positional control of 2-DOF robotic arm driven by electro-hydraulic servo system. *ISA Trans* **59**, 55–64 (2015)

6. Yang, S., Han, J., Xia, L., Chen, Y-H.: An optimal fuzzy-theoretic setting of adaptive robust control design for a lower limb exoskeleton robot system. *Mech. Syst. Signal Process.* **141**, 06706 (2020)
7. Korayem, M.H., Irani, M., Nekoo, S.R.: Analysis of manipulators using SDRE: a closed loop nonlinear optimal control approach. *Scientia Iranica. Trans. B Mech. Eng.* **17**, 456–467 (2010)
8. Korayem, M.H., Irani, M., Nekoo, S.R.: Load maximization of flexible joint mechanical manipulator using nonlinear optimal controller. *Acta Astronaut.* **69**, 458–469 (2011)
9. Korayem, M.H., Nekoo, S.R.: State-dependent differential Riccati equation to track control of time-varying systems with state and control nonlinearities. *ISA Trans.* **57**, 117–135 (2015)
10. Korayem, M.H., Nekoo, S.R.: Finite-time state-dependent Riccati equation for time-varying nonaffine systems: rigid and flexible joint manipulator control. *ISA Trans.* **54**, 125–144 (2015)
11. Lima, J.J., Tusset, A.M., Janzen, F.C., Piccirillo, V., Nascimento, C.B., Balthazar, J.M., Brasil, M.R.L.F.: Nonlinear state estimation and control applied to a manipulator robotic including drive motor. *Math. Eng. Sci. Aerosp.* **5**, 413–425 (2014)
12. Lima, J.J., Tusset, A.M., Janzen, F.C., Piccirillo, V., Nascimento, C.B., Balthazar, J.M., Brasil, M.R.L.F.: SDRE applied to position and vibration control of a robot manipulator with a flexible link. *J. Theor. Appl. Mech.* **54**, 1067–1078 (2016)
13. Lima, J.J., Rocha, R.T., Janzen, F.C., Tusset, A.M., Bassinello, D.G., Balthazar, J.M.: Position control of a manipulator robotic arm considering flexible joints driven by a DC motor and a controlled torque by a MR-brake. In: *SME 2016 International Mechanical Engineering Congress and Exposition*, vol. 4, Dynamics, Vibration, and Control, Phoenix, AZ, USA, pp. V04BT05A022 (2017)
14. Lima, J.J., Balthazar, J.M., Rocha, R.T., Janzen, F.C., Bernardini, D., Litak, G., Tusset, A.M., Bassinello, D.: On positioning and vibration control application to robotic manipulators with a nonideal load carrying. *Shock. Vib.* **2019**, 1–14 (2019)
15. Tusset, A.M., Piccirillo, V., Bueno, A.M., Balthazar, M.J., Sado, D., Felix, J.L.P., Brasil, M.R.L.F.: Chaos control and sensitivity analysis of a double pendulum arm excited by an RLC circuit based nonlinear shaker. *J. Vib. Control* **22**, 3621–3637 (2016)